THE UNIVERSITY OF TEXAS AT AUSTIN
CENTER FOR TRANSPORTATION RESEARCH

TECHNICAL REPORT 0-6916-1
TxDOT PROJECT NUMBER 0-6916

Seismic Vulnerability and Post-Event Actions for Texas Bridge Infrastructure

Farid Khosravikia
Anderson Potter
Vyacheslav Prakhov
Georgios Zalachoris
Tianjian Cheng
Ayushi Tiwari
Patricia Clayton
Brady Cox
Ellen Rathje
Eric Williamson
Jeffrey Paine
Cliff Frohlich

December 2017; Published November 2018

http://library.ctr.utexas.edu/ctr-publications/0-6916-1.pdf

Technical Report Documentation Page

1. Report No. FHWA/TX-18/0-6916-1	2. Government Accession No.	3. Recipient's Catalog No.
4. Title and Subtitle Seismic Vulnerability and Post-Event Actions for Texas Bridge Infrastructure		5. Report Date December 2017; Published November 2018 6. Performing Organization Code
7. Author(s) Farid Khosravikia, Anderson Potter, Vyacheslav Prakhov, Georgios Zalachoris, Tianjian Cheng, Ayushi Tiwari, Patricia Clayton, Brady Cox, Ellen Rathje, Eric Williamson, Jeffrey Paine, Cliff Frohlich		8. Performing Organization Report No. 0-6916-1
9. Performing Organization Name and Address Center for Transportation Research The University of Texas at Austin 3925 W. Braker Lane, 4th Floor Austin, TX 78759		10. Work Unit No. (TRAIS) 11. Contract or Grant No. 0-6916
12. Sponsoring Agency Name and Address Texas Department of Transportation Research and Technology Implementation Office P.O. Box 5080 Austin, TX 78763-5080		13. Type of Report and Period Covered Technical Report (07/01/2015–12/30/2017) 14. Sponsoring Agency Code
15. Supplementary Notes Project performed in cooperation with the Texas Department of Transportation and the Federal Highway Administration.		
16. Abstract The research investigates the seismic vulnerability of bridges in Texas by characterizing seismic hazards in the State, developing computational tools to estimate the likelihood of seismic damage to various bridge types, and providing TxDOT tools to inform post-earthquake response planning and decision-making.		
17. Key Words Seismic hazard, vulnerability, fragility, nonlinear bridge modelling	18. Distribution Statement No restrictions. This document is available to the public through the National Technical Information Service, Springfield, Virginia 22161; www.ntis.gov.	

19. Security Classif. (of report) Unclassified	20. Security Classif. (of this page) Unclassified	21. No. of pages 350	22. Price

Form DOT F 1700.7 (8-72) Reproduction of completed page authorized

THE UNIVERSITY OF TEXAS AT AUSTIN
CENTER FOR TRANSPORTATION RESEARCH

Seismic Vulnerability and Post-Event Actions for Texas Bridge Infrastructure

Farid Khosravikia
Anderson Potter
Vyacheslav Prakhov
Georgios Zalachoris
Tianjian Cheng
Ayushi Tiwari
Patricia Clayton
Brady Cox
Ellen Rathje
Eric Williamson
Jeffrey Paine
Cliff Frohlich

CTR Technical Report:	0-6916-1
Report Date:	December 2017; Published November 2018
Project:	0-6916
Project Title:	Seismic Vulnerability and Post-Event Actions
Sponsoring Agency:	Texas Department of Transportation
Performing Agency:	Center for Transportation Research at The University of Texas at Austin

Project performed in cooperation with the Texas Department of Transportation and the Federal Highway Administration.

Center for Transportation Research
The University of Texas at Austin
3925 W. Braker Lane, 4th floor
Austin, TX 78701

http://ctr.utexas.edu/

Disclaimers

Author's Disclaimer: The contents of this report reflect the views of the authors, who are responsible for the facts and the accuracy of the data presented herein. The contents do not necessarily reflect the official view or policies of the Federal Highway Administration or the Texas Department of Transportation (TxDOT). This report does not constitute a standard, specification, or regulation.

Patent Disclaimer: There was no invention or discovery conceived or first actually reduced to practice in the course of or under this contract, including any art, method, process, machine manufacture, design or composition of matter, or any new useful improvement thereof, or any variety of plant, which is or may be patentable under the patent laws of the United States of America or any foreign country.

Engineering Disclaimer

NOT INTENDED FOR CONSTRUCTION, BIDDING, OR PERMIT PURPOSES.

Research Supervisor: Dr. Patricia Clayton

Acknowledgments

The authors would like to extend appreciation to the Texas Department of Transportation for providing the funding for this project. In particular, the authors would like to thank Joe Adams, the TxDOT Project Manager, and members of the Project Monitoring Committee for their assistance and guidance with the research.

Table of Contents

List of Tables

List of Figures

Chapter 1. Introduction

1.1. Overview

Historically, seismic activity in the State of Texas has not been a source of concern due to the infrequency and low magnitudes of seismic events experienced in the state. Thus, standard bridge details and design practices developed and used by the Texas Department of Transportation (TxDOT) have not explicitly considered seismic hazards. In recent years, however, seismologists have detected a significant increase in the frequency of seismic events occurring across the state (e.g., an average rate of two seismic events per year prior to 2008 has increased to an average of almost twelve events per year in recent years), many of which are thought to be a result of human activity (Frohlich et al. 2016a).

The largest earthquakes that have been recorded to date in the State of Texas are the 1931 Valentine Earthquake (6.3 moment magnitude) and the 1995 Alpine Earthquake (5.7 moment magnitude), both thought to be from natural causes. The events in Texas that are believed to be human-induced have yet to reach such large magnitudes. For example, the largest human-induced event in Texas is believed to be the 2011 Fashing earthquake, registering a moment magnitude of 4.8; however, the 2011 earthquake in Prague, Oklahoma (moment magnitude 5.7) and the 2016 earthquake in Pawnee, Oklahoma (moment magnitude 5.8) indicate that potentially human-induced earthquakes can reach higher magnitudes.

When considering the lack of seismic detailing for bridges in Texas, the sharp increase in seismicity across the state and the potential for larger magnitude earthquakes (i.e., greater than magnitude 5) has raised significant concern about the seismic vulnerability of Texas bridges. Bridges are vital links in a highway transportation system, and their functionality following an earthquake event plays a major role in the response and recovery of the affected region. With almost 53,000 bridges in the state of Texas, it is important for TxDOT to evaluate the vulnerability of these critical structures and to develop an effective plan to assess the functionality of the state's transportation network following a seismic event.

To evaluate the potential seismic risks to bridges in the State of Texas, it is necessary to characterize the seismic hazards in the State and the seismic vulnerability, or fragility, of the Texas bridge population. Seismic hazard maps can be used to geographically show the distribution of level of shaking that is expected in an earthquake event. To develop seismic hazard maps for Texas, one must develop models to predict the intensity of ground shaking based on earthquake magnitude, distance from the epicenter, and local soil, or site, conditions. Additionally, maps characterizing the local soil conditions across the State must also be developed, which is particularly necessary in Texas where such data are limited. This report presents the research done to characterize and map seismic hazards and site classification (i.e., characterized by the V_{s30} parameter) across the State.

Additionally, to characterize the seismic vulnerability of the bridge infrastructure in Texas, fragility curves can be produced to predict the likelihood of bridge damage following a given level of earthquake shaking. Developing seismic fragility curves for Texas bridges requires an understanding of the inventory, structural detailing, and seismic behavior of typical bridges in the

State. Computational models of representative bridge archetypes subjected to Texas-specific ground motions can be used to evaluate seismic vulnerability. Ultimately, fragility curves produced in this research project can be used to develop a post-event action plan to identify bridge types and bridge components more likely to experience damage. Establishing a post-event response plan based on such a seismic vulnerability assessment can help ensure public safety and facilitate economic and timely bridge inspections following a seismic event.

1.2. Project Objectives and Report Outline

The main goal of the present project is to evaluate the seismic vulnerability of Texas bridges and to recommend a plan of action for post-earthquake response based on the seismic vulnerability of various bridge types. To do so, the following major tasks, each of which are discussed in separate chapters in this report, are included in this project:

- Assessing the seismicity of Texas and surrounding areas. (Chapter 2)
- Assessing the geologic conditions in Texas and estimate the Vs30 maps over the state of Texas. (Chapter 3)
- Developing a suite of ground motions representative of the seismic hazards and geologic conditions across the State of Texas. (Chapter 4)
- Introducing seismic hazards of Texas and developing hazard maps for deterministic earthquake event scenarios. (Chapter 5)
- Characterizing the Texas bridge inventory and creating continuous and simply-supported steel, prestressed, and reinforced concrete bridge samples with geometric and material properties representative of those found in the TxDOT inventory. (Chapter 6)
- Developing nonlinear bridge component models for those bridge samples based on past experimental, analytical, and numerical research done on bridge components, and assembling these component models into full bridge models for response-history analysis. (Chapter 7)
- Generating fragility curves for various bridge classes, which describe the probability of a bridge structure reaching a certain level of damage when subjected to different levels of ground motion intensity. (Chapter 8)
- Recommending a post-event action plan for TxDOT to identify and prioritize the most vulnerable bridges for inspection and repair efforts, given earthquake location and magnitude. (Chapter 9)

Chapter 2. Seismicity of Texas and Surrounding Regions

2.1. Overview

This chapter provides relevant background information pertaining to seismicity of Texas and surrounding regions. Much of this chapter, prepared by Dr. Cliff Frohlich as part of this research project, is published in an article entitled, "A historical review of induced earthquakes in Texas," authored by Frohlich, Heather DeShon, Brian Stump, Chris Hayward, Matt Hornbach, and Jake Walter, which was published in the *Seismological Research Letters* in August 2016 (Frohlich et al. 2016b). This chapter discusses what is known about induced (human-caused) and natural (tectonic) earthquakes in Texas. Because earthquake hazards vary across the state, a discussion of induced and natural seismicity is provided separately for four specific regions of Texas, including Gulf Coast, Northeast Texas, West Texas, and Texas Panhandle. Then, the seismicity of neighboring states that may affect Texas, including Oklahoma, Louisiana, and New Mexico, are discussed.

2.2. Historical Background

In Texas, earthquakes have occurred in close association with activities accompanying petroleum production since 1925. Frohlich et al. (2016a) developed a five-question test to categorize individual events as "tectonic," "possibly induced," "probably induced" or "almost certainly induced." In Texas, the probably induced and almost certainly induced earthquakes are broadly distributed geographically—in the Fort Worth Basin of north Texas, the Haynesville Shale play area of east Texas, along the Gulf Coast in south Texas, and the Permian Basin of west Texas. As the technologies applied to manage petroleum fields have evolved, induced earthquakes have been associated with different practices. In fields being driven by primary recovery prior to 1940, earthquakes occurred in fields extracting high volumes of petroleum from shallow strata. Subsequently, as field pressures decreased and secondary recovery technologies became common, earthquakes also occurred in association with waterflooding operations. Since 2008, the rate of earthquakes with magnitudes greater than 3 has increased from about two per year to twelve per year; much of this change is mostly attributable to earthquakes occurring within a few km of wastewater disposal wells injecting at high monthly rates. For three sequences monitored by temporary local seismograph networks, most hypocenters had focal depths at and deeper than the depth of injection and occurred along mapped faults situated within two km of injection sites. The record clearly demonstrates that induced earthquakes have been broadly distributed in several different geographic parts of Texas over the last 90 years.

There has been widespread recognition among seismologists since the 1960s that wastewater injection and other activities commonly associated with petroleum production can sometimes induce earthquakes (Healy et al. 1968; Nicholson and Wesson 1990; Suckale 2009). In recent years there has been a renaissance of interest in induced earthquakes, beginning after October-November

2008 when ten felt earthquakes occurred near an injection well on the Dallas-Fort Worth airport (Frohlich 2012). Figure 2.1 represent the rate of the earthquakes with magnitude greater that three in the state of the Texas. Earthquakes are as cataloged in Table A1 (available in the appendices to this report). Note that beginning about 2008, the rate increased from about two per year to about 12 per year, and this increase occurred in the Northeast, Gulf Coast, and West Texas regions, but not in the Panhandle. As seen in the figure, the events in north Texas were subsequently followed by noticeable increases in the occurrence rate of earthquakes elsewhere in the midwestern U.S. (Petersen et al. 2015), especially in Oklahoma (Keranen et al. 2014; Walsh and Zoback 2015), Arkansas (Horton 2012) and other regions in Texas. There have been 162 Texas earthquakes having M≥3 occurring since 1975 and reported by the National Earthquake Information Center (NEIC) and the International Seismological Centre (ISC); of these, 94 have occurred since 2008. For more information upon these earthquakes one can visit Table A-1 and Table A-2.

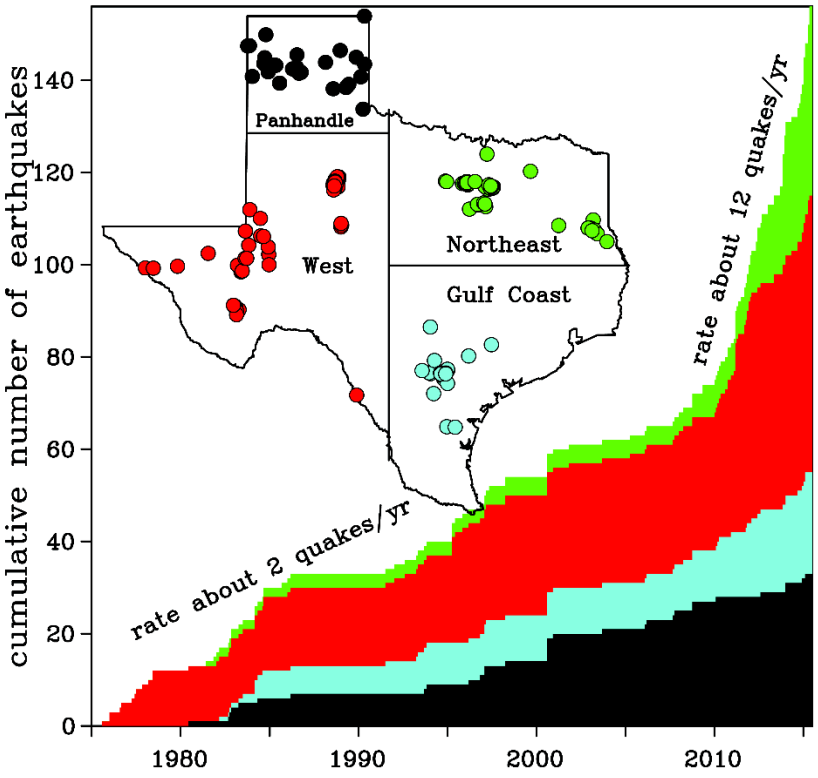

Figure 2.1: Earthquakes in Texas with magnitude M ⩾3 since 1975

Few geographic regions have had a petroleum industry for as long as, or as vigorous as, Texas. Thus, a review of Texas earthquakes associated with petroleum production activities is useful for comparison with induced earthquakes elsewhere and provides insight about how this phenomenon changes over time scales of decades or greater. One objective of this review is to assemble the available evidence concerning induced Texas earthquakes, including difficult-to-find publications describing older events.

Another objective is to evaluate and categorize individual Texas earthquake using a standardized set of criteria. Towards this end we apply a five-question test to evaluate the strength of evidence suggesting an earthquake is induced (Frohlich et al. 2016a). This five-question test (Table 2.1) is based on similar tests proposed some twenty years ago (Davis and Frohlich 1993; Davis et al. 1995). However, the questions have been simplified to apply to both injection- and extraction-induced earthquakes and some questions relating to subsurface pressures and geomechanical modeling have been removed because this information is available for only a small fraction of reported earthquakes. From scoring the answers to these questions, we categorize individual earthquakes as "almost certainly induced," "probably induced," "possibly induced" or "tectonic."

Table 2.1: Five questions to assess how strongly the evidence suggests an earthquake is induced

QT. *Timing:* In this location, are earthquakes of this character known to begin only after the commencement of nearby petroleum production or fluid injection operations that could induce seismic activity?	For each earthquake and each question QT, QS, QD, QF and QP, answer "Yes," "Possibly," or "No" and then score: +1.0 if answer is "Yes; +0.5 if answer is "Possibly"; +0.0 if answer is "No." Then, to assess how likely it is the earthquake is induced, sum the scores and: If sum = 0.0-1.0: T tectonic. If sum = 1.5–2.0: PsI possibly induced. If sum = 2.5–3.5: PrI probably induced. If sum = 4.0-5.0: ACI almost certainly induced.
QS. *Spatial correlation:* Are the epicenters spatially correlated with such production or injection operations; i.e., within 5 km for well-determined epicenters, or within 15 km otherwise?	
QD. *Depth:* Is information available concerning focal depths of earthquakes at this location, and does this suggest some depths are shallow, probably occurring at or near production or injection depths	
QF. *Faulting:* Near production or injection operations, are there mapped faults, or linear groups of epicenters that appear to lie along a fault? Here "near" is within 5 km if the earthquake or earthquake sequence of interest has well-determined epicenters, or within 15 km otherwise.	
QP. *Published analysis:* Is there a credible published paper or papers linking the seismicity to production or injection operations?	

Texas earthquakes associated with petroleum operations and here categorized as induced have occurred since 1925, but the amount and quality of data available to evaluate a possible causal relationship has changed considerably over time. Figure 2.2 represents seismograph stations in Texas over time. Prior to about 1970 Texas had few seismograph stations, and much of the available information came from felt-report studies. As late as 2005, there were only six continuously-operating seismic stations in Texas providing publicly available data (Figure 2.2), and thus epicenters reported by the NEIC typically had uncertainties of 5–10 km or more (Frohlich 2012; Petersen et al. 2015). At present, there are 17 permanent seismograph stations providing continuous real-time waveform data, and in 2015 the Texas legislature, in response to concern

about induced earthquakes, funded a program to install 22 additional stations and establish a statewide monitoring network (Texas House Bill 2 2015). This legislative action and the anticipated expansion of seismic monitoring in Texas provide additional motivation to categorize previously recorded earthquake activity, as we are presently transitioning to an era where Texas seismicity will be more effectively monitored. In addition to these broadband stations, Oklahoma, Arkansas, and New Mexico presently operate statewide seismograph networks to monitor regional seismic activity.

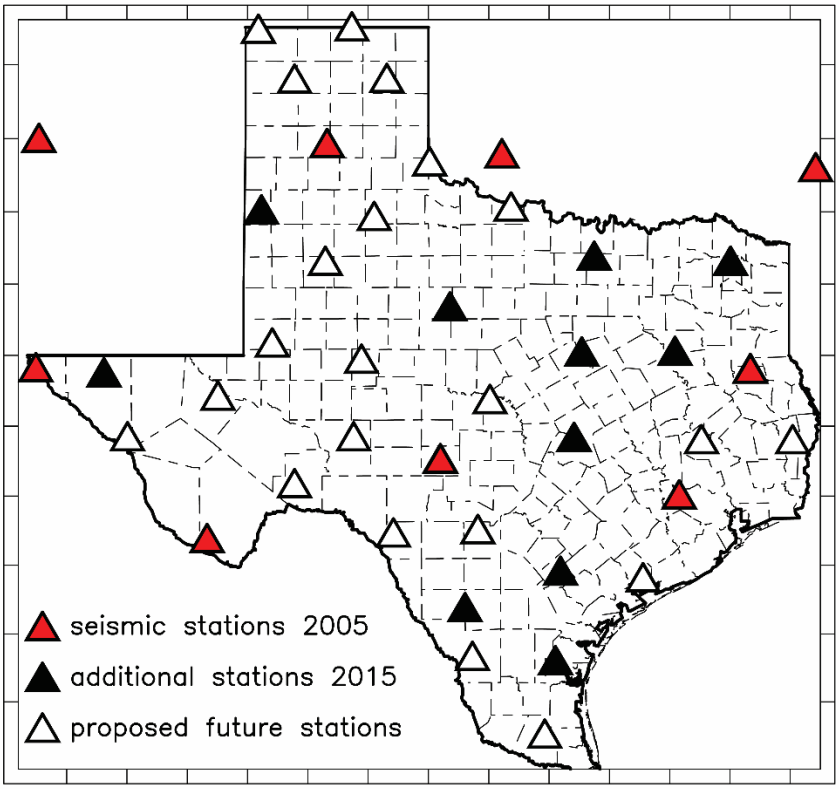

Figure 2.2: Texas seismograph stations

Figure 2.3 presents Texas oil and gas wells. The map shows historically significant petroleum fields, and active oil and gas wells as compiled in 2013 by the Texas Bureau of Economic Geology from data supplied by the Texas Railroad Commission. As seen in the figure, petroleum production has been broadly distributed across Texas for almost a century (Hinton and Olien 2002; Olien 2010). The first oil field in Texas with a substantial economic impact was in 1894 near Corsicana, situated about midway between Dallas and Mexia in northeast Texas. The famed Spindletop strike was in 1901 close to Beaumont along the Gulf Coast near the Louisiana border. The Goose Creek Field, south of Houston on the Gulf Coast, opened in 1908 and reached maximum production in 1918. During the 1920s, oil production continued along the Gulf Coast and in northeast Texas. The Mexia and Wortham Fields were discovered in 1920 and 1924. Fields also began producing at numerous locations in the Panhandle and the Permian Basin. The Panhandle Field began producing commercially in 1921; several fields in west Texas opened between 1921 and 1929. In the 1930s and subsequently development of new fields across Texas continued, and earthquakes

have been associated with several of these fields: 1930 marked the discovery of the East Texas Field, then one of the largest in the world, and probably responsible for the 1957 Gladewater earthquake; the Stratton Field, apparently responsible for the 1997 and 2010 Alice earthquakes, opened in 1938; the Kelly-Snyder and Cogdell Fields opened in 1948 and 1949; the Imogene and Fashing Fields opened in 1944 and 1958.

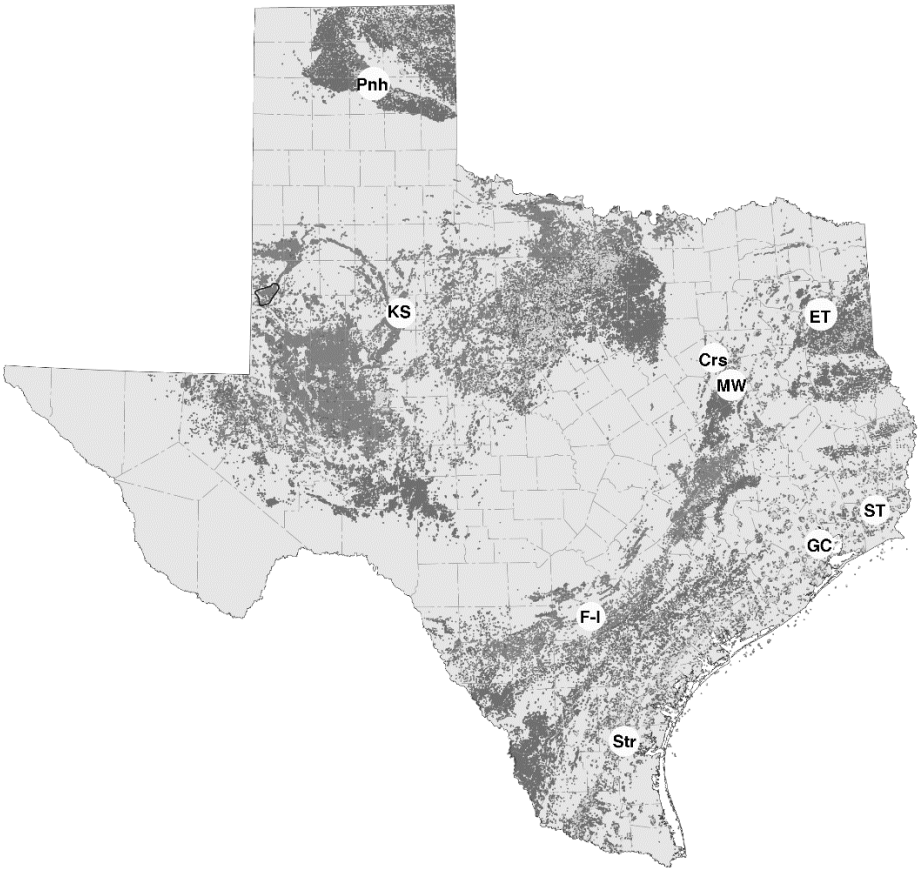

Crs: Corsicana	ET: East Texas	F-I: Fashing-Imogene
GC: Goose Creek	KS: Kelly-Snyder	MW: Mexia-Wortham
Pnh: Panhandle	ST: Spindletop	Str: Stratton

Figure 2.3: Texas oil and gas wells

The production of oil and gas is often accompanied by the extraction of significant amounts of connate water—water trapped in sedimentary pore spaces. Since the 1930's much of this produced water has been re-injected into the producing reservoir to improve hydrocarbon recovery. Two such methods are re-injection to maintain reservoir pressure, and waterflooding operations that move oil laterally from water-injection wells to producing wells. Finally, the process of injecting chemicals and/or gases such as CO_2 to bring about "tertiary recovery" or "enhanced oil recovery" is widespread nowadays, and has been in use for decades. These technologies are contrasted with the "primary recovery" phase of production, when natural subsurface pressures are sufficient to produce petroleum without waterflooding or other treatments.

In other fields, no commercial benefit is achieved from injecting into the producing reservoir, and because produced water is often highly saline, alternate means of water disposal must be employed. Most often, this is accomplished by injection into specially designed and permitted water disposal wells. These disposal wells are numerous and many have been in operation for decades; there are currently tens of thousands of active disposal wells in Texas (Figure 2.4).

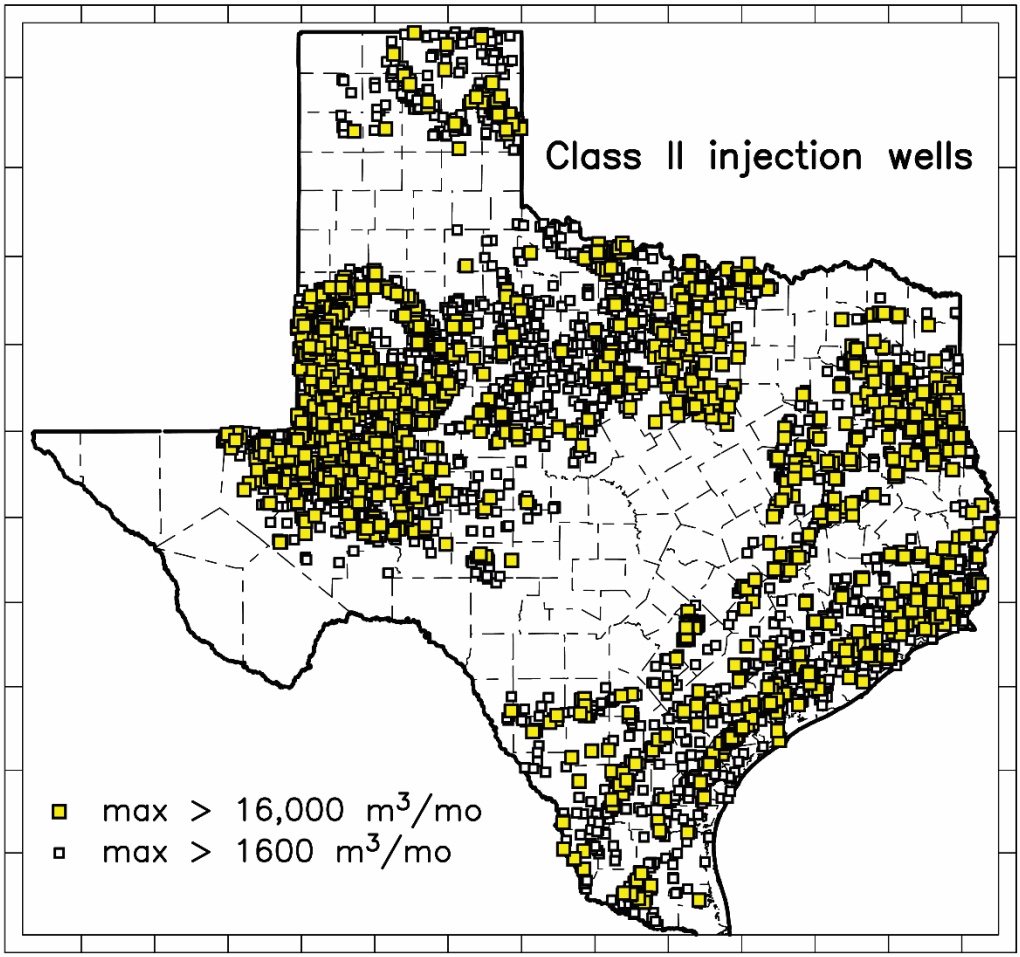

Figure 2.4: Location and maximum monthly injection volumes for active injection wells in Texas

Much of the present concern about induced seismicity focuses on the development of so-called "unconventional" sources of petroleum—gas or oil that is bound up in strata having permeabilities too low to allow fluid to flow easily. The combination of the technologies of horizontal drilling and hydrofracturing made it possible to selectively increase subsurface permeability and thus exploit unconventional sources. Both technologies had been developed more than 60 years ago, but only began to be exploited on a massive scale in Texas since about 2003 in the Barnett Shale of northeast Texas, since about 2008 in the Haynesville Shale of east Texas, since about 2009 in the Eagle Ford of south Texas, and since about 2011 in the Permian Basin of west Texas. Hydrofracturing in a horizontally-drilled well typically requires water volumes two to three times greater than in a vertical well (Nicot and Scanlon 2012). And when hydrofractured wells enter the

production phase much of the injected water returns to the surface as wastewater that requires disposal. For the most part, induced seismicity associated with unconventional petroleum development is associated with wastewater disposal, not the hydrofracturing process itself.

2.3. Induced Earthquake Activity in Four Regions of Texas

By applying the five-question test and scoring system to our compilation of Texas earthquakes with reported magnitudes of 3 and greater (Table A-1 and Table A-2, available in the appendices to this report), Figure 2.5 shows the strength of evidence supporting an induced cause for Texas earthquakes 1847–2015. As seen in the figure, it is found that induced earthquakes occurred between 1925 and the present. Some earthquakes are associated with fluid injection, while others are associated with production and/or fluid extraction. Most of these earthquakes are small (magnitude $M \leq 4$); however, at least four have had magnitudes of 4.6 and higher. Altogether, for the 162 Texas earthquakes having $M \geq 3$ and occurring between 1975 and 2015, 42 (26%) are characterized as almost certainly induced, 53 (33%) as probably induced, 45 (28%) as possibly induced, and the remaining 21 (13%) as tectonic. In the remainder of this section, the most significant induced earthquakes and earthquake sequences in four different geographic regions of Texas are described.

2.3.1. Texas Gulf Coast

Goose Creek – 1925: probably induced. Small earthquakes accompanied ground subsidence of up to a meter associated with the production of more than 16×10^6 m^3 of oil, beginning in 1916, from the Goose Creek Field along San Jacinto Bay east of Houston, now called Baytown (Figure 2.6 and Figure 2.7). Gray-shaded areas in Figure 2.6 indicate extent of the Permian Basin, the Barnett Shale, the Haynesville Shale producing area, and the Eagle Ford Shale producing area. None of the available sources list specific dates for the occurrence of these earthquakes, but contemporary descriptions noted that they "shook the houses, displaced dishes, spilled water, and disturbed the inhabitants generally" (Pratt and Johnson, 1926). Commercially important production in the Goose Creek field came from sand lenses at depths of 1000 to 4000 ft (300 to 1200 m). In Pratt and Johnson (1926) and Yerkes and Castle (1976) there are maps of the subsided region, pictures of surface faults or "fractures," and discussion of the mechanics.

Because the subsidence submerged much of the land surface overlying the field to below sea level, the State of Texas, hoping to collect the revenues from oil produced, sued Humble Oil for the rights to the field, which no longer being on land, was not subject to private ownership (Pratt and Johnson 1926). The State lost the suit as the court ruled that the subsidence was an "act of man" caused by the extraction of oil and was not a natural event. Thus, one notable feature of the Goose Creek earthquakes is that there is a court ruling and a 90-year-old precedent supporting the assertion that oil and gas activities induce land subsidence, and accompanying earthquakes in Texas.

Fashing – 1973–2012: almost certainly induced. Since Christmas Eve (local time) in 1973, several felt earthquakes have occurred near Fashing in Atascosa County, TX. Events include an

M3.6 on 23 July 1983 (Pennington et al., 1986), an M4.3 on 9 April 1993 (Davis et al. 1995), and an M_W4.8 20 October 2011 (Frohlich and Brunt 2013). The highest felt intensities were reported as modified Mercalli intensity (MMI) VI, occurred in and near the Fashing gas field in both 1993 and 2011, and fell off to MMI III or less at distances beyond 30 km (Figure 2.6 and Figure 2.8). Focal mechanism for this event is as reported by St. Louis University (Herrmann et al., 2011). The highest-intensity region of this earthquake was situated more than 15 km from the nearest active injections wells, and thus is unlikely to be induced by injection. However, Frohlich and Brunt (Frohlich and Brunt, 2013) showed that earthquakes here in 1973, 1983 and this event followed increases in the rate of extraction of water and petroleum from wells situated within the MMI V-VI region shown here (redrawn from Frohlich and Brunt, 2013). A focal mechanism for the 2011 earthquake (Frohlich and Brunt 2013; Herrmann et al. 2011) indicated normal faulting along a NE-SW trending fault (see Figure 2.8).

Pennington et al. (1986) summarized the history of gas production at the Fashing Field. The Fashing Field is in the Edwards Limestone along the upthrown side of a normal fault. Production began in 1958 from horizons at 3.4 km depth; initial bottomhole pressure was 35.2 MPa in 1958 but by 1983 pressures along the fault had dropped to 7.1 MPa, or about 20 per cent of the initial values. Their investigation concluded the Fashing earthquakes up to that time were related to fluid withdrawal (i.e., gas production operations).

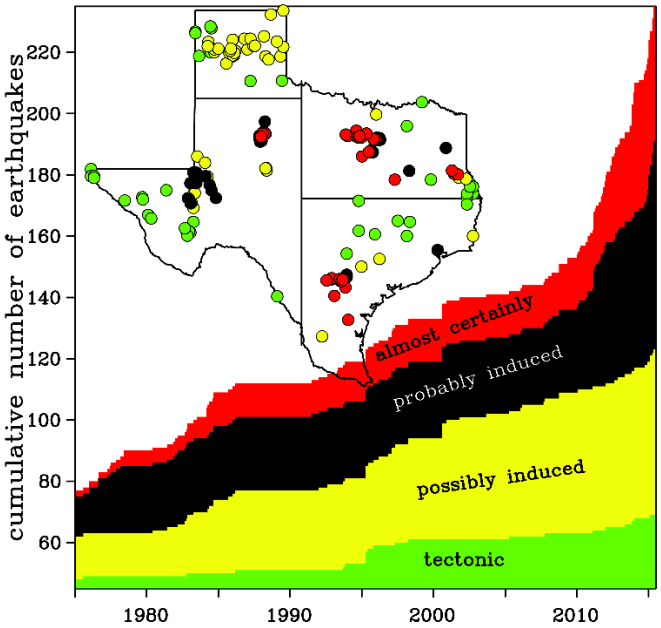

Figure 2.5: Strength of evidence supporting an induced cause for Texas earthquakes 1847–2015

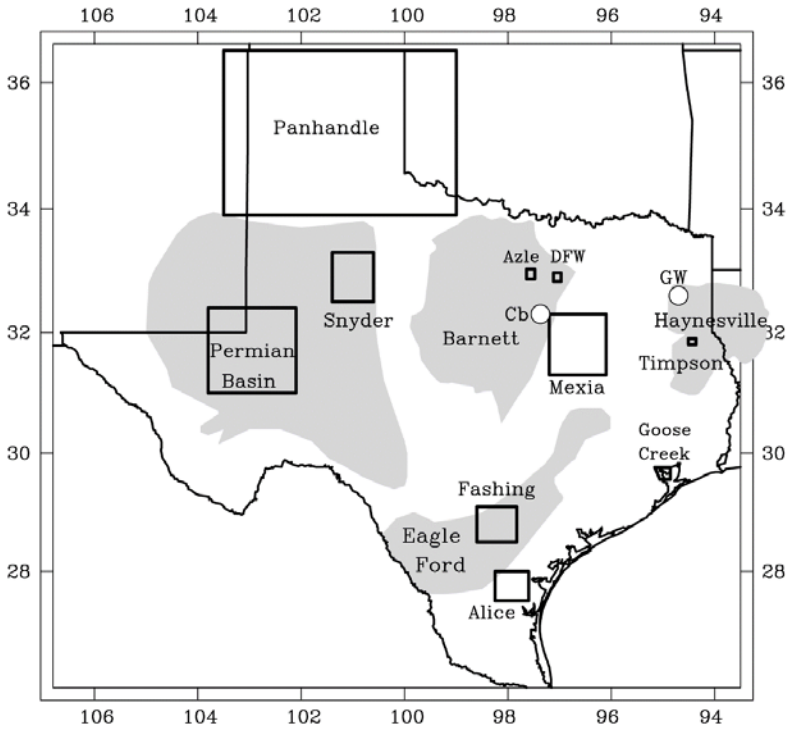

Cb: locations of 2009–2011 earthquakes near Cleburne

GW: locations of 1957 earthquakes near Gladewater

Figure 2.6: Map locations of earthquake sequences discussed in this report

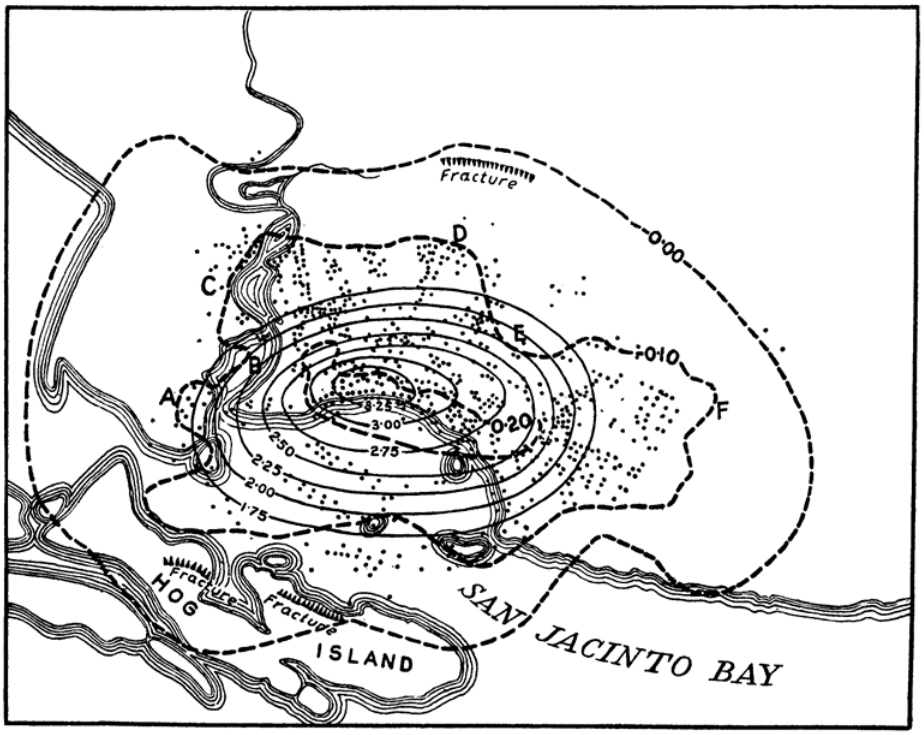

Note: Here, subsidence contours are in feet, and dots are locations of oil wells.

Figure 2.7: Map of subsidence in the Goose Creek Oil Field, Texas (Pratt and Johnson 1926)

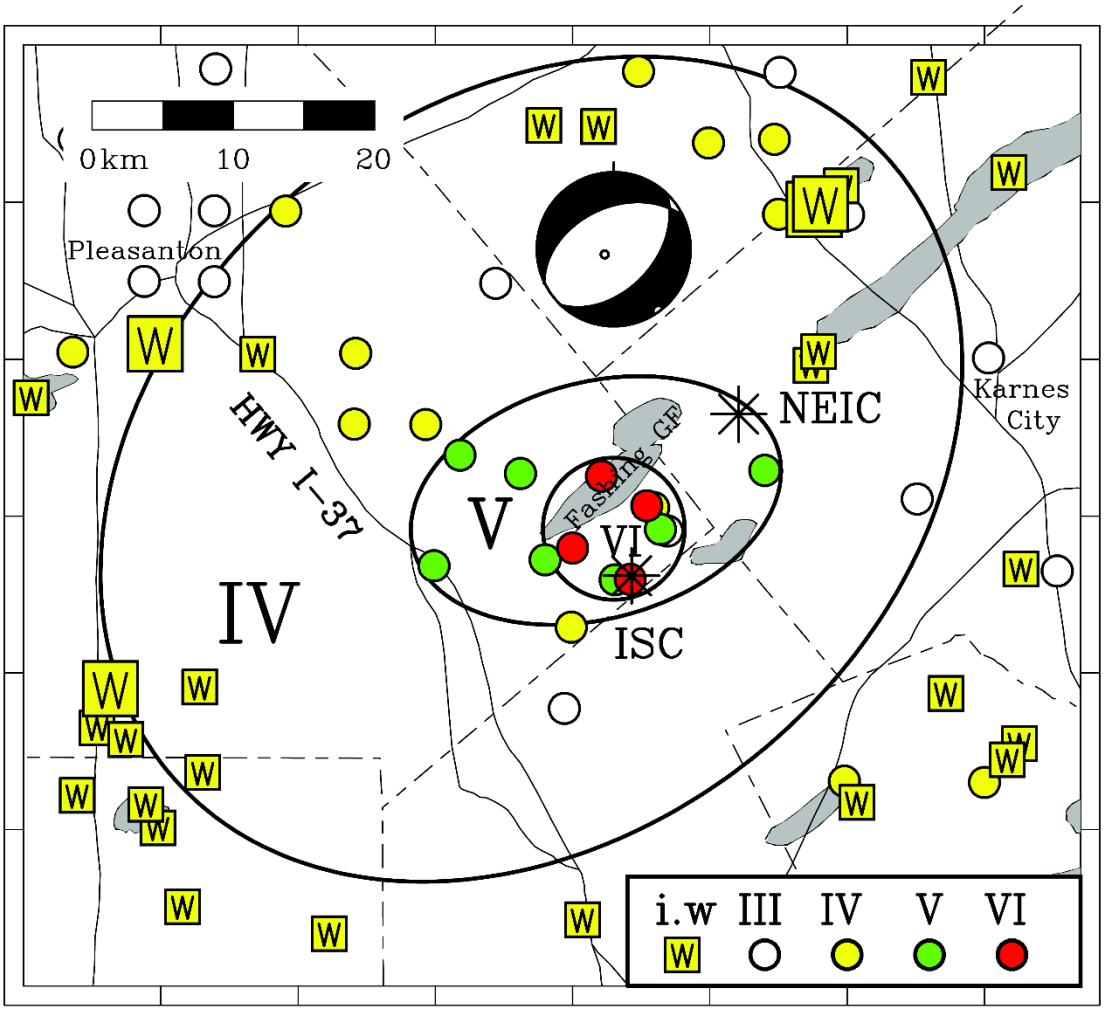

Circles:	indicate locations and MMI values of felt reports
Squares:	injection disposal wells
Grey:	gas fields
NEIC:	the epicenter as reported by the National Earthquake Information Center
ISC:	the epicenter as reported by the International Seismological Centre

Figure 2.8: Felt reports and injection disposal wells near the 20 October 2011 MW4.8 Fashing earthquake

Investigations of the subsequent earthquakes in 1993 and 2011 reached similar conclusions (Davis et al. 1995; Frohlich and Brunt 2013). Frohlich and Brunt (2013) noted that the 1973, 1993, and 2011 earthquakes all coincided with marked increases in extraction volumes of oil and water from wells in the region experiencing MMI V and greater during the 2011 earthquake. In the five years prior to the 2011 earthquake the nearest active injection disposal wells were 15 km and more distant from the epicentral region. The studies conclude that all the Fashing earthquakes are induced but caused by extraction, not injection.

Alice – 1997 and 2010: almost certainly induced. Two nearly identical m_{bLg}3.9 earthquakes occurred on 24 March 1997 (Bilich et al., 1998) and 25 April 2010 (Frohlich et al., 2012) near Alice, TX, about 75 km west of Corpus Christi (Figure 2.6 and Figure 2.9). Labels of MMI levels III and V-VI, in Figure 2.9, indicate locations where individuals provided felt information. Three individuals within the MMI V-VI isoseismal region reported experiencing MMI V or MMI VI. Location labeled "crack" indicates the reported location of 1.6 km-long northeast-southwest crack following the 1997 earthquake. Symbols +, X, and *, respectively, indicate the NEIC epicenters for the 1997 and 2010 earthquakes, and the location for both events determined by Frohlich et al. (2012). Dark and light grey areas are oil and gas fields; mapped faults are from Ewing (1990). Figure reproduced from Frohlich et al. (2012). Their intensities reached MMI V-VI in a region about 10–20 km SE of Alice and approximately along the mapped trace of the Vicksburg Fault and the boundary of the Stratton oil and gas field, which has produced $76x10^9$ m^3 of gas and about $16x10^6$ m^3 of oil since production commenced in 1938. Analysis of secondary arrivals and surface waves suggested the earthquakes had focal depths of 3 km or less, the approximate depth of the producing Frio formation in the Stratton Field. Following the 1997 earthquake, one resident reported that a 1.6 km-long SW-NE-trending crack had appeared in fields within the highest-intensity region.

Evidence that supports an induced cause includes the absence of any previously reported regional earthquakes, the shallow focal depths, and the epicenters near the boundary of a field that has produced high volumes of oil and gas for many decades.

Elsewhere along the Gulf Coast. Small felt earthquakes occurring in 1984 and subsequently have occurred in Atascosa County about 35 km northwest of Fashing near Pleasanton and Jourdanton, coincident with the Imogene Oil Field. As in the Fashing Field, production in the Imogene Field is also from an upthrown normal fault, at 2.4 km depth, and began in 1944. Following the 1984 earthquake, a small local seismograph network recorded aftershocks that were "found to be at or near the fault contact of the producing horizon of the Imogene Field" (Pennington et al. 1986). This suggests these earthquakes are almost certainly induced, although caused by extraction, not injection.

Felt earthquakes have also been reported in Falls City, TX, about 20 km northeast of Fashing in Karnes County (Davis et al. 1995; Olson and Frohlich 1992). These include a magnitude m_{bLg}3.6 on 20 July 1991 and an m_{bLg}4.3 on 7 April 2008. Although Olson and Frohlich (1992) suggested that the 1991 event might be caused by fluid withdrawal, Frohlich and Brunt (2013) noted that the 1991 quake followed an increase in injection beginning in 1990 at nearby disposal wells. Increases in both injection and production occurred prior to the 2008 earthquake. A focal mechanism for the 2008 earthquake (Herrmann et al. 2011) indicated normal faulting along a NE-SW trending strike. As suggested by all the investigations mentioned here, these earthquakes are probably induced.

2.3.2. Northeast Texas

Mexia-Wortham – 9 April 1932: almost certainly induced. This earthquake, with an estimated magnitude of M4.0, shook down bricks from several chimneys in Wortham but was only barely

perceptible to people at several towns about 20 miles away (Figure 2.6 and Figure 2.10). As seen in Figure 2.10, the relatively high intensities (MMI VI) coinciding with the Wortham Field, and the much lower intensities (III and less) at distances exceeding about 20 km suggest a shallow focal depth. Figure redrawn from Frohlich and Davis (2002).This indicates the focal depth must have been quite shallow. Sellards (1933) reported that the earthquake caused a crack that extended across the highway between the towns of Wortham and Mexia. The regions of highest intensities included the Wortham and Mexia Fields, which had produced more than $15x10^6$ m^3 of oil at that time.

Sellards (1933) noted that "the fact that the tremor was centered in a region of large oil production lends force to the idea that the tremor may have been caused by adjustment in the land surface incident to operations in the oil fields," and subsequent publications have also reached this conclusion (Yerkes and Castle 1976).

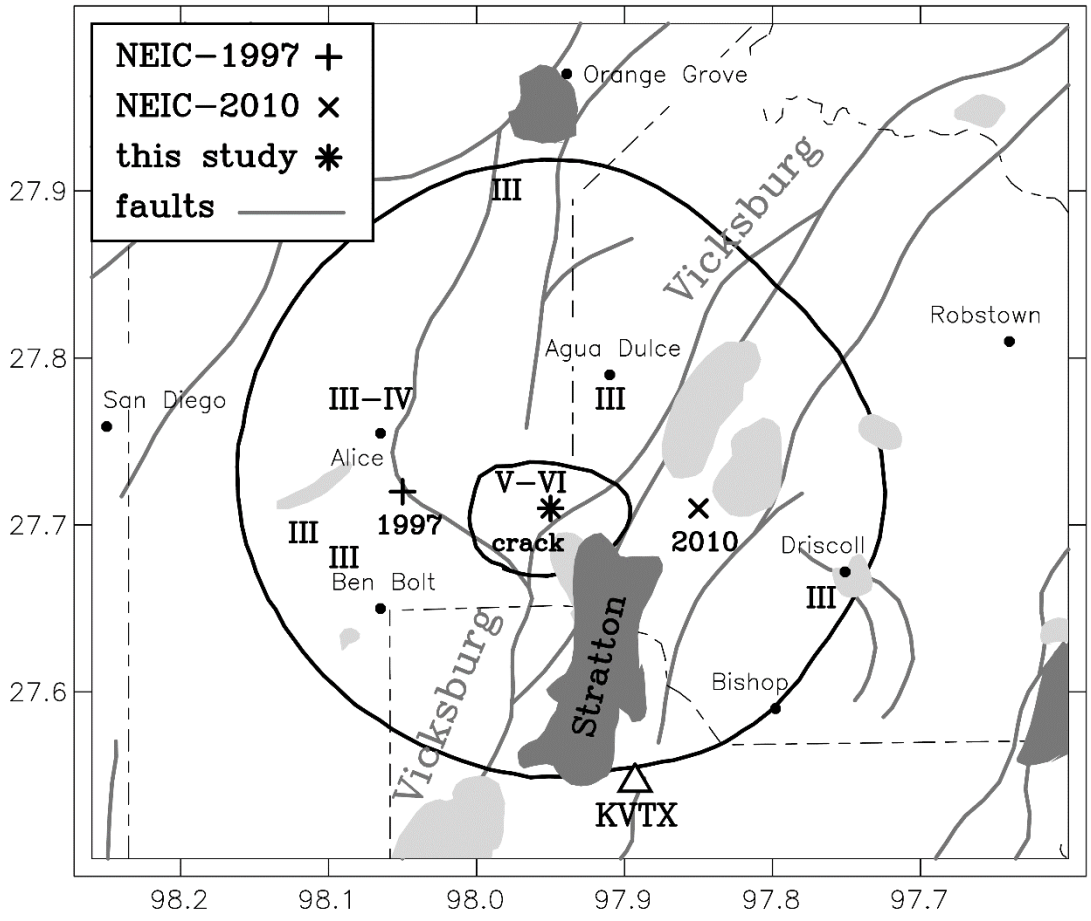

Figure 2.9: Felt report summary for the 25 April 2010 m3.9 Alice earthquake

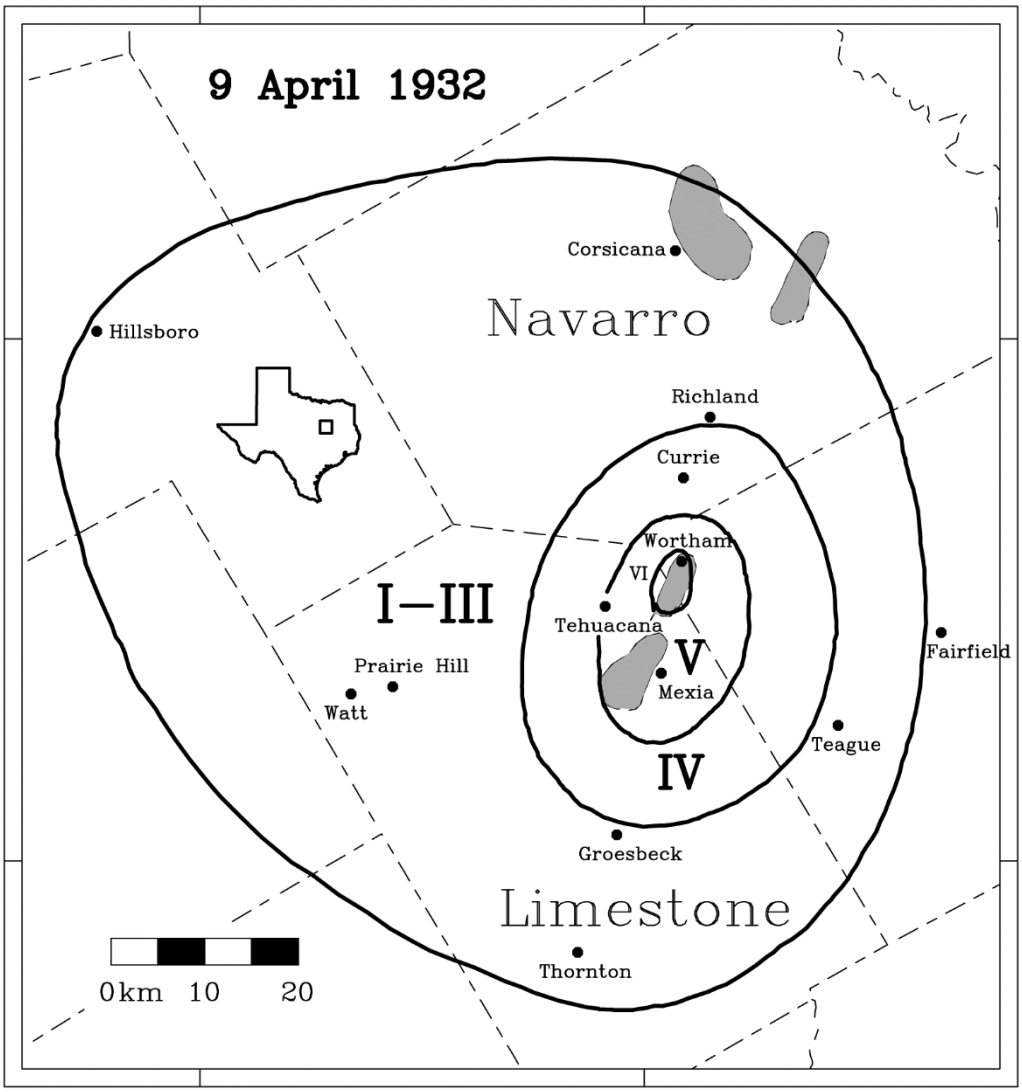

Roman numerals:	Modified Mercalli Intensities
dashed lines:	county boundaries
Shaded regions	major oil fields established prior to 1932

Figure 2.10: Felt report summary for the 9 April 1932 M4.0 Wortham-Mexia earthquake

Gladewater – 19 March 1957: probably induced. A series of four earthquakes, the largest having magnitude M4.7, were felt most strongly between Gladewater and Longview and occurred directly above the northern part of the East Texas Field in the area of the highest density of wells. Frohlich and Davis (2002) presented arguments both for and against an induced cause, noting that "The East Texas Field was, at the time of discovery in 1930, the largest field in the Western Hemisphere. By [1957] more than 600×10^6 m^3 of oil had been extracted from the field. The relatively high magnitude and large felt area (45,000 km^2) are difficult to explain if it was induced by fluid withdrawal. Moreover, it seems unlikely that a quake with magnitude as great as 4.7 would occur at the relatively shallow production depth of 1 km." The available information doesn't provide accurate information about the epicenter or focal depth of this earthquake.

Unfortunately, there is no detailed published case history describing the 1957 Gladewater sequence and evaluating its relationship to regional petroleum operations; Frohlich and Davis's (2002) two-page summary is the most comprehensive source available. Nevertheless, because historical earthquakes are unknown at this location, because of the huge volume of fluid removed from the East Texas Field, because fluid removal over decades-and-longer intervals appears to have induced many of the earthquakes elsewhere in Texas described above, and because published sources have suggested the Gladewater earthquakes may have been induced (Yerkes and Castle 1976), we now categorize this sequence as probably induced.

Dallas-Fort Worth International Airport – 2008–2013: almost certainly induced. Beginning on 30 October 2008 people living near the Dallas-Fort Worth International Airport reported experiencing felt earthquakes (Figure 2.6 and Figure 2.11). In Figure 2.11, triangles are 11 earthquakes occurring in 2008 and 2009 and located using data collected by a six-station temporary network; squares are injection disposal wells; circles and white pentagons are bottom-hole and surface locations, respectively, of producing horizontal natural gas wells. Earthquake focal depths were approximately 4.5 km; their epicenters were within 0.5 km of a well that began injecting about 16,000 m3/mo at 4.2 km depth, beginning about seven weeks before the first earthquake was reported. Figure 2.11 is reproduced from Frohlich et al. (2011). These were the first earthquakes known in the Dallas-Fort Worth metropolitan area (DFW) in historical times (i.e., since about 1860). Scientists at Southern Methodist University (SMU) deployed a six-station seismograph network that recorded numerous aftershocks between November 2008 and January 2009. Analysis of these data (Frohlich et al., 2011; Reiter et al., 2012) indicated that all well-recorded events occurred at focal depths of about 4.5 km along an approximately 1-km-long NE-SW linear trend coinciding with a previously mapped fault. The epicenters were within about a km of a wastewater disposal well on the DFW airport property. This well had begun injection operations only seven weeks before the first earthquakes occurred, injecting into the Ellenburger formation at rates of about 48,000 m^3/mo between 12 Sept. 2008 and August 2009. Activity at the airport continued well after injection ceased in 2009; the largest earthquake with magnitude m_{bLg}3.4 occurred on 30 September 2012.

About eight months after injection ceased, a second sequence of earthquakes began to the NE along the extension of the NE-SW trending linear cluster about 2 km from the injection well. Because this sequence began after injection ceased, Janska and Eisner (2012) suggest the entire DFW airport sequence may be tectonic in origin and unrelated to injection. However, the fact that earthquakes sometimes occur after injection ceases is well known (Healy et al. 1968; Nicholson and Wesson 1990; Petersen et al. 2016b; Suckale 2009) Ellsworth, 2013). Thus, we and others (Frohlich et al., 2011; National Research Council, 2012) conclude that the DFW airport earthquakes were induced because of the absence of historical seismicity prior to injection, the proximity of the injection well to a known mapped fault, the onset of activity only six weeks after injection commenced in 2008, the frequency and magnitude of these events compared to other active, naturally occurring EQ zones, and the earthquake depths at and below the depth of injection.

Cleburne – 2009–2012: almost certainly induced. Beginning in June 2009 residents of Cleburne, situated about 60 km south of Fort Worth, reported experiencing felt earthquakes that continued until at least June 2012. The largest reported magnitude was m_{bLg}3.5 for an earthquake on 24 June 2012. Scientists at Southern Methodist University installed a five-station temporary network to record this activity (Justinic et al. 2013) and were able to locate accurately 38 earthquakes occurring along a 2–3 km-long NS trending linear feature, with best-determined focal depths of 3.5–4.2 km. The centroid of these locations was 1.3 km from a saltwater disposal well that began injecting in 2007 at depths of 2.4–3.1 km, and 3.2 km distant from a well that injected at depths of 3.2–3.3 km from September 2005 through July 2009. We know of no mapped faults in the public archive for this location, but faulting throughout the oil and gas production layers in the Fort Worth basin in neighboring counties is not uncommon (Railroad Commission of Texas, 2015). Focal mechanisms determined for two events indicate normal faulting along a NS-trending direction that corresponds to the linear trend of located events.

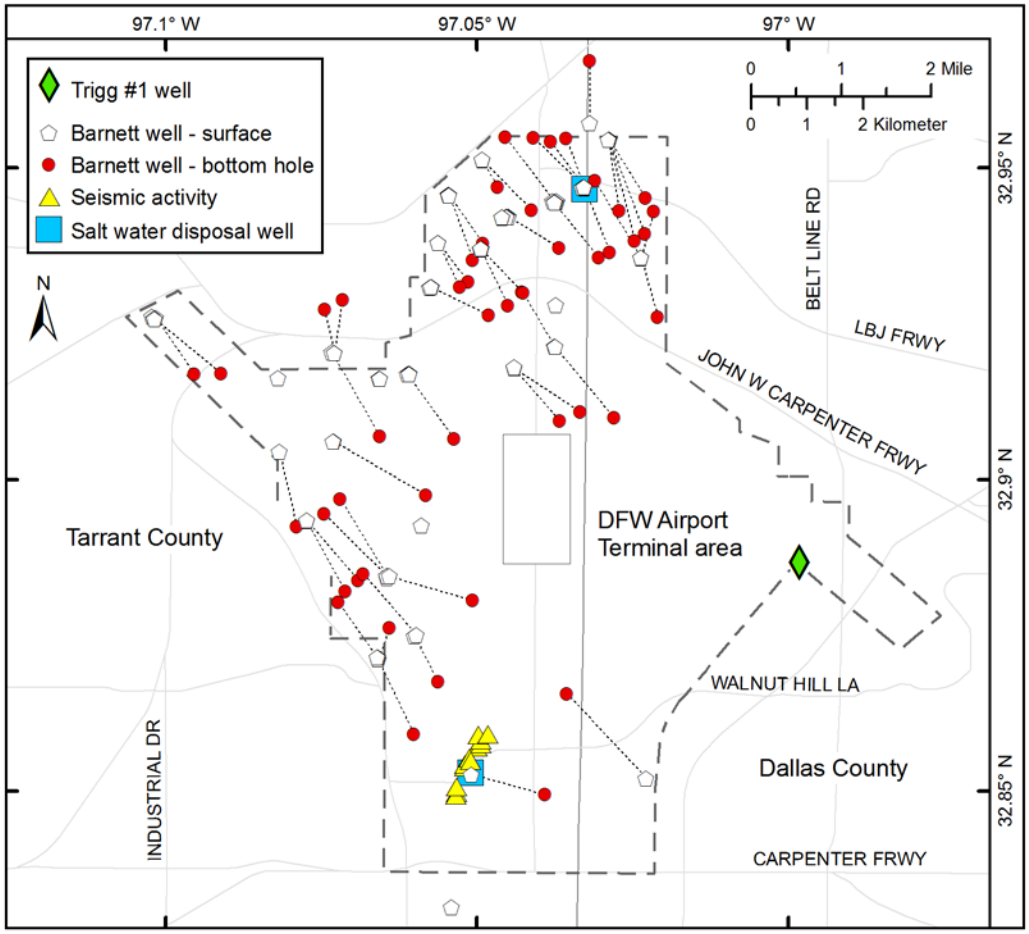

Figure 2.11: Earthquakes, injection wells, and production wells at the Dallas-Fort Worth International Airport

Because of the absence of historical seismicity prior to injection, the proximity of the injection wells, and the depths of some earthquakes depths near the depth of injection, we conclude this sequence is almost certainly induced.

Timpson – 2012–2014: almost certainly induced. On 10 May 2012 an earthquake with M_W3.9 occurred in east Texas a few km southeast of Timpson (Figure 2.6 and Figure 2.12); on 17 May 2012 there was a larger M_W 4.8 event that produced intensities up to MMI VII. Waveform modeling for the 17 May mainshock was consistent with a focal depth of 4.5 km (Frohlich et al. 2014). Focal mechanisms reported for this event indicated strike-slip faulting (Figure 2.12). Note that best-located events form a planar group extending from about 2–5 km depth (see cross section A-A' in Figure 2.12) coinciding with a mapped fault (dark line near B-B' on map in Figure 2.12), and situated within 1–3 km of wells 'south' and 'north' injecting at ~1.8 km depth. Prior to the 2012 mainshock, injection rates at north well were ~16,000 m3/mo; at south well they were ~24,000–48,000 m3/mo. Figures redrawn from Frohlich et al. (2014).

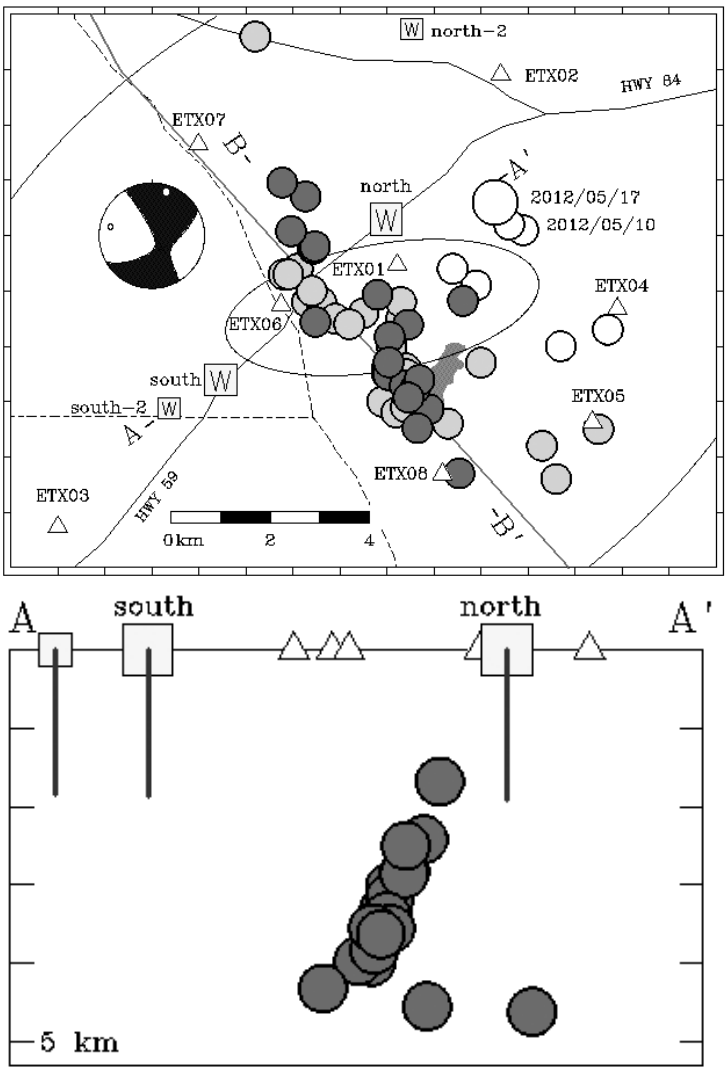

Circles:	earthquakes	White circles:	epicenters for earthquakes occurring prior to installation of temporary network, including the MW4.8 17 May 2012 event.
Triangles:	temporary seismic stations	Grey circles:	epicenters determined when network was partially installed; darkest circles are
Squares:	injection disposal wells	darkest circles:	best-located hypocenters occurring after installation of all eight stations.

Figure 2.12: Earthquakes and injection wells in the 2012–13 Timpson sequence

By February 2013 eight temporary seismograph stations had been installed (Frohlich et al., 2014). These stations recorded numerous aftershocks with epicenters situated along a NW-SE trending, SW dipping mapped fault that had been reported by Jackson (1982). Focal depths for the best-determined aftershocks were between 1.5 and 4.5 km. The aftershock sequence was situated about 2–3 km from two wastewater injection wells that had been injecting 16,000 m^3/mo or more since 2006–2007 at depths of about 1.9 km. A search of records at station NATX in Nacogdoches, about 35 km distant, revealed that several small earthquakes apparently from the same focus had

occurred in 2008, 2010 and 2011 (Frohlich et al. 2014) and subsequent reanalysis of Transportable Array data revealed additional earthquakes that occurred between 2010 and 2012 (Walter et al. 2016). Fan et al. (2014) simulated the spatial and temporal evolution of the pore pressure and stress fields in this region using a coupled finite-element geomechanical model and concluded that it was plausible that injection induced this earthquake sequence.

Even in the absence of the modeling, the sequence occurrence along a mapped fault, the focal depths of the events, and the proximity, timing and volume of the injection, all support the conclusion that this sequence was almost certainly induced.

Azle – 2013–2015: almost certainly induced. Beginning in November 2013, a series of earthquakes occurred near the city of Azle, about 25 km northwest of Fort Worth. As of 2015 the sequence includes eight earthquakes having magnitude $M \geq 3$; the two largest were M_{bLg}3.6 events occurring on 20 November 2013 and 8 December 2013. Like other Fort Worth Basin event sequences, there was no history of prior seismic activity. Scientists at SMU and the USGS deployed a temporary seismograph network and were able to locate accurately 283 events occurring between December 2013 and April 2014 (Figure 2.6 and Figure 2.13) (Hornbach et al. 2015). Figure 2.13 is revised from Hornbach et al. (2015). The seismicity occurred at depths between 1.5 km and 8 km on two steeply dipping, conjugate faults consistent with the general strike of the Newark East fault zone, a mapped fault system that extends NE-SW across the seismically active region. Focal mechanisms were consistent with normal faulting.

There are two wastewater injection wells and multiple production wells within 3 km of the seismic activity. Between June 2009 and 2014 injection was ongoing at the closest disposal well at depths of about 2.5 km and rates of 30,000–80,000 m^3/mo. Two gas and brine producing wells of interest were situated directly above the earthquake activity, but specific monthly production volumes of brines were not available. Geomechanical modeling of pore-pressure diffusion (Hornbach et al. 2015) indicated that the combination of brine production and wastewater injection was sufficient to generate subsurface pressure changes that could induce earthquakes on near-critically stressed faults.

Because of the absence of historical seismicity prior to injection, the proximity of the injection wells, the relatively high volumes injected compared to other regional wells, the timing of high injection rates with felt seismicity, and the depths of earthquakes at and below the depth of injection, we conclude this sequence is almost certainly induced.

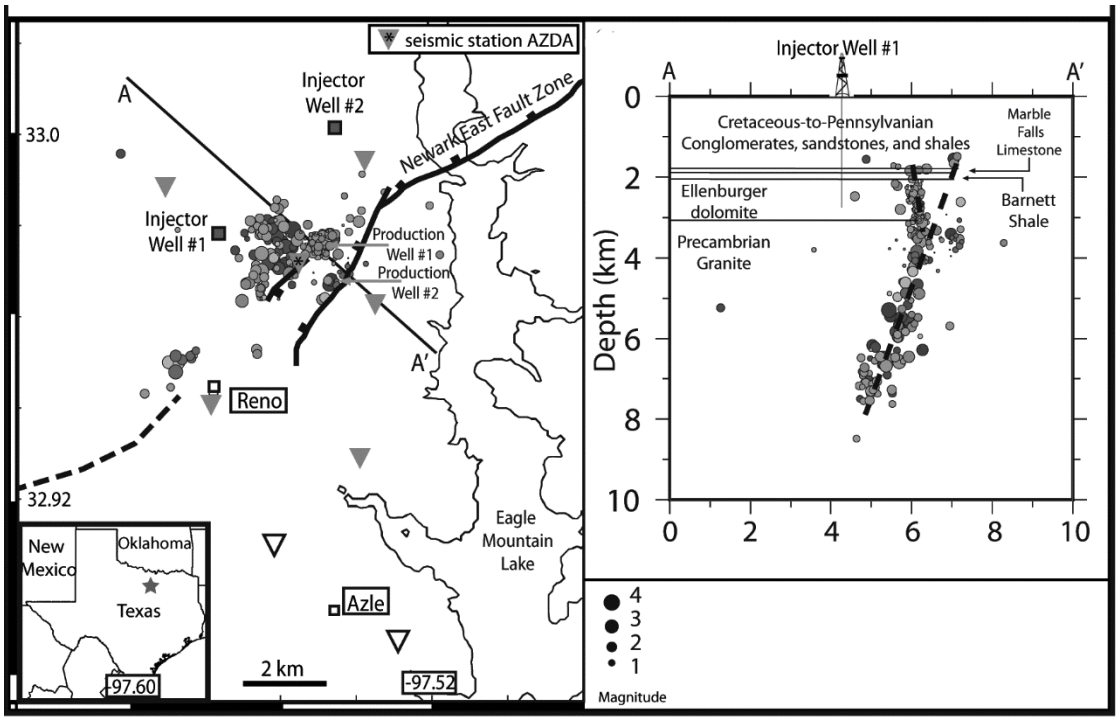

Circles: earthquake epicenters Triangles: Temporary seismograph station Star: Map location

Figure 2.13: Earthquakes near Azle and regional geologic structure

Elsewhere in northeast Texas: Frohlich (2012) analyzed data collected between November 2009 and September 2011 by the EarthScope Transportable Array and located 67 earthquakes. All of the more accurately located events were grouped in eight distinct locations, and each of these groups was situated within 3.2 km of one or more injection disposal wells having maximum injection rates of 24,000 m^3/mo or more. Two of these groups (Dallas-Fort Worth and Cleburne) are among those discussed above. Because of the proximity to high-volume injection wells and the absence of regional historical seismicity, earthquakes in the remaining six groups are probably induced.

The most numerous of the eight groups had 32 earthquakes and was situated in northeastern Johnson County near Venus, about 40 km southeast of Fort Worth and 30 km northeast of Cleburne. This focus has continued to be seismically active up into 2015, including an M_{bLg}4.0 earthquake on 7 May 2015. To further investigate this activity, scientists at Southern Methodist University and The University of Texas at Austin have installed several temporary seismograph stations. A focal mechanism for this 2015 earthquake indicates normal faulting.

2.3.3. West Texas

Snyder – 1974–1982: almost certainly induced. Two sequences of earthquake activity have occurred in association with the Cogdell Field about 20 km north of Snyder. The first began in 1974 and lasted until 1982; the largest earthquake, with magnitude m_b 4.6, occurring on 16 June

1978. The field began producing in 1949, and waterflooding of the producing reservoir began in April 1956. The injection began at the edges of the field and migrated inward over time; the injection rates increased and exceeded more than 300,000 m^3/mo by November 1974 when the first known earthquake occurred. A surface-wave analysis of the 1978 earthquake (Voss and Herrmann 1980)found normal faulting and estimated a depth of 3 km. The USGS operated a temporary seismograph network from February 1979 to August 1981 (Harding 1981) and recorded 20 locatable earthquakes having mean depths of 1.9 km. Both results are consistent with the injection depth of 2.1 km. Davis and Pennington (1989) investigated this sequence and attributed it to the waterflooding of the Cogdell oil field. They modeled fluid pressures in the field and concluded that the earthquakes occurred at the boundaries of regions having low fluid pressures adjacent to higher-pressure regions. We conclude this sequence is almost certainly induced because of the absence of historical earthquakes prior to 1974, the huge and sustained injection volumes, the earthquake depths at about the depth of injection, and the supporting modeling evidence.

Snyder – 2006–2012: probably induced. Following more than 20 years with no reported earthquakes, a second sequence of activity in the Cogdell oil field (Figure 2.6 and Figure 2.14) began in 2006; between 2006 and 2015 NEIC reported 24 earthquakes having $M \geq 3$, including an M_W 4.4 earthquake on 11 September 2011. Four focal mechanisms determined for this sequence included two strike-slip and two normal faulting events (Figure 2.14). Earthquakes occurring 1974–1982 in the Cogdell Field have been attributed to waterflooding operations in the Cogdell Field (Davis and Pennington, 1989). However, the 2000–2011 earthquakes mapped here appear to be associated with super-critical CO2 gas injection (Gan and Frohlich, 2013). As the history of waterflooding and gas injection are highly similar in the Cogdell, Kelly-Snyder, and Salt Creek Fields, it is presently unclear why earthquakes occur primarily in and near the Cogdell Field. Gan and Frohlich (2013) evaluated EarthScope Transportable Array records to investigate this sequence. They found no evidence that this second sequence was attributable to waterflooding; instead they found that it coincided with a program to inject super-critical CO_2 in the Cogdell Field. For the Cogdell Field, super-critical CO_2 injection rates averaged about 113 million m^3/mo between 2004 and 2012, and there was a temporary increase to more than 225 million m^3/mo in August 2006, just as the first earthquake in the sequence occurred. Although we have no knowledge of mapped regional faults or information about the focal depths of this sequence, we conclude it is probably induced. If so, the M_W4.4 earthquake is the largest known earthquake induced by injection of super-critical CO_2.

Permian Basin 1966–present: probably induced. Between December 1975 and September 1979 a 12-station seismograph network was deployed in west Texas to assess seismic risk associated with a proposed nuclear waste disposal site in southeastern New Mexico (Figure 2.6 and Figure 2.15). The network recorded more than 2000 earthquakes of which about 1300 were located. There were several different investigations analyzing these data (Doser et al. 1992; Keller et al. 1987; Rogers and Malkiel 1979); all found that much of this seismicity occurred within several active oil and gas fields, notably the War-Wink, Kermit-Keystone, and Apollo-Hendrick Fields. The investigations all concluded the seismicity was probably induced, but more than one mechanism

was responsible. For example, some events seemed to be associated with enhanced recovery efforts, and others with production.

Felt earthquakes had not been reported in or near the locations of these petroleum fields prior to 1966; between 1966 and 1978 there have been several reported earthquakes having $M \geq 3$, including one with M3.9 on 25 January 1976. Because the region was settled much earlier, Rogers and Malkiel (1979) suggest that earthquakes were mostly rare or absent prior to about 1966. Although the relationship between seismicity and petroleum operations appears to be complex, and many active fields there have no earthquakes, we conclude that the majority of Permian basin earthquakes are probably induced.

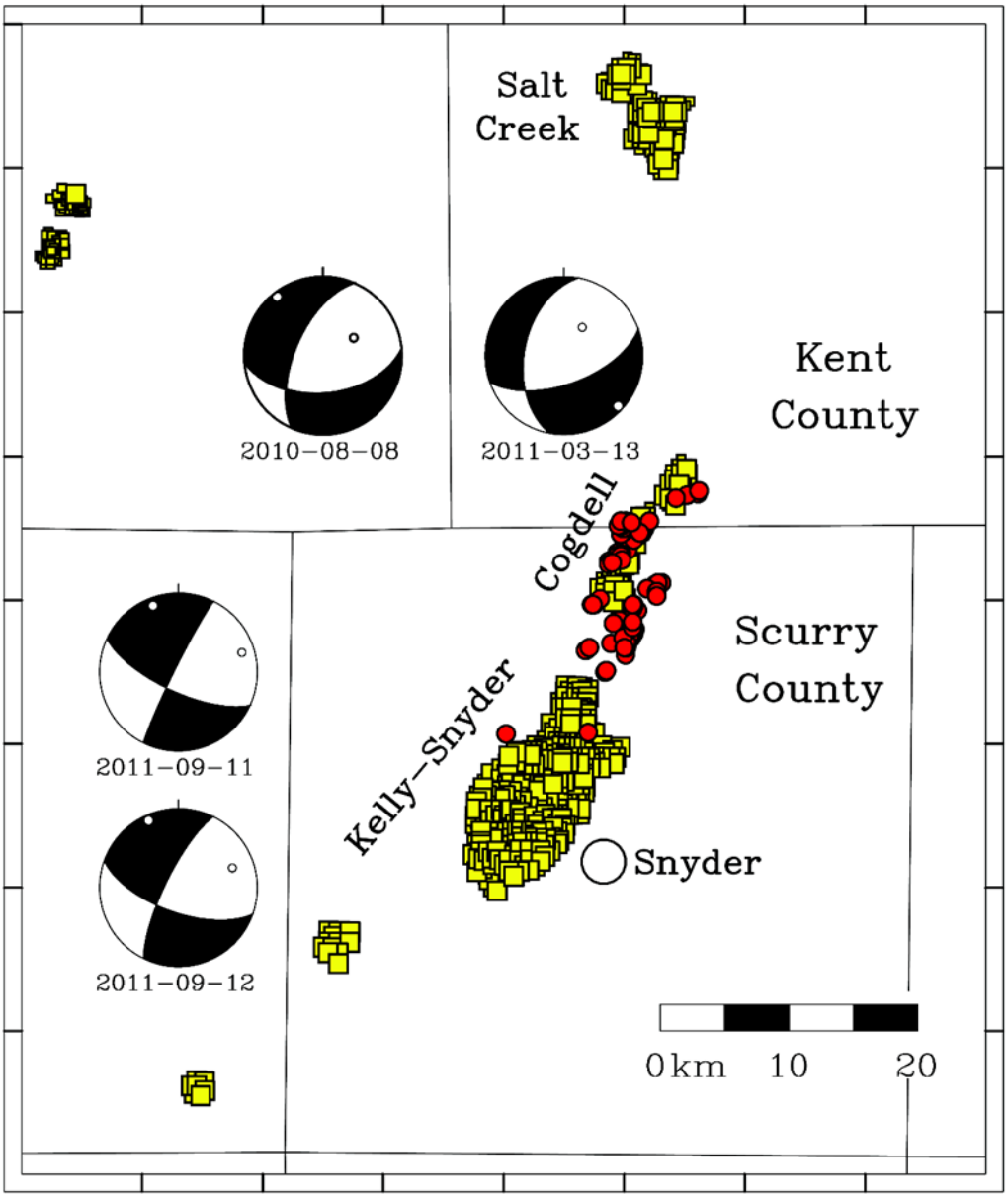

Filled circles	Earthquakes located by Gan and Frohlich (2013) using data from nearby USArray temporary stations
Squares	Super-critical CO2 gas injection wells
Beach-balls	Reported focal mechanisms for four of the mapped earthquakes

Figure 2.14: Earthquakes 2009–2011 and gas injection wells near Snyder TX

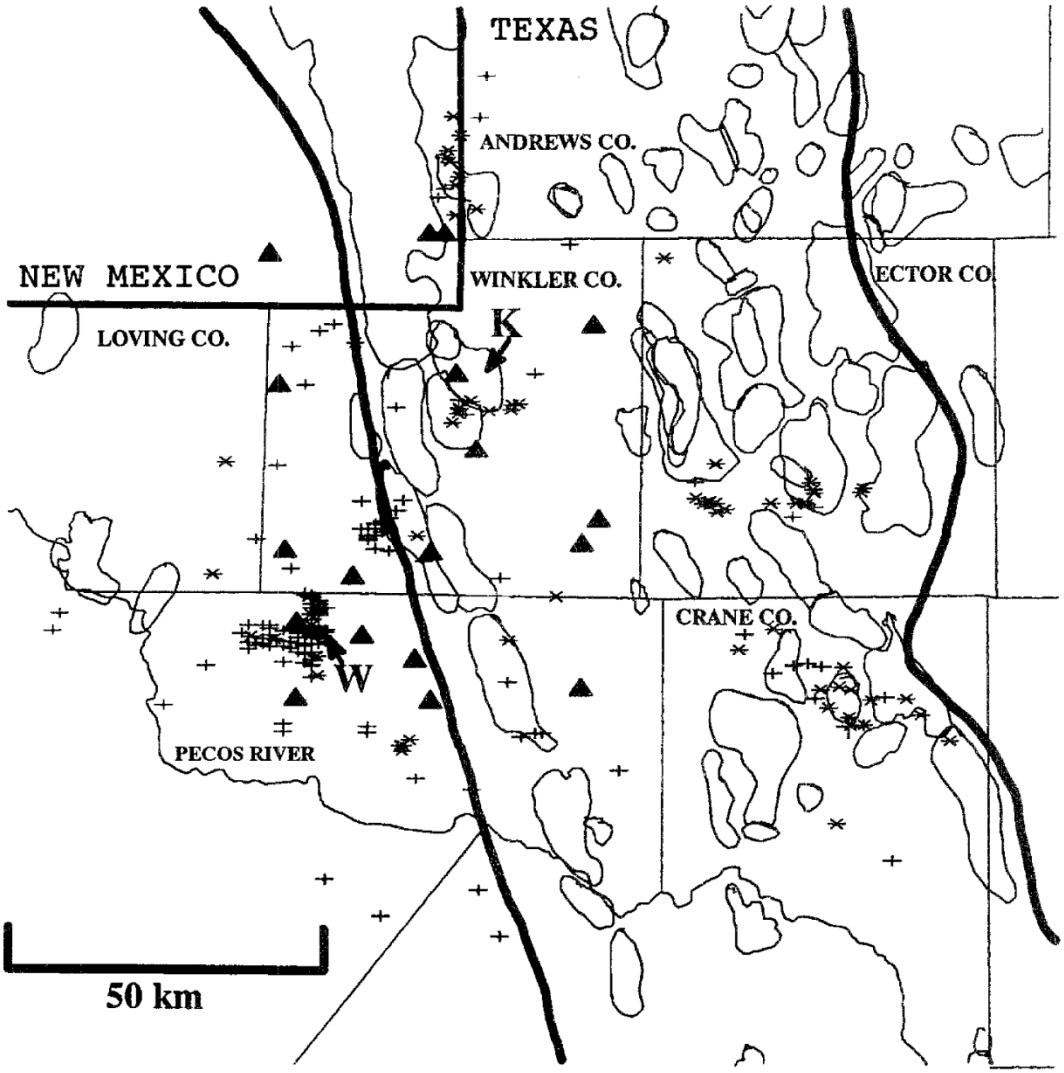

Note: Symbols "*" and "+" are epicenters relocated using data collected by temporary seismograph stations (triangles) operational from 1976–1979; "+" symbols are epicenters located with data from fewer than 4 stations. Oil fields are irregular-shaped regions enclosed by thin lines; bold lines are boundaries of the Central Basin Platform. Several investigators have noted that earthquakes are associated with the Keystone (labeled K) and War Wink (W) Fields, and seismicity within Crane County and Ector County is generally co-located with oil field outlines. Figure reproduced from Doser et al. (1992).

Figure 2.15: Seismicity 1976–1979 and oil fields of the Permian Basin

2.3.4. Texas Panhandle

In Texas, the largest historical earthquakes other than the 1931 and 1995 west Texas events occur in the Panhandle, where earthquakes having magnitudes exceeding M5 (as determined from felt areas) have occurred on 20 July 1925 (M5.4), 20 June 1936 (M5.0), and 12 March 1948 (M5.2) (Frohlich and Davis 2002). Of these, the 1948 earthquake was centered in the northwest corner of the Panhandle where we know of no contemporaneous petroleum production. However, for both

the 1925 and 1936 earthquakes (Figure 2.6 and Figure 2.16), the region of maximum intensities coincided with the giant Panhandle oil and gas field.

This, along with the observation that no confirmed earthquakes are known in the region prior to 1910 when petroleum was first discovered here, has led to speculation that Panhandle earthquakes are induced (Frohlich and Davis 2002; Pratt and Johnson 1926). Although the assertion would be credible for the 1936 earthquake (more than $50x10^6$ m^3 of oil were produced from the Panhandle Field prior to 1938), it is less plausible in 1925, as vigorous petroleum production was just getting underway then. Moreover, prior to 1910 the population of the Panhandle was scant, and earthquakes occurring then might have gone unnoticed. No information is currently available concerning the focal depths of Panhandle earthquakes, and epicentral locations are not very accurate.

Nevertheless, many of the Panhandle earthquakes in Tables A1 and A2 (available in the appendices to this report) have occurred near active production or injection operations. But while it is possible some Panhandle earthquakes are induced, at present there is insufficient evidence to conclude an induced cause is probable. However, in the analysis of Weingarten et al. (2015), some Panhandle events do qualify as earthquakes "associated" with injection. Clearly, more research concerning Panhandle earthquakes is warranted.

2.4. Natural Earthquakes in Texas

2.4.1. Texas Gulf Coast

The Gulf Coast and some communities in central Texas to the north (such as Austin) were settled in the first half of the 19th century. For smaller earthquakes (M < 4.5) occurring prior to 1970 or so the only information available often comes from felt reports, as there were few or no regional seismograph stations then. Searches of contemporary newspapers and journals has uncovered a few reports of apparent earthquakes occurring between 1847 and 1952. Very approximate magnitudes have been assigned to these events from an assessment of the felt reports. None of these apparent earthquakes was assigned a magnitude larger than 4.1.

These reported apparent earthquakes occurred in Seguin (14 February 1847, M3.6), Manor (1 May 1873, M3.1), Paige (5 January 1887, M4.1), Wellborn (31 January 1887, M3.3; Austin (Creedmoor, 9 October 1902, M3.9), Hempstead (8 May 1910, M3.8), and Orange (17 October 1952, M3.3).

2.4.2. Northeast Texas

Analysis of contemporary accounts suggests an earthquake may have occurred near Rusk on 8 January 1891 (M4.0), although there is some question about this (see Frohlich and Davis, 2002).

Sellards (1935) performed a field study investigating an earthquake occurring 12 April 1934 (M4.2) along the Texas-Oklahoma at Trout Switch (a spur on the railroad).

Between 24 April and 19 August 1964, a series of small earthquakes (largest, M4.4) occurred in Sabine County near Hemphill, and many of these were recorded on a temporarily-deployed seismograph. These events occurred while the nearby Sam Rayborn Reservoir dam was under construction, and before construction began on the nearby Toledo Bend Reservoir dam; thus, they appear to be natural, and not reservoir-induced earthquakes.

On 31 May 1997 a small earthquake (M3.4) occurred in Hunt County near Commerce.

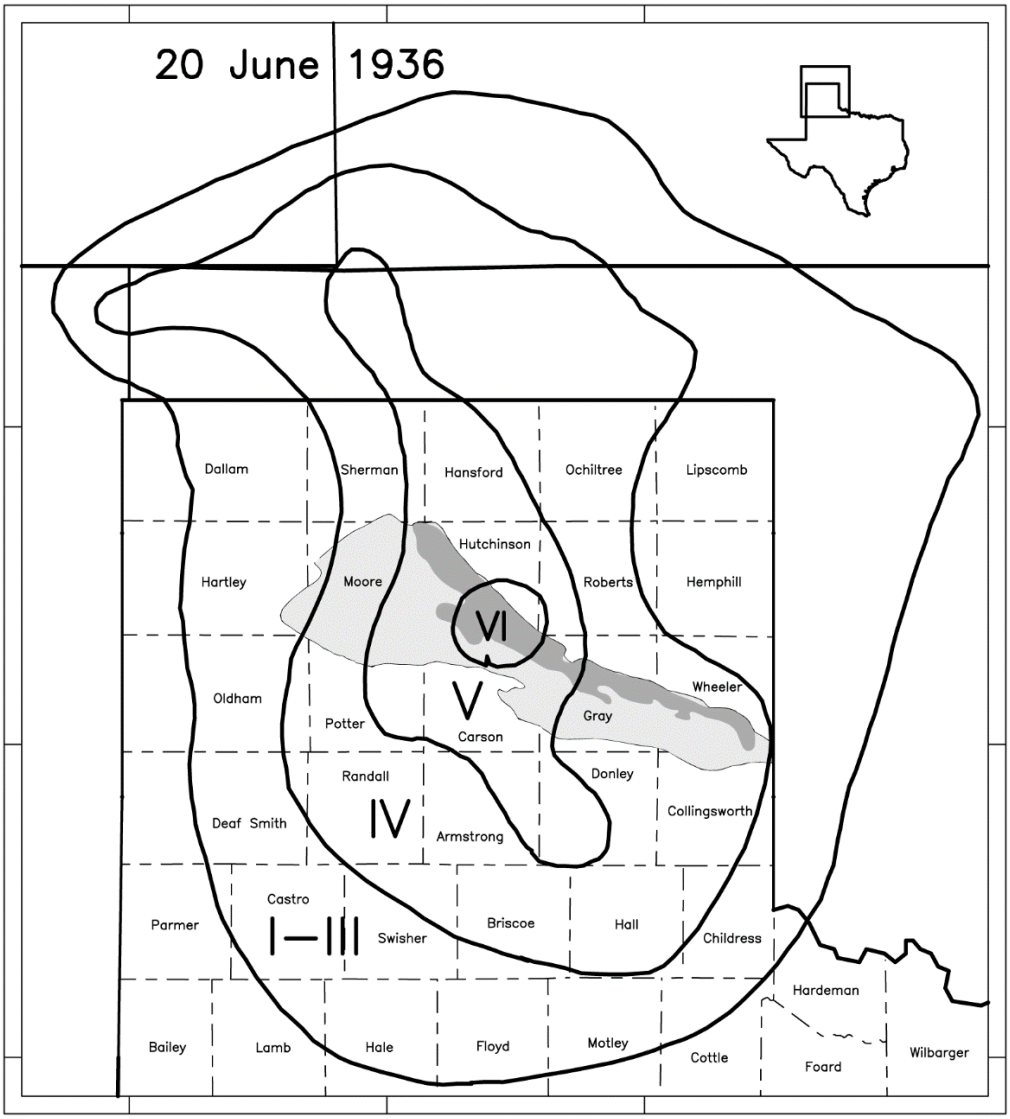

Roman numerals: Modified Mercalli Intensities
Dark grey: Oil field
Light grey: Gas field

Figure 2.16: Petroleum fields and felt intensities for the 20 June 1936 Panhandle earthquake (Frohlich and Davis 2002)

2.4.3. West Texas

The state's largest historical natural earthquakes are in West Texas—one occurring near Valentine (16 August 1931, M6.0), the other near Alpine (14 April 1995, M5.7). The 1931 earthquake had intensities as high as MMI IX in the epicentral area; both earthquakes were felt over most of Texas (Figure 2.17). Both these earthquakes are part of a band of natural seismicity extending from El Paso roughly southeast and paralleling the Rio Grande River; this is the seismically most active region in Texas.

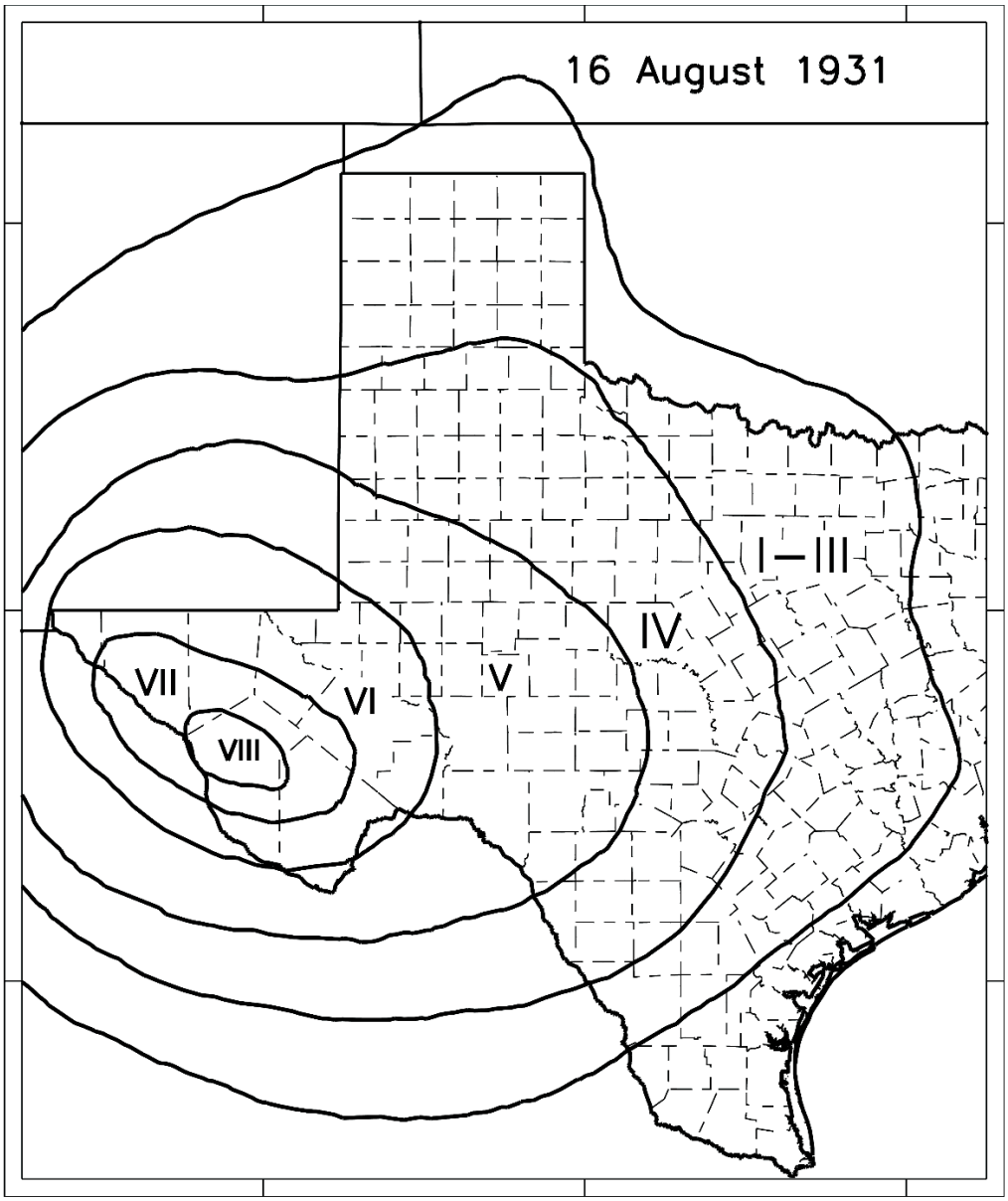

Roman numerals: Modified Mercalli Intensities
dashed lines: county boundaries

Figure 2.17: Felt area map for the 16 August 1931 Valentine earthquake (Frohlich and Davis 2002)

There are two contemporary studies of the 1931 Valentine earthquakes (Sellards, 1933), and Doser (1987) analyzed regional records to determine a focal mechanism. Perhaps surprisingly, the 1995 Alpine earthquake is less well-studied, as there has been no journal publication focusing on this event, although several published papers have used seismic waves from this earthquake to investigate regional crustal and mantle structure.

2.4.4. Texas Panhandle

The Texas Panhandle is the second most active seismic region in Texas, as numerous earthquakes with M>3 have occurred there in the 20th century, including three with magnitudes of M5.0 or greater. These occurred on 30 July 1925 (Borger, M5.4), 20 June 1936 (Borger, M5.0), and 12 March 1948 (Dalhart, M5.2). Of these the 1948 Dalhart earthquake is surely natural, as it occurred in the northwest corner of the Panhandle where there was little or no petroleum production.

However, both the 1925 and 1936 Borger earthquakes occurred within or on the boundary of the Panhandle Field, a huge oil and gas field that was undergoing development prior to 1925. There is little information to evaluate whether these earthquakes are induced or natural, as virtually the only published investigations are Udden (1926), Sellards (1939) and Frohlich and Davis (2002). No confirmed earthquakes are known in the Panhandle region before petroleum development began somewhat before 1920. However, census records indicate that there were virtually no inhabitants in the Panhandle prior to 1900, possibly explaining the absence of reported earthquakes, if earthquakes there are of natural origin.

2.5. Seismicity in Regions Neighboring Texas

2.5.1. Oklahoma

The largest historically reported earthquakes in Oklahoma had magnitudes of about M5.6. These occurred on 22 October 1882 near Fort Gibson (M5.6, Frohlich and Davis, 2002), 9 April 1952 near El Reno (M5.7, Frohlich and Davis), and 5 November 2011 near Prague and Sparks (M5.6). All historical Oklahoma earthquakes having magnitudes exceeding M5 have occurred in the central and northern parts of the states; none have occurred near the Oklahoma-Texas border (Figure 2.18). Note that activity is relatively sparse in the southern half of the state.

However, the Meers Fault in southern Oklahoma (Figure 2.19) is visible at the surface and has been investigated extensively (Crone and Luza 1990; Ramelli and Slemmons 1990). Paleoseismic studies involving trenching, etc., indicate that the Meers Fault was seismically active 1200–1300 years ago, and activity could have magnitudes of M7.0–7.5 or larger. There is some evidence that recurrence intervals are ~100,000 years; however, this is not well established.

2.5.2. The New Madrid Region

Between December 2011 and February 1812 three earthquakes occurred near New Madrid, Missouri, which have been widely reported to have magnitudes as large as M8 (Johnston and

Schweig, 1996). A more recent analysis by Hough et al. (2000) concluded that the magnitudes were probably significantly smaller (M7.4–7.5). However, for many locations in northeastern Texas it is likely that the 1811-1812 earthquakes are the source of the highest MMI levels experienced over the past several hundred years (Figure 2.20). At these distanced (~800 km) the peak frequencies of shaking would be relatively low, but are of interest as these might affect some components of bridges. There were no felt reports in Texas due to the low population density in 1811. Isoseismal lines shown in Figure 2.20 were inferred from a summary of felt reports from east of the Mississippi River.

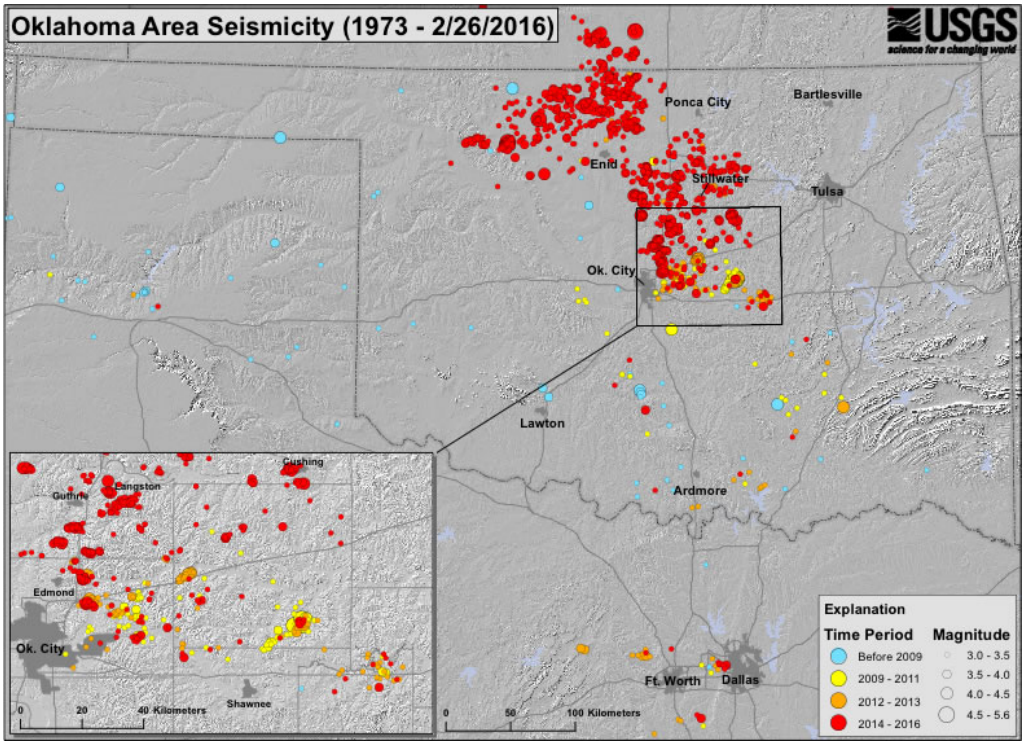

Figure 2.18: Seismicity of Oklahoma for 1973–2016, as reported by the U.S. Geological Survey

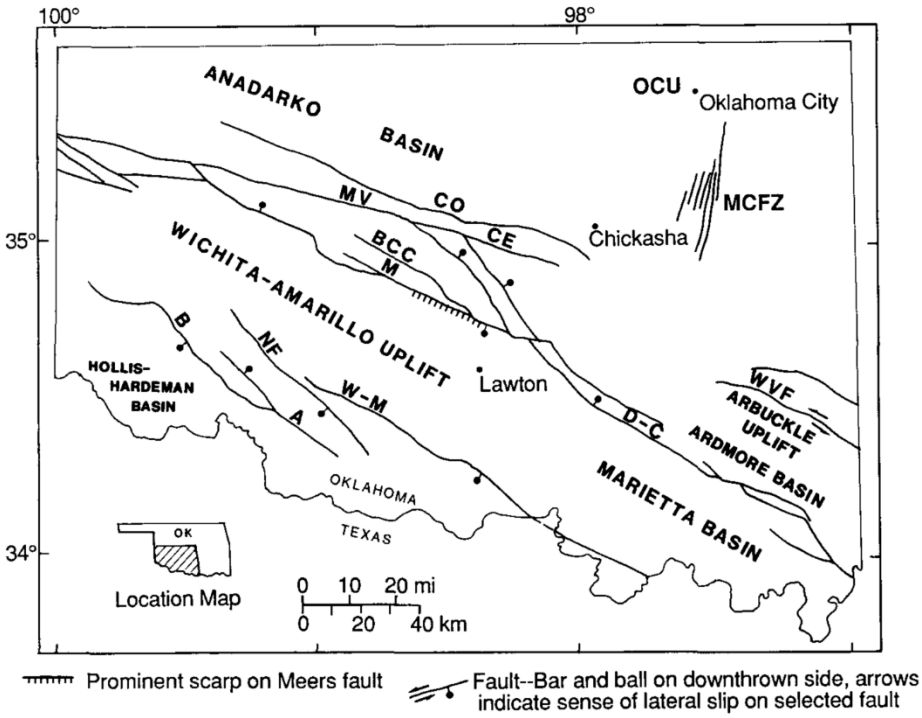

Figure 2.19: Location of mapped faults in southern Oklahoma, including the Meers Fault (M) (Crone and Luza 1990)

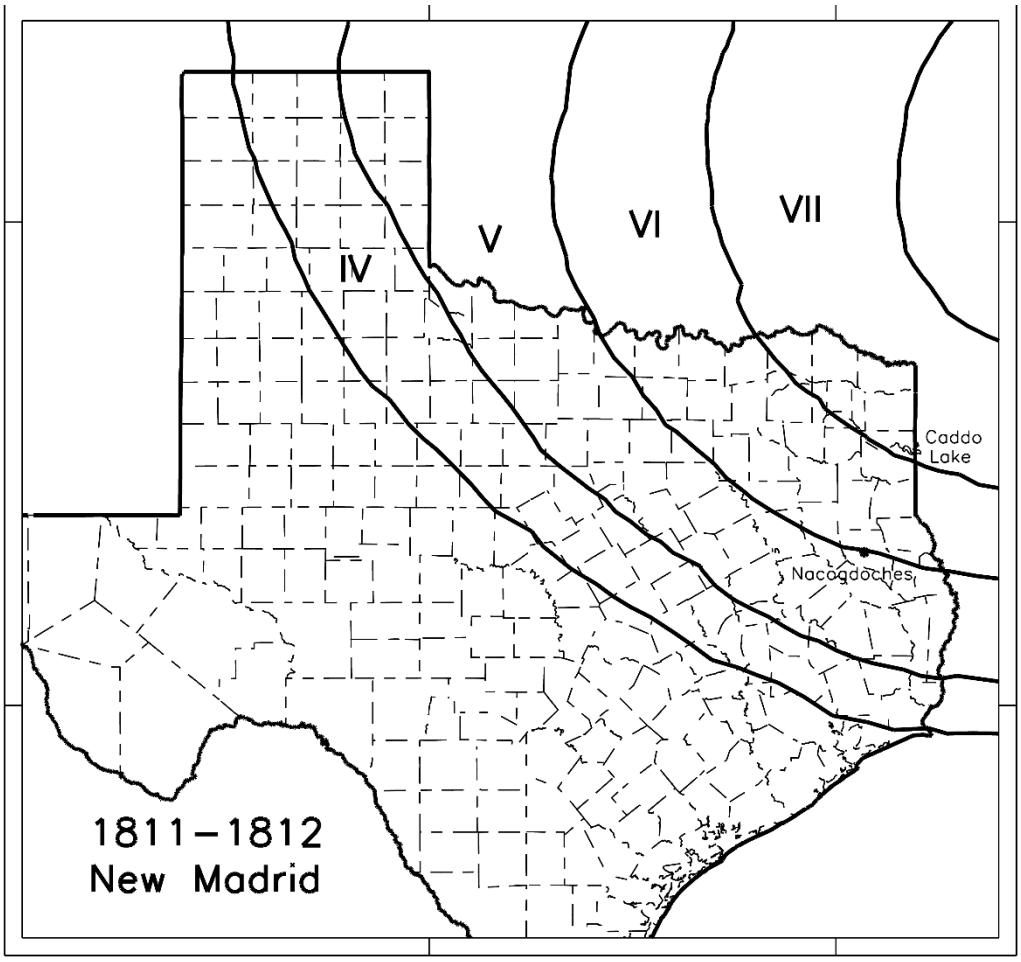

Note: Dashed lines are county boundaries.

Figure 2.20: Estimated felt area map for the New Madrid, Missouri earthquake, December 1811

2.5.3. Louisiana, New Mexico, and the Gulf of Mexico

Earthquakes are relatively rare in Louisiana. The largest historical earthquakes have had magnitudes of about M4.0. These include the 16 October 1983 earthquake in Lake Charles (M3.9; Stevenson and Agnew, 1988), with an epicenter relatively close to the Texas-Louisiana border. Recent evidence suggests that some small (~M2) Louisiana earthquakes may be induced (Walter et al. 2016).

Most of the larger historically recorded felt earthquakes in New Mexico occurred in the central and western part of the state, in the neighborhood of Socorro and Albuquerque. None of these appear to have had a magnitude as large as M6.0.

On 2 January 1992 an earthquake with magnitude M5.0 occurred in Rattlesnake Canyon in Lea County New Mexico, near the Texas-New Mexico border. Sanford et al. (1993) investigated this event, determined a focal mechanism, and suggested it might be induced.

Seismicity in the Gulf of Mexico is generally rare, although an M5.8 earthquake occurred on 10 September 2006 in the eastern Gulf, more than 400 km from the Texas-Louisiana boundary. Along the Texas coast the Gulf of Mexico is virtually aseismic (Frohlich, 1983).

2.5.4. Mexico

Earthquakes with magnitudes of M7.5–8.0 occur with regularity in Mexico. However, these large events are all situated on the Pacific coast, with epicenters more than 600 km from any location in Texas. Although surface waves from some of these earthquakes might occasionally be felt in Texas and causes low-frequency effects (perceptible swaying of tall building, sloshing of swimming pools, seiches) they don't otherwise pose a hazard.

2.6. Discussion

2.6.1. Induced Earthquakes across Texas through Time

Earthquakes induced by human activity occur in several different areas of Texas (Figure 2.5), and for some events the evidence they are induced is exceptionally strong. This is particularly true for three recent sequences of earthquakes associated with wastewater disposal in deep wells. These are the Dallas-Fort Worth International Airport sequence of 2008–2013 (Frohlich et al., 2011); the Timpson sequence surrounding the M4.8 earthquake of 17 May 2012 (Frohlich et al., 2014); and the Azle sequence beginning in 2013 (Hornbach et al. 2015). All three sequences occurred in regions where prior seismic activity was unknown; all three had accurately-determined epicenters situated within about two kilometers of active injection wells with maximum monthly injection rates of 24,000 m^3 or greater; all three sequences had accurately-determined hypocenters with focal depths at approximately the depth of injection and at greater depths; and epicenters for all three sequences occurred within a few km of known mapped subsurface faults.

Induced earthquakes are not just a recent phenomenon in Texas. The evidence that petroleum operations induced earthquakes in 1925 (Goose Creek) and 1932 (Mexia-Wortham) is credible, in spite of the fact that no seismographs recorded these events. In both cases careful field investigations (Pratt and Johnson, 1926; Sellards, 1933) established the presence of surface cracks, and in Mexia a pattern of felt reports suggested the source was shallow and coincident with the area where high-volume extraction was underway. The geologists who performed these field investigations, Wallace E. Pratt and Elias H. Sellards, were established and well-respected scientists with strong ties to industry—Pratt was employed by Humble Oil and was among the founders of the American Association of Petroleum Geologists, and Sellards was Director of the Texas Bureau of Economic Geology. Both made statements in academic publications suggesting the earthquakes were caused by petroleum extraction: Pratt and Johnson (1926) noted the earthquakes accompanied land subsidence and concluded that this was "directly caused by extraction of oil, water, gas, and sand from beneath the surface." Sellards (1933) noted that "the tremor may have been caused by adjustment of the land surface incident to the operations in the oil fields" and to support this, presented calculations indicating that cumulative production in the

fields was 60–100x10^6 m^3 of oil and water, and 20x10^6 m^3 of gas. Their statements suggesting an induced cause for the Goose Creek and Mexia-Wortham earthquakes are notable, especially as induced earthquakes were virtually unknown at that time.

2.6.2. The Multiple Causes of Induced Earthquakes in Texas

Mechanisms other than wastewater injection appear to be responsible for several Texas earthquake sequences. These mechanisms include fluid extraction for the 1932 Mexia-Wortham earthquake and the M4.8 2011 earthquake near Fashing (Pennington et al., 1986; Frohlich and Brunt, 2013); near-surface subsidence associated with fluid extraction (Goose Creek); enhanced oil recovery (Snyder earthquake M4.6 1978: Davis and Pennington, 1989); and super-critical CO_2 injection (Snyder earthquake M4.3 2011: Gan and Frohlich, 2013).

Indeed, over the past century in Texas, the apparent causes of induced earthquakes have changed as the technologies used to extract petroleum have evolved. Prior to 1940 most fields in Texas produced from relatively shallow strata, were in the primary recovery phase, and often were managed to produce oil as quickly as possible. The resulting removal of large volumes often led to changes in subsurface stress conditions, surface and/or subsurface faulting and cracking, and (sometimes) earthquakes. The 1925 Goose Creek and 1932 Wortham-Mexia earthquakes are prime examples.

As subsurface pressures declined in some of the larger fields, operators realized that waterflooding was necessary to maintain production (secondary recovery). This process began as early as 1938 in the East Texas Field, and was in widespread use across Texas when it was initiated in 1956 in the Cogdell Field near Snyder. Pennington et al. (1986) argue that waterflooding was responsible for the 16 June 1978 Snyder earthquake sequence. For the 1957 Gladewater earthquake, waterflooding of the East Texas Field may have contributed to its occurrence; however, an alternate cause is redistribution of subsurface stress, which is a plausible mechanism considering the huge volumes of petroleum produced here from strata at depths of 1–2 km.

Like the East Texas Field, many other fields in Texas have long and complex production histories, sometimes making it difficult to assign a single cause to associated earthquakes. Examples of such fields are in the Permian Basin, where numerous fields were discovered in the 1920s and subsequently have produced large volumes of petroleum from different strata, and over the decades have undergone various episodes of secondary and tertiary recovery. New shale-play fields, typically in basinal settings not co-located with the older fields, today are undergoing vigorous hydrofracturing operations. Other fields with long and various production histories and earthquakes include the Stratton Field (and the 1997 and 2010 Alice earthquakes) along the Gulf Coast, and the Fashing Field (and its earthquakes 1974–2011) south of San Antonio; in both cases the earthquakes are almost certainly induced, but the complex history makes it difficult to isolate one causal mechanism.

In contrast, the evidence indicates that a single cause—wastewater injection that activates nearby subsurface faults—is primarily responsible for many induced Texas earthquake sequences

occurring since 2008. These include the 2008–2013 Dallas-Fort Worth International Airport sequence, the 2009–2010 Cleburne sequence, the 2012 Timpson sequence, and the 2013–2015 Azle sequence. There also appear to be several other persistent loci of seismic activity associated with injection disposal wells elsewhere in northeast Texas (Frohlich 2012). However, if we compare the seismicity in northeast Texas and Oklahoma, the Texas seismicity tends to be clustered around a small number of distinct sites whereas in Oklahoma, the associated seismicity is aerially more extensive and distributed geographically over a much larger area (Walsh and Zoback 2015). There are also considerably fewer Texas earthquakes having M>3. The difference may occur because the injection in northeast Texas is mostly to dispose of fluids produced following hydrofracturing operations, and the seismicity is concentrated around a few wells having higher rates of injection (Frohlich 2012). In contrast, in Oklahoma much of the disposal is from large volumes of water coproduced during conventional oil production, and subsequently reinjected into deeper sedimentary formations that appear to be in hydraulic communication with crystalline basement (Walsh and Zoback 2015). In Oklahoma, the overpressuring and associated seismicity appears to extend over entire formations, rather than just around individual wells.

Although the Texas data support the assertion that when earthquakes occur, they often are situated within a few km of high-rate injection wells, or near fields where large volumes of oil and gas have been produced over many years from relatively shallow strata, the converse is not true. That is, the majority of high-rate disposal wells and highly productive petroleum fields are not associated with nearby earthquakes. Nevertheless, it is important to emphasize that while association is not causation, we cannot dismiss the correlations in time and space over a long operational history, reported at multiple sites and noted in numerous peer-reviewed publications. At present it is still poorly understood why seismicity occurs in some environments and not in other apparently similar situations. For Texas, we anticipate that this understanding will improve over time as the Texas seismograph network improves and more seismic data are collected, and as future research efforts target areas like the Panhandle and the Permian basin that have been seismically active and where considerable information is available about regional geology.

While Texas provides examples of earthquakes associated with extraction, secondary recovery, and wastewater injection, at present there have been no reported examples where hydrofracturing operations themselves directly caused felt earthquakes or earthquakes with magnitudes M3 or greater, such as have been observed in Alberta, British Columbia, Ohio, Oklahoma and elsewhere (Eaton and Mahani 2015; Farahbod et al. 2015; Holland 2011; Skoumal et al. 2015). However, this is unsurprising considering that earthquakes associated with hydrofracturing are usually small-magnitude events and seismic station coverage in Texas is relatively sparse.

Similarly, we are unaware of any reservoir-induced earthquakes in Texas (i.e., earthquakes associated with the filling of surface-water impoundments). This is unsurprising considering that nearly all such earthquakes occur beneath reservoirs having maximum depths of 50 m or more (Gupta 2002). Only two reservoirs in Texas have depths exceeding 50 m (Lake Travis at 65 m, and Lake Amistad at 60 m), and neither have nearby earthquakes.

2.7. Summary

Earthquakes induced by human activity occur in several different areas of Texas, and for some events the evidence they are induced is exceptionally strong. Induced earthquakes are not just a recent phenomenon in Texas. The evidence that petroleum operations induced earthquakes in 1925 (Goose Creek) and 1932 (Mexia-Wortham) is credible, in spite of the fact that no seismographs recorded these events. Mechanisms other than wastewater injection appear to be responsible for several Texas earthquake sequences. These mechanisms include fluid extraction for the 1932 Mexia-Wortham earthquake and the M4.8 2011 earthquake near Fashing; near-surface subsidence associated with fluid extraction (Goose Creek); enhanced oil recovery; and super-critical CO_2 injection (Snyder earthquake M4.3 2011). Indeed, over the past century in Texas, the apparent causes of induced earthquakes have changed as the technologies used to extract petroleum have evolved.

Chapter 3. Texas Geologic Conditions and V_{S30} Maps

3.1. Overview

The influence of local soil and rock conditions including local rock type and geologic context on ground motion and potential earthquake damage has been recognized for many years (Kramer 1996). In general, less rigid soil and rock types (e.g., unconsolidated sand, gravel and clay) undergo more severe ground motion than do more rigid soil and rock types (e.g., granite, limestone and sandstone) for a far field seismic event. Given that measurements of near-surface rock properties are sparse and unequally distributed across Texas, one approach to estimating seismic properties statewide is to leverage knowledge of the distribution and types of rocks and sediments from previously published geologic maps and group the units by some parameters that reasonably correlate with seismically relevant properties.

One approach to estimating the geographic variation in seismic response from geologic maps has been to group geologic units by age, under the assumption that younger units are associated with a larger seismic response than are older rocks in most cases. In many large geographic areas, there is a general correlation between the age of a geologic unit and its rigidity, but that correlation may only be a secondary one that reflects the greater proportion of rigid, crystalline rocks in regions dominated by older Paleozoic and Precambrian units, and the corresponding greater proportion of less rigid sedimentary strata (shales, mudstones, and semi-consolidated gravel, sand, and clay) in geologically younger areas.

An alternative approach, if the data are available, is to associate dominant rock types with mapped geologic units, estimate physical properties of those major rock types from published analyses of these or similar rock types, and then group the geologic units by dominant rock types with similar physical properties regardless of geologic age. Across Texas, initial project-related investigations suggest that there may be as many as 30 or 40 primary rock types that could be derived from published geologic maps and could form the basis for a map depicting the distribution of those primary types. The primary lithologic units could then be aggregated into a smaller number of rock units having similar seismic response. The goal is to combine the dozens of primary types into perhaps four or five aggregated units that would likely range from the least-rigid group (unconsolidated sands, silts, and clays) to the most rigid group (crystalline rocks). Using this approach, similar rock types of differing ages would be grouped together and considered to have similar seismic properties rather than be assigned properties based on age of the mapped unit alone.

To conduct the grouping process by physical properties of soil and rock, a parameter is needed to relate the physical properties and ground motion amplification. V_{S30}, as the time-averaged shear wave velocity of the top 30m, has been proved to be a proper evaluation of ground motion amplification and adopted as the key parameter for seismic design in ASCE 7 and AASHTO Seismic Design Specifications. Therefore, this chapter also provides a brief discussion on the existing shear wave velocity profiles and V_{S30} proxy methods. Then, the in-situ V_{S30} measurements

made as part of this research project are presented. Finally, the V_{S30} maps developed for Texas using in-situ measurements and proxy methods are shown.

3.2. Geologic Maps of Texas

Maps showing the distribution of geologic units over parts of the state have been created by numerous individuals, groups, and agencies and exist at a variety of scales. Most of the regionally systematic mapping ranges from 7.5-minute quadrangle scale (1:24,000) showing the most detail (but incomplete statewide coverage), to statewide compilations at 1:500,000 (Barnes, 1992). The most detailed maps of the entire state are the 1:250,000-scale maps of the Bureau of Economic Geology's Geologic Atlas of Texas. This series, consisting of 38 maps (Figure 3.1 and Table 3.1) that each cover one degree of latitude and two degrees of longitude, was published as a compilation of more detailed maps at larger scales where available, along with new mapping at the 1:250,000 scale. These maps, published between 1964 and 1987 in print-only format, are periodically revised and updated as new mapping is completed. Atlas-series maps have been combined to produce the 1:500,000-scale statewide geologic map of Texas (Figure 3.2).

Table 3.1: List of the 1:250,000-scale geologic maps of the Bureau of Economic Geology's Geologic Atlas of Texas series

Map sheet	Author	Map sheet	Author
Abilene	Brown and others, 1972	**Llano**	Barnes, 1981
Amarillo	Eifler and Barnes, 1969	**Lubbock**	Eifler and others, 1967
Austin	Proctor and others, 1974a	**Marfa**	Twiss and Barnes, 1979
Beaumont	Shelby and others, 1968	**McAllen-Brownsville**	Brewton and others, 1976b
Beeville-Bay City	Aronow and others, 1975	**Palestine**	Shelby and others, 1967
Big Spring	Eifler and others, 1974	**Pecos**	Eifler and Barnes, 1976
Brownfield	Eifler and others, 1974	**Perryton**	Eifler and others, 1970
Brownwood	Kier and others, 1976	**Plainview**	Eifler and others, 1968
Clovis	Eifler and others, 1978	**San Angelo**	Eifler and others, 1975
Corpus Christi	Aronow and Barnes, 1968	**San Antonio**	Brown and others, 1974
Crystal City-Eagle Pass	Brown and others, 1976	**Seguin**	Proctor and others, 1974b
Dalhart	Eifler and others, 1984	**Sherman**	McGowen and others, 1967
Dallas	McGowen and others, 1972	**Sonora**	McKalips and Barnes, 1981
Del Rio	Waechter and Barnes, 1977	**Texarkana**	Shelby and others, 1966
Emory Peak-Presidio	Brown and others, 1979	**Tucumcari**	Eifler and others, 1983
Fort Stockton	Anderson and others, 1982	**Tyler**	Pieper and others, 1964
Hobbs	Eifler and others, 1976	**Van Horn-El Paso**	Dietrich and others, 1967
Houston	Aronow and Barnes, 1968	**Waco**	Proctor and others, 1970
Laredo	Brewton and others, 1976a	**Wichita Falls-Lawton**	Hentz and Brown, 1987

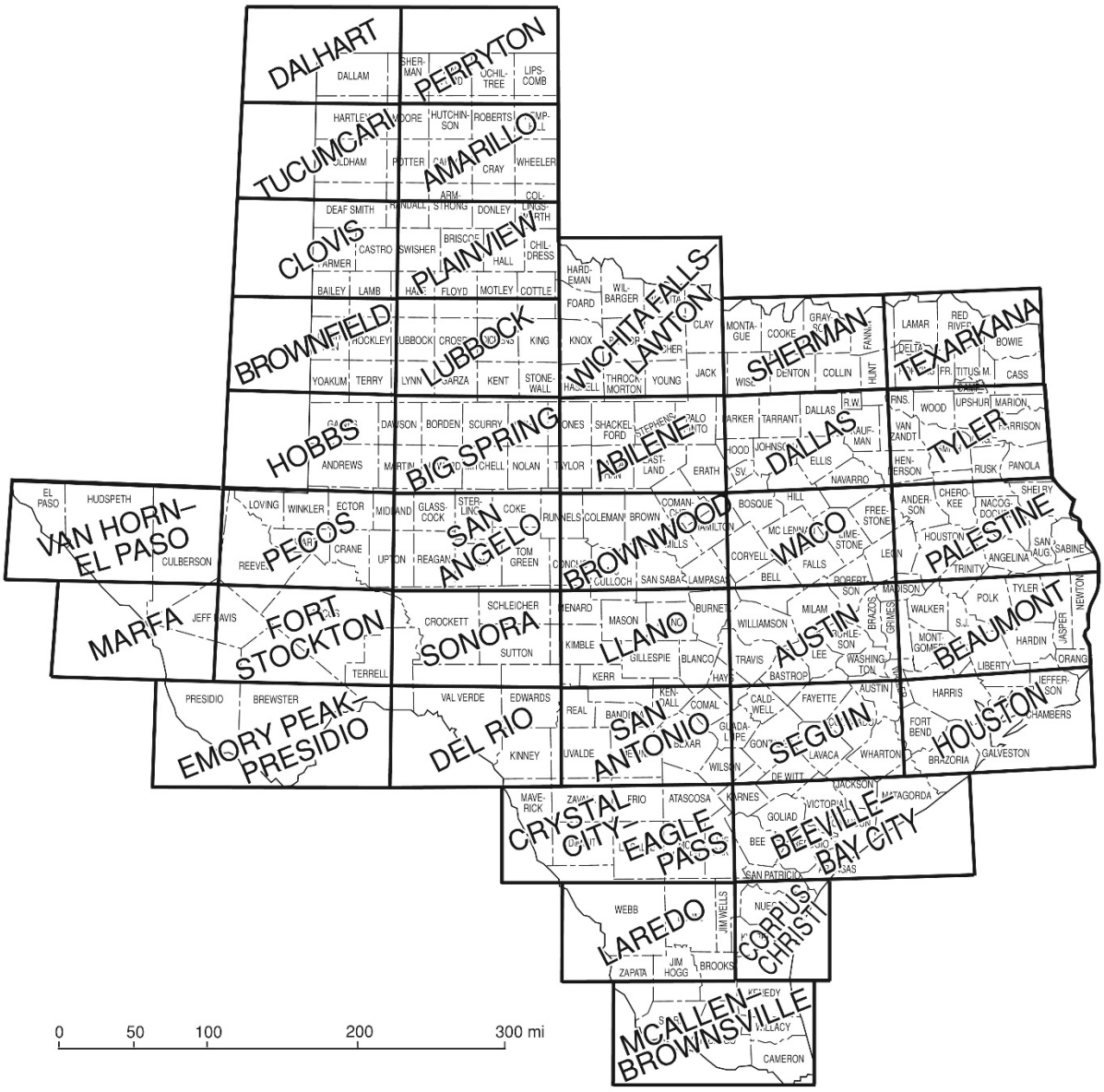

Figure 3.1: Map showing the distribution of the 38 map sheets that comprise the Geologic Atlas of Texas

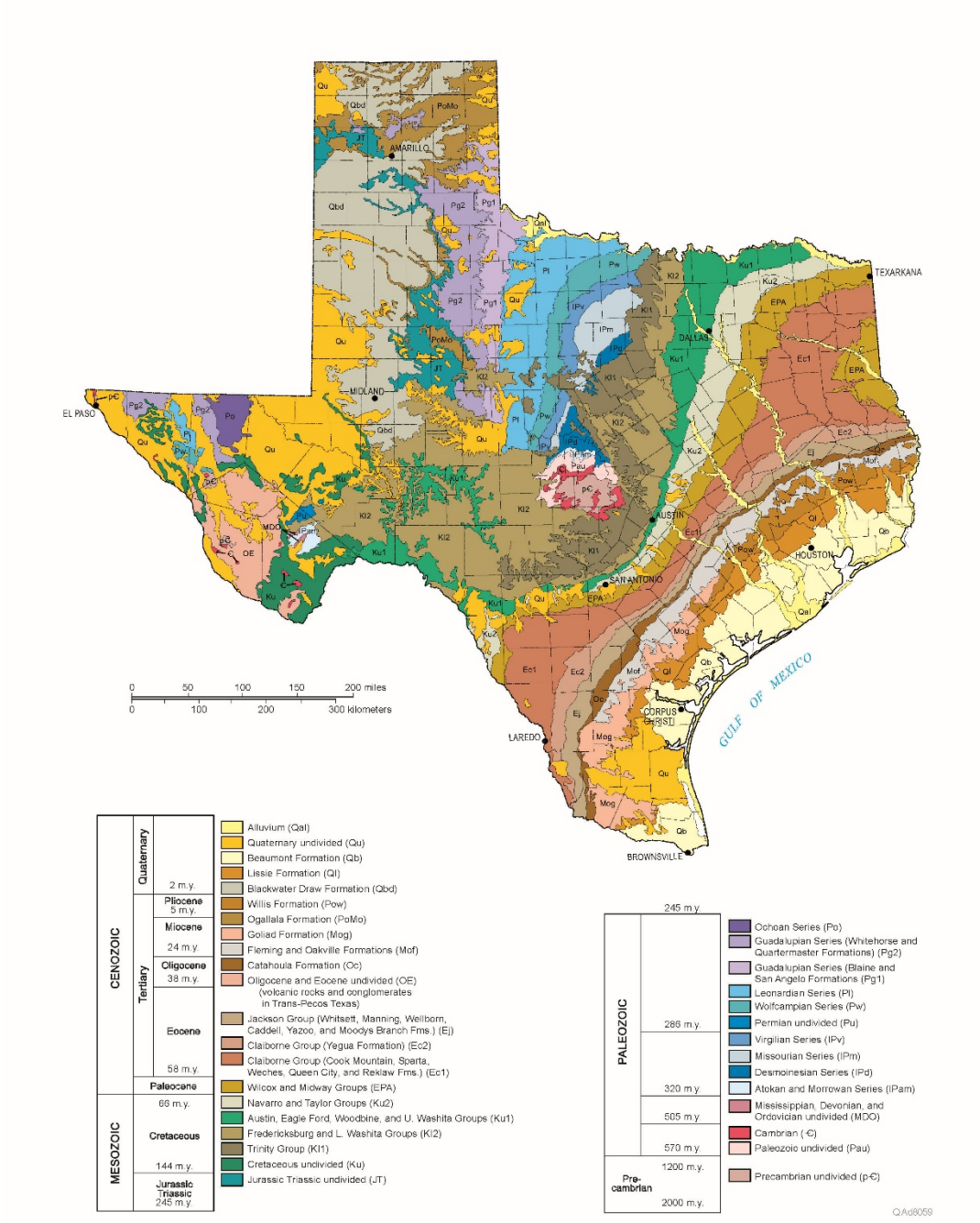

Figure 3.2: Generalized geologic map of Texas (modified from Barnes, 1992)

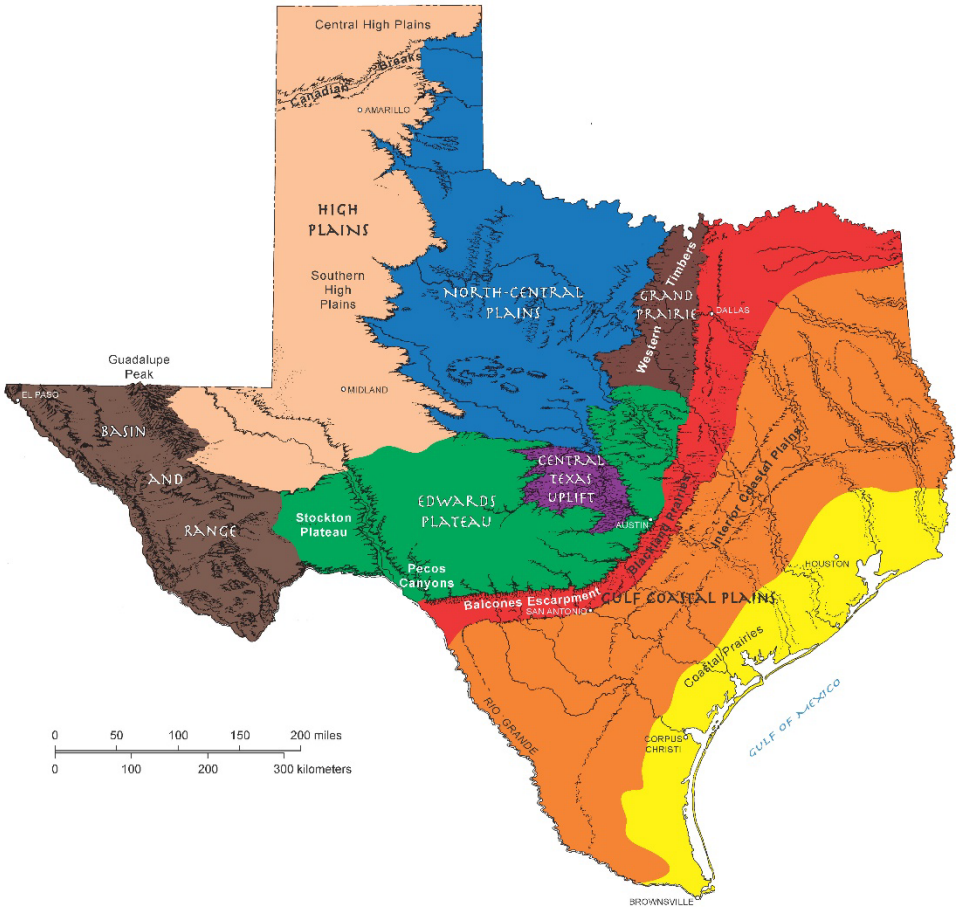

PROVINCE	MAX. ELEV. (ft)	MIN. ELEV. (ft)	TOPOGRAPHY	GEOLOGIC STRUCTURE	BEDROCK TYPES
Gulf Coastal Plains					
Coastal Prairies	300	0	Nearly flat prairie, <1 ft/mi to Gulf	Nearly flat strata	Deltaic sands and muds
Interior Coastal Plains	800	300	Parallel ridges (questas) and valleys	Beds tilted toward Gulf	Unconsolidated sands and muds
	1000	450	Low rolling terrain	Beds tilted south and east	Chalks and marls
	1250	450	Low stairstep hills west; plains east	Strata dip east	Calcareous east; sandy west
	3000	450	Flat upper surface with box canyons	Beds dip south; normal faulted	Limestones and dolomites
	2000	1200	Steep-walled canyons		Limestones and dolomites
	4200	1700	Mesa-formed terrain; highs to west	Unfaulted, near-horizontal beds	Carbonates and alluvial sediments
	2000	800	Knobby plain; surrounded by questas	Centripetal dips, strongly faulted	Granites; metamorphics; sediments
	3000	900	Low north-south ridges (questas)	West dip; minor faults	Limestones; sandstones; shales
High Plains					
Central	4750	2900	Flat prairies slope east and south	Slight dips east and south	Eolian silts and fine sands
Canadian Breaks	3800	2350	Highly dissected; local solution valleys		
Southern	3800	2200	Flat; many playas; local dune fields		
	8750	1700	North-south mountains and basins	Some complex folding and faulting	Igneous; metamorphics; sediments

Figure 3.3: Physiographic map of Texas (modified from Wermund, 1996)

The aforementioned 1:250,000-scale Geologic Atlas of Texas maps have now been digitized and converted to an ArcGIS-compatible format. For each of the 38 sheets, geologic units were mapped as individual polygons associated with attribute fields including the geologic formation symbol. The symbols include letters designating the geologic age and an abbreviation for the formation name. The symbols and the detailed formation descriptions were used to create new attribute fields that designate the geologic unit ages and primary and secondary lithologic types. That process, along with some standardization of lithologies, yielded 48 different primary lithologies.

A simplified version of the 1:500,000-scale geologic map of Texas (Figure 3.2) shows the regional distribution of geologic units that can serve as the basis for grouping rock units with similar seismic response. When combined with the similarly scaled map of the major physiographic regions of Texas (Figure 3.3), which is largely controlled by the distribution of geologic units and their topographic expression, a framework for grouping geologic units can be developed that takes into account primary rock types, geologic and geomorphic setting, and landscape age. Subsequently, the 48 different primary lithologies were divided into 6 different groups of lithologic types based on the relative stiffness of the formation. Table 3.2 presents the six different groups of lithologic types. The first three groups refer to lithologic descriptions attributed to soil deposits, while the last three groups include primary rock types associated with soft-to-hard rock formations. More specifically, Group A includes alluvium or terrace deposits, Group B contains fine-grained sediments of clay, silt, and loess, and Group C includes coarse-grained sediments of sand and gravel. Group D includes units of soft-rock formations of varying degrees of cementation, such as mudstone, claystone, siltstone, sandstone, conglomerate, marl, and shale. Groups E and F consist of units characterized by hard-rock formations, such as chalk, limestone, and evaporate (Group E), and chert, basalt, granite, and rhyolite (Group F). Table 3.2 lists all of the primary lithologies included for each of the 6 rock-type groups. Figure 3.4a shows the spatial distribution of the mapped units based on the 6 rock-type groups, and Figure 3.4b shows the spatial distribution of the same units based on geologic age. The distribution of the geologic units based on primary lithology and geologic age can be used to estimate seismic properties, such as V_{S30}, statewide.

Table 3.2: Primary lithologic descriptions for the six rock types defined in this study

Rock Type Group	Primary Lithologic Description
A	alluvium, colluvium
B	clay, fill, mud, silt
C	gravel, rock debris, sand
D	breccia, caliche, claystone, conglomerate, marl, mudstone, sandstone, shale, siltstone
E	chalk, dolomite, gypsum, limestone
F	agglomerate, amphilbolite, andesite, ash, basalt, chert, diorite, extrusives, gneiss, granite, igneous rocks, ignimbrite, intrusive, leptite, melarhyolite, meta-igneous rocks, metaquartzite, meta-sedimentary rocks, porphyry, pyroclastics, rhyolite, schist, serpentinite, syenite, trachyte, tuff

As seen in Figure 3.4, the Gulf Coastal Plain consists predominantly of Tertiary to Quaternary age formations that are dominantly unconsolidated to semi-lithified terrigenous deposits (Groups A, B, and C). Cretaceous-age marls and chalks (Groups D and E) border the upper Gulf Coastal Plain and underlie a substantial fraction of the urban corridor that includes parts of San Antonio, Austin, and Dallas. These strata are likely more rigid than those of the Gulf Coastal Plain, but not as rigid as the dominant limestones and dolomites of the Cretaceous rocks forming the adjacent Edwards Plateau (Group E). Lithified Paleozoic strata underlie the North-Central Plains, and consist of sandstones, siltstones, shales, and carbonates (Groups D and E) with Vs that can be as large as those of the Edwards Plateau limestones or as small as those of the Tertiary-age sediments of the upper Gulf Coastal Plain (Groups B and C). The Precambrian granites and metamorphic rocks that underlie the Central Texas Uplift are among the oldest and stiffest rocks in Texas. The mountains and intervening basins within the Basin and Range province of far west-Texas are underlain by geologic units that range in age from Precambrian to Quaternary and in lithology from soft unconsolidated sediments that fill the basins to stiff igneous and metamorphic rocks that form the ranges. In the High Plains province of northwestern Texas, semi-consolidated to unconsolidated sediments of Tertiary and Quaternary age overlie stiffer sedimentary rocks of Paleozoic and Mesozoic age. The thickness of the younger units and associated burial depth of the generally stiffer Paleozoic and Mesozoic strata are important characteristics that will influence seismic properties such as V_{S30}.

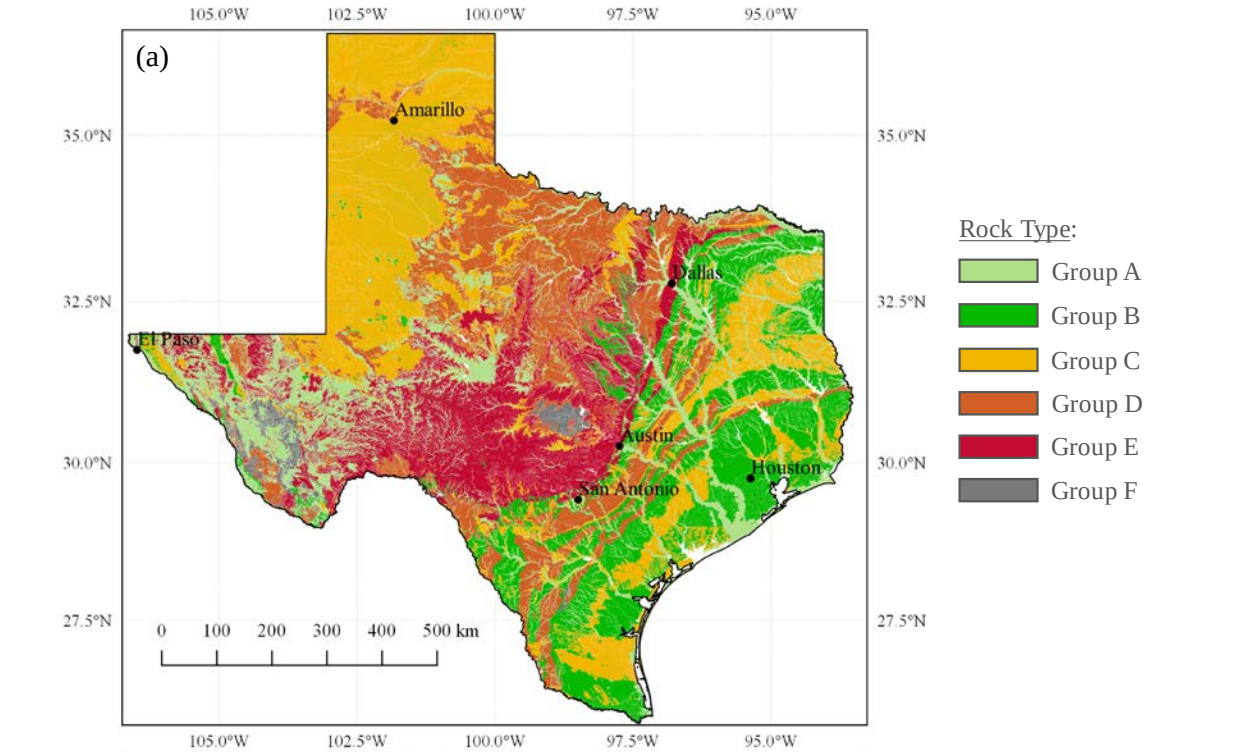

a) based on primary rock type group (Table 3.2)

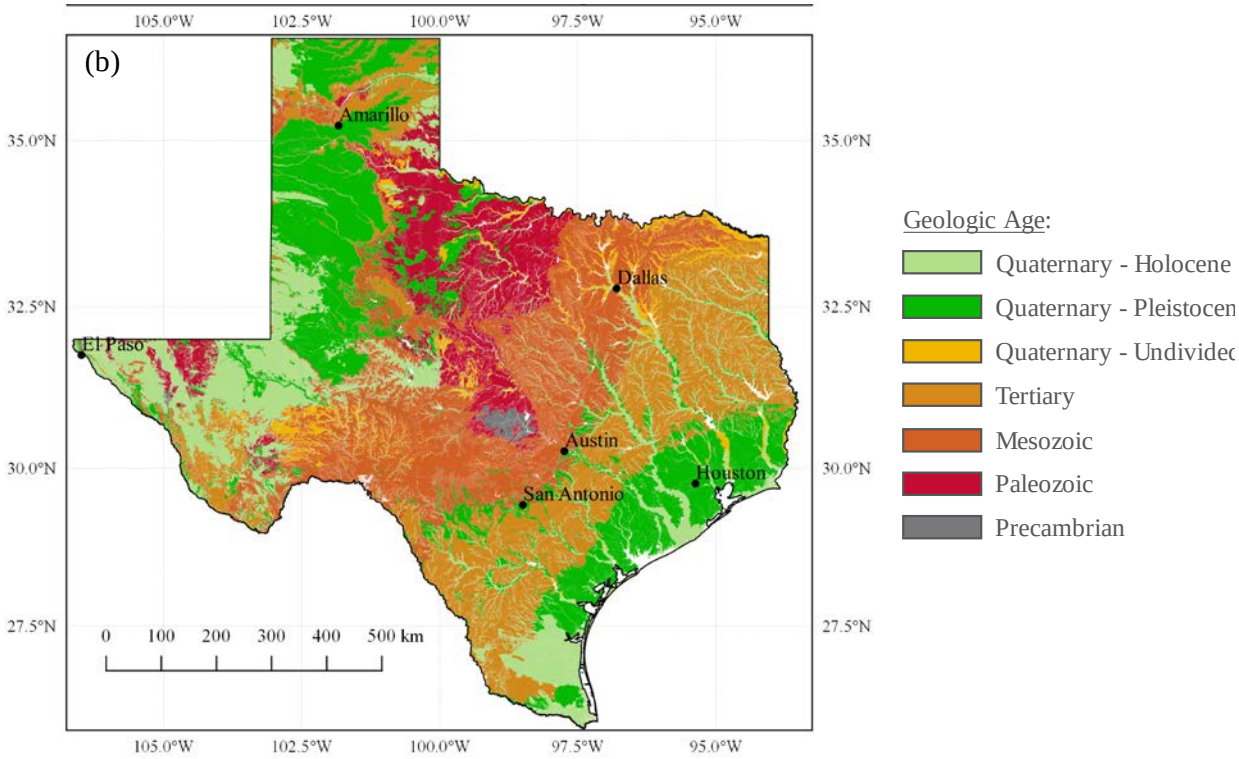

b) based on geologic age

Figure 3.4: Spatial distribution of mapped units

3.3. Existing Shear Wave Velocity Profiles

As stated in Section 3.1, V_{S30} is important in quantifying physical properties of geological units and evaluating ground motion amplification. A major objective of this research project is to provide a map of V_{S30} values across the State of Texas for more accurate estimations of ground shaking hazards. Thus, it is necessary to retrieve V_{S30} values from existing shear wave velocity profiles to provide reference for representative V_{S30} values for each geological units. Additional in-situ V_{S30} measurements are made as part of this project, as described in Section 3.6, to supplement the existing shear wave velocity profiles.

As part of the PEER Next Generation Attenuation – East (NGA-East) project (http://peer.berkeley.edu/ngaeast/), a database of 2,754 shear wave velocity (*Vs*), measured profiles in Central and Eastern United States (CEUS), were retrieved from the literature (Goulet et al. 2014). In this database, a limited number of shear wave velocity measurements within the state of Texas can be found. Table 3.3/Table 3.4 summarize the information regarding these *Vs* profiles in Texas, in terms of their literature source, location, reported V_{S30} value, as well as the associated rock unit name and geologic period. Figure 3.5 illustrates the color-coded median V_{S30} value for each location. As it can be seen from Figure 3.5, almost all available *Vs* measurements in Texas are located along the Gulf Coastal Plain, with the only exception being a few *Vs* in situ data from the Comanche Peak Nuclear Power Plant.

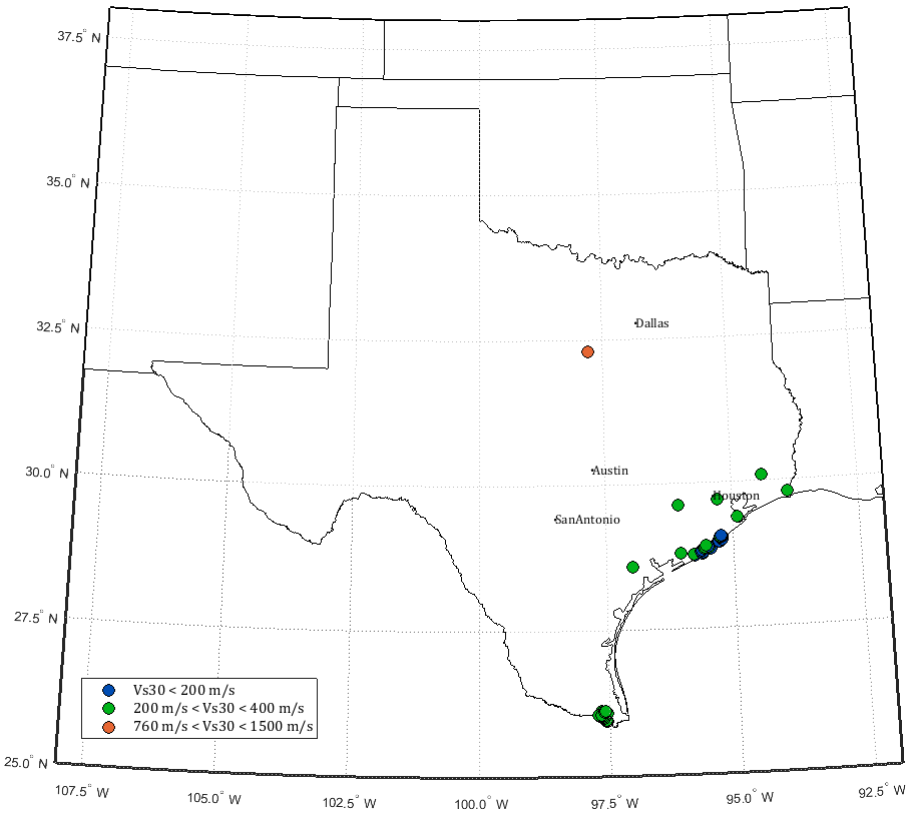

Figure 3.5: Locations of Vs measurements in Texas

Table 3.3 Measured shear wave velocity profiles in Texas

Source	Location	Latitude (deg)	Longitude (deg)	Reported V_{S30} (m/s)	Rock Unit Name	Period
Dames and Moore (1974)	Alien's Creek	29.63	-96.06	309.84	Beaumont Formation	Quaternary
	Comanche Peak	32.30	-97.79	1188.32	Glen Rose Formation	Cretaceous
Holzer et al. (2010)	CMN001	25.95	-97.55	217.00	Alluvium	Quaternary
	CMN002	25.95	-97.56	214.00		
	CMN003	25.96	-97.57	201.00		
	CMN005	25.97	-97.58	233.00		
	CMN006	25.97	-97.59	233.00		
	CMN007	25.98	-97.60	233.00		
	CMN008	25.99	-97.60	236.00		
	CMN011	26.02	-97.61	236.00		
	CMN013	26.03	-97.63	236.00		
	CMN015	26.03	-97.65	234.00		
	CMN022	26.05	-97.62	259.00		
	CMN016	26.04	-97.66	221.00		
	CMN019	26.04	-97.70	232.00		
	CMN021	26.06	-97.62	227.00		
	CMN023	26.07	-97.62	225.00		
	CMN027	26.12	-97.66	221.00		
	CMN032	26.07	-97.58	236.00		
	CMN024	26.08	-97.63	231.00		
	CMN031	26.09	-97.54	201.00		
	CMN025	26.09	-97.64	228.00		
	CMN026	26.11	-97.65	232.00		
	CMN004	25.96	-97.58	232.00		
	CMN009	26.00	-97.60	240.00		
	CMN010	26.01	-97.61	240.00		
	CMN012	26.02	-97.62	236.00		
	CMN014	26.03	-97.64	275.00		
	CMN018	26.04	-97.68	247.00		
	CMN017	26.05	-97.67	241.00		
	CMN020	26.05	-97.72	234.00		
	CMN028	26.06	-97.67	221.00		
	CMN029	26.11	-97.61	224.00		
	CMN030	26.12	-97.57	228.00		
	MGA001	28.75	-95.77	197.00		
	MGA002	28.76	-95.77	199.00		
	MGA003	28.77	-95.79	211.00		
	MGA004	28.77	-95.61	155.00		
	MGA008	28.79	-95.63	158.00		
	MGA005	28.80	-95.60	174.00		
	MGA007	28.80	-95.62	158.00		
	MGA006	28.80	-95.61	175.00		
	MGA010	28.83	-95.64	168.00		
	MGA009	28.83	-95.64	167.00		

Table 3.4: Measured shear wave velocity profiles in Texas (cont'd)

Source	Location	Latitude (deg)	Longitude (deg)	Reported V_{S30} (m/s)	Rock Unit Name	Period
Holzer et al. (2010)	BZA014	28.87	-95.59	248.00	Alluvium	Quaternary
	BZA004	28.87	-95.45	188.00		
	BZA015	28.88	-95.58	229.00		
	BZA016	28.88	-95.57	214.00		
	BZA017	28.88	-95.56	195.00		
	BZA019	28.88	-95.58	226.00		
	BZA005	28.89	-95.48	222.00		
	BZA018	28.89	-95.57	219.00		
	BZA006	28.90	-95.51	179.00		
	BZA007	28.91	-95.55	211.00		
	BZA002	28.98	-95.30	159.00		
	BZA003	28.98	-95.27	181.00		
	BZA001	28.98	-95.29	155.00		
	BZA020	29.01	-95.22	175.00		
	BZA013	29.04	-95.27	200.00		
	BZA011	29.06	-95.23	192.00		
	BZA008	29.06	-95.27	154.00		
	BZA012	29.06	-95.24	195.00		
	BZA009	29.07	-95.26	210.00		
	BZA010	29.07	-95.25	199.00		
Luminant Generation Company LLC (2009)	unknown location	32.30	-97.79	663.79	Glen Rose Formation	Cretaceous
	B-1000	32.30	-97.79	1035.47		
	B-1012	32.30	-97.79	1061.33		
	B-2000	32.30	-97.79	1199.23		
STP Nuclear Operating Company (2011)	STP 4	28.80	-96.04	271.30	Beaumont Formation (sand)	Quaternary
	STP 3	28.80	-96.04	279.76		
	STP 1	28.80	-96.04	284.83		
	STP 2	28.80	-96.04	288.50		
Exelon Nuclear Texas Holdings LLC (2008)	Victoria County Power Block	28.58	-97.00	238.74	Lissie Formation undivided	Quaternary
Hoar and Stokoe (1982)	1 Amoco Oil Refinery, Site No.2	29.40	-94.90	190.31	Beaumont Formation	Quaternary
	2 Amoco Oil Refinery, Site No.2	29.40	-94.90	203.95		
	1 Amoco Oil Refinery, Site No.1	29.40	-94.90	206.84		
	2 Amoco Oil Refinery, Site No.1	29.40	-94.90	207.62		
	3 Amoco Oil Refinery, Site No.1	29.40	-94.90	209.15		
	3 Amoco Oil Refinery, Site No.2	29.40	-94.90	216.09		
Stokoe and Mok (1987)	S. R. Bertron Electric Generating Station 1	29.70	-95.30	204.53	Beaumont Formation	Quaternary
	S. R. Bertron Electric Generating Station 2	29.70	-95.30	210.39		
	S. R. Bertron Electric Generating Station 3	29.70	-95.30	213.11		
	S. R. Bertron Electric Generating Station 4	29.70	-95.30	226.42		
Stokoe et al. (1983)	Site of Union Texas Petroleum Gas Plant near Sour Lake, Texas 1	30.10	-94.40	198.86	Beaumont Formation (sand)	Quaternary
	Site of Union Texas Petroleum Gas Plant near Sour Lake, Texas 2	30.10	-94.40	206.06		
	Site of Union Texas Petroleum Gas Plant near Sour Lake, Texas 3	30.10	-94.40	207.25		
Stokoe (1983)	American Petrofina Plant 1	29.80	-93.90	225.00	Alluvium	Quaternary
	American Petrofina Plant 2	29.80	-93.90	228.91		
	American Petrofina Plant 3	29.80	-93.90	232.01		

3.4. V_{S30} Proxy Method

Due to the lack of existing shear wave velocity profiles, there is a strong demand to measure V_{S30} values along Texas. However, since measurements can only be conducted at limited locations, a reliable V_{S30} proxy method is also needed to map the V_{S30} values for the whole State of Texas by exploiting these measurements. Generally, V_{S30} proxy can be done by geologic units or P-wave seismogram. Here, an overview of these existing V_{S30} proxy methods is presented.

3.4.1. V_{S30} Proxy by Geologic Units

3.4.1.1. West Coast America

Wills and Silva (1998) were the first to publish a geology-based V_{S30} proxy relationship for estimating V_{S30}. Their relationship was developed only for the state of California. It was based on a statistical study of 556 sites with measured V_{S30} values and known surface geology. They predominantly grouped sites into the following five main geologic categories, each with a number of sub-categories (refer to Table 3.5), except the Great Valley Sequence:

a) Quaternary Units with nine sub-categories

b) Tertiary Sedimentary Rocks with twelve sub-categories

c) Great Valley Sequence

d) Franciscan Complex with seven sub-categories

e) Crystalline Rocks with four sub-categories

When choosing the sites with measured V_{S30}, Wills and Silva (1998) used sites where geologic units are similar in the upper 30m and excluded sites where the soil profile has an abrupt geologic transition in the upper 30m. This kind of sites usually exist near the boundaries between two zones with distinct surface geologic conditions and mean V_{S30} value, so the estimated V_{S30} values in Table 3.5 may not be applicable for the boundary areas. In fact, since soil profiles in the upper 30m near the boundaries may not be able to be attributed to any single geologic unit, the problem to estimate V_{S30} values for these boundary areas may not be solved by the V_{S30} proxy method itself.

While average V_{S30} values and standard deviations were calculated for most of the geologic sub-categories, the variability of V_{S30} values within each sub-category could be considerable. For example, Figure 3.6 shows the distribution of 189 measured V_{S30} values for Quaternary alluvium as a sub-category in Quaternary Units (refer to Table 3.5). The V_{S30} values in this sub-category have a mean value of 284 m/s with a standard deviation of 85 m/s. However, the V_{S30} values often ranged from about 100 to 500m/s, with a few outliers up to 650 m/s. According to NEHRP site classification (Table 3.6), this wide range of V_{S30} values includes soil profiles from Site Class C to E. Thus, further sub-categorization within units of similar geologic age is clearly important.

Furthermore, the mean V_{S30} values for some sub-categories may fall near the boundary V_{S30} values between two adjacent site classes. For instance, the Quaternary (older) alluvium has a mean V_{S30}

value of 368m/s with a standard deviation of 80m/s, as shown in Table 3.5. The mean V_{S30} value is near the boundary V_{S30} value (i.e., 360m/s) between Site Class C and D. Therefore, it would be difficult to determine which site class the Quaternary (older) alluvium belongs to. A good solution is to resort to other V_{S30} proxy methods when encountering such a situation.

Table 3.5: Geology-based V_{S30} proxy relationships for California from Wills and Silva (1998)

	Geologic unit	#	Vs30	std	type S-
Quaternary units	Qi (intertidal mud)	38	159	45	E
	af/Qi (Fill over intertidal mud)	19	204	50	D
	Quaternary alluvium	189	284	85	D
	Qal (including thin alluvium)	237	298	92	
	Quaternary (older) alluvium	79	368	80	C?
	Qs	17	329	54	D
	Qm (marine terraces)	4	278	47	D
	QT (Merced Fm)	3	316		D
	QT (Santa Clara, Ukiah, & Paso Robles)	8	512	204	C
Tertiary sedimentary rocks	Briones	1	776		C?
	Butano	4	414	18	C
	Castaic	1	550		C
	Claremont	1	552		C
	Colma	2	442		C
	Lambert shale	1	576		C
	Pico Fm (including Fernando & Repetto)	7	362	63	?
	Poway Grp	1	345		?
	Puente & Modelo Fms	9	401	103	C
	Purisima Fm	1	295		?
	Topanga	2	406		C
	Towsley	2	419		C
	All Tertiary sedimentary rocks	40	421	109	C
Great Valley seq.	Panoche Fm	4	864		B
Franciscan complex	KJF (undifferentiated)	8	1171	223	B
	KJF chert	1	582		?
	KJF greenstone	2	715		?
	KJF "sheared"	2	482		C
	KJF ss	12	966	437	B
	KJF ss & greenstone	1	584		?
	serpentine	3	549		C
	All KJF	29	902	387	B
crystalline rocks	Tertiary volcanic rocks	7	685	195	C
	gneiss	1	825		B
	"granitic"	8	767	279	?
	granitic grus	1	384		C
	All plutonic and metamorphic	18	715	242	C

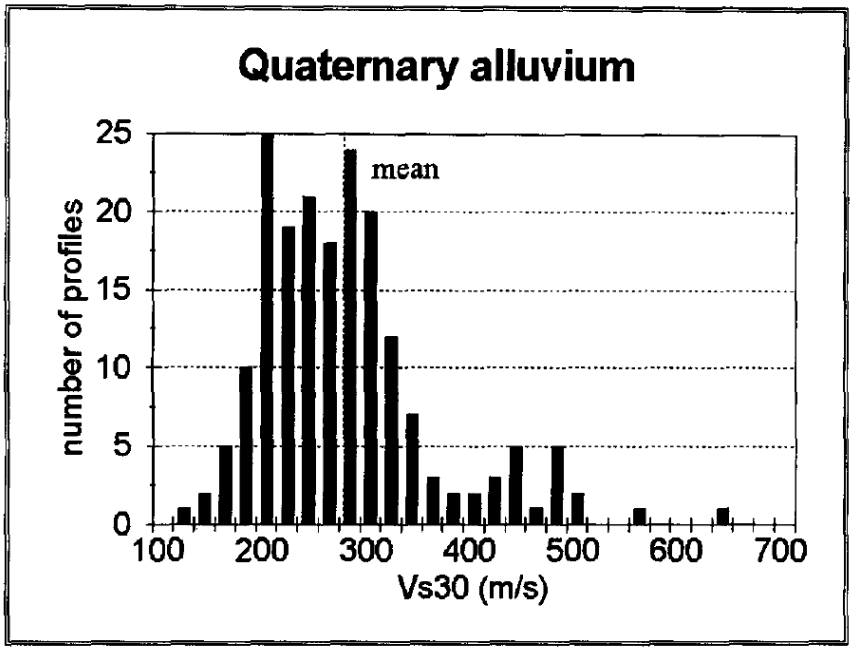

Figure 3.6: Histogram showing the distribution of all measured V_{S30} values for Quaternary alluvium from Wills and Silva (1998)

Table 3.6: NEHRP seismic site classes based on V_{S30}, from BSSC (2001)

Site Class	Soil Profile Name	V_{S30} (m/s)	
		Minimum	Maximum
A	Hard rock	>1500	
B	Rock	>760	1500
C	Very dense soil and soft rock	>360	760
D	Stiff soil	180	360
E	Soft soil		<180

Wills et al. (2000) developed a site-condition map for the State of California based on geology and NEHRP site classification, as shown in the left of Figure 3.7. In their approach, geologic units were first grouped with similar age and properties (e.g., grain size, hardness). Then, a V_{S30} class based on NEHRP site classification was assigned to each group. For geologic units which had a typical V_{S30} value near the boundary value of two V_{S30} classes, intermediate classes (i.e., class BC, CD, DE) were assigned and the mean V_{S30} values of the two adjacent classes were set as the start and end values for corresponding intermediate classes. Groups with the same V_{S30} class or intermediate class were regarded as one site condition, so there are in total 7 site conditions, namely B, BC, C, CD, D, DE, E. To validate the accuracy of the NEHRP site classification map, the 556 sites with measured V_{S30} values in Wills and Silva (1998) were plotted onto the map to check if the measured V_{S30} values fall in the site classification assigned to the site location. The result was 74% of the sites with measured V_{S30} values fell in the expected site classifications. Many of the

misclassified sites have a soil profile where harder material at shallow depth were found below a thin, young alluvium at the surface (Wills and Clahan 2006). This phenomenon justifies the statement that sites where the soil profile has an abrupt geologic transition in the upper 30m may not be classified properly only by geology-based V_{S30} proxy relationships.

Wills and Clahan (2006) refined the geology-based V_{S30} proxy relationship developed by Wills et al. (2000) by using 19 geologic categories instead of the 7 site conditions, as shown in the right of Figure 3.7 and Table 3.7. Three features are used to describe each category. The first feature is the general geologic unit (e.g., Qal, Quaternary alluvium) and the second feature is a qualitative description of the unit (i.e., thickness and particle size). The last feature is the location of each category within California, which indicates that local conditions are important in some cases and caution should be exercised when extrapolating region-specific studies to other areas. By following this V_{S30} proxy relationship the originally misclassified sites in the site-condition map developed by Wills et al. (2000) fell in the right category, but the cost is that each category is specifically for a certain area and the geology-based V_{S30} proxy relationship loses generality.

While it is possible that geology-based V_{S30} proxy relationships developed for California may provide some insights into V_{S30} estimates in Texas, most geology units shown in Table 3.7 refer to very specific areas in California, for which similar conditions may not exists in Texas, or may only exist in a small area. For instance, Qal (Quaternary alluvium) within California is divided into seven sub-categories in Table 3.7, but Qal is very limited in Texas (refer to Figure 3.2) and only exists along river drainages in the Gulf Coastal Plains. Furthermore, Mesozoic and Paleozoic formations account for large parts of Central Texas, and these units are not referred to in Table 3.5 and Table 3.7.

3.4.1.2. Central and Eastern Region of North America

Kottke et al. (2012) developed geology-based V_{S30} proxy relationships for central and eastern North America, as the geologic conditions are quite different from that of western North America. They developed their V_{S30} proxy by dividing the geologic conditions in central and eastern North America into 3 main types: glaciated, non-glaciated and residual soils, as shown in Table 3.8. Each main type was split based on geologic age, resulting in 5 major units, and further sub-divided based on depositional environment, resulting in 19 categories in total. The V_{S30} values reported for non-glaciated units are mean values based on Vs measurements. For glaciated units, the V_{S30} values are computed from a simple calculation based on a two-layer model. The first layer is a sediment layer of specified thickness (refer to Table 3.8) and shear wave velocity typical of an analogous soil type in non-glaciated units. The second layer is a rock layer with a shear wave velocity of 3000m/s. Due to a lack of data, V_{S30} values for residual soils, Old Glacial Sediments and some of the Non-Glacial Sediments were not proposed. Since glacial deposits do not exist in Texas, the only available data in Table 3.8 that might be applicable to Texas are the V_{S30} values for Young and Old Non-Glacial Sediments.

Table 3.7: Geology-based V_{S30} proxy relationships for California from Wills and Clahan (2006)

Geologic Unit	Geologic Description	No. of profiles	Mean Vs30	S.D.	Vs30 from Mean of ln	S.D. of ln	Mean of ln of Vs30
Qi	Intertidal Mud, including mud around the San Francisco Bay and similar mud in the Sacramento/San Joaquin delta and in Humboldt Bay	20	160	39	155	0.243	5.046
af/qi	Artificial fill over intertidal mud around San Francisco Bay	44	217	94	202	0.357	5.310
Qal, fine	Quaternary (Holocene) alluvium in areas where it is known to be predominantly fine	13	236	55	229	0.238	5.437
Qal, deep	Quaternary (Holocene) alluvium in areas where the alluvium (Holocene and Pleistocene) is more than 30 m thick; generally much more in deep basins	161	280	74	271	0.250	5.604
Qal, deep, Imperial V	Quaternary (Holocene) alluvium in the Imperial Valley, except sites in the northern Coachella Valley adjacent to the mountain front	53	209	31	207	0.135	5.335
Qal, deep, LA Basin	Quaternary (Holocene) alluvium in the Los Angeles basin, except sites adjacent to the mountain fronts	64	281	85	270	0.275	5.599
Qal, thin	Quaternary (Holocene) alluvium in narrow valleys, small basins, and adjacent to the edges of basins where the alluvium would be expected to be underlain by contrasting material within 30 m	65	349	89	338	0.244	5.825
Qal, thin, west LA	Quaternary (Holocene) alluvium in part of west Los Angeles where the Holocene alluvium is known to be thin, and is underlain by Pleistocene alluvium	41	297	45	294	0.150	5.684
Qal, coarse	Quaternary (Holocene) alluvium near fronts of high, steep mountain ranges and in major channels where the alluvium is expected to be coarse	18	354	82	345	0.223	5.845
Qoa	Quaternary (Pleistocene) alluvium	132	387	142	370	0.273	5.916
Qs	Quaternary (Pleistocene) sand deposits, such as the Merritt Sand in the Oakland area	15	302	46	297	0.171	5.697
QT	Quaternary to Tertiary (Pleistocene–Pliocene) alluvial deposits such as the Saugus Formation of southern California, Paso Robles Formation of central coast ranges, and the Santa Clara Formation of the Bay Area.	18	455	150	438	0.266	6.083
Tsh	Tertiary (mostly Miocene and Pliocene) shale and siltstone units such as the Repetto, Fernando, Puente, and Modelo Formations of the Los Angeles area	55	390	112	376	0.272	5.930
Tss	Tertiary (mostly Miocene, Oligocene, and Eocene) sandstone units such as the Topanga Formation in the Los Angeles area and the Butano sandstone in the San Francisco Bay area	24	515	215	477	0.386	6.169
Tv	Tertiary volcanic units including the Conejo Volcanics in the Santa Monica Mountains and the Leona Rhyolite in the East Bay Hills	3	609	155	597	0.240	6.392
Kss	Cretaceous sandstone of the Great Valley Sequence in the central Coast Ranges	6	566	199	539	0.332	6.291
serpentine	Serpentine, generally considered part of the Franciscan complex	6	653	137	641	0.204	6.464
KJf	Franciscan complex rock, including melange, sandstone, shale, chert, and greenstone	32	782	359	712	0.432	6.569
xtaline	Crystalline rocks, including Cretaceous granitic rocks, Jurassic metamorphic rocks, schist, and Precambrian gneiss	28	748	430	660	0.489	6.493

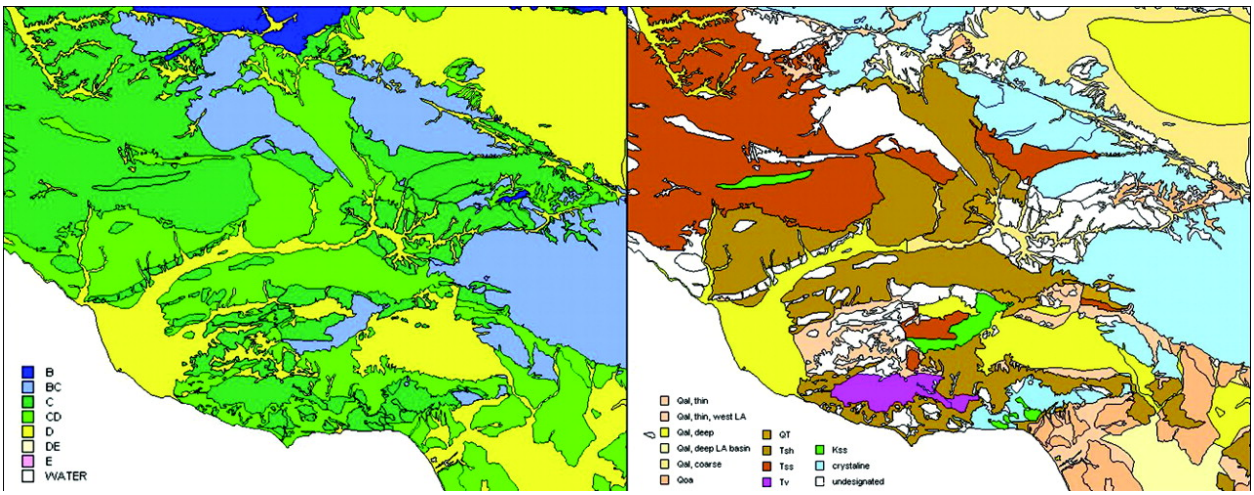

Figure 3.7: California maps showing 7 site conditions in the left and 19 geologic categories. In the right from Wills and Clahan (2006)

Table 3.8: Geology-based V_{S30} proxy relationships for central and eastern North America from Kottke et al. (2012)

Major Unit (Age)	Sub-unit	Abbrev.	Thick. (m)	Soil Class	Mean V_{s30} (m/s)	σ_{lnV} (m/s)
Old Glacial Sediments (Older than Wisconsin)	Glaciomarine and Lacustrine	OGm	9	ONm	--	--
	Outwash and alluvium	OGo	7	ONa	--	--
	Tills	OGt	16	ONa	--	--
Young Glacial Sediments (Wisconsin and younger)	Glaciomarine and Lacustrine	YGm	8	YNm	520	0.53
	Outwash and alluvium	YGo	11	YNa	470	0.67
	Tills	YGt	16	YNa	300	0.45
	Discontinuous Till	YGd	5	YNa	1050	0.39
Old Non-Glacial Sediments (Mid-Pleistocene and older)	Alluvium	ONa			--	--
	Colluvium	ONc			--	--
	Loess	ONl			250	0.11
	Lacustrine, Marine and Marsh	ONm			290	0.22
Young Non-Glacial Sediments (Holocene and late Pleistocene)	Alluvium	YNa			220	0.14
	Colluvium	YNc			--	--
	Loess	YNl			--	--
	Lacustrine, Marine and Marsh	YNm			230	0.12
	Beach, dune, and sheet sands	YNs			210	0.18
Residual Sediments	Residual from metamorphic and igneous rock	RRm			--	--
	Residual from sedimentary rock	RRs			--	--
	Residual from soils	RSs			--	--

Parker et al. (2016) developed a new geology-based V_{S30} proxy relationships for central and eastern North America based on statistical analysis of 2754 sites with measured V_{S30} values. The sites were first grouped by attributes including geologic age, lithology, glaciation history and location relative to know basins. An F-test (Cook and Weiberg, 1999; Akritas, 2015) was performed to test if there are distinct trends in the log mean of V_{S30}, standard deviation of the log mean and trend with 30 arc-sec slope gradient. The sites were regrouped until all groups passed the F-tests. Finally, the sites were classified into 16 groups, as shown in Table 3.9. The relationship between the V_{S30} values and 30 arc-second slope gradients are also investigated by semi-log and log-log regression:

$$\ln(V_{s30}) = c_0 + c_1 s \tag{3-1}$$

$$\ln(V_{s30}) = c_2 + c_3 \ln(s) \tag{3-2}$$

where V_{S30} is the mean shear wave velocity in the upper 30m in units of m/s, s is the 30 arc-second slope gradients in units of m/m, and c_0, c_1, c_2, c_3 are regression parameters.

If either c_1 or c_3 exceed their 95% confidence intervals, there are statistically significant relationship between gradient and V_{S30} and the value of these parameters would be reported in Table 3.9. Table 3.9 provides useful reference values for Cenozoic units, but still only limited values for Mesozoic and Paleozoic units, which are common in Texas. It also shows geomorphology such as basins may have a significant effect on local V_{S30} values.

Table 3.9: Geology-based V_{S30} proxy relationships for central and eastern North America from Parker et al. (2016)

Category							Group Moments		Gradient Relationship					
Group	Era	Period	Epoch	Prior Glaciation?	Other Criteria	N	μ_{lnV} (m/s)	σ_{lnV}	LL/SL*	c_0	c_1	c_2	c_3	σ_{lnV}
1	C	Q	H	No	Alluvium, fluvial, & deltaic	301	209	0.226						
2	C	Q	H	No	All other lithology	166	226	0.297						
3	C	Q	H	Yes	In Ottawa, Canada	981	232	0.675	SL	5.38	9.30			0.673
4	C	Q	H	Yes	Not in Ottawa, Canada	46	307	0.738	LL			8.06	0.389	0.655
5	C	Q	Pli	No		213	250	0.277						
6	C	Q	Pli	Yes	In Ottawa, Canada	167	600	0.678	LL			7.19	0.147	0.666
7	C	Q	U	No	Not in sedimentary basin	46	257	0.342						
8	C	Q	U	No	In sedimentary basin	208	280	0.288						
9	C	Q	U	Yes	Not in sedimentary basin	56	202	0.318	SL	5.23	37.4			0.291
10	C	T				109	319	0.335	LL			6.14	0.071	0.312
11	M					21	792	0.68						
12	P				In the Illinois Basin	48	272	0.525						
13	P			No	Not in the Illinois Basin	201	483	0.627						
14	P			Yes	Not in the Illinois Basin	125	694	0.831						
15	p€			No		21	987	0.892						
16	p€			Yes		63	1250	0.873						
*LL for log-log relationship, SL for semi-log relationship in the Y direction (Eqs. 4-5).														

3.4.1.3. Other Areas of the World

Cox et al. (2011) conducted a seismic site classification microzonation for Port-au-Prince, Haiti based on 35 shear wave velocity profiles and a regional geologic map, as shown in Figure 3.8. The representative V_{S30} value for each geologic unit is taken as the median V_{S30} value for all V_{S30} values derived from shear velocity profiles for corresponding geologic units, as shown in Table 3.10.

Cox et al. (2011) also noted that further efforts are required for accurate site classification. For instance, potential presence of soft clay or liquefiable soil may alter the classification of some areas with Holocene alluvial deposits and coastal artificial fills from Site Class C or D to Site Class E or F. Since such details vary from region to region, it would be important to perform specific investigations of the targeted area.

Stewart et al. (2014) compiled shear wave velocity profiles for Greece and tested a geology-based V_{S30} proxy method (Wills and Clahan 2006), a gradient-based V_{S30} proxy method (Wald and Allen 2007) and a terrain-based V_{S30} proxy method (Yong et al. 2012). Results show all methods are biased towards the collected data. Then Stewart et al. (2014) developed a geology-topography hybrid V_{S30} proxy method for Greece similar to what has already been discussed above in regards to Parker et al. (2016). Sites were grouped by geological units and Eq. (3.2) were used to correlate gradient with V_{S30} in each geological unit. Therefore, there was one pair of parameters (c_2, c_3) for each geological unit except the Mesozoic unit, where no strong relationship between gradient and V_{S30} was found and simply a mean V_{S30} value was assigned. The whole process of testing existing V_{S30} proxy methods and development of new V_{S30} proxy methods suggest the V_{S30} proxy methods developed in one area may not be not be proper for other areas and new V_{S30} proxy methods for the area of interest should be considered.

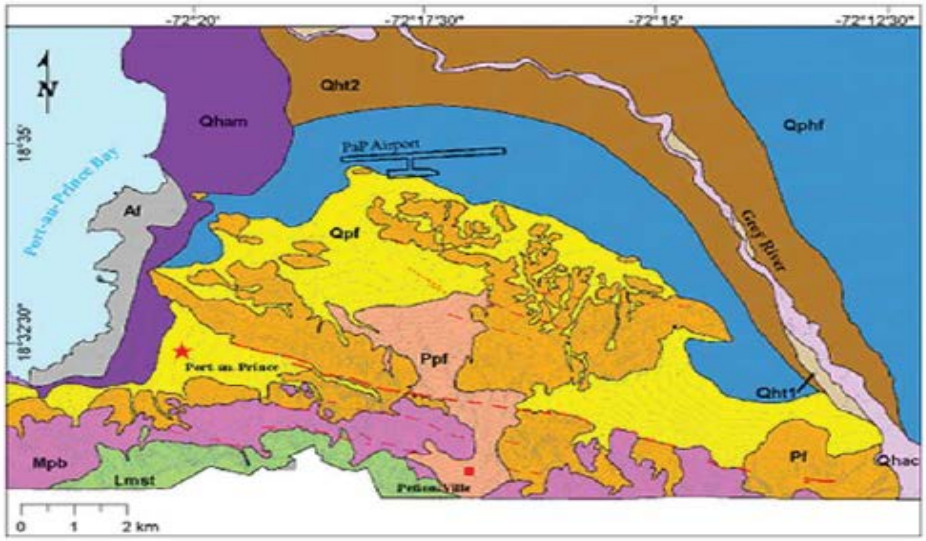

Explanation

Af	Artificial fill forming reclaimed land west of the mapped 1785 shoreline
Qhac	Stream channel alluvium; typically well-sorted, bedded, unconsolidated sand, silty sand, and gravel within the active channels of major streams
Qham	Marine/estuarine deposits interfingered with alluvial fan deposits and local fill
Qht1	Lower alluvial terrace deposits/surfaces within areas of historic flood inundation
Qht2	Elevated alluvial terrace deposits/surfaces bordering major streams and margins of intermontane valleys
Qphf	Alluvial fan/plain deposits
Qpf	Fan deposits forming steep fans at the rangefront
Ppf	Broad, deeply incised strath surface (or thin deposit veneer) developed over Pliocene fan
Pf	Pliocene fan deposits forming a deeply dissected paleofan complex along the rangefront
Mpb	Fanglomerate/talus deposits consisting of coarse, angular "breccia"
Lmst	Limestone bedrock exposed along rangefront

Faults - Long dashes indicate relatively high degree of confidence on location
Short dashes express less certain location

Inferred primary fault cutting Mio-Pliocene fan deposits

Inferred secondary fault cutting Mio-Pliocene fan deposits

Figure 3.8: Geologic map for Port-au-Prince, Haiti from Cox et al. (Cox et al. 2011)

Table 3.10: Median V_{S30} values for surficial geologic units (Cox et al. 2011)

Geologic Unit	Number of Profiles	Median V_{S30} (m/s)	NEHRP Site Class
Af	3	278	D
Qham	3	335	D
Qht2	1	346	D
Qphf	2	480	C
Qpf	8	499	C
Ppf	1	504	C
Pf*	7	564	C
Mpb	3	513	C
Lmst	1	1014	B

To get an idea of the similarity of V_{S30} values for the same geological units in different areas, Typical V_{S30} values of Holocene units are summarized and presented in Figure 3.9. Note the data collected from glaciated areas in Central and Eastern North America are excluded since it is expected to yield distinct V_{S30} values for geologic conditions that do not exist in Texas. While all mean values of V_{S30} fall in Site Class D, the four sets of data clearly show distinct trends. V_{S30} values for Holocene soils in Central and Eastern North America are generally lower than V_{S30} values in other areas and may even fall in Site Class E, which has high amplification factors. Another interesting phenomenon is that Greece, which has neither the most collected data nor largest area, shows the highest variance of V_{S30} values and has more than 40% percent possibility to fall in Site Class C. This comparison shows that while geology-based V_{S30} proxy may provide some good reference to start with, specific investigation into correlations between V_{S30} values and local geological conditions are usually needed.

3.4.2. V_{S30} Proxy by Topographic Slope

The idea behind using topographic slope as a proxy for estimating V_{S30} is almost intuitive: stiff (i.e., high shear wave velocity) materials are more likely to support a steep slope after millions of years of geotectonic movement and weathering. While void ratio and mean effective stress are the main factors controlling shear modulus of soil (Fumal and Tinsley 1985), mean effective stress does not vary greatly from site-to-site over the top 100 ft/30 m of subsurface. However, void ratio, particle size/shape, and cementation can vary significantly from site-to-site and these factors have a strong influence on both topographic slope and shear stiffness in soils. For rock, shear modulus is mainly determined by hardness and fracture spacing, which are also indicated by topography.

Wald and Allen (2007) first correlated V_{S30} with topographic slope on the basis of large datasets of measured V_{S30} values from the U.S., Taiwan and Italy. The data are divided into two categories according to local tectonic structure: active tectonic regions and stable continental regions. Wald and Allen (2007) suggest areas with a mean slope less than 0.05m/m be classified as a stable continental region, otherwise the area should be classified as an active tectonic region. Correlations

between V_{S30} and topographic slope are developed for each category, as shown in Figure 3.10 and Table 4.9. Thus, V_{S30} estimates can be derived if local topographic data is available.

One obvious advantage of the slope-based V_{S30} proxy method is the ease with which it can be applied over large regions. The only data required is a regional topographic map, which is easy to obtain with the aid of satellite imaging. The other advantage over geology-based V_{S30} proxy methods is that unlike geologic units, topographic slope is a quantitative factor that enables smooth transitions of V_{S30} over large areas. Wald and Allen (2007) developed a V_{S30} map for the Central and Eastern U.S., including Texas, as shown in Figure 3.11. While the general qualitative trend of the map is consistent with basic conditions in Texas, note that data used to develop the map involves no data from Texas so general and local bias may exist. For example, when the slope-based V_{S30} proxy relationships were applied to Salt Lake City, Utah, the V_{S30} estimates were found to be significantly higher, on average, than those from measured Vs profiles, as the green crosses were generally lower than the color-coded polygons shown in Figure 3.10(a). Wald and Allen (2007) also found V_{S30} and topographic slope are hard to correlate for specific geological terrains and processes. The explanation behind the inconsistency is that other mechanism may also have a significant influence on V_{S30}, such as aging, weathering, and cementation. Besides that, different resolution in topographic data may affect the correlation, especially for large-scale mapping. Nevertheless, topographic slope is a valuable parameter worth investigating for estimating V_{S30} and the correlation may be adapted to conditions in Texas by utilizing measured V_{S30} values. Color-coded polygons represent V_{S30} and slope ranges are consistent with ranges given in Table 3.11 from Wald and Allen (2007).

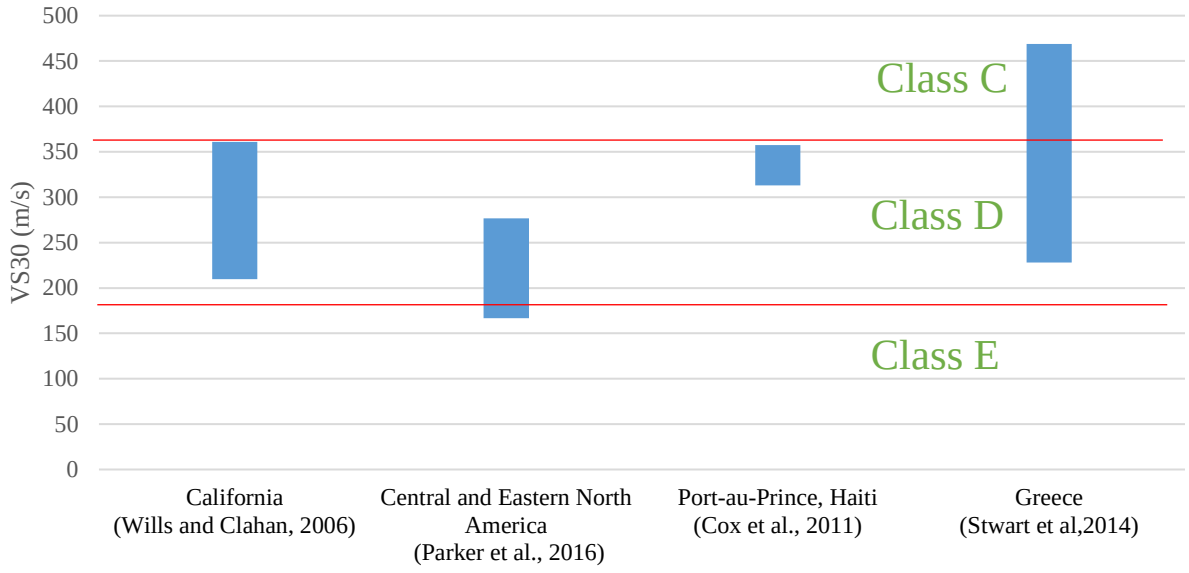

Note: boxes show V_{S30} from Mean of ln (V_{S30}) $\pm$ Standard Deviation of ln (V_{S30})

Figure 3.9: Typical V_{S30} values for Holocene units in different areas

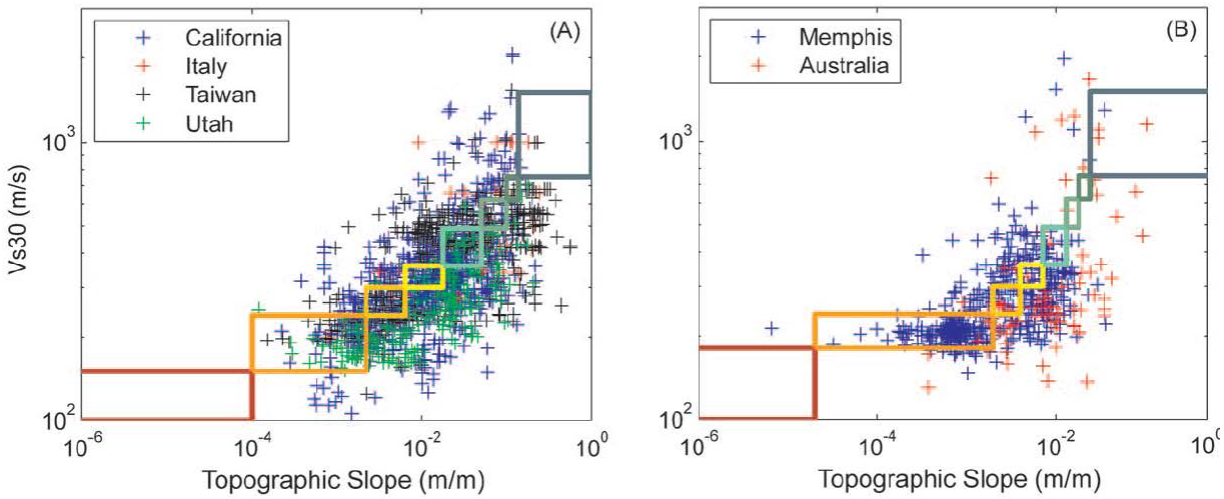

(a) Active tectonic region (b) Stable continental region (Wald and Allen 2007)

Figure 3.10: Correlations of measured V_{S30} (m/sec) versus topographic slope (m/m)

Table 3.11: Summary of slope ranges for V_{S30} categories from Wald and Allen (2007)

Class	V_S^{30} Range (m/sec)	Slope Range (m/m)	
		Active Tectonic	Stable Continent
E	<180	<1.0E−4	<2.0E−5
	180–240	1.0E−4–2.2E−3	2.0E−5–2.0E−3
D	240–300	2.2E−3–6.3E−3	2.0E−3–4.0E−3
	300–360	6.3E−3–0.018	4.0E−3–7.2E−3
	360–490	0.018–0.050	7.2E−3–0.013
C	490–620	0.050–0.10	0.013–0.018
	620–760	0.10–0.138	0.018–0.025
B	>760	>0.138	>0.025

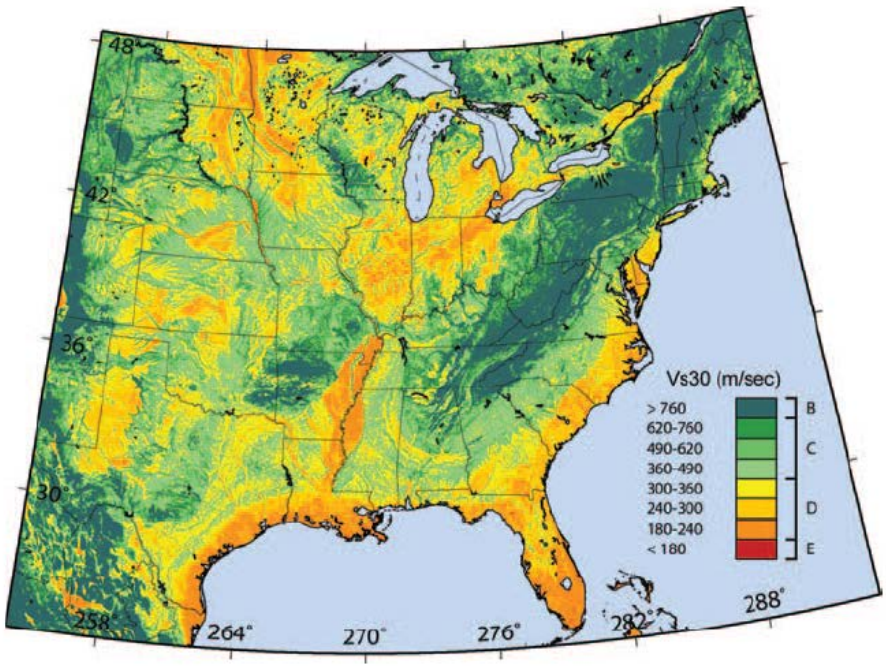

Note: This figure is derived from topographic slope and slope-V_{S30}correlations for stable continental regions from Wald and Allen (2007).

Figure 3.11: Estimated V_{S30} map for the continental United States east of the Rocky Mountains

Yong et al. (2008) developed another topography-based V_{S30} proxy method by applying an integrated digital imaging analysis approach. The method was divided into 5 steps:

1) Identify slopes from the relative Digitalized Elevation Model (rDEM) and assign terrain units as classes including mountains, piedmonts and basins according to slopes.
2) Discriminate the lithology using spectral features in Advanced Spaceborne Thermal Emission and Reflection Radiometer (ASTER). For details refer to Kahle and Rowan (1980), Abrams and Hook (1995) and Yong (2007).
3) Compare the spatial distribution of lithology determined in step 2 with terrain units determined in step 1 to verify the correlation between physical properties and terrain units.
4) Assign the range of shear-wave velocities for all terrain units based on Wills and Silva (1998).
5) Verify the identified lithology with independent geological investigations.

Yong et al. (2011) applied similar technique for seismic microzonation of Port-au-Prince, Haiti except measured shear-wave velocity profiles from Cox et al. (2011) were used for calibration. The resulted seismic microzonation agreed well with that from Cox et al. (2011).

Essentially this method correlates topography with geology and used geology-based V_{S30} proxy methods for seismic microzonation. It uses more satellite data than Wald and Allen (2007) to establish a robust correlation between topography with geology. However, on the crucial step of assigning V_{S30} values it inherits the advantage and disadvantages in geology-based V_{S30} proxy

methods. Thus, an accurate correlation between local geology and V_{S30} values is the prerequisite for this method.

3.4.3. V_{S30} Proxy by Terrain

Yong et al. (2012) introduced a terrain-based V_{S30} proxy method for the State of California. The approach consists of two steps. The first step is to classify the targeted area into different terrain types. An automated topography classification scheme introduced by Iwahashi and Pike (2007) was adopted to perform the classification based on Shuttle Radar Topography Mission Digital Elevation Models (30 arcsec SRTM DEMs). In the scheme three parameters representing the geometric signature were specified: slope gradient, local convexity and surface texture. Slope gradient was the most important parameter of all the three and could be easily inferred from DEMs. Local convexity was defined as the percentage of convex-upward cells with an arbitrary 10-cell radius and was a necessary parameter to classify areas with low-relief features. Local convexity can be derived from DEMs by applying an image-processing operation called a Laplacian filter. Surface texture is used to quantify topographic spacing in DEMs. It was defined as the number pits and peaks within a radius of ten cells. The pits and peaks were identified from differences between the original DEM and a second DEM derived by a spatial convolution filtering technique called median filtering. After the three parameters were extracted from the SRTM DEM, a straightforward process was applied to divide the targeted area into 16 terrain types based on the mean value of all three parameters.

To better illustrate the terrain type determination process, after each partition the group which has a value higher than the mean value is labelled as *Hi*, whereas the group which has a value lower than the mean value is labelled as *Li*. Here, *i* represents the corresponding parameter used for partitioning, where *i* = *g*, *c*, *t* refers to the slope gradient, local convexity, and surface texture, respectively. For example, group HgLc means data in this group has a gradient higher than the mean gradient in the first partition and a convexity lower than mean convexity in the second partition. The process can be described by these steps:

1) Calculate the mean gradient Mg_0, mean convexity Mc_0 and mean texture Mt_0 of the whole dataset.
2) Do the first partition on the whole dataset based on gradient using Mg_0. Results are either Hg or Lg.
3) Do the second partition on the Hg group based on convexity using Mc_0. Results are either HgHc or HgLc.
4) Do the third partition on the HgHc and HgLc groups based on texture using Mt_0. Results are either HgHcHt, HgHcLt, HgLcHt, or HgLcLt. These are the first four final terrain types.
5) Calculate the mean gradient Mg_1, mean convexity Mc_1 and mean texture Mt_1 of the group Lg.
6) Repeat step 1 for the Lg group. Meaning re-partition the Lg group based on gradient using Mg_1. Results are either LgHg or LgLg.

7) Repeat step 2 for only the LgHg group. Meaning, re-partition the LgHg group based on convexity using Mc1. Results are either LgHgHc or LgHgLc.

8) Repeat step 3 for both the LgHgHc and LgHgLc groups. Meaning, re-partition these groups based on texture using Mt1. Results are either LgHgHcHt, LgHgHcLt, LgHgLcHt, LgHgLcLt. These are the fifth through eighth final terrain types.

9) Calculate the mean gradient Mg_2, mean convexity Mc_2 and mean texture Mt_2 of the group LgLg.

10) Repeat step 1 for the LgLg group. Meaning re-partition the LgLg group based on gradient using Mg_2. Results are either LgLgHg or LgLgLg.

11) Repeat step 2 for both groups. Meaning re-partition the LgLgHg and LgLglg groups based on convexity using Mc_2. Results are either LgLgHgHc, LgLgHgLc, LgLgLgHc, LgLgLgLc.

12) Repeat step 3 for all resulted groups in step 9. Meaning re-partition the LgLgHgHc, LgLgHgLc, LgLgLgHc and LgLgLgLc groups based on texture using Mt_2. Results are the last eight final groups.

Readers can also refer to Figure 3.12 and Figure 3.13 for the whole process. Note Figure 3.12 and Figure 3.13 provides the partition methods to group areas into 8, 12 and 16 terrain types. The principles are essentially the same and the method to group areas into 16 terrain types are used here. In Figure 3.12, criteria are mean values of slope gradient, local convexity, and surface texture, which change to accommodate increasingly low-relief topography depending on number of classes requested (8, 12, or 16). Grid cells steeper than the mean gradient of the study area are distributed among classes 1–4 by first threshold calculation in all three options; for an eight-class output, the remaining cells fall into classes 5–8; for 12 classes, the latter cells are instead allotted among classes 5–12 by reduced parameter means (second threshold); for 16 classes, cells not placed in classes 1–8 are similarly parsed at the third threshold into classes 9–16.

By applying this process Yong et al. (2012) divided California into 16 terrain types, as shown in Figure 3.14. Yong et al. (2012) used 853 measured and inferred V_{S30} values (locations shown in Figure 3.14) to assign average values in each terrain type, except terrain type 13 due to a lack of data, as shown in Figure 3.15. Yong et al. (2012) also compared this method with the geology-based method of Wills et al. (2000) and the topography-based method of Wald and Allen (2007) based on the 853 measured and inferred V_{S30} values. Results showed that the terrain-based method had the lowest typical standard deviation. Yong et al. (2012) stated this method took into account both the geology and topography information so it was more robust than a proxy method based solely on either geology or topography.

The key step in most V_{S30} proxy methods is to classify areas into meaningful groups that could be representative of common shear wave velocity. While personal knowledge and experience are heavily involved in this step for geology- and topography-based methods, this terrain-based method is relatively automatic and objective. Classifications are done only according to relative values of local areas (i.e., mean values of slope gradient, local convexity and surface texture). This feature enables application of this method to any part of the world without any modification.

However, typical V_{S30} values assigned to each terrain type in one area of the world may provide little information for the same terrain type in other areas because they may have distinct shear stiffness properties relative to the absolute mean values of slope gradient, local convexity and surface texture. Thus, this method heavily depends on the abundance of existing local measured and reliably inferred V_{S30} values. For now, only a limited number of Vs profiles are available in Texas and most of them are located along the Gulf Coastal Plain. More data need to be collected to apply this method for Texas.

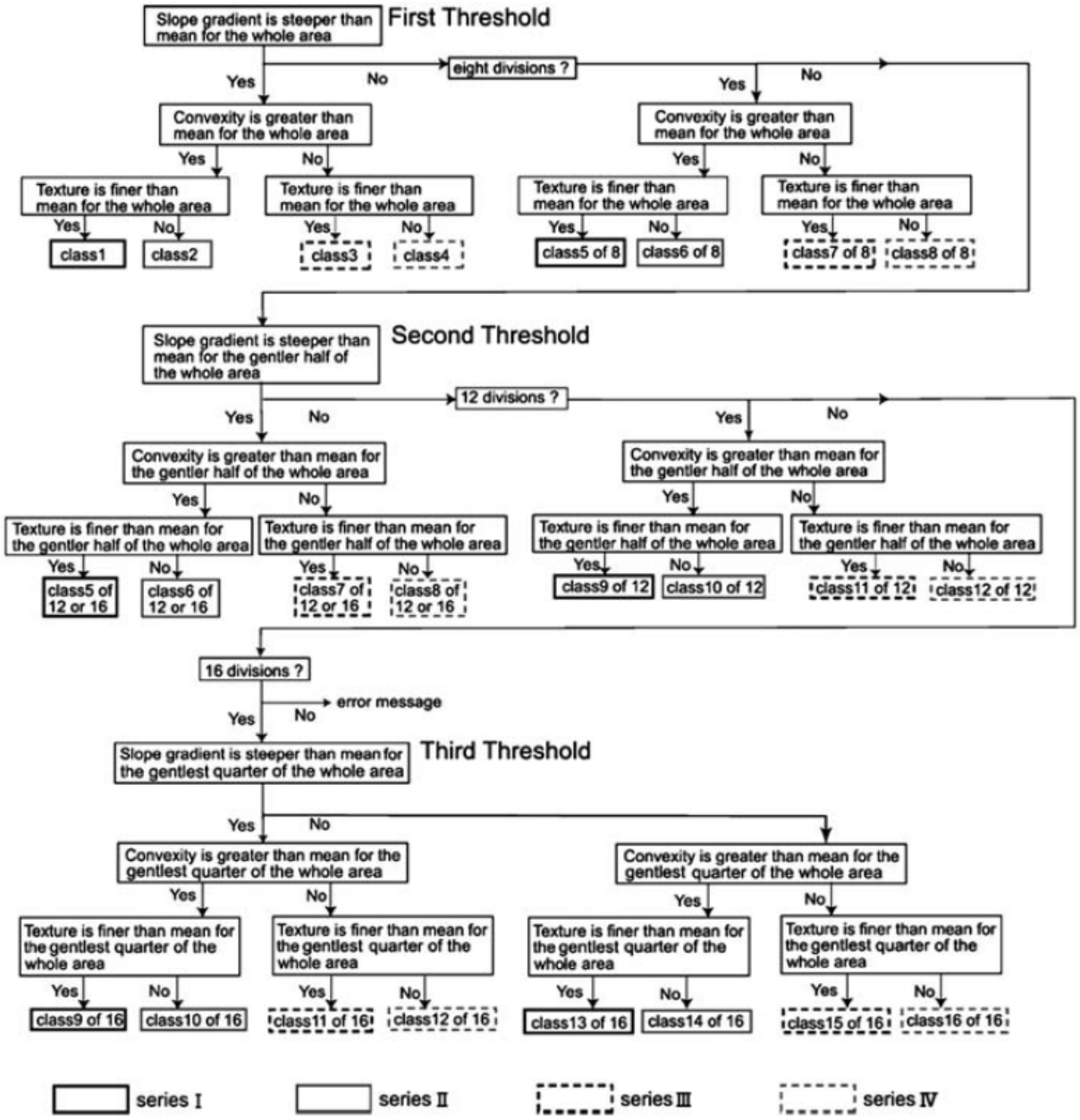

Figure 3.12: Flow chart (Iwahashi and Pike 2007) for automated nested-means classification of topography

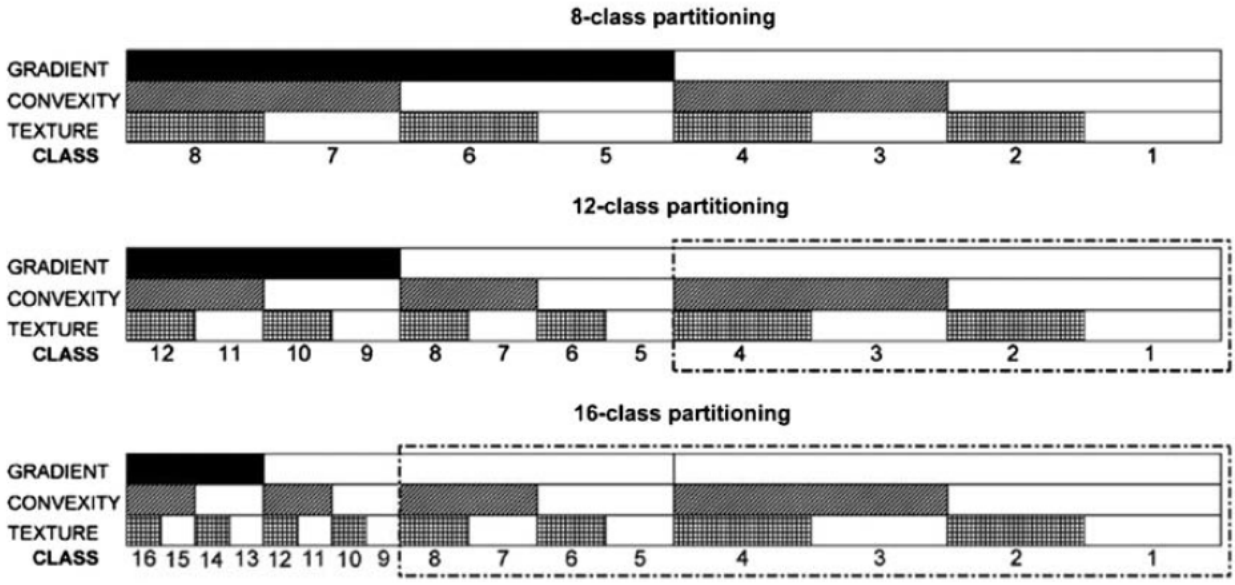

Note: sequence of operations proceeds from top down. Shaded rectangles represent grid cells below the mean of variable in that row; open rectangles are cells above the mean; rectangles within two dot–dashed boxes are same as those immediately above. Rectangle size is symbolic only and does not represent number of grid cells.

Figure 3.13: Nested-means half/half partitioning shown diagrammatically (Iwahashi and Pike 2007) for gray-scaled images of three input variables and 8, 12, and 16 output classes

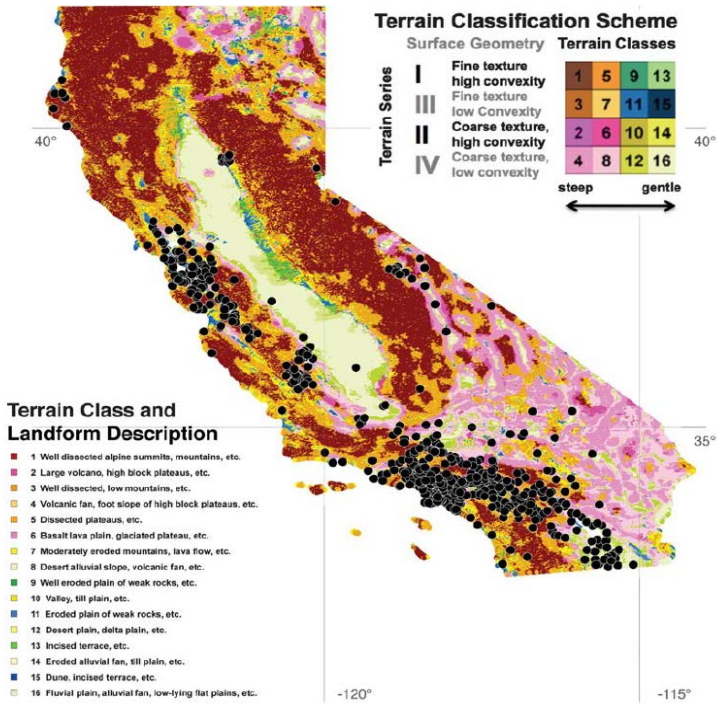

Figure 3.14: Terrain map of California (Iwahashi and Pike 2007) with locations (black circles) of 853 V_{S30} values (Yong et al. 2012)

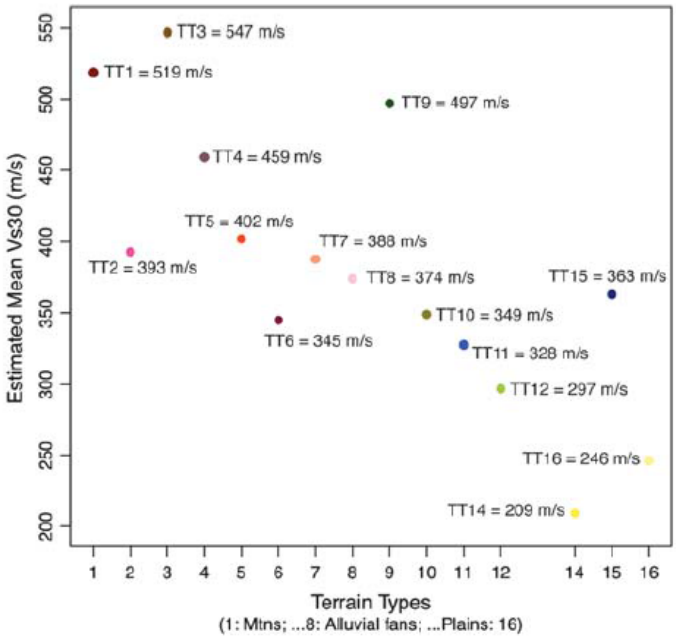

Note: No estimate is provided for Terrain-type 13 (Yong et al. 2012)

Figure 3.15: Plot describing mean V_{S30} values found in terrain types in California

3.4.4. V_{S30} Proxy by P-wave Seismogram

Kim et al. (2016) proposed a new method to infer V_{S30} by P-wave seismogram. The theoretical background is an analytic expression of the radial displacement to vertical displacement ratio on

the free-surface of a half-space from a single, incident plane P-wave, as shown in Figure 3.16. The ratio can be derived from the solution by Aki and Richards (2002) as:

$$\frac{\dot{U}_R}{\dot{U}_Z} = \frac{-2V_S\, p \cos j}{1 - 2{V_S}^2 p^2} \tag{3-3}$$

where $\dot{U}_R$ is the radial displacement at the ground surface, $\dot{U}_Z$ is the vertical displacement at the ground surface, V_S is the shear wave velocity of the half-space medium, j is the angle of the shear wave reflected back down from the ground surface, and p is the ray parameter. The ray parameter can be expressed as:

$$p = \frac{\sin j}{V_S} \tag{3-4}$$

By substituting Eq. (3-4) into Eq. (3-3), Eq. (3-5) becomes:

$$\frac{\dot{U}_R}{\dot{U}_Z} = -\tan 2j \tag{3-5}$$

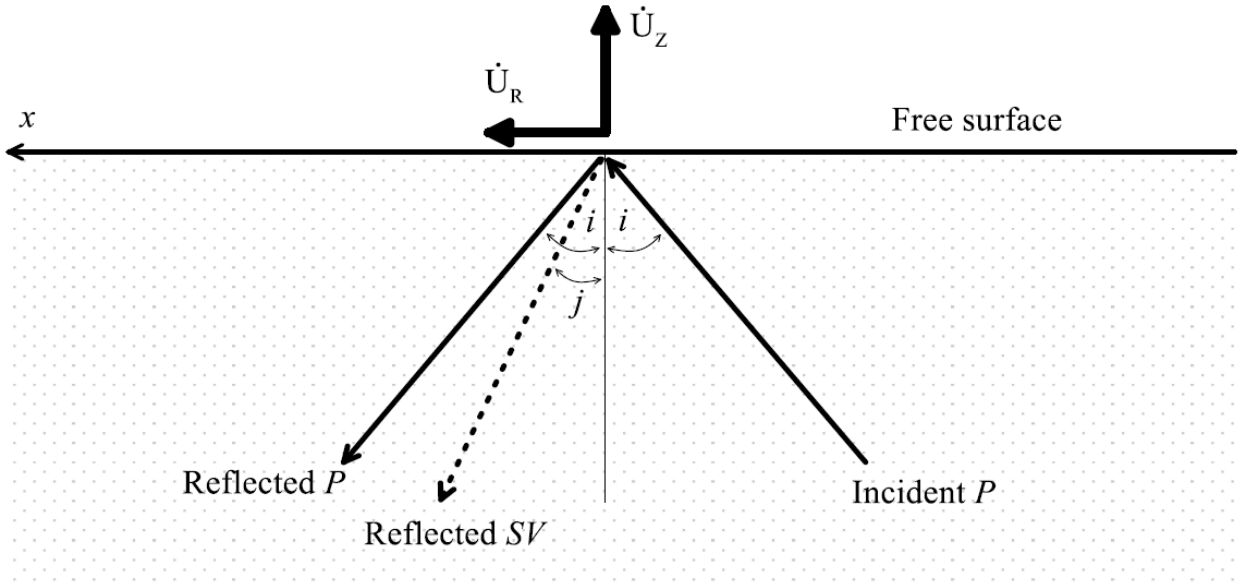

Figure 3.16: Schematic sketch showing the incident P-wave and reflected P- and SV-waves (Kim et al. (2016))

$\dot{U}_R$ and $\dot{U}_Z$ can be retrieved from recorded ground velocity time histories or integration of ground acceleration time histories. The direction $\dot{U}_R$ is from hypocenter to station and can be derived by rotating two recorded horizontal components numerically. Kim et al (2016) suggested using the first portion of the time series to get rid of the interference from other waves. Figure 3.16 is an example from Kim et al (2016) used to illustrate how $\dot{U}_R$ and $\dot{U}_Z$ are retrieved from velocity time histories. The two records are from the 2011-03-16 M 4.3 Hawkesbury earthquake at station

CN.OTT and the 2005-05-01 M 4.2 Shady Grove earthquake at station NM. TUMT. The lower two plots in Figure 3.17 are the zoomed-in views at the very beginning of the velocity histories. Basically, Kim et al (2016) used the first peak value of $\dot{U}_Z$ and corresponding value of $\dot{U}_R$ at the same moment to get *j* by Eq. (3-5).

Kim et al (2016) estimated ray parameter *p* by assuming a simplified two-layer crustal velocity model, as shown in Figure 3.18. The ray parameter can be calculated from solving Eq. (3-6):

$$p = \frac{\sin(\arctan(\frac{R_1}{D_1}))}{V_{p_1}} = \frac{\sin(\arctan(\frac{R_2}{D_2}))}{V_{p_2}} \qquad (3\text{-}6)$$
$$R_1 + R_2 = R$$

where R_1 *and* R_2 are the horizontal travelled distances of P-wave in the upper and lower layers, respectively, between the station location and the epicenter, $D_1$is the thickness of the upper layer, D_2 is the vertical distance from the hypocenter to the boundary of the upper and lower layer, V_{P1} *and* V_{P2} are the P-wave velocity of the upper and lower layer, respectively, and R is the horizontal distance from the epicenter to station.

V_{P1}, V_{P2}, D_1, D_1 are retrieved from an assumed crustal model. Kim et al (2016) used crustal models from EPRI (1993) for Central and Eastern North America (CENA). R can be easily calculated once the earthquake hypocenter is known. Then, *p* can be solved from Eq. (3-4).

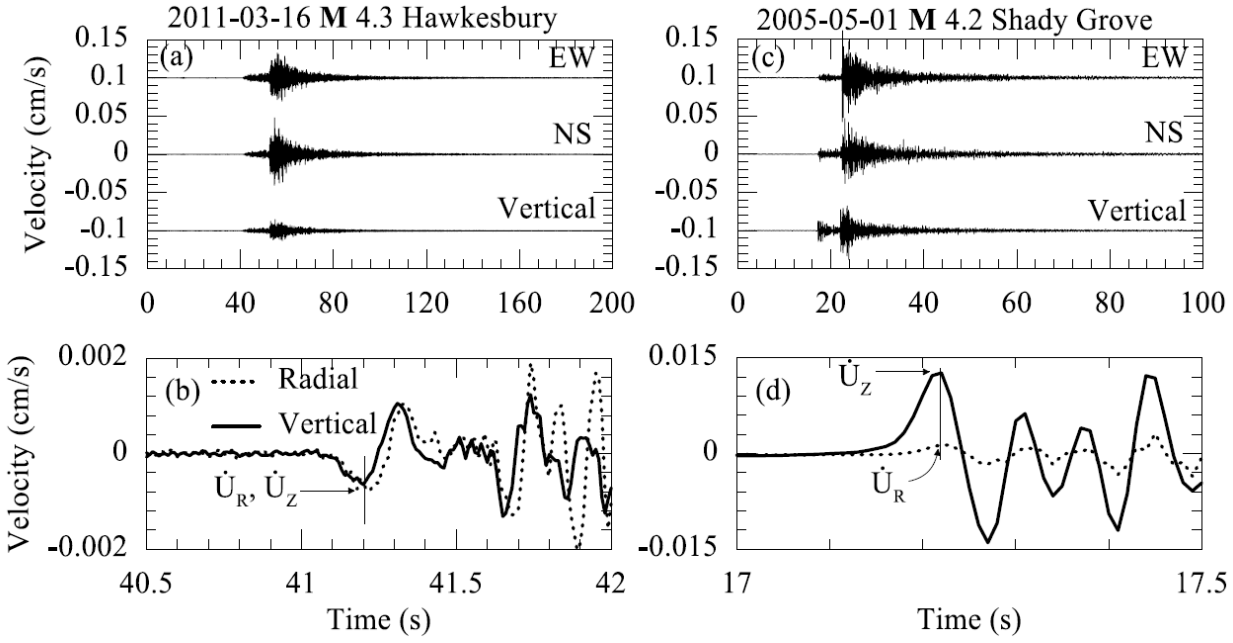

Figure 3.17: Surface ground motion (velocity) time series

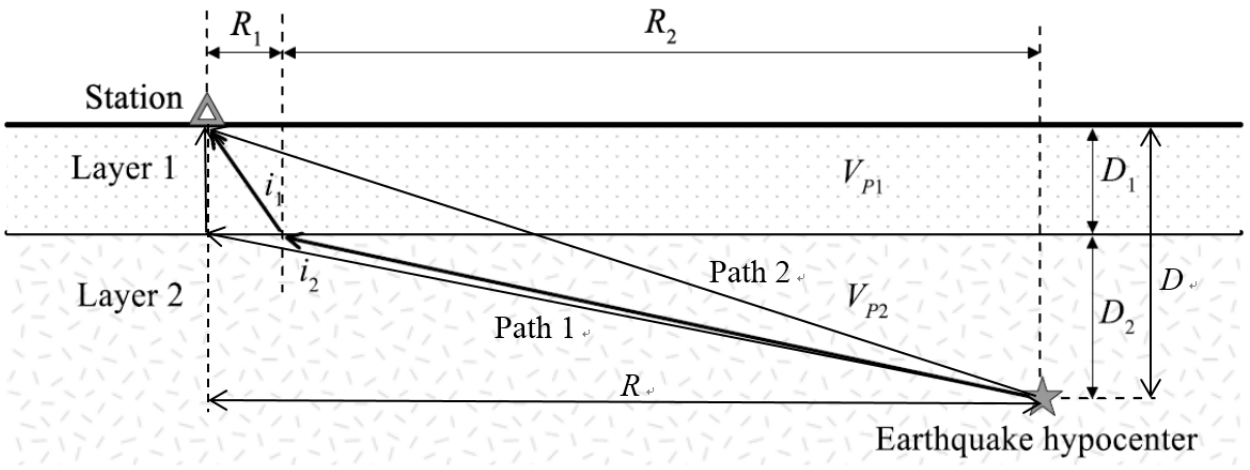

Figure 3.18: Schematic sketch of ray path for the crustal structure simplified to two layers (Kim et al. 2016)

For distant earthquakes, usually *R*>>*D*, then

$$p \approx 1/V_{p2} \tag{3-7}$$

In most cases $V_{P1} < V_{P2}$ because generally P-wave velocity increases with increasing depth. Therefore, the estimation can be justified by considering two extreme cases:

Case 1: $V_{P1} \to 0$, Based on the principle that waves travel in the fastest path from source to receiver, P-waves travel to the boundary between layer 1 and layer 2 right below the station, then it travels almost vertically to the station (Path 1), as shown in Figure 3.18, $\sin i = \frac{1}{\sqrt{1+(\frac{D_2}{R})^2}}$.

Case 2: $V_{P1} \to V_{P2}$, the two-layer crustal model reduces to a one-layer crustal model and waves travel in a straight path from source to receiver. So P-wave travels in Path 2, as shown in Figure 3.18, $\sin i = \frac{1}{\sqrt{1+(\frac{D}{R})^2}}$.

Since *R*>>*D*>*D*$_2$, in both cases $\sin i \approx 1$, so $p = \frac{\sin i}{V_{P2}} \approx 1/V_{P2}$. This relationship should be valid for any intermediate value of V_{P1}.

Once $\dot{U}_R$, $\dot{U}_Z$ and *p* are known, *j* can be computed from Eq. (3-5), thus V_S can be computed from Eq. (3-2). The estimated *Vs* from this method is equivalent to the time-averaged shear-wave velocity from the ground surface to a depth z (*Vs*$_Z$). Kim et al. (2016) assumed the depth z to be the product of the pulse duration of the source time function and the shear wave velocity ($\tau_p \times$ *Vs*$_Z$). Kim et al. (2016) also recommended using velocity time histories from small earthquakes with a magnitude M_W of 3-4 and a pulse duration of 0.1 seconds for these small earthquakes.

There is still a need to convert *Vs*$_Z$ to V_{S30}. According to the study of Boore et al. (2011) and Boore (2004), there is a strong correlation between V_{S30} and *Vs*$_Z$. Kim et al. (2016) developed the correlation between *Vs*$_Z$ to V_{S30} as:

$$\log V_{s30} = c_0 + c_1 \log V_{sz} \tag{3-8}$$

To determine the constants c_0 and c_1, Kim et al. (2016) used a database of 821 *Vs* profiles measured in CENA from published reports and Nuclear Power Plant (NPP) license applications. For z<30m, Vs_{30} and Vs_Z from z=1~29m with an interval of 1m (i.e., Vs_1, Vs_2,…, Vs_{29}) are extracted from these measured *Vs* profiles. For Vs_Z at each depth, two pairs of c_0 and c_1 are developed by regression. One pair is for *Vs* profiles in glaciated regions and the other pair is for *Vs* profiles in non-glaciated regions. So, there are 58 pairs of c_0 and c_1 in total.

For z>30m, pairs of c_0 and c_1 for z=50~200m and intervals of 25m are developed. However, at each depth the same values of c_0 and c_1 are developed for glaciated and non-glaciated region due to lack of data.

In short, the method can be divided into the following steps:

a) Determine $\dot{U}_R$, and $\dot{U}_Z$ from velocity time histories and calculate *j* by Eq. (3-5).

b) Apply appropriate crustal models and calculate the ray parameter *p* by Eq. (3-6) or Eq. (3.7).

c) Calculate Vs_Z by Eq. (3-2) and determine z as $Vs_Z/10$.

d) Use z to find corresponding pair of c_0 and c_1. Then use Eq. (3.8) to convert Vs_Z to Vs_{30}.

Kim et al. (2016) compared the estimated Vs_Z with measured Vs_Z for 31 selected stations, as shown in Figure 3.19. The number next to the station name in Figure 3.19 represents the number of earthquake events used to estimate the shear-wave velocities. Boxplot shows the minimum and maximum (outside bars), 25th and 75th percentile (gray box), and the median (bar inside of gray box). It appears that there are differences between the mean estimated Vs_Z and the measured Vs_Z for more than half of the selected stations are more than 20%. Furthermore, the range in estimated Vsz values spans hundreds of meters per second in most cases. So, while this method is attractive and a potentially valuable tool to estimate V_{S30} over large, well-instrumented areas, results may be quite unstable. There are possibly two reasons for this instability. One reason is that the selection of $\dot{U}_R$ and $\dot{U}_Z$ is subjective. Theoretically the ratio between $\dot{U}_R$ and $\dot{U}_Z$ is constant at every moment according to Eq. (3-3), but in reality, it is very common for the velocity time histories of $\dot{U}_R$ and $\dot{U}_Z$ to show completely different trends at different moments in time. Under such circumstances is it appropriate to use the first peak value or an averaged value over a short duration? Since the answer is unclear, for now it is a good strategy to use only “good” velocity time histories. Here are a few recommendations for picking “good” velocity time histories.

a) Use records from small, distant earthquakes (i.e., M_W <5). It is critical since the very foundation of this method, Eq. (3-3), is only valid for linear elastic (i.e., constant modulus at different strain) material. For large earthquakes soil may enter nonlinear state and Eq. (3-3) should not be used anymore.

b) Use records with an evident first peak in velocity time histories for $\dot{U}_R$ and $\dot{U}_Z$ to distinguish earthquake induced P-waves from background noise.

c) Use records with similar trend of velocity time histories for $\dot{U}_R$ and $\dot{U}_Z$. That is, the two velocity time histories have similar shape. In this way the ratio between $\dot{U}_R$ and $\dot{U}_Z$ can be close at different moments in time.

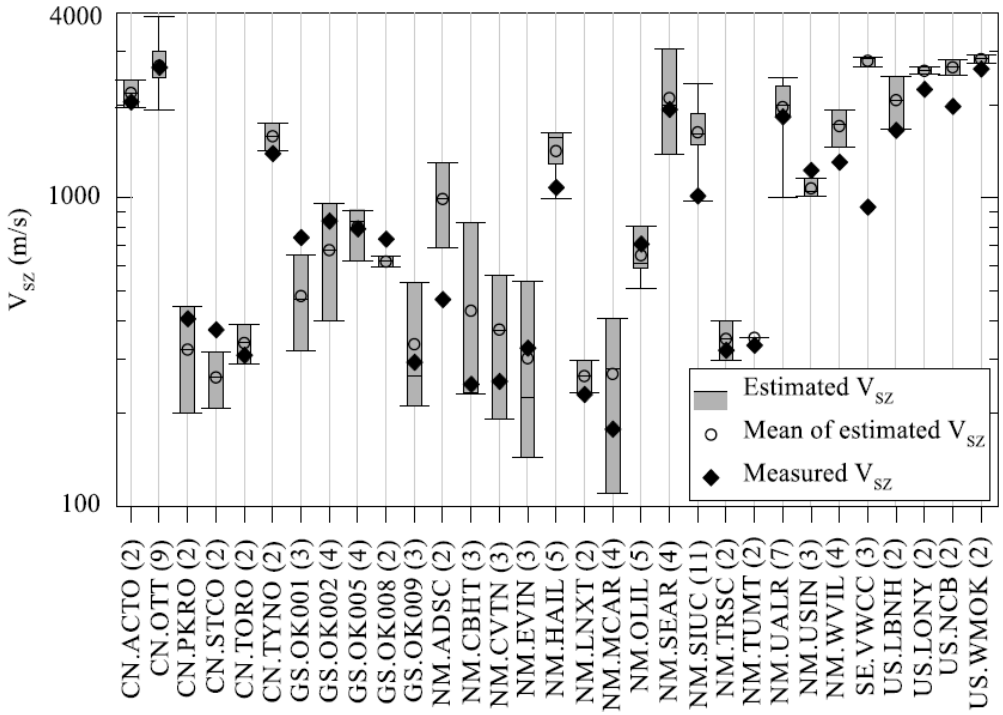

Figure 3.19: Shear-wave velocities to depth z (Vs_Z) estimated for 31 selected stations.

The other reason for unstable results of this method is the uncertainty of V_{P2}, which has a great influence on the ray parameter *p*, as indicated by Eq. (3-7). Figure 3.20 shows the crustal models in EPRI (1993). The crustal models are based on the scale of 60km in depth. However, most small earthquakes happen at a depth of no more than 10km and each crustal model gives only one to two rough values of P-wave velocity at the top 10km. So, there could be large error in V_{P2} due to the coarse nature of the P-wave velocity models. After all, P-wave velocity varies from thousands of meters per second at a depth of 10km to hundreds of meters per second near the earth's surface. In fact, Kim et al. (2016) reduced V_{P2} from crustal models in EPRI (1993) by 14% to better fit measured Vs_Z, but large error still exists, as shown in Figure 3.19. More refined crustal models of a small area focusing on the top 10km is required to give a better estimation of V_{P2}.

It is also worth noting that the assumption of the depth z for Vs_Z to be the product of the pulse duration of the source time function and the shear wave velocity ($\tau_p \times Vs_Z$) stills needs further investigation since it is not thoroughly explained in Kim et al. (2016).

Although picking appropriate values of parameters (i.e., $\dot{U}_R$, $\dot{U}_Z$, V_{P2}) in this method is a challenge, there is still a great merit in this method. Despite the fact that an empirical relation is used to convert Vs_Z to V_{S30}, physical derivation is incorporated in this method, unlike geology or

topography based V_{S30} proxies, for which quantitative relations are purely derived by statistical study.

In summary, this method can be used to derive V_{S30} estimates at discrete locations (i.e., locations of ground motion stations). The estimated V_{S30} values at these locations can be added into database for statistical study of other V_{S30} proxies, or they can be simply used as a way to validate other V_{S30} proxies. The positive aspect of this approach is that it is based on measurements of wave propagation. However, many simplifying assumptions are required in order to convert the measured ground motions into V_{S30} estimates. Thus, one should be aware that the estimates may have significant scatter and may deviate substantially from measured values.

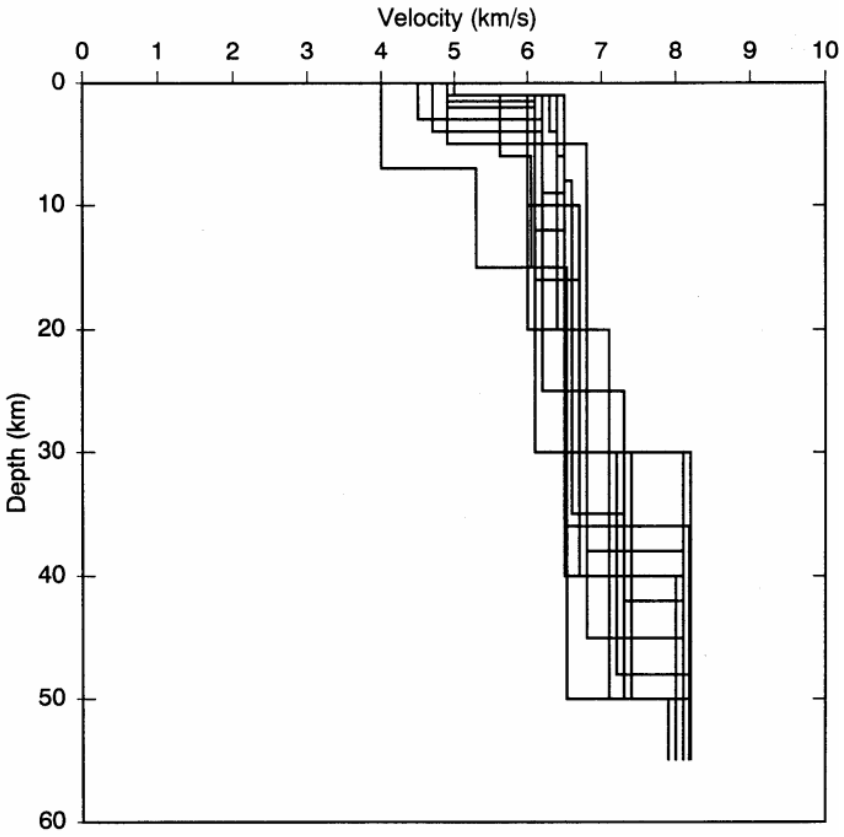

Figure 3.20: P-wave velocity profiles of 16 crustal models in EPRI report: Guidelines for Determining Design Basis Ground Motions (EPRI, 1993)

3.5. Initial Proxy-based V_{S30} Maps of Texas

As discussed earlier, due to the lack of existing in-situ measurements of shear wave velocity profiles in Texas, reliable proxy estimates of V_{S30} values are necessary. Such proxy estimates can be used to develop proxy-based V_{S30} maps, which can subsequently be further informed by any existing in-situ measurements of V_S profiles in Texas. An approach in estimating V_{S30} is the P-wave seismogram method, described in detail in Section 3.4.4 (Kim et al. 2016; Ni et al. 2014),

which uses earthquake recordings from seismic stations and theoretical wave propagation considerations to estimate V_{S30}.

Zalachoris et al. (2017) used the P-wave seismogram method to estimate VS30 at 251 seismic station locations in Texas, Oklahoma, and Kansas (Figure 3.21a). Based on the obtained VS30 estimates, Zalachoris et al. (2017) developed a spatially-interpolated VS30 map of Texas, Oklahoma, and Kansas (Figure 3.21b). Furthermore, the researchers investigated the relationship between the VS30 estimates and the geologic conditions at the locations of each site, as documented by large-scale geologic maps retrieved from United States Geological Survey (USGS) Division of Mineral Resources (DMR). Based on the findings of Zalachoris et al. (2017), developed protocols for assigning VS30 values to locations in Texas, Oklahoma, and Kansas for situations where in-situ measurements of shear wave velocity are not available. These protocols incorporate combined geologic age and rock type proxy groups, as listed in Table 3.12 under "All Data." Further study of the data from Zalachoris et al. (2017) indicated statistically significant differences between the V_{S30} of the Quaternary units along the Gulf Coast and the Quaternary units outside the Gulf Coast region. Thus, for this study, the protocols were revised to separate the Quaternary units within the Gulf Coast from those outside the Gulf Coast, as shown in Table 3.12.

Excluding the Basin and Range region in West Texas, where the density of stations for which V_{S30} estimates were developed is scarce, the interpolated V_{S30} map shown in Figure 3.21 captures the broad variations of V_{S30} across Texas as related to the generic geologic features observed in the geologic maps of Texas (Figure 3.4). For example, the computed V_{S30} values are smaller (i.e., < 400 m/s) within the Quaternary unconsolidated sediments along the Gulf Coast, and larger (i.e., > 760 m/s) within at the Precambrian and Paleozoic igneous and metamorphic units of the Llano Uplift and within the Paleozoic shales, siltstones, and sandstones of the North-Central Plains. Nonetheless, it should be noted that the interpolated V_{S30} map shown in Figure 3.21 does not capture short distance variations in geology and subsurface conditions, because the spacing between V_{S30} estimates is generally large (about 75 km).

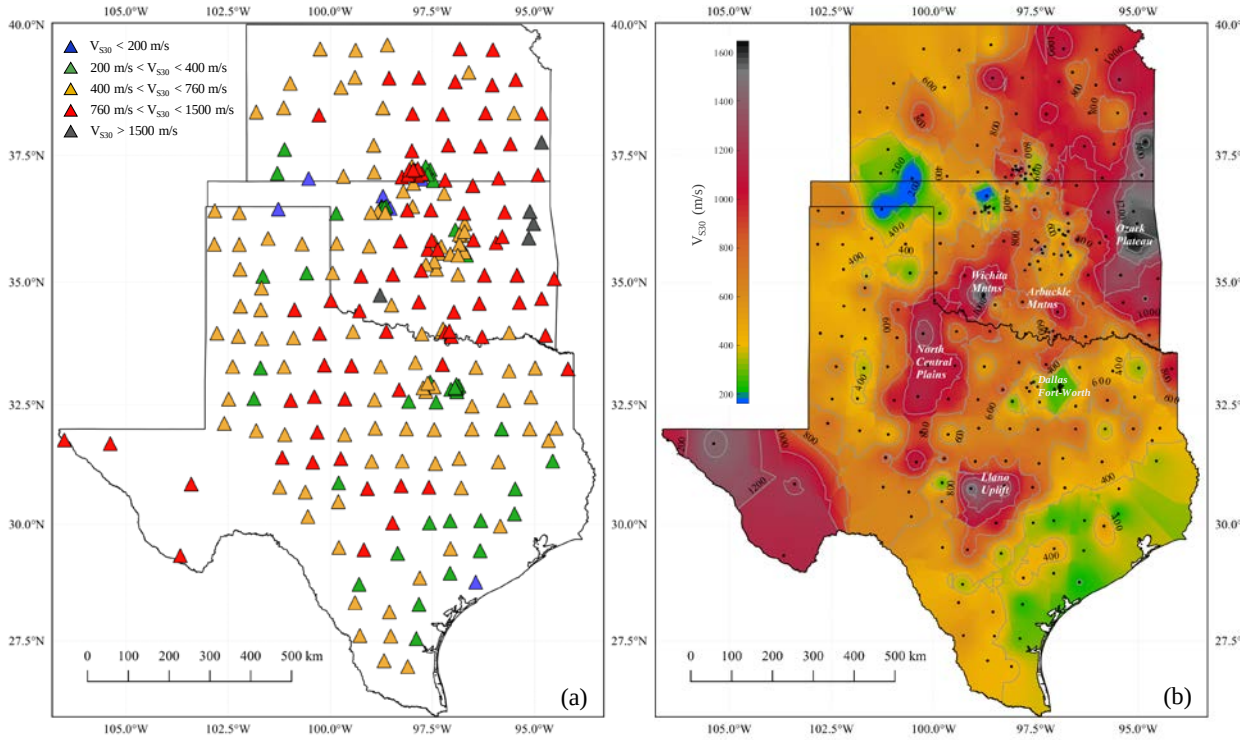

(a) color-coded stations based on median V_{S30} estimates

(b) interpolated map based on median V_{S30} estimates (Dots represent V_{S30} estimate locations)

Figure 3.21: *Distribution of* V_{S30} *across Texas, Oklahoma, and Kansas (Zalachoris et al. 2017)*

Table 3.12: Mean V_{S30} (μ_{lnV}) and standard deviation (σ_{lnV}) values for different geologic age and rock type groupings, based on data from Zalachoris et al. (2017)

		All Data			Gulf Coast Data			Outside Gulf Coast Data		
Geologic Age	**Rock Type Group**	**Npts**	**μ_{lnV} (m/s)**	**σ_{lnV}**	**Npts**	**μ_{lnV} (m/s)**	**σ_{lnV}**	**Npts**	**μ_{lnV} (m/s)**	**σ_{lnV}**
Quaternary - Holocene	A/C	13	363	0.44	8	284	0.31	5	544	0.31
Quaternary - Pleistocene	A/B/C	36	440	0.61	3	376	0.71	33	447	0.62
Quaternary - Undivided	A/B/C	20	512	0.52	3	380	0.42	17	540	0.53
Tertiary	B	13	349	0.25						
	C/D	28	478	0.3						
	F	1	1077	N/A						
Mesozoic*	C/D*	15	455	0.47						
	E	20	727	0.37						
Paleozoic*	D*	11	893	0.26						
	E	12	981	0.27						
Paleozoic / Precambrian	F	5	1519	0.06						

*Note: only data within Texas have been considered for this study

The revised protocols for proxy VS30 assignment shown in Figure 3.21 were used to develop two initial proxy-based VS30 maps of Texas (Figure 3.22). The first map (Figure 3.22a) is based on spatial interpolation of the individual VS30 estimates from the P-Wave Seismogram method, while

the second map (Figure 3.22b) was created by assigning a proxy VS30 value to each mapped polygon of the Geologic Atlas of Texas (Figure 3.4) based on the associated geologic age, the primary lithologic description, and the associated average VS30 value in Table 3.12.

The two maps illustrated in Figure 3.22 show some obvious similarities, but also exhibit significant differences. Specifically, both maps indicate V_{S30} values less than 400 m/s along the Gulf Coast, V_{S30} values between 400 m/s and 600 m/s within the Panhandle and north Permian Basin regions, and V_{S30} values greater than 800 m/s within the Llano Uplift and the North Central Plains. Nonetheless, the spatial resolution of the V_{S30} map based on the geology-based proxy is significantly higher, because it is defined by the scale of the mapped polygons of the different geologic units (Figure 3.4). The interpolated V_{S30} map based on the P-Wave Seismogram method provides a useful illustration of the gradual change in V_{S30} between two measurement points, but it does not capture local changes in geology between measurement points. The geology-based map captures these local changes in geology but displays distinct jumps in V_{S30} at geologic boundaries because it assigns a single V_{S30} value to each geologic unit.

3.6. V_{S30} from In-Situ Measurements

As stated earlier, in-situ measurements of near-surface V_S profiles are sparse and unequally distributed across Texas. Almost all of these *Vs* measurements are located along the Gulf Coast, with the only exception being a few *Vs* profiles from the Comanche Peak Nuclear Power Plant. Acknowledging the lack of existing shear wave velocity profiles, a series of in-situ measurements of V_S profiles were performed at seismic station locations in the Dallas-Fort-Worth area. Overall, in-situ V_S measurements at 29 sites were performed as part of this research project, using a combination of linear array active-source and 2D array ambient-wavefield surface wave testing. After inversion of the Rayleigh wave dispersion data into V_S profiles, V_{S30} values at each site were obtained. Additionally, the in-situ V_{S30} values were approximated from the Rayleigh wave phase velocity at a 40 m wavelength (V_{R40}) using $V_{S30} \sim 1.045 \cdot V_{R40}$ (Brown et al. 2000). The V_{S30} and V_{R40} values computed from the in-situ surface wave measurements in the DFW area are shown in Table 3.13, along with the corresponding P-Wave V_{S30} estimates at the co-located seismic stations and geology-based V_{S30} proxy values (Table 3.12) at each location. Figure 3.23 illustrates the locations of all existing measured shear wave profiles within the state of Texas, color-coded based on the corresponding V_{S30} value for each location.

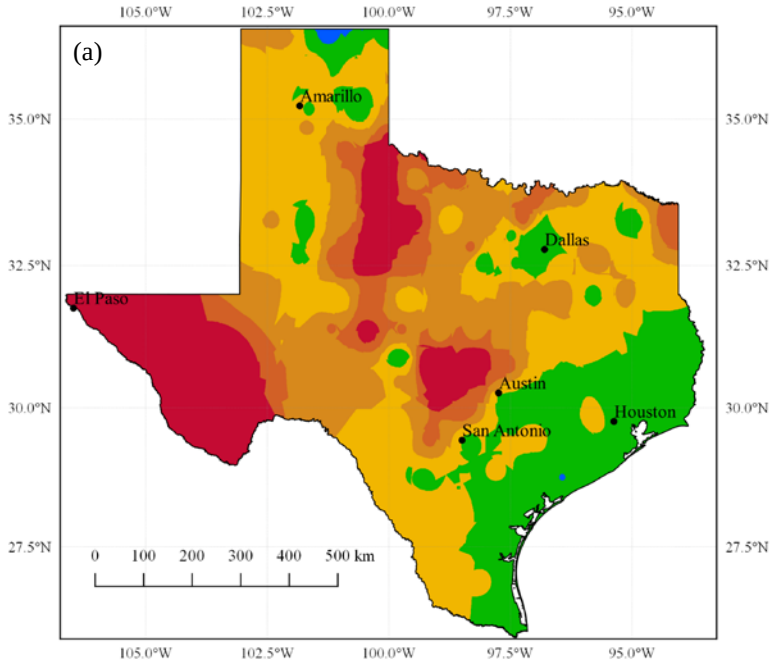

a) P-Wave Seismogram V_{S30} estimates from Zalachoris et al. (2017)

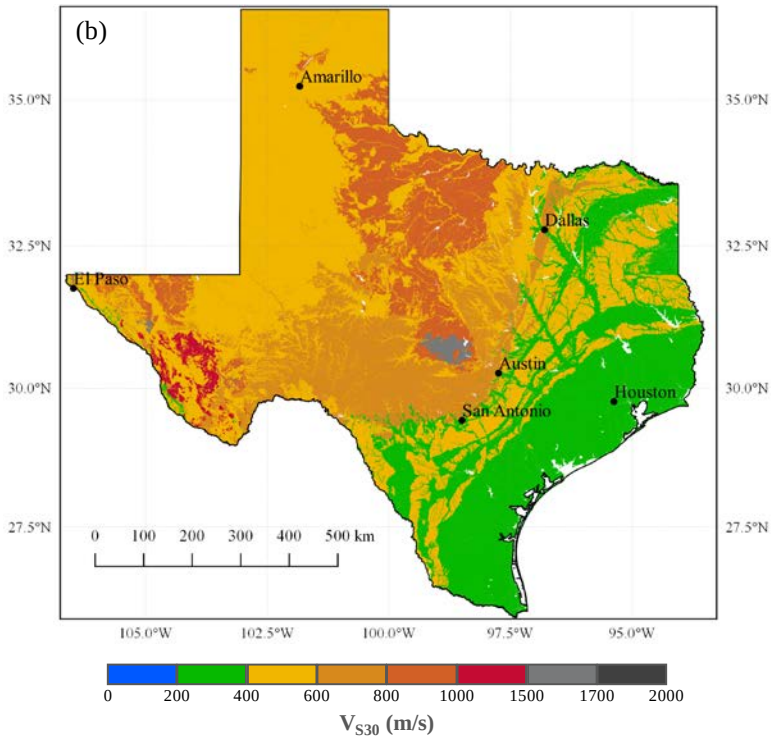

b) Geology-based V_{S30} *protocol (Table 3.12)*

Figure 3.22: Proxy-based V_{S30} *map of Texas*

To assess the accuracy of both the P-Wave Seismogram V_{S30} estimates and the geology-based V_{S30} proxies, we compare them with the V_{S30} values obtained via the in-situ V_S measurements (Figure

3.24). Additionally, the VS measurement at the Wichita Mountains in Oklahoma, which was performed at the Paleozoic granitic site of the US.WMOK seismic station (measured VS30 = 1,859 m/s, P-wave Seismogram VS30 = 1,663 m/s, geology-based proxy VS30 = 1,519 m/s) is also considered. In Figure 3.24, error bars for the VS30 values are shown. For the in-situ measurements the error bars represent +/- 1 standard deviation from the Vs inversion results (Table 3.13). For the P-wave seismogram results, the error bars represent +/- 1 standard deviation (in ln units) from the VS30 estimates obtained at a seismic station from multiple earthquake recordings. When only one or two motions could be successfully used in the P-wave seismogram method at a station, a standard deviation of 0.4 (in ln units) was assigned based on the data presented in Zalachoris et al. (2017). Finally, for the geology-based proxy values of VS30 the error bars represent +/- 1 standard deviation (in ln units) of the VS30 values measured for that geologic unit.

Based on Figure 3.24, it can be observed that the P-Wave seismogram VS30 values provide a relatively good estimate of the VS30 values obtained from in-situ surface wave measurements (Figure 3.24a). There is no systematic under or over-prediction of the estimated VS30 values by the P-Wave Seismogram method as compared with the measurements. Similarly, the geology-based proxy method (Table 3.12) also compares favorably with the in-situ measured VS30 values (Figure 3.24b). However, because the geology-based proxy method assigns the same VS30 value to sites within the same geologic unit, Figure 3.24b shows many sites with the same VS30 value because they are all located within the same geologic unit. Therefore, it can be concluded that VS30 estimates based on P-Wave Seismogram and the geology-based proxy methods can be used with a certain degree of confidence at locations where in-situ measurements of V_S are not available.

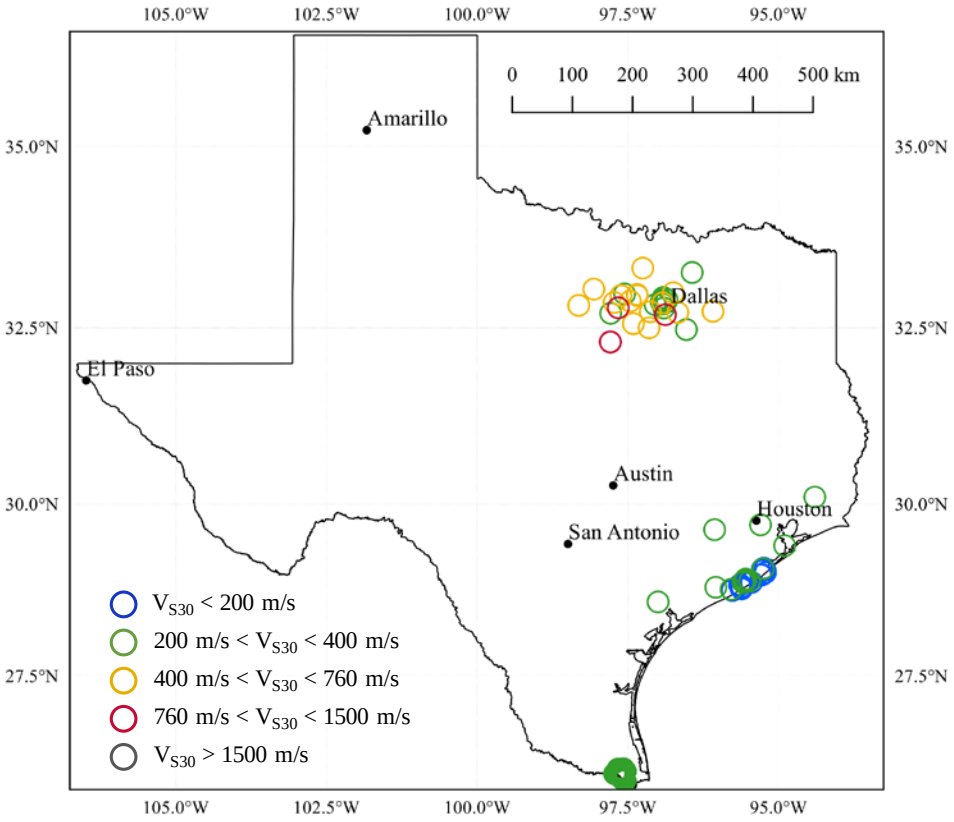

Figure 3.23: Locations of V_S *measurements in Texas, color-coded based on* V_{S30} *values*

Table 3.13: V_{R40} and V_{S30} values at seismic station locations in the Dallas/Fort Worth obtained in-situ surface wave measurements

					Dispersion V_{R40}			Inversion V_{S30}			P-Wave Seismogram V_{S30}	
Station	**Latitude**	**Longitude**	**Geologic Age**	**Primary Lithology**	**Mean**	**+1σ**	**-1σ**	**Median**	**+1σ**	**-1σ**	**Estimate**	**Geology Protocol**
135A	32.557300	-97.409900	Cretaceous	marl	607	637	577	626	647	606	389	455
136A	32.474600	-96.529700	Quaternary	alluvium	349	367	331	388	419	361	481	363
AFDA	32.822600	-97.048400	Cretaceous	shale	402	422	382	398	413	383	212	455
AZDA	32.972800	-97.555300	Cretaceous	sandstone	-	-	-	348	362	334	271	455
AZE2	32.949400	-97.615200	Cretaceous	sandstone	482	506	458	433	451	416	633	455
AZFC	32.853100	-97.728600	Cretaceous	sandstone	-	-	-	438	456	421	579	455
AZHL	32.965600	-97.348300	Cretaceous	limestone	775	824	726	736	798	679	-	727
AZWP	32.779500	-97.660000	Cretaceous	limestone	942	989	895	800	910	703	526	727
AZWR	32.812647	-98.315843	Pennsylvanian	limestone	716	752	680	743	800	690	840	981
DJLW	32.730433	-96.089294	Tertiary	limestone	-	-	-	696	809	599	-	727 (N/A)
EML1	32.873500	-97.460300	Quaternary	alluvium	534	561	507	457	507	421	404	363
FW01	32.684047	-96.878336	Cretaceous	chalk	-	-	-	1230	1341	1120	-	727
FW02	32.950190	-97.342550	Cretaceous	limestone	478	502	454	493	536	454	-	727
FW03	33.039624	-98.065202	Pennsylvanian	sandstone	401	421	381	440	470	412	-	893
FW04	32.847630	-96.923250	Cretaceous	shale	381	412	350	406	446	369	-	455
FW05	32.988669	-96.747081	Cretaceous	chalk	-	-	-	486	493	479	-	727
FW07	32.702466	-97.786092	Cretaceous	sandstone	429	450	408	382	394	371	-	455
FW08	32.714410	-96.672990	Cretaceous	chalk	-	-	-	474	492	457	-	727
FW11	32.722730	-97.127870	Cretaceous	sandstone	463	490	436	462	485	440	-	455
FW12	32.498996	-97.148597	Cretaceous	shale	479	506	452	449	474	425	-	455
IFBF	32.923700	-96.913500	Holocene	alluvium	363	382	344	362	385	340	270	363
IFDF	32.775600	-96.904400	Holocene	alluvium	327	343	311	323	336	310	247	363
IFS3	32.831200	-96.921100	Cretaceous	shale	295	310	280	306	317	296	341	455
ILCC	32.861000	-96.947200	Cretaceous	shale	403	424	382	363	389	339	353	455
IPD1	32.889000	-96.933300	Holocene	alluvium	373	392	354	362	381	344	210	363
ITL1	32.848900	-96.899000	Holocene	alluvium	355	374	336	290	315	267	265	363
ITSC	32.890300	-96.849800	Cretaceous	shale	333	350	316	310	314	306	260	455
Z35A	33.330800	-97.253000	Cretaceous	limestone	764	802	726	667	766	581	875	727
Z36A	33.270200	-96.434400	Cretaceous	clay	394	415	373	368	397	341	520	455

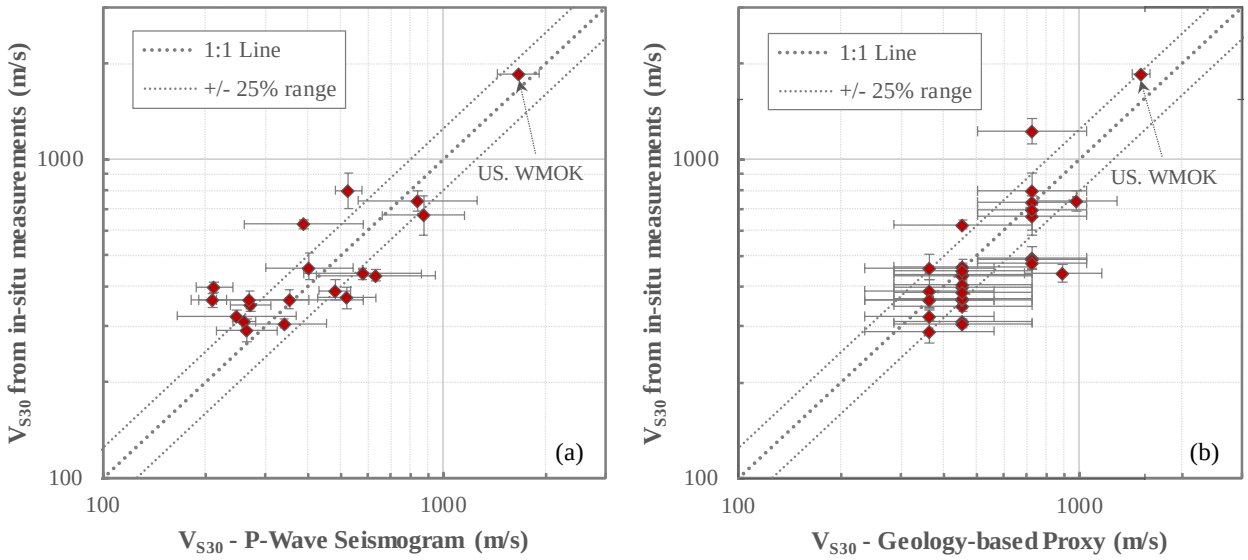

Figure 3.24: Comparison of estimated V_{S30} *values and* V_{S30} *values obtained from in-situ measurements at seismic stations in Dallas-Fort-Worth area*

3.7. V_{S30} Maps of Texas

Leveraging the information from the in-situ shear wave velocity measurements, the V_{S30} maps of Texas presented in Figure 3.22 were updated to more accurately depict the spatial variation of V_{S30} across the state (Figure 3.25). First, the V_{S30} map constructed based on spatial interpolation of the individual V_{S30} P-Wave Seismogram estimates (Figure 3.22a) was updated by incorporating the V_{S30} values obtained from the in-situ V_S measurements described above. At the locations where both a measured V_S profile and a V_{S30} P-Wave Seismogram estimate are available, the V_{S30} value from the in-situ measurement was used. Figure 3.25 presents the revised interpolated V_{S30} map of Texas using both the in-situ measurements and P-wave seismogram V_{S30} estimates. The revised map in Figure 3.25 is only slightly different than the previous map in Figure 3.22a, with the most significant differences occurring in the DFW area.

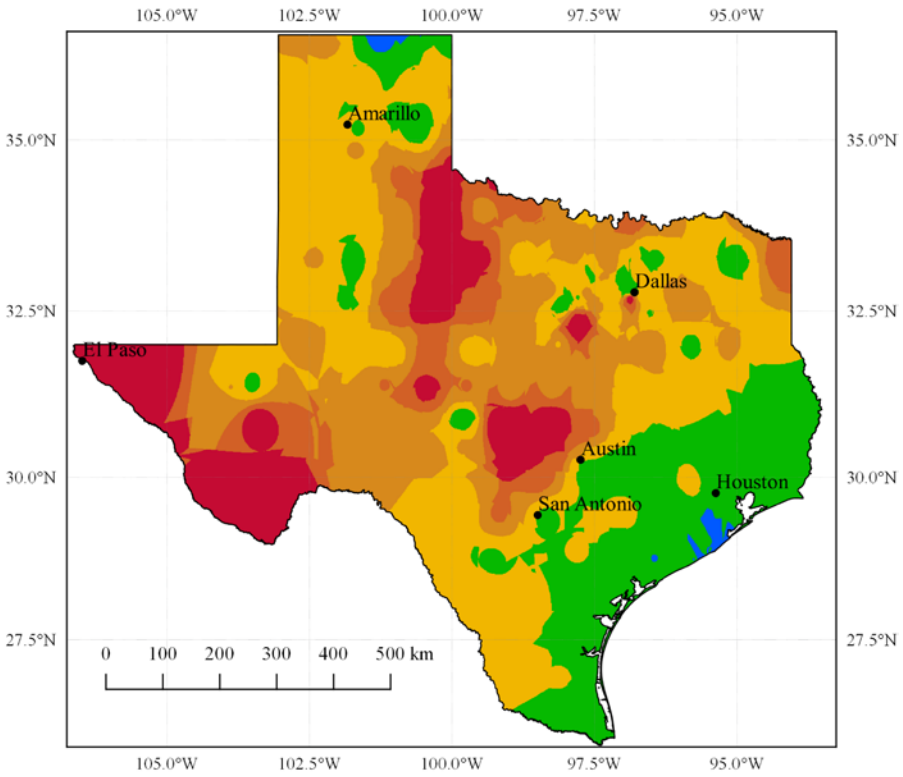

Figure 3.25: Spatial interpolation of V_{S30} *across Texas based on in-situ* V_S *measurements and P-wave seismogram* V_{S30} *estimates*

To develop the most comprehensive V_{S30} map of Texas that accounts for spatial variations in V_{S30} and local changes in geology, the V_{S30} values from the in-situ measurements and the P-Wave seismogram method are combined with the mapped geologic units of the Geologic Atlas of Texas (Figure 3.4) and the associated geology-based protocol for V_{S30} proxy assignment. To develop this comprehensive V_{S30} map based on the integrated V_{S30} data, a 1 km-by-1 km grid of individual points was created and a V_{S30} value was assigned to each point according to the following criteria:

$$V_{s30} = \begin{cases} V_{s30,M} & R \le 0.5km \\ 0.8V_{s30,M} + 0.2V_{s30,G} & 0.5km < R \le 2km \\ 0.5V_{s30,M} + 0.5V_{s30,G} & 2km < R \le 5km \\ 0.2V_{s30,M} + 0.8V_{s30,G} & 5km < R \le 15km \\ V_{s30,G} & R > 15km \end{cases} \quad (3\text{-}9)$$

where R is the distance of the grid point from the nearest location with a V_{S30} value either from in-situ V_S measurement or P-Wave Seismogram, $V_{S30,M}$ is the V_{S30} value at the measurement location (i.e., V_S measurement or P-Wave Seismogram), and $V_{S30,G}$ is the V_{S30} value assigned to the geologic unit where the grid point is located, according to the geology-based V_{S30} protocol (Table 3.12). The criteria in Eq. 3.7-1 weights $V_{S30,M}$ more heavily when close to a measurement location and increases the weight assigned to $V_{S30,G}$ when further from a measurement location. If no measurement location is within 15 km of a grid point, then $V_{S30,G}$ is assigned. After V_{S30} values

were assigned to each of grid point, spatial interpolation was performed to develop the final, recommended V_{S30} map of Texas (Figure 3.26). This map has the advantage of retaining much of the detail of the local geology from the mapped polygons of the Geologic Atlas of Texas, while incorporating the spatial interpolation derived from the locations where V_{S30} estimates or measurements are available.

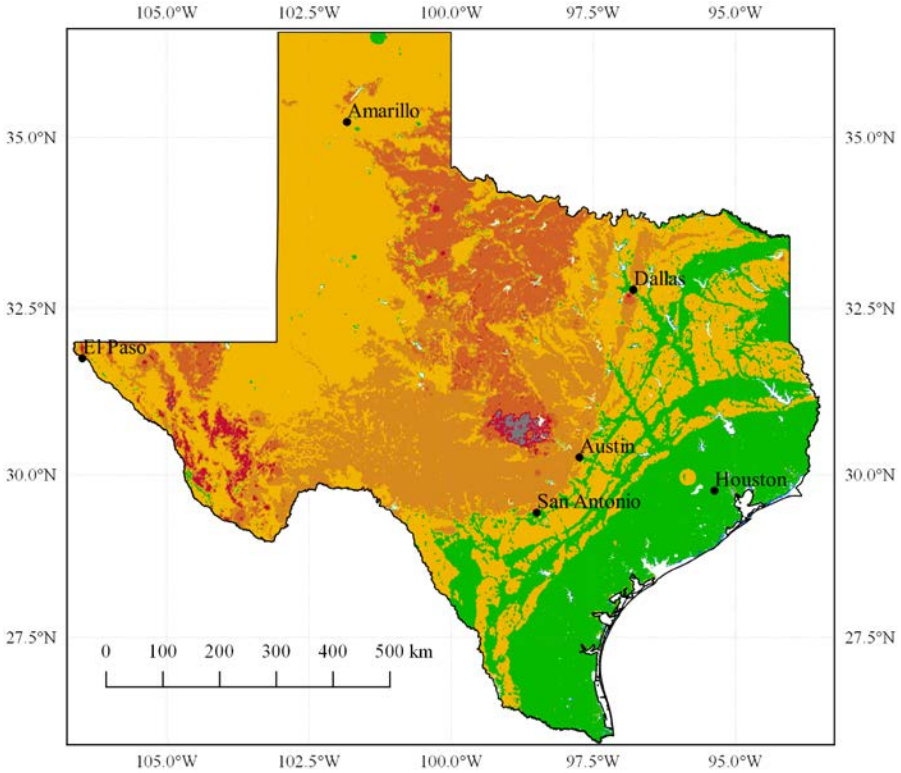

Figure 3.26: Recommended V_{S30} *map of Texas based on integrated* V_{S30} *data from in-situ* V_S *measurements, P-wave seismogram* V_{S30} *estimates, and geology-based* V_{S30} *protocol*

3.8. Summary

A series of V_{S30} maps of the state of Texas derived from different V_{S30} sources and approaches were presented. The processes associated with the development of these maps were discussed. A description of the geologic conditions in the state of Texas, as provided by the Geologic Atlas of Texas, was provided. For each mapped unit, information regarding the primary lithology and the geologic age was then used to guide the development and assessment of proxy-based V_{S30} maps of Texas. Two initial proxy-based V_{S30} maps of Texas were developed. The first map was based on spatial interpolation of the individual V_{S30} estimates from the P-Wave Seismogram method, while the second map was created by assigning a proxy V_{S30} value to each mapped polygon of the Geologic Atlas of Texas based on the associated geologic age and primary lithologic description. Values of V_{S30} obtained from in-situ shear wave velocity measurements, predominantly from the Dallas-Fort-Worth area, were presented, and an assessment of the accuracy of the proxy-based estimates of V_{S30} was made. Finally, the proxy-based V_{S30} maps were merged with the V_{S30} values from in-situ measurements to develop a final, comprehensive V_{S30} map of Texas.

Chapter 4. Representative Ground Motions

4.1. Overview

This chapter discusses development of an ensemble of ground motions to be used for seismic analysis of bridges in Texas. A catalog of earthquake recordings is constructed, and the seismic recording stations used to retrieve ground motion data are presented. The signal processing procedures applied to the recorded ground motion database are summarized. Finally, the processes and criteria associated with the selection of the ground motions to be used for bridge seismic analysis are presented. These ground motions are compared to responses predicted by existing CEUS GMPEs and the Texas region-specific ground motion models (GMMs) developed by Rathje and Zalachoris (2017).

4.2. Catalog of Earthquake Events

Currently, there is not a complete, consistently processed and widely utilized ground motion database for potentially induced earthquakes in Texas, Oklahoma, and Kansas. To obtain a substantial number of earthquake ground motions representative of earthquake shaking in Texas, a catalog of earthquake events with epicenters located in Texas and the surrounding States/areas was created. For that purpose, the comprehensive database, accessed via the website of the Incorporated Research Institutions for Research, IRIS (https://www.iris.edu/hq/), was utilized. Accordingly, 556 earthquake events occurring after January 2005, with magnitudes greater than 3.0, were selected. The locations and magnitudes of the selected earthquakes are illustrated in Figure 4.1a. The moment magnitudes (M_W) of the selected earthquakes were either known through IRIS, or computed using 1-Hz pseudo-spectral amplitudes (PSA) of the vertical component of the ground motion records (Atkinson and Mahani 2013; Atkinson et al. 2014). Nonetheless, it is important to note that the developed catalog does not distinguish between natural and induced seismicity.

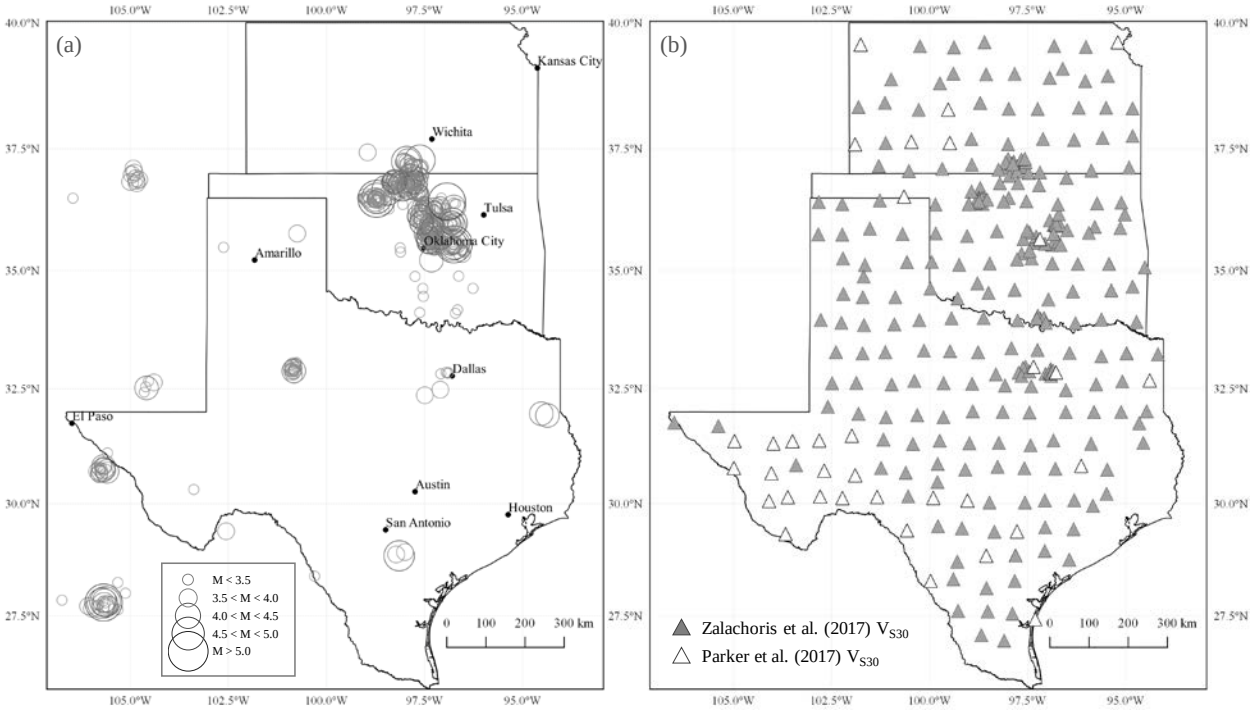

Figure 4.1: (a) Locations and magnitudes of selected earthquake events, (b) Locations of seismic recording stations in Texas, Oklahoma, and Kansas

4.3. Seismic Stations in Texas, Oklahoma, and Kansas

As seen in Figure 4.1a, most of the earthquake events of the developed database did not occur within the state of Texas. In fact, the majority of the earthquake epicenters are found in Northern Oklahoma (Figure 4.1a) Therefore, understandably, the distances between the epicenters of the selected earthquakes and the seismic recording stations located in Texas are generally large. Such large distances unavoidably result in recorded ground motions of very low amplitude. Because the 1-year seismic hazard at several areas within the state of Texas (i.e., West Texas) can be quite substantial (i.e., PGA ~ 0.25 g,), it was decided to include recordings retrieved from seismic stations located in Oklahoma and Kansas, for which the epicentral distances are shorter and the accelerations larger, to develop a more inclusive database of potential earthquake ground shaking in Texas.

Throughout the last 30 years, more than 400 seismic stations have been operating at various locations and at various times in the states of Texas, Oklahoma and Kansas (Incorporated Research Institutions for Research, IRIS - https://www.iris.edu/hq/) to monitor seismic activity. These seismic stations were part of several seismic networks, either at a local, state, federal, or global level (i.e., USArray of Transportable Array – TA; United States National Seismic Network – US; Global Seismograph Network – IU). Most of these stations remained operational for at least a brief period of time (i.e., 2 years for the TA stations), while a few are still operational. Figure 4.1b shows the locations of the past and existing seismic stations in Texas, Oklahoma and Kansas.

As discussed in Chapter 3, to quantify site amplification most Ground Motion Prediction Equations (GMPEs) use the time-averaged shear wave velocity of the upper 30 m (i.e., V_{S30}) as a measure of the physical properties of the near-surface geologic conditions. Due to the lack of existing in-situ measurements of shear wave velocity profiles in Texas, Oklahoma, and Kansas, reliable proxy estimates of V_{S30} values in these States are necessary. As part of the Next Generation Attenuation – East (NGA-East) project (http://peer.berkeley.edu/ngaeast/), V_{S30} estimates at sites throughout CEUS were developed using a hybrid slope-geology proxy method (Parker et al. 2017). These proxy-based estimates were assigned directly from the statistical proxies based on the local geology and slope, and did not involve any physics-based derivation. An alternative approach is the P-wave seismogram method (Kim et al. 2016; Ni et al. 2014), which uses recordings from seismic stations and theoretical wave propagation considerations to estimate V_{S30}. Zalachoris et al. (2017) used the P-wave seismogram method to estimate V_{S30} at 251 seismic station locations in Texas, Oklahoma, and Kansas. In this study, the V_{S30} values as estimated by Zalachoris et al. (2017) were used, with the exception of seismic station locations where P-wave seismogram V_{S30} estimates were not available. At these stations, the hybrid slope-geology proxy V_{S30} values, as defined by Parker et al. (2017), were utilized. Figure 4.1b distinguishes the seismic stations in Texas, Oklahoma, and Kansas for which a V_{S30} estimate is available from those with no available V_{S30} estimate.

4.4. Selection of Ground Motions for Structural Response History Analyses

Ground motion data recorded at Texas, Oklahoma, and Kansas stations (Figure 4.1b) were retrieved using tools available on the website of the Incorporated Research Institutions for Research, IRIS (https://www.iris.edu/hq/) (i.e., Standing Order for Data -SOD- software, https://ds.iris.edu/ds/nodes/dmc/software/downloads/sod/). The retrieved ground motion database includes three component ground motion recordings from the events within the earthquake catalog shown in Figure 4.1a. The collected data and associated metadata were quality assured and reviewed several times.

All collected time series were processed in a unified manner. The recordings were instrument corrected and the mean was removed. The records were examined for obvious irregularities (i.e., clipping, distortion, apparent high noise) on an individual basis. Then, 5% cosine tapering, acausal Butterworth filtering, and baseline correction were applied. The high-pass and low-pass filter frequencies were determined based on a Signal-to-Noise Ratio (SNR) threshold of 3. Any records with SNR values consistently less than 3 within the examined bandwidth were rejected. Overall, the developed ground motion database of this study consists of 5,345 three-component ground motion records from 295 seismic stations. Finally, rotation-angle-independent ground motion intensity measures (RotD50) (Boore 2010) were computed for 429 spectral periods, as per the NGA-East database (Goulet et al. 2014).

Figure 4.2a illustrates the moment magnitude (M_W)-hypocentral distance (R_{hyp}) coverage of the developed ground motion database. The selected ground motions for use in this project are shown

in red. Data from events with magnitudes between M_W = 2.5 and M_W = 5.8, and distances R_{hyp} = 4–500 km are included. In particular, the database has approximately 926 records with R_{hyp} < 50 km (Figure 4.2a). Moreover, Figure 4.2b shows the distribution of the considered seismic stations based on their National Earthquake Hazards Reduction Program (NEHRP) site classification. It is estimated that 106 of the considered seismic stations are located on "rock" site conditions, defined as locations with V_{S30} greater than 760 m/s (site class A and B, Figure 4.2b).

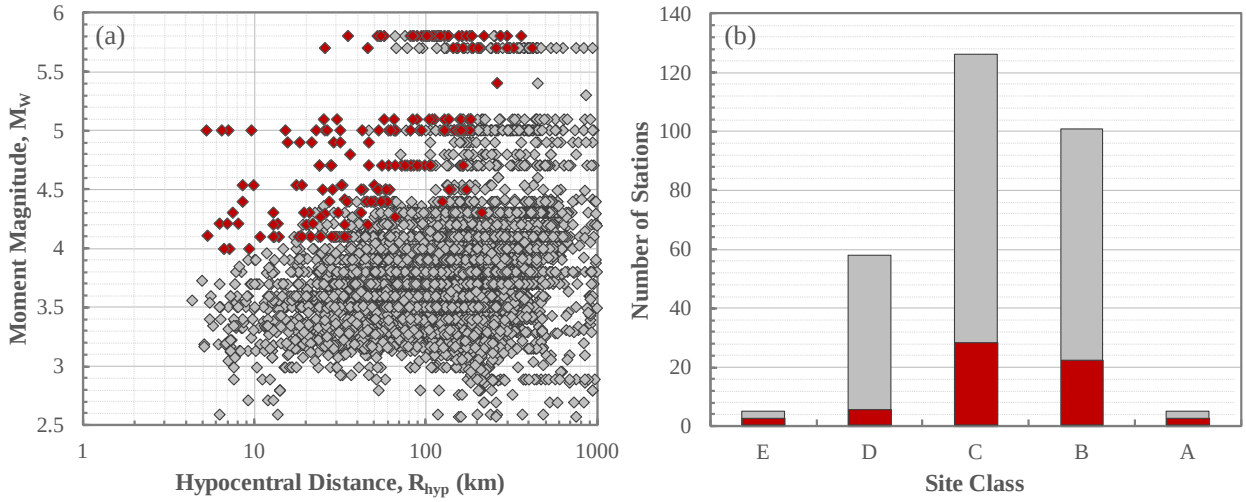

a) Moment Magnitude (M_W) – Hypocentral Distance (R_{hyp}) distribution

b) Number of stations per NEHRP site classification

Figure 4.2: Ground motion database utilized in this study

As discussed earlier, the ground motions to be used in this project need to be representative of the seismic hazard in Texas. To effectively test the response of structural elements of bridges across the state of Texas, records from larger magnitude earthquakes (i.e., $M_W \geq 4.0$) are required. Thus, from the developed ground motion database (Figure 4.2), 50 recordings within each of 4 magnitude bins (i.e., $4.0 \leq M_W < 4.5$, $4.5 \leq M_W < 5.0$, $5.0 \leq M_W < 5.5$, and $M_W \geq 5.5$) were selected. These motions were selected to capture high intensity motions with larger PGA, as well as motions with long period content. Table B-1 (see Appendix B) presents the relevant information regarding the selected recordings (i.e., event date/time, event location, magnitude/depth, recording station information, etc.). Overall, 200 three-component recordings from 36 earthquake events and 68 seismic stations are included in this list. The magnitude – distance, and site class distributions of the selected recordings are indicated in Figure 4.2a and Figure 4.2b, respectively, using red symbols. Moreover, Figure 4.3 illustrates the locations of the earthquake events (Figure 4.3a) and seismic stations (Figure 4.3b) associated with the selected ground motions. In Figure 4.3b, the seismic stations have been color-coded based on their corresponding V_{S30} estimate.

Based on Table B-1, the maximum PGA of the selected records is 0.595 g while the minimum is 0.0025 g, with 23 ground motions having PGA values greater than 0.05 g. Hypocentral distances span from 5.2 km to 420.1 km, with 67 of the selected ground motions recorded at distances less than 35 km, and 71 recorded at distances greater than 100 km (Figure 4.2a). In an effort to illustrate

the ground motion characteristics of the selected motions, Figure 4.4 shows a series of histograms for several ground motion parameters (PGA, spectral accelerations at 0.2 sec, 0.3 sec, and 1.0 sec, as well as peak ground velocity – PGV) associated with the selected recordings. As seen in Figure 4.4, most records are characterized by PGA values between 0.01 g and 0.03 g. Additionally, it is observed that with increasing spectral period, there is a shift of the computed spectral accelerations to smaller values.

To effectively evaluate the ground motion frequency content which could be considered as representative for the recordings in Texas, the response spectra of the selected recordings were compared with target response spectra derived based on the USGS 1-year hazard maps (Petersen et al. 2017). That is, the general steps defined by the International Building Code (IBC) were followed for the generation of a "target" response spectrum Figure 4.5.

Accordingly, the parameter SDS as the spectral acceleration at a period of 0.2 sec is determined from the USGS 1-year hazard map, and the parameter SD1 as the spectral acceleration at 1.0 sec is determined from the USGS 1-year hazard map (Petersen et al. 2017). TS is taken as SD1/SDS, while T0 = 0.2×TS. Acknowledging the fact that the seismic hazard is not uniform across Texas, three target response spectra were developed; for the Dallas-Fort Worth area, for West Texas, and for the rest of Texas (Figure 4.6), respectively.

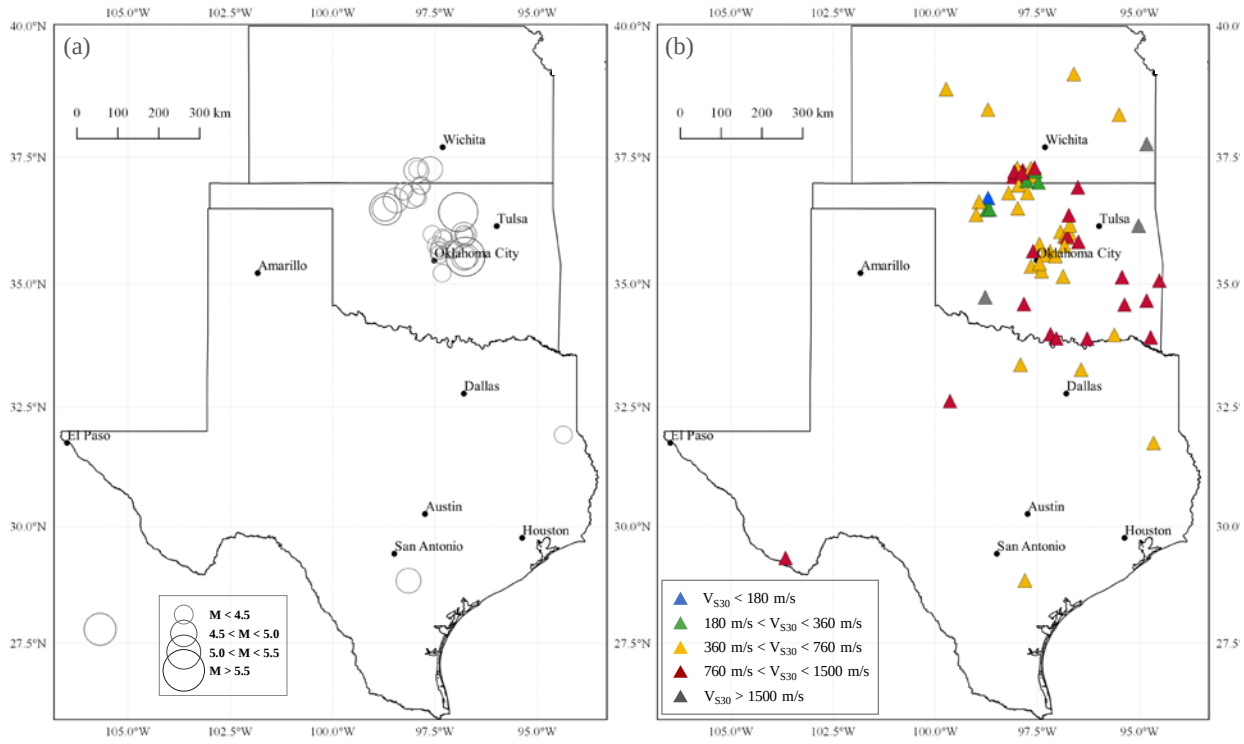

(a) Locations and Magnitudes (b) Locations of seismic recording

Figure 4.3: Earthquake events selected for this study

Figure 4.7 illustrates the computed response spectra for the selected ground motions. Response spectra are categorized based on the corresponding peak ground acceleration. Both horizontal components are included. Four PGA bins were defined; PGA < 0.05 g, 0.05 g ≤ PGA < 0.1 g, 0.1 g ≤ PGA < 0.3 g, and PGA > 0.3 g. Figure 4.7 also depicts the median response spectra for the recordings from each PGA bin (red line), as well as the target spectra for the three distinct regions. Accordingly, 357 individual component records were characterized by PGA less than 0.05 g, 26 records had PGA between 0.05 g and 0.1 g, 12 records had PGA values between 0.1 g and 0.3 g, while 5 records had PGA values greater than 0.3 g.

Based on Figure 4.7, the selected ground motions can be considered representative of the seismic hazard in Texas, as estimated via the constructed target spectra (Figure 4.6). Although the ground motions having PGA less than 0.05 g produce response spectral values that are slightly lower than the Rest of Texas target spectrum, this target spectrum was constructed as the upper limit response for most areas in Texas excluding West Texas and the Dallas-Fort Worth area. Records with PGA between 0.05 g and 0.1 g compare relatively well with the Dallas-Fort Worth target spectrum, while ground motions with PGA greater between 0.1 g and 0.3 g produce spectral accelerations that on average match the West Texas target spectrum. Nonetheless, it is important to note that since most motions with PGA between 0.05 g and 0.3 g are recorded at short distances and are from relatively smaller magnitude earthquakes (median M_W = 4.9 and R_{hyp} = 18 km for motions with 0.05 g ≤ PGA < 0.1 g; median M_W = 4.3 and R_{hyp} = 7 km for motions with 0.1 g ≤ PGA < 0.3 g), they are lacking long period energy. Thus, these motions do not compare well with the target spectra at periods greater than approximately 0.2 sec. These comparisons with the target spectra indicate that the recorded motions need to be scaled to larger intensities to better represent the expected frequency content at periods greater than 0.2 sec. Finally, the ground motions with PGA > 0.3 g produce substantially higher spectral accelerations than the three target spectra, for all periods. Even though these records do not seem to be representative of the seismic hazard within the state of Texas, as defined by the 1-year seismic hazard maps, they can provide an upper limit, worst case scenario for the assessment of critical infrastructure across Texas.

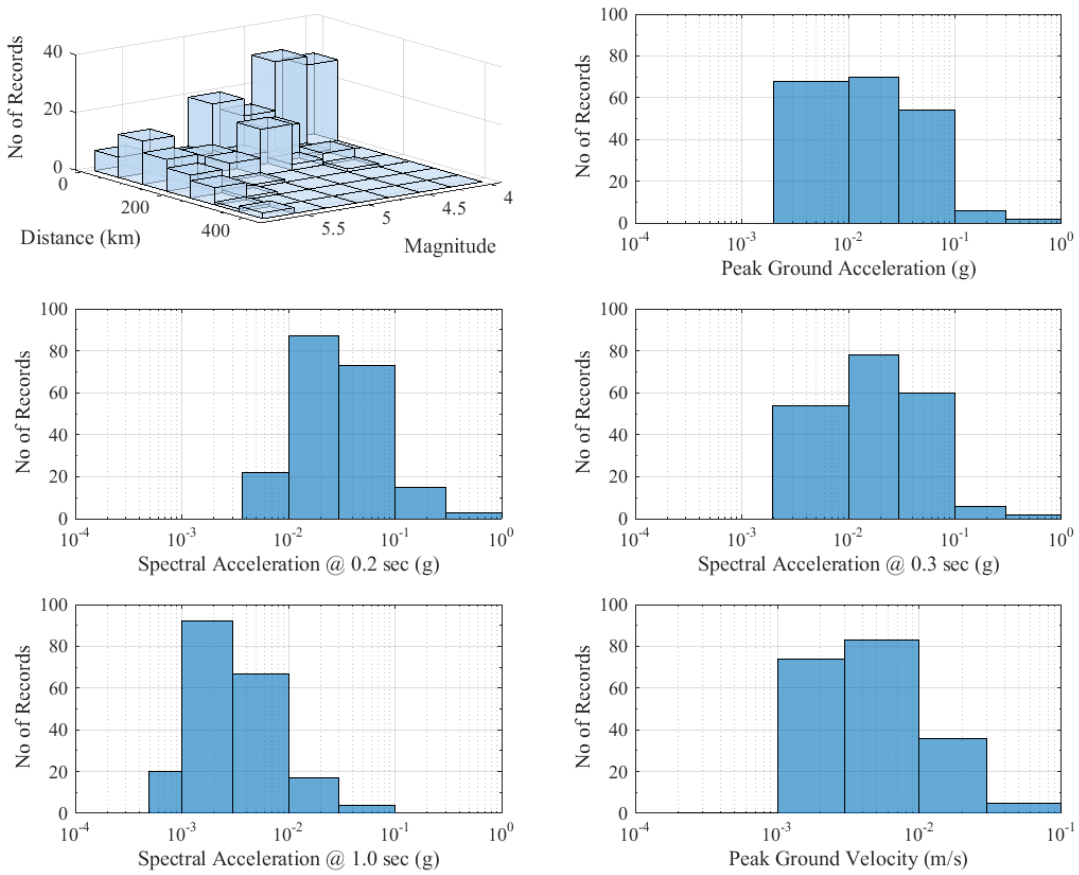

Figure 4.4: Histograms of ground motion parameters for the selected recordings

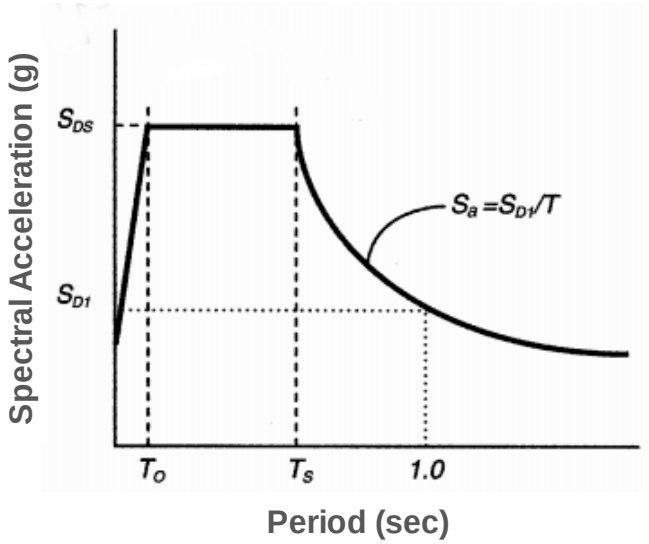

Figure 4.5: Schematic of the determination of a target response spectrum based on IBC

	Dallas	West Texas	Rest of Texas
S_{DS} (g)	0.18	0.35	0.05
S_{D1} (g)	0.025	0.035	0.01

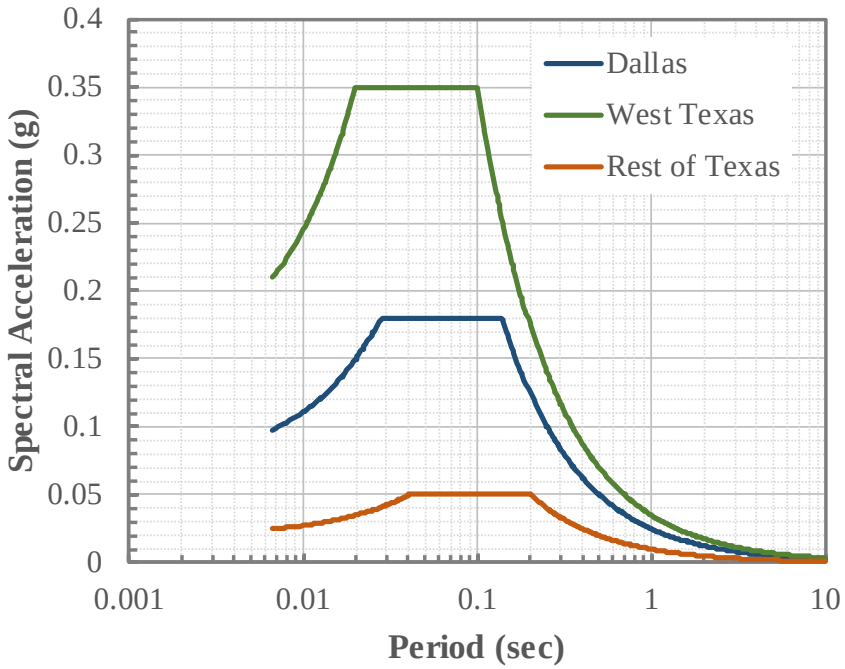

Figure 4.6: Estimated target response spectra for Dallas and West Texas

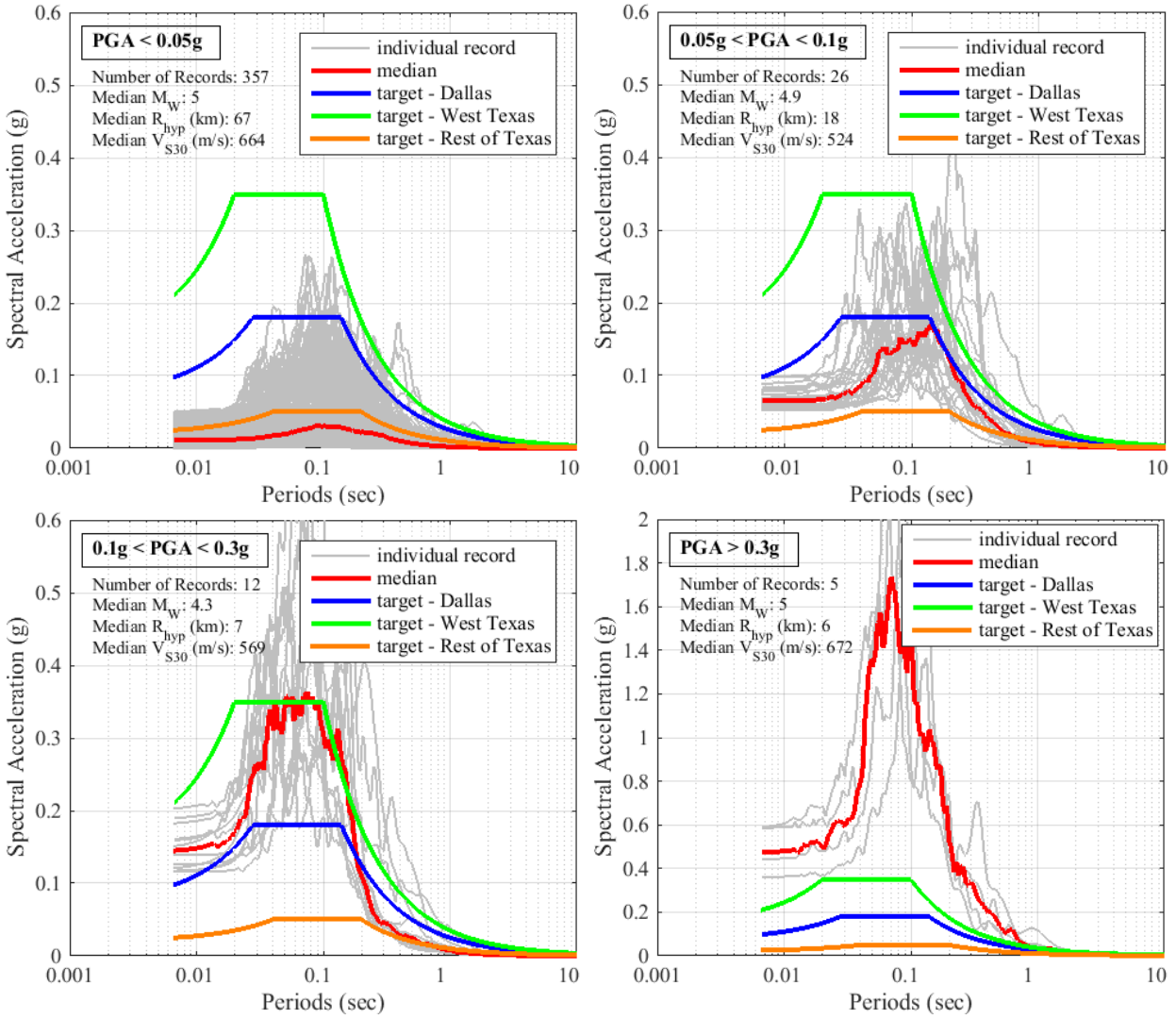

Figure 4.7: Response spectra of the selected ground motions for different bins of PGA values

To further assess the frequency content of the selected ground motions, the spectral accelerations of the selected recordings are compared against predictions by several ground motion models (GMMs), for four magnitude bins ($4.0 \leq M_W < 4.5$, $4.5 \leq M_W < 5.0$, $5.0 \leq M_W < 5.5$, and $M_W \geq 5.5$) in Figure 4.8. The median M_W, R_{hyp}, and V_{S30} values for each magnitude bin (Figure 4.8) are used to compute the model predictions. All spectral accelerations are normalized by the corresponding PGA values (Figure 4.8) to better evaluate the frequency content of the motions. The following ground motion predictive models are used as reference: i) the Hassani and Atkinson (2015) (*HA15*), developed as part of the Next Generation Attenuation (NGA)-East project; ii) the Atkinson (2015) (*A15*) model developed for small-to-moderate events at short hypocentral distances with application to regions with induced seismicity; and iii) the Adjusted Hassani and Atkinson (2015) model (Zalachoris and Rathje, 2017) (*Adjusted HA15*).

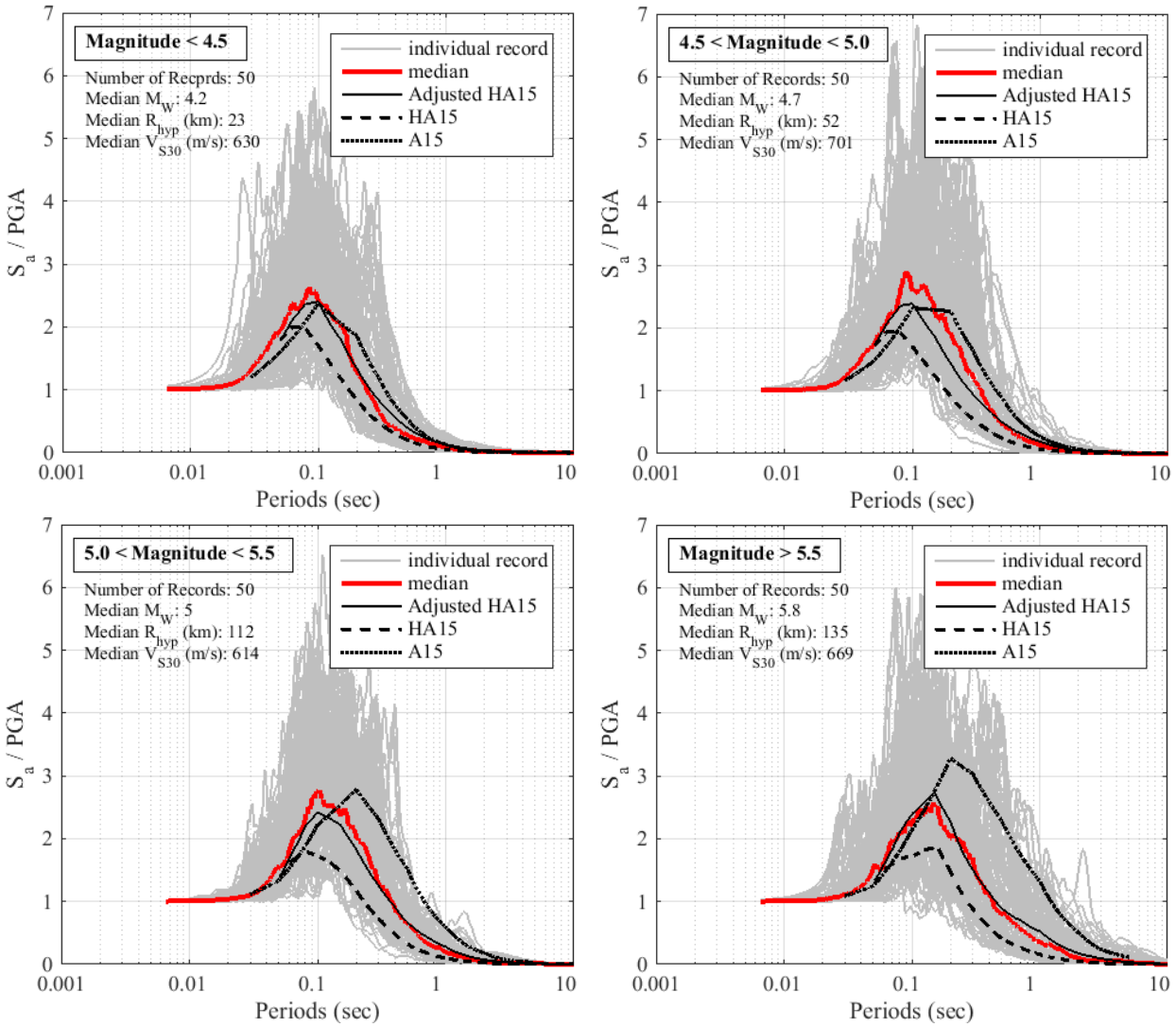

Figure 4.8: Comparison of normalized response spectra between the selected ground motions with and predictions by GMPEs

The Adjusted HA15 model, developed by Zalachoris and Rathje (2017), using the ground motion database for Texas, Oklahoma, and Kansas described in Section 4.2, understandably, provides the best fit to the selected ground motions, for all magnitudes. The "small-magnitude" A15 model, developed using data from Western United States (WUS), predicts a response spectral shape richer at periods greater than 0.1 s. This difference is expected because of the difference in attenuation characteristics between WUS and CEUS. Finally, the HA15 GMPE, developed using the NGA-East ground motion database, seems to provide a spectral shape that peaks at relatively lower periods (i.e., T < 0.1 s) than the selected ground motions. This is possibly due to the fact that the selected ground motions were recorded during potentially induced events in Texas, Oklahoma, and Kansas, which are believed to be associated with lower stress drops (Hough 2014), and thus lower corner frequencies than natural seismicity. Contrary, the NGA-East ground motion database (Goulet et al. 2014) primarily includes data from natural events in CEUS, hence the difference in the frequency content observed in Figure 4.8.

4.5. Summary

This chapter described a suite of ground motions to be used in this study to represent Texas seismicity. The processes associated with the creation of a database of over 5,000 ground motions recorded in Texas, Oklahoma, and Kansas was presented. A subset of 200 three-component recordings were selected from the ground motion database to be used for the structural response history analyses to be presented in Chapter 9 of this report. The selected ground motions span a magnitude range from 4 to 5.8 and a range of hypocentral distances from 5 km to 420 km. It was shown that the corresponding computed PGA values, which range from 0.0025 g to 0.595 g, are generally consistent with the seismic hazard in the state of Texas, as assessed by USGS. Furthermore, the frequency content of the selected ground motions was evaluated by comparing the spectral accelerations from the selected motions with several ground motion prediction models.

Chapter 5. Texas Hazard Maps

5.1. Introduction

This chapter provides hazard maps developed for Texas, as well as a description of the process associated with the development of these hazard maps. The organization of this chapter is as follows. First, a brief description of the seismic hazard in the Central and Eastern United States (CEUS) is provided. Such a description is used to define the level of ground motion that can be considered "representative" at different locations throughout the CEUS, and particularly in the State of Texas. Subsequently, the Ground Motion Model (GMM), as well as the V_{S30} map of Texas used for the development of the final hazard maps are discussed. Finally, the constructed hazard maps for two deterministic earthquake scenarios occurring at four different locations in Texas are presented.

5.2. Seismic Hazard in the State of Texas

One of the most recent assessments of the seismic hazard in the Central and Eastern United States (CEUS) that includes contributions from both induced and natural earthquakes was published by the United States Geological Survey (USGS) by Petersen et al. (2016a, 2017). More specifically, the USGS developed short-term, 1-year seismic hazard forecasts for 2016 and 2017 for the CEUS using input models, which consider alternative earthquake catalogs, maximum magnitudes and ground motion models. As a result, seismic hazard maps for 1-percent probability of exceedance in 1 year were developed. Figure 5.1 and Figure 5.2 illustrate the corresponding 2017 seismic hazard maps for peak ground acceleration (PGA) and spectral acceleration (S_a) at a period of 1.0 sec, respectively. Based on Figure 5.1, the ground shaking corresponding to 1-percent probability of exceedance in 1 year reaches 0.25 g and 0.125 g in West Texas and the Dallas-Fort Worth area, respectively, while for the rest of the state of Texas the hazard does not exceed 0.025 g.

The aforementioned assessment by USGS (Petersen et al. 2016a, 2017) utilized a probabilistic framework for the quantification of the seismic hazard in CEUS. Nonetheless, the present report focuses on providing simplified hazard maps based on deterministic scenarios of earthquake events. This report presents extreme earthquake scenarios, namely events with magnitudes M = 5.0 and M = 6.0, occurring at four different locations, selected based on population density and/or current seismicity trends. These four locations were selected: i) Dallas, ii) Dallas-Fort Worth International Airport, iii) Fort Worth, and iv) El Paso. To develop the hazard maps for these scenarios, we use a newly developed Ground Motion Model (GMM), particularly tuned to the observed—and potentially induced—seismicity in the States of Texas, Oklahoma, and Kansas (Zalachoris and Rathje 2017). Moreover, to account for the effects of the local site conditions on the expected level of ground shaking, the comprehensive V_{S30} map of Texas, as presented in Chapter 3, is utilized.

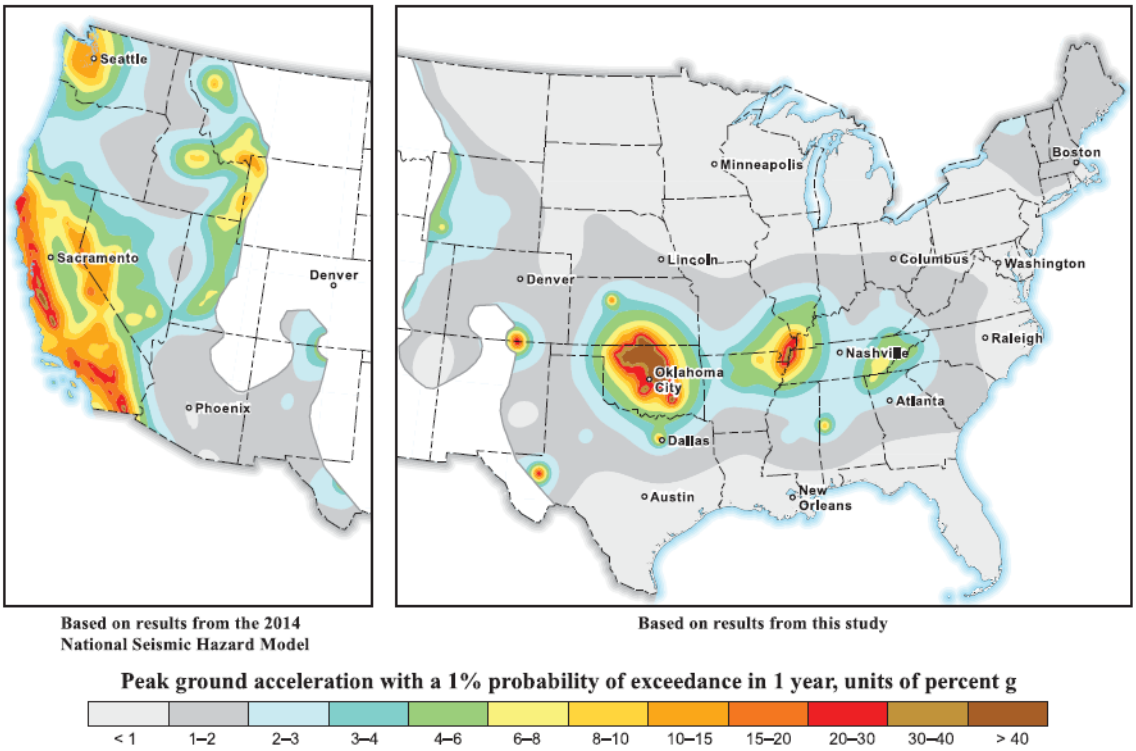

Figure 5.1: USGS 2017 1-year seismic hazard map – PGA (Petersen et al. 2017)

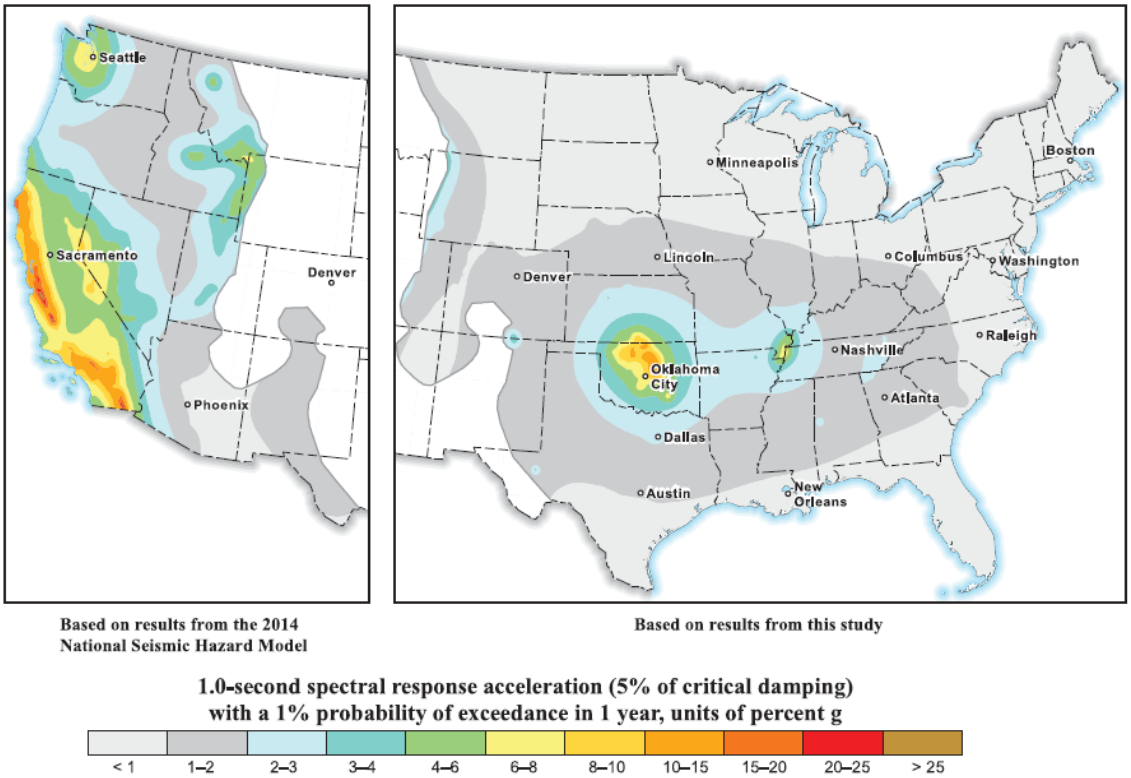

Figure 5.2: USGS 2017 1-year seismic hazard map – S_a (1.0 sec)(Petersen et al. 2017).

5.3. Ground Motion Model for Texas Hazard Maps

Earthquake engineering design and assessment requires reliable estimates of ground motions that may be produced by future earthquakes. Such prediction requires a detailed and accurate modeling of earthquake source and attenuation characteristics. The increasing number of recorded motions from past events provide an empirical basis to constrain the model parameters for ground motion prediction. Taking advantage of the observational data, numerous statistical models have been developed that predict the probability distributions of observed ground motion parameters. These statistical models are generally referred to as Ground Motion Prediction Equations (GMPEs) or Ground Motion Models (GMMs).

Typically, GMMs are based on regression analysis that fit a predefined functional form to data from recordings. As a result, a ground motion parameter is related to a set of variables describing the earthquake source, the wave propagation path, and local site conditions (Douglas, 2003). The models generally are in the form:

$$\ln(\boldsymbol{Y}) = \boldsymbol{f_{source}}(magnitude, mechanism) + \boldsymbol{f_{distance}}(magnitude, distance) + \boldsymbol{f_{site}}(i.e., shear\ wave\ velocity, V_S) \quad (5.1)$$

where f_{source} is the earthquake source term, $f_{distance}$ is the site-to-source distance term, f_{site} is the site effects term (or "Site Amplification Model"), and Y is the ground motion parameter. Common predicted ground motion parameters are: *Peak Ground Acceleration* (**PGA**), *Peak Ground Velocity* (**PGV**), and *Pseudo Spectral Acceleration* (**PSA**) at various spectral periods (**T**). As expressed by Equation (5.1), the key elements of most GMPEs include:

Earthquake Magnitude, as quantified through Moment Magnitude (M_W)

Style of faulting (mechanism): Reverse (RV), or Strike-Slip (SS), or Normal (N)

Source-to-site distance, typically quantified via R_{RUP}: the distance to fault rupture

Soil conditions, usually parameterized via V_{S30}: the time-averaged shear wave velocity of the upper 30 m

Depth to bedrock (i.e., $Z_{1.0}$, depth to $V_S = 1.0\ km/s$)

In the past decades, hundreds of GMMs have been developed (Douglas 2016) for application in various tectonic regions (i.e., shallow crustal, subduction zones, stable continental). The selection of the most appropriate GMM for a certain application is one of the most crucial decisions for the development of seismic hazard maps.

In particular, for the State of Texas, the observed seismicity has been associated with and possibly "induced" by human activities, such as fluid injection or extraction (Hough 2014). Due to their nature, the induced events are likely to be of smaller magnitude and at shallower focal depth than natural earthquakes. These characteristics of induced seismicity often make the development of application-specific GMMs a necessity. Acknowledging the lack of a ground motion model

developed entirely based on regional data, Zalachoris and Rathje (2017) utilized recordings at seismic stations in Texas, Oklahoma, and Kansas (presented previously in Section 4.2 of this report), to develop a new GMM for small-to-moderate earthquake events particularly tuned to the characteristics of the observed seismicity in these States. The new model (hereafter ZR18) was developed by modifying a CEUS GMM using regional observations of shaking. The Hassani and Atkinson (2015) model (hereafter HA15), which was developed as part of the Next Generation Attenuation—East (NGA-East) project (PEER, 2015), was selected as the reference CEUS GMM. Additional details on development of this GMM can be found in Zalachoris and Rathje (2018).

The reference site condition of the Zalachoris and Rathje (2017) model, in terms of the time-average shear wave velocity of the upper 30 m (V_{S30}), is V_{S30} = 760 m/s. The variation of the predicted peak ground acceleration (PGA) and spectral acceleration at a period of 1.0 sec (Sa(1.0s)) with epicentral distance (R_{epi}) for the two scenarios (M = 5.0 and M = 6.0) considered in this study, for hard rock (i.e., V_{S30} = 760 m/s) and soft soil (i.e., V_{S30} = 200 m/s), are illustrated in Figure 5.3 As seen in Figure 5.3a, the Zalachoris and Rathje (2017) GMM predicts reference rock (i.e., V_{S30} = 760 m/s) PGA values as high as 0.45g and 0.62g at very close epicentral distances (R_{epi} < 1 km), and values of 0.015g and 0.043g at an epicentral distance of R_{epi} = 50 km, for M = 5.0 and M = 6.0, respectively. Similarly, for soft soil conditions (V_{S30} = 200 m/s) (Figure 5.3b), ZR18 results in PGA values of 0.37g and 0.38 g at very close epicentral distances (R_{epi} < 1 km), and values of 0.018g and 0.048g at an epicentral distance of R_{epi} = 50 km, for M = 5.0 and M = 6.0, respectively. To account for the effects of the local site conditions on the expected level of ground shaking, the comprehensive V_{S30} map of Texas, as developed as part of the present project and presented in Chapter 3, is used as an input for the Zalachoris and Rathje (2017) predictive model.

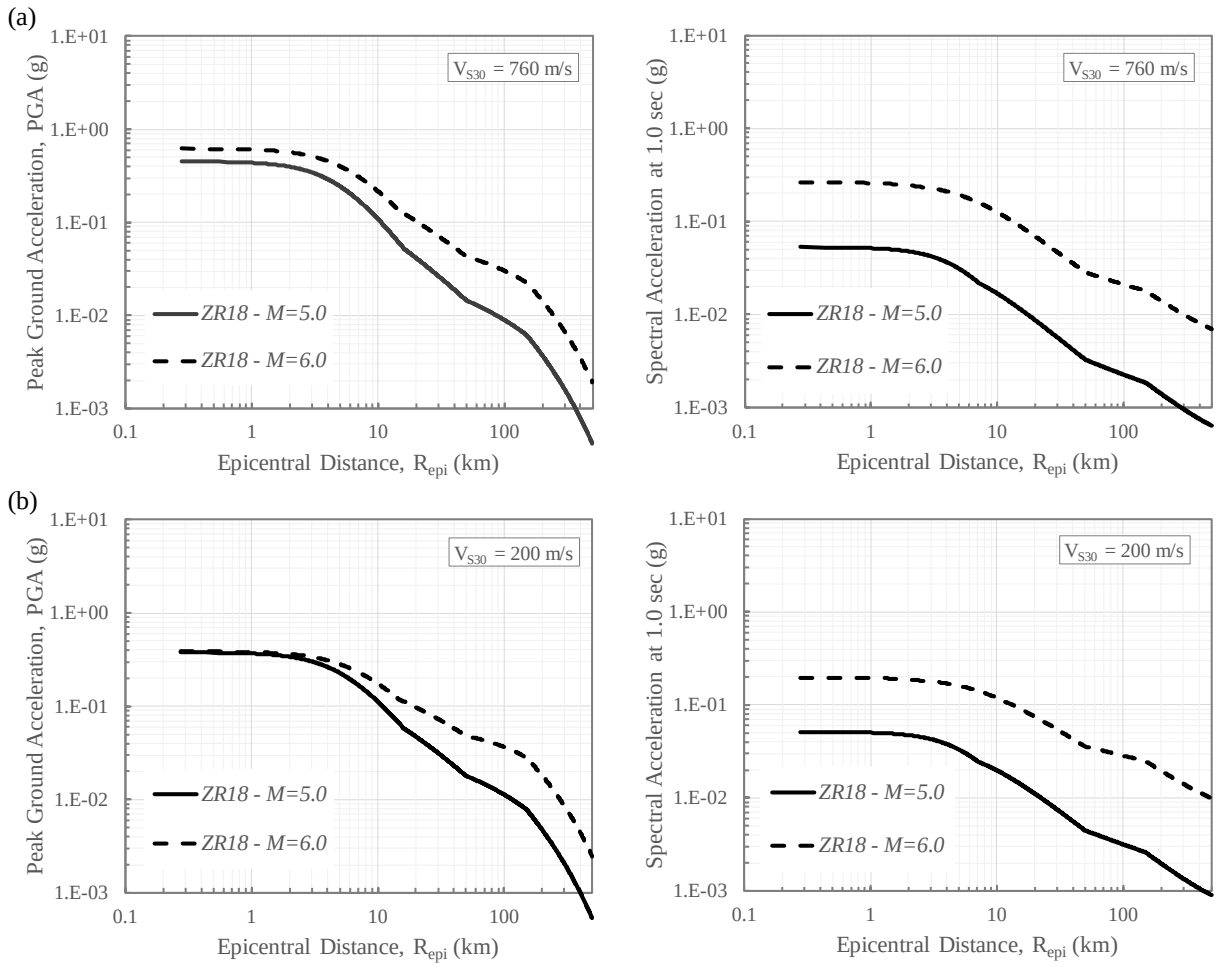

Figure 5.3: Variation of peak ground acceleration (PGA), and spectral acceleration at 1.0 sec with epicentral distance

5.4. Hazard Maps for Deterministic Earthquake Event Scenarios

Using the aforementioned Ground Motion Model developed by Zalachoris and Rathje (2017), as well as the V_{S30} map of Texas shown in Figure 3.26, a series of maps were constructed, depicting the median predicted ground motion within a distance of 80–100 km of the four epicentral locations considered in this study; namely Dallas, Dallas-Fort Worth International Airport, Fort Worth, and El Paso. Figure 5.4 shows the detailed V_{S30} distribution across the Dallas-Fort Worth basin and the El Paso study area. Two deterministic earthquake events with magnitudes M = 5.0 and M = 6.0 were considered. Accordingly, eight hazard maps (four locations × two magnitudes) were constructed for peak ground acceleration (PGA), as well as for spectral acceleration at a period of 1.0 sec (Sa(1.0s)). These maps are shown in Figure 5.5 through Figure 5.12. Additional Shapefiles containing the PGA and Sa(1.0s) contour lines corresponding to the hazard maps of Figure 5.5 through Figure 5.12, are provided as supplemental electronic material to this report. The depicted hazard maps of Figure 5.5 through Figure 5.12 correspond to the PGA and Sa(1.0s) vs. Epicentral Distance relationships provided by ZR18 model, using V_{S30} values from the

constructed V_{S30} Map of Texas (Figure 3.26). At this point, it has to be noted that due to the lack of V_{S30} maps outside of the State of Texas, the hazard maps for El Paso (Figure 5.11 and Figure 5.12) were developed assuming V_{S30} = 760 m/s for areas in New Mexico and Mexico. As seen in Figure 5.5 through Figure 5.12, at the vicinity of the earthquake epicenter, the PGA values range between 0.42g (for El Paso, Figure 5.11) and 0.50g (for DFW, Figure 5.7), for M = 5.0, and between 0.54g (for El Paso, Figure 5.11) and 0.63g (for DFW, Figure 5.7), for M = 6.0. Similarly, the Sa(1.0s) values range between 0.047g (Figure 5.12) and 0.065g (Figure 5.8), for M = 5.0, and between 0.22g (Figure 5.12) and 0.29g (Figure 5.8), for M = 6.0. Nonetheless, these values decrease relatively quickly with distance, with PGA at R_{epi} = 30 km being on the order of 0.03g and 0.1g, and Sa(1.0s) on the order of 0.006g and 0.05g, for M = 5.0 and M = 6.0, respectively. In addition to the hazard maps and contour lines corresponding to the deterministic hazard maps for PGA and Sa(1.0s), the Shapefiles supplementing this manuscript also contain contour lines of spectral accelerations at periods of 0.05s and 0.2s for the four locations and two event scenarios considered.

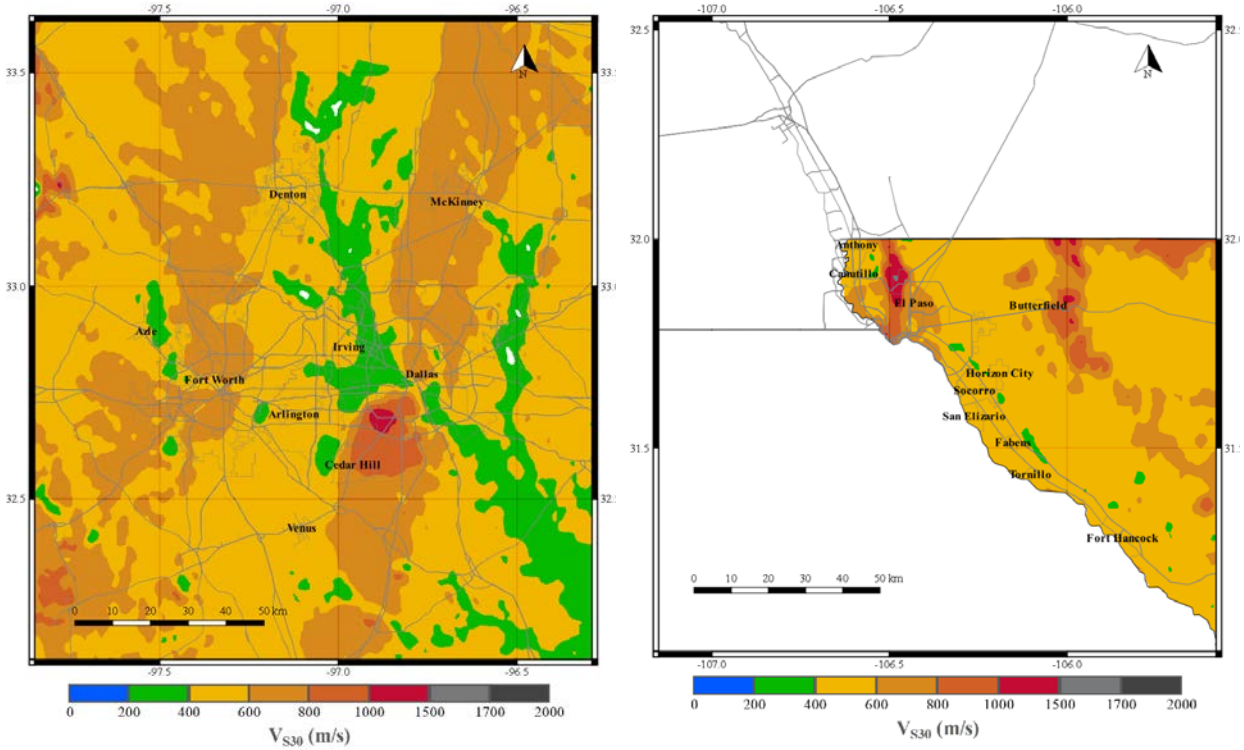

Figure 5.4: Detailed V_{S30} distribution across the Dallas-Fort Worth basin and the El Paso study areas

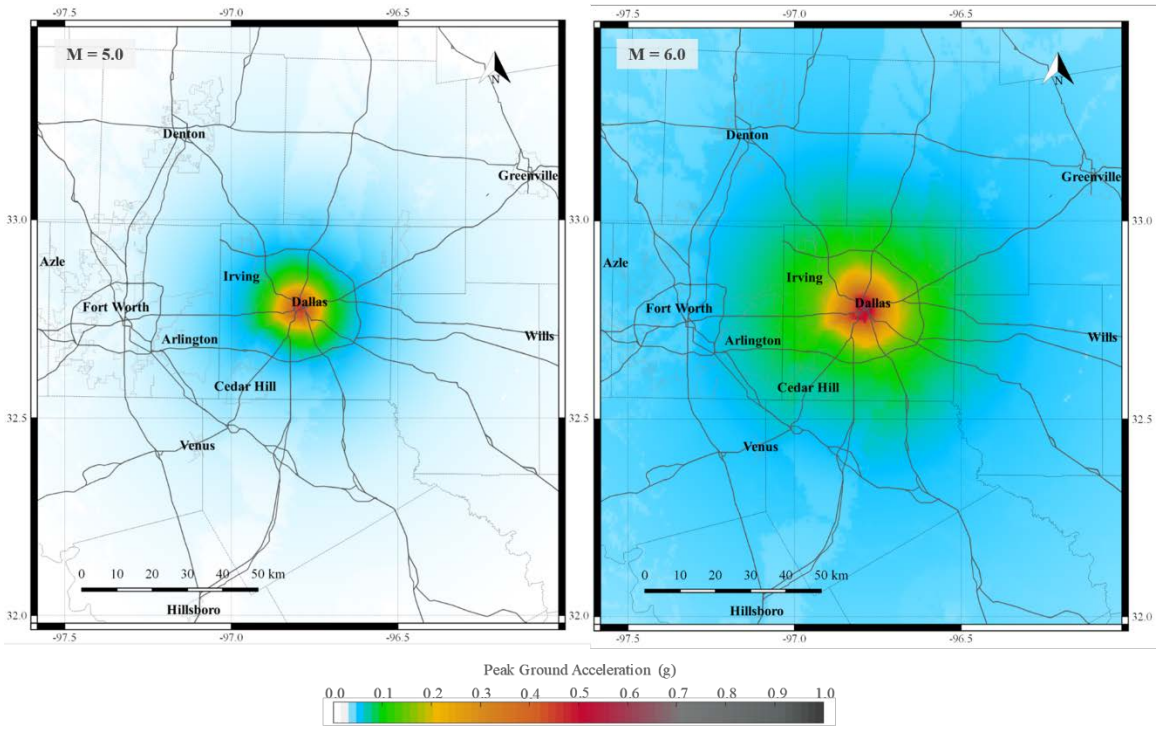

Figure 5.5: Hazard maps for peak ground acceleration, for M = 5.0 and M = 6.0 – Dallas

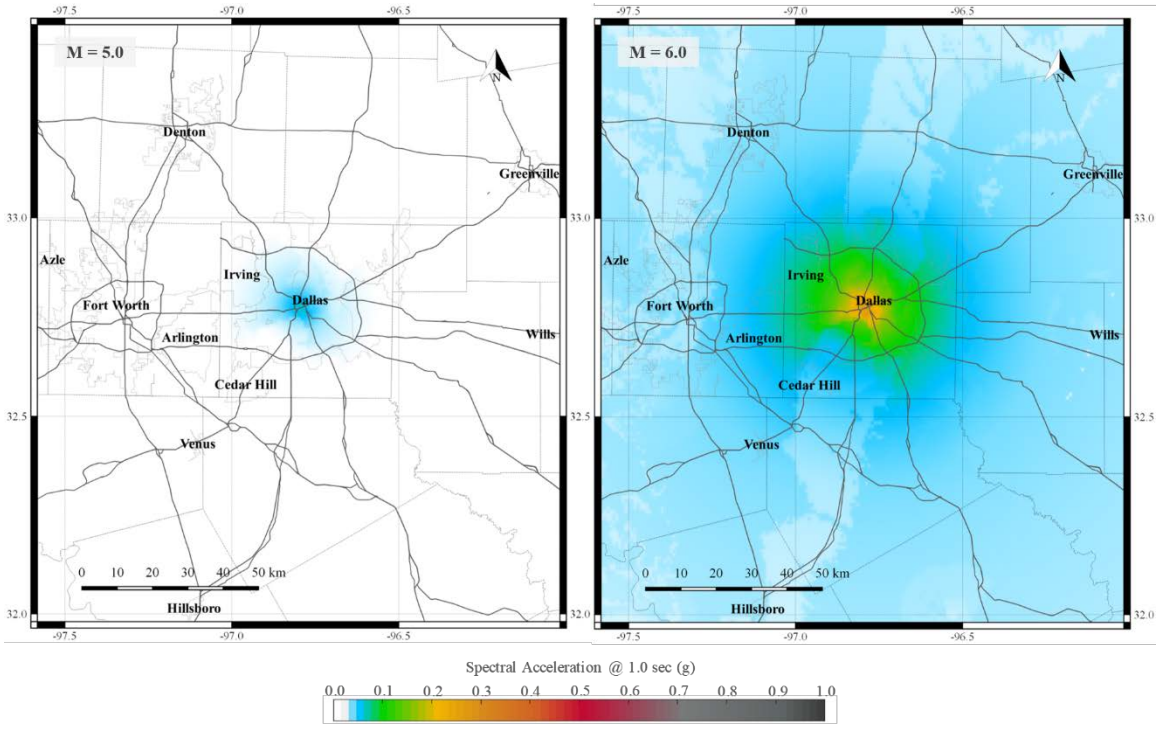

Figure 5.6: Hazard maps for spectral acceleration at 1.0 sec, for M = 5.0 and M = 6.0 – Dallas

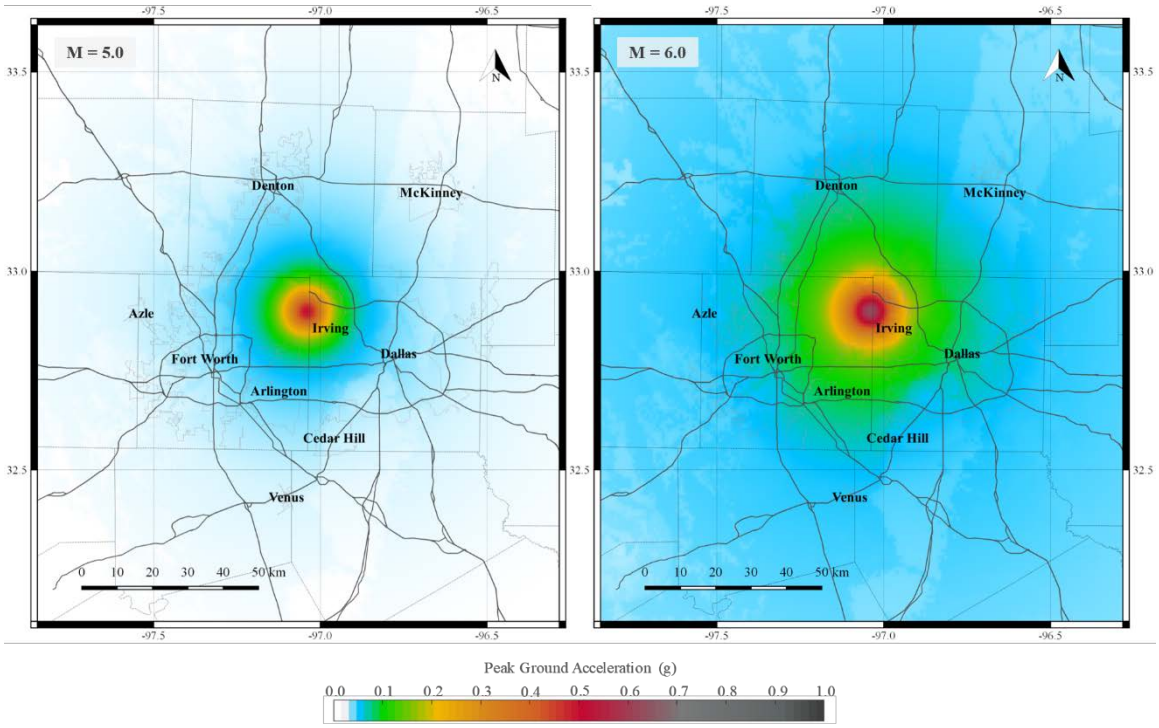

Figure 5.7: Hazard maps for peak ground acceleration, for M = 5.0 and M = 6.0 – Dallas-Fort Worth International Airport

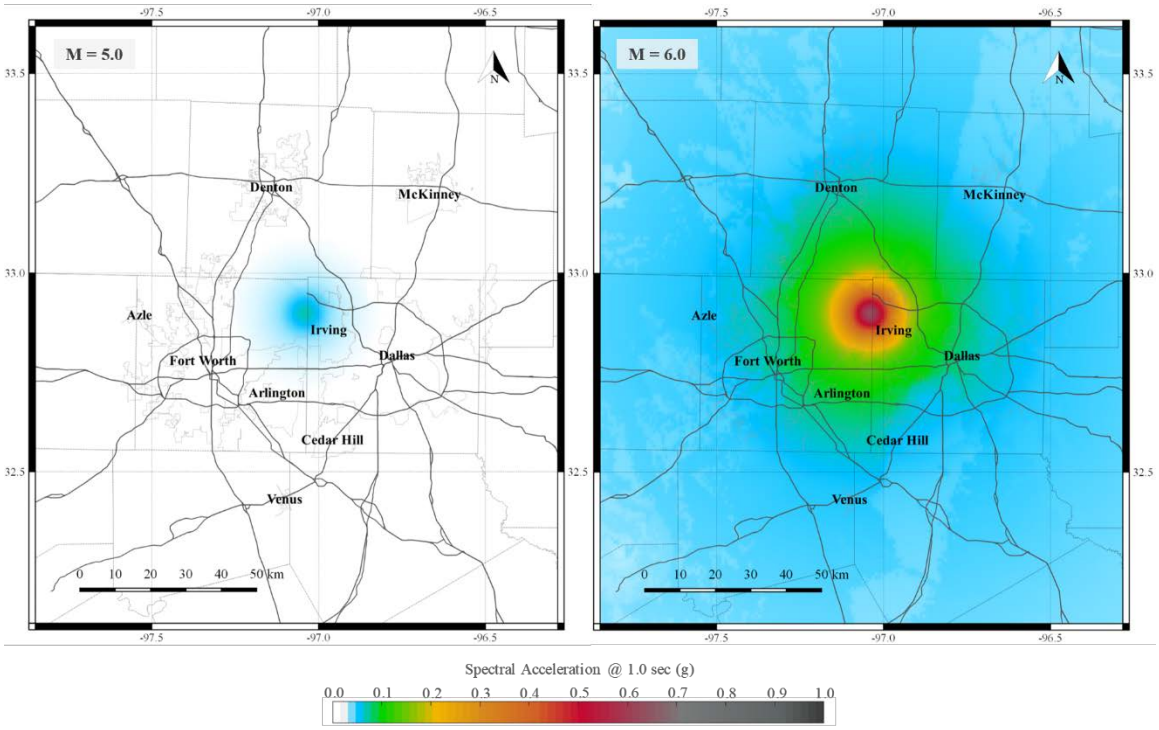

Figure 5.8: Hazard maps for spectral acceleration at 1.0 sec, for M = 5.0 and M = 6.0 – Dallas-Fort Worth International Airport

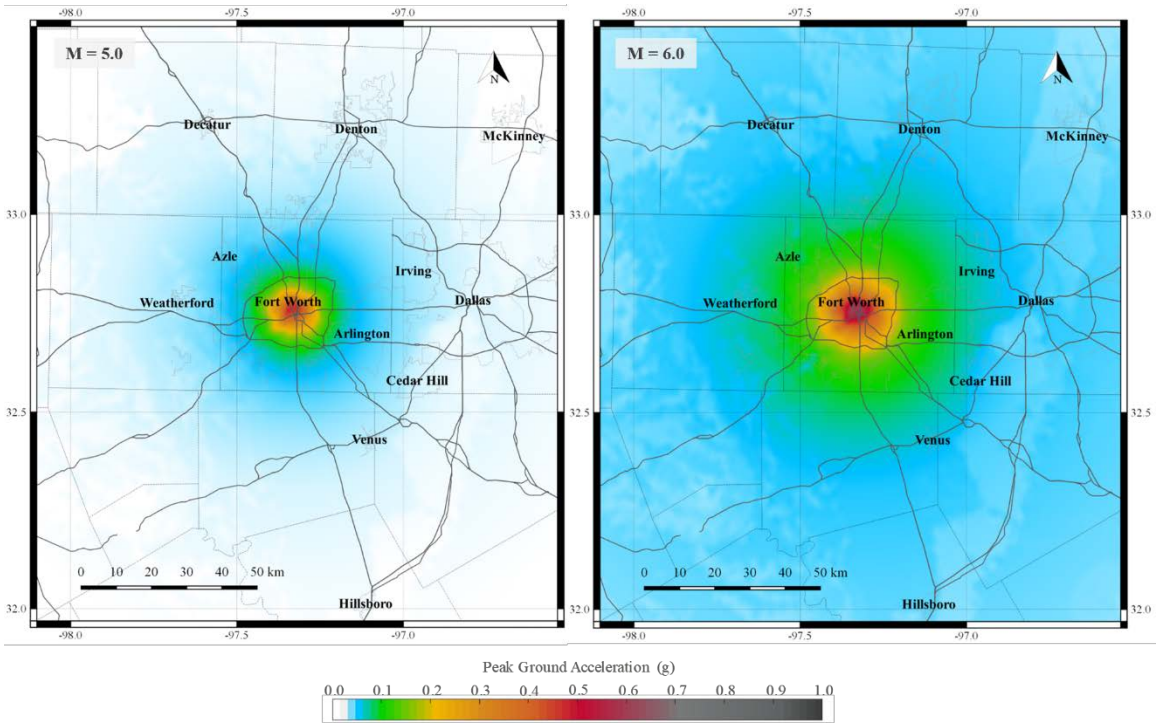

Figure 5.9: Hazard maps for peak ground acceleration, for M = 5.0 and M = 6.0 – Fort Worth

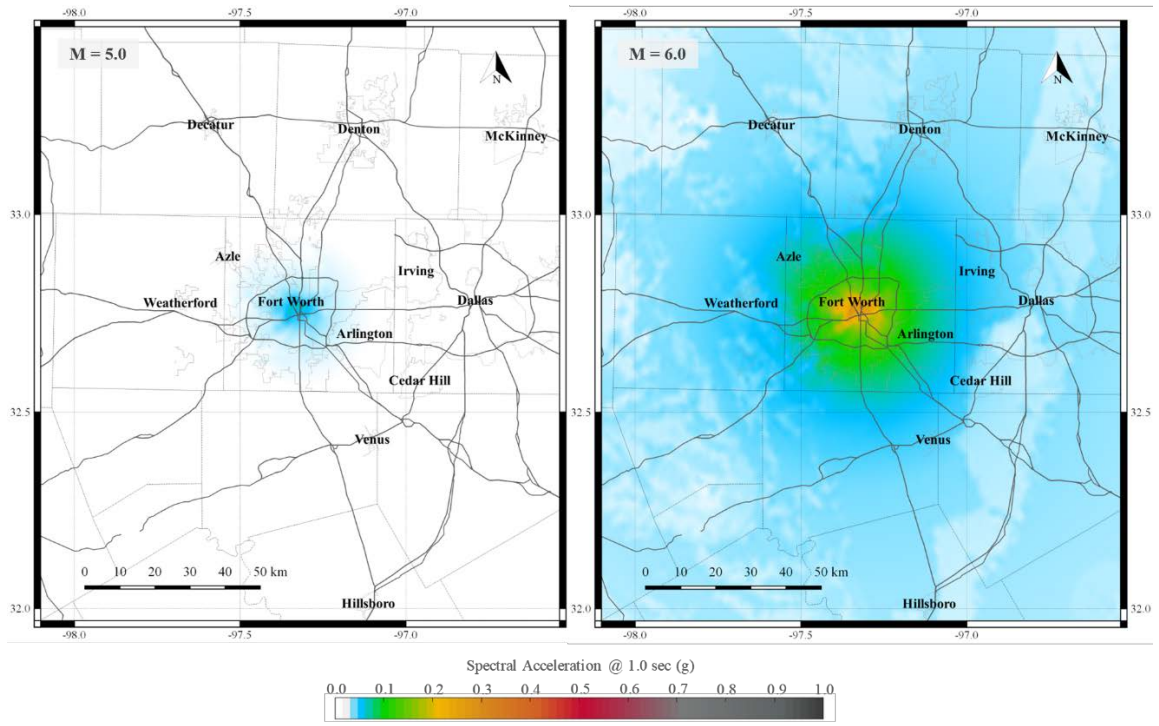

Figure 5.10: Hazard maps for spectral acceleration at 1.0 sec, for M = 5.0 and M = 6.0 - Fort Worth

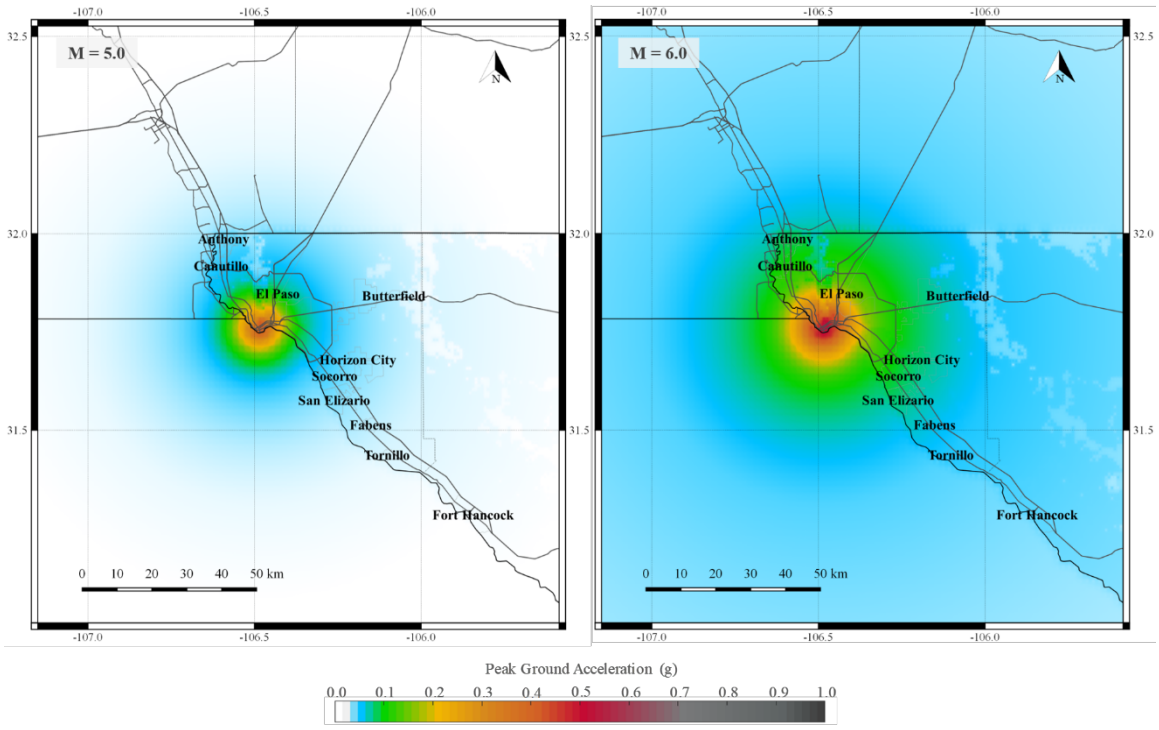

Figure 5.11: Hazard maps for peak ground acceleration, for M = 5.0 and M = 6.0 – El Paso

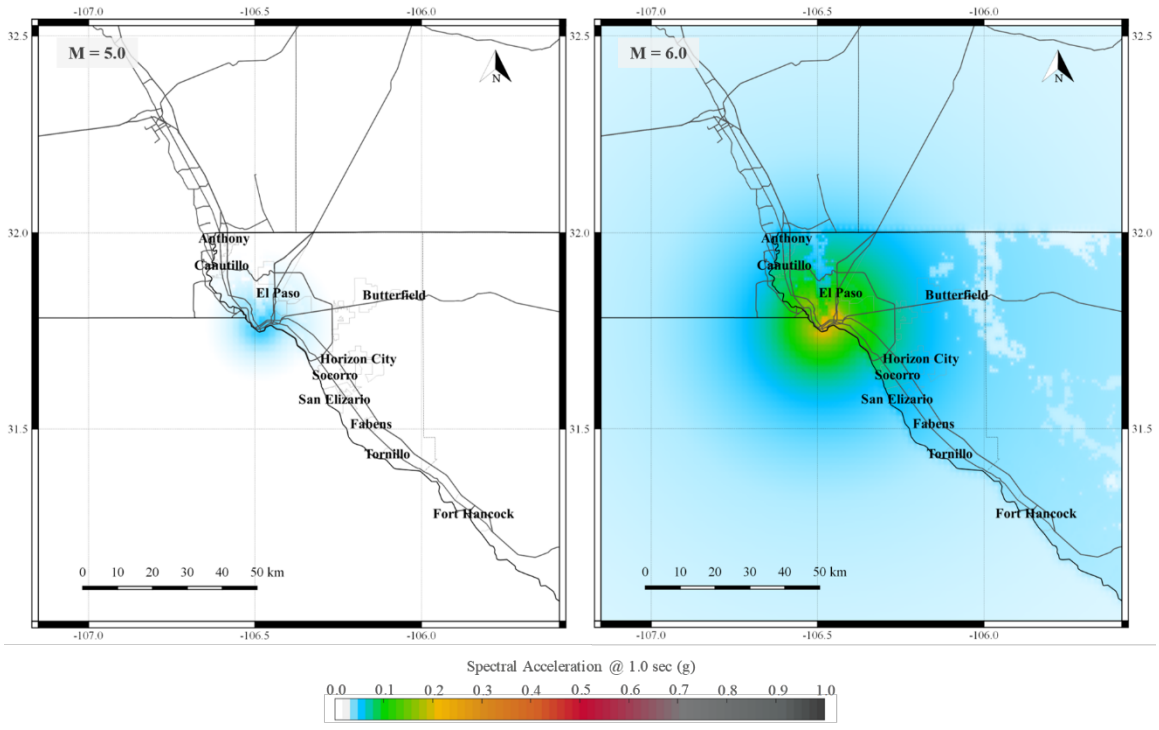

Figure 5.12: Hazard maps for spectral acceleration at 1.0 sec, for M = 5.0 and M = 6.0 – El Paso

5.5. Summary

A series of hazard maps presented in this study are presented. Initially, the seismic hazard in the CEUS, and particularly in the State of Texas, as recently assessed by USGS, was presented. Subsequently, the Zalachoris and Rathje (2018) Ground Motion Model was briefly discussed, which was utilized for predicting median spectral amplitudes, as well as the V_{S30} map of Texas developed as part of this project. Then, seismic hazard maps were constructed for four locations (Dallas, Dallas-Fort Worth International Airport, Fort Worth, El Paso) and two deterministic scenario events (M = 5.0 and M = 6.0). Ground motion predictions are provided for four spectral periods; namely, PGA, 0.05 sec, 0.2 sec, and 1.0 sec.

Chapter 6. TxDOT Bridge Inventory and Representative Bridges

6.1. Overview

When performing fragility analysis on a bridge network for a large region or state, such as Texas, a challenge that arises is determining an accurate way to estimate the seismic vulnerability of the entire bridge inventory without having to assess every individual structure. The first step in addressing this challenge is developing a thorough understanding of the bridge inventory for the area of study. In this chapter, an analysis of the TxDOT highway bridge inventory is conducted using the FHWA National Bridge Inventory (NBI), as well as additional information provided by TxDOT. Information of interest in characterizing the bridge inventory for seismic fragility analysis includes, but is not limited to, bridge structural system and material, era of construction, and geometry. Moreover, the chapter discusses specific components and structural details of Texas bridges. Bridge design and construction techniques not only vary among the different bridge classes, but also may vary based on era of construction. The second step in this process is using the information from the bridge inventory analysis to create representative bridge samples that are statistically significant yet nominally similar. This chapter is also intended to provide an overview of the sampling methods used to determine the representative bridge samples used in this study.

6.2. Bridge Classes

When assessing the seismic vulnerability of an individual bridge, ideally one would generate fragility curves using representative models of the specific bridge in question. However, when assessing the vulnerability of a bridge network for a region or state, developing fragility curves for individual bridges is not feasible. An alternative approach is to generate fragility curves for typical bridge classes representative of the bridge population in question. Thus, an important part of the fragility assessment is understanding and characterizing the bridge inventory for the area of study. This is typically done by gathering data from the National Bridge Inventory database, and supplementary information from standard bridge drawings or owner expertise.

The National Bridge Inventory (NBI) is a database compiled by the Federal Highway Administration (FHWA) to help track and record bridge inspection data. The NBI was first created in the 1970s following the implementation of the National Bridge Inspection Standards, which required every bridge located on a public road be inspected at least once every two years (FHWA, 1994). The database does not provide a complete description of each bridge; however, it does provide basic information that can be used to create generalized highway bridge classes. The NBI contains 116 fields of information including identification information, design types, material types, geometric data, functional descriptions, condition and inspection ratings, etc. The *Recording and Coding Guide for the Structure Inventory and Appraisal of the Nation's Bridges* (NBI Coding Guide, 1995) is used to decode the information in each of the 116 fields.

When creating bridge classes for use in a seismic fragility assessment, it is important to characterize the bridge classes such that the bridges assigned to them are expected to have similar seismic behavior. Typically, bridge classes are represented by design type, material type, number of spans, and span continuity (Nielson, 2005; Ramanathan, 2012). In this study, bridge classes are represented by superstructure design type, material type, number of spans, and span continuity. Table 6.1 and Table 6.2 show possible material and design types as listed in NBI.

Table 6.1: Superstructure material types listed in NBI

Description
Concrete (Simply Supported)
Concrete Continuous
Steel (Simply Supported)
Steel Continuous
Prestressed Concrete (Simply Supported)
Prestressed Concrete Continuous
Wood or Timber
Masonry
Aluminum, Wrought Iron, or Cast Iron
Other

Table 6.2: Superstructure design types listed in NBI

Description	
Slab	Suspension
Stringer/Multi-beam or Girder	Stayed Girder
Girder and Floor Beam System	Movable-Lift
Tee Beam	Movable-Bascule
Box Beam or Girders-Multiple	Movable-Swing
Box Beam or Girders-Single or Spread	Tunnel
Frame	Culvert
Orthotropic	Mixed Types
Truss-Deck	Segmental Box Girder
Truss-Thru	Channel Beam
Arch-Deck	Other
Arch-Thru	

According to the NBI, there are 52,937 bridges in the state of Texas; however, only 33,586 of them are considered on-system, i.e., maintenance responsibility belongs to TxDOT. For the purposes of this study, only on-system bridges are considered in the analysis. Of the 33,586 on-system bridges, 13,441 are listed in NBI as culverts, which are assumed out of scope for this project. Table 6.3 shows the remaining 20,145 on-system bridges separated into 11 different bridge classes based on superstructure system and material, along with an abbreviated name and the frequency of each bridge class.

Table 6.3: Texas bridge classes

Bridge Type	Abbreviation	Amount	Percentage (%)
Multi-Span Continuous Reinforced Concrete-Slab	**MCRC-Slab**	**1,068**	**5.30**
Multi-Span Simply Supported Reinforced Concrete-Slab	**MSRC-Slab**	**1,566**	**7.77**
Multi-Span Simply Supported Reinforced Concrete-Girder	**MSRC**	**3,336**	**16.56**
Multi-Span Simply Supported Reinforced Concrete-Tee Beam	-	829	4.12
Single Span Reinforced Concrete-Girder	-	137	0.68
Multi-Span Simply Supported Prestressed Concrete-Girder	**MSPC**	**6,808**	**33.79**
Single Span Prestressed Concrete-Girder	**SSPC**	**1,753**	**8.70**
Multi-Span Simply Supported Prestressed Concrete-Box Girder	-	849	4.21
Multi-Span Continuous Steel-Girder	**MCSTEEL**	**2,075**	**10.30**
Multi-Span Simply Supported Steel-Girder	**MSSTEEL**	**457**	**2.27**
Single Span Steel-Girder	-	141	0.70
Other	-	1,126	5.59
Total		**20,145**	**100.00**

As seen in Table 6.3, seven out of the twelve bridge classes (those in **bold** in Table 6.3) make up 88.7% of the total on-system bridges in Texas. Based on the research requested by TxDOT in the project problem statement, these seven classes are those considered in this study. The five non-bold face entries in Table 6.3 are considered outside the scope for this study. As seen in the table, Single Span Reinforced Concrete-Girder and Single Span Steel-Girder bridges consist of a very small percentage (1.38%) of the total on-system inventory. The class listed as "Other" makes up 5.59% of the total bridge inventory, but it consists of a large number of smaller bridge types that by themselves have no real significance towards the total percentage (e.g., bridges of different materials such as wood and masonry, cable-stayed bridges, suspension bridges, etc.). The other two bridge classes, i.e., Multi-Span Simply Supported Reinforced Concrete-Tee Beam and Multi-Span Simply Supported Prestressed Concrete-Box Girder bridges, represent a reasonable percentage (4.21% and 4.12%, respectively) of the total; however, neither of these systems were indicated by TxDOT as a superstructure type of initial interest in the research problem statement, and are considered out of scope for this study.

Figure 6.1 shows the locations of all on-system bridges considered in the scope of this study indicating those with pre-stressed concrete girders (MS PC-Girder and SS PC-Girder), steel girders (MC Steel-Girder and MS Steel-Girder, and those not falling into either of these categories. This figure shows trends in the geographic distribution of Texas bridges. While bridges tend to be concentrated in and around larger cities, this concentration is particularly true for steel girder bridges. Similarly, PC girder bridges tend to be concentrated along major interstate highways in Texas. This concentration of specific bridge classes near highly populated areas and along major

interstate thoroughfares could be of interest, as damage to these types of bridges during an earthquake event could have greater impact on the public and state commerce.

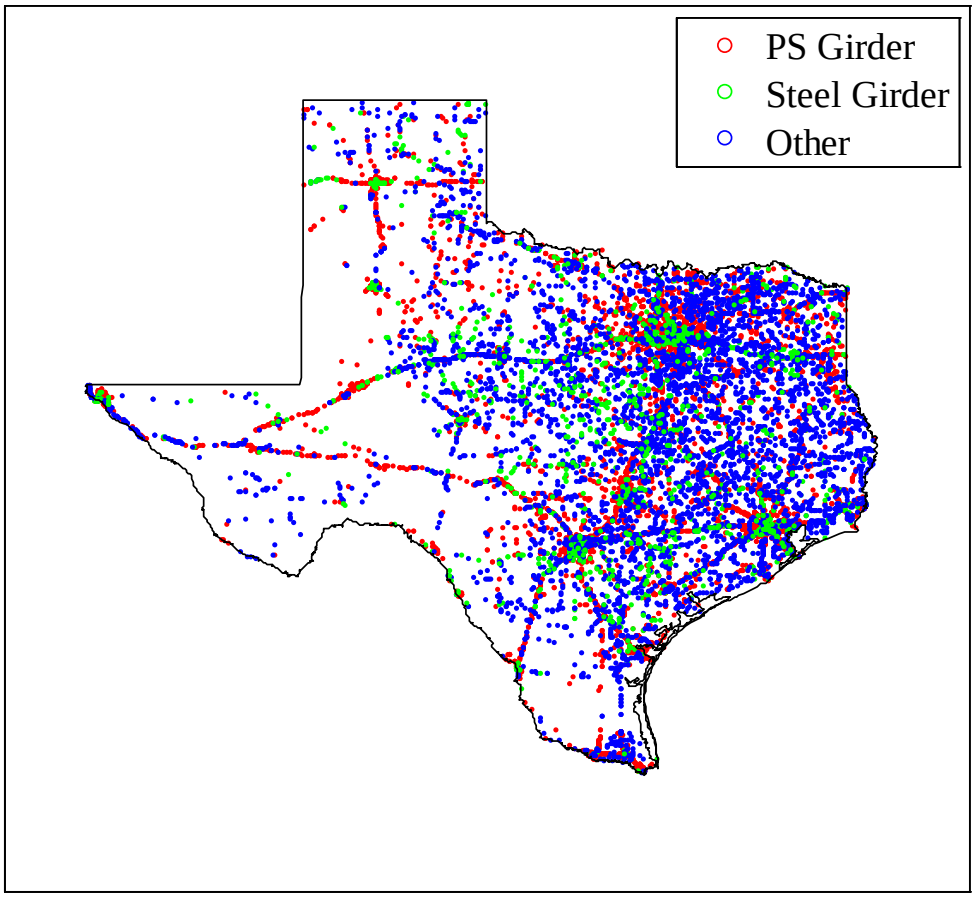

Figure 6.1: TxDOT bridge locations in scope of study

6.3. Bridge Geometric Statistics

With the general bridge classes defined, the next step is to examine the characteristics of each individual bridge class. The main parameters for bridge characterization are number of spans, maximum span length, deck width, vertical under-clearance, skew angle, substructure type, year of construction. These parameters were retrieved from NBI and the TxDOT bridge database and are analyzed to identify general geometric trends throughout the entire bridge population, as well as within each bridge class. In this regard, probabilistic distributions of the geometric parameters and age of the bridge population were developed and reported in this chapter. These parameters, which are depicted in Figure 6.2 and Figure 6.3, are critical for developing numerical bridge models to simulate seismic behavior, as these parameters greatly affect structural stiffness, mass, and fundamental periods of vibration.

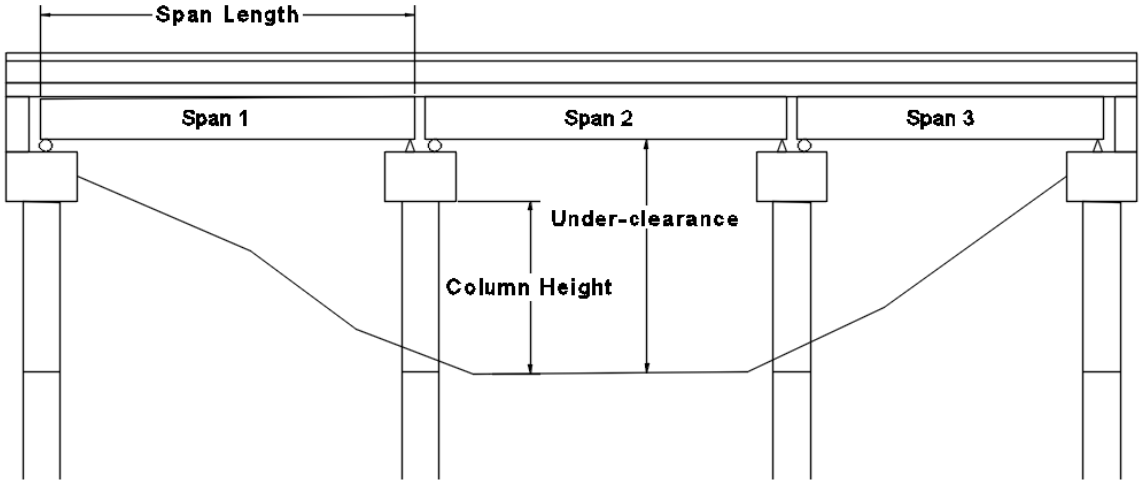

Figure 6.2: Profile of a typical three-span bridge

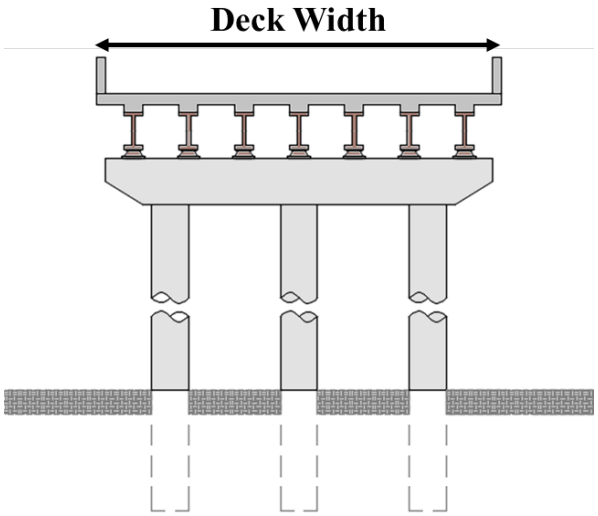

Figure 6.3: Cross section of a typical steel girder bridge

6.3.1. Number of Spans

The number of spans parameter takes the form of distinct integer values, and therefore, can be examined through counting the frequency of data at each span number. In this study, probability mass functions (PMFs) are generated and used to analyze the number of spans for each bridge class. Figure 6.4 and Figure 6.5 show PMFs of number of spans for simply supported and continuous span bridges, respectively. PMFs are generated by dividing the number of bridges having a particular span number by the total number of bridges in that class.

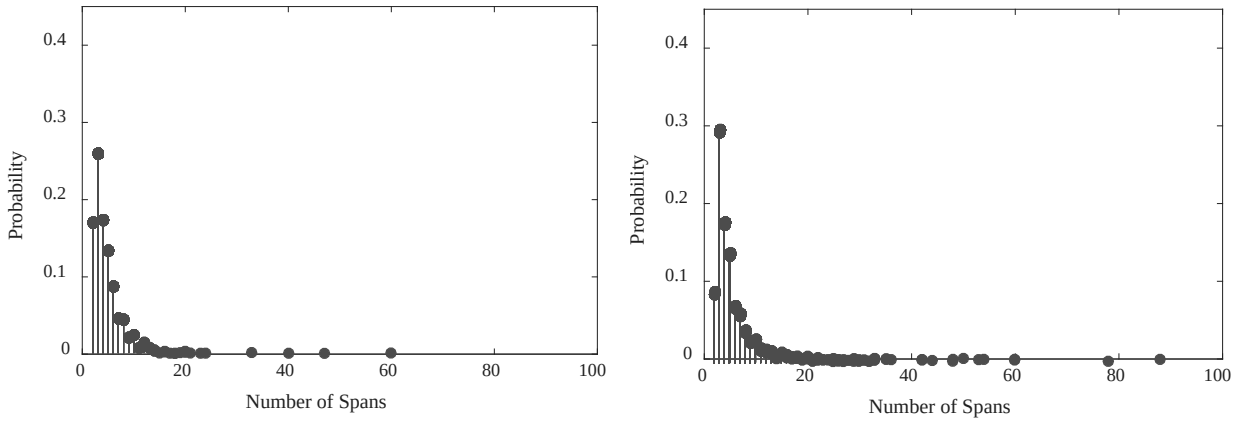

a) MSRC-Slab

b) MSRC

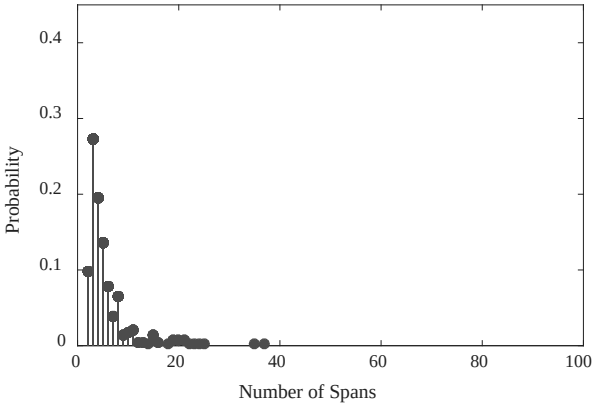

c) MSSTEEL

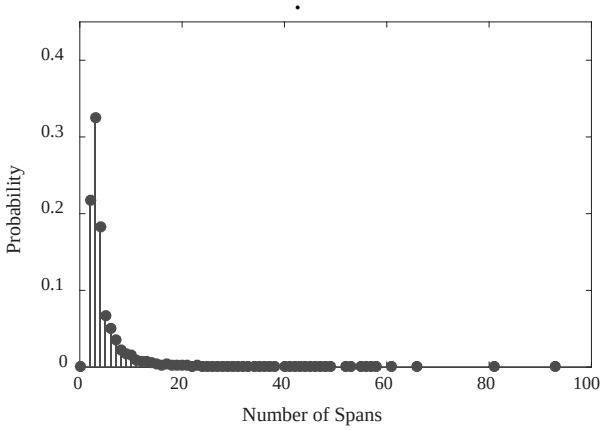

d) MSPC

Figure 6.4: PMFs of number of spans for multi-span simply supported bridge classes

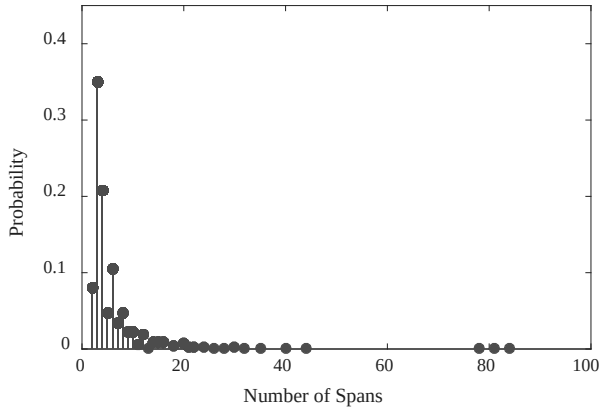

a) MCRC-Slab

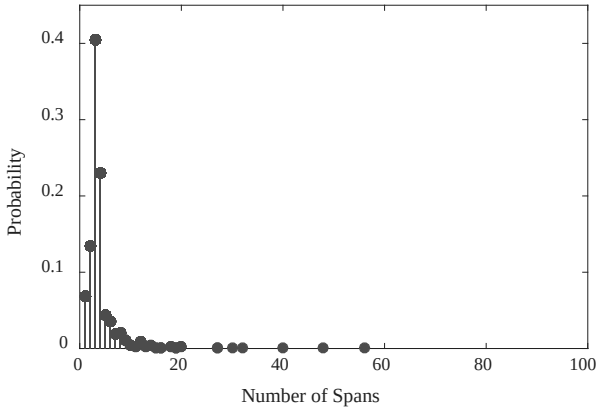

b) MCSTEEL

Figure 6.5: PMFs of number of spans for multi-span continuously supported bridge classes

Table 6.4 shows statistics for the number of spans for each bridge class. The data shows the typical span configuration is between two and six spans, with three spans being the most common. On average, 75% of the simply supported bridges have less than six spans, while 80% of the continous bridges have less than six spans.

Table 6.4: Span number statistics

Bridge Class	Mean	Std Dev.	Median	Mode
MCSTEEL	4.10	3.33	3	3
MSSTEEL	5.40	4.08	4	3
MSPC	4.86	5.40	3	3
MSRC	5.72	6.91	4	3
MCRC-Slab	5.70	7.35	4	3
MSRC-Slab	4.78	3.52	4	3

For each bridge class, the distributions for number of spans were modified before sampling to reduce unnecessary complexities in the modeling process. For example, for each bridge class, there are some bridges in the population that have a very large number of spans (e.g., 12 or more). Using a Latin Hypercube Sampling approach, described in more detail in Section 6.7, would result in samples with a similarly large number of spans that would result in a significant increase in computational expense during the nonlinear response-history analyses, while the expected damage is not expected to be significantly different from a bridge with significantly fewer spans (Sullivan and Nielson 2010).

Thus, in this study, the number of spans considered in the sampling methods are reduced to only two to five span configurations to avoid having models with an excessive number of spans. This range of spans covers over 70% of the population for all bridge classes (see Figure 6.4 and Figure 6.5 for span number distributions), except for the multi-span continuous concrete slab bridges with only 67% of the population having between two to five spans (see Figure 6.6). This modification is done once again to reduce the computational expense for the large number of nonlinear response-history analyses that are conducted in the seismic fragility assessment.

Following this reasoning and the guidance of HAZUS (FEMA 2003), most past fragility analysis studies such as Choi (2002), Nielson (2005), Pan (2007), Ramanathan (2012), and Tavares et al. (2013) have only considered a constant three-span bridge configuration. In some cases, fragility results from the base three-span configuration can be extrapolated to predict the response of bridges with a larger number of spans (FEMA 2003; Sullivan and Nielson 2010); however, the number of spans, ranging from two to five, are explicitly considered as a variable in this study. Table 6.17 and Table 6.23 at the end of this chapter present the randomly generated number of spans for 8 different configurations of each bridge class.

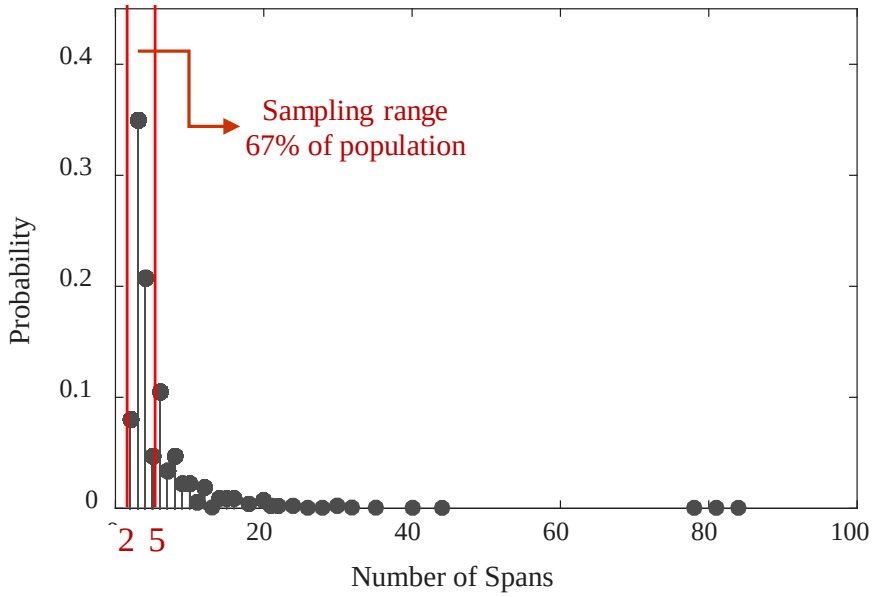

Figure 6.6: Sampling range for number of spans of MCRC-slab bridge class

6.3.2. Span Length

Recording the length of every span in every bridge in the NBI would not be feasible; however, the maximum span length is recorded in the NBI and can be used along with some common assumptions to establish a generalized span configuration. The two assumptions adopted in this study are: 1) span lengths are symmetrical along the length of the bridge; 2) approach span lengths are constant within a certain bridge class. For example, a two-span bridge would have two spans with lengths equal to the maximum. A bridge with three or more spans would have interior spans with lengths equal to the maximum, while the end spans would be considered the approach spans with a standard length. Approach span length is not listed in the NBI; however, approach span lengths are determined from bridge drawings acquired from TxDOT and are used to define a typical approach span length for each bridge class. Table 6.5 shows some statistics to show general trends of maximum span length for each bridge classes, and Figure 6.7 through Figure 6.9 show histograms of the actual data. For each bridge class, the span length for each bridge configuration are randomly generated using the information listed in Table 6.5.

Table 6.5: Maximum span length statistics

Bridge Class	Mean (ft)	Std Dev. (ft)	Median (ft)	Coefficient of Variation
MCSTEEL	102.13	52.82	88.00	0.52
MSSTEEL	48.20	26.57	40.03	0.55
MSPC	86.60	28.20	80.00	0.33
MSRC	34.51	5.18	30.84	0.15
SSPC	96.30	23.70	98.00	0.25
MCRC-Slab	32.81	11.98	29.86	0.37
MSRC-Slab	23.52	3.48	24.93	0.15

After examining the data, there are a few trends that should be noted. First, as expected, the continuous span bridge types have longer span lengths than their simply supported counterparts. For example, the MCSTEEL class has an average span length of 103 feet, while the MSSTEEL class only has an average of 48 feet. Second, for the simply supported bridge classes, the MSPC class has the longest spans, exceeding the MSSTEEL class by almost 50%, the MSRC by 60%, and the MSRC-Slab class by almost 70%. Figure 6.7 through Figure 6.9 show that most of the bridge classes have one or two prominent span lengths; however, the MSPC and SSPC classes appear to have lengths more evenly distributed between a given range.

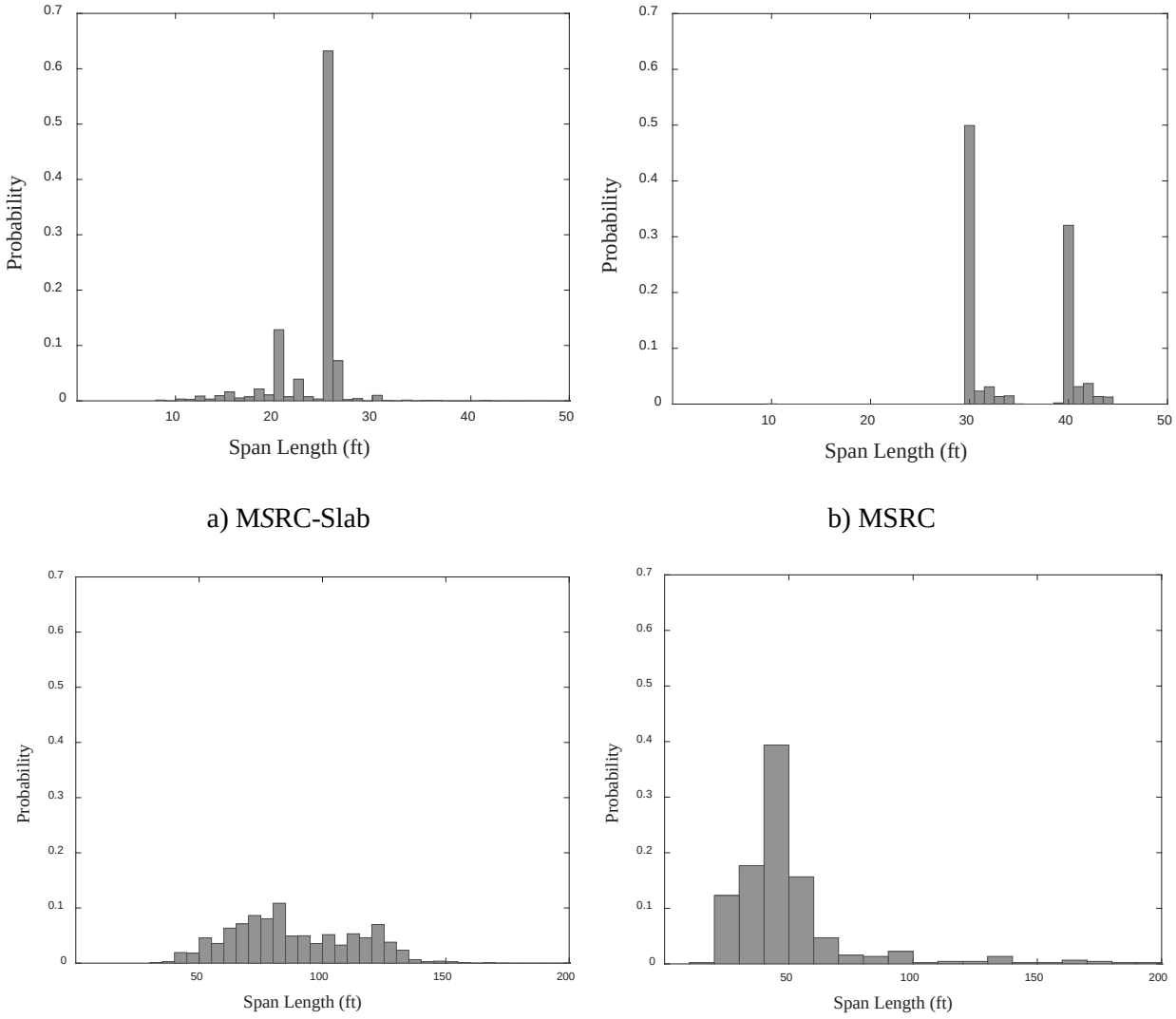

a) MSRC-Slab

b) MSRC

c) MSPC

d) MSSTEEL

Figure 6.7: Histograms of maximum span length for multi-span simply supported bridge classes

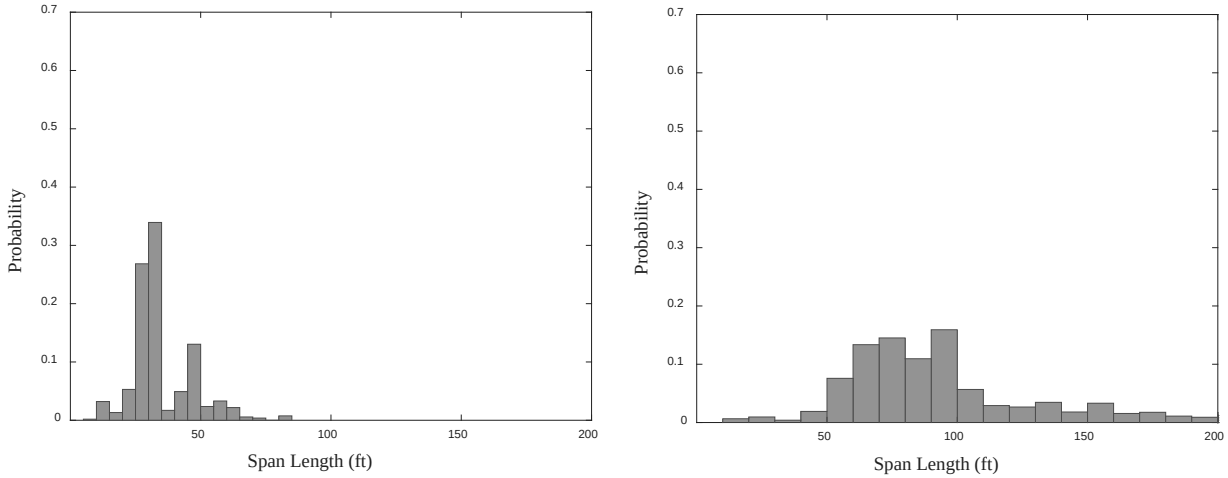

a) MCRC-Slab b) MCSTEEL

Figure 6.8: Histograms of maximum span length for multi-span continuous bridge classes

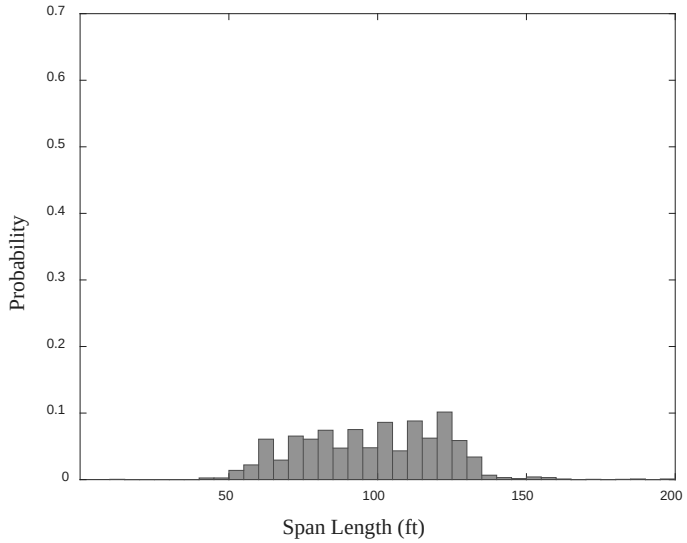

Figure 6.9: *Histogram of maximum span length for single span bridge types*

Highway bridges with three or more spans typically consist of a combination of main spans and approach spans. Main spans are typically the longer spans at the middle of the structure, while the approach spans are designated as the shorter spans used on either end of the bridge. To develop representative bridge models, it important to understand and utilize appropriate approach span lengths for each bridge class. As previously mentioned, approach span lengths are not listed in the NBI database and are, therefore, commonly determined through review of relevant bridge plans (Nielson 2005; Ramanathan 2012). Through review of Texas as-built drawings, it was determined that span lengths are typically symmetrical along the length of the bridge, and approach span lengths follow noticeable trends among each bridge class. Some of these trends and the approach span lengths selected for each bridge class in this study are presented below.

Approach span length for the multi-span, simply supported prestressed and steel girder bridge classes (i.e., MSPC and MSSTEEL) varies between 40 feet and 65 feet; however, an approach span length of 40 feet was found to be the most common, and is used in this study for both of these bridge classes. For the continuous span steel girder bridge class (MCSTEEL), it was determined that the approach span lengths had more variability and were directly correlated to the main span length. After a thorough investigation of as-built drawings (see Appendix C for list of relevant as-built drawings), it was concluded that approach span lengths for the MCSTEEL bridge class range between 60 to 80 percent of the main span length.

The reinforced concrete bridge classes (i.e., MSRC, MSRC-Slab, and MCRC-Slab) tend to have very different trends when it comes to approach span lengths. For example, the MSRC and MSRC-Slab type bridges do not typically have shorter approach spans; instead, the main span length is utilized for all spans throughout the length of the structure. This is predominantly due to the heavily standardized design and construction processes used for these particular bridge types. Whether pre-cast or cast-in place construction is used, standardized forms and span lengths are often utilized for ease of design and construction. This standardization in the distributions of main span lengths for each of these bridge classes, which show that the majority of the MSRC Girder and Slab bridges in the Texas inventory, utilize one or two prominent span lengths (e.g., 30 or 40 feet span lengths, and 25 feet span lengths, respectively). The continuous reinforced concrete slab bridge class (i.e., MCRC-Slab) varies from its simply supported counterpart, utilizing approach spans that are typically shorter than the main spans. Review of relevant bridge plans showed that an approach span length of 25 feet is the most commonly used value for the MCRC-Slab bridge class; thus, it is assumed for all the MCRC-Slab bridges in this study.

In summary, the length of approach spans, i.e., shorter spans used on either end of the bridge, takes constant values of 25 feet for MCRC-Slab bridges, 40 feet for MSPC and MSTEEL bridges. Therefore, for these three bridges classes, it is not a random variable. However, for MCSTEEL, it is a random variable that is uniformly distributed between 60 to 80 percent of the main span length. Moreover, for MSRC and MSRC-Slab bridges, it is the same as the length of the main spans, which are randomly generated based on the information in Table 6.5.

6.3.3. Deck Width

The deck width (i.e., outer to outer distance of the bridge deck railings) is used to define the number of girders in a bridge and estimate the total seismic weight. Table 6.6 reports the basic statistics for this deck widths reported in the NBI, and Figure 6.10 through Table 6.24 show the distributions. One trend worth noting is the prestressed concrete girder bridges on average have wider decks than the steel and reinforced concrete girder bridges. Both the MSPC and SSPC classes have an average deck width of about 53 feet, while the steel girder classes have an average deck width around 45 feet, and the RC classes have an average around 40 feet. However, the median deck width values for the MSPC and SSPC classes are lower than the average values and are consistent with the other bridge types, indicating there are some larger deck width outliers that area causing the average to

be higher. This trend could be due to the fact that PC girder types tend to be more prevalent in newer construction, which would correspond with higher traffic demands and wider roadways.

Table 6.6: Deck width statistics

Class	Mean (ft)	Std Dev. (ft)	Median (ft)	Coefficient of Variation
MCSTEEL	47.72	22.97	41.67	0.48
MSSTEEL	45.17	17.88	44.20	0.40
MSPC	52.60	25.26	44.30	0.48
MSRC	38.59	13.81	37.30	0.36
SSPC	53.05	25.43	44.30	0.48
MCRC-Slab	44.98	16.57	42.00	0.37
MSRC-Slab	35.94	15.62	29.53	0.43

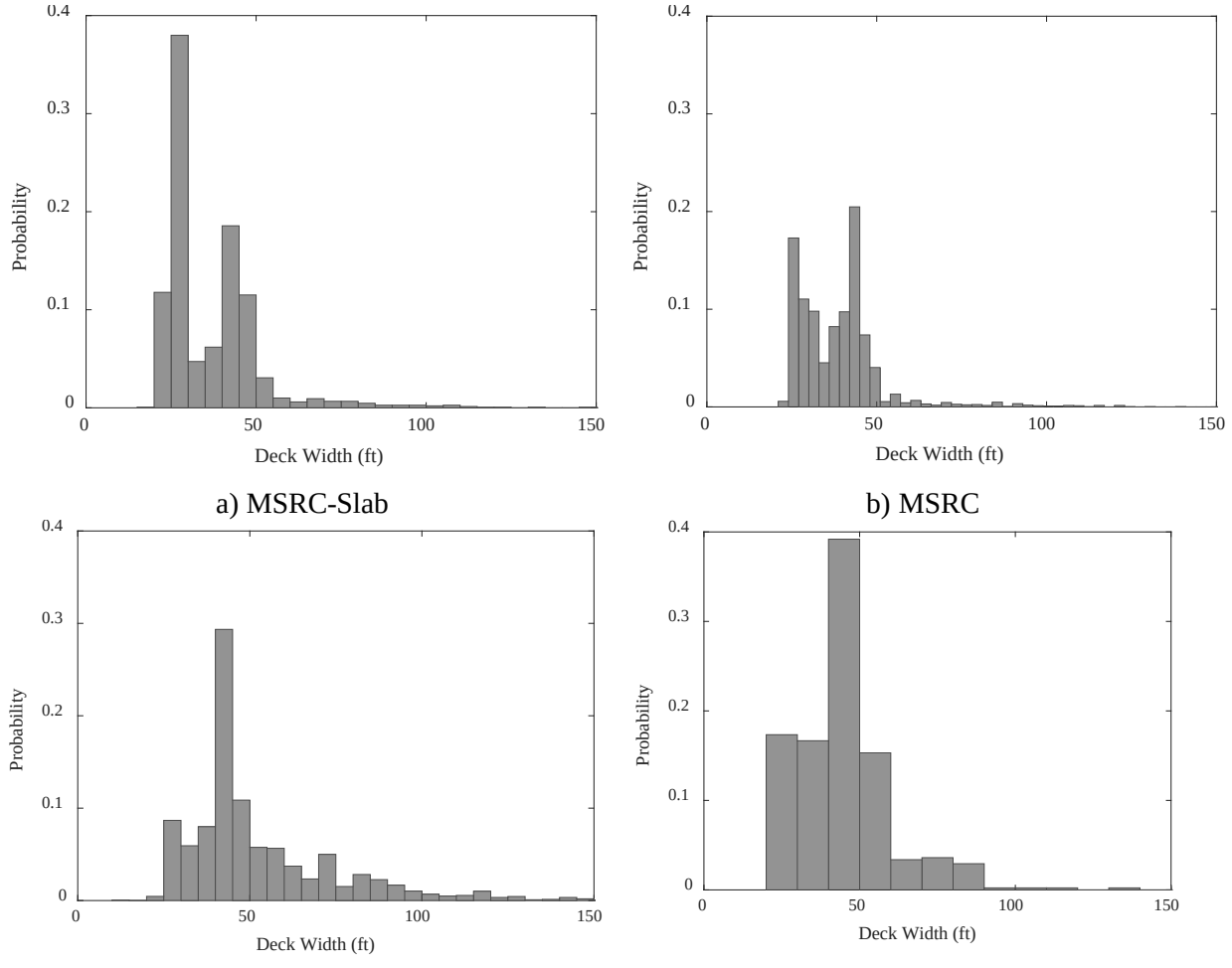

a) MSRC-Slab

b) MSRC

c) MSPC

d) MSSTEEL

Figure 6.10: Histograms of deck width for multi-span simply supported bridge types

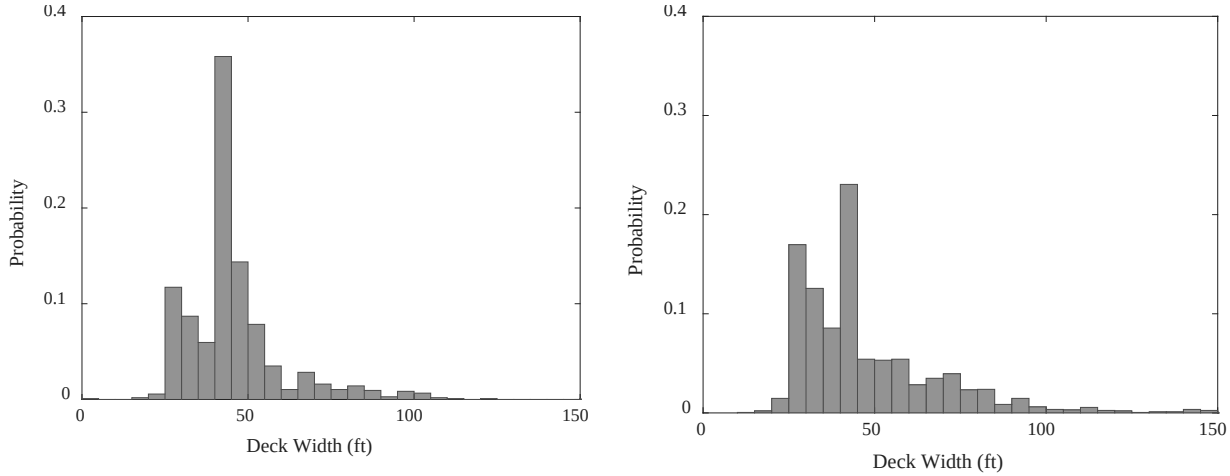

a) MCRC-Slab b) MCSTEEL

Figure 6.11: Histograms of deck width for multi-span continuous bridge types

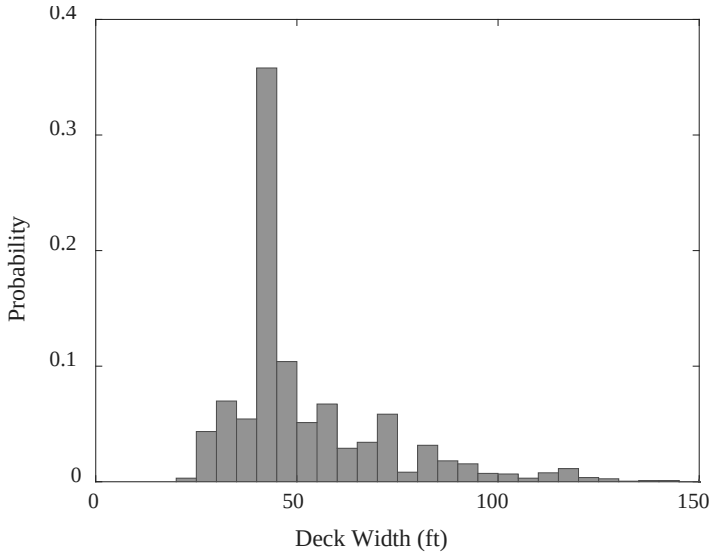

Figure 6.12: Histogram of deck width for single span bridge types

For each bridge class, the distributions for deck width, which are presented in Table 6.6, were modified before sampling analysis to reduce unnecessary complexities in the modeling process. To ensure that the bridge samples capture the vast majority of the bridge inventory without generating unnecessarily complex and computationally expensive bridge models, the deck width was only sampled from the 10th to the 90th percentile of the entire inventory for each class. For example, the multi-span prestressed concrete girder (MSPC) bridge class has deck widths that range from 10 feet to 223 feet, but were sampled between 31 feet and 86 feet (i.e., the 10^{th} and 90^{th} percentiles, see Figure 6.13). Not only do the very narrow and excessively wide bridges only represent a very small percentage of the population, but the excessive deck width significantly increases the computational expense of the nonlinear analyses and is not expected to have a significant effect on seismic performance.

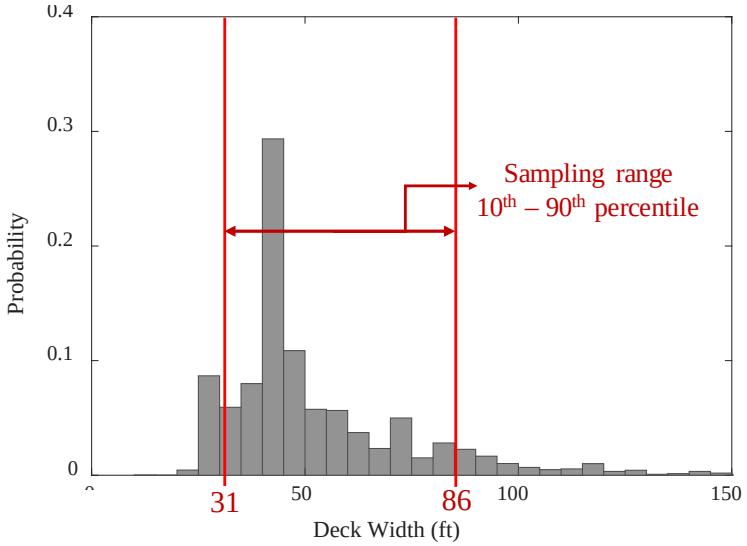

Figure 6.13: Sampling range for deck width of MSPC

6.3.4. Vertical Under-Clearance

The height of a bridge column or bent plays can significant affect the bridge's seismic response due to its correlation with lateral stiffness and natural periods of vibration. Unfortunately, NBI does not explicitly record column height. NBI does, however, record vertical under-clearance data, which can be used to infer column height. Unfortunately, under-clearance data is only listed in NBI for bridges that span over a roadway or railway. Since not all bridges span roadways or railways, the amount of data available to estimate column height is limited and may not be representative of all bridges in the state. In fact, only 43% (about 7,600 bridges) of the in-scope bridges in this study have under-clearance data listed, and some classes have no under-clearance data at all. To gather a large enough dataset to be statistically significant, the under-clearance data for all seven bridge classes are lumped together. It is possible that the available under-clearance data from NBI and TxDOT sources do not capture the actual range of column heights in the bridge population, as it does not account for bridges over water crossings or multi-level flyovers; however, the vertical under-clearance data is the best available source for information on column height.

Vertical under-clearance is measured from the bottom of the superstructure to the top of the roadway or railroad surface below. Figure 6.14 shows the distribution for under-clearance data from NBI. From this figure, the under-clearance parameter appears to take on a bimodal distribution. As shown in Figure 6.14, the most prominent mode is at an under-clearance value of about 17 feet, and the second mode is around 23 feet. The average under-clearance is 17.7 feet with a standard deviation of 3.5 feet. For all bridge classes, under-clearance was sampled from the same distribution.

For modeling purposes, the actual column height, not the under-clearance measurement, is needed. Column height is calculated by subtracting the depth of the bent cap from the under-clearance

value. Therefore, column height was customized to each bridge class by using a typical bent cap depth that is specific to each class as described in Section 6.4.3.1.

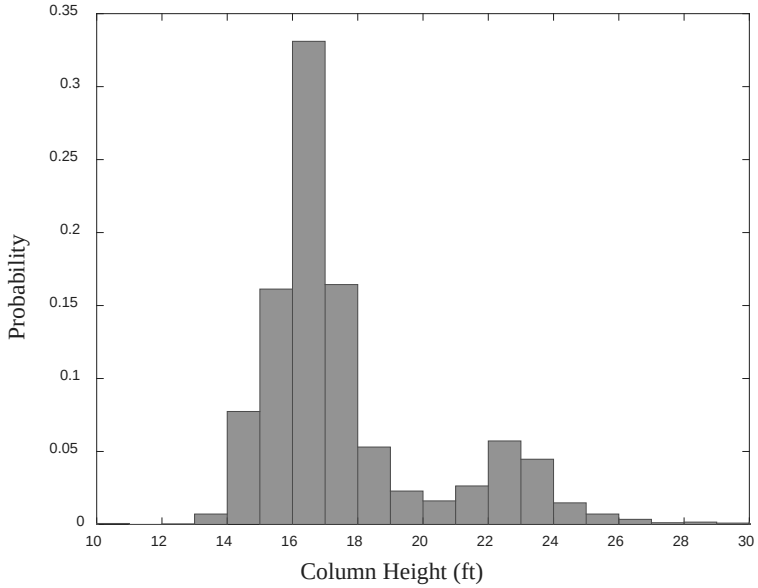

Figure 6.14: Histogram for vertical under-clearance

6.3.5. Skew Angle

Skew angle is another geometric parameter that can greatly affect the seismic response of a bridge (Pottatheere and Renault 2008; Sullivan and Nielson 2010). As seen in Figure 6.15, skew angle is measured as the angle between the centerline of supports and a line perpendicular to the centerline of the roadway. In the NBI, skew angle is recorded based on structural plan drawings or a field measurement; however, for curved bridges or bridges where the skew angle varies, the average skew is recorded in NBI. In certain cases where there is a large variance in skew along the length of the bridge and cannot be accurately represented by an average value, a value of 99 is recorded to indicate this variation. For the purposes of this study, bridges with this large variance value (i.e., skew angle values of 99) have been excluded when determining class statistics.

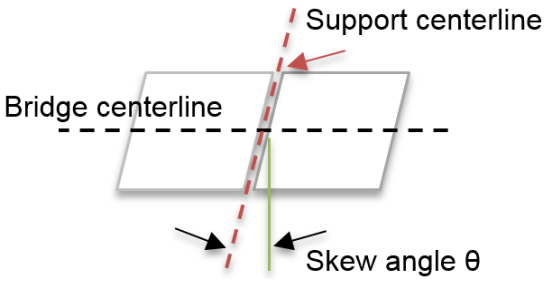

Figure 6.15: Diagram depicting skew angle

Small changes in skew angle do not have a significant effect on seismic response; therefore, instead of looking at the overall distribution of skew, it is more beneficial to look at certain ranges of skew angles (Nielson 2005). The four ranges of interest in this study are $\theta = 0°$, $1° < \theta < 15°$, $15° < \theta <$

30°, and θ > 30°. The percentage of bridges that fall into each range, along with some basic statistics for each bridge class are shown in Table 6.7. It is evident the majority of bridges have no or very little skew. On average, a given bridge class has about 75% of bridges with less than fifteen degrees of skew. Sullivan and Nielson (2010) found that a skew angle less than fifteen degrees has little to no effect on seismic vulnerability of a bridge; therefore, skew is neglected in this study. Therefore, no skew angle is considered for the bridge representatives in this study. However, it should be noted that both MSPC and SSPC classes, as well as the MCSTEEL class, do have a notable proportion of bridges with skew angles greater than 15 degrees.

Table 6.7: Skew angle statistics

Class	Mean (deg)	Std Dev. (deg)	Median (deg)	Mode	0° (%)	1° - 15° (%)	15° - 30° (%)	> 30° (%)
MCSTEEL	15.02	19.05	0.00	0.00	51	9.06	13.85	26.08
MSSTEEL	6.63	13.72	0.00	0.00	77.49	3.48	2.78	16.24
MSPC	12.23	16.24	0.00	0.00	52.1	10.82	16.17	20.89
MSRC	5.22	12.18	0.00	0.00	81.7	4.89	7.65	5.79
SSPC	10.55	14.70	0.00	0.00	53.5	13.56	17.3	15.7
MCRC-Slab	3.96	10.01	0.00	0.00	82.4	5.28	6.23	6.13
MSRC-Slab	9.17	17.02	0.00	0.00	72.4	0.32	3.2	24.07

6.3.6. Year of Construction

Year built is not a geometric parameter; however, it still is a parameter of significance when simulating seismic behavior. Knowing the year that a bridge was built can indirectly provide information on typical construction and detailing practices of the time, including material properties, girder and bent cross-section geometry, bearing details, standard reinforcement and bracing layouts, etc. Table 6.8 shows the median year of construction and average age for each bridge class, and Figure 6.16 through Figure 6.18 show the distributions for year built. This inventory analysis shows that PC girders tend to be the most current design type, as the median year of construction is 1991 for the single span and 1989 for the multi-span types. MSSTEEL bridges tend to be the oldest construction, with a median year of construction of 1940. The year of construction for each bridge configuration is randomly generated based on its distributions shown in Figure 6.16 through Figure 6.18. Table 6.17 through Table 6.23 at the end of this chapter present the randomly generated year of construction for eight different configurations of each bridge class.

Table 6.8: Construction year statistics

Class	Median (year)	Median age (in 2017)
MCSTEEL	1965	52
MSSTEEL	1940	77
MSPC	1989	28
MSRC	1966	51
SSPC	1994	23
MCRC-Slab	1958	59
MSRC-Slab	1952	65

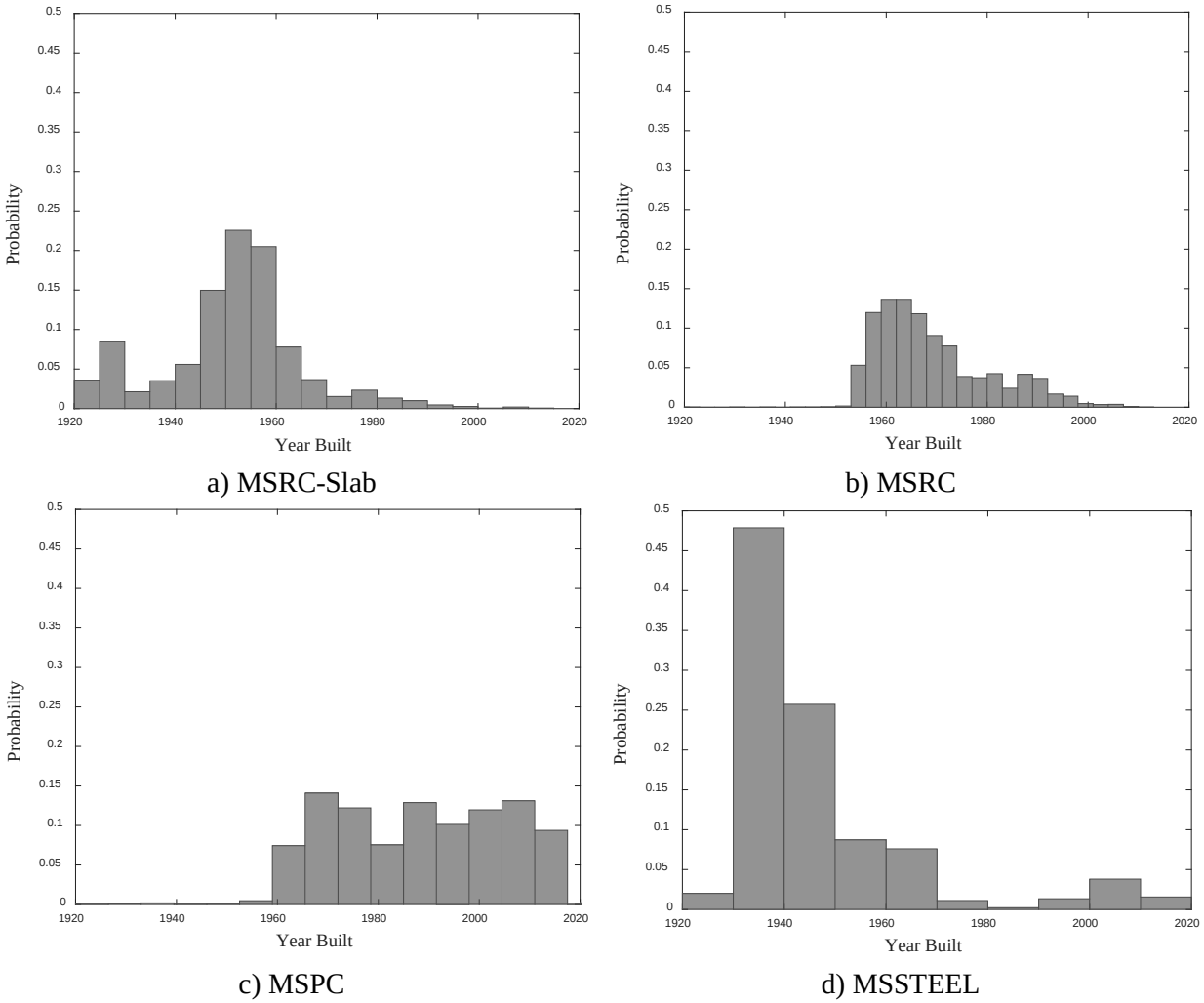

a) MSRC-Slab

b) MSRC

c) MSPC

d) MSSTEEL

Figure 6.16: Histograms of construction year for multi-span simply supported bridge classes

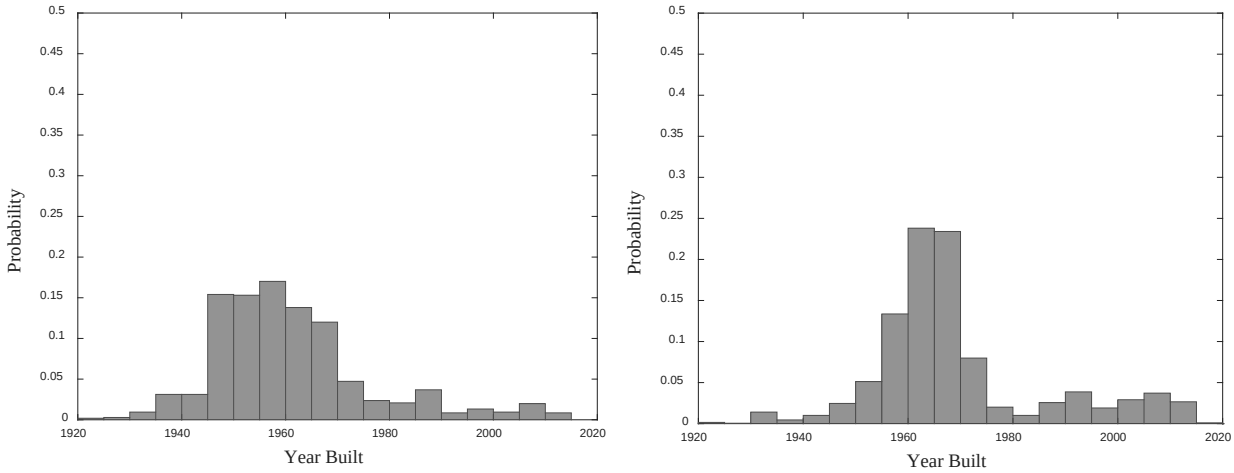

a) MCRC-Slab b) MCSTEEL

Figure 6.17: Histograms of construction year for multi-span continuous bridge types

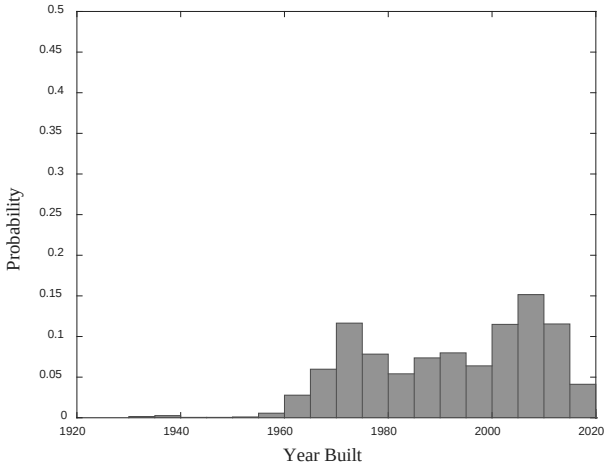

Figure 6.18: Histograms of construction year for single span bridge types

6.4. Bridge Components and Typical Details

A highway bridge can be separated into three main components: the superstructure, the substructure, and the bearings as illustrated in Figure 6.19. Information on structural member layout, cross-sectional properties, and connection details for each of these main components are necessary for creating computational bridge models; however, such detailed information is not documented in the NBI or TxDOT bridge database. To determine typical structural component layout and cross-sectional parameters, information from TxDOT standards and as-built drawings of TxDOT bridges were compiled and synthesized in the following sections.

6.4.1. Material Properties

Reinforced concrete is a common material used in bridge construction. Reinforced concrete is frequently used in foundations, bents, bridge decks, and other superstructure elements. In this study, the uncertainties in concrete compressive strength and steel reinforcement strength are considered explicitly. Bournonville et al. (2004) conducted a study looking at the properties of A615 grade 40 steel bars (fy = 40ksi, which are commonly used in pre 1990s TxDOT bridge construction) and found that the yield strength, fy, tends to follow a right skew distribution. Therefore, in this study, a lognormal distribution was chosen to model uncertainty of reinforcement yield strength. The median value and standard deviation for grade 40 reinforcing bars is 55,000 psi and 4,900 psi, respectively (Bournonville et al. 2004). Concrete compressive strength, f'c, is assumed to follow a normal distribution following the guidance of Unanwa and Mahan (2012). Concrete bridge construction dating back to the 1950s is expected to have lower bound or nominal compressive strengths between 3,000 psi and 5,000 psi. However, ASCE 41 (2014) suggests that expected strengths are closer to 1.5 times the lower bound. To capture a wide range of compressive strengths in this study, a median value of 4,500 psi is used, and again following guidance from Unanwa and Mahan (2012), a coefficient of variation of 0.19 is used to estimate a standard deviation of 850 psi.

6.4.2. Superstructure

The superstructure consists of the roadway surface, the railings, and some type of structural system such as steel or concrete girders. As shown earlier, bridge superstructures can be made of a variety of different construction materials and various types of structural systems. This study specifically focuses on four different types of superstructure including steel girders, prestressed concrete girders, reinforced concrete girders, and reinforced concrete slabs, which are shown in Figure 6.19.

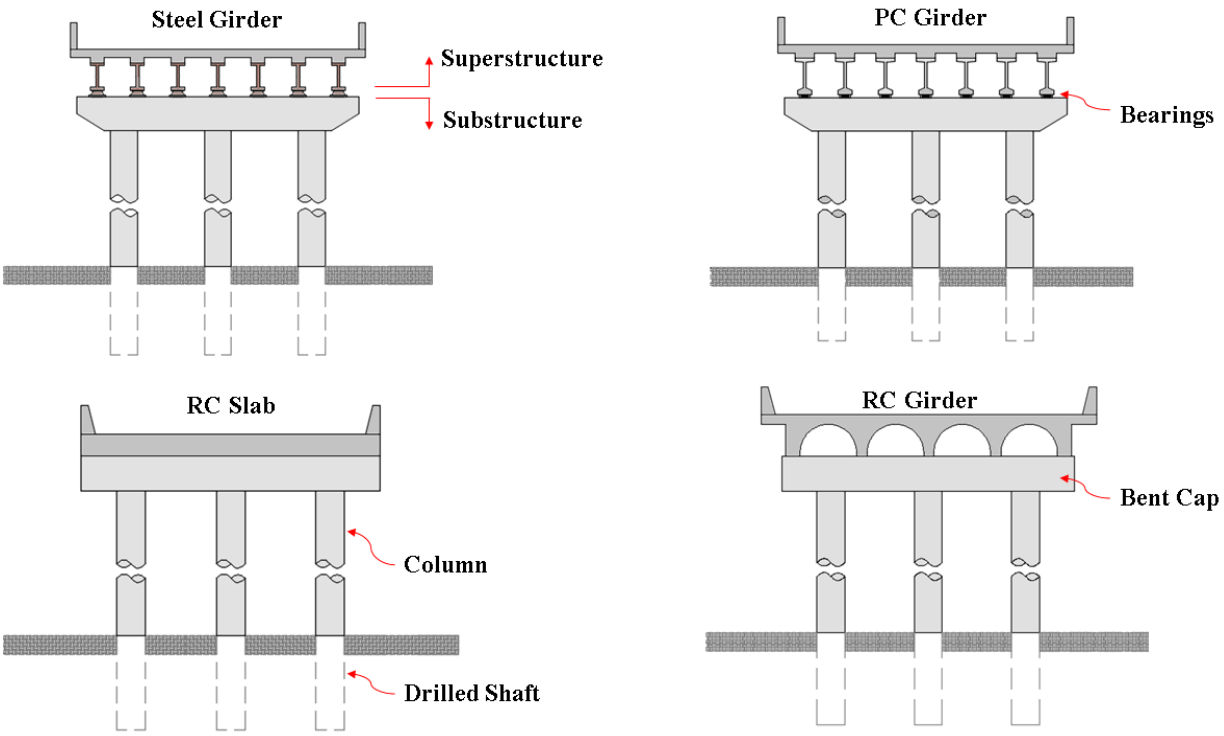

Figure 6.19: Bridge component classification for different bridge classes

6.4.2.1. Steel Girders

Structural characteristics of the different superstructure types are necessary to accurately assign the stiffness and mass to the superstructure elements of a computational bridge model. Steel girders, for example, have different girder sections based on span length, girder spacing, and span continuity. Simply supported steel girder bridges with span length less than approximately 100 feet, are typically supported by standard rolled wide-flange, or W–shape, sections. Table 6.9 shows examples of steel beam sections allowed per the TxDOT standard drawings (TxDOT 2006) based on span length and roadway width. From this table, it is evident that there are a several different girders with varying section properties and weights that can be used for a given bridge geometry. Thus, a sampling technique is employed to select beam sizes and section properties that are representative of those that could be used for steel girders in the Texas bridge population. In the sampling process, the available girder sections were determined from the TxDOT standards based on span length, and then a single girder section was randomly selected for each geometric bridge sample. Table 6.10 shows the girders and the section properties used for each simply-supported steel bridge sample.

Table 6.9: Table of required beam sizes (TxDOT 2015)

	30 - 50ft Span	60ft Span	70ft Span	80ft Span	90ft Span
24ft Roadway	W18 x 130	W21 x 166	W24 x 207	W27 x 235	W30 X 261
	W21 x 122	W24 x 146	W27 x 178	W30 X 211	W33 X 221
	W24 x 104	W27 x 146	W30 X 173	W33 X 169	W36 X 231
	W27 x 146	W30 X 173	W33 X 130	W36 X 150	W40 X 199
	W30 X 173	W33 X 118	W36 X 135	W40 X 149	
	W33 X 118	W36 X 135	W40 X 149		
	W36 X 135	W40 X 149			
	W40 X 149				
28ft Roadway	W18 x 130	W21 x 166	W24 x 207	W27 x 235	W30 X 261
	W21 x 132	W24 x 131	W27 x 178	W30 X 191	W33 X 241
	W24 x 117	W27 x 146	W30 X 173	W33 X 201	W36 X 231
	W27 x 146	W30 X 173	W33 X 141	W36 X 170	W40 X 199
	W30 X 173	W33 X 118	W36 X 135	W40 X 167	
	W33 X 118	W36 X 135	W40 X 149		
	W36 X 135	W40 X 149			
	W40 X 149				
30ft Roadway	W18 x 130	W21 x 132	W24 x 162	W24 x 229	W27 x 258
	W21 x 111	W24 x 117	W27 x 146	W27 x 194	W30 X 211
	W24 x 104	W27 x 146	W30 X 173	W30 X 173	W33 X 201
	W27 x 146	W30 X 173	W33 X 118	W33 X 152	W36 X 231
	W30 X 173	W33 X 118	W36 X 135	W36 X 150	W40 X 199
	W33 X 118	W36 X 135	W40 X 149	W40 X 149	
	W36 X 135	W40 X 149			
	W40 X 149				

Table 6.10: Section properties of sampled girders for MSSTEEL configurations

Bridge Sample	Member	Depth (in)	Area (in^2)	I_x(in^4)	I_y(in^4)
1	W24×104	24.06	30.7	3100	259
2	W18×130	19.25	38.3	2460	278
3	W30×191	30.68	56.1	9200	673
4	W21×122	21.68	35.9	2960	305
5	W30×173	30.44	50.9	8230	598
6	W27×146	27.38	43.2	5660	443
7	W30×173	30.44	50.9	8230	598
8	W36×135	35.55	39.9	7800	225

For MCSTEEL bridges with span lengths less than 100 feet, it was determined that, similar to their simply supported counterparts, are built using rolled wide flange sections. Therefore, the girder sections for continuous bridge samples with spans less 100 feet were selected using the same method as discussed for MSSTEEL bridges. However, continuous span construction is often used

to achieve longer span lengths than are practical with simply supported construction. This trend is depicted in the span length distributions shown in Section 6.3.2, where the average span length for the MSSTEEL bridge class is 48 feet, while the average for the MCSTEEL bridge class is 102 feet. MCSTEEL bridges with span length longer than 100 feet often require girder depths well beyond the available rolled wide-flange sections. In fact, design engineers typically use built-up I-girder sections for the longer span continuous girders. When built-up plate girders are designed, time and care is typically taken to determine an efficient plate girder design for each specific bridge to minimize the cost of material and fabrication. Consequently, TxDOT does not have a set of standard drawings for continuous steel girders, making it more challenging to determine typical section properties for the bridges in the multi span steel girder bridge class. One approach to obtaining properties for continuous steel girders is to conduct a full superstructure design following the TxDOT design manual for each bridge sample in this class. This approach, however, would be very time consuming, and may not reflect design practices representative of the era when much of the MCSTEEL bridges were constructed. However, design engineers often follow several "rules of thumb" to develop a preliminary section that can then be refined to fit to the design requirements. These "rules of thumb" assumed in this study are listed below:

- Span length (L)/girder depth (D) ≈ 32
- Girder depth (D)/web thickness (t_w) ≈ 137
- Flange width (b_f)/girder depth (D) ≈ 0.33
- Flange width (b_f)/(2*flange thickness (t_f)) ≈ 9.2

In the design process, span length is often governed by predetermined site constraints. For example, the bridge needs to span a four-lane highway, a 120-foot waterway, or needs to avoid existing utility lines. Thus, span length can be used as the starting point in determining the girder depth. Once the girder depth is selected, the remaining guidelines help the designer determine the remaining properties of the girder section. Since these "rules of thumb" or guidelines are only intended to provide a preliminary girder section, it is expected that these particular parameters (e.g., L/D, D/t_w, b_f/D, and $b_f/(2*t_f)$) for the final girder design have some variation. To gain understanding of how much variation is expected, several as-built drawings for long span continuous steel girder bridges (span lengths ranging from 115 to 240 feet; TxDOT, 2007; TxDOT, 1975; TxDOT, 1971a; TxDOT, 1971b; TxDOT, 1965) were used to compare preliminary and final design parameters. Table 6.11 shows this comparison. This table verifies the variance in the final design, which should be considered in selecting accurate built-up girder sections. In this study, girder sections are selected using the linear regressions shown in Figure 6.20.

Table 6.11: MCSTEEL girder parameter comparison

	L (ft)	L/D	D/t_w	b_f/D	$b_f/2t_f$
Final Design	115	30	123	0.26	8
	140	28	160	0.23	9.33
	150	30	137	0.30	12
	150	33.33	123	0.26	9.33
	240	30	170	0.21	10
Preliminary design		32	137	0.33	9.2

L: Span Length, D: girder depth, t_w: web thickness, b_f: flange width, t_f: flange thickness

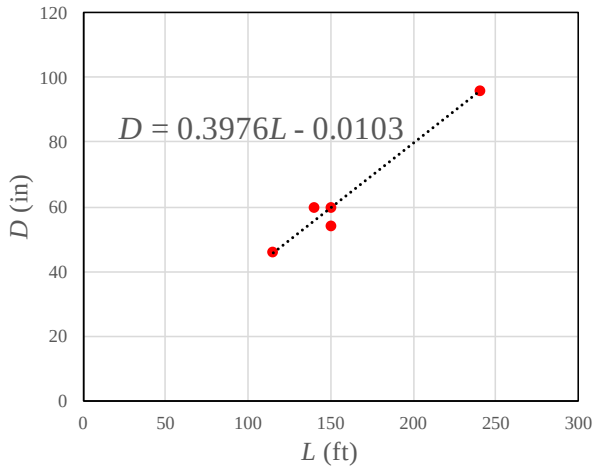

Span Length vs. Girder Depth

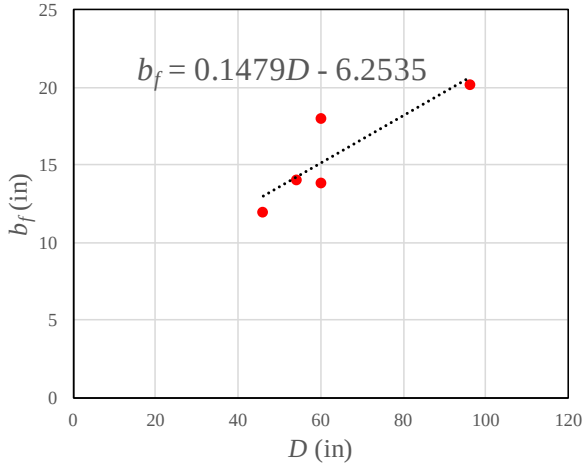

Girder Depth vs. Flange Width

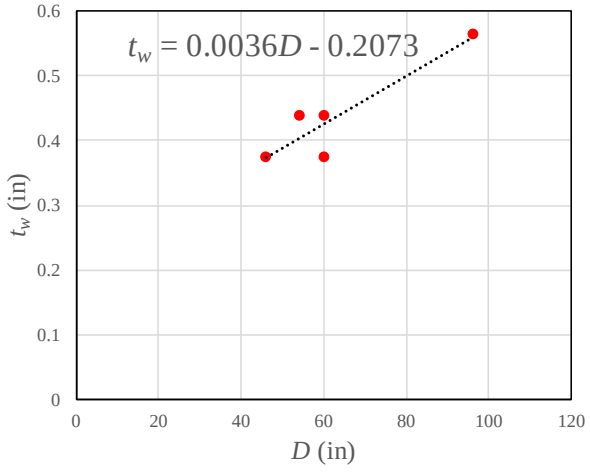

Girder Depth vs. Web Thickness

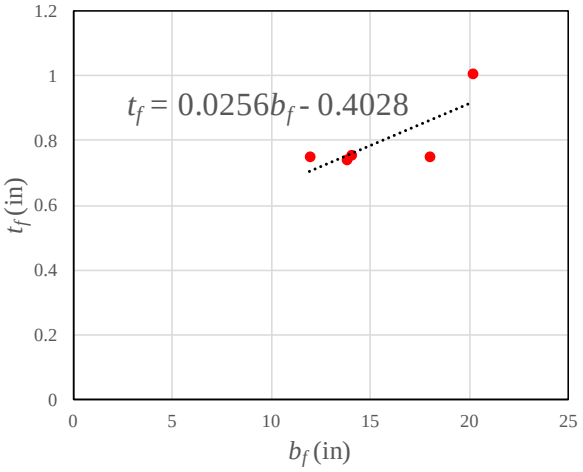

Girder Depth vs. Flange Thickness

Figure 6.20: Linear regressions of girder sections of MCSTEEL bridges

The section properties used for the MCSTEEL bridge samples, in this study, are show in Table 6.12. It should be noted that continuous steel girders often utilize flange cover plates or web stiffeners to increase section capacity at certain places along the length of the span (e.g., cover plates at the mid span and at interior supports, and web stiffeners at bearing locations). The section properties for MCSTEEL bridges used in this study neglect these additional components (e.g., cover plates, bearing stiffeners, and web stiffeners).

Table 6.12: MC steel girder section properties

Bridge Sample	Depth (in)	Area (in^2)	I_x(in^4)	I_y(in^4)
1	38.2	43.98	9800	229
2	38.7	58.8	14900	695
3	31.6	77	13100	959
4	46.0	36.2	12736	225
5	38.2	43.98	9800	229
6	58.0	50.9	27906	493
7	35.9	44.3	9040	270
8	96.0	92.9	129187	1335

In addition to knowing the size and type of girders used in a superstructure, it is also important to know the number and spacing of girders for determining mass and stiffness properties in the computational model. Review of TxDOT standard and as-built drawings for steel girder bridges showed that depending on the deck width, girder spacing is typically specified in 4-inch intervals with a lower and upper bound of 5 feet and 9 feet, respectively. To improve economy in the superstructure design, a design engineer commonly chooses to minimize the number of girders, while maintaining a reasonable girder spacing and a reasonable amount of overhang (e.g., the distance from the center line of exterior girder to the outside of the bridge deck, see Figure 6.21). This design process can lead to a variety of different girder spacings. For example, a bridge with a 26 feet deck width, as shown in Figure 6.21, can have four girders spaced at 7.33 feet and an overhang of 2 feet, four girders spaced at 7 feet with an overhang of 2.5 feet, three girders spaced at 9 feet with an overhang of 4 feet, and a variety of other combinations. After further investigation of standard and as-built drawings it was found that overhang distance ranges from 2 to 5 feet; however, it is evident that an overhang of approximately 2 to 3 feet is preferred. In this study, girder spacing for bridge models is selected from a range of 6 to 9 feet, at intervals of 4 inch, based on which spacing value produces an overhang closest to 2 feet. The number of girders and girder spacing for each bridge sample are presented in Appendix D.

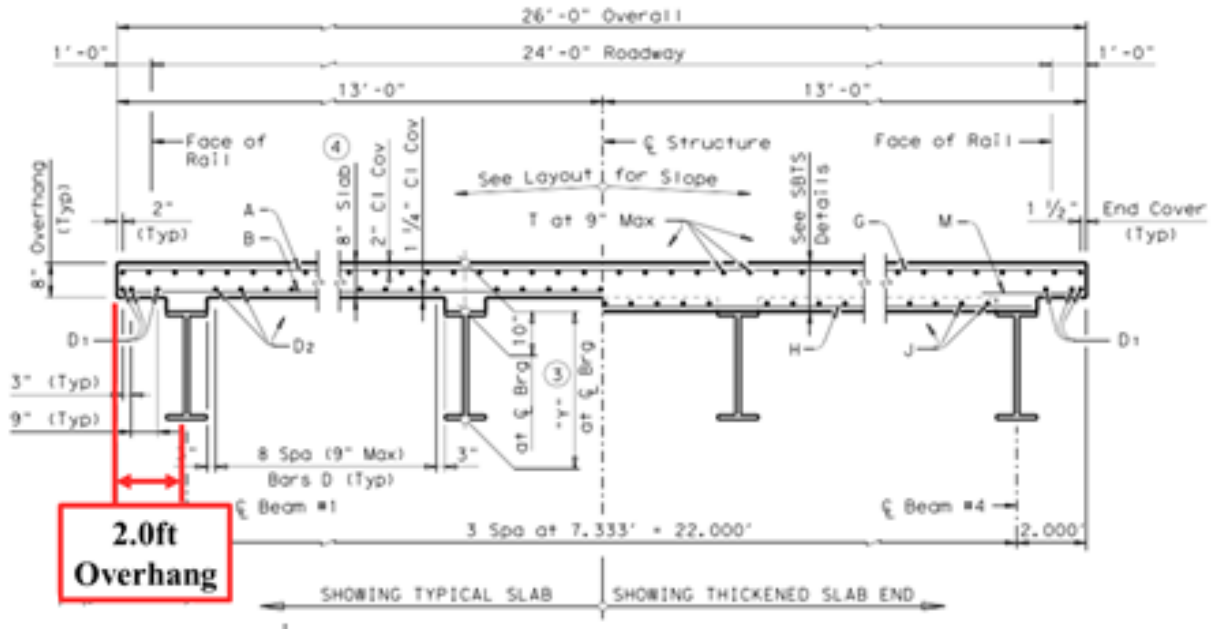

Figure 6.21: Typical transvers superstructure cross-section (TxDOT 2004)

6.4.2.2. Prestressed Concrete Girders

Determining the section properties and mass of prestressed concrete girder spans (MSPC bridge class) is relatively simple compared to the steel girder spans due to the limited number of prestressed concrete standard sections. Historically the American Association of State Highway and Transportation Officials (AASHTO) has provided standard prestressed sections to be used in highway bridge design. Most state departments of transportation have adopted and used the AASHTO standard sections; however, TxDOT is one of the few states that has developed and used their own standard sections. The overall shape of the two designs are similar; however, there are minor differences in the dimensions resulting in slightly different section properties. Figure 6.22 shows the generic shape and the dimensions of both the AASHTO girders (i.e., Type II, III, and IV) and the TxDOT girders (i.e., Type B, C, 54, and 72). It also should be noted that in 2008 TxDOT revised their prestressed girder sections to bulb-T sections (see Figure 6.22), which are used in new highway bridge construction.

In this study, the section properties and mass of the MSPC bridge samples were selected from the old TxDOT sections if the construction year of the sample was prior to 2008 and from the new Tx girder sections for samples constructed after 2008. More specifically, after reviewing as-built drawings and standards for bridges constructed before 2008, it was determined that Type B girders are typically used for spans less than 70 feet, Type C girders for spans between 70 feet and 90 feet, and Type 72 girders for spans greater than 90 feet. Following TxDOT's recommendations for the new Tx girders, Tx 40 girders were used for samples with spans less than or equal to 90 feet, and Tx 62 girders for spans larger than 90 feet.

The number and spacing of girders for prestressed girders follows the same procedure as that presented for steel girders. In fact, depending on the deck width, girder spacing is typically specified in 4-inch intervals with a lower and upper bound of 5 feet and 9 feet, respectively. The number of girders and girder spacing for each bridge sample are presented in Appendix D.

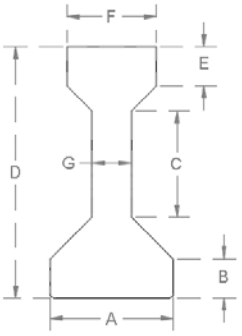

TxDOT and AASHTO prior 2008

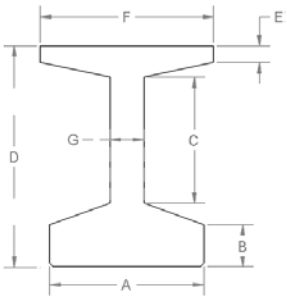

TxDOT Bulb – T girders

AASHTO I-Girders

Beam Type	A (in)	B (in)	C (in)	D (in)	E (in)	F (in)	G (in)
II	18	6	15	36	6	12	6
III	22	7	19	45	7	16	7
IV	26	8	23	54	8	20	8

TxDOT I-Girders

Beam Type	A (in)	B (in)	C (in)	D (in)	E (in)	F (in)	G (in)
B	18	6	14	34	4	12	6.5
C	22	7	16	40	6	14	7
54	16	8	32	54	4	16	6
72	22	11	40.5	72	5.5	22	7

Tx Girders (TxDOT Bulb-T)

Beam Type	A (in)	B (in)	C (in)	D (in)	E (in)	F (in)	G (in)
Tx 28	32	6.75	9	28	3.5	36	7
Tx 34	32	6.75	12	34	3.5	36	7
Tx 40	32	6.75	18	40	3.5	36	7
Tx 46	32	8.75	22	46	3.5	36	7
Tx 54	32	8.75	30	54	3.5	36	7
Tx 62	32	8.75	37.5	62	3.5	42	7
Tx 70	32	8.75	45.5	70	3.5	42	7

Figure 6.22: PC girder sections

6.4.2.3. Reinforced Concrete Girders

Reinforced concrete girder bridges (MSRC class), also known as pan formed girders, are a style of cast-in-place concrete superstructure that was most commonly employed in the 1960s and 1970s. Figure 6.23a shows a standard RC girder cross-section typically used in Texas. In this figure, the superstructure depth is shown as 24 inches; however, TxDOT does have a 33-inch RC girder section as well. Following the guidance of the as-built and standard drawings, the 24-inch section depth is assumed for span lengths less than 40 feet, while the 33-inch depth is assumed for spans of 40 feet and longer.

To simplify calculations section properties for the RC pan girder in the computational models (described in more detail in Chapter 7 of this report), the cross-section was transformed into a T-section with equal cross-sectional area and similar moments of inertia to ensure an accurate representation of the RC girder mass and stiffness. Figure 6.23b shows an example of the transformed section used to calculate section properties.

Reinforced concrete girder bridges are built using standard sections, as shown in Figure 6.23a, which are designed with a standard girder spacing of 3 feet and a 1 feet overhang. In this study,

girder spacings for the RC girder bridge samples are assumed to be 3 feet, and the number of girders is determined resulting in an overhang as close to 1 foot as possible.

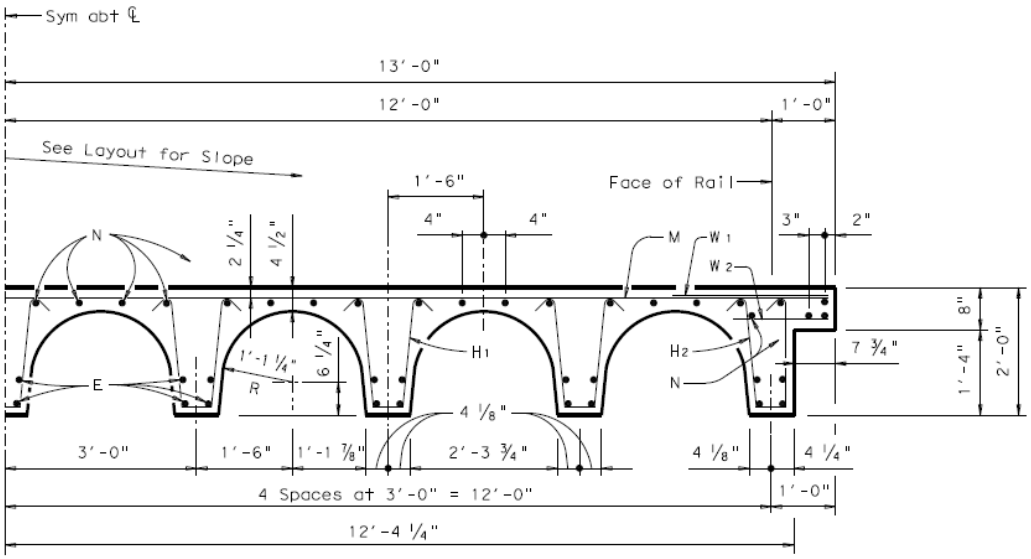

(a) Typical Half Transverse section (TxDOT 2005)

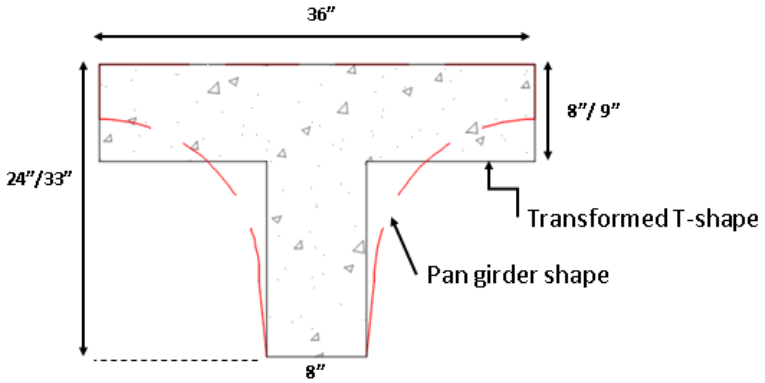

(b) Transformed T-section

Figure 6.23: RC girder standard section

6.4.2.4. Reinforced Concrete Slabs

The last superstructure bridge class is the RC slab class, in which the structural system comprises either a cast-in-place reinforced concrete slab or pre-cast reinforced concrete slab panels. In Texas, the RC slab superstructure was most popular in the early to mid-1900s (e.g., 1930s-1970s). This slab superstructure type can be constructed as either simply supported or continuous spans and is typically used in structures requiring much shorter span lengths. For instance, it is used in simply supported spans of approximately 25 feet, and continuous spans of approximately 35 to 40 feet. Current TxDOT standard drawings and standards from the 1980s and 1990s indicate that in modern construction, MSRC-slab bridges are specified to have a 16-inch thick slab, whereas MCRC-slab bridges have 14-inch thick slabs for span lengths less than 30 feet and 16-inch thick slabs for spans greater than or equal to 30 feet. However, as-built drawings from RC slab bridges

constructed prior to the 1980s indicate that MSRC-slab bridges from this era were typically built with 12-inch slabs, and MCRC-slab bridges were typically built with either a 12-inch or 14-inch slab. Based on the typical age of RC slab bridges in the Texas bridge population, in this study, the MSRC-slab bridges are assumed to have a 12-inch slab, and the MCRC-slab bridges are assumed to have a 12-inch slab for spans less than 30 feet and a 14-inch slab for spans greater than or equal to 30 feet.

6.4.2.5. Bridge Deck and Railings

In addition to the girders themselves, the concrete bridge deck and railings also contribute significantly to the superstructure mass and stiffness. In steel girder construction, it is common to have composite slabs (i.e., shear studs connecting the girders and concrete slab), in which part of the slab contributes to the flexural stiffness of the superstructure. Past fragility studies such as Nielson (2005) and Pan et al. (2010) have considered composite construction for steel girder classes, i.e., MCSTEEL and MSSTEEL classes; however, TxDOT did not adopt composite construction until the mid to late 1980s, while the majority of the steel bridges in Texas were built between the 1940s and 1970s. Therefore, this study does not consider any contribution from the bridge deck in determination of the girder flexural stiffness. In terms of superstructure mass, however, the bridge deck does have a big contribution. The current TxDOT standards for the MSSTEEL bridge class requires an 8-inch bridge deck; however, a 7.25-inch deck was commonly found in the as-built drawings from bridges built in the 1930s to1950s.

The MSPC girder class has similar variation in deck thickness as the current standard specifies an 8.5-inch deck, while the as-built drawings indicate that a 7.25 to 8-inch deck is typical for bridges built in the 1960s to 1990s. Due to these variations in deck thickness observed in as-built drawings and limited information regarding deck detailing for the entire bridge population, the bridge deck for both the MSSTEEL and MSPC classes are assumed to be 8 inches thick. The typical deck thickness for the MCSTEEL bridge class is assumed to be 6.5 inches based on as-built drawings from the 1940s to 1970s, which were used in this study. For the MSRC and MSRC-slab bridge classes, the bridge deck is part of the structural system; thus, no additional mass or stiffness from the bridge deck is considered in the model.

Bridge railings, i.e., traffic barriers placed along the edge of the bridge deck, certainly contribute to superstructure mass; however, the weight of the barrier is a relatively small percentage (i.e., approximately 4 to 5%) of the total weight of the superstructure. TxDOT has a variety of different sizes and shapes of railings in their standard drawings. Determining a typical size and shape for railings of a specific bridge class is difficult, as railings are specified by roadway type and traffic demands. Due to the uncertainty in railing type and design, the railing mass is not explicitly considered in this study; however, the increased superstructure mass due to railings were considered through a mass factor applied to the entire superstructure mass. In fact, Following the guidance of Ramanathan (2012), this mass factor is assumed to follow a uniform distribution with bounds of 110% to 140% of superstructure mass calculated from given geometries and material densities. The railings are assumed to have no effect on the superstructure stiffness.

Moreover, deck gaps are used in bridge design to allow for expansion and contraction of the superstructure. These gaps can be found at designated expansion joints at both the abutments and interior bents. Temperature variations as well as construction imperfections can create large uncertainties in the expansion gaps; hence, it is important to account for this in the modeling process. Expansion joint details vary between the bridge classes and are typically selected based on the expected thermal movement and any anticipated shortening. Common types of joints include poured sealant and neoprene compression sealant, which are common in RC slab and RC girder construction, and armor joint and sealed expansion joints, which are common in PC girder and steel girder construction. Following the study by Ramanathan (2012), the gaps at both the abutments and interior bents are assumed to follow a uniform distribution, with two sampling ranges for small and large gaps. Looking through the TxDOT standards and as-built drawings, it was observed that the poured sealant, neoprene sealant, and the armored expansion joints have a much smaller movement range than their sealed expansion joint counterpart.

6.4.3. Substructure

The substructure (i.e., bridge bents, columns, foundation, and abutments) supports the superstructure. Unlike the superstructure, the substructure is expected to see highly nonlinear behavior during a seismic event, requiring a more complex computational model to accurately capture these behaviors and potential failure modes. Computational modeling techniques and specific details regarding modeling are found in Chapter 7, while the following sections focus on TxDOT typical details used to develop the substructure models used in this study. As mentioned earlier, the NBI does not provide substructure information; however, with the help of TxDOT the research team was able to obtain and analyze substructure type data from TxDOT's in-house bridge database. The information found in this database is split into three parts: the above ground substructure (i.e., bridge bent or column), the below ground substructure (i.e., foundation), and type of bent cap. Each of these three substructure components must be determined to model bridges and simulate seismic behavior.

6.4.3.1. Bridge Bents

The above ground substructure includes the intermediate supports along the length of a bridge, which are often referred to as bridge bents or piers. Piers are usually comprised of a single support (e.g., single column or pier wall), while bents are typically comprised of multiple supports such as multiple columns or piles. There are a number of different bent types used in bridges, such as hammer-head bents, wall bents, and multi-column bents. In general, the above ground substructure, i.e., bridge bents, can take on one of the following nine configurations: pile bents, single column bents, multiple column bents, concrete column bent with tie beam, concrete column bent wall, concrete pier, masonry pier, trestle (steel, concrete, or timber), or other. Figure 6.24 shows the probability of occurrence of each above ground substructure type for each individual bridge class Based on the substructure information gathered from TxDOT's bridge database. This figure reveals that the overwhelming majority of PC girder bridges (i.e., MSPC and SSPC), as well as the MCSTEEL bridges are supported by multiple column bents. The remaining four bridge

classes (i.e., MSRC-Slab, MSRC, MSSTEEL, and MCRC-Slab) are split between pile bents and multiple column bents. The MSRC and MCRC-Slab classes are split almost evenly with 49% and 42%, respectively, for pile bents, and 48% and 53%, respectively, for multiple column bents. The MSRC-Slab class tends to more commonly employ pile bents with 63%; however, the MSRC-Slab class still has a significant percentage with multiple column bents as well, with 30%. For this reason, multiple column bents are assumed as the above ground substructure for the generalized computational bridge models in this study.

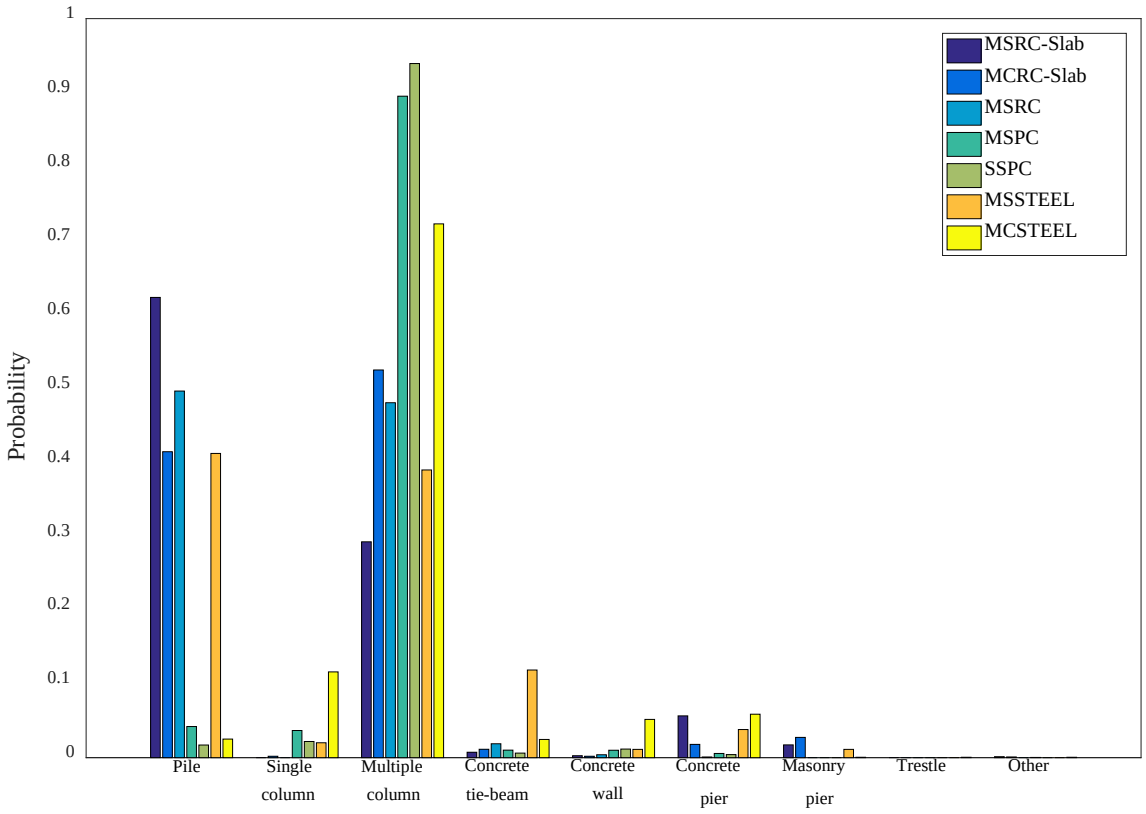

Figure 6.24: Histogram for types of above ground substructure

As discussed above, it was determined that the majority of bridges in Texas have either multi-column or pile bents. Multi-column bents are predominantly built with cylindrical reinforced concrete columns, while pile bents can be built using either steel H-pile or concrete piles (either reinforced or prestress concrete). Bridge bents with either concrete columns or piles are constructed with a reinforced concrete bent cap, while steel pile bents have either reinforced concrete or steel caps. TxDOT recognizes four bent cap materials in their inventory database: concrete, steel, timber, and masonry. Figure 6.25 represent a schematic view of the typical configuration of multi-column bents. The bent cap distributes the load from the superstructure to the individual columns, which are attached to the pile or drilled shaft foundation.

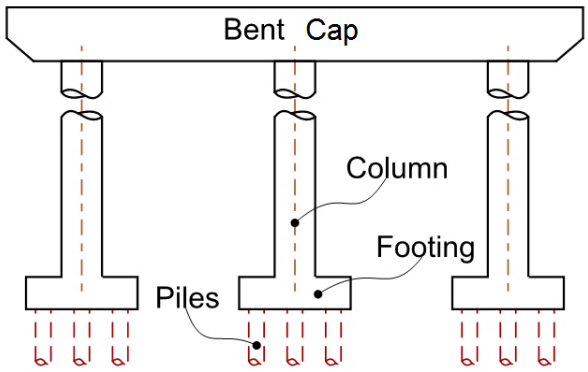

Figure 6.25: Multi-column bent (Nielson 2005)

Figure 6.26 shows the distribution of types of bent caps among the seven bridge classes. This figure shows that even though TxDOT uses four different bent cap materials, the overwhelming majority of bridges employ concrete bent caps. For all seven bridge classes the probability of having a concrete bent cap is greater than 90%. As seen in Figure 6.26, reinforced concrete bent caps are by far the most prominent in the Texas bridge inventory.

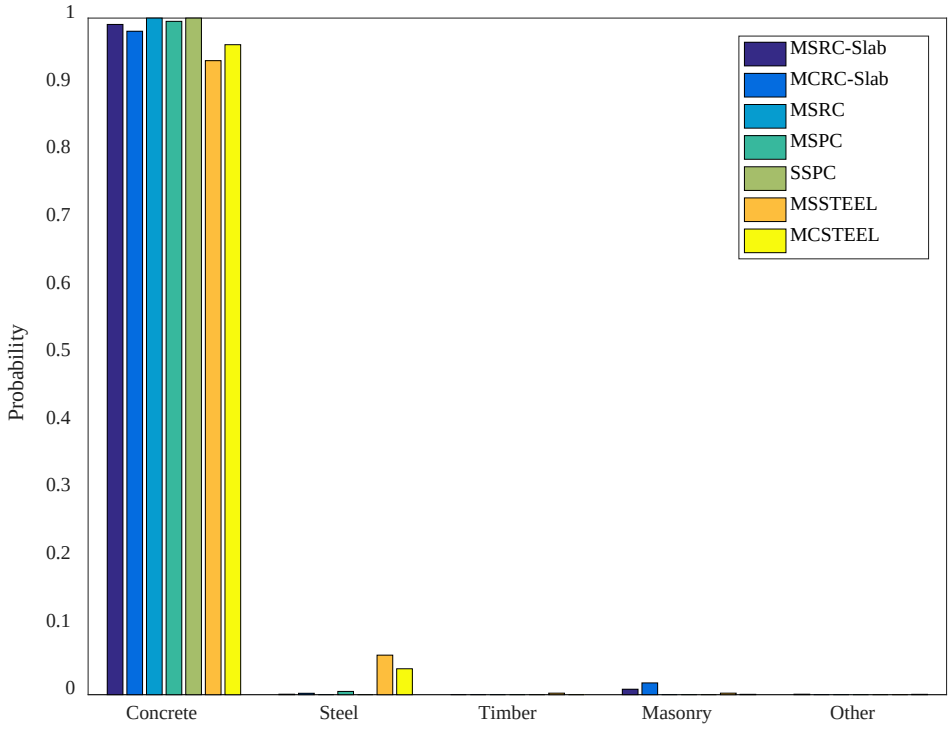

Figure 6.26: Histogram for types of bent caps

To model the behavior of a bridge bent, it is important to know typical member sizes and details for both the columns and bent caps. Bent caps are typically much stiffer than the columns below them and are often assumed to remain elastic for seismic analysis. Thus, the basic geometry, i.e., depth and width, of a typical bent cap is all that is needed to calculate section properties and mass for the modeling process. As seen in Figure 6.27, concrete bent caps used in Texas typically have

a square or rectangular cross-section; however, the dimensions may vary between the different bridge classes and are typically governed by span length and column diameter.

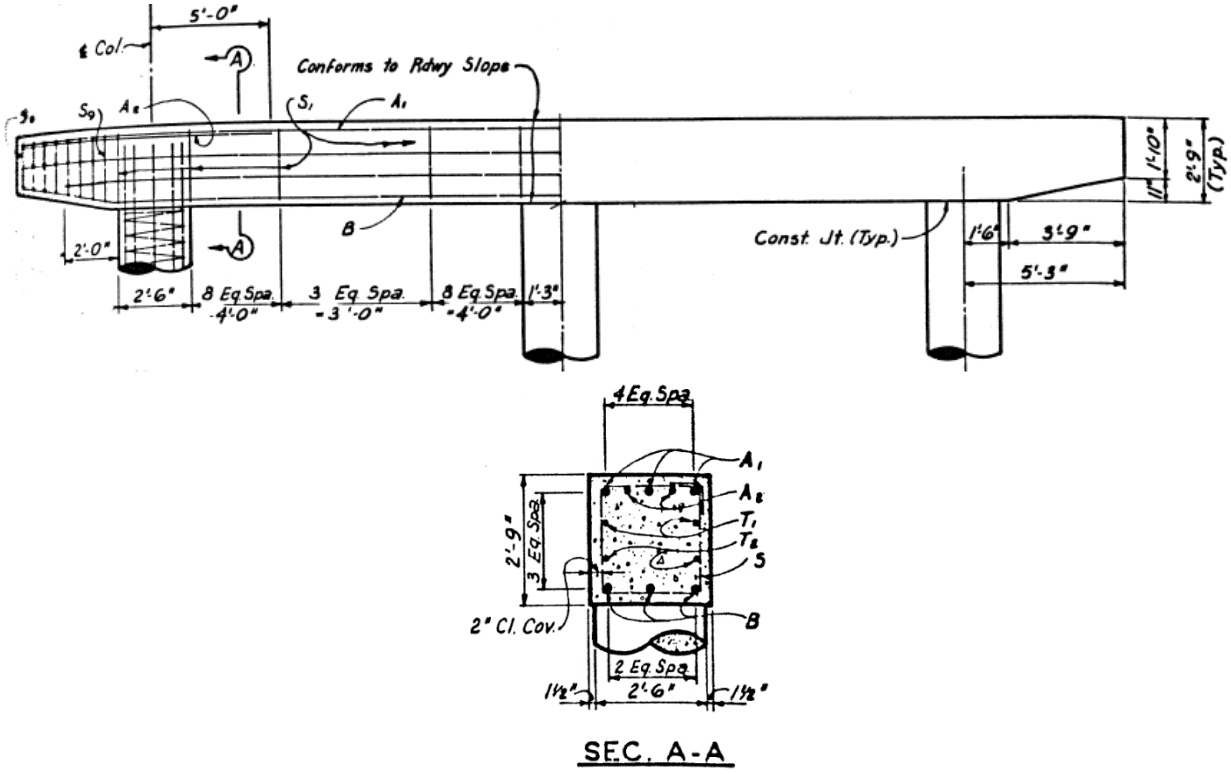

Figure 6.27: Typical bridge bent, and bent cap detail (TxDOT 1962)

The bent cap dimensions for each bridge class are generally based on a combination of as-built drawings from the 1930s to 1990s, TxDOT standard drawings from the 1980s to 1990s, as well as current TxDOT standard drawings. The different dimensions of the bent caps that are used in this study are listed in Table 6.13.

Table 6.13: Bent cap dimensions per bridge class

	Bent Cap Dimensions	
Bridge Class	Width	Depth
MCSTEEL	2.5	3
MSSTEEL	3	3
MSPC (Circa 2008)	2.75	2.75
MSPC (2009–Present)	3.5*	3.5*
MSRC	2	2.5
MCRC-Slab	2	2.5
MSRC-Slab	2	2.5

Note: for span lengths > 100 ft, the width and depth should be 4 ft.

6.4.3.2. Columns

Columns contribute significantly to seismic vulnerability and are expected to experience highly nonlinear behavior when subjected to large seismic demands. To capture this nonlinear behavior in the modeling process, it is important to simulate the flexural and shear strength of the reinforced concrete column section, as well as potential longitudinal reinforcement development length and splicing failure modes. See Chapter 7 for details on simulating these failure modes. The flexural and shear strength of a cylindrical concrete column is directly related to the cross-sectional dimensions and the reinforcing layout.

Investigation of TxDOT standard drawings and as-built bridge drawings from the 1930s to 2000s indicated that TxDOT multi-column bents have historically utilized either 30-inch diameter or 24-inch diameter columns. However, since approximately 2008, TxDOT has started specifying 36-inch and 42-inch columns for the new PC girder bridges (TxDOT 2017). Among the two main column sizes, i.e., 30-inch diameter and 24-inch diameter, there are minor differences in the reinforcing details; however, they do follow some general trends. For example, it is standard for all columns to have a #3 spiral reinforcing cage with a 6-inch pitch along the entire length of the column. Longitudinal bars are typically detailed to extend straight into bent caps and foundations without any 90-degree hooks. Figure 6.28 shows typical reinforcing details for both a 30-inch and 24-inch diameter columns. It should be noted that Texas bridges, in general, have different column sizes and reinforcing details than bridges considered in previous CEUS studies. Past seismic vulnerability studies focusing on the CEUS (Choi 2002; Nielson 2005) used 30-inch and 36-inch diameter columns with transverse reinforcement at 12-inch spacing. Like the current study, these past studies assume similar details for the column-to-bent cap and column-to-foundation joints, where longitudinal bars extend straight through the joint. This type of joint reinforcement detailing without any 90-degree hooks is consistent with detailing used in low seismic hazard regions such as Texas and the CEUS, whereas 90-degree hooks are more commonly employed in moderate and high seismic regions. The specific column sizes and details used for each bridge class are found in Table 6.14.

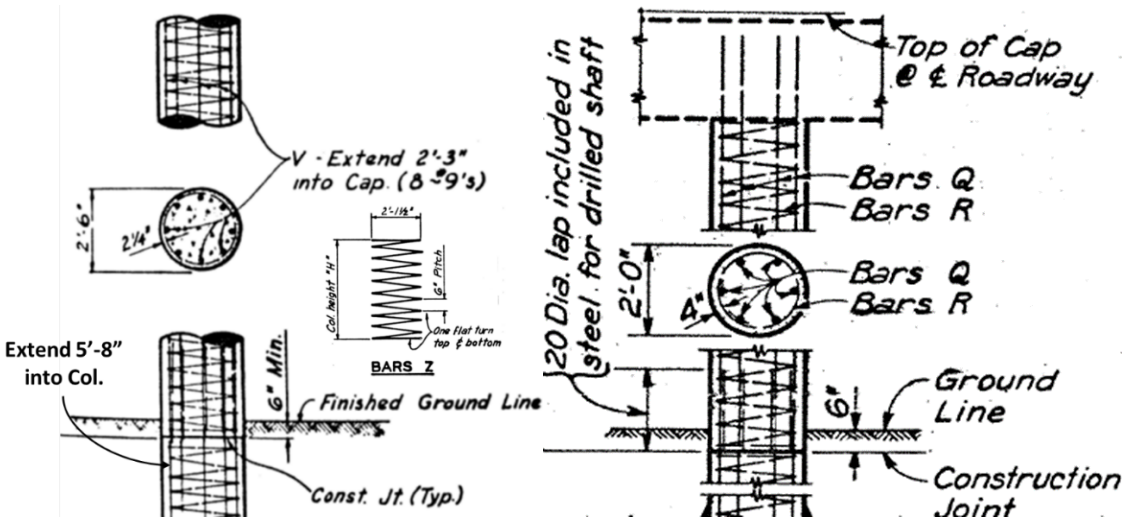

Figure 6.28: Typical column cross-section and details (TxDOT 1962) for (a) 30-inch diameter and (b) 24-inch diameter (TxDOT 1970) columns

Table 6.14: Column properties and reinforcing details for column with different sizes

Diameter (in)	**24**	**30**	**36**	**42**
Number of longitudinal bars	8	8	10	14
Longitudinal spacing (equal, or inches)	Equal	Equal	Equal	Equal
Longitudinal bar size	#7	#9	#9	#9
Transverse type (spiral, tie)	Spiral	Spiral	Spiral	Spiral
Transverse spacing/pitch (in)	6	6	6	6
Transverse bar size	#3	#3	#4	#4
Cover (to center of trans. bar) (in)	2.25	2.25	3	3
Reinforcement coating	None	None	None	None
Embedment length-Cap (ft)	2	2.25	2.75	2.75
Embedment length-drilled shaft (ft)	2.25	3	4.5	4.5

Column diameter is typically governed by span length and, in some cases, year of construction. For MSPC bridge class, bridge samples with span lengths less than 100 feet and constructed prior to 2009 are assumed to have 30-inch diameter columns, while bridge samples constructed in 2009 or later and have spans less than 100 feet are assumed to have 36-inch diameter columns. If a MSPC bridge sample has a span length longer than 100 feet, a 42-inch diameter column is used regardless of when the bridge was constructed. Again, this was determined through review of current TxDOT standards and as-built drawings for PC girder bridges built in the 1960s through early 2000s. For the MSSTEEL and MCSTEEL bridges, column sizes are governed solely by span

length. In fact, if a bridge sample has span length less than 100 feet, it is assumed to have 30-inch diameter columns, or if the span length is greater than 100 feet, 42-inch diameter columns are used. The reinforced concrete girder and slab bridges, on average, have much shorter span lengths (e.g., average span lengths of 34 feet and 23 feet, respectively) requiring much lower column demands. For these bridge classes, i.e., MSRC, MCRC-Slab, and MSRC-Slab, it assumed that all bridge samples utilize 24-inch diameter columns.

The number and spacing of columns also has a big influence on overall bent behavior under lateral loads. Determining a standard column number and spacing for all bridge classes and samples is not a trivial task, as these parameters vary with deck width and design details, including slab overhang, and column inset from end of bent cap. By studying standard and as-built drawings; however, one can identify common trends—such as max spacing, minimum spacing, and spacing intervals—that can be used to develop a standard procedure for determining number of columns and column spacing for a generic multi-column bridge bent in this study. For example, in this study, it was determined that column-to-column spacing is typically between 7 feet and 16.5 feet, typically specified at 6-inch intervals. The next step in determining column spacing of a generic multi-column bent is to find a relationship between deck width, length of the bent cap, and distance from edge of cap to the first column. Again, typical standard and as-built drawings indicated that for RC-Slab and MSRC classes, the length of the bent cap is the same as the deck width, while other classes have some variability in cap length. However, the bent cap was generally found to be 2 feet shorter than the width of the superstructure. Typically, in multi-column bents, as shown in Figure 6.27, there is a certain amount of column inset, indicating the bent cap extends beyond the outside columns. An estimation of this typical column inset is necessary to determine the number of columns and overall multi-column bent layout. In as-built and standard drawings, this column inset dimension, i.e., the distance from edge of bent cap to center of outside column, varies significantly, as this distance is typically varied in order to optimize column spacing. Nonetheless, knowing the upper and lower limits as well as a typical value for column inset inform the bent layout for sampled bridges. Based on bent dimensions found in drawings, a lower limit of 2 feet, an upper limit of 6 feet, and a typical value of 4 feet are assumed for the column inset dimension used to determine the column spacing and layout within a bent.

In summary, the process of determining the number of columns and column spacing in a multi-column bent relies on: the deck width, the width of the bent cap, and the typical column inset. The process is iterative and is as follows: Subtract 10 feet from the sampled deck width to get the center-to-center distance between outside columns (i.e., subtract 2 feet to get width of cap, and 8 feet to account for column inset on either side of cap). Then, divide this value in half (which initially assumes three columns per bent) to get an initial column spacing estimate. If the initial spacing is larger than 16.5 feet, columns are added until the spacing is adequate (i.e., less than 16.5 feet). The final step is to round the column spacing to the nearest 6-inch interval (e.g., a 12.23 foot spacing would be rounded to 12 feet, and a 12.36 foot spacing would be rounded to 12.5 feet). The number of columns and column spacing for each of the bridge samples used in this study are found in Appendix D.

6.4.3.3. Foundations

Foundations are considered as the below ground portion of the substructure, which transfers the structural loads to the surrounding soil or rock. Foundations can take on a variety of different configurations depending on the loading demands, soil type, and other site-specific constraints such as superstructure type, overhead clearances, existing utilities, and so on. The below ground substructure, just like its above ground counterpart, is split into nine different types in the TxDOT bridge inventory data. These foundation types are steel piling, concrete piling, timber piling, drilled shafts, spread footings, pile cap on steel piling, pile cap on concrete piling, pile cap on timber piling, and other. Figure 6.29 shows the distribution of foundation types among the seven bridge classes. Below ground substructure seems to be more varied between different types than the above ground substructure; however, the PC Girder classes (i.e., MSPC and SSPC) and the MCSTEEL class again tend to have one substructure type, with 83%, 86%, and 73%, respectively, of bridges in these classes having drilled shaft foundations. The MCRC-Slab and MSRC classes tend to have drilled shafts and concrete pilings, while the MSRC-Slab and MSSTEEL classes are distributed between drilled shafts, concrete piling, spread footings, and steel piling.

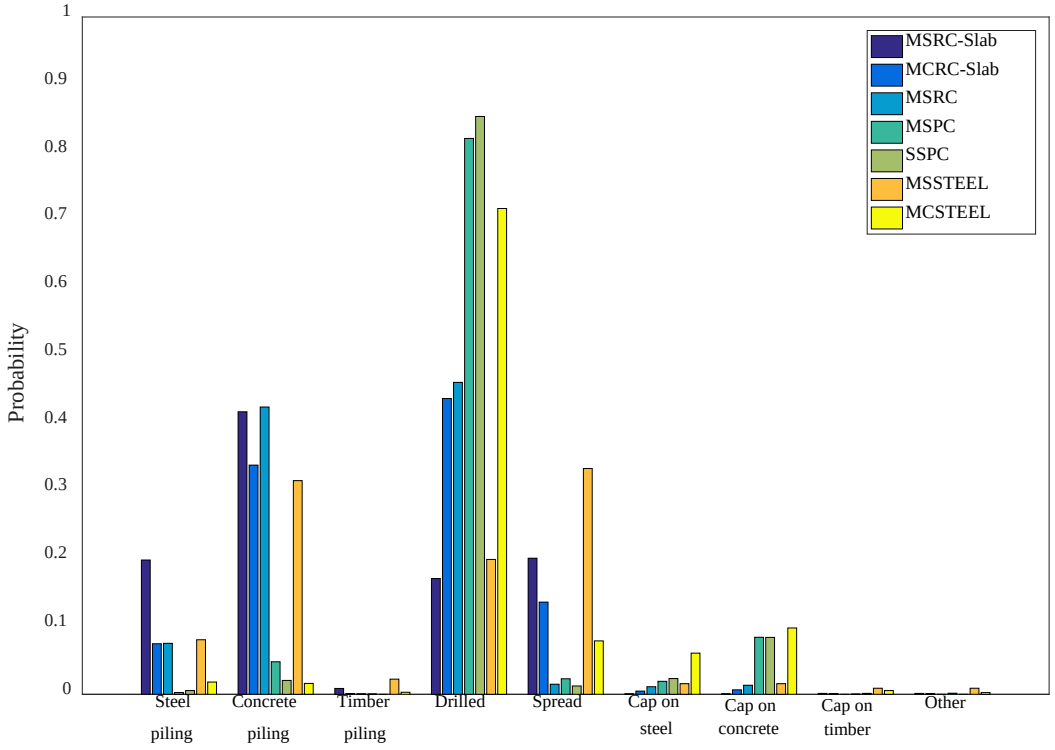

Figure 6.29: Histogram for types of below-ground substructure

In general, the following foundation systems are the most common in Texas: integrated pile/column (i.e., drilled shafts or pile), spread footings, or pile footings. Figure 6.30 shows examples of these foundations systems. Spread footings (Figure 6.30a) are considered shallow foundations and are typically used in locations where firm soil or rocky conditions are found at relatively shallow depths.

Pile supported foundations typically consist of either driven steel H-pile, precast (reinforced or prestressed) concrete pile, or cast in drilled holes (CIDH) connected with a concrete pile cap. In certain cases, the pile cap can be continuous along all columns in a bent (e.g., a strip footing), but more commonly each column has an individual pile footing (Figure 6.30d/e). Regardless of the pile type, it is important to have adequate embedment into the pile to ensure the proper force transfer. Pile footings, shown in Figure 6.30d/e, are typically considered deep foundations.

Integrated column/pile, shown in Figure 6.30b and c, are referred to as an integral column/shaft. The integral shaft or integral pile foundations are the most common and are considered as the prominent foundation types in this study. As shown in Figure 6.30b, when subjected to lateral loading, the critical section or plastic hinge region of an integral shaft foundation consisting of the same diameter column is below the ground line. The plastic hinge typically forms at a depth of about twice the pile diameter below the surface (Priestley et al. 1996), which makes it difficult to identify during a post-earthquake inspection. The integral shaft foundations with an oversized shaft, shown in Figure 6.30c, have an increase in stiffness at the shaft-column joint, forcing the plastic hinge to form at the base of the column, which is typically at or above the ground line. This case of damage above the soil surface is much easier to identify during a visual inspection. Both of these drilled shaft types are used in Texas. According to the TxDOT *Geotechnical Design Manual* (TxDOT, 2012), drilled shafts are most economical in competent soil or rock, while the pile foundations are best suited for softer soils.

Moreover, based on the substructure distribution for Texas bridges (Figure 6.29), it is here assumed that MSRC and MSSTEEL bridge classes consist of pile foundations, while drilled shaft foundations are assumed for the remaining bridge classes (i.e., MSPC, SSPC, MSRC-Slab, MCRC-Slab, and MCSTEEL). Based on the database available for Texas, it is concluded that approximately 80% of bridges with pile foundations utilize concrete piles. Concrete piles are either plain reinforced or prestressed square piles ranging in size from 16 inches up to 24 inches. When steel piles are used, TxDOT standards typically specify the use of HP14, 16, or 18. For drilled shaft foundations, TxDOT standard drawings show details for drilled shafts with diameters from 18 inches up to 48 inches. Due to insufficient data regarding actual shaft diameters, this study assumes the shaft diameters of sample bridges are the same size as the columns specified above.

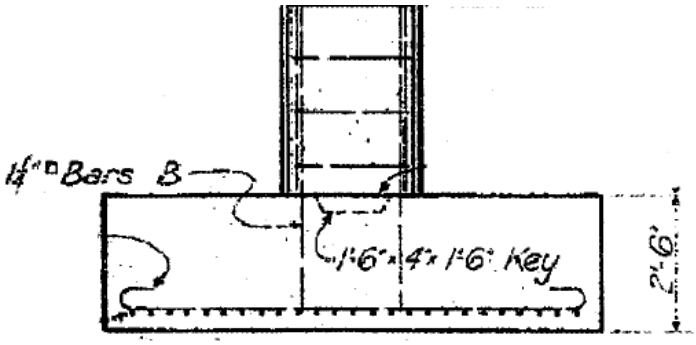

(a) Spread footing (TxDOT, 1939)

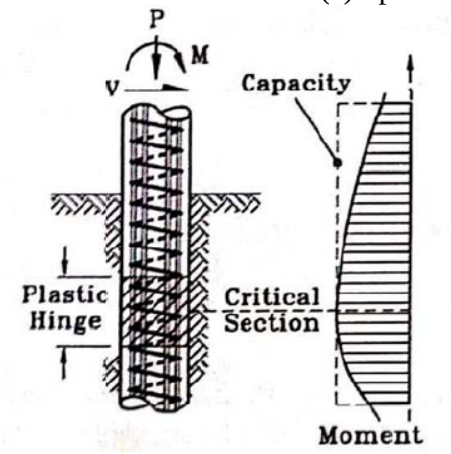

(b) Integral pile/column (Ramanathan, 2012)

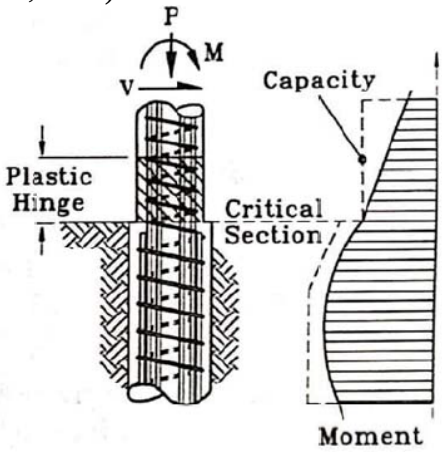

(c) Integral pile/column (oversized pile) (Ramanathan, 2012)

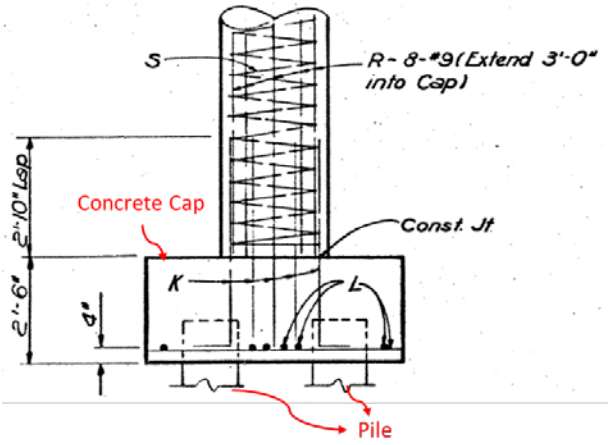

(d) Pile footing, as adopted from TxDOT (1962)

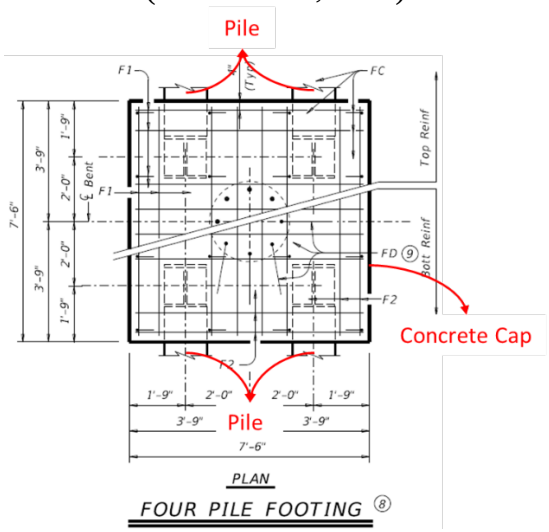

(e) Pile footing, as adopted from TxDOT (2015)

Figure 6.30: Typical foundation systems

To model the foundation, which is discussed in Chapter 7, two main parameters should be determined as: number of piles per footing and stiffness of the foundation. First, the number of piles per footing is addressed. Based on thorough review of TxDOT design standards and as-built

drawings, typical footings consist of three to five piles per column. For the purpose of this study, a footing supported by four piles per column (Figure 6.30d) is chosen as the basis for modeling.

Second, translational stiffness of the foundation is addressed. For footings, due to the lack of data on relevant foundation testing data in Texas, the Caltrans (1999) recommendation on the foundation stiffness is utilized in this study. Caltrans (1999) suggests a constant initial stiffness for of 40 kip/inch for a pile regardless of pile material or geometry. To take into account the uncertainty, this parameter is modeled as a random variable with uniform distribution with median of 40 kip/inch, as well as lower and upper bounds of 20 kip/inch per pile and 75 kip/inch per pile, respectively. Therefore, a translational foundation stiffness ranging between 80 kip/inch and 300 kip/inch in both the transverse and longitudinal direction can be considered for the four-pile group foundation in Texas. For drilled shafts, the stiffness of the foundation is computed based on the diameter of the foundation. The following paragraphs discuss how to correlate shaft diameter to foundation stiffness for modeling purposes.

Ramanathan (2012) performed an analysis on a variety of drilled shaft/pile systems and soil profiles using the software called LPILE, which is a program used for the analysis and design of piles and drilled shafts under lateral loads. Ramanathan (2012) determined that the translational stiffness of an integral column and shaft/pile is linearly related to the diameter of the shaft/pile (see Table 6.15 and Figure 6.31). Following the linear relationship shown in Figure 6.31 and using a typical shaft diameter found in Texas (e.g., 30-inch dia. for the MSPC girder bridge class), a median translational stiffness for an integral column and shaft/pile was found to be 173 kip/inch. Comparing this stiffness to a four-pile group foundation with a median pile stiffness of 40 kip/inch per pile (i.e., 160 kip/inch translational foundation stiffness for the four-pile group), it is evident that the four-pile group foundation and the 30-inch diameter integral column/shaft foundation have similar stiffnesses. For the case of simplicity, in this study, the translational foundation stiffness for drilled shaft foundations is determined by the sampled value of initial pile stiffness (i.e., 20 kip/inch/pile to 75 kip/inch/pile) multiplied by a relevant coefficient that is determined based on the relationship between shaft diameter and equivalent pile group. For example, a 24-inch shaft is assumed to have a stiffness equivalent to that of 3 piles (median of 120 kip/inch), a 30-inch diameter shaft has a stiffness equivalent to 4 piles (median of 160 kip/inch), a 36-inch shaft has a stiffness equivalent to 6 piles (median of 240 kip/inch), and a 42-inch shaft has a stiffness equivalent to 8 piles (median of 320 kip/inch).

In summary, where pile foundations are used, it was assumed that four piles were used per column, and where drilled shafts are used, the shaft diameter was correlated to an equivalent stiffness of a pile group as mentioned above.

Table 6.15: Translation foundation stiffness (Ramanathan 2012)

Foundation Type	Translational stiffness (kip/in)
16 in intergral pile column	30
6 ft dia. Drilled shaft	600
8 ft dia. Drilled shaft	900

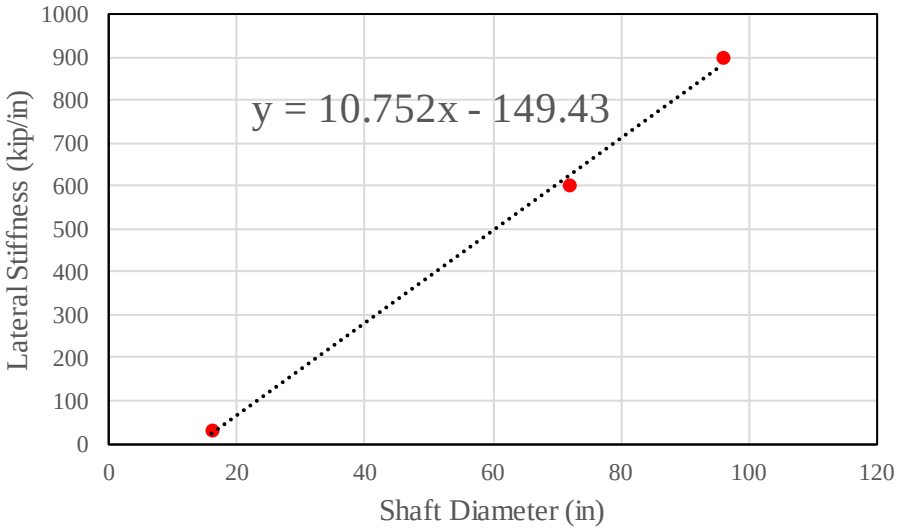

Figure 6.31: Translational foundation stiffness vs. shaft/pile diameter

6.4.3.4. Abutments

Abutments are a component of the substructure that can have multiple functions. First, abutments are the end bridge bents that provide the vertical and horizontal support for the superstructure. Abutments can also provide soil retention at grade separations. Lastly, abutments provide the link between the superstructure and the roadway approach. There are a variety of different types and designs of abutments; however, they can be broken down into two main categories, seat type and integral abutments. Seat type abutments, as shown in Figure 6.32, act like a bent cap where the superstructure rests on the bridge seat allowing movement independent from the abutment. However, integral abutments, as shown in Figure 6.33, are built monolithically with the superstructure. Integral abutments tend to provide a much stiffer structure and help prevent unseating of the superstructure during a seismic event (Ramanathan 2012). Following an in-depth review of TxDOT standard and as-built drawings, it was concluded that seat type abutments, and more specifically pile-bent-type abutments, shown in Figure 6.32d, are the most common among Texas bridges.

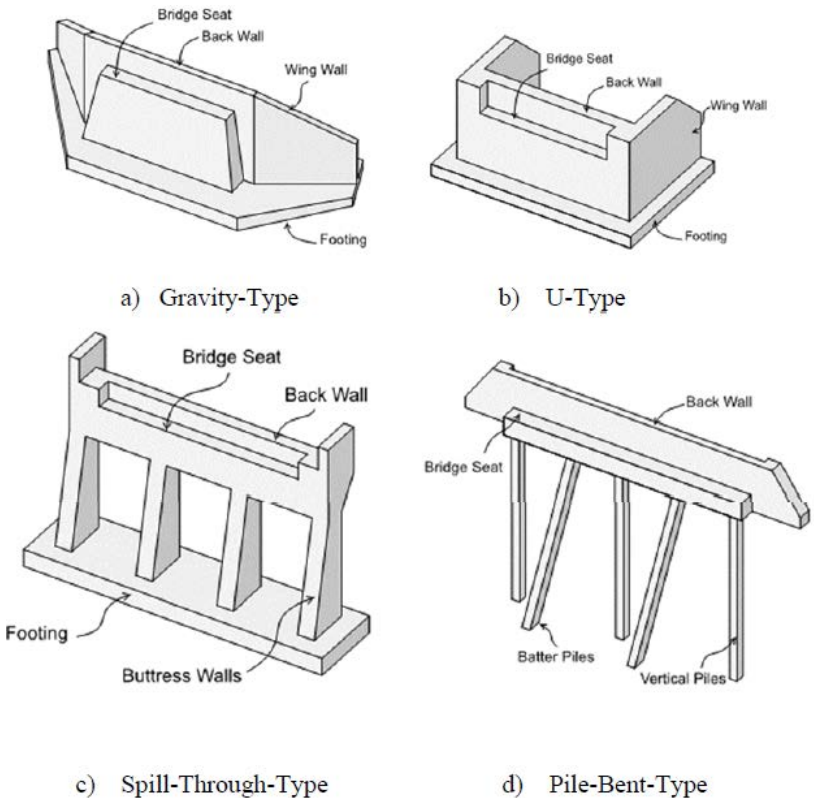

Figure 6.32: Common seat type abutments (Nielson 2005)

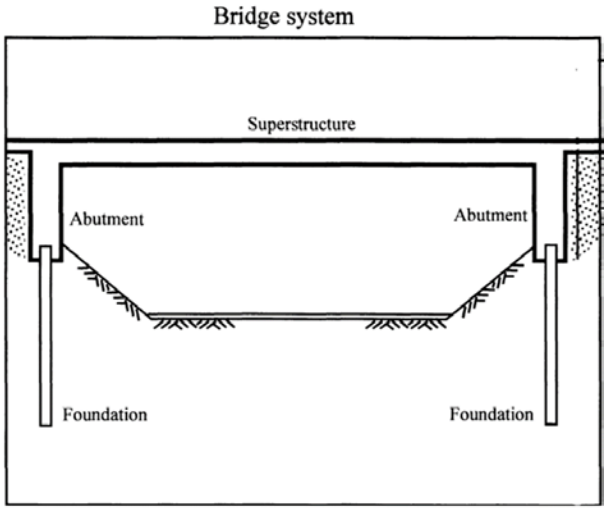

Figure 6.33: Integral type abutment

In addition to vertical gravity loads, abutments also experience horizontal loads during a seismic event. Two types of horizontal resistance are present during loading in the longitudinal direction as shown in Figure 6.34. The first one is a passive resistance, which is developed as the abutment backwall is pressed into the soil backfill. In this case, the resistance is provided by the soil and the shafts/piles. The other type is active resistance, which is developed from the shafts/piles when the

abutment pulls away from the backfill. The resistance in the transverse direction is provided by the shafts/piles and wing walls (Nielson 2005).

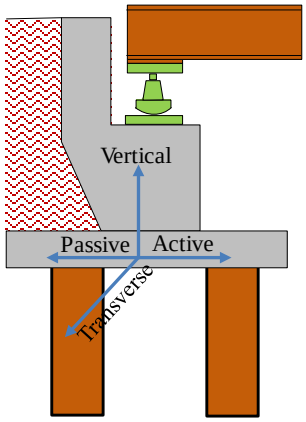

Figure 6.34: Horizontal abutment behavior

The active stiffness, as well as transverse resistance, is directly related to the number of piles (or shafts) in the abutment, which can act in either the longitudinal or transverse directions. Pile bent abutments can be constructed with either driven piles or drilled shafts. For ease of design and construction, abutment foundations typically utilize the same foundation type and layout as the interior bents. Therefore, the active abutment behavior for a specific bridge class is assumed to be the same as the foundation types discussed earlier. In fact, active abutment stiffness is equal to the translational foundation stiffness. For example, a MSPC bridge is modeled with an active abutment stiffness based on the diameter of the drilled shafts. A MSSTEEL bridge is modeled with an active abutment stiffness based on the stiffness of four piles per column location.

The passive stiffness is provided by both the soil behind the abutment and the piles. The passive stiffness thus depends on both the number of piles and the size of the abutment (i.e., abutment height and width). Borzorgzadeh et al. (2007) suggested that the initial stiffness per unit length of a 5.5 feet tall abutment, k_i, in the passive direction is 20 kip/inch per foot of abutment length; however, the abutment stiffness, k_{abut}, can be adjusted proportionally to the backwall height as follows:

$$k_{abut} = k_i (= 20.0 \frac{kip/in}{ft}) \times b \times \left(\frac{h_{abut}}{5.5} \right) \quad (6\text{-}1)$$

where, b is the width of the backwall and h_{abut} is the height of the abutment. Borzorgzadeh et al. (2007) also showed that the k_i is dependent on other variables such as soil properties, vertical wall movement, and area of structural backfill. Due to insufficient data on the distribution of initial stiffness, this parameter is assumed to follow a uniform distribution between 20 kip/inch per foot of abutment length and 50 kip/inch per foot of abutment length based on recommendation from Caltrans (1999). The abutment width is considered to be the width of the bridge deck, while the height is considered as the summation of the depth of the bent cap, shown in Table 6.13, and the height of the backwall. Backwalls are intended to support the approach slab and retain soil, so they typically extend from the top of the bent cap to the bottom of the approach slab. Therefore, the

backwall height for prestressed concrete and steel girder bridges is determined by the depth of the girder plus the height of the bearing. For the reinforced concrete girder bridge class, the slab is actually part of the girder depth; therefore, the backwall height is 8 to 10 inches less than the total superstructure depth. Reinforced concrete slab bridges do not actually have a backwall as the approach slab typically rests directly on the bent cap.

6.4.4. Bearings

The final component needed to develop a bridge model are the bearings. The bearings transfer loads from the superstructure to the substructure. These loads are mainly vertical live and dead loads, longitudinal and transverse loads, and material thermal expansion loading. During a seismic event, bridge bearings typically experience much larger demands than are considered for in-service conditions. In fact, during the earthquake, they experience significant longitudinal and transverse loadings, which can introduce structural vulnerability. Thus, it is important to accurately represent and capture bearing behavior in the modeling process. There are two main types of bearings used in this study: steel bearings and elastomeric bearings.

When it comes to modeling bearing behavior, there are several parameters that requires attention: coefficient of friction (COF), stiffness, dowel strength (concrete bridges only), and dowel gap (concrete bridges only). All of these parameters are dependent on the material and configuration of the particular bearing, and are discussed in the following sections.

6.4.4.1. Steel Bearings

Historically, steel bearings have most commonly been used in non-seismically detailed steel bridges. A typical steel bearing consists of a masonry plate on the bottom that is attached to the abutment or bent with anchor bolts, and a sole plate on the top that is attached to the underside of the girder. These types of bearings were prominent in steel girder bridge construction prior to the 1990s. There are two types of steel bearings: fixed bearings and expansion bearings. Fixed bearings are intended to transfer vertical and horizontal loading to the foundation while accommodating superstructure rotations relative to the substructure. Expansion bearings are intended to relieve material expansion forces by accommodating large relative longitudinal displacements, while also maintaining their vertical load carrying capacities and transferring transverse loading (Mander et al. 1996). In fact, fixed bearings are restrained in both the longitudinal and transverse directions, and expansion bearings are restrained only in the transverse direction. Figure 6.35 shows examples of fixed and expansion steel bearings. In simply supported spans, one can often find alternating fixed and expansion constraints. In continuous spans, the fixed type bearing is typically at the interior girder supports, while the expansion bearings are at the exterior girder supports.

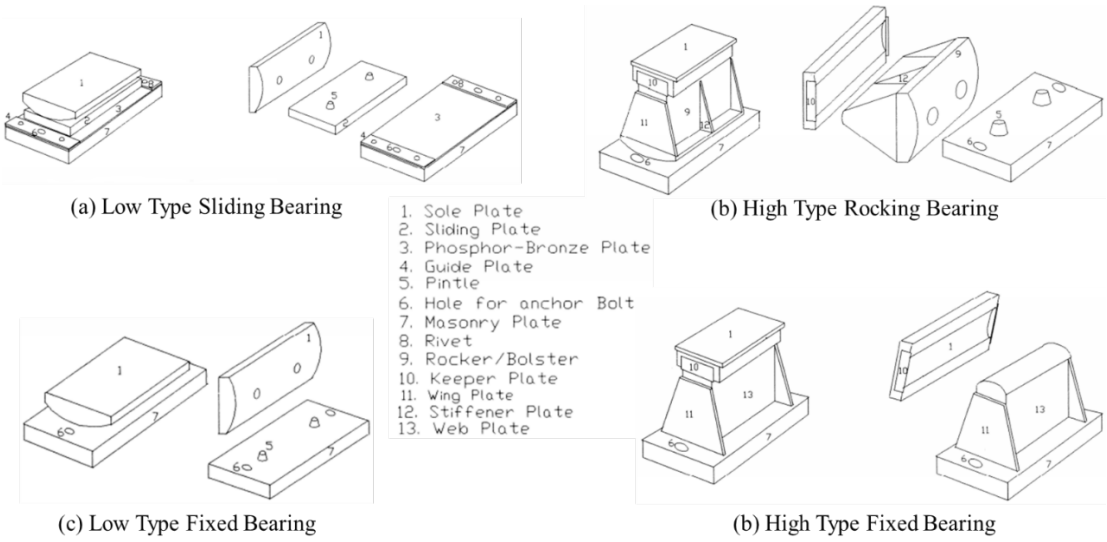

Figure 6.35: Typical steel bearings (Mander et al. 1996)

Steel bearing designs may vary in different areas of the country; however, most steel bearings have the same general geometry and main components. Figure 6.36 shows a typical high type rocker bearing used in Texas, which shows an example of these design variations when compared with the bearings in Figure 6.35. Due to the lack of experimental data and the similarities in the overall bearing designs, however, the Texas-specific bearings in this study, are assumed to follow the behavior of the steel bearings presented in the Mander et al. (1996) study, which are shown in Figure 6.35. Mander et al. (1996) conducted a study looking at the behavior of steel bearings under cyclic lateral loading and determined values for both COF and stiffness. They suggested that the COF, depending on the level of corrosion, varies from 0.2 to 0.6 for low-type sliding, and from 0.04 to 0.12 for high-type steel rocker bearings. The lower bound and upper bound of the suggested ranges represent clean to heavily corroded conditions. Moreover, Mander et al. (1996) suggested a mean value of 765 kip/in and 114 kip/in for initial stiffness of steel bearings in the longitudinal transverse directions, respectively. To take into account the uncertainty on the initial stiffness of steel bearings, it is assumed that this variable is a random variable with a uniform distribution with lower and upper bounds of 50% and 150% of the mean value (Nielson 2005).

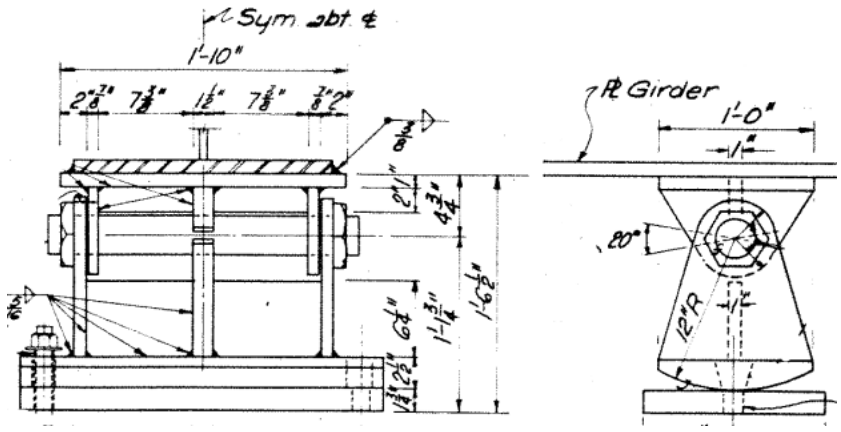

Figure 6.36: Typical steel rocker bearing used in Texas

These steel bearing types are susceptible to corrosion and deterioration. In addition, they can exhibit non-ductile behavior, such as toppling and bolt fracture. As a result, these types of bearings are known to be vulnerable to seismic loading (NCHRP, 1977). Consequently, steel bearings have been replaced with elastomeric type bearings for steel girder bridges in the current TxDOT standards for new steel girder bridge construction. However, studying the bridge class statistics, it is evident that the majority, i.e., 83%, of steel girder bridges, both simply supported and continuous steel girder bridges, were built between the 1930s and the 1970s. Therefore, in order to accurately capture the vulnerability of the existing steel girder bridge population, steel bearings were assumed to model the behavior of the MSSTEEL and MCSTEEL bridge classes. One thing that should be noted is that this study only considers the high type steel bearings. Due to lack of data on the bearings used in the entire Texas bridge population, it is not possible to determine which bridges use high type versus low type bearings. A thorough review of as-built drawings of Texas bridges from the 1930s to the 1970s, did however indicate that high type bearings were commonly employed in both steel bridge classes.

6.4.4.2. Elastomeric Bearing

Elastomeric bearings are a very common bearing type used for prestressed concrete girder bridges. These types of bearings consist of an elastomeric rubber pad, with or without steel dowels that are anchored into the bent cap extending through the pad into the bottom of the girder. The elastomeric pad transfers horizontal loads through a frictional force at the interface with the concrete bent cap, while the dowels transfer load through beam type dowel action (Nielson 2005). As with steel bearings, elastomeric bearings also have both a fixed type and expansion-type bearings. To relieve material expansion forces through longitudinal movement, elastomeric expansion bearings are equipped with slotted holes in the rubber pad and in the bottom of the concrete girder such that bearings accommodate translation in the longitudinal direction without engaging the dowel. Figure 6.37 shows the typical configuration for an elastomeric bearing.

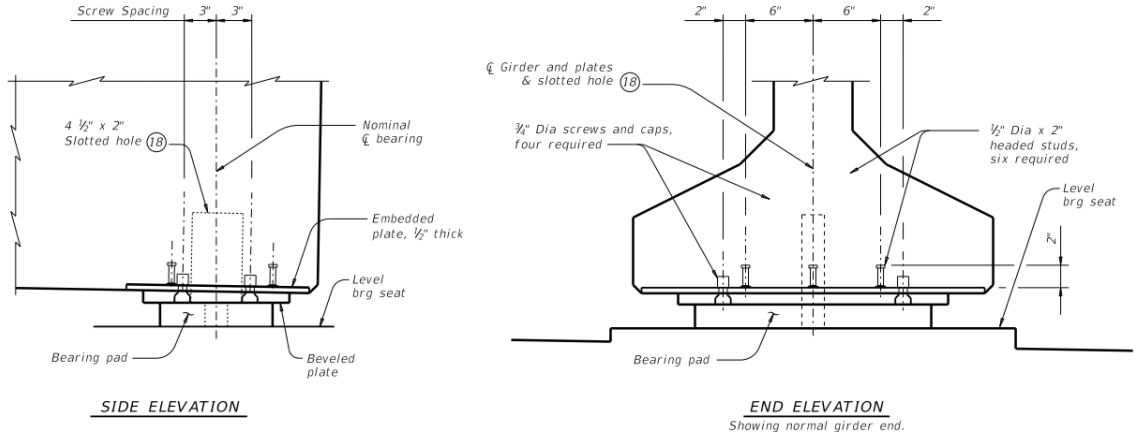

Figure 6.37: Typical elastomeric bearing (TxDOT 2017)

During an earthquake event, it is possible for an elastomeric bearing to undergo deformation in the rubber pad, displacement due to sliding, deformation in the steel dowel, or a combination of all three. To model these behaviors, it is important to understand the bearing material and geometry. For example, deformation in the elastomeric pad is directly related to the stiffness of the elastomer, as well as the surface area and the thickness of the pad. Initial stiffness of the elastomeric bearing can be estimated using the following equation:

$$k_0 = \frac{GA}{h_r} \tag{6-2}$$

where, G is shear modulus of the elastomer; A is area of pad; and h_r is thickness of the pad. Past studies have shown that variability in G has a strong correlation with the variability in hardness of the elastomer. For instance, the elastomer experiences an increase in hardness with age as it is exposed to external elements (Mtenga 2007). AASHTO Design specifications (2016) implies that G ranges from 0.66 MPa (96 psi) to 2.07 MPa (300 psi); however, there is insufficient information on the actual distribution within this range. Thus, in this study, G is assumed to have a uniform distribution between the AASHTO-specified limits. Pad area and thickness vary with girder dimensions and span length. Current TxDOT standards specify elastomeric pad dimensions as 8-inch by 21-inch for Tx28 through Tx54 girders, and 9-inch by 21-inch pad dimensions for Tx62 and Tx70 girders with a minimum pad thickness of approximately 2.75 inches. Review of as-built drawings revealed that bearing pads for older PC girders have a standard width of 6-inches, a length that is 2 to 3 inches shorter than the flange width, and a minimum thickness of 0.75-inch for bridges with spans up to 60 feet then increasing by 1/8 inch for every additional 10 feet in span length. Therefore, the pad area and pad thickness parameters were deterministically selected from standard bearing details from the corresponding era of construction.

Displacement due to sliding also depends on the surface area of the bearing pad, as well as the coefficient of friction (COF), the weight of the superstructure, and the gap between the dowel and the hole in the pad. For elastomeric bearings, the mean of COF for elastomeric pads are computed as follows:

$$\mu = 0.05 + \frac{0.4}{\sigma_m} \tag{6-3}$$

where μ is the mean of COF. As seen, μ is a function of the normal stress, σ_m, on the bearing. The σ_m and μ are calculated based on the associated gravity loads acting on each specific bearing. To account for uncertainty in the COF, a multiplication factor is applied to the computed COF. The multiplication factor is assumed to follow a lognormal distribution with a mean of zero and a standard deviation of 0.1 (Ramanathan 2012).

Deformation in the steel dowel is directly related to the size of the dowel and the strength of the dowel. To accurately capture the full behavior of an elastomeric bearing, the dowel strength and the gap between the dowel and the slotted hole in the bottom of the girder must be considered. During a seismic event, it is possible that the dowel could experience significant inelastic deformations. Following the guidance of Choi (2002), it is assumed that the ultimate strength of the dowel is directly related to the ultimate strength of the steel. Attempting to better understand the behavior of dowels in an earthquake event, Choi (2002) developed a finite element model of a typical dowel (i.e., a 1 inch diameter dowel that projected 3 inches into the bottom of the girder). Choi (2002) found that the ultimate lateral strength of this typical dowel was approximately 58kN (13 kips). However, if a different size dowel is used, the strength is assumed to be quadratically proportional. This relationship is owing to the fact that the strength scales according to the cross-sectional area ratio between the two dowels. In Texas, it is common to use a 1.25 inch diameter dowel (as opposed to the 1 inch diameter dowels in the Choi (2002) study); therefore, in this study, it is assumed that the average ultimate lateral strength is 20 kips. To account for variation, the dowel strength is assumed to follow a lognormal distribution with a mean value of 20 kips and a coefficient of variation (COV) of 0.08. Accounting for the fact that the dowel is not sitting perfectly in the middle of the slotted holes in the girders (i.e., slotted holes only at expansion bearings), it is important to capture the variations in the dowel gap in the model. Thus, in this study, it is assumed that dowel gap varies uniformly between 0 and 2.75 inches based on the maximum length of slot in the bottom of the girder minus the dowel diameter, i.e., a 4-inch slot and 1.25-inch dowel.

One additional note that should be mentioned is the TxDOT current standards for elastomeric bearing pads utilize thin layers of steel shims embedded within the elastomeric pad to increase the vertical stiffness and durability of the pad. Based on observations during review of as-built drawings and the age of PC girder bridges considered in this study, this type of bearing with steel shims was not determined to be representative of the existing Texas highway bridge inventory and, therefore, is not used in this study.

6.4.4.3. Alternative Concrete Bearing

In certain regions of the US, elastomeric bearings are the bearing of choice for any concrete superstructure such as PC I-girders, PC box-girders, RC slabs, and RC girders (Nielson 2005). For instance, Nielson (2005) determined that these types of bridges in the CEUS utilize elastomeric bearings. Nonetheless, in Texas, the RC girder and slab bridge classes do not typically utilize elastomeric bearings, predominantly due to the cast in place construction used for these

superstructure types. TxDOT does have some precast slab and beam type bridges in their system that utilize elastomeric bearings; however, this type of superstructure and bearing configuration is more typical of modern construction and was not found to be representative of the RC superstructures considered in this study, which were typically built between the 1920s and 1990s. Careful review of standard and as-built drawings was necessary to determine typical bearing details for RC girder and RC slab superstructure types. Figure 6.38 shows an example of the alternative concrete bearings used for RC girder and slab construction in Texas.

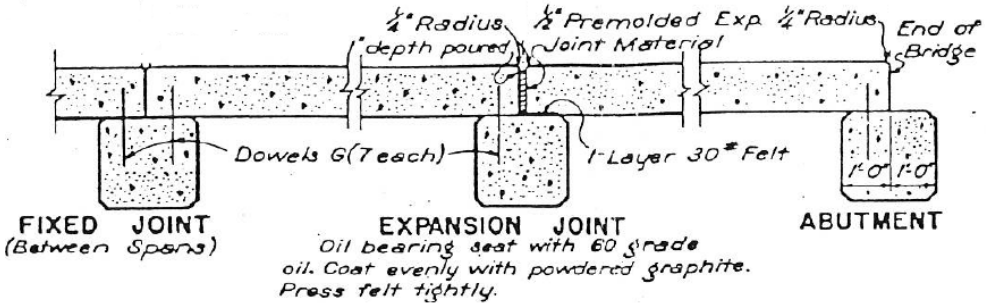

(a) RC slab (TxDOT, 1955)

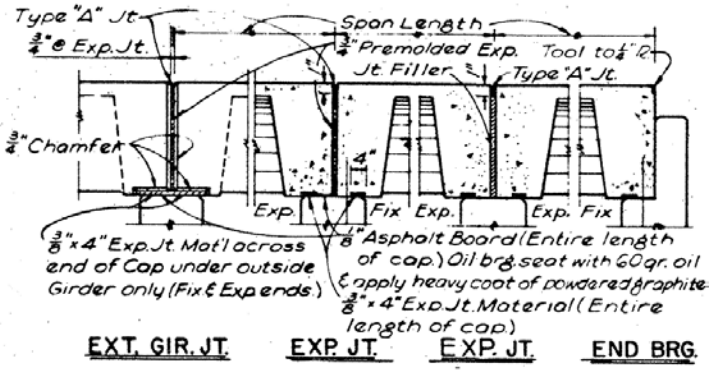

(b) RC girder (TxDOT, 1966)

Figure 6.38: RC girder and slab bearing details

As with both the steel and elastomeric bearings, Figure 6.38 shows both fixed and expansion type bearings for RC girder and slab superstructures. For the expansion type bearings, it is common to coat the bridge seat with some kind of lubricant such as 60 grade oil or powdered graphite, and then utilize a thin material barrier such as roofing felt or asphalt board between the concrete superstructure and concrete bridge seat. Figure 6.38 also shows the elimination of retention dowels at the expansion bearing locations. Fixed bearing locations vary slightly between the two details shown in Figure 6.38. For RC slab bridges, it is typical for the concrete slab to sit directly on the concrete bridge seat with #6 (¾-inch diameter) dowels, spaced at 2-foot intervals along the length of the bridge seat. For the RC girder bridge class, a thin piece of expansion joint material is placed along the face of the bridge seat and #6 dowels are placed at each girder location. The expansion joint material helps protect the edge of the bridge seat due to small deflections and rotations in the superstructure. These materials are, however, very thin and narrow (e.g., 3/8-inch thick and 4

inches wide) and may degrade over decades of exposure to the elements. Thus, it is reasonable to assume that the concrete girder is likely in direct contact with the concrete cap.

Modeling the behavior of these alternative concrete bearings includes resistance due to sliding friction and the dowels. The material used in the bearings shown in Figure 6.38 are significantly thinner than the elastomeric pads and are assumed to contribute negligible stiffness to the bearing model. For the fixed and expansion bearings, it is assumed that the concrete superstructure sits directly on the concrete bridge seat; therefore, a coefficient of friction (COF) for concrete on concrete can be assumed.

Following the guidance of the ACI 318 building code (2014), the median value of COF for a hardened concrete on concrete surface is assumed to be 0.6. To consider uncertainty in the COF, a multiplication factor is applied in the same fashion as discussed previously for the elastomeric bearing. This assumption is again based on the thin nature of the bearing material used in these alternative expansion joint details, as well as the age of the RC girder and RC slab bridge classes, which indicates that the bridges from these classes have been exposed to weathering for a median age of 50 years and 64 years, respectively, leading to deterioration of the bearing material and lubricant.

The dowels found in these alternative type bearings are 0.75-inch steel dowels. They are assumed to behave in the same fashion as the dowels in the elastomeric bearing, with a slight reduction in stiffness due to the reduction in cross sectional area. In fact, the ultimate strength of the 0.75-inch dowel can be calculated assuming that the dowel strength can be scaled by the cross-sectional area ratio as for dowels used in the elastomeric bearing. Thus, a median ultimate dowel strength of 7 kips and COV of 0.08 are used to model these types of bearings.

6.4.5. Damping Ratio

Damping ratio for bridges typically ranges from 0.02 to 0.07 of critical damping, which represents the 2nd and 98th percentiles according to Chen et al. (2003). Fang et al. (1999) found that damping in tall buildings follow a normal distribution, which can be extended to bridges (Nielson 2005; Ramanathan 2012). Therefore, in this study uncertainty in damping ratio are represented by a normal distribution with a mean of 0.045 and standard deviation of 0.0125.

6.4.6. Loading Direction

Torbol and Shinozuka (2012) conducted a study looking at the effect of the angle of incidence (i.e., the angle of “attack” of the ground motion) on bridge fragility curves. Their results indicated that the angle of seismic incidence could lead to significant variation in the fragility of a bridge, and ultimately could lead to the underestimation of the vulnerability of the structure. Determining the angle of incidence of a seismic event on a particular structure is not easy; however, with enough site-specific information and knowledge of seismic fault activity one could argue that a particular angle of incidence could be generated with reasonable error. In the present study, an entire network of bridges with very different site information and orientations are being assessed. Thus, it is not

possible to determine bridge-specific loading directions for unknown earthquake sources. Following the guidance of Torbol and Shinozuka (2012), in this study, the angle of seismic incidence is considered a random variable sampled from 0 to 360 degrees.

6.4.7. Summary of Random Variables

A summary of all the material properties and component behaviors described in Section 6.4, and their respective distribution characteristics can be found in Table 6.16.

Table 6.16: Summary of parameters and distribution characteristics

			Probability Parameters		
Parameter Description	**Abbreviation**	**Distribution**	***a****	***b****	**Units**
Concrete strength	Conc Str	Normal	4200	850	psi
Reinforcing strength	Reinforcing Str	Lognormal	55,000	4900	psi
Steel fixed - longitudinal	Steel Fix - Long	Uniform	424.8	637.2	kip/in
Steel fixed - transverse	Steel Fix - Trans	Uniform	22.8	34.2	kip/in
Elastomeric shear modulus	Elasto shear mod	Uniform	96	300	psi
Steel fixed COF - longitudinal	Steel Fix COF-Long	Uniform	0.168	0.252	--
Steel fixed COF - transverse	Steel Fix COF-Trans	Uniform	0.296	0.444	--
Steel Rocker COF - longitudinal	Steel Rocker COF-Long	Uniform	0.032	0.048	
Steel Rocker COF - transverse	Steel Rocker COF-Trans	Uniform	0.08	0.12	
Elastomeric-Multipl. factor	Elasto MF	Lognormal	0	0.1	--
Dowel Strength	Dowel Str	Lognormal	20	1.6	kip
Dowel Gap	Dowel Gap	Uniform	0	2.75	in
Passive Stiffness	Abt-Pas Stf	Uniform	20	50	kip/in/ft
Pile Stiffness	Pile Stf	Uniform	20	60	kip/in per pile
Superstructure mass	Mass	Uniform	110	140	%
Damping ratio	Damp Ratio	Normal	0.045	0.0125	--
Deck Gaps - Large (MCSTEEL)	Large Gap	Uniform	1	6	in
Deck Gaps - Large (MSSTEEL)	Large Gap	Uniform	1	2	in
Deck Gaps - Small (MSSTEEL)	Small Gap	Uniform	0.7	1.3	in
Loading direction	Load Dir	Uniform	0	360	degrees

*For normal and lognormal distributions, *a* and *b* indicate the median and dispersion, respectively, and for uniform distribution, *a* and *b* represent the lower and upper bounds, respectively.

6.5. Bridge Configurations

In the present study, first, eight representative samples per class were selected to represent the variation in bridge geometry. These representative bridges were developed by sampling from the distributions of five geometry and age parameters, including number of spans, deck width, span length, year of construction, and under-clearance, which provides an approximate estimation of

column height. To properly account for material uncertainties and variations in component behavior, the geometrically representative bridge samples are each paired with eight samples of the material properties and component behaviors, creating the 64 bridge samples per bridge class to be used in the nonlinear response-history analyses. The parameters used to capture variation in material properties and component behaviors include, but are not limited to, steel and concrete strength, steel bearing stiffness, elastomeric bearing shear modulus, coefficient of friction for bearings, deck gap size, abutment stiffness, mass density, and inherent damping ratio. Therefore, in this study, 448 randomly generated bridges are generated to represent Texas bridge inventory. In this section, first, the sampling technique, which is the Latin Hypercube Sampling method, is discussed in details. Then, the geometric parameters of each bridge configuration of different bridge classes are shown. Finally, the bridge parametric samples generated for each bridge configuration are presented.

6.5.1. Sampling Methodology

A major part of this study is analyzing the seismic vulnerability of the entire TxDOT bridge inventory. As previously mentioned, it is not feasible to analyze each individual structure; therefore, a set of bridge samples representing the variations in the Texas bridge inventory must be used. Based on experience from past studies (Choi 2002; Nielson 2005; Pan 2007; Ramanathan 2012) a large number of bridge samples are required to capture the variations in seismic performance. In this project, a total of 64 bridge samples are selected for each bridge class of concern (i.e., MCSTEEL, MSSTEEL, MSPC, MSRC, MCRC-Slab, MSRC-Slab, SSPC).

Creating a computational bridge model requires a number of different variables to fully and accurately define each bridge. Some of these variables may be geometric parameters such as span length, deck width, number of spans, etc. While other variables are used to model material properties such as concrete strength, steel reinforcing strength, soil stiffness, pile stiffness, bearing stiffness, etc. As seen in past studies (Nielson 2005; Pan 2007; Ramanathan 2012), the number of modeling parameters can be quite large with upwards of 18 to 20 variables per model. To account for uncertainties in geometry and materials, one must sample from a probabilistic distribution for several, if not all of these variables. Thus, it is important to find an accurate yet efficient way to sample each of these parameters.

Over the past several decades, a lot of research and effort has been invested in developing efficient and reliable probabilistic analysis methods used in engineering research (Olsson and Sandberg 2002). Several different methods have been used (e.g., Taylor series expansion and Neumann series expansion methods); however, Monte Carlo simulations, which are a probabilistic based sampling approach, have become the most popular approach in many engineering analysis applications. A concern that often arises when using a Monte Carlo simulation is the computational expense. Straight Monte Carlo simulations randomly select samples for each uncertain variable in an engineering problem based on their associated probabilistic distributions, which requires a large number of samples in order to accurately represent the entire distribution (e.g., on the order of 1,000 to 10,000 samples, in some cases even more). In certain applications where only, a small

collection of samples are used, the clustering of samples in the high probability region becomes a concern in that the selected samples are no longer representative of the entire range of the population they are meant to represent.

To reduce the size of the sampling set (and thus reducing computational cost) without affecting the ability to capture the full range of the population, other variations of Monte Carlo simulations have been developed. According to Huntington and Lyrintzis (1998), Latin Hypercube Sampling (LHS), which utilizes a stratified random sampling technique, is the best variant of Monte Carlo that utilizes smaller samples. In this approach, the cumulative distribution function for the parameters of interest are divided up into *n* (i.e., the desired number of samples) equal sections or bins, and then a sample is randomly selected from within each bin (e.g., see Figure 6.39). This approach allows for the full probabilistic distribution to be represented in just a small number of samples. In this study, sixty-four bridge samples are to be modeled for each of the seven bridge classes considered in this study. Thus, the modeling parameters (which will be discussed in the following section) for each bridge were sampled using a Latin Hypercube technique. More specifically, following the work of Iman and Conover (1982) a ranked Latin Hypercube method was used in order to match the sampled correlation matrix as closely as possible to the empirical correlation matrix. In other words, the correlation between variables in the sample set should be representative of the correlation between variables in the entire population. The majority of the parameters used in this study show essentially zero correlation, and are thus assumed to have no correlation. It is still recommended, however, to use the ranked sampling method in order to eliminate the introduction of random or accidental correlation. For example, if deck width and column height are uncorrelated in the bridge inventory data, the ranked sampling approach would prevent the deck width and column height from generating a positive correlation during the random sampling process to avoid producing results unrepresentative of the actual population.

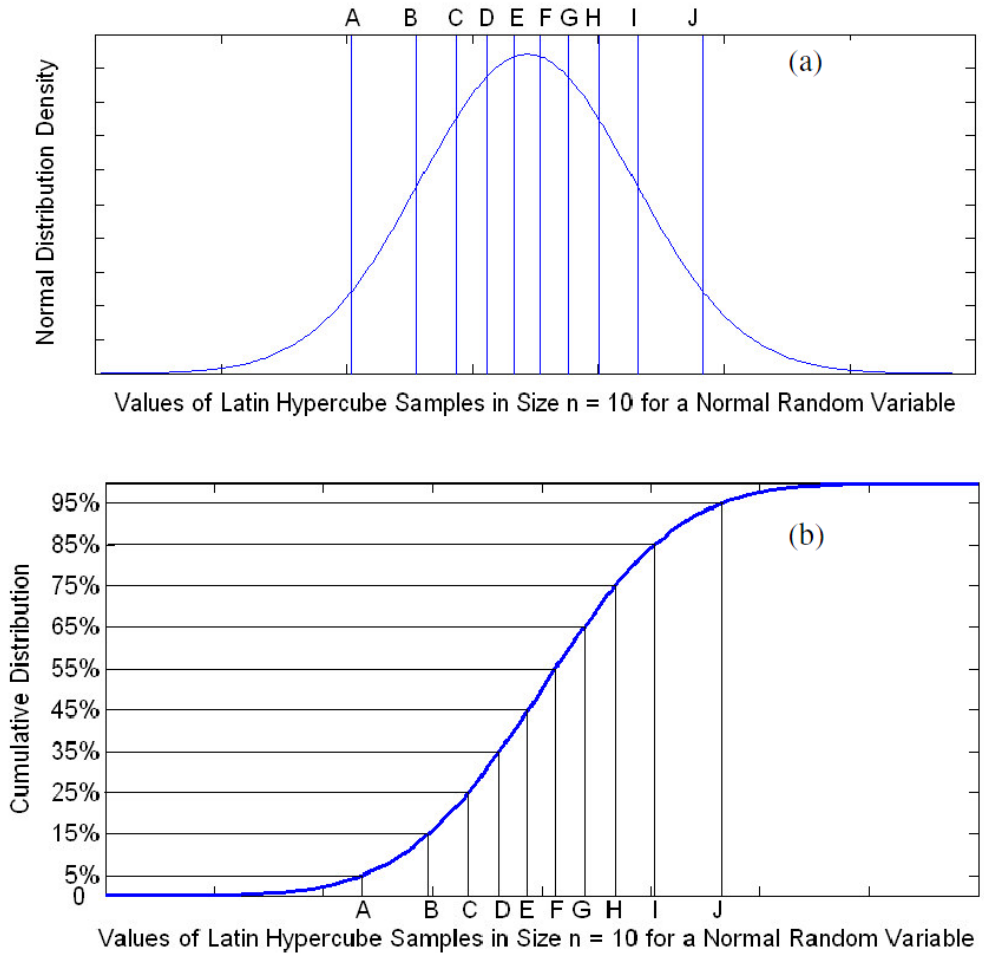

Figure 6.39: Generation of bridge parameter samples by the Latin Hypercube Sampling Approach (Pan 2007)

6.5.2. Bridge Geometric Samples

The geometrically representative bridge samples that are used for each bridge class in this study can be seen below in Table 6.17 through Table 6.23.

Table 6.17: Geometric samples of multi-span continuous steel girder (MCSTEEL) bridges

Bridge No.	Deck Width (ft)	Span Length (ft)	Number of Spans	Year Built	Under Clearance (ft)
1	66	60	3	1970	13.8
2	27.88	90	4	1962	15.50
3	31.20	87	3	1967	14.58
4	53.70	118	4	1964	13.83
5	41.43	40	3	1970	16.08
6	43.20	145	4	1973	15.25
7	40.00	70	3	1959	15.50
8	35.20	240	2	2004	17.33

Table 6.18: Geometric samples of multi-span steel girder (MSSTEEL) bridges

Bridge No.	Deck Width (ft)	Span Length (ft)	Number of Spans	Year Built	Under Clearance (ft)
1	42.00	33	3	1938	18.00
2	31.33	40	4	1955	14.25
3	32.64	77	4	1999	14.00
4	23.33	45	3	1939	15.83
5	46.00	35	2	1946	13.33
6	18.00	46	3	1940	17.83
7	21.30	24	5	1933	13.63
8	16.33	50	3	1935	15.67

Table 6.19: Geometric samples of multi-span prestressed concrete girder (MSPC) bridges

Bridge No.	Deck Width (ft)	Span Length (ft)	Number of Spans	Year Built	Under Clearance (ft)
1	45.30	37	5	1938	17.08
2	40.98	107	4	1997	20.58
3	40.00	84	2	1969	18.42
4	36.30	60	3	2006	16.08
5	71.00	72	2	1985	16.67
6	57.20	121	3	1973	15.67
7	62.00	80	3	2015	14.75
8	44.30	100	3	1994	17.50

Table 6.20: Geometric samples of multi-span reinforced concrete girder (MSRC) bridges

Bridge No.	Deck Width (ft)	Span Length (ft)	Number of Spans	Year Built	Under Clearance (ft)
1	45.80	41	5	1971	15.50
2	25.70	40	4	1982	18.08
3	32.00	40	3	1963	15.08
4	39.18	30	2	1990	16.33
5	28.30	30	3	1959	16.92
6	42.30	40	3	1961	21.58
7	24.70	30	3	1954	16.50
8	44.20	30	5	1968	17.75

Table 6.21: Geometric samples of single span prestressed concrete girder (SSPC) bridges

Bridge No.	Deck Width (ft)	Span Length (ft)	Number of Spans	Year Built	Under Clearance (ft)
1	42.00	60	1	1999	17.50
2	60.80	112	1	2010	16.75
3	82.82	70	1	1975	16.08
4	35.91	95	1	1983	17.00
5	46.00	115	1	1962	15.92
6	40.00	80	1	1993	21.08
7	44.30	100	1	2015	18.33
8	46.20	120	1	2006	15.17

Table 6.22: Geometric samples of multi-span continuous reinforced concrete slab (MCRC-slab)

Bridge No.	Deck Width (ft)	Span Length (ft)	Number of Spans	Year Built	Under Clearance (ft)
1	54.11	30	3	1947	16.75
2	42.00	55	5	1961	22.67
3	46.00	25	4	1964	21.50
4	40.00	30	4	1969	16.92
5	32.30	25	3	1957	17.33
6	40.00	30	3	1952	16.33
7	46.00	45	2	1986	14.42
8	41.80	32	4	1959	15.67

Table 6.23: Geometric samples of multi-span reinforced concrete slab (MSRC-slab) bridges

Bridge No.	Deck Width (ft)	Span Length (ft)	Number of Spans	Year Built	Under Clearance (ft)
1	23.3	22	2	1948	23.08
2	42.2	25	4	1956	14.75
3	41.15	25	3	1952	16.42
4	27.5	25	5	1960	20.83
5	25.3	25	3	1942	15.83
6	25.30	18	4	1928	16.50
7	25.3	25	3	1963	17.00
8	46	25	2	1953	17.42

6.5.3. Bridge Parametric Samples

As an example, Table 6.24 through Table 6.31 show the parameter samples for the MSPC bridge class that are to be matched with the geometric representative bridge samples from that bridge class. The parameter samples for the rest of the bridge classes (i.e., MS RC girder, MS RC slab, MS Steel girder, MC RC Slab, MC Steel girder, and SS PC girder) are presented in Appendix E.

Table 6.24: MSPC parameters for geometric sample 1

	Modeling Sample							
Parameter	1	2	3	4	5	6	7	8
Conc Str	4303	4703	5437	5558	3669	4783	3932	3165
Reinf Str	53867	53215	48248	56264	58834	50585	58016	63368
Elasto Shear Mod	294	103	206	140	241	272	197	153
Elasto MF	1.19	0.97	0.84	0.91	1.03	1.08	0.96	1.04
Dowel Str	23.96	23.32	28.90	27.97	26.22	25.12	26.65	25.68
Dowel Gap	3.087	2.000	2.746	1.575	1.144	2.340	0.237	0.792
Abt-Pas Stf	29.5	42.6	49.3	40.4	21.4	27.4	32.6	35.6
Pile Stf	22.3	56.2	70.7	30.5	38.5	50.0	43.6	63.6
Fnd-Rot Stf	648	1329	1013	503	1100	1186	908	786
Fnd-Tran-Stf	328	215	449	378	356	151	246	297
Mass	131	121	111	134	123	127	116	137
Damp Ratio	0.077	0.044	0.029	0.055	0.049	0.048	0.041	0.032
Large Gap	4.34	5.99	5.02	2.04	0.31	2.70	3.61	1.21
Load Dir	336	42	249	271	194	96	158	77

Table 6.25: MSPC parameters for geometric sample 2

	Modeling Sample							
Parameter	1	2	3	4	5	6	7	8
Conc Str	5186	4920	4761	3461	4208	5718	4438	3878
Reinf Str	55543	59314	56588	43373	53625	51135	52159	61557
Elasto Shear Mod	160	123	212	258	237	107	299	178
Elasto MF	1.03	1.05	1.00	1.08	0.92	0.96	0.75	1.14
Dowel Str	23.39	25.58	23.85	25.03	27.77	28.85	27.18	26.15
Dowel Gap	1.080	0.159	0.735	2.544	2.339	1.252	3.141	1.720
Abt-Pas Stf	42.5	20.3	38.7	31.1	24.8	48.0	44.3	33.1
Pile Stf	39.7	43.1	63.0	48.8	25.0	72.0	31.0	57.1
Fnd-Rot Stf	682	1001	785	1197	559	845	1112	1332
Fnd-Tran-Stf	224	218	284	320	451	373	412	145
Mass	119	122	125	129	111	139	114	135
Damp Ratio	0.035	0.016	0.040	0.064	0.048	0.044	0.051	0.059
Large Gap	1.32	2.08	5.26	2.29	4.02	0.37	3.48	4.67
Load Dir	8	300	141	258	190	63	359	103

Table 6.26: MSPC parameters for geometric sample 3

	Modeling Sample							
Parameter	1	2	3	4	5	6	7	8
Conc Str	3419	4152	3904	5322	6624	4743	5050	4256
Reinf Str	52631	55994	51354	57827	53348	49364	61097	59225
Elasto Shear Mod	247	273	220	130	116	294	172	179
Elasto MF	1.16	0.93	1.04	0.80	1.02	0.95	1.00	1.10
Dowel Str	29.02	23.70	24.91	26.62	28.07	26.23	21.59	25.78
Dowel Gap	1.308	1.894	2.191	0.918	2.801	0.761	0.183	3.053
Abt-Pas Stf	24.0	29.9	23.5	31.4	47.6	40.9	44.0	37.4
Pile Stf	69.2	42.2	67.3	53.7	36.1	24.3	33.0	57.0
Fnd-Rot Stf	1333	801	678	831	1041	1086	1294	554
Fnd-Tran-Stf	424	186	279	373	255	172	306	399
Mass	122	121	126	130	137	114	113	136
Damp Ratio	0.050	0.060	0.029	0.049	0.057	0.043	0.039	0.031
Large Gap	3.76	3.01	4.58	0.19	5.50	0.95	1.92	2.70
Load Dir	21	110	227	213	303	346	65	163

Table 6.27: MSPC parameters for geometric sample 4

	Modeling Sample							
Parameter	1	2	3	4	5	6	7	8
Conc Str	6293	3988	3839	4764	5242	2458	4836	4392
Reinf Str	50209	52627	56148	56967	59285	67869	47694	54304
Elasto Shear Mod	246	208	144	119	161	293	250	185
Elasto MF	1.13	0.83	1.03	0.96	0.93	1.12	1.07	0.99
Dowel Str	28.31	25.90	26.47	24.12	24.68	27.10	30.36	23.57
Dowel Gap	1.657	1.312	0.795	1.065	0.120	2.547	2.346	3.141
Abt-Pas Stf	35.5	44.6	29.8	40.3	33.9	23.4	26.1	49.2
Pile Stf	21.8	53.4	33.3	43.8	56.1	69.3	35.7	62.0
Fnd-Rot Stf	1008	1131	773	508	1406	622	1284	886
Fnd-Tran-Stf	214	173	417	364	406	233	297	334
Mass	136	126	121	123	117	113	132	134
Damp Ratio	0.039	0.033	0.051	0.082	0.049	0.043	0.054	0.025
Large Gap	4.62	5.60	4.34	1.10	0.12	2.84	3.21	1.60
Load Dir	140	190	229	134	317	312	77	23

Table 6.28: MSPC parameters for geometric sample 5

	Modeling Sample							
Parameter	1	2	3	4	5	6	7	8
Conc Str	5522	3251	4653	5463	4363	3939	3831	4844
Reinf Str	55396	47291	54070	57045	50139	63356	52291	59464
Elasto Shear Mod	271	293	236	126	103	185	201	148
Elasto MF	1.14	0.90	1.09	0.97	0.89	0.95	1.07	1.03
Dowel Str	28.41	27.19	25.60	24.04	23.50	25.18	26.37	31.12
Dowel Gap	2.139	1.044	2.968	1.241	0.494	0.120	1.987	2.685
Abt-Pas Stf	36.6	43.4	34.3	21.9	41.1	23.8	46.5	27.9
Pile Stf	39.3	73.6	64.5	33.2	59.6	43.1	26.1	50.2
Fnd-Rot Stf	1236	1109	618	874	741	1366	514	1042
Fnd-Tran-Stf	255	290	391	309	184	352	420	154
Mass	133	132	140	126	125	114	111	118
Damp Ratio	0.025	0.034	0.079	0.045	0.058	0.048	0.038	0.051
Large Gap	2.86	5.67	1.13	4.60	1.71	0.28	3.68	4.42
Load Dir	86	304	198	337	4	150	113	241

Table 6.29: MSPC parameters for geometric sample 6

	Modeling Sample							
Parameter	1	2	3	4	5	6	7	8
Conc Str	4443	6231	3686	5014	3459	5309	4660	4204
Reinf Str	57262	53086	45119	55641	50264	61685	59832	53879
Elasto Shear Mod	150	235	118	250	177	298	140	213
Elasto MF	1.07	0.93	0.93	0.83	1.16	1.00	1.01	1.04
Dowel Str	23.06	28.11	25.43	24.71	24.24	26.37	29.34	27.12
Dowel Gap	2.764	0.003	1.299	1.859	0.516	2.235	0.890	3.105
Abt-Pas Stf	30.6	33.9	43.0	24.2	40.7	21.5	47.3	38.2
Pile Stf	43.5	24.7	56.6	31.0	39.1	52.7	65.5	74.8
Fnd-Rot Stf	670	832	1038	1241	774	493	1179	1324
Fnd-Tran-Stf	221	423	319	411	339	204	268	149
Mass	118	115	123	136	128	133	132	110
Damp Ratio	0.057	0.047	0.038	0.062	0.029	0.050	0.032	0.043
Large Gap	2.86	1.53	5.60	4.56	0.27	1.38	3.71	4.49
Load Dir	1	125	311	344	147	63	205	229

Table 6.30: MSPC parameters for geometric sample 7

	Modeling Sample							
Parameter	1	2	3	4	5	6	7	8
Conc Str	4815	4439	3255	5308	3665	3945	6135	4566
Reinf Str	54529	55672	63954	57096	49895	59551	47218	51657
Elasto Shear Mod	204	195	248	289	271	122	149	98
Elasto MF	1.08	0.80	0.93	1.25	0.94	0.99	1.04	1.00
Dowel Str	23.15	26.53	27.16	28.42	23.74	27.54	25.18	25.56
Dowel Gap	0.830	3.017	2.092	0.294	0.560	2.605	1.640	1.590
Abt-Pas Stf	47.0	40.0	44.2	24.9	35.2	28.9	20.7	34.3
Pile Stf	22.5	32.0	37.7	60.1	48.3	65.8	73.6	42.0
Fnd-Rot Stf	1204	1160	798	992	606	1320	875	590
Fnd-Tran-Stf	206	167	438	307	291	349	390	226
Mass	120	125	110	135	122	114	129	140
Damp Ratio	0.028	0.049	0.062	0.035	0.042	0.053	0.056	0.041
Large Gap	2.09	0.84	5.21	2.39	4.48	0.44	5.55	3.60
Load Dir	168	334	70	116	268	33	214	283

Table 6.31: MSPC parameters for geometric sample 8

	Modeling Sample							
Parameter	1	2	3	4	5	6	7	8
Conc Str	4717	4064	3039	5663	4406	5088	3842	4842
Reinf Str	55711	50887	59420	54204	49258	52551	62232	57574
Elasto Shear Mod	181	132	264	297	101	217	160	228
Elasto MF	1.10	1.02	1.04	1.13	0.94	0.84	0.98	0.90
Dowel Str	23.47	27.91	27.22	28.66	26.09	24.48	25.38	25.11
Dowel Gap	1.132	0.601	1.629	1.426	2.561	2.270	0.392	3.131
Abt-Pas Stf	37.9	34.0	29.7	20.0	39.1	47.9	25.3	46.0
Pile Stf	65.2	43.0	71.0	56.1	22.5	30.3	47.9	36.5
Fnd-Rot Stf	1123	807	548	1195	975	895	1310	697
Fnd-Tran-Stf	403	309	288	416	246	174	354	188
Mass	136	122	140	131	128	114	118	111
Damp Ratio	0.052	0.047	0.030	0.060	0.058	0.035	0.042	0.038
Large Gap	3.98	2.83	4.52	0.77	5.78	0.50	1.50	3.16
Load Dir	147	256	18	55	220	289	96	329

6.6. Summary

The NBI database, along with additional information provided by the in-house TxDOT bridge database, was used to provide statistical information on the TxDOT bridge inventory. Seven bridge classes, representing 84.7% of the on-system bridges in Texas, were identified by TxDOT as being of primary importance in this seismic vulnerability study. Statistical information on the following parameters were determined using the NBI and TxDOT databases: number of spans, maximum span length, deck width, vertical under-clearance, skew angle, substructure type, and year built. This information is used in selection of sample bridges for each bridge class that are representative of those found in the inventory.

Moreover, TxDOT standard drawings and as-built drawings were used to identify specific components and structural details commonly used for the bridges and construction eras of interest. Information on typical superstructure, substructure, and bearing details, gleaned from extensive review of TxDOT standard and as-built bridge drawings, provides guidance in developing the representative bridge models used in this study, which are addressed in next chapter.

When conducting a fragility analysis for a large transportation network, an important step is developing samples that accurately represent the entire network. The Texas bridge inventory consists of bridges of many different types, materials, sizes, and construction eras. This chapter's second focus of was creating bridge samples that are statistically representative of the entire bridge population. First, geometric parameters, including deck width, span length, number of spans, year of construction, and under-clearance, were sampled to create eight geometrically representative bridge samples for each bridge class. Second, material properties and component behaviors such as concrete strength, steel strength, bearing stiffness, coefficient of friction, mass, damping ratio, loading direction, deck gaps, and abutment and foundation stiffness, were sampled eight times and assigned to each of the geometric samples, creating a total of 64 bridge samples. These

representative bridge samples are used to create computational bridge models, as described in Chapter 7, and are used to conduct a computational seismic fragility analysis, as described in Chapter 8.

Chapter 7. Model Development

7.1. Overview

This chapter describes the bridge component numerical modeling approaches used for the nonlinear response-history analyses. In this chapter, first, the general modeling parameters selected for the analyses, such as selection of the software, model dimensionality, and the element types used, are discussed. Then, numerical models for each component of the bridges are discussed in details. Finally, the model assembly approach is described, as well as an example of response history analysis of a bridge sample.

7.2. General Modeling Assumptions

7.2.1. 2D and 3D Models

Generation of fragility curves requires accurate numerical bridge models capable of simulating nonlinear behavior. The first decision that needs to be made is whether the models should be constructed in two dimensions (2D) or three dimensions (3D). The main advantage of a 2D model is its simplicity compared to a 3D model. An important question arises concerning whether bridges should be modeled in their longitudinal or transverse directions when using a 2D approach. Numerous studies such as Rashidi and Ala Saadeghvaziri (1997) and Shinozuka et al. (2000b) suggest that the longitudinal direction controls the response, while others (Lou and Cheng 1996) believe the transverse direction is critical.

Rashidi and Ala Saadeghvaziri (1997) argued that seismic motion acting in the longitudinal direction of a bridge causes more damage to multi-span bridges than transverse motions due to impact between adjacent bridge decks and abutments. Additionally, the study revealed that many bridge bearings are designed inadequately in the longitudinal direction, claiming that a significantly-sized earthquake will cause girder unseating and bridge collapse. A seismic fragility study of the bridges in California arrived at a similar conclusion, stating that the analysis of bridges with ground motions in the transverse direction produced lower levels of damage (Shinozuka et al. 2000b).

With the ubiquity of computationally-efficient finite element software capable of conducting 3D analyses, the guidelines for nonlinear analysis of bridge structures prepared by the Pacific Earthquake Engineering Research Center (PEER) recommend using 3D bridge models to accurately capture the interaction of bridge response in both orthogonal directions (Aviram et al. 2008). Research performed by the Nielson (2005) assessing the seismic fragility of bridges in the Central and Southeastern United States similarly employed 3D models in the analyses to capture these effects. The distribution of forces in critical bridge components such as columns, bearings, abutments, and superstructure, depends on their relative longitudinal and transverse stiffnesses, coupled with ground shaking components in the longitudinal and transverse directions. For that reason, three-dimensional models are used in this study.

7.2.2. Types of Analysis

To accurately predict the response and level of damage in bridge components, nonlinear models are required. Linear models are only able to predict the response within elastic limits (prior to steel yielding, concrete cracking, and spalling) and will not capture cyclic yielding and strength-degrading behaviors of structural components, deck pounding, nonlinear soil effects, nonlinear abutment behavior, and other factors. These behaviors are particularly important in seismic analysis, where response of a system depends on the ductility and energy dissipation capacities of its components (Aviram et al. 2008).

Two types of nonlinearities need to be considered. The first type is material nonlinearity, accounting for inelastic stress-strain behavior of elements, as well as the presence of gaps that can open and close (deck joints, clearance between bearing dowels and slotted holes, etc.). The second type represents geometric nonlinearity, accounting for second-order (P-Δ) effects and stability. Most modern structural analysis software has the capability to perform a second-order analysis (Aviram et al. 2008).

Establishing accurate demand-response relationships for seismic fragility curves requires accurate nonlinear models that are capable of simulating damage-related behavior as well as representative ground motions to perform nonlinear response-history analyses. Contrary to static analysis methods, where seismic activity is expressed as externally-applied inertial loads acting on nodes throughout the height of the structure, response-history analysis directly applies ground accelerations as a function of time in a dynamic analysis. In a nonlinear response-history analysis, ground motions with up to three orthogonal components (i.e., two horizontal acceleration components and, optionally, one vertical acceleration component) are applied to the nonlinear structural analysis model, and responses (displacements, forces, and bending moments) of key nodes and elements are recorded. Bridge modes of deformation tend to be sensitive to particular ground motions; therefore, a suite of different ground motions needs to be considered to determine the bridge critical response (Aviram et al. 2008).

There are various finite element analysis software packages capable of performing response-history analysis, including SAP2000 (CSI 2016), RISA-3D (RISA-Technologies 2016), and OpenSees (McKenna et al. 2000). For the purpose of this study, OpenSees is selected as the primary nonlinear analysis tool. The main advantages of OpenSees include its computational efficiency and code-based input, allowing bridge models to be created automatically using secondary scripts, as well as the fact that OpenSees is an open-source framework, giving researchers the opportunity to freely develop and distribute their own material and element models. Numerous nonlinear material models are already built into the software, allowing users to simulate a wide variety of nonlinear hysteretic behaviors (McKenna et al. 2000).

A rectangular coordinate system is used for 3D bridge modeling. As shown in Figure 7.1, the X-axis is the chord connecting the abutments (longitudinal), the Y-axis is orthogonal to it in the horizontal plane (transverse), and the Z-axis is in the vertical direction. For non-skewed bridges,

local axis orientation of frame elements, indicated by numbered axes in Figure 7.1, typically coincides with the global axis directions.

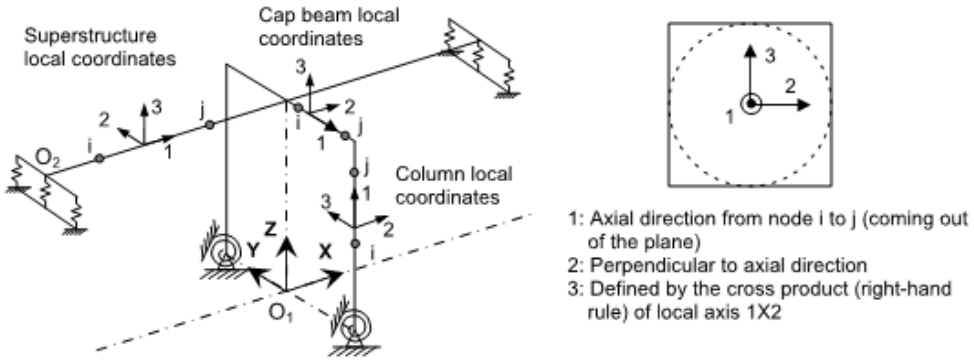

Figure 7.1: Bridge global and local coordinate systems (Aviram et al. 2008)

7.2.3. Modeling Approach

Nonlinear dynamic analysis and damage assessment of large explicit three-dimensional bridge models for earthquake loading is computationally demanding; hence, bridge structural components such as girders, bent caps, and columns are usually simplified to line elements. Nonlinear material behavior can be defined through distributed plasticity beam-column elements, where fiber cross-sections can be defined along the length of an element with specified nonlinear material behaviors. Alternatively, elastic beam-column elements can be used, where nonlinear springs can be assigned at specific locations where nonlinear behavior is expected to occur. For example, nonlinear rotational springs can be placed at the ends of a beam-column element expected to exhibit flexural hinging.

In OpenSees, these nonlinear springs are modeled using nonlinear zero-length elements. As implied by its name, a zero-length element lumps inelastic behavior to an infinitesimal point. It can act as a translational spring in any direction with force-displacement behavior assigned to it, or as rotational spring in any direction with moment-rotation behavior assigned to it. Multiple springs in any degrees of freedom can be used between two nodes located at the same coordinates. Unlike distributed plasticity elements, zero-length springs lump all inelastic behavior in one point, making it significantly more computationally efficient. Creation of bridge fragility curves requires multiple bridge models to be analyzed using response-history analysis with suites of different ground motions, making computational time an important aspect to take into account. Additionally, some bridge nonlinear effects, such as shear failure, pounding, or soil deformation, have to be estimated with empirical relationships, which can be assigned to a spring element, whereas distributed plasticity fiber elements are only capable of capturing axial and flexural behavior. As a result, zero-length springs are used in this study to simulate nonlinearity effects in the bridge models.

Dynamic analysis of a structure requires appropriate assignment of translational and rotational masses to the nodes of the structure. To provide a realistic distribution of inertial forces throughout a structure, translational masses can be assigned to multiple nodes along the length of the superstructure. To capture global torsional behavior of a bridge, nodal translational masses can be assigned along the superstructure's width without requiring input of rotational masses if a 3D model is used (Amirihormozaki et al. 2015). In most cases, the torsional mode of a bridge is unlikely to control bridge response during a seismic event; however, in rare cases when that mode controls, it will affect the behavior and damage of the whole structure, and therefore should not be ignored (Aviram et al. 2008).

Another important phenomenon that needs to be accounted for in the model is damping, i.e., energy dissipation of the bridge components during their dynamic response. A common way to model structural damping is through Rayleigh damping, in which the amount of damping force is proportional to velocity. Most studies covering bridge seismic analysis (Choi 2002; Filipov 2012; Nielson 2005) generally use a damping ratio of 5% for all bridge types, as is commonly assumed in design. In this study, the damping ratio is assumed to be a random variable that is sampled on as described in Section 6.5 of this report, and this damping ratio is assigned to the first two modes using a Rayleigh damping model.

In summary, 3D models are used to capture deformation in the longitudinal, transverse, and vertical bridge directions. Nonlinear zero-length springs are used to simulate nonlinear behavior concentrated at a single point. Translational masses are distributed throughout the structure to simulate inertial forces. Damping is modeled as mass and stiffness proportional Rayleigh damping. In the following sections, the nonlinear model that is assigned to each bridge component is discussed in details.

7.3. Superstructure

As mentioned earlier, bridge superstructures are typically composed of a concrete deck and steel or concrete girders. Depending on the age of construction, the bridge deck and girders may or may not act compositely. When conducting a dynamic seismic analysis, the superstructure is the main contribution of mass for the bridge system, which must be accounted for in the model. Bridge superstructures are assumed to be significantly stiffer and stronger laterally than the columns and bearings underneath them in both the longitudinal and transverse directions. Hence, the superstructure is expected to stay in the elastic range during a seismic event. For this reason, the bridge superstructure is often modeled using elastic beam-column elements for seismic analysis (Filipov 2012; Nielson 2005; Tavares et al. 2013). If bridge superstructure or diaphragm inelasticity are possible, the assumption of linear elasticity should be checked at the end of the analysis (Filipov 2012). Beam-column elements are able to capture combined axial and flexural demands without explicit consideration of shear deformations, which has been assumed to be adequate for simulation of sufficiently long spans. The effects of shear deformations only become significant for span/depth ratios less than two, which is atypical for bridge girders (Patel et al. 2014).

Elastic analysis implies a linear relationship between stress and deformation of the superstructure elements; however, for concrete members it is important to account for the effects of cracking on flexural and torsional stiffness. To account for cracking, gross flexural moments of inertia of concrete girders are multiplied by 0.5 (AASHTO 2016), and the torsional constant is multiplied by 0.2 (Caltrans 2013). NHI (2014) recommendations to use unmodified section properties (i.e., no reduction in flexural rigidity) were not followed in this study. Even though it is true that prestressed girders are designed to remain uncracked during service loads, it is unknown whether they remain so during a seismic load. Hence, a factor of 0.5 was used for prestressed girders as well as conventionally reinforced concrete girders.

As noted, the superstructure is assumed to remain elastic during a seismic analysis; hence, the entire superstructure cross-section can be lumped into a single beam-column element representing mass and stiffness of the entire deck width (Aviram et al. 2008; Nielson 2005; Pan et al. 2010). This simplified single beam element approach, however, does not capture vertical and horizontal distribution of mass along the width of the bridge superstructure.

Alternatively, the distribution of mass, gravity loads, and stiffness along the width of the superstructure can be modeled using multiple beam-column elements aligning with the girder lines, which is termed a deck-grid model (Amirihormozaki et al. 2015; Filipov 2012; Tavares et al. 2013). One of the biggest advantages of the deck-grid model is its ability to distribute superstructure mass and stiffness along bridge width. The beam-column elements along the girder lines consider the stiffness of the girder and its tributary concrete deck area. In cases where the deck is not composite, the contribution of stiffness from the deck can be neglected. A conservative assumption is also to neglect concrete rail stiffness, as if the rails are cast separately from the deck, resulting in larger deformation estimates than if rail stiffness was considered. However, if there is good evidence of a rigid connection between the deck and concrete rails, their stiffness should be included because it will result in smaller superstructure deflection in the transverse direction.

Figure 7.2 shows bridge deck grid model proposed by Filipov (2012). As seen in the figure, the longitudinal beam-column elements are connected in the transverse direction via beam-column elements simulating the transverse stiffness of the deck and other transverse bracing elements. No mass is assigned to the transverse elements because it is already included in the longitudinal elements (Amirihormozaki et al. 2015). In the case of steel bridges, where cross-frames provide transverse bracing between the girders, those members are more likely to experience inelastic behavior during a seismic event compared to concrete diaphragms. Cross-frames may be modeled as nonlinear components, being able to dissipate some of the seismic energy and reduce the shear demands on columns through their inelastic deformation; however, in the absence on cross-frame nonlinear behavior models, such cross-frame models were not used in this study (Hamidreza et al. 2010). Diaphragms and cross-frames at the locations of bents and abutments are expected to experience the largest loads, whereas loads at intermediate diaphragms or cross-frames are significantly lower. For this reason, some researchers (Amirihormozaki et al. 2015) have suggested that explicit modeling of bracing elements at these intermediate locations is not necessary;

however, it is still important to assign a rotational constraint to the girder nodes at each intermediate diaphragm or cross-frame location to account for their bracing effects.

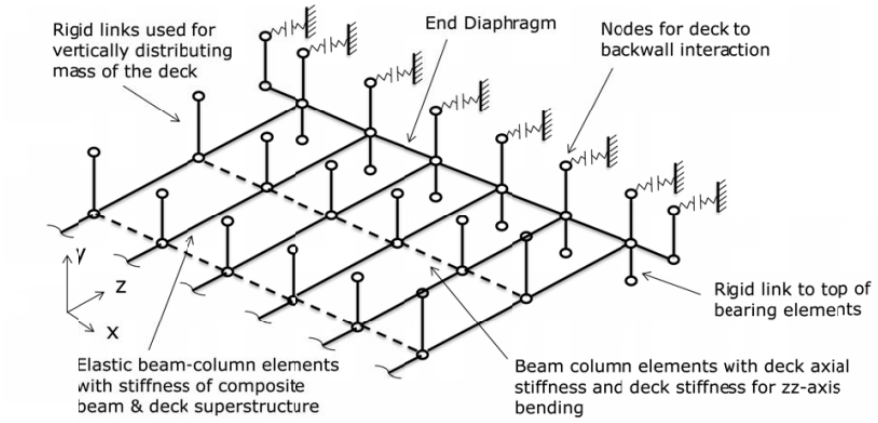

Figure 7.2: Bridge deck grid model (Filipov 2012)

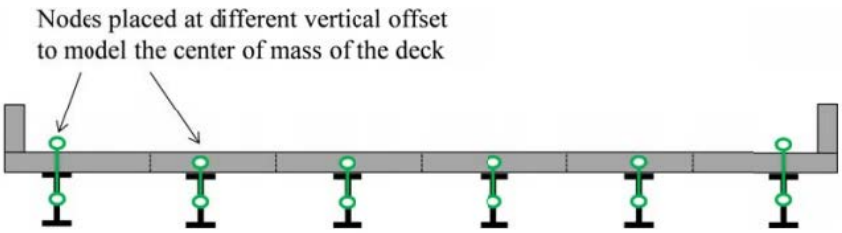

Figure 7.3: Deck mass distribution (Filipov 2012)

Accurate mass assignment and distribution is essential for getting accurate solutions from response-history analyses. All bridge dead loads need to be considered as part of the seismic mass, including slab, girders, wearing surface, and rails. Live loads typically do not need to be considered as part of the seismic mass. Figure 7.3 shows deck mass distribution. As seen in the figure, in the deck-grid model, the mass is assigned to nodes representing the vertical distribution of mass in the superstructure system. This vertical distribution of mass accounts for overturning effects that may be caused by the center of mass not aligning with the center of transverse stiffness (Filipov 2012).

In order to accurately represent mass distribution along the span, intermediate nodes (girder and deck) were used, as opposed to only having nodes at the supports. Spreading the mass to intermediate nodes did not significantly affect superstructure translation, but it did change the amount of rotation, particularly in approach spans. The exact number of intermediate girder nodes must be determined on a case-by-case basis, where a sensitivity study can be used to make this determination. For this research project, a minimum of three intermediate nodes per span is used.

In the case of slab bridges, which do not have any girders, the slab itself acts as the main flexural element. Hence, slab sections were modeled with beam-column elements with appropriate

sectional and material properties. The number of sub-sections used to subdivide the slab can range from one (rectangular section representing the entire slab width) to nearly infinitely many sections of infinitesimal width. In this study, the number of slab sections was selected so that the spacing between them will be similar to typical bridge girder spacing. Deck lumped mass nodes were still used, but only to represent wearing surface and rail mass, if present. The mass of the slab is accounted for through beam-column mass per unit length assignment.

To simulate bridge diaphragm behavior, a rigid diaphragm constraint was used for girder nodes within a simply-supported span or for all girder nodes in continuous spans. This command makes all of the assigned nodes within a span translate and rotate in the horizontal plane as a rigid body.

Even though superstructure is expected to stay elastic under gravity and earthquake loading, deck damage may occur due to pounding effects at deck joint locations. The numerical model capable of simulating this phenomenon is presented in the following section.

7.4. Joint

Deck pounding is caused by out-of-phase motion of adjacent bridge sections. It is a common cause of bridge seismic damage, including girder unseating and concrete deck crushing and spalling. The bridges that are the most susceptible to this kind of damage are multi-span simply supported bridges with joints between adjacent spans. Pounding damage can still occur in single-span and continuous bridges between superstructure and abutments.

The research performed by Muthukumar (2003) extensively studied the effects of pounding and methods of numerically model it. There are two main methods to model pounding effects: (1) the stereomechanical approach and (2) the contact element approach. The stereomechanical approach is a macroscopic attempt to model dynamic impact of two colliding bodies (labeled 1 and 2) using an assumed coefficient of restitution (e). Impact is assumed to be instantaneous, and the principle of momentum balance is applied to relate the velocities before (v_1 and v_2) and after impact (v_1' and v_2') per Equation (8.1) (Goldsmith 1978).

$$e = \frac{v_2' - v_1'}{v_1 - v_2} \tag{7.1}$$

The coefficient of restitution ranges from zero (perfectly-plastic impact) to 1.0 (perfectly-elastic impact), and depends on material and geometric properties of the two colliding bodies. Previous research using the stereomechanical approach, however, has shown little effect of variation of e on the structural response due to pounding (DesRoches and Fenves 1997). The stereomechanical approach is limited in its application due to what is typically an unknown duration of contact. If the impact duration is sufficiently long, the assumption of instantaneous impact is no longer correct (Muthukumar 2003). Finally, the approach cannot be modeled using available structural analysis software, including OpenSees; therefore, it is not used in this study.

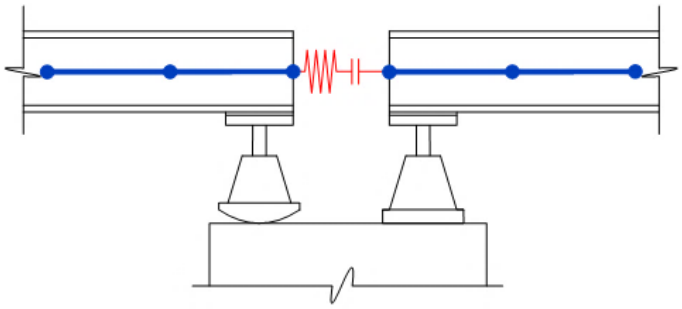

Figure 7.4: Deck pounding model (Nielson, 2005)

The contact element approach is the preferred impact modeling method to implement in nonlinear analyses. As shown in Figure 7.5, impact is simulated by a contact spring between two colliding bodies. Initially, when the gap between components is open, the spring provides no stiffness. Thus, it does not resist deformation in any way. Once the gap is closed, however, the contact element is engaged with a high stiffness, which depends on material and geometric properties of the colliding bodies. Many previous studies including Maison and Kasai (1990), Wolf and Skrikerud (1980), and Anagnostopoulos (1988) used an elastic behavior to model pounding, which is as shown in Figure 7.5. However, an elastic model is unable to simulate energy dissipation without using additional damper elements, making the resulting behavior unrealistic.

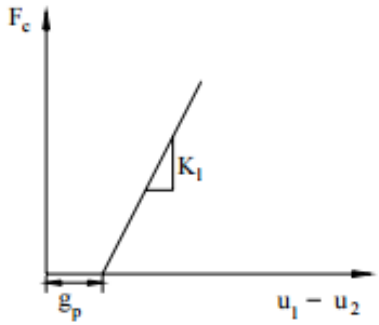

Figure 7.5: Linear contact spring behavior

In contrast to the previous research, Muthukumar (2003) developed a bilinear pounding model to capture energy dissipation during bridge deck collision. The energy lost during the impact (ΔE) is based on the stereomechanical approach as follows:

$$\Delta E = \frac{1}{2}\frac{m_1 m_2}{m_1 + m_2}(1 - e^2)(v_1 - v_2)^2 \qquad (7.2)$$

where m_1 and m_2 are masses of the colliding bodies; v_1 and v_2 are velocities of the colliding bodies; and e is restitution coefficient, which is typically taken as 0.6–0.8 for concrete decks. The relative velocity of two colliding bodies at the onset of impact can be related to the maximum penetration during the collision, as follows:

$$(v_1 - v_2)^2 = \left[\frac{2(m_1 + m_2)}{m_1 m_2}\right]\left[\frac{k_h \delta_m^{n+1}}{n+1}\right] \tag{7.3}$$

where k_h is impact stiffness parameter, which is typically taken as 25,000 k-in$^{-3/2}$; n is Hertz coefficient, which is typically taken as 3/2; and δ_m is maximum penetration of two decks, which is assumed as 1 inch. Combining the Equations (7.2) and (7.3) yields:

$$\Delta E = \frac{k_h \partial_m^{n+1}(1 - e^2)}{n+1} \tag{7.4}$$

The theoretical energy loss estimate serves as a basis behind the bilinear model by Muthukumar (2003). According to the assumption, the amount of energy lost is equal to the area under the hysteresis curve, which is shown in Figure 7.6, with the maximum displacement equal to the assumed maximum penetration of two decks.

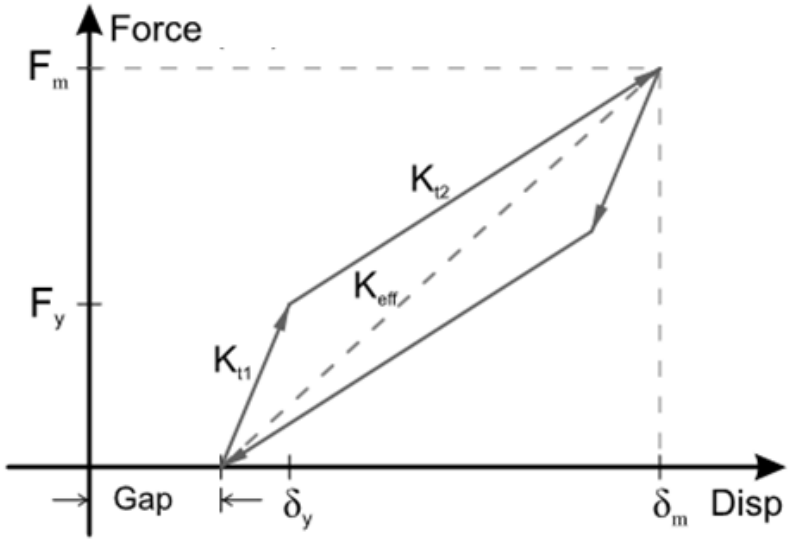

Figure 7.6: Bilinear pounding element behavior

The pounding element is modeled using a nonlinear spring with the bilinear pounding model shown in Figure 7.6 assigned in the longitudinal direction; the remaining five degrees of freedom are unconstrained. The material model requires definition of the initial gap between two deck segments or a deck segment and abutment. The initial stiffness (K_1), secondary stiffness (K_2), and yield displacement (δ_y) must also be defined, and these parameters are computed based on the estimated energy loss as follows:

$$K_1 = k_h\sqrt{\delta_m} + \frac{\Delta E}{a{\delta_m}^2} \tag{7.5}$$

$$K_2 = k_h\sqrt{\delta_m} - \frac{\Delta E}{(1-a){\delta_m}^2} \tag{7.6}$$

$$\delta_y = a\delta_m \tag{7.7}$$

where, a is typically taken as 0.1. Figure 7.7 shows a sample hysteretic response for a joint with an initial gap of 0.5 inch. The pounding element is a compression-only spring that gets activated once the gap length closes; no resistance is provided in the tensile direction.

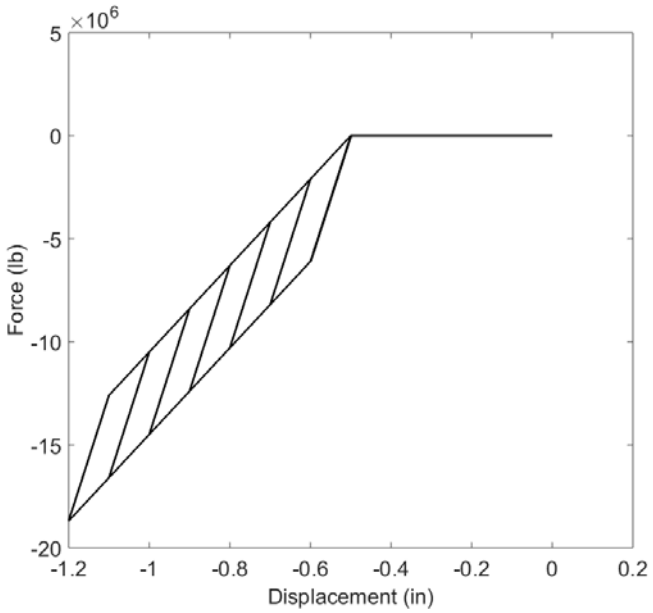

Figure 7.7: Pounding element hysteresis

7.5. Bearings

Another potential cause of bridge seismic damage is girder unseating due to excessive bearing deformation and/or instability. Numerical models for typical bearing types found in Texas highway bridges are presented in the following sections. As noted in Chapter 6, bridge bearings transfer vertical and horizontal loads from the bridge superstructure to the substructure. Two common types of bearings are steel bearings and elastomeric bearings. In the following sections, the numerical modeling of each bearing type is discussed in detail.

7.5.1. Steel Bearings

In general, steel bearing behavior can be separated into two primary mechanisms: bilinear friction and hysteretic restraining behaviors. As shown in Figure 7.8, Coulomb friction is assumed to govern friction of the bearings, which is because of sliding and rocking of the steel bearings. Elastic stiffness before sliding or rocking, k_e, is very large, and inelastic stiffness after sliding or rocking, k_p, is very small or zero (assuming no corrosion or debris). The friction force, F_f, is proportional to the normal reaction, N, and the coefficient of sliding or rocking friction, μ, as follows:

$$F_f = \mu N \tag{7.8}$$

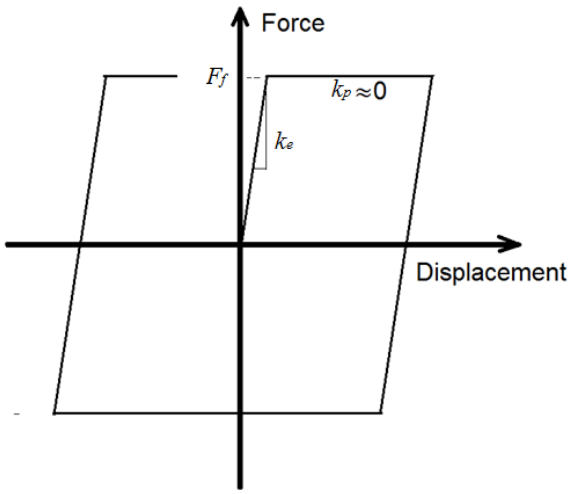

Figure 7.8: Nonlinear behavior associated with friction

The restraining behavior, which is mainly because of collision with guide plates, keeper plates, pintles, anchor bolts, is represented using a nonlinear hysteretic function. Figure 7.9 shows the hysteretic behavior that is considered in this study. This type of modeling is commonly used in previous studies (Mander et al. 1996).The bilinear friction behavior and hysteretic restraining behavior is combined in parallel (i.e., the stresses and stiffnesses are added together) to simulate behavior of an entire bearing.

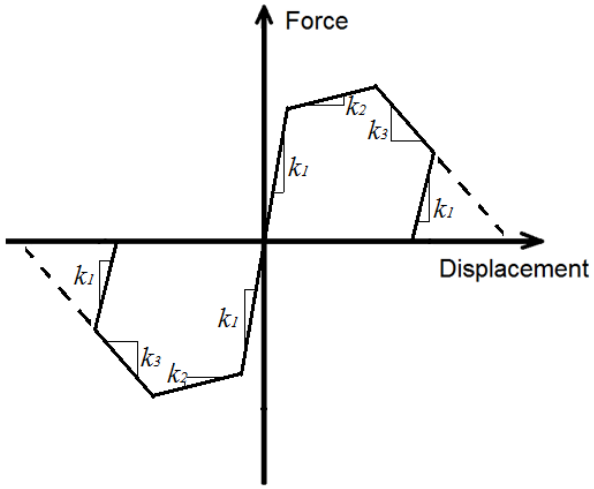

Figure 7.9: Nonlinear behavior associated with restraining

Cyclic tests of each type of steel bearing have been conducted by Mander et al. (1996). Parameters for defining the combination of bilinear and hysteretic analytical functions to represent the behavior in the longitudinal and transverse directions for each bearing type were determined empirically and are detailed in Mander et al. (1996). For the purpose of evaluating the analysis parameters, the models for each bearing type were analyzed using the same displacement history from their respective tests. The results from the analyses are overlaid with the experimental data for comparison for each bearing type. Note, hysteretic forces from the bilinear and hysteretic

springs, which act in-parallel, were added in order to compare to the experimental force-displacement results. For the purpose of analysis, symmetric clearances at anchor bolts, pintles, and keeper plates are assumed in the proposed models, although this will not always be true in the real-world scenarios (Mander et al. 1996).

7.5.1.1. Low-Type Sliding Bearings

The longitudinal response of the low-type sliding bearing (Figure 7.10) can be approximated with a bilinear friction response alone (Figure 7.11) because the element is free to translate. As for the transverse response, both bilinear friction and hysteretic restraining behaviors need to be included. Once the bearing force of μN is exceeded, the bearing translates in the direction of the slide prior to contacting a hysteretic element, a guide plate in this case. The contact between the sliding plate and the guide plates provides resistance prior to guide plate anchor fracture. Additionally, the clearance between the sliding and guide plate (3mm in the details shown in Figure 7.10) needs to be included as it will allow free translation within that gap region as shown in Figure 7.12 (Mander et al., 1996). Stiffness and strength parameters for modeling the bilinear and hysteretic behaviors were proposed by Mander et al. (1996).

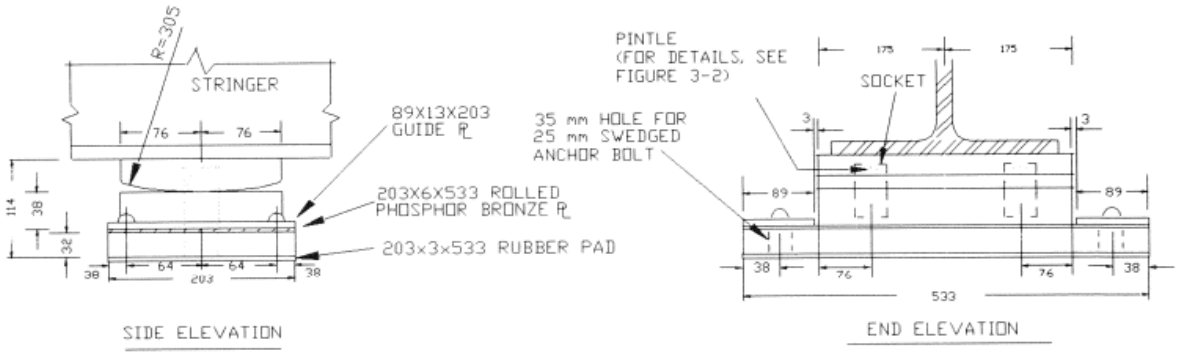

Figure 7.10: Low-type sliding bearing specimen (Mander et al. 1996)

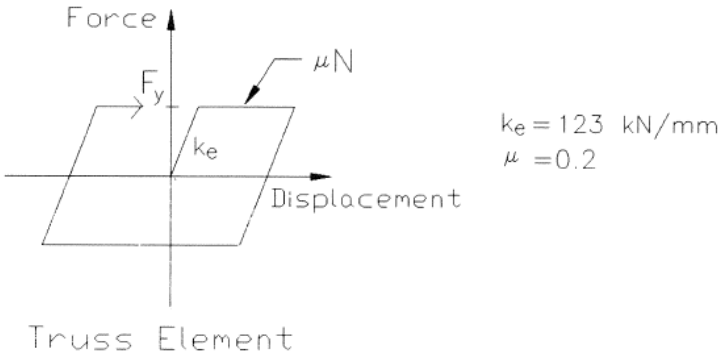

Figure 7.11: Low-type sliding bearing, longitudinal model (Mander et al. 1996)

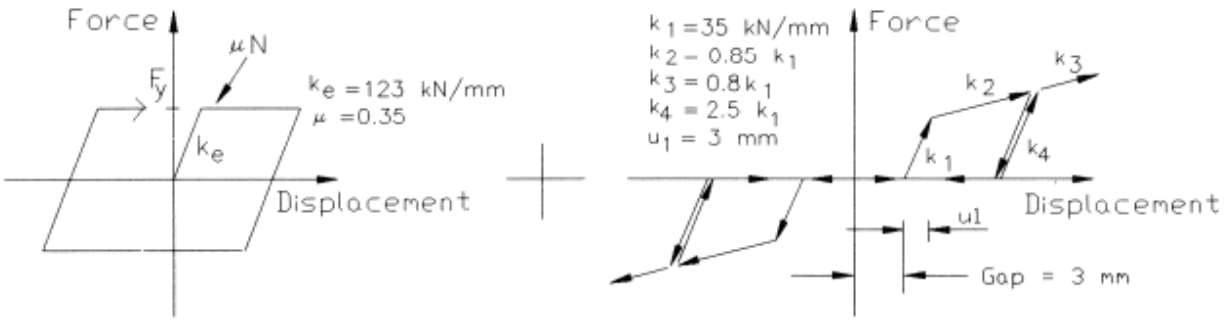

Figure 7.12: Low-type sliding bearing, transverse model (Mander et al. 1996)

Figure 7.13 and Figure 7.14 show the comparison between the low-type fixed bearing test performed by Mander et al. (1996) and the computational pushover analysis using the same displacement history in the longitudinal and transverse directions, respectively. The *y*-axis on the plots is base shear coefficient, which is equal to the ratio of horizontal bearing force to normal force. Due to convergence issues associated with using zero-stiffness during sliding in the longitudinal direction, the value of post-yielding stiffness ratio (relative to the initial stiffness) was adjusted to 0.001. Hence, there is a non-zero slope on the graph in the post-yield region.

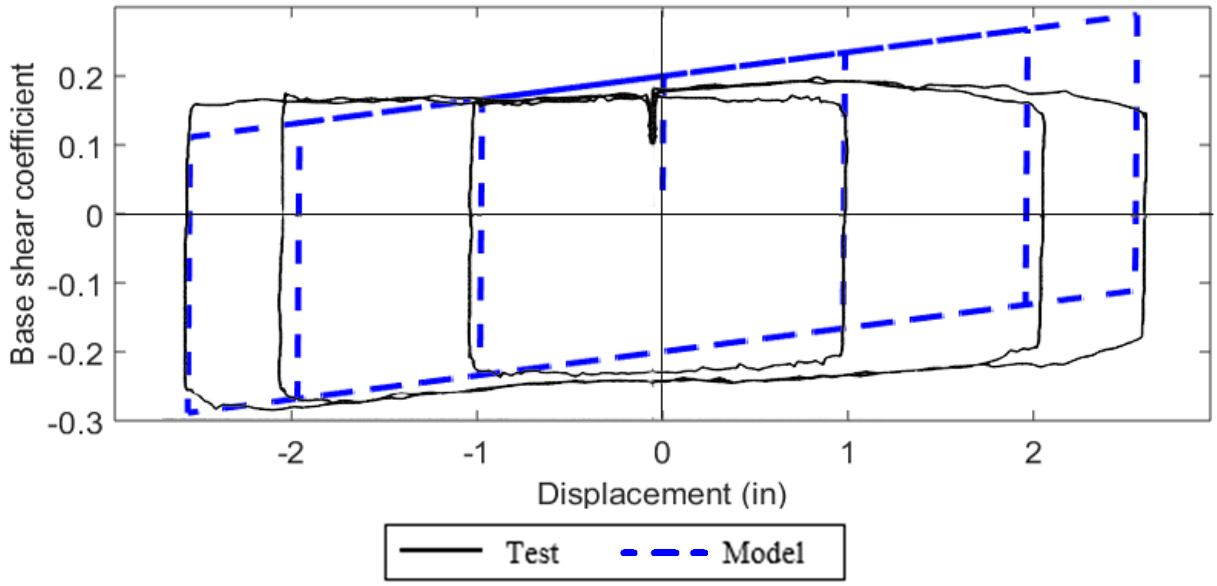

Figure 7.13: Low-type sliding bearing, longitudinal model-test comparison

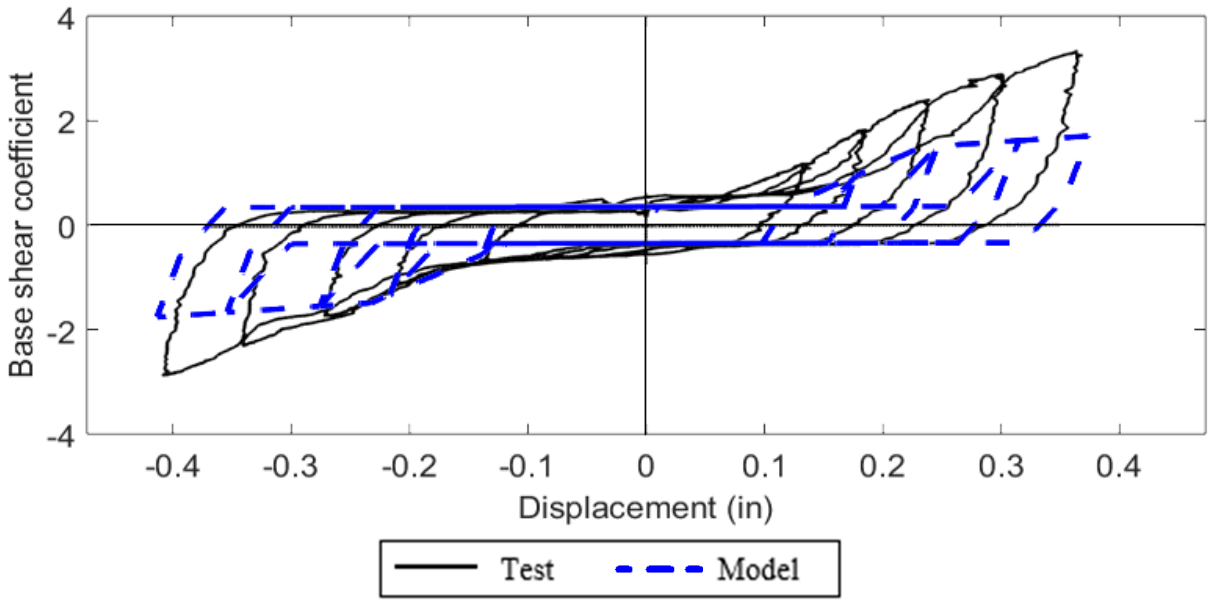

Figure 7.14: Low-type sliding bearing, transverse model-test comparison

7.5.1.2. Low-Type Fixed Bearings

This type of bearing, shown in Figure 7.15, exhibits both friction and pintle restraining/deformation behaviors in both the longitudinal and transverse directions (Figure 7.16 and Figure 7.17, respectively). The gap in this hysteretic restraining model accounts for the clearance between pintle (trapezoidal extrusion from the masonry plate) and socket (pintle slotted hole).

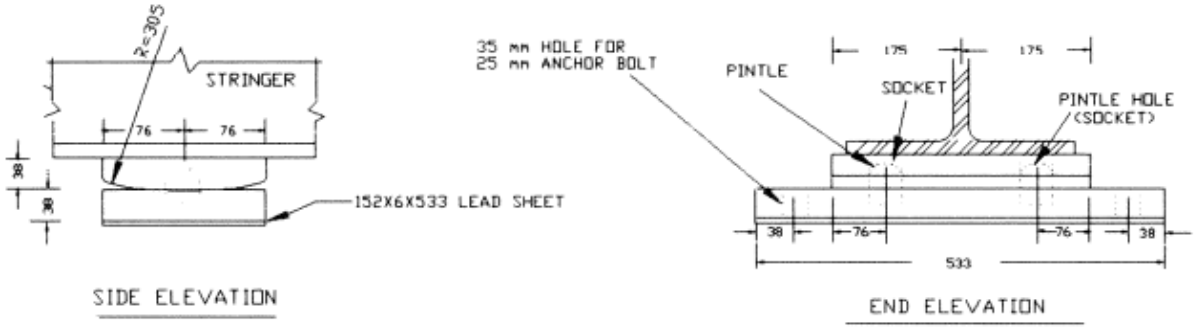

Figure 7.15: Low-type fixed bearing specimen (Mander et al. 1996)

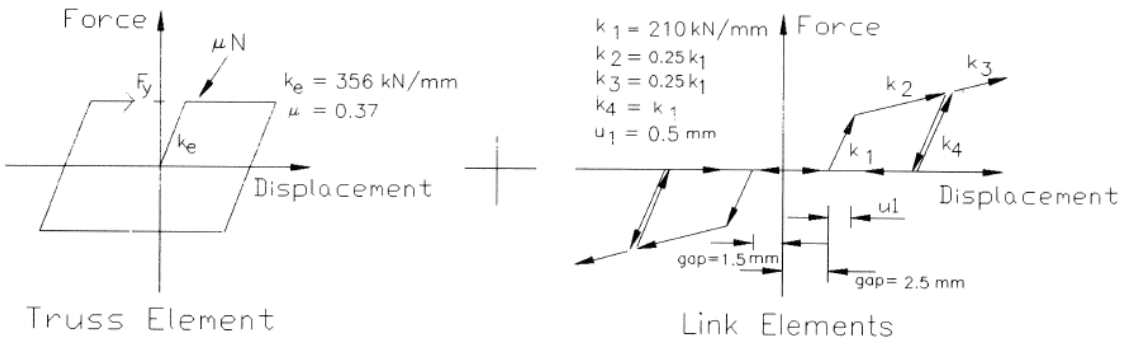

Figure 7.16: Low-type fixed bearing, longitudinal model (Mander et al. 1996)

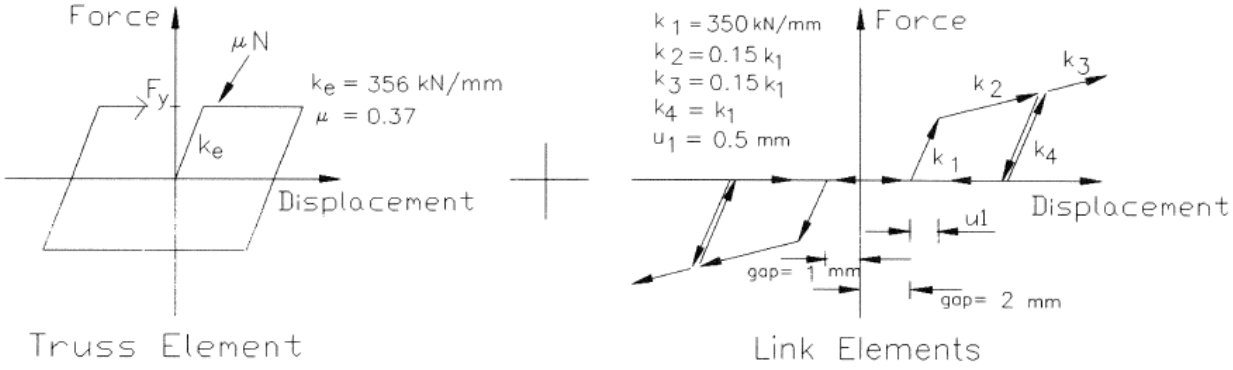

Figure 7.17: Low-type fixed bearing, transverse model (Mander et al. 1996)

Similar to the low-type sliding bearings, Figure 7.18 and Figure 7.19 show the comparison between testing and numerical modeling for the loading in the longitudinal and transverse directions, respectively.

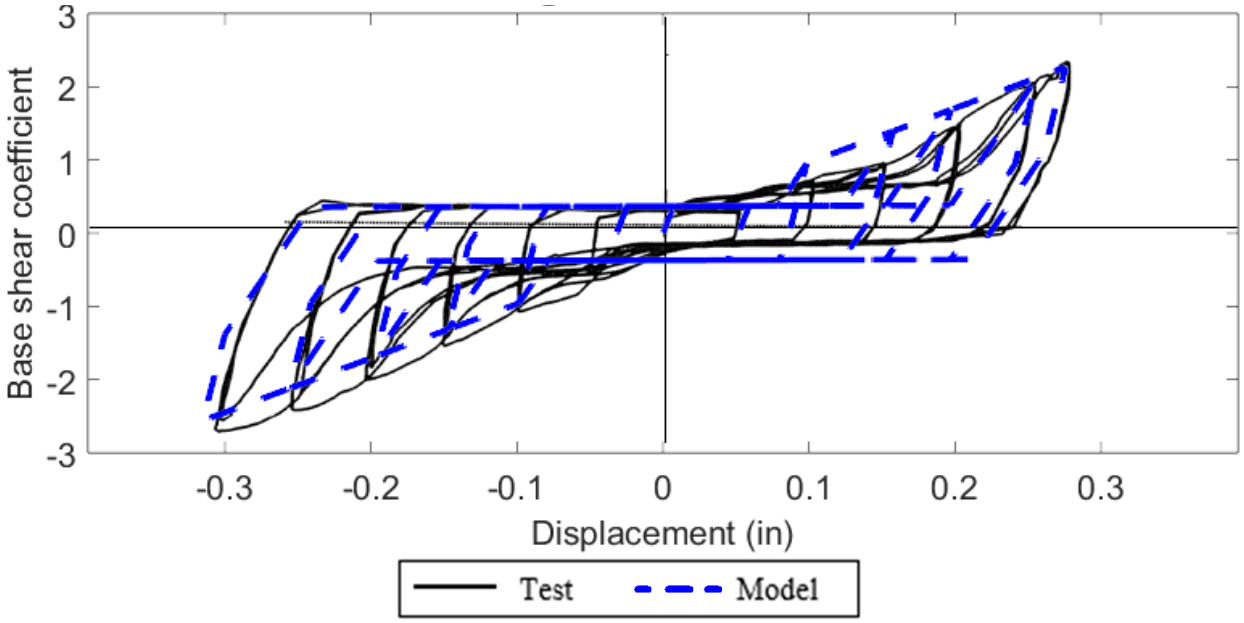

Figure 7.18: Low-type fixed bearing, longitudinal model-test comparison

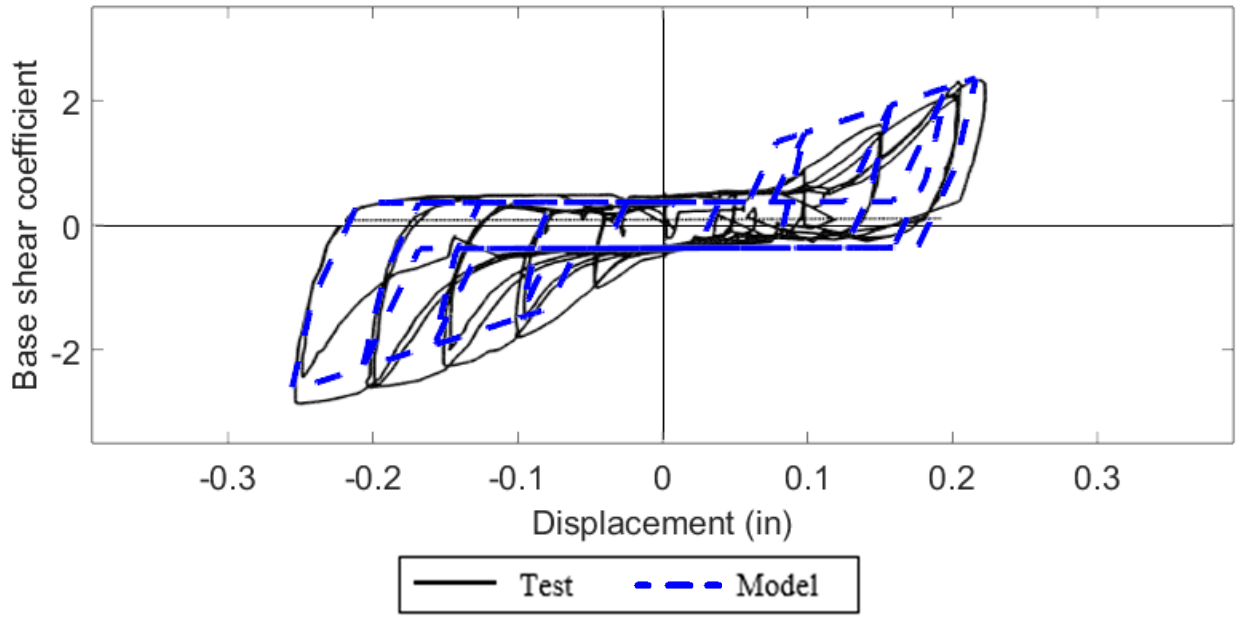

Figure 7.19: Low-type fixed bearing, transverse model-test comparison

7.5.1.3. High-Type Rocker Bearings

For high-type rocker bearings, which is shown in Figure 7.20, the longitudinal behavior depends on a combination of rolling resistance at the base of the rocker and Coulomb friction at the hinge of the sole plate-rocker interface. This combined rolling and friction resistance is modeled with a bilinear function (Figure 7.21). Ideally, the inelastic stiffness is zero in case of a uniform curvature and smooth rocking surface. However, Mander et al. (1996) recommend using non-zero k_p values

to account for debris buildup. In case of the particular high-type bearing tested in this experimental program, it is about 1.8% of the elastic stiffness.

The transverse behavior of the high-type bearing needs to be described with both bilinear rolling and friction models and hysteretic restrainer models as shown in Figure 7.22. Note that the keeper plates exhibit a more brittle behavior under bearing compared to the ductile hysteretic bearing behavior shown for other bearing types. The keeper plate is located on both sides of the bearing; hence, the behavior is identical in both transverse directions.

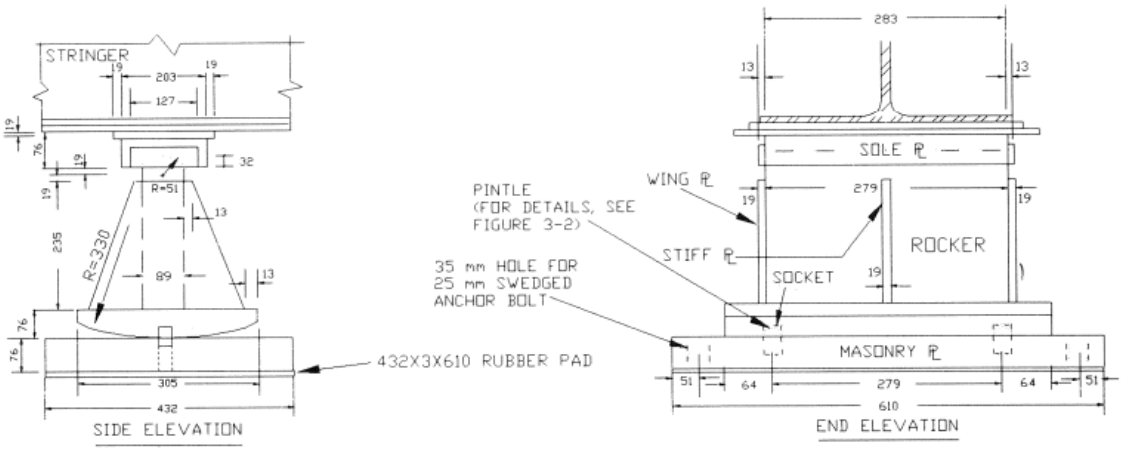

Figure 7.20: High-type rocker bearing specimen (Mander et al., 1996)

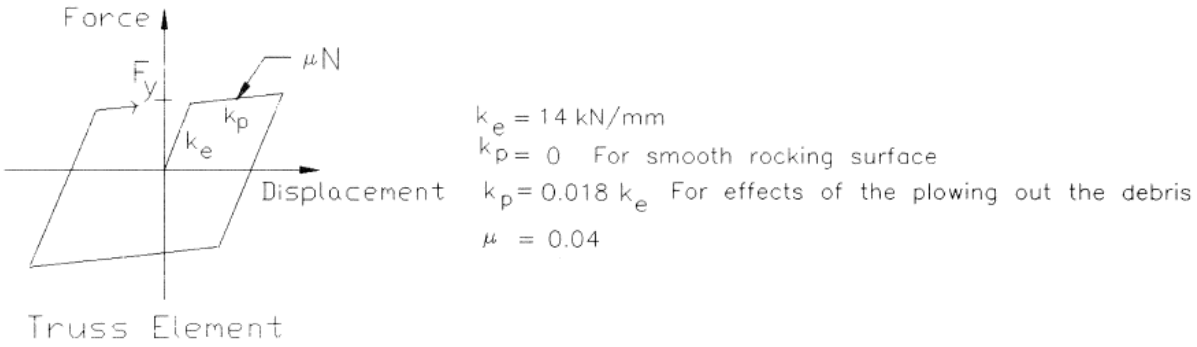

Figure 7.21: High-type rocker bearing, longitudinal model (Mander et al., 1996)

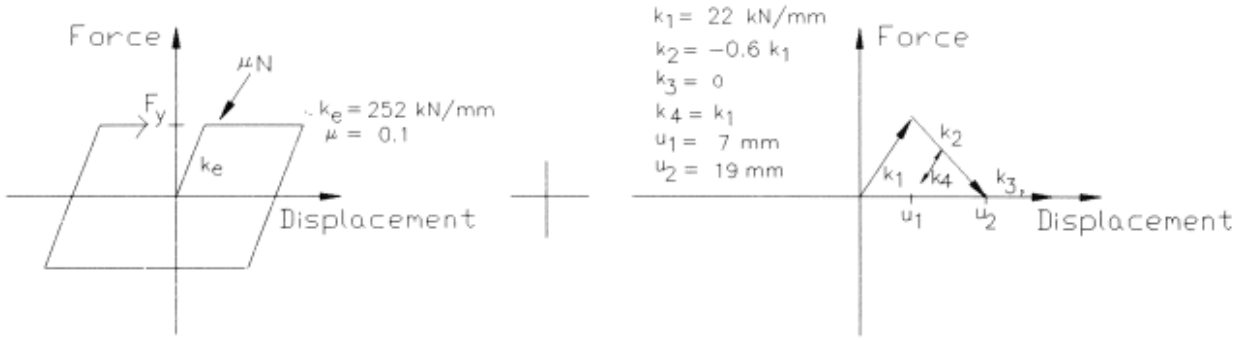

Figure 7.22: High-type rocker bearing, transverse specimen (Mander et al., 1996)

Figure 7.23 shows the comparison between testing and modeling results in the longitudinal direction, and Figure 7.24 displays the comparison for the specimen loaded in the transverse direction. Note, during transverse loading of the rocker bearing specimen, it failed due to instability during the first cycle; hence, there is only one hysteresis loop.

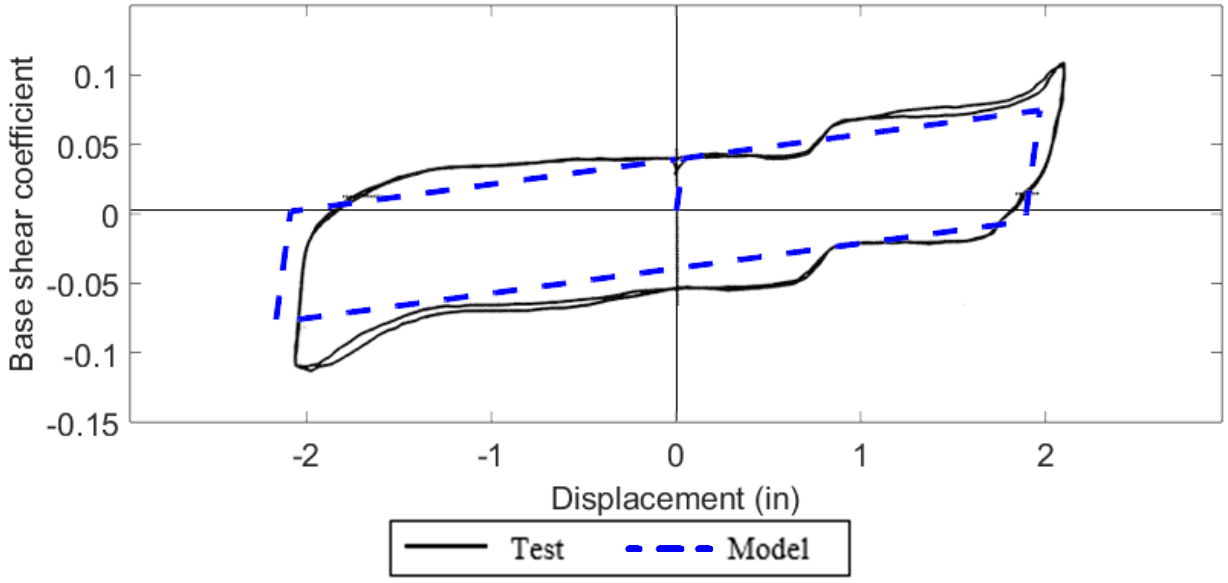

Figure 7.23: High-type rocker bearing, longitudinal model-test comparison

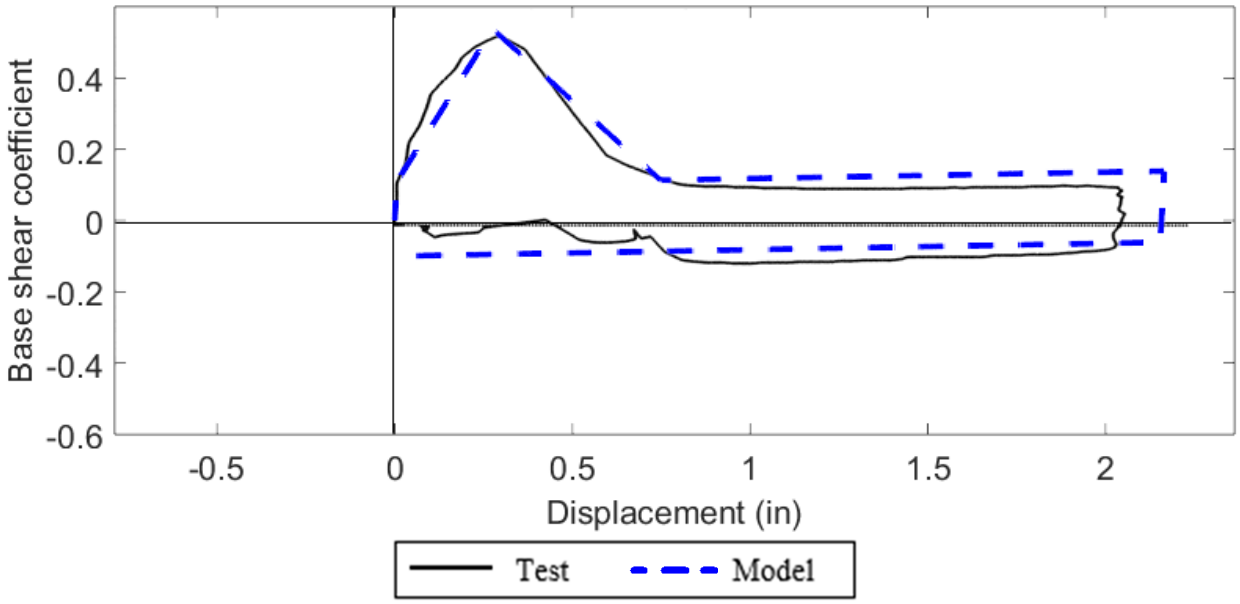

Figure 7.24: High-type rocker bearing, transverse model-test comparison

7.5.1.4. High-Type Fixed Bearings

For high-type fixed bearings (Figure 7.25), the transverse behavior is nearly the same as the rocker bearing, though there are some variations in the strength and stiffness parameters. Sliding is not permitted in the longitudinal direction, but longitudinal deformation due to prying of the masonry plate on the rubber pad has been observed. A bilinear model has been proposed to simulate this prying behavior and can be added in parallel with the hysteric bearing behavior to simulate anchor bolt deformations and concrete pullout/breakout (Mander et al., 1996).

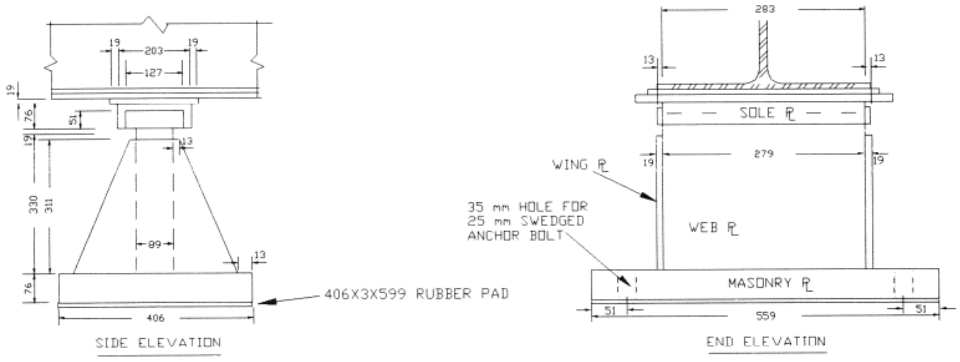

Figure 7.25: High-type fixed bearing specimen (Mander et al., 1996)

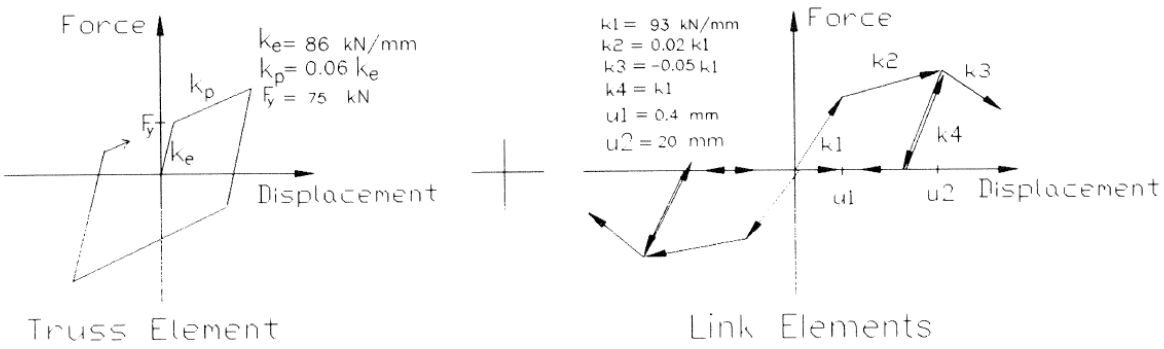

Figure 7.26: High-type fixed bearing, longitudinal model (Mander et al., 1996)

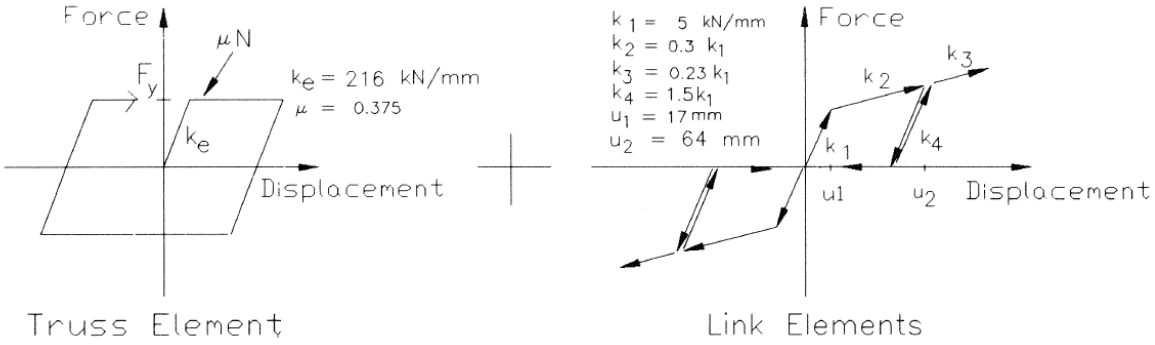

Figure 7.27: High-type fixed bearing, transverse specimen (Mander et al., 1996)

Figure 7.28 and Figure 7.29 show the comparison between hysteretic behavior for the high-type fixed bearing specimens loaded in the longitudinal and transverse directions, respectively.

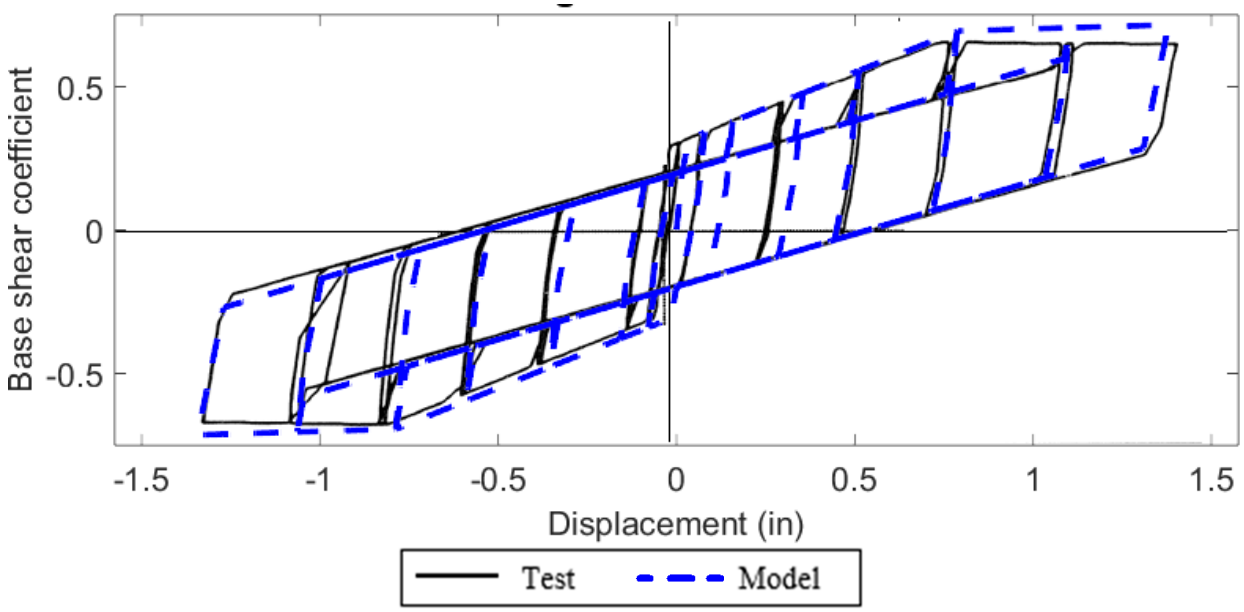

Figure 7.28: High-type fixed bearing, longitudinal model-test comparison

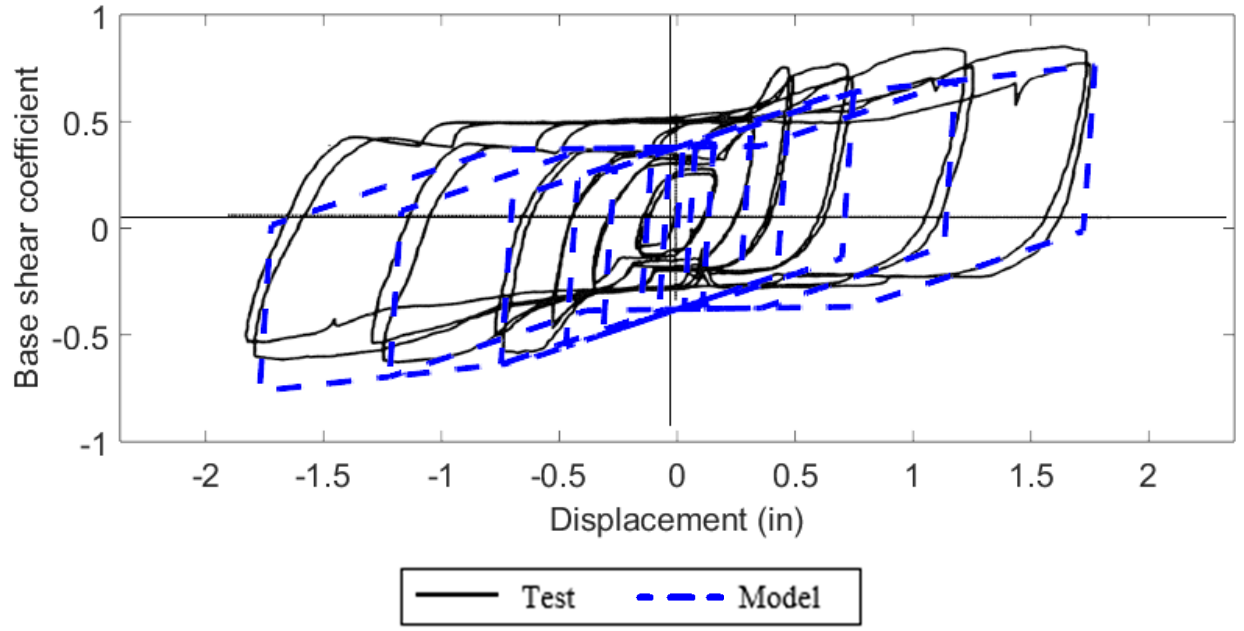

Figure 7.29: High-type fixed bearing, transverse model-test comparison

7.5.2. Elastomeric Bearings

As discussed in Chapter 6, elastomeric bearings are a common type of bearings used in prestressed concrete girder and slab bridges, as well as modern steel bridges. Each component of the bearing system provides a distinct contribution to the system. The elastomeric pad transfers horizontal load via shear stiffness of the elastomeric pad and frictional resistance, and the steel dowels provide resistance through beam-type action. Therefore, the model for each component can be developed

separately and then applied in parallel to simulate the composite action, as was done in other bridge fragility studies (Nielson 2005).

When subjected to a lateral loading, the bearing pad undergoes shear deformation with uniform elastic stiffness until the frictional resistance ($F_f = \mu N$) is exceeded, then the stiffness changes to nearly zero. The coefficient of friction used to determine the frictional resistance between bearing pad and concrete was obtained empirically with Eq (6.10). The initial stiffness is approximated with Eq. (6-9).

Bridge bearing dowels are expected to stay elastic under service loads, but they can undergo significant inelastic deformation during a moderate seismic event, deforming as a cantilever beam. As discussed in Section 6.4.4.2, the dowel models developed by Choi (2002), which used detailed finite element models of a typical steel dowel used in the region to determine key response parameters, forms the basis of the dowel models in this study. Figure 7.30 present the model developed by Choi (2002) for 25.4 mm (1 in.) diameter steel dowel. As seen in the figure, the initial stiffness of each dowel was calculated to be 46 kN/mm (262.7 kip/in), and the estimated yield and ultimate strengths were approximately 56.0 kN (12.6 kip) and 58.0 kN (13.0 kip), respectively. Choi (2002) proposed that if a dowel diameter other than 1 in. is used, the strength and stiffness are assumed to be quadratically proportional.

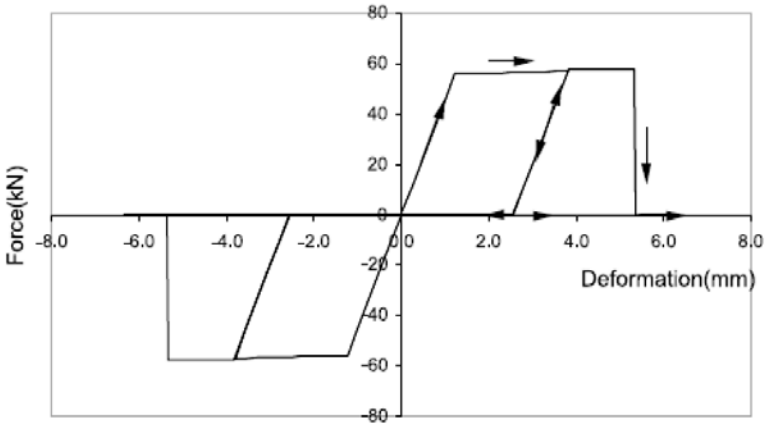

Figure 7.30: Steel dowel analytical model (Choi, 2002)

The combined elastomer shear deformation-friction model is added in parallel with the dowel hysteretic model. The behavior of the fixed elastomeric bearing is identical in the longitudinal and transverse directions. For expansion bearings, the gap is much larger in the longitudinal direction than the transverse direction because the slot is designed to accommodate translation. The stiffness and strength parameters, however, remain the same.

7.6. Bent

Bearings transfer lateral loads from the superstructure to the bents at bridge intermediate supports, which adds to the flexibility of the structure. Numerical models of bridge bents (columns and bent caps) are presented in the following sections. As discussed earlier, the bent cap distributes the load

from the superstructure to the individual columns, which are attached to the pile or drilled shaft foundation. To model bridge bents, Nielson (2005) suggests the use of beam-column elements for columns and bent caps at their respective centroidal axes. Bent cap and column elements are connected using rigid links. Columns are susceptible to damage during an earthquake. Thus, models capable of simulating this nonlinear behavior are necessary and are described in more detail below.

7.6.1. Columns

There are multiple approaches to modeling the nonlinear behavior of bridge columns (Figure 7.31) which include (a) concentrated plasticity models, (b) hinge region models, (c) fiber section models, and (d) 3D solid element models.

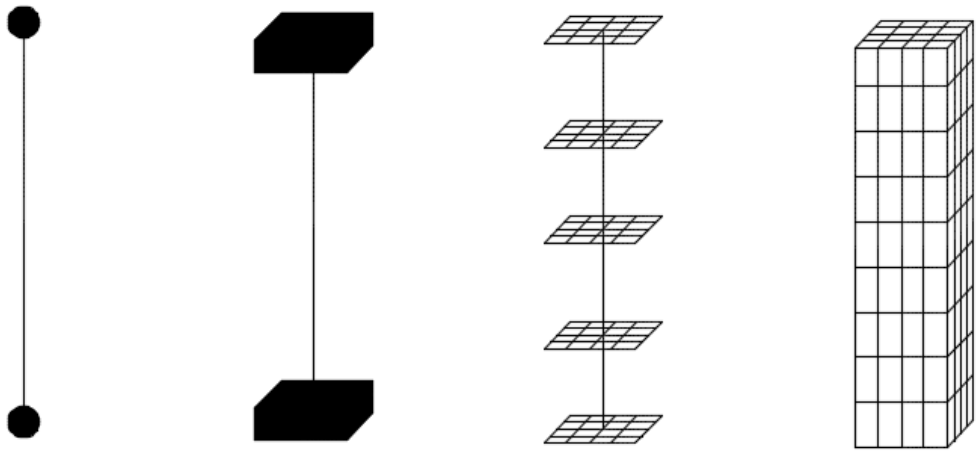

(a) (b) (c) (d)

Figure 7.31: Column modeling approaches

The 3D solid finite-element model (Figure 7.31d) in which concrete as well as all reinforcing bars are modeled explicitly with solid elements with contact models that simulate bond-slip behaviorsis capable of modeling complex concrete column behavior including different failure modes; however, this approach is very complex and requires numerous assumptions and experimental data to accurately calibrate e. In addition, solid FEM models are significantly more computationally demanding, which is a big disadvantage when running many nonlinear response history analyses of full bridge systems, as required for fragility analysis. Therefore, 3D finite element models were not considered for use in this study.

The distributed plasticity (Figure 7.31c) approach is a common method to model column behavior that has been used in previous bridge fragility studies (Nielson 2005) as it is capable of simulating coupled axial and flexural behavior by assigning fiber sections throughout a member. For the case of a reinforced concrete column, each section can be modeled with fibers that are assigned with uniaxial material models for concrete or reinforcing steel that are located according to the geometry of the cross-section and locations of longitudinal steel bars as shown in Figure 7.32.

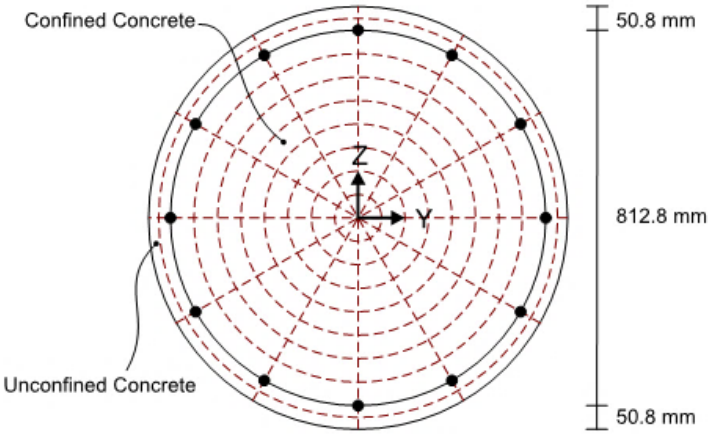

Figure 7.32: Column fiber section (Nielson 2005)

The models with nonlinear behavior governed by axial-flexural fiber cross-sections (Figure 7.31c) and predefined plastic hinge regions (Figure 7.31b) assume the column is able to reach its full moment capacity prior to shear failure and bar buckling. Such models are reasonable for those regions where columns are seismically detailed and capacity designed to avoid such non-ductile failure modes. However, the fiber-based models that simulate axial and flexural failure modes of bridge columns may not be appropriate for regions where seismic detailing has not been considered and other, less ductile failure modes are expected. As shown in Figure 7.33, typical column transverse reinforcement consists of a #3 spiral evenly spaced at 6-inch pitch. The longitudinal bars typically run straight into bent and pile caps with no hooks. Contrarily, modern seismic design involves tighter spiral spacing in plastic hinge regions (both ends of the column) for enhanced ductility, as well as anchorage of longitudinal and transverse reinforcement with hooks. Poor anchorage and light transverse reinforcement in non-seismically detailed bridge columns make them prone to a potential bar pullout or shear failure during a seismic event, which cannot be captured with either distributed or lumped plasticity approaches because fiber sections only account for axial-bending interaction.

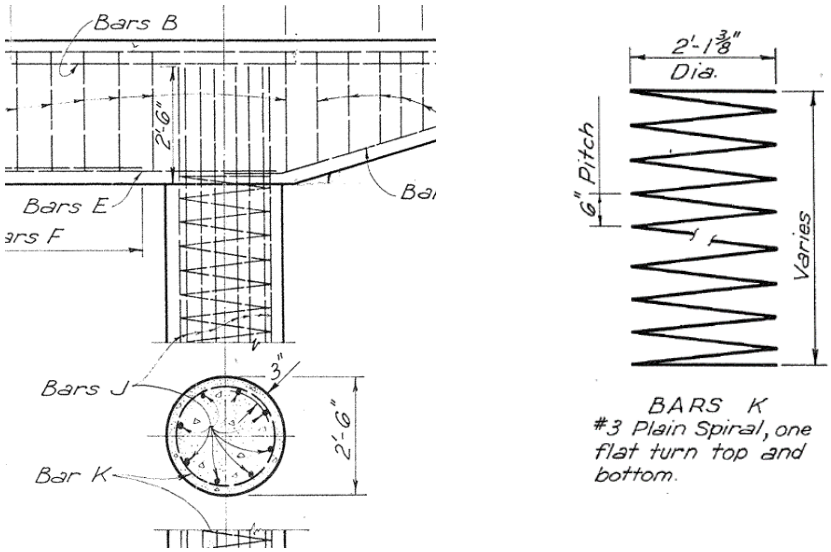

Figure 7.33: Typical column reinforcement in Texas (TxDOT 1962)

For this study, a lumped plasticity model (Figure 7.31a) is used, as it is the most computationally-efficient solution for the scope of the project. Columns are modeled with elastic beam-column elements with rotational springs (i.e., zero-length elements) at the top and bottom acting in two orthogonal directions (longitudinal and transverse). Each spring is assigned a nonlinear moment-rotation behavior based on the section's flexural and shear strength, as well as longitudinal reinforcement development length and splicing considerations.

The column nonlinear spring behavior is primarily based on the work done by the ACI 369 committee (2016) for the ASCE 41-17 standard. The equations for nonlinear behavior were based on a large experimental database of columns of various sizes and steel reinforcement layouts (including low transverse reinforcement) with cyclic loading in single and double curvatures. The experimental database includes 319 rectangular and 171 circular column tests without lap-splices (Ghannoum and Sivaramakrishnan 2012a; b), as well as 39 rectangular columns with lap splices (Al Aawar 2015). The database includes column specimens that failed in flexure, flexure-shear, and shear.

The generalized backbone curve used in ASCE 41 (2014) is shown in Figure 7.34. Line A-B represents initial elastic behavior, line B-C delineates a reduced stiffness response, line C-D represents a sudden loss of strength, and finally line D-E represents the spring behavior at a residual capacity prior to a column collapse at point E. To avoid convergence issues, as well as uncertainty about the slope of line C-D, strength degradation is assumed to occur linearly between points C and E, as shown in Figure 7.35.

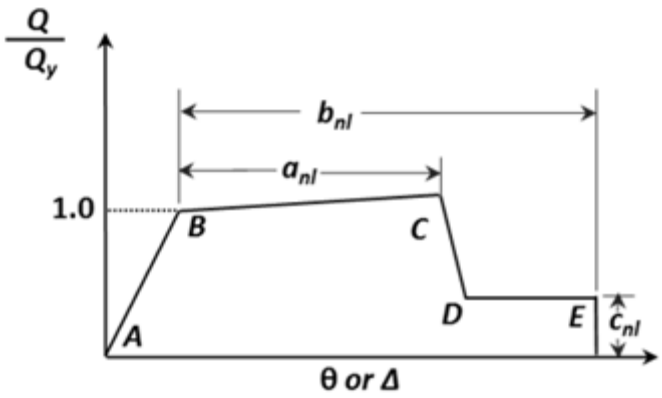

Figure 7.34: Column backbone curve (ACI 2016)

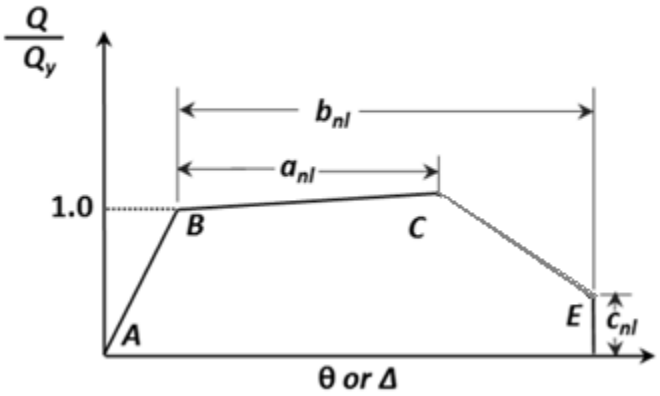

Figure 7.35: Modified column backbone curve

The backbone curves for these rotational springs represent moment-rotation behavior and are defined in ASCE 41 using the three parameters, a_{nl}, b_{nl}, and c_{nl}. The parameters a_{nl} and b_{nl} describe column inelastic rotation capacities to the points that limit the hardening region and strength degradation respectively, whereas c_{nl} represents residual capacity ratio. ACI (2016) provides different equations to define these parameters depending on whether the column is controlled by inadequate development/splicing or not. Table 7.1 outlines the nonlinear modeling parameters for both cases.

Table 7.1: Column nonlinear modeling parameters (ACI 2016)

Modeling Parameter	Not Controlled by Inadequate Development/Splicing	Controlled by Inadequate Development/Splicing
a_{nl} (radians)	$0.042 - 0.043\frac{N_{UD}}{A_g f'_{cE}} + 0.63\rho_t - 0.023\frac{V_{yE}}{V_{OE}} \geq 0.0$	$0.0 \leq \frac{1}{8}\frac{\rho_t f_{ytE}}{\rho_l f_{ylE}} \leq 0.02$
b_{nl} (radians)	$\frac{0.5}{5 + \frac{N_{UD}}{0.8A_g f'_{cE}}\frac{1}{\rho_t}\frac{f'_{cE}}{f_{ytE}}} - 0.01 \geq a_{nl}$	$a_{nl} \leq 0.012 - 0.085\frac{N_{UD}}{A_g f'_{cE}} + 12\rho_t \leq 0.06$
c_{nl}	$0.24 - 0.4\frac{N_{UD}}{A_g f'_{cE}} \geq 0.0$	$0.15 + 36\rho_t \leq 0.4$

where A_g is Gross cross-sectional area; f'_{cE} *i*s Expected concrete compressive strength; f_{ylE} is expected yield strength of longitudinal reinforcement; f_{ytE} is expected yield strength of transverse reinforcement; N_{UD} is member axial force; V_{yE} is shear demand at expected flexural yielding of the column; V_{OE} is expected shear strength of the column; ρ_l is Longitudinal reinforcement ratio; ρ_t *is* Transverse reinforcement ratio. Expected strength is defined as the mean value of strength of a component at the deformation level anticipated for a population of similar components considering the variability in material strength as well as strain-hardening and plastic section development. For reinforced concrete $f'_{cE} = 1.5f'_c$, $f_{ylE} = 1.25f_{yl}$, $f_{ytE} = 1.25f_{yt}$, where f_c, f_{yl}, f_{yt} are nominal concrete compressive strength, longitudinal reinforcing steel yield strength, and transverse reinforcing steel yield strength, respectively (ACI 2016).

To calculate the shear demand at expected flexural yielding of the column, it is required to know the expected deformed shape (i.e., the boundary conditions) of the column to determine the moment-shear relationship. For simplicity, two limiting cases are considered, single curvature and double curvature. Moment-shear relationships can be established using structural analysis and assumed fixed or pinned end conditions as shown in Figure 7.36. For single curvature $V=M/L$, whereas for double curvature $V=2M/L$, where V = shear (constant along the column length), M = bending moment at the end(s) of the column, L = column length. As mentioned previously, the assumption of single curvature for column longitudinal deformation and double curvature for transverse deformation is reasonable for multi-column bents (Aviram et al. 2008).

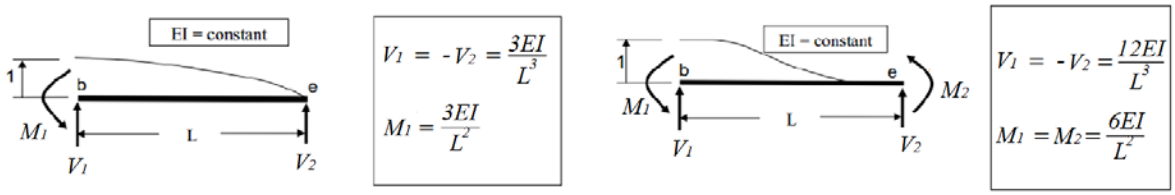

a) single curvature b) double curvature

Figure 7.36: Flexural member stiffness coefficients

To determine whether or not the column is controlled by inadequate development/splicing, the ACI (2016) equation for maximum stress that can be developed in anchored or spliced reinforcement (f_s) can be used as shown in Eq. (7-9). If $f_s = f_y$, then the column is not controlled by inadequate development/splicing. if $f_s < f_y$, longitudinal bars cannot develop their full yield strength and therefore the column is controlled by inadequate development/splicing. In addition, in that case steel yield strength is limited to the value of f_s.

$$f_s = 1.25\left(\frac{l_b}{l_d}\right)^{2/3} f_{yL} \leq f_y \tag{7.9}$$

where f_y is yield strength of longitudinal reinforcing steel (lower-bound or expected); f_{yL} is lower-bound yield strength of longitudinal reinforcing steel; l_d is development length of reinforcing steel; l_b is available length of straight development, lap splice, or standard hook. Chapter 25 of the ACI 318-14 (2014) standard defines development length (l_d) as the length required for reinforcement to be embedded in order to develop sufficient bond between concrete and steel to achieve full yield strength of the reinforcement, as shown in Eq. (7.10).

$$l_d = \frac{3}{40}\frac{f_y}{\lambda\sqrt{f'_c}}\frac{\Psi_t\Psi_e\Psi_s}{\left(\frac{c_b + K_{tr}}{d_b}\right)}d_b \tag{7.10}$$

where c_b is lesser of the distance from center of a bar to nearest concrete surface and one-half the center-to-center spacing of bars or wires being developed; d_b is bar diameter; K_{tr} is transverse reinforcement index defined in the following equation:

$$K_{tr} = \frac{40A_{tr}}{sn} \tag{7.11}$$

where A_{tr} is area of transverse reinforcement; s is spacing/pitch of transverse reinforcement; n is number of bars developed/spliced at the same location.

Additionally, the confinement term $(c_b + K_{tr})/d_b$ shall not exceed 2.5. For the calculation of development length, modification factors shall be in accordance with ACI 318 (2014) values outlined in Table 7.2.

Table 7.2: Modification factors for development length (ACI, 2014)

Condition	Value
Lightweight concrete	0.75
Normalweight concrete	1.0
Epoxy-coated or zinc and epoxy dual-coated reinforcement with clear cover less than $3d_b$, or clear spacing less than $6d_b$	1.5
Epoxy-coated or zinc and epoxy dual-coated reinforcement for all other conditions	1.2
Uncoated or zinc-coated (galvanized) reinforcement	1.0
No. 7 and larger bars	1.0
No. 6 and smaller bars and deformed wires	0.8
More than 12 in. of fresh concrete placed below horizontal reinforcement	1.3
Other	1.0

As mentioned previously, ACI (2016) depicts column plastic deformation and damage as a moment-rotation behavior. The strength parameters, i.e., the y-axis values of the points *B*, *C*, and *E* on the backbone curve (Figure 7.35) are moment values. In cases when flexural strength controls the capacity of the column, point *B* represents nominal column moment strength (M_n). The ordinate value of point *E* is equal to the moment at point *B* multiplied by c_{nl}.

Slope B-C approaches the value of probable moment strength (M_{pr}) at a rotation of 0.04 radians; however, the backbone curve is very unlikely to reach that point because the plastic rotation is limited by a_{nl}. ACI 318 (2014) defines M_{pr} as a probable flexural capacity with a tensile stress of longitudinal bars taken as $1.25f_y$. It is important to note that the reinforcement yield capacity is still limited by f_s, which itself is a function of a lower-bound yield strength.

Flexural or flexure-shear failure may not always control the failure mechanism, as is the case for a column with limited transverse reinforcement, which is prone to fail in shear; therefore, the column strength also needs to be limited by the column's shear capacity. ACI (2016) determines column shear strength (V_{col}) as follows:

$$V_{col} = \alpha_{col}\left(\frac{A_{tr}f_{yt}d}{s}\right) + \lambda\left(\frac{6\sqrt{f'_c}}{M_{UD}/V_{UD}d}\sqrt{1+\frac{N_{UG}}{6\sqrt{f'_c}A_g}}\right)0.8A_g \qquad (7.12)$$

where d is effective depth of column reinforcement; M_{UD}/V_{UD} is largest ratio of moment to shear developed in the column; and α_{col} is 1.0 for $s/d \leq 0.75$ and 0.0 for $s/d \geq 1.0$. α_{col} varies linearly from 1.0 to 0.0 for $0.75 \leq s/d \leq 1.0$

If the column nominal shear capacity is less than the shear demand at the nominal flexural capacity, it is considered to be shear-controlled. In this case, the ordinate of point B on the moment-rotation

backbone curve (Figure 7.35) is equal to the moment expected at the nominal shear strength, and the column never reaches flexural yielding. Unlike flexural yielding, no hardening is assumed for a shear failure mode; therefore, the slope of line B-C is zero. For computational purposes, due to the fact that zero slope may cause convergence issues, the slope was assigned a low non-zero number. The equations for a_{nl} and b_{nl} remain the same for both flexure- and shear-controlled cases. However, both variables depend on the amount of column transverse reinforcing and, therefore, will be lower for columns controlled by shear failure.

Through the inspection of TxDOT bridge plans and typical details, it was determined that a vast majority of the multi-column bents were built with circular concrete columns (Figure 7.33); therefore, only circular column sections were considered in this study. Determination of flexural capacity of a circular section was determined through a fiber section analysis, where the column dead load is considered for axial-flexural interaction.

After flexural and shear capacities, as well as associated plastic backbone rotations are calculated using the aforementioned procedures, the column lumped plasticity model can be constructed. The column assembly (Figure 7.37) consists of an elastic beam-column element with zero-length moment-rotation springs at the ends. The elastic beam-column element requires input of two end nodes, cross-sectional area (A), elastic (E) and shear (G) moduli, torsional constant (J), flexural moments of inertia in both directions (I_z and I_y), and a function related to element coordinate transformation.

Elastic modulus (E) of steel girders are assumed to be 29,000 ksi. For concrete material, the elastic modulus is obtained per ACI 318 (2014) equation, as follows:

$$E = 57000\sqrt{f'_c} \tag{7-13}$$

Shear modulus for both materials, i.e., steel and concrete, are obtained using the following equation:

$$G = \frac{E}{2(1+\nu)} \tag{7-14}$$

where ν = Poisson's ratio, and is set to be 0.3 for steel and 0.15 for concrete.

Post-peak crushing strength of concrete (f'_{cu}) is assumed to be zero. Concrete strain at maximum strength, according to Kent and Part (1971), is taken as a ratio of twice the compressive strength divided by concrete secant modulus as follows:

$$\varepsilon_c = \frac{2f'_c}{E} \tag{7.15}$$

where $f'c$ in Equation shall be used in psi. Concrete crushing strain is assumed to be 0.003, a typical value used in reinforced concrete design.

Confined concrete compressive strength (f'_{cc}) and corresponding strain (ε_{cc}) are calculated based on Mander et al. (1988) equations, which is shown in Eq. (8.5). Concrete crushing strength is

assumed to be zero as well, while crushing strain is scaled by the ratio of $\varepsilon_{cc}/\varepsilon_c$. The latter value is not particularly important for the pushover analysis where finding flexural capacity (M_n) is the primary interest, and the outer unconfined portion of the section will reach crushing strength first.

$$f_{cc} = f_c\left(-1.254 + 2.254\sqrt{1 + \frac{7.94f'_l}{f_c}} - 2\frac{f'_l}{f_c}\right) \tag{7.16}$$

$$\epsilon_{cc} = \epsilon_c\left(1 + 5\left(\frac{f_{cc}}{f_c} - 1\right)\right) \tag{7.17}$$

where $f_l^{'}$, which is refer to lateral confining pressure can be computed as follows:

$$f'_l = \frac{1}{2}K_e\rho_s f_{yt} \tag{7.18}$$

$$K_e = \frac{1 - \frac{s_{clear}}{2d_{core}}}{1 - \rho_{cc}} \tag{7.19}$$

where ρ_s is the ratio of the volume of transverse confining steel to the volume of concrete core; K_e is confinement coefficient; s_{clear} is clear spacing between transverse reinforcement; d_{core} *is* diameter of concrete core within transverse reinforcement; ρ_{cc} is ratio of the volume of longitudinal steel to the volume of concrete core.

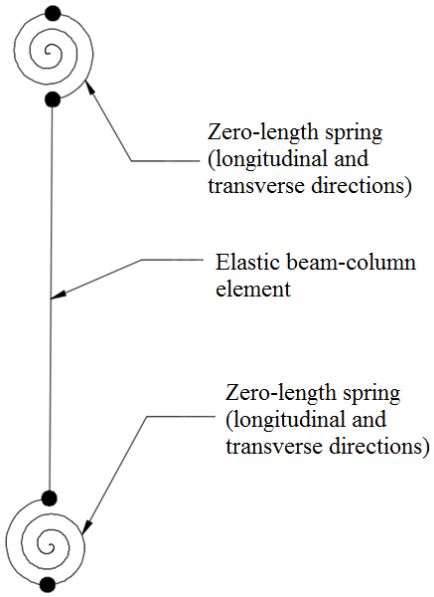

Figure 7.37: Column model

The rotational springs are meant to simulate the plastic rotation behavior of the column. The elastic portion of the rotational lumped plasticity spring backbone is supposed to be rigid theoretically, allowing all deformations to come only from the elastic beam-column element. However,

numerically simulating rigidity with a very high stiffnesses approaching infinity can create difficulties in convergence. Instead, the elastic portion of the backbone curve was set to span from -0.1θ_y to 0.1θ_y, where θ_y is rotation associated with reaching nominal moment or shear capacity (whichever happens first) based on the preliminary column pushover analysis. To compensate for the additional flexibility provided by the elastic rotational capacity of the springs, the modulus of elasticity of the elastic beam-column element was increased by a factor of 1/(1 - 0.1) = 1.11. Once the column reaches its rotational capacity, the backbone curve input for the material model is defined according to a_{nl}, b_{nl}, and c_{nl} per ACI (2016). A sample column rotational spring pushover curve is shown in Figure 7.38.

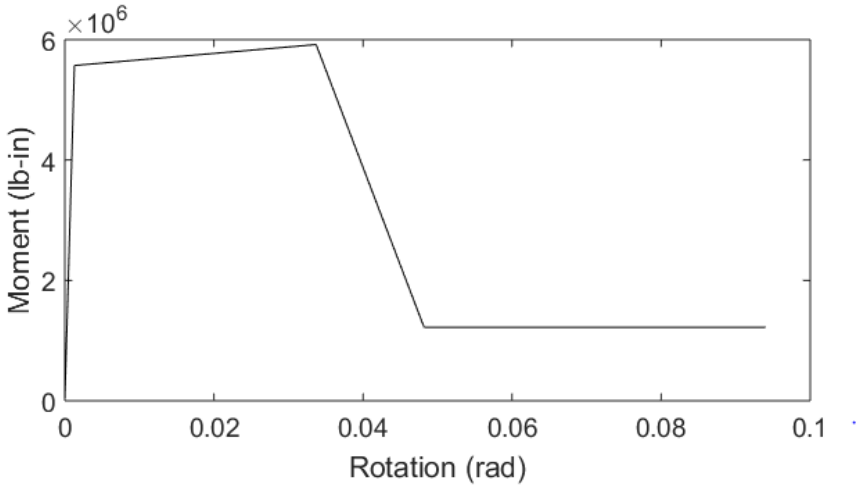

Figure 7.38: Sample column backbone curve

In addition to backbone parameters, the nonlinear models for the springs also requires to input parameters that will control column unloading, pinching, and damage parameters. There is no definitive theoretical approach or analytical model that defines all of the unloading and reloading parameters for reinforced concrete, mainly due to variability of the cyclic behavior of damaged reinforced concrete members. Therefore, these parameters were calibrated based on available column testing data from the literature. The datasets used for calibration were based on experimental cyclic pushover tests performed by various researchers that were compiled into databases for unspliced column specimens by Ghannoum & Sivaramakrishnan (2012a; b) and spliced column specimens by Al Aawar (2015). Those tests include columns loaded in both single and double curvature.

Based on geometric and material properties of each test specimen, lumped plasticity column models were created to simulate their behavior according to ACI (2016) backbone curve provisions. Additionally, the nonlinear column specimen models were subjected to the cyclic displacement histories for their respective tests in OpenSees. Finally, load-displacement hysteresis curves from the experiment and from the numerical model were compared to each other to calibrate the model hysteresis parameters.

The main criterion that was used for calibration of unloading, damage, and pinching parameters was energy dissipation capacity of the column, which is equal to the area under the hysteresis. Additionally, the maximum strength of the column test specimen and numerical model were compared to determine whether the ACI (2016) approach underestimates or overestimates the actual capacity. A sample comparison of a column test and results from a nonlinear pushover analysis for a column specimen that failed in shear is shown in Figure 7.39. It is impossible to define material parameters that will perfectly fit results from every specimen of the data set; therefore, an approach was chosen that resulted in slightly underestimated column energy dissipation compared to the test data. This approach was used since the nonlinear analyses are intended to evaluate bridge system damage, and the underestimation of energy dissipation is expected to produce worst case estimations for displacement-based column damage states.

The column load-deformation data from the 71 different circular flexure-shear- and shear-critical column tests conducted by different researchers was found to vary significantly from specimen to specimen; however, one clear observation was made that shear-critical columns (as shown in Figure 7.39) typically have significantly more pinching than the flexure-controlled columns, as shown in Figure 7.40.

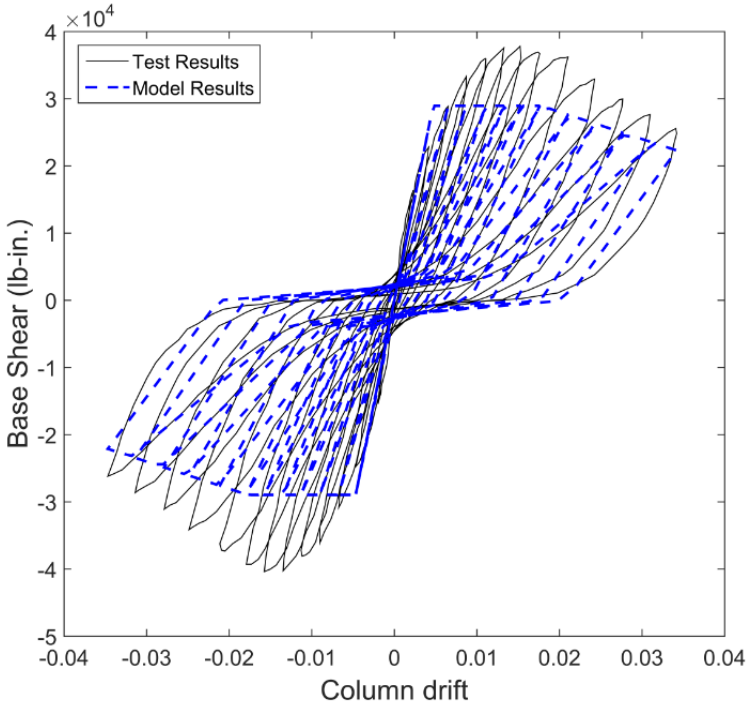

Figure 7.39: Column testing vs. modeling hysteresis (shear controlled)

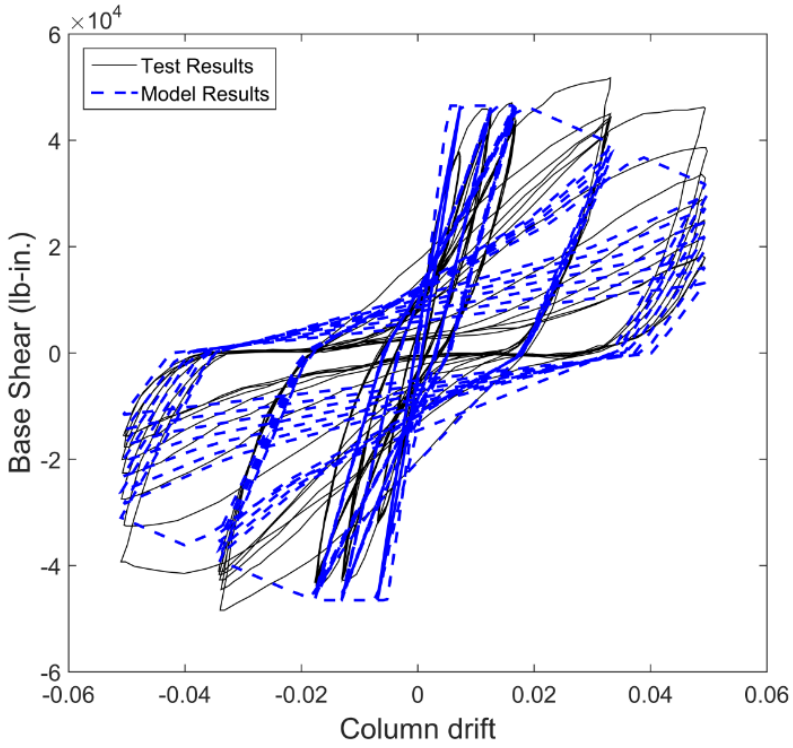

Figure 7.40: Column testing vs. modeling hysteresis (flexure-controlled)

Numerous values for pinching and damage factors were evaluated against the experimental data using a trial and error approach until acceptable results (lowest variation and reasonable underestimation of energy dissipation) were obtained.

7.6.2. Bent Caps

Bent caps are significantly stiffer than the columns below and are not expected to exhibit inelastic behavior under lateral loading; therefore, the bent caps are modeled with linear elastic beam-column elements. The maximum moment demands developed in the bent cap elements were compared to their flexural capacity to verify this assumption following the response-history analyses. Gross flexural moments of inertia are multiplied by a factor of 0.5 per ACI (2016), and gross torsional constant is multiplied by 0.2 per Caltrans (2013) to account for reduced stiffness due to cracking.

7.7. Foundation

Bridge columns extend down to foundations embedded into soil. There are two ways to model foundation behavior: (1) the direct method involves a finite element model that explicitly considers soil-structure interaction, and (2) the substructure simplified method, which simulates soil and foundation behavior via a set of translational and rotational springs (Nielson 2005). Usage of idealized pinned or fixed foundation supports to model foundations is discouraged because those

supports are not able to capture the effects of soil flexibility and energy dissipation (Aviram et al. 2008).

An example of the direct method is a nonlinear Winkler foundation (dynamic p-y) analysis. In such an analysis, piles are modeled explicitly as beam-column elements, and the soil-structure interaction is approximated through a set of nonlinear p-y springs acting transverse to the pile. P-y spring behavior can be simulated using backbone parameters for sand and clay soils based on experimental testing by Boulanger et al. (1999). The properties of each spring depend on the pile length tributary to it; therefore, any number of springs can be applied throughout the pile height. A greater number of springs increases accuracy of the analysis, but also increases the computational demand due to a greater number of degrees of freedom in the model. Pile vertical response due to friction can be modeled through a set of nonlinear springs applied longitudinally along the pile (t-z method). Pile bearing is modeled with vertical spring applied at the tip of the pile (Q-z method). The overall element assembly is shown in Figure 7.41.

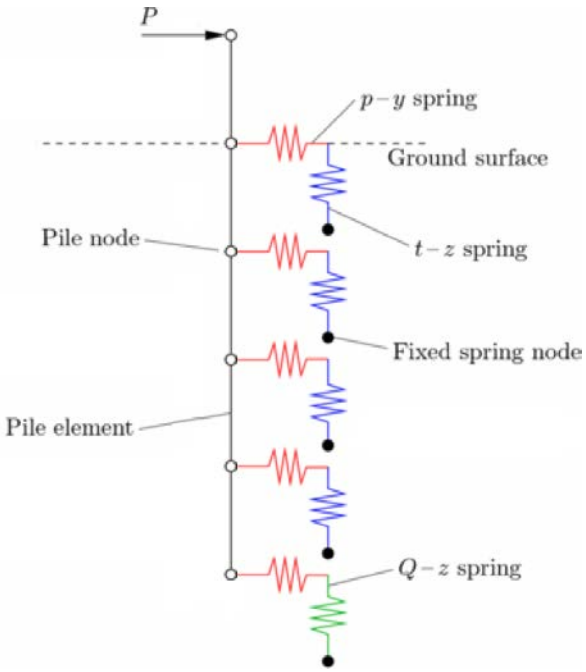

Figure 7.41: Winkler Foundation Model (McGann et al. 2011)

The direct method is computationally expensive because it significantly increases the number of degrees of freedom in the model (e.g., multiple nodes per pile) and involves plastic deformations in numerous spring elements. It is a good approach to use for specific bridge models where foundation details and soil properties are known. However, for the large number of generic bridge samples used in this study to represent many bridges across the state, such computational cost is not justified based on the uncertainty and variability in soil and foundation properties and details needed to define the different model components. As a result, the substructure simplified method was used in the study.

Similar to the bearing models described in Section 7.5, foundation behavior was modeled in this study using a nonlinear translation springs, where rotational degrees of freedom are assumed to be fixed. The foundation model proposed by Choi (2002) was used to simulate pile/shaft behavior. The elastic translational stiffness is based on the pile/shaft configuration as described in Section 6.4.3.3. The displacement corresponding to a pile/shaft reaching its maximum capacity is taken as 1 in. (Nielson 2005). The foundation behavior was approximated as a tri-linear curve. The demands at first yield was assumed to occur at 30% of the ultimate deformation and 70% of the ultimate strength (Choi 2002). Figure 7.42 shows a sample pile/shaft hysteresis curve with 40 kip/in effective stiffness. Similar to the bearing models and consistent with pile/shaft modeling in past fragility studies (Choi 2002; Nielson 2005), the behavior is assumed to be fully pinched, the unloading slope is assumed to be equal to the elastic stiffness, and no reloading stiffness degradation was considered. For the foundations under bridge bents, only the pile/shaft resistance is considered, and soil resistance is neglected due to relatively low pile/shaft surface area. At the abutment foundations, on the other hand, the resistance of the soil at abutments in the longitudinal direction cannot be ignored due to large abutment-soil interface; therefore, soil resistance is considered in addition to the pile/shaft resistance. The numerical model for abutments, including the soil resistance, is presented in the section below.

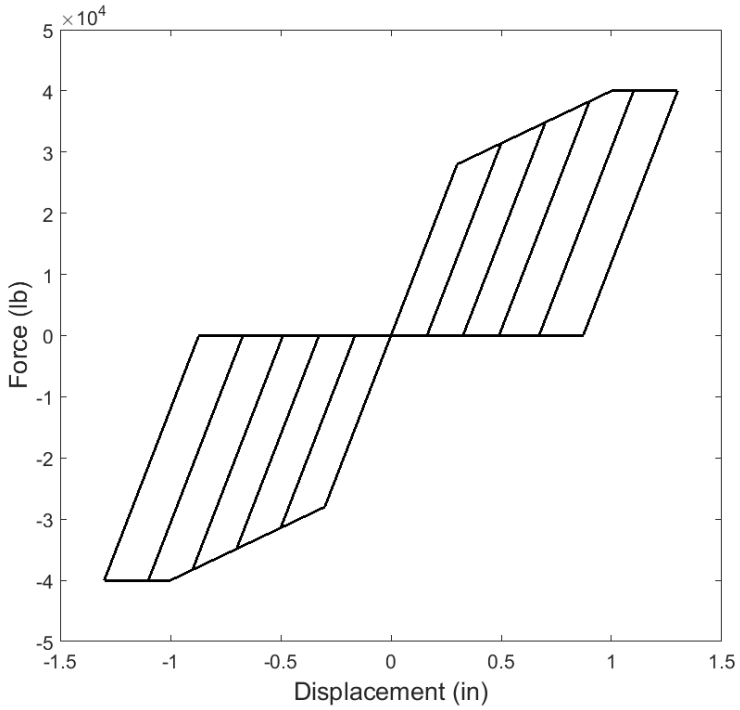

Figure 7.42: Pile/shaft element hysteresis

7.8. Abutment

Abutment behavior was modeled using nonlinear translational springs placed in parallel, with one representing soil resistance and the other representing pile/shaft resistance as shown in Figure 7.43. The multi-linear model used by Choi (2002) is employed in this project for the passive soil

resistance. All strength and deformation values used to define the model are based on the soil elastic stiffness, ultimate soil pressure, and ultimate soil displacement. The approach used in this study, based on the Choi (2002) model, simplifies nonlinear soil force-deformation behavior to a quad-linear curve (i.e., a backbone curve described by four linear segments in the negative direction). The multi-linear material model available in OpenSees, however, is only able to simulate a tri-linear relationship; therefore, the approach used by Choi (2002) was modified to use only three linear segments to define the backbone response. The post-yielding behavior was truncated, as shown in Figure 7.44. This modification slightly underestimates the soil energy dissipation capacity compared to the proposed Choi (2002) model; however, there is insufficient experimental data to justify any other simplification of the quad-linear backbone curve.

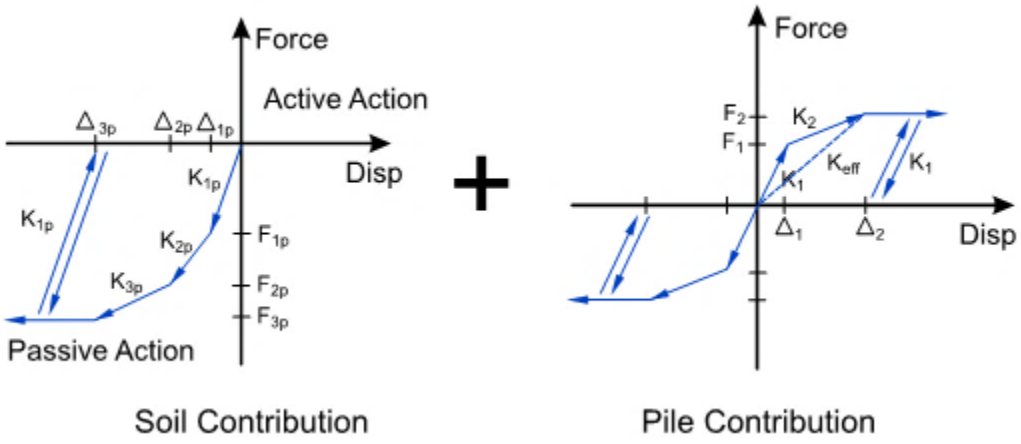

Figure 7.43: Abutment models (Nielson, 2005)

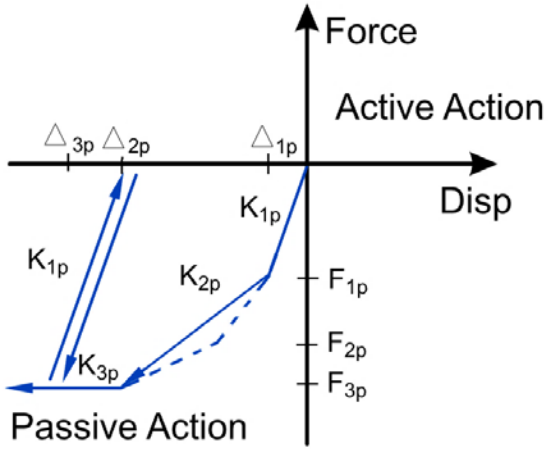

Figure 7.44: Modified soil model

The soil backbone curve is only defined in the negative (passive) direction. Soil is assumed to have no active resistance due to its negligible tensile strength; therefore, negligible strength values were assigned for the material in the positive direction. The nonlinear soil behavior was only used for

the springs in the longitudinal direction, and soil passive resistance in the transverse direction was ignored. Figure 7.45 shows an example hysteresis curve for a 30-ft-wide abutment with a height of 10 ft, and coarse cohesionless soil conditions.

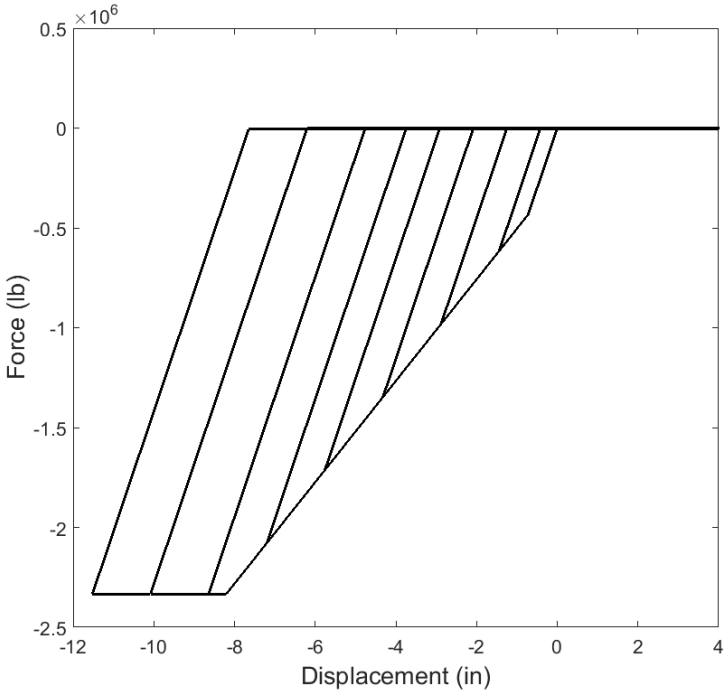

Figure 7.45: Abutment soil element hysteresis

7.9. Assembly

Each of the previously described components are assembled into a full bridge model based on the randomly sampled geometry and material properties described in Chapter 6. A model schematic for continuous bridges is shown in Figure 7.46, and a model schematic for simply-supported bridges is shown in Figure 7.47. As described earlier, bridge girders, bent caps, and columns are modeled using beam-column elements with material and cross-sectional properties assigned corresponding to the bridge members they represent to simulate their associated mass and stiffness. Elements are located at their respective centers of mass to accurately represent distribution of mass along bridge height. Inherently, this modeling approach results in separation between the girder, bent cap, and column elements in the vertical direction. Therefore, connectivity of those elements was ensured by usage of rigid links. Nonlinearity effects in the columns, bearings, abutments, foundations, and joints are modeled in OpenSees using translational and rotational nonlinear spring (i.e., zero-length) elements in both longitudinal (L) and transverse (T) directions; no nonlinear vertical springs were used in the model.

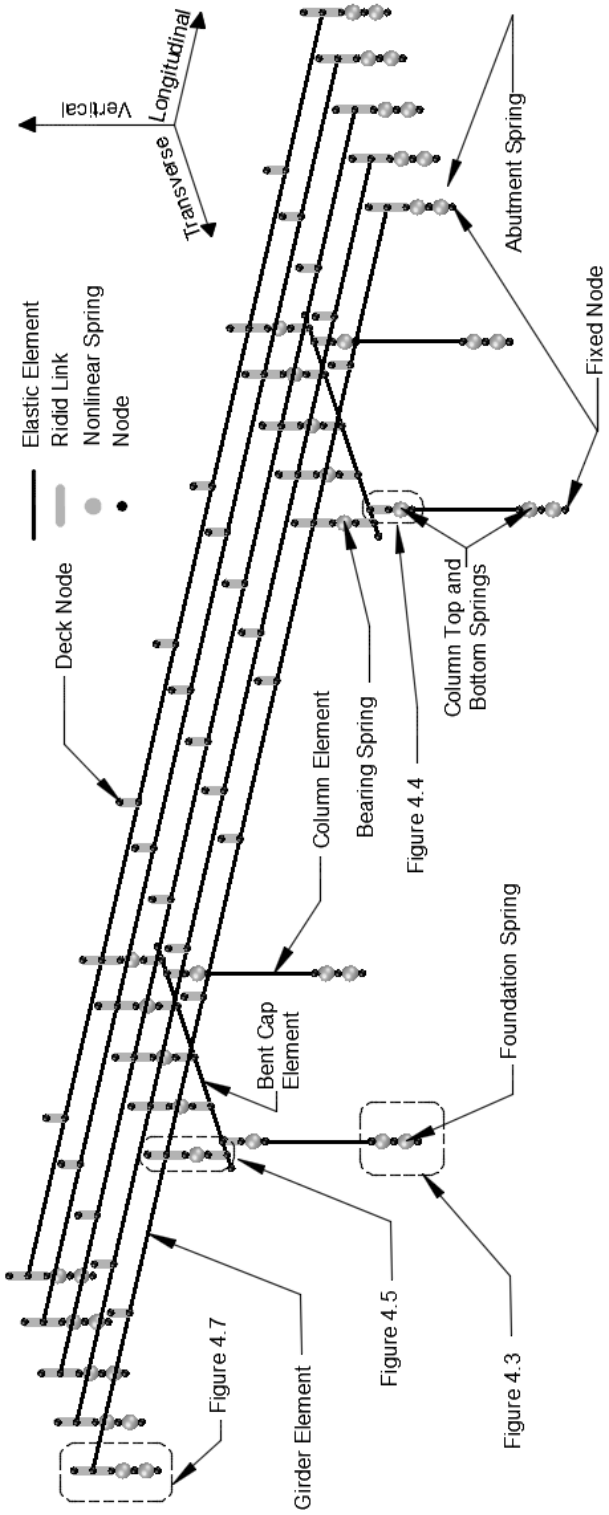

Figure 7.46: Model schematic for a continuous bridge

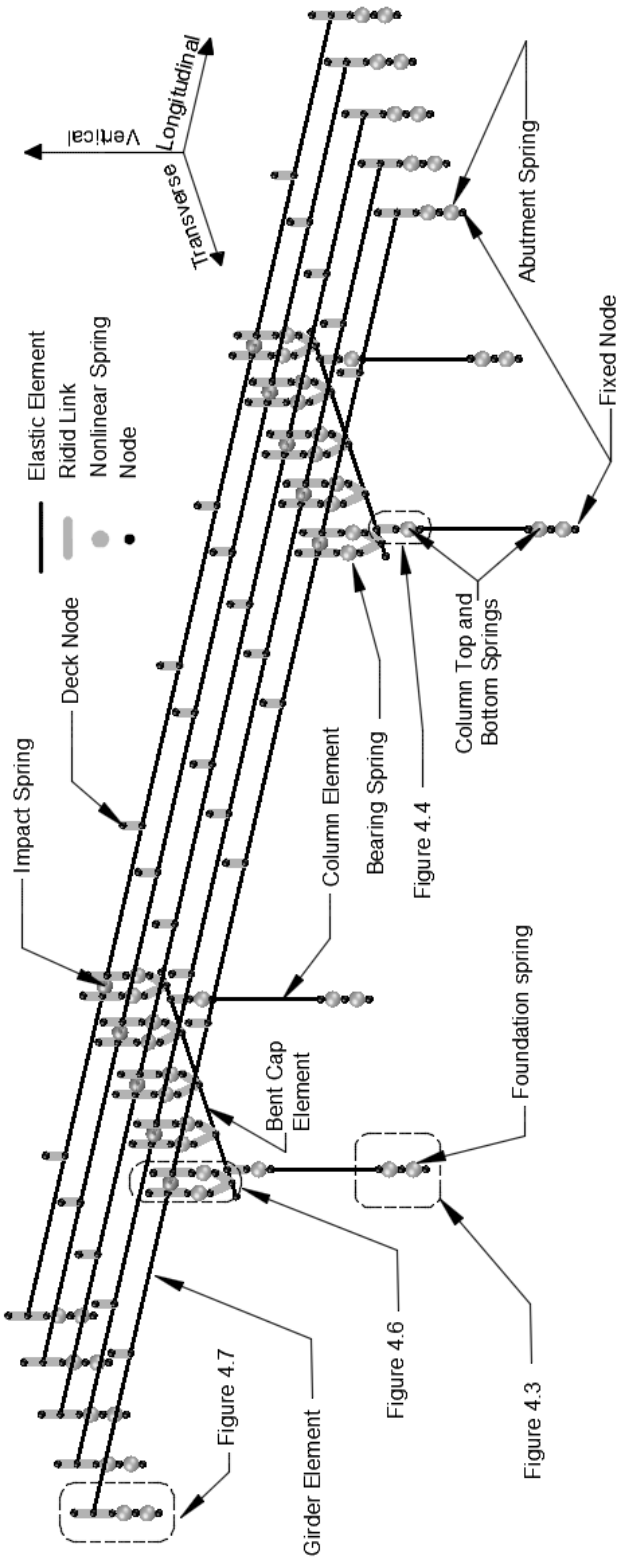

Figure 7.47: Model schematic for a simply-supported bridge

Figure 7.48 depicts the spring layout used at the bottom of column elastic elements. The assembly involves three nodes (labeled as bottom hinge, bottom end, and fixed nodes) located at the exact same coordinates, though shown at different locations in the figure for clarity. The column hinge node, which is located at the end of elastic column flexural element, is connected to the column end node via zero-length rotational springs representing nonlinear column plastic rotation and degrading behaviors in the longitudinal and transverse directions (refer to Section 7.7). All other degrees of freedom (rotation about column axis and all three displacements) were constrained, i.e., not allowing any relative displacements and rotations in directions where the springs do not act, preventing any instability issues in the model. The column end node is connected to the fixed node via translational (longitudinal and transverse) springs, simulating the foundation behavior. Degrees of freedom not affected by the springs (vertical displacement and all three rotations) were constrained. As implied by its name, all six degrees of freedom of fixed node are restrained from movement.

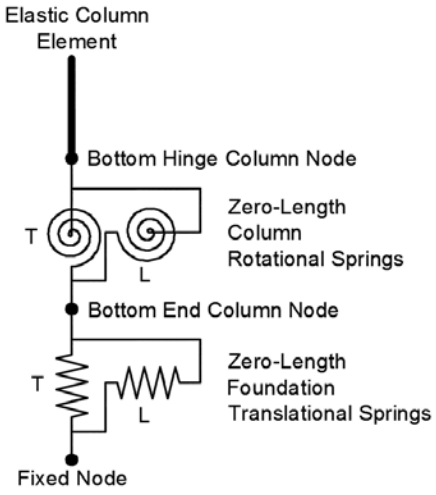

Figure 7.48: Element layout at column bottom

Figure 7.49 shows the spring layout at the top of column elastic elements. Similar to the column bottom layout, it involves rotational springs acting in longitudinal and transverse directions simulating column behavior once it exceeds its elastic capacity. Similar to bottom columns, translations as well as rotations about columns axis were constrained to be equal at the two column nodes. Due to the fact that the column top and the bent caps centers of mass are located at different heights, those two nodes are connected with a rigid link.

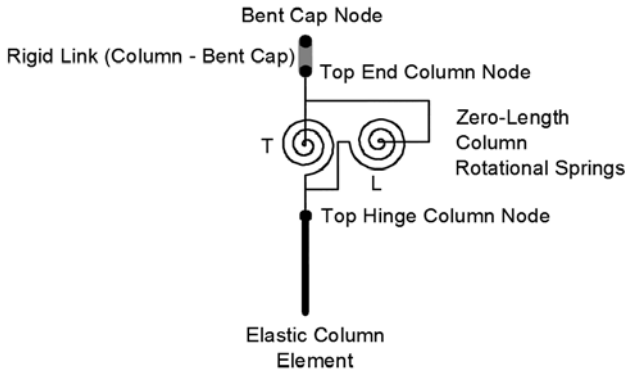

Figure 7.49: Element layout at column top

Figure 7.50 shows the spring layout at bent locations for continuous bridges. It involves flexural elements representing bridge girders located at their center of mass locations. Nodes with lumped tributary deck mass are located above girder nodes at a vertical location representing the deck center of mass, and the two nodes are connected via a rigid link. Additionally, a rigid link is used to tie the nodes representing the center of girder mass and girder bottom (top bearing node). Bearing nodes are connected with two sets of nonlinear springs in both horizontal directions, one representing bearing bilinear behavior and the other representing hysteretic restraining behavior as described in Section 7.5. The springs are connected in parallel, which indicates that they have equal displacements but unequal forces. Hence, their stiffnesses are added together. In cases where restraining mechanisms are not provided in the bearing (e.g., for steel rocker bearings in the longitudinal direction), only the bilinear springs are used. The top and bottom bearing node constraints include vertical translation, as well as rotation in the transverse direction and rotation about the vertical axis. Rotation in the longitudinal direction was not constrained because bearings are usually designed to allow in-plane girder rotation. The bottom bearing node is connected to the bent cap center of mass via a rigid link.

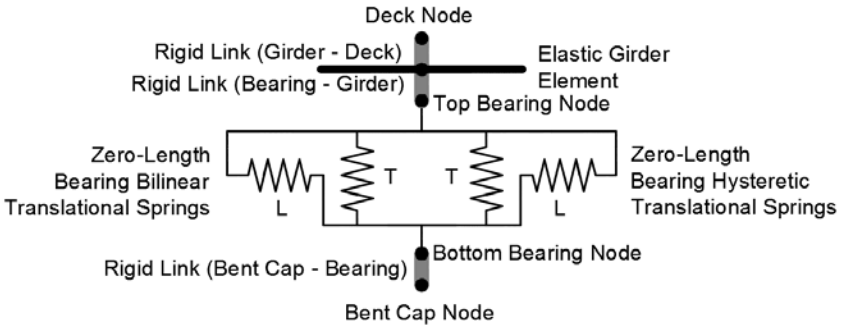

Figure 7.50: Element layout at bent for a continuous bridge

Figure 7.51 shows the element assembly at bent locations for simply-supported bridges. In this case, girder elastic elements are not connected to each other, enabling bridge spans to move independently from each other. However, as the bridge joint gap closes, the impact spring is engaged, simulating deck pounding effects as described in Section 7.4. The impact deck stiffness is assumed to be equally divided among girders. The joint impact spring only acts in the

longitudinal direction; thus, no resistance is provided by the element in the transverse direction. Both bearings under each simply-supported girder are attached to the same bent cap node.

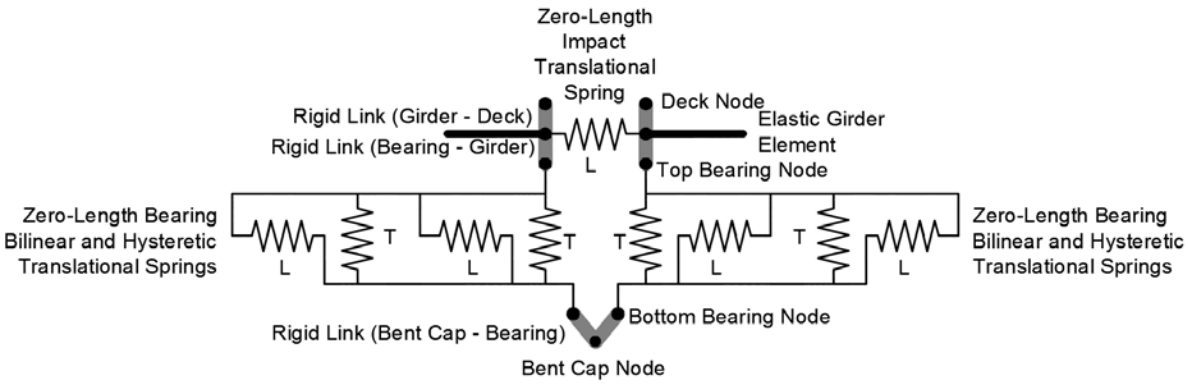

Figure 7.51: Element layout at bent for a simply-supported bridge

Figure 7.52 displays the element layout at the abutment locations. Similar to the bent locations, the girder element node is tied to the deck and bearing nodes via rigid links. In addition to bilinear and hysteretic elements representing bearing behavior, a longitudinal impact spring is added in parallel, representing the gap between deck and abutment back wall. Once that gap is closed, the superstructure can no longer move relative to the abutment without deck pounding. Resistance in the transverse direction is provided only by bearing elements.

The bearing and impact spring assembly at the abutment is connected in series to foundation and abutment springs, which are acting in parallel. Foundation and abutment soil stiffnesses, based on the number and size of piles and/or shafts under the abutment and the back wall width, are assumed to be equally distributed among girders. As previously discussed, soil passive resistance is only assumed to be acting in the longitudinal direction; therefore, there is no transverse abutment spring in the layout. Vertical translations and all rotations were constrained between the spring nodes.

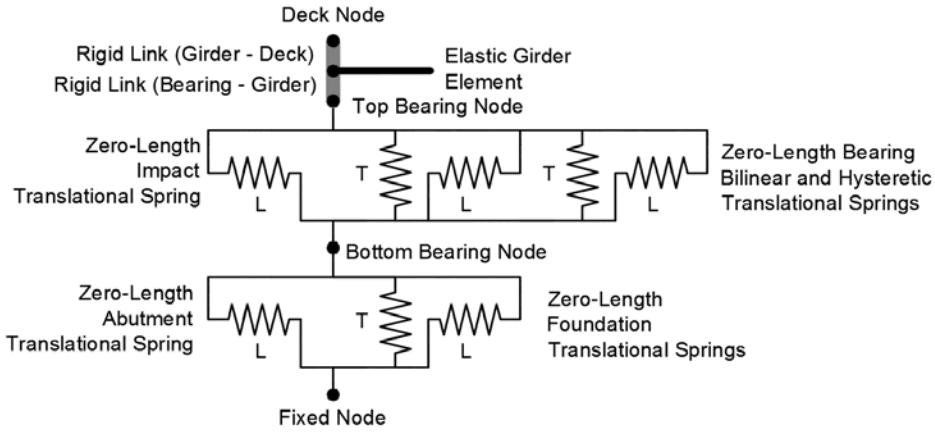

Figure 7.52: Element layout at abutment

As discussed earlier in Section 7.3, the rigid diaphragm assumption is used for the superstructure. Additionally, rigid diaphragm constraints are assigned to the nodes below the bearings at each abutment. This constraint is done for the purpose of preventing relative motion between bottom bearing nodes, which are meant to be representing abutment seats. If no constraint is assigned to those nodes and two adjacent bearings have different stiffnesses (e.g., bearings under the exterior girder have a dowel and bearings under the interior girder do not), the bottom bearing nodes will translate independently from each other, which is not representative of abutment seat behavior. For the model developed, abutments are assumed to act as a rigid body; therefore, the bottom bearing nodes can translate or rotate as a rigid body with the abutment seat. For dynamic analyses, the initial time step for response-history analysis is set at 0.001 seconds, which is shorter than the time step in typical ground acceleration records used in this project (0.01-0.025 seconds); therefore, no ground motion acceleration data is lost due to time step being too large. Additionally, the implicit Newmark average acceleration time-stepping method, unlike some of its alternatives, is unconditionally stable, meaning it does not have an instability issue due to analysis time step being too large relative to structure's natural period.

The presence of numerous nonlinear spring elements with different loading and unloading stiffnesses, yield strengths, hardening, and degradation parameters makes the model prone to convergence issues. The Newmark-Raphson nonlinear algorithm is used to find a converged state at each analysis step; however, several techniques are implemented to address convergence issues that may arise during a response-history analysis. Firstly, the script contains if-statements which gradually reduce the time step to 1/100 of the initial value. If reducing the time step does not produce a converged solution for that analysis step, the analysis uses different solution algorithms to solve the nonlinear equations of motion including Modified Newton-Raphson, Krylov-Newton, and Broyden solution algorithms. If neither reducing the time step nor changing the nonlinear solution algorithm helps to find a converged state in that analysis step, the script tries one small linear (explicit) analysis step using stiffness values calculated during the last successfully converged step. After the small linear analysis step, the analysis returns to the implicit Newton-Raphson algorithm for future analysis steps. Because using a linear analysis step can result in the structure being in an unrealistic (i.e., not in equilibrium) state; results from an analysis that required a linear analysis step should be carefully reviewed to determine if the response is reasonable. In some instances, a small linear step is needed to get through a particularly tough situation in terms of convergence, after which the implicit methods can resume finding converged solutions for subsequent analysis steps. If the model does not go back to convergence after one linear step, the analysis stops.

7.10. Example Nonlinear Time-History Analysis

To demonstrate the results that can be obtained from a nonlinear response-history analysis, a sample bridge model and ground motion were assumed for a demonstration. A three-span simply-supported steel girder bridge was chosen. The length of the approach spans is 27 ft and the length of the main span is 37 ft. The superstructure consists of five W18x130 steel girders and a 40-ft-wide 8-in.-thick non-composite concrete deck. Each bent consists of three 30-in-diameter, 20.4-ft-

tall circular concrete columns tied together by concrete bent caps. Steel bearings were used in the model, with high-type fixed bearings at one end of the simply-supported spans, and high-type rocker bearings at the opposite end. Drilled shafts are used for foundations under both abutments and bents. Schematic drawing for the model is shown in Figure 7.53. Note, only elastic flexural elements (girders, bent caps, and columns) located at their respective centers of mass are shown in the figure. The connectivity is provided through zero-length elements and rigid links, not shown on the drawing.

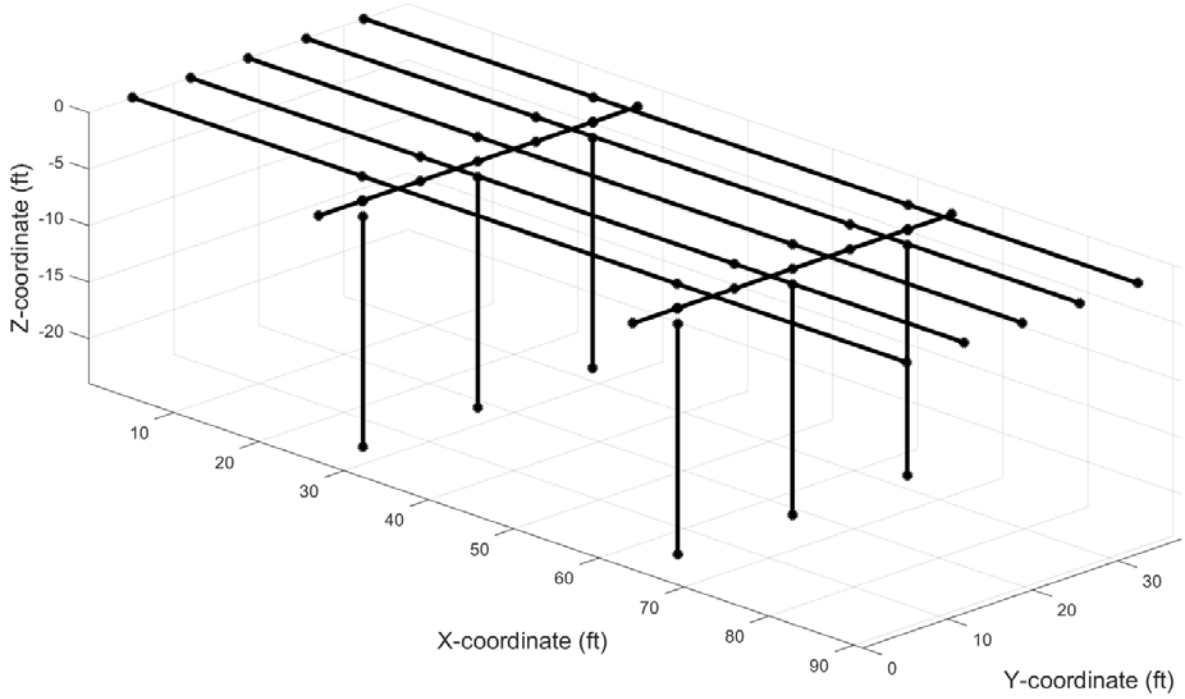

Figure 7.53: Bridge model schematic

Prior to execution of response-history analysis, an eigenvalue analysis was performed in order to obtain natural periods and mode shapes of the structure. Figure 7.54 shows the mode shape corresponding to the longest period of the structure (0.51 s). The displacements were deliberately amplified to make the mode shapes more prominent and do not represent realistic bridge deformations expected from seismic loading. Note, beam-column elements, are defined in the figure by drawing straight lines between two end nodes of a member. In the actual OpenSees model, flexural elements are assigned using appropriate finite-element shape functions, and internally simulate flexural deformations in elements. For the case of this bridge, the lowest mode of vibration is deck transverse displacement.

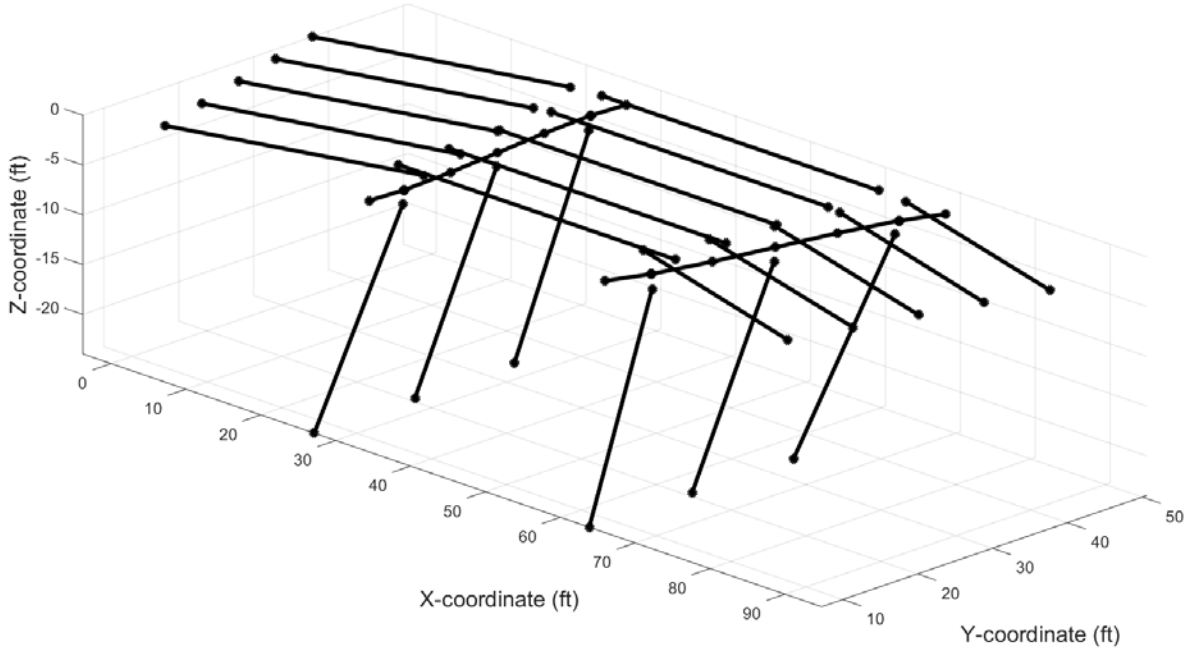

Figure 7.54: Bridge mode shape, transverse displacement (Period = 0.51 s)

Figure 7.55 shows the mode shape for the deck longitudinal direction movement. The natural period of this mode is 0.39 s. In this case, deck support stiffnesses are symmetric in the direction parallel to the translation, resulting in no deck rotation. Figure 7.56 shows the mode shape associated with bent out-of-phase transverse displacement, resulting in rotation of the middle span. The approach spans, on the other hand, translate without any rotation. The natural period of this mode is 0.35 s.

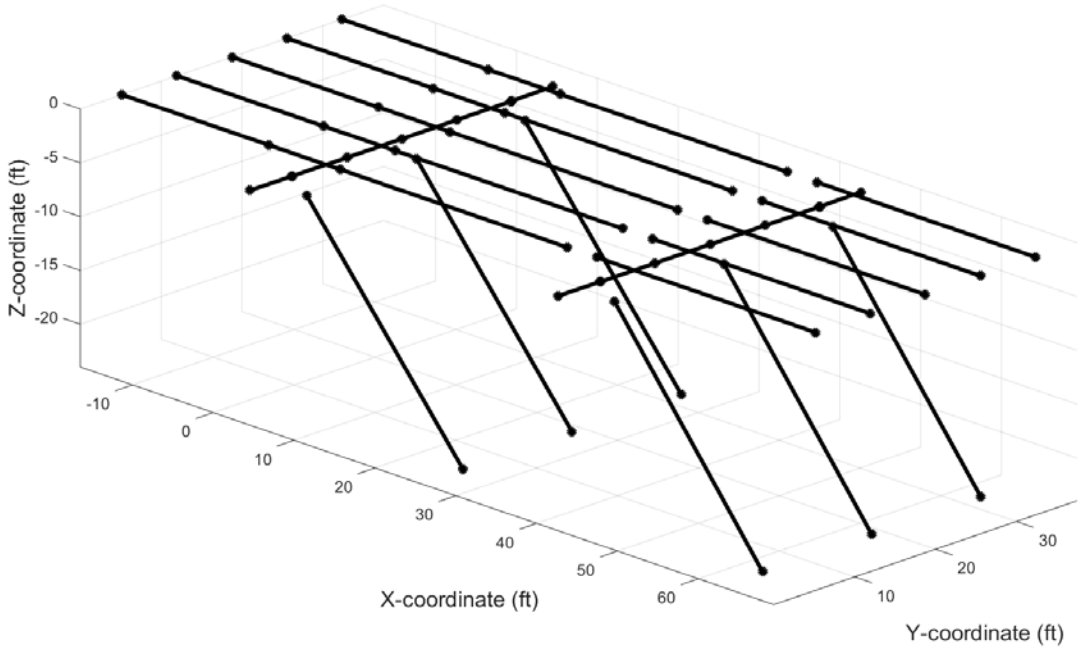

Figure 7.55: Bridge mode shape, longitudinal translation (Period = 0.39 s)

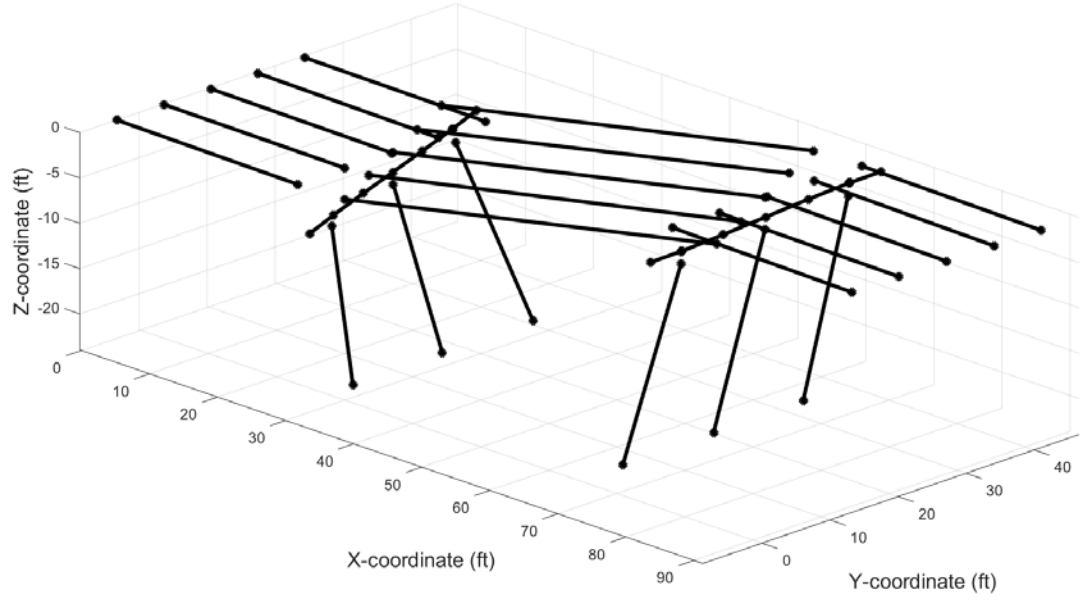

Figure 7.56: Bridge mode shape, rotation (Period = 0.35 s)

A ground motion time-history (shown in Figure 7.57) recorded during the 1994 Northridge earthquake was selected for this demonstration analysis (McKenna et al., 2006). The ground motion was applied at a 45-degree angle to the bridge span direction to invoke both longitudinal and transverse bridge deformations. The amplitude of the record was scaled by a factor of two, resulting in a maximum PGA of 0.84g to induce inelastic deformations in the nonlinear springs for demonstration purposes.

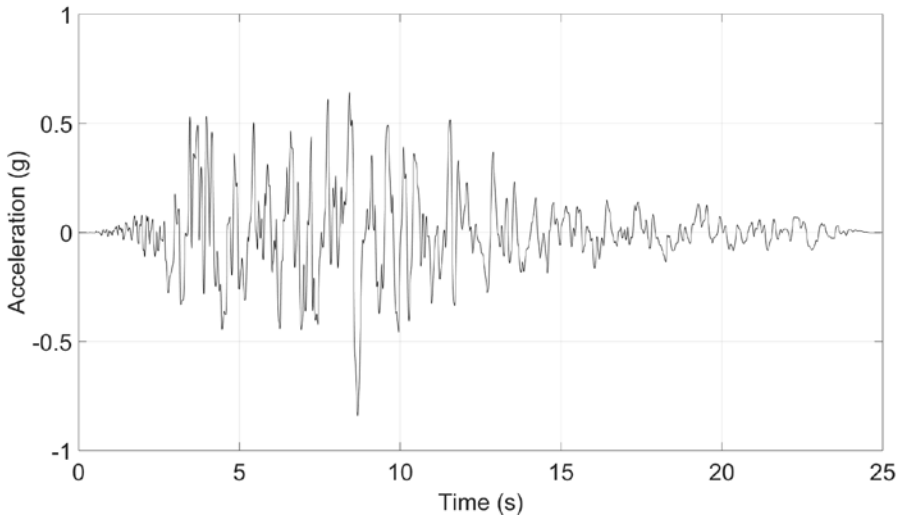

Figure 7.57: Sample ground motion history

Figure 7.58 shows the deck displacement response-history for all three bridge spans in the longitudinal direction. The displacement values are taken as the average displacements of the deck nodes over the middle girder at both ends of the spans. As evident in the figure, the simply-supported spans translate mostly in-phase with each other with similar periods of motion, though they have different amplitudes.

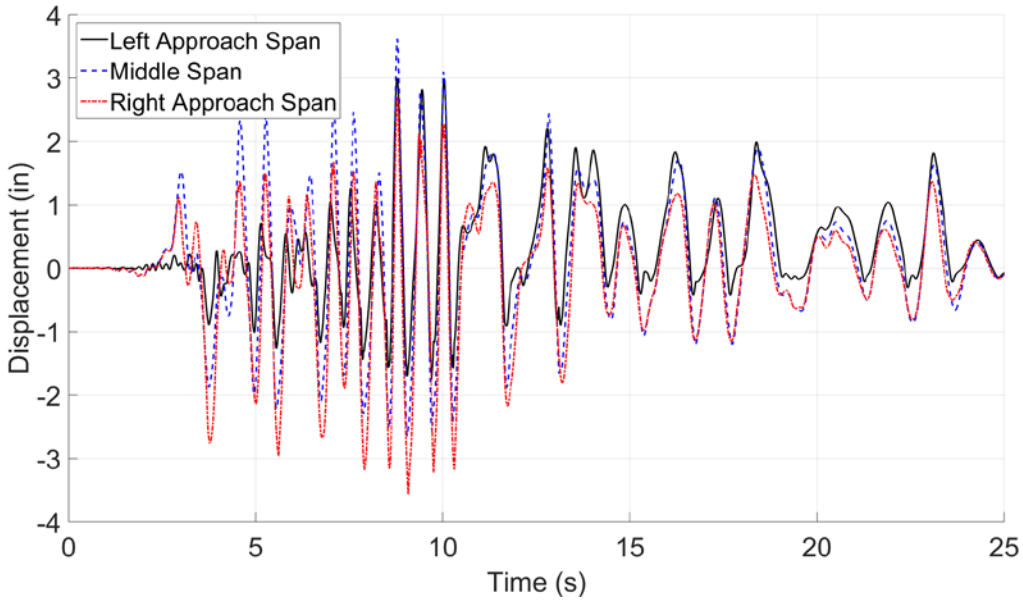

Figure 7.58: Deck displacement response-history (longitudinal direction)

Figure 7.59 shows the deck displacement response-history of the spans in the transverse direction. The transverse response has similar trends to the response in the longitudinal direction, except the period of vibration is noticeably higher, which is expected because the bridge natural period is longer in the transverse direction. Figure 7.60 shows the deck rotation response-history throughout the ground excitation. As shown in the plot, all three deck spans underwent small amounts of in-

plane rotation, including the middle span, which shows contribution of the third (rotational) mode to the overall bridge response. However, the amount of middle span rotation is negligible after the strong shaking phase (amplitudes less than 0.5g).

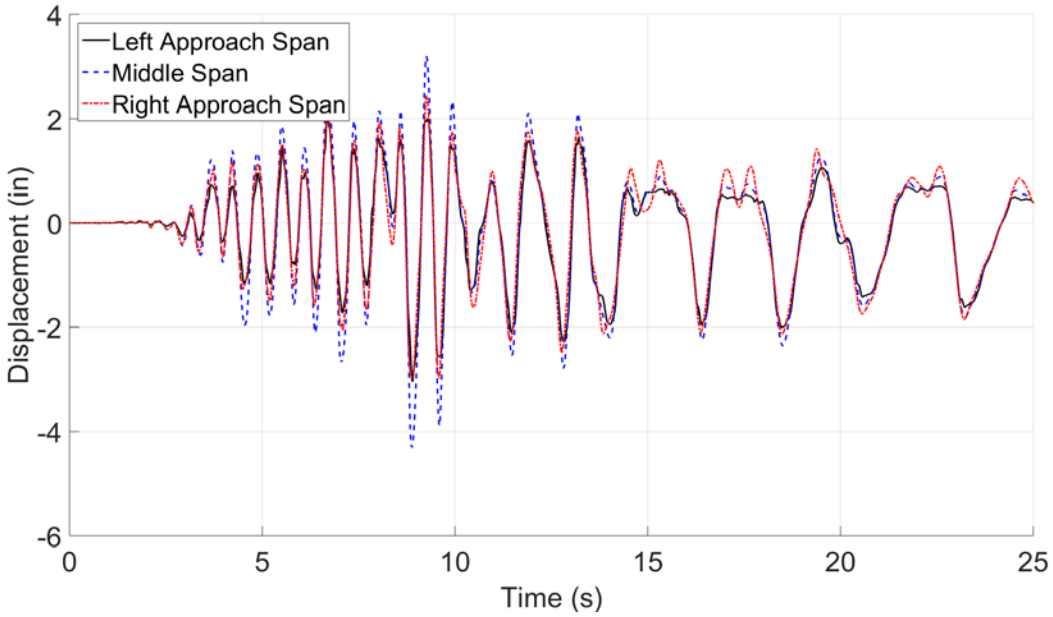

Figure 7.59: Deck displacement response-history (transverse direction)

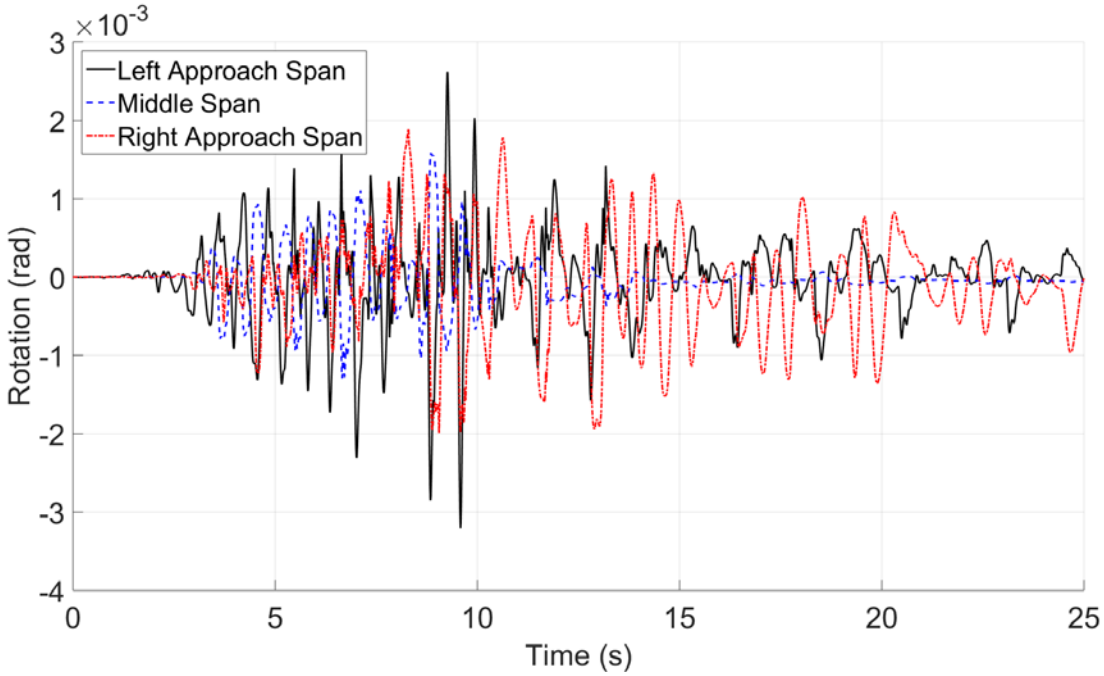

Figure 7.60: Deck rotation response-history

The displacement response-history is a general indicator of global bridge behavior; however, it does not provide any information about a structure's state of damage. To assess the bridge condition, the level of inelastic deformation, or lack thereof, needs to be quantified. For the models developed for this project all nonlinear effects are simulated with lumped plasticity (zero-length) springs. Each spring (column, bearing, foundation, etc.) needs to be assessed individually and the amount of inelastic deformation needs to be compared to selected limit states representing the levels of slight, moderate, extensive, and complete damage, which are described in detail in Chapter 8.4.

The bridge columns used in the example model were found to be flexure-controlled as previously described in Section 7.6.1. Figure 7.61 shows hysteretic plots of one of the bottom column springs in the longitudinal and transverse directions. Both springs exceeded their elastic capacities. The plastic rotation was higher in the longitudinal direction than in the transverse direction. Figure 7.62 displays hysteretic plots for one of the top column springs in both directions. The top longitudinal spring reached significantly lower moment demands compared to the bottom spring, confirming the initial assumption that bridge columns bend primarily in single curvature in the longitudinal direction. The moment demand in the top and bottom column springs in the transverse direction are more similar, though not equal, supporting the assumption that the column responds in double curvature in the transverse direction. Based on the plots in Figure 7.61 and Figure 7.62, hinging only occurred at the bottom of the column as indicated by the springs' nonlinear response.

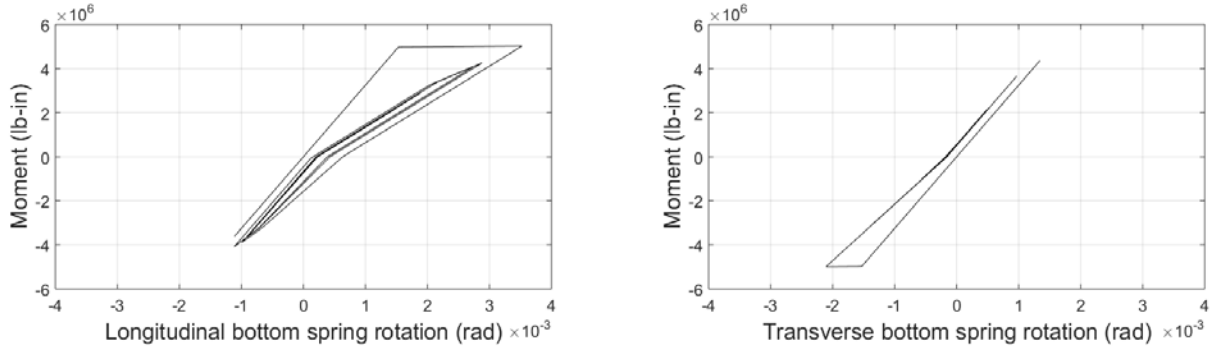

Figure 7.61: Column bottom spring hysteresis

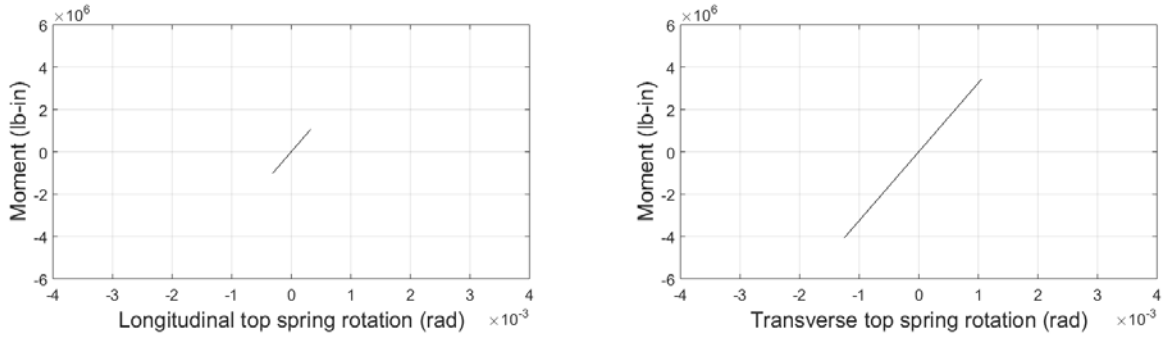

Figure 7.62: Column top spring hysteresis

Figure 7.63 displays the bearing bilinear spring response of one of the fixed bearings located at abutment. For the case of high-type fixed bearings, the bilinear spring represents prying behavior of masonry plate on rubber pad in both directions. Figure 7.64 shows the hysteretic response of the hysteretic element at the same bearing location in the longitudinal and transverse directions acting in parallel with the bilinear springs. In this case, the hysteretic spring represents resistance and deformation of bearing anchor bolts, which are shown to exhibit inelastic behavior in both directions in this demonstration analysis.

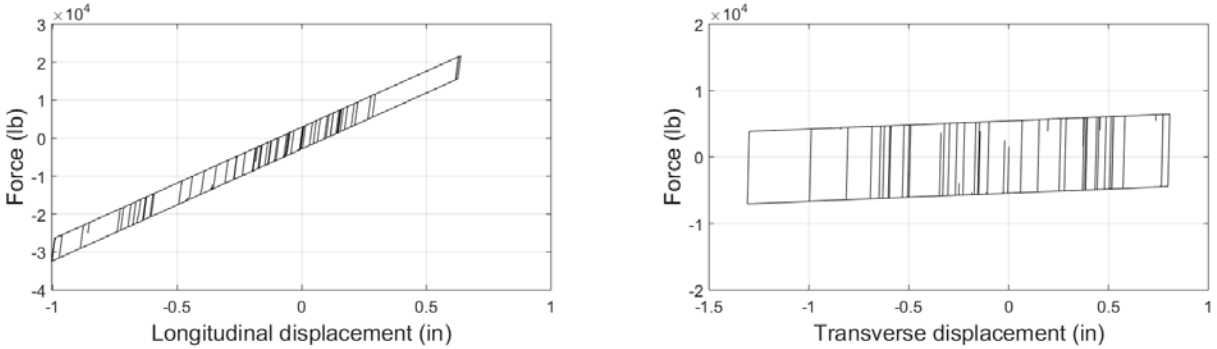

Figure 7.63: Fixed bearing bilinear spring hysteresis

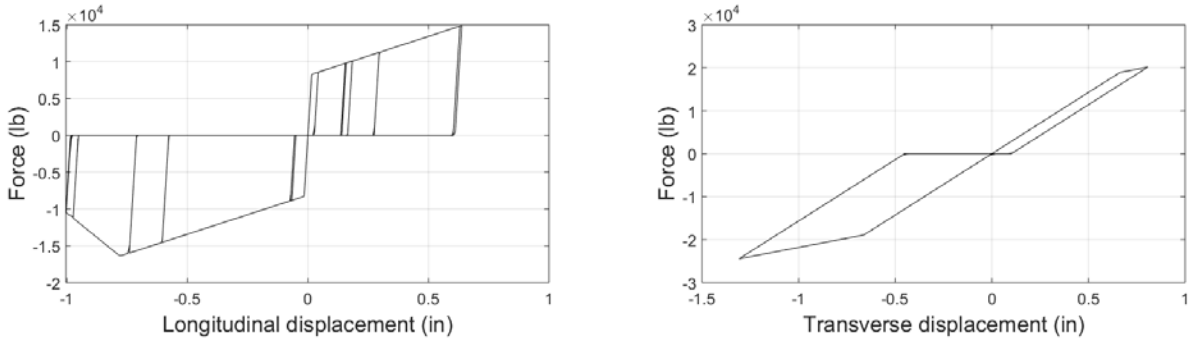

Figure 7.64: Fixed bearing hysteretic spring hysteresis

The following two figures present the response of one of the rocker expansion bearings on the opposite end (attached to the bridge bent) of the span for which the fixed bearing behavior was just shown. Figure 7.65 shows the bilinear spring response, where the behavior in the longitudinal direction represents rocking of the bearing, and the behavior in the transverse direction represents masonry plate prying. Figure 7.66 shows the behavior of the hysteretic element. Because there is no restraint in rocker bearings in the longitudinal direction, only the transverse restraint spring is used. The expansion bearings at the bent location experienced relatively small displacements in the transverse direction with the hysteretic element remaining elastic.

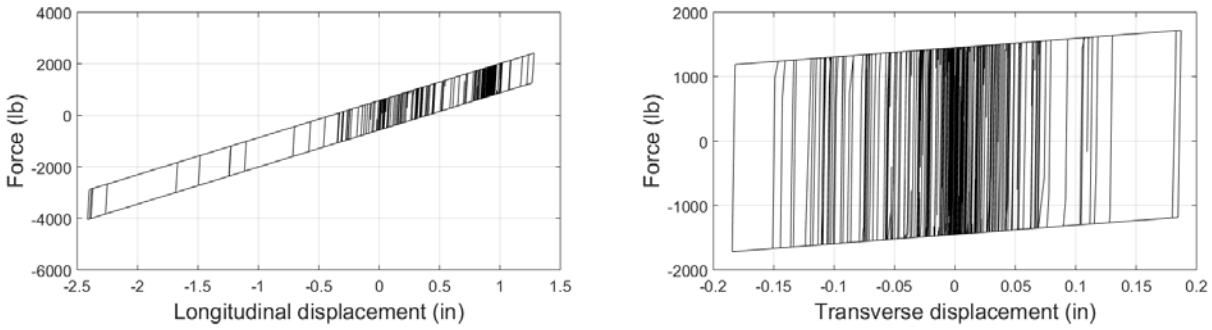

Figure 7.65: Rocker bearing bilinear spring hysteresis

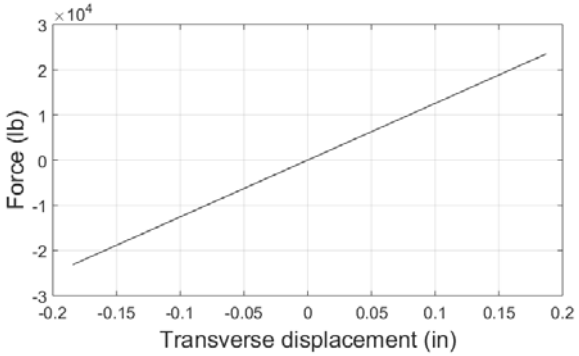

Figure 7.66: Rocker bearing hysteretic spring hysteresis

Figure 7.67 shows the impact spring response at both abutment locations. As evident in the figure, 1-in. gaps between deck and backwall were fully closed during the excitation. The impact force, however, was not high enough to exceed elastic capacity of the springs, meaning there was no concrete spalling caused by pounding. Figure 7.68 shows the longitudinal backwall soil resistance at both abutment locations. As shown, the soil backfill at one of the abutments experienced inelastic behavior.

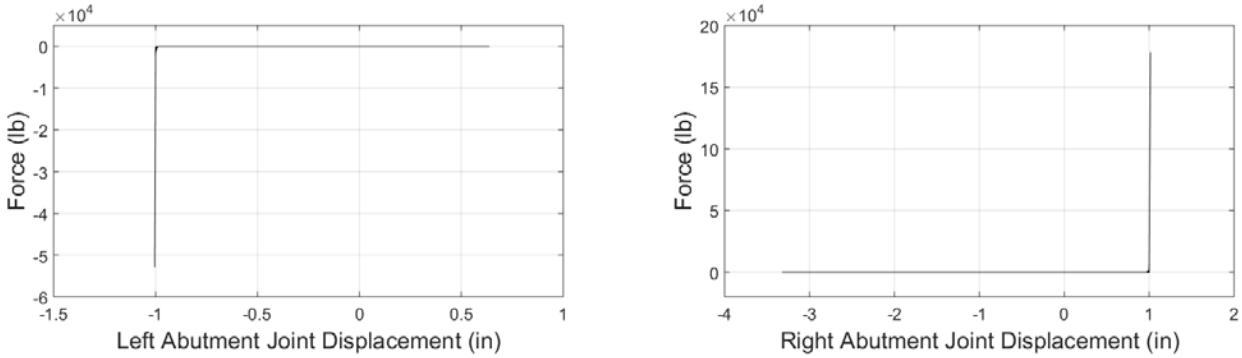

Figure 7.67: Impact spring hysteresis

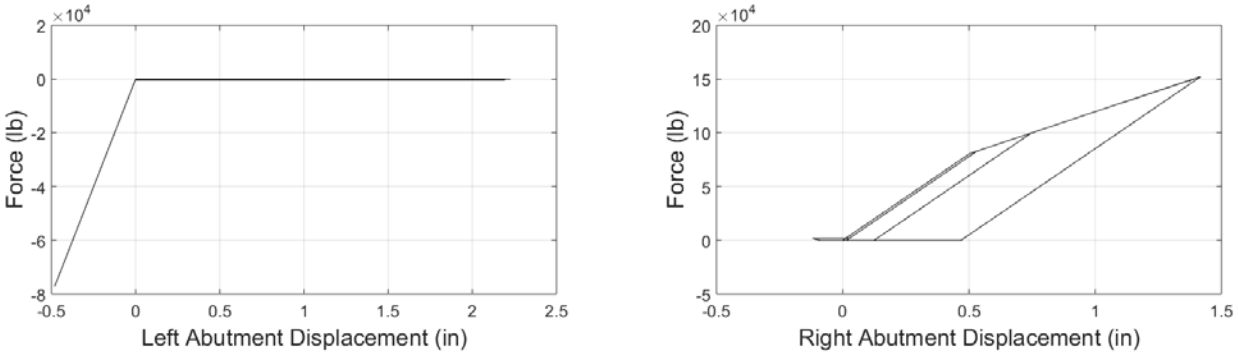

Figure 7.68: Abutment soil spring hysteresis

Figure 7.69 depicts behavior of a drilled shaft under one of the abutments, experiencing inelastic behavior in both orthogonal directions. Figure 7.70 shows the drilled shaft behavior under a bent column. Similarly, both springs experienced inelastic deformations.

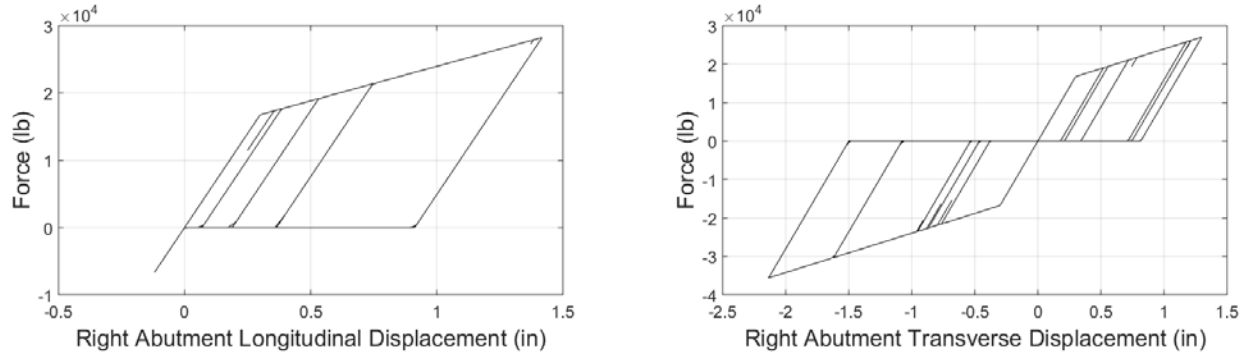

Figure 7.69: Abutment shaft spring hysteresis

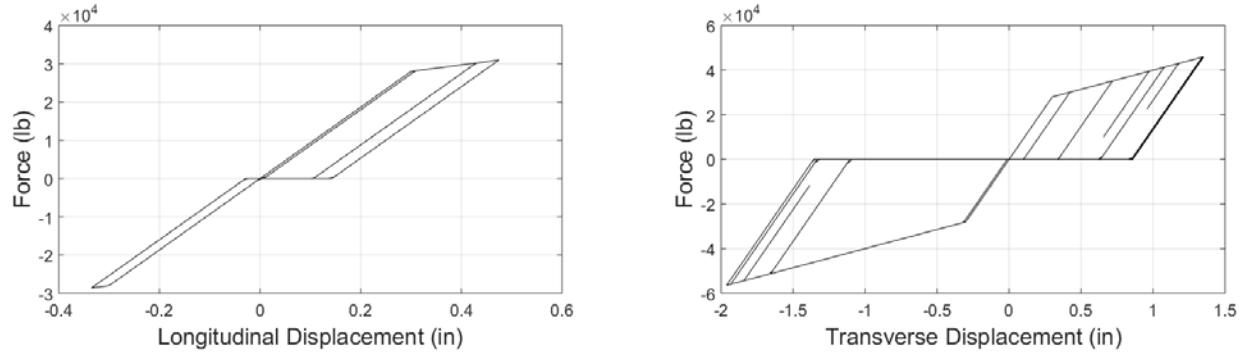

Figure 7.70: Bent shaft spring hysteresis

7.11. Model Properties of Representative Bridges

In the following, the fundamental period and mode shapes of the sampled bridges (see Section 6.5 for details) are discussed. The natural frequency of a system is an inherent property of the system that is dependent only on the initial stiffness of the structure and its seismic mass. It is not dependent on the load function. The natural period of a structure can be used to approximate peak

force and displacement demands using ground motion and/or design response spectra with other simplifications to account for multiple mass degrees of freedom and nonlinear effects (Chopra 2012).

7.11.1. Steel Girder Bridges

Table 7.3 present the fundamental periods for steel girder bridges, i.e., MCSTEEL and MSSTEEL classes. In particular, this table shows the minimum, average, and maximum of the fundamental (i.e., first mode) periods of the eight bridges that are generated for each bridge geometric configuration. Detailed information on the geometric configurations of MCSTEEL and MSSTEEL bridges can be found in Table 6.17 and Table 6.18, respectively. As seen in the table, the fundamental translational period of MCSTEEL bridges varies between 0.32 second and 0.80 second. According to Table 6.17, these values are associated with bridge configurations that have the shortest and longest span lengths. In fact, by investigating the effect of the geometric and material parameters on the natural period of the bridges, it is found that the span length is the most important factor, which is mainly because of the fact that span length controls the amount of the mass of the bridges. Therefore, longer span lengths tend to result in larger masses, without significant changes in lateral stiffnesses. It is worth noting that by looking into the mode shapes of the bridges in this class, the longitudinal translation mode (similar to the one shown in Figure 7.55, is the fundamental mode for the majority of the bridge models; however, some of the bridge models have a fundamental mode shape representative of transverse direction translation (similar to the one shown in Figure 7.54).

For MSSTEEL bridge classes, Table 7.3 shows that the fundamental period varies between 0.26 and 0.42 second. Although the 0.42 second period is associated with the bridge geometric configuration that has the longest span length, the 0.26 second period is for geometric configuration number 5, which, according to Table 6.18, does not have the shortest span length. In fact, the span length (and thus the mass as described previously) is not the only factor that controls the fundamental period. For this bridge class, other parameters such as deck width (and thus number of columns), under clearance (and thus column height), as well as girder type and size have a significant effect on the bridge stiffness, and thus its period. Similar to the MCSTEEL class previously described, the fundamental (i.e., first) mode of the majority of MSSTEEL bridges are modes associated with longitudinal direction translation, Finally, it is worth noting that MSSTEEL bridges generally have lower periods compared to MCSTEEL bridges, which is mainly due to the fact that MCSTEEL bridges have continuous and longer spans, which results in more mass without significant changes in lateral stiffness.

Table 7.3: Fundamental period of steel girder bridges in the horizontal direction

Geometric Configurations	T_n (second)					
	MCSTEEL			MSSTEEL		
	Min	Average*	Max	Min	Average*	Max
1	0.32	0.34	0.36	0.30	0.32	0.37
2	0.46	0.50	0.52	0.30	0.32	0.33
3	0.42	0.45	0.47	0.36	0.39	0.42
4	0.42	0.44	0.49	0.30	0.33	0.35
5	0.30	0.32	0.34	0.26	0.27	0.29
6	0.49	0.53	0.57	0.35	0.35	0.36
7	0.37	0.40	0.44	0.26	0.28	0.30
8	0.70	0.74	0.80	0.29	0.32	0.34

*This parameter refers to the average of the eight generated samples corresponding to each bridge geometric configuration.

7.11.2. Concrete Girder Bridges

Table 7.4 shows the fundamental periods of reinforced and prestressed concrete girder bridges in the horizontal direction. As seen in the table, the fundamental period varies between 0.50 to 1.07 seconds, and 0.36 to 1.18 seconds for MSPC and SSPC girder bridges, respectively. For reinforced concrete bridges, this range is between 0.12 to 0.52 second. In fact, reinforced concrete bridges are much stiffer than prestressed concrete girder bridges, mainly because of the bearing type. Prestressed concrete girder bridges contain elastomeric bearings which are more flexible than concrete-to-concrete friction bearings used in reinforced concrete girder bridges. For more information on the bearing types and modeling parameters, see Sections 6.4.4 and 7.5. Moreover, it is worth noting that for concrete girder bridges considered in this study, the longitudinal translation mode shape controls the fundamental period of the bridges.

Table 7.4: Fundamental period of reinforced and prestressed concrete girder bridges

Geometric Configurations	MSPC			SSPC			MSRC		
	Min	Average*	Max	Min	Average*	Max	Min	Average*	Max
1	0.57	0.64	0.73	0.36	0.45	0.58	0.39	0.41	0.43
2	0.91	1.07	1.26	0.75	0.92	1.13	0.47	0.49	0.52
3	0.70	0.81	1.00	0.41	0.54	0.69	0.26	0.29	0.32
4	0.50	0.59	0.69	0.59	0.73	0.96	0.12	0.16	0.21
5	0.62	0.75	0.92	0.72	0.86	1.13	0.19	0.21	0.24
6	0.80	0.96	1.17	0.49	0.60	0.73	0.28	0.31	0.37
7	0.67	0.80	1.07	0.75	0.91	1.16	0.20	0.22	0.25
8	0.66	0.81	1.05	0.72	0.88	1.18	0.28	0.31	0.36

*This parameter refers to the average of the eight generated samples corresponding to each bridge geometric configuration.

7.11.3. Concrete Slab Bridges

Table 7.5 shows the fundamental periods of reinforced concrete slab bridges. As seen in the table, for continuous slab bridges, the fundamental period varies between 0.13 to 0.42 seconds, which correspond respectively to geometric configuration 5 with the shortest span length and geometric configuration 2 with the longest span length. For simply-supported spans, the fundamental period varies between 0.09 to 0.38 second. Like steel girder bridges, the continuous bridges have higher natural period, which is mainly because of longer spans and larger masses without significant changes in lateral bridge stiffness.

Moreover, concrete slab bridges have lower periods compared to other bridge classes including steel girder bridges (MCSTEEL and MSSTEEL), prestressed concrete girder bridges (MSPC and SSPC), and reinforced concrete girder bridges (MSRC). This observation is mainly owing to the fact that slab bridges have generally shorter spans and stiffer bearings. In fact, slab bridges consist of concrete-to-concrete friction bearings, which are much stiffer than steel bearings in steel girder bridges and elastomeric bearings in prestressed concrete bridges. Finally, it is worth noting that their fundamental modes in these concrete slab bridge classes are different from the ones discussed in other bridge classes. In fact, for most of simply-supported reinforced concrete slab bridge (MSRC-Slab), the transverse mode shape forms the fundamental mode shape of the bridges.

Table 7.5: Fundamental period of reinforced concrete slab bridges

Geometric Configurations	T_n (second)					
	MCRC-Slab			MSRC-Slab		
	Min	Average*	Max	Min	Average*	Max
1	0.16	0.19	0.26	0.09	0.11	0.15
2	0.27	0.32	0.42	0.24	0.25	0.27
3	0.16	0.20	0.27	0.18	0.21	0.23
4	0.17	0.21	0.28	0.34	0.36	0.38
5	0.13	0.17	0.22	0.18	0.20	0.21
6	0.15	0.18	0.25	0.20	0.21	0.22
7	0.15	0.19	0.25	0.19	0.20	0.23
8	0.18	0.22	0.29	0.13	0.15	0.20

*This parameter refers to the average of the eight generated samples corresponding to each bridge geometric configuration.

7.12. Summary

In this chapter, the numerical models developed to simulate the seismic behavior of Texas bridges are presented. OpenSees was selected as the structural analysis framework for the study due to its computational efficiency, broad availability of material and element models, as well as code-based input which allows the models to be created through automated scripts. Automated model creation is a significant benefit for this study due to large number of different response-history analyses that need to be performed for fragility curve development. Three-dimensional modeling was selected for bridge models to capture various damage limit states in both longitudinal and transverse directions.

Bridge girders were modeled as elastic beam-column elements with corresponding mass and cross-sectional properties assigned to them. The mass of the deck and bridge railings was lumped in deck nodes connected to girder elements with rigid links. Deck pounding effects between adjacent simply-supported spans, as well as pounding between the superstructure and abutment backwalls was modeled using nonlinear translational springs in the direction parallel to bridge span (longitudinal direction). Bridge bearings were modeled with nonlinear springs in the longitudinal and transverse directions. One spring has a bilinear material assigned to it, simulating effects of bearing sliding, rocking, or prying, while the other spring has a nonlinear hysteretic material assigned to it to simulate the resistance and damage associated with restraining elements such as anchor bolts, pintles, and dowels. Bent columns were simulated as lumped plasticity elements, i.e., they were modeled with elastic beam-column elements with nonlinear rotational springs on both ends. The rotational springs capture both flexural and shear damage (whichever occurs at a lower demand). Spring rotational capacities are calculated based on column concrete strength, axial load, longitudinal and transverse reinforcement, and reinforcement development/anchorage. Hysteretic unloading/reloading and stiffness degradation parameters were calibrated based on available experimental data. Foundations under bents and abutments were modeled with translational

springs in the longitudinal and transverse directions using nonlinear hysteretic materials representing pile or shaft behavior. Effects of soil-structure interaction were ignored due to high uncertainty about soil behavior as well as variability in foundation design. The effects of soil passive resistance when the abutment backwall is displacing toward the soil were simulated with nonlinear longitudinal translational springs at both bridge ends. Soil active resistance (the abutment displacing away from the soil) was ignored due to soil negligible tensile strength. Resistance in the transverse direction was not included as well. Example results from a nonlinear response-history analysis of a bridge were shown for demonstration, and dynamic properties (i.e., fundamental periods and mode shapes) were presented for the bridge samples used in this study.

Chapter 8. Fragility Curves

8.1. Overview

In this chapter, nonlinear response history analyses (NRHAs) are conducted for bridge samples that are generated in Chapter 6. Each of these bridge samples is subjected to unique ground motion pairs (i.e., multi-directional shaking) representative of Texas seismic hazards. The outputs of the NRHAs are set as input for computational probabilistic models, such as Monte Carlo simulation, to produce bridge component fragility curves, as well as system-level bridge fragility curves for each bridge class. These fragility curves can be used to estimate the likelihood of damage in Texas bridges following an earthquake, which can help to inform post-event actions and inspection prioritization and to identify bridge components and classes that are most vulnerable to earthquake shaking.

8.2. Analytical Fragility Procedure

Vulnerability assessment in this study is done using fragility functions. Fragility functions provide the conditional probability that gives the likelihood of whether a structure meets or exceeds a pre-defined level of damage (limit states) given a ground motion intensity measure. In this study, Peak Ground Acceleration (PGA) is used as ground motion intensity measure. These fragility functions can be then used to make retrofit decisions, to make post-earthquake inspection decisions, and to estimate the total loss of the bridges after an earthquake. In this study, the fragility curves are used to give guidance for post-earthquake inspection decisions for Texas bridges. Fragility curves can be developed following three main methodologies (1) expert based fragility functions, (2) empirical fragility functions, and (3) analytical fragility functions.

Expert based fragility curves were first developed in the 1980's, when the Applied Technology Council (ATC) put together a panel of 42 experts in order to develop damage probability matrices for various components of California infrastructure (ATC 1985). These matrices provided estimations of damage likelihood given certain ground motion intensity based on judgement and experience-level of each expert. This method was used again in the work of Padgett and DesRoches (2007) to develop improved bridge functionality relationships to be used in fragility analysis. Expert based fragility functions rely solely on the experience and the number of experts involved, which brings about a major concern of subjectivity. Due to these concerns, and the collection of post-earthquake damage data, and the development of analytical probabilistic models, this method is rarely used.

Empirical fragility curves are developed from actual earthquake damage data. Following the 1989 Loma Prieta, 1994 Northridge, and the 1995 Kobe earthquakes, the empirical method became fairly popular. Examples of empirical fragility curves can be found in the studies of Basoz and Kiremidjian (1996), Yamazaki et al. (1999), Der Kiureghian (2002), Shinozuka et al. (2003), and Elnashai et al. (2004). Although this method provides a very realistic risk assessment of earthquake

damage, it does have its limitations. These limitations being, (i) statistical insignificant results due to small sample sizes and (ii) inconsistencies in the post-earthquake assessments as different inspectors could report different levels of damage. This methodology is not feasible for Texas because of lake of available data that has been reported because of earthquake.

When actual post-earthquake damage and ground motion data is not available, analytical methods must be used to develop fragility curves. Throughout the last decade researchers have been developing and using analytical methodologies and procedures to generate fragility curves (Choi 2002; de Felice and Giannini 2010; Karim and Yamazaki 2003; Mackie and Stojadinović 2001; Nielson and DesRoches 2007a; Nielson 2005; Pan 2007; Ramanathan 2012; Shinozuka et al. 2000a). Analytical fragility functions can be generated using seismic response data from elastic-spectral analysis, non-linear static analysis, or non-linear time history analysis. Despite being one of the most computationally demanding methods, the non-linear time history method is often viewed as one of the more reliable methods available (Shinozuka et al. 2003). This methodology forms the framework used in the present vulnerability assessment.

This study utilizes a probabilistic framework, which considers uncertainty in ground motions and local soil conditions, as well as uncertainty in design and detailing practices over the past several decades when the bridge population was constructed. In this framework, fragility functions are provided to evaluate the vulnerability of Texas bridges to these natural and induced seismic hazards. There are three key parameters in this framework as follows: structural demand, *D*, which refers to the responses of the bridges from nonlinear time-history analysis; structural capacity, C; and the probability of the damage, p_f, which is the probability that the structural demand, *D*, meets or exceeds the structural capacity, C, and reads:

$$p_f = P\left[\mathrm{D/C} > 1 \mid \mathrm{PGA}\right] \tag{8-1}$$

Assuming lognormal distributions for demand and capacity, Cornell et al. (2002) showed that the above-mentioned probability can be computed using the following equation:

$$p_f = \Phi\left[\frac{\ln(S_\mathrm{D}/S_\mathrm{C})}{\sqrt{\beta_{\mathrm{D|PGA}}{}^2 + \beta_\mathrm{C}{}^2}} \mid \mathrm{PGA}\right] \tag{8-2}$$

where S_D and $\beta_{\mathrm{D|PGA}}$ are, respectively, the median and logarithmic dispersion of the seismic demands conditioned on PGA, and S_C and β_C are, respectively, the median and dispersion of the capacity and Φ is the standard normal cumulative distribution function. Therefore, to compute the probability of damage, statistical models are required to estimate the median and dispersion of the seismic demands and capacities.

The main steps to produce analytical fragility curves are shown in Figure 8.1. To take into account the uncertainty in the ground motion, the first step is to obtain a suite of ground motions that represent the seismic hazards of the studied area (Chapter 4). Second, bridge samples are randomly generated to be statistically representative of the Texas bridge inventory (Chapter 6). Recall that this study classified the Texas bridges into seven different classes that the bridges in each class have similar seismic behavior. For each bridge class, 64 bridge samples are generated by taking

into account the uncertainty in geometric as well as modeling parameters (Chapter 6). Each selected bridge sample is simulated with a nonlinear computational model (Chapter 7) and is subjected to a randomly selected ground motion that is scaled to various PGA levels. Then, for each ground motion-bridge pair, a nonlinear time history analysis is conducted for a variety of PGA levels.

The outputs of the nonlinear analyses, the PGA of the selected ground motion, and the demands of different components (e.g., bearing deformations, abutment deformations, and column rotations) are set as an input for the probabilistic seismic demand model (PSDM) to predict the S_D and $\beta_{D|PGA}$ for each bridge component. In addition, for each component, the probabilistic seismic capacity model (PSCM) is developed to predict S_C and β_C. Having both PSDM and PSCM for each component, the fragility curves can be computed using Eq. (8-2). Finally, by developing the fragility curves for each component, the fragility functions for a particular bridge class can be computed. The first two steps of this numerical fragility procedure, including ground motion and bridge selection and bridge nonlinear modeling, were discussed in detail in the previous chapters (Chapter 4, 6, and 7, respectively). The other steps are described in detail in the following sections.

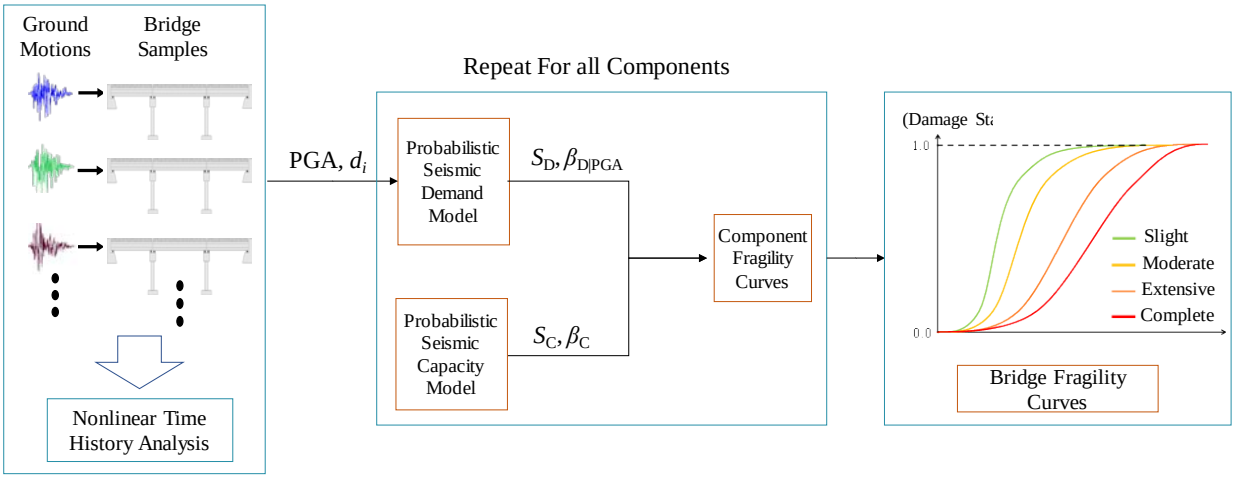

Figure 8.1: Analytical fragility function procedure

8.3. Probabilistic Seismic Demand Model

Probabilistic Seismic Demand Models (PSDMs) establish a relationship between the component demands (e.g., plastic rotation of column, bearing displacement, abutment displacement, etc.) and the selected ground motion intensity measure, which can be used to develop component level fragility functions. PSDMs are developed by recording peak component demands, d_i, from each ground motion-bridge model pair, and by plotting the demand versus the ground motion intensity measure values for that ground motion. Cornel et al. (2002) showed that the median of seismic demands tends to follow a power function of intensity measure as follows:

$$S_D = a\text{PGA}^b \tag{8-3}$$

This equation can be transformed to logarithm space where $\ln(S_D)$ follows a linear function with respect to PGA, with an intercept of $\ln(a)$ and a slope of b as follows:

$$\ln(S_D) = \ln(a) + b \times \ln(\text{PGA}) \tag{8-4}$$

Figure 8.2 presents a schematic of a typical PSDM as well as the linear function of Eq. 8.3 through the peak demand data obtained from nonlinear response-history analyses. As seen in the figure, coefficients *a* and *b* can be computed by fitting a linear regression to the lognormal of the outputs from nonlinear time history analyses.

Cornell et al. (2002) proposed that the conditional seismic demands typically follow a lognormal distribution, resulting in normal distribution with median of ln(S_D) and dispersion of $\beta_{D|PGA}$, in the transformed space (Figure 8.2). The variation or dispersion of the seismic demands about the mean, given the intensity measure, is the conditional lognormal standard deviation of the seismic demand ($\beta_{D|PGA}$). According to Padgett et al. (2008), $\beta_{D|PGA}$ is approximately estimated by computing the dispersion of the data around the fitted linear regression using the following equation:

$$\beta_{D|IM} = \sqrt{\frac{\sum_{i=1}^{N}[\ln(d_i) - \ln(S_D)]^2}{N-2}} \tag{8-5}$$

Recall that in this study, the seismic demands of columns, bearings, and abutments are recorded. In particular, the seismic demands comprise the plastic rotation of columns, the longitudinal and transverse deformations of bearings, and deformations in passive, active, and transverse directions of abutments. The parameters of the PSDM for the aforementioned seismic demands are shown in Table 8.1 through Table 8.7 for the different bridge classes considered in this study.

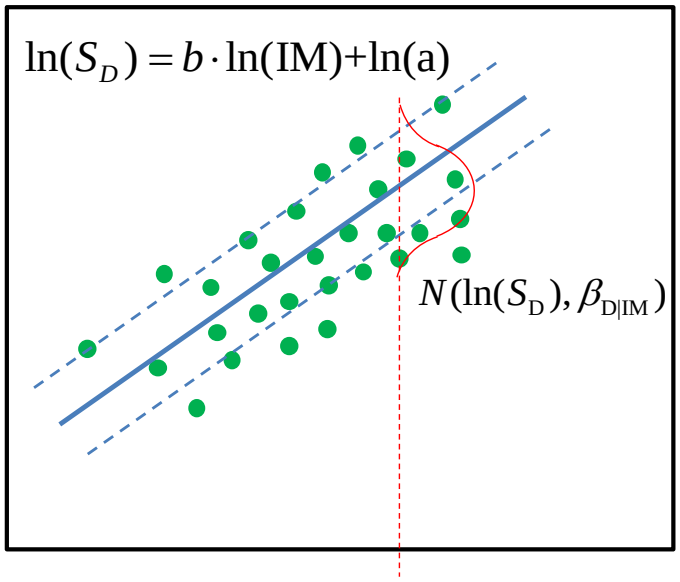

Figure 8.2: Illustration of parameters of the PSDM in the transformed space

Table 8.1: PSDM parameter estimations for MCSTEEL bridges

Component	Abbreviation	a	b	$\beta_{D\|PGA}$
Column	Rot	0.003	1.03	1.10
Fixed bearing-Long.	fx_L	0.11	0.92	1.11
Fixed bearing-Trans.	fx_T	0.48	1.50	1.19
Expan. bearing-Long.	ex_L	1.23	0.69	0.74
Expan. bearing-Trans.	ex_T	0.48	1.16	0.89
Abutment-Active	abut_A	0.03	0.23	0.69
Abutment-Passive	abut_P	0.02	0.58	1.37
Abutment-Trans.	abut_T	0.33	0.40	0.82

Table 8.2: PSDM parameter estimations for MSSTEEL bridges

Component	Abbreviation	a	b	$\beta_{D\|PGA}$
Column	Rot	0.0027	0.96	0.92
Fixed bearing-Long.	fx_L	0.58	1.19	0.84
Fixed bearing-Trans.	fx_T	0.65	1.70	0.98
Expan. bearing-Long.	ex_L	1.26	0.83	0.67
Expan. bearing-Trans.	ex_T	0.52	1.59	0.98
Abutment-Active	abut_A	0.07	0.41	1.24
Abutment-Passive	abut_P	0.05	0.65	1.43
Abutment-Trans.	abut_T	0.12	0.46	0.54

Table 8.3: PSDM parameter estimations for MSPC bridges

Component	Abbreviation	a	b	$\beta_{D\|PGA}$
Column	Rot	0.003	0.98	0.91
Fixed bearing-Long.	fx_L	1.28	1.02	1.09
Fixed bearing-Trans.	fx_T	1.31	1.19	1.19
Expan. bearing-Long.	ex_L	1.43	0.89	0.88
Expan. bearing-Trans.	ex_T	1.35	1.19	1.07
Abutment-Active	abut_A	0.08	0.40	0.97
Abutment-Passive	abut_P	0.16	0.88	1.41
Abutment-Trans.	abut_T	0.11	0.54	0.89

Table 8.4: PSDM parameter estimations for MSRC bridges

Component	Abbreviation	a	b	$\beta_{D\|PGA}$
Column	Rot	0.0026	1.2	1.01
Fixed bearing-Long.	fx_L	0.52	1.32	0.95
Fixed bearing-Trans.	fx_T	0.15	1.72	1.35
Expan. bearing-Long.	ex_L	0.84	1.19	0.67
Expan. bearing-Trans.	ex_T	0.40	2.08	1.14
Abutment-Active	abut_A	0.14	0.36	0.59
Abutment-Passive	abut_P	0.22	0.79	0.86
Abutment-Trans.	abut_T	0.11	0.47	0.53

Table 8.5: PSDM parameter estimations for SSPC bridges

Component	Abbreviation	a	b	$\beta_{D\|PGA}$
Fixed bearing-Long.	fx_L	2.03	0.98	0.85
Fixed bearing-Trans.	fx_T	1.42	1.03	0.93
Expan. bearing-Long.	ex_L	1.81	0.90	0.83
Expan. bearing-Trans.	ex_T	1.42	1.03	0.93
Abutment-Active	abut_A	0.08	0.17	0.71
Abutment-Passive	abut_P	0.30	0.82	0.88
Abutment-Trans.	abut_T	0.09	0.41	0.83

Table 8.6: PSDM parameter estimations for MCRC-slab bridges

Component	Abbreviation	a	b	$\beta_{D\|PGA}$
Column	Rot	0.0028	0.96	0.94
Fixed bearing-Long.	fx_L	0.00	0.80	0.96
Fixed bearing-Trans.	fx_T	0.01	1.10	1.06
Expan. bearing-Long.	ex_L	0.68	1.42	0.95
Expan. bearing-Trans.	ex_T	0.67	1.77	1.12
Abutment-Active	abut_A	0.11	0.17	0.46
Abutment-Passive	abut_P	0.08	0.38	0.81
Abutment-Trans.	abut_T	0.10	0.15	0.47

Table 8.7: PSDM parameter estimations for MSRC-slab bridges

Component	Abbreviation	a	b	$\beta_{D\|PGA}$
Column	Rot	0.003	0.95	0.91
Fixed bearing-Long.	fx_L	0.37	1.18	0.93
Fixed bearing-Trans.	fx_T	0.16	1.49	1.40
Expan. bearing-Long.	ex_L	0.72	1.19	0.66
Expan. bearing-Trans.	ex_T	0.63	1.97	1.01
Abutment-Active	abut_A	0.05	0.22	0.54
Abutment-Passive	abut_P	0.09	0.71	1.11
Abutment-Trans.	abut_T	0.05	0.29	0.53

8.4. Probabilistic Seismic Capacity Model

For each component, four levels of damage (i.e., limit states) are defined as slight, moderate, excessive, and complete. The first step in developing the capacity models requires establishing a qualitative definition for each damage state. In past bridge fragility studies, it is common to adopt the damage states used in the FEMA loss assessment package HAZUS-MH (Choi 2002; Nielson 2005; Padgett 2007; Tavares et al. 2013) to ensure compatibility between the developed fragility functions and the HAZUS framework. Engineering judgment can, however, be used in refining these damage states as they can vary greatly depending on the condition, age, and type of the structure (Choi et al. 2004). The qualitative definitions for the slight, moderate, extensive, and complete damage states as given in HAZUS can be found in Table 8.8. These qualitative descriptions are given in terms of visual damage indicators for various components, and in some cases indications of potential component failures and loss of load-carrying capacity. The qualitative damage state definitions adopted in this study (Table 8.8) follow the HAZUS framework, with slight modifications in terminology to be more consistent with the TxDOT Bridge Inspection Manual and the TxDOT “Elements” Field Inspection and Coding Manual.

Table 8.8: Qualitative damage state descriptions considering Texas specific details

Damage State	Description
Slight	Minor cracking and spalling of the abutments, appearance of minor cracking at bridge seat, minor inelastic deformation of elastomeric bearing, minor spalling and cracking of columns (damage requires no more than cosmetic repair, and no exposed reinforcing), or minor cracking of the deck (distressed area less than 2% of deck area).
Moderate	Any column experiencing moderate (shear cracks) cracking and spalling (column still sound structurally), moderate movement of the abutment (<2″), prying of masonary plate (e.g., moderate cracking or spalling of bearing area) or severaly bent anchor bolts, rocker bearing instability, or moderate approach settlement.
Extensive	Any column degrading without collapse-shear failure, (column structurally unsafe), significant inelastic bearing displacement, anchor bolt failure, bearing instability iminent (e.g., overturned bearing), extensive elastomeric pad damage, major approach settlement, vertical offset of the abutment
Complete	Any column collapsing, any bearing no longer supported which may lead to imminent deck collapse, tilting of substructure caused by foundation failure.

After defining qualitative limit states, the next step in developing capacity models is determining quantitative metrics to evaluate the occurrence of the described limit states. Quantification of these damage metrics is often based on individual component capacities or limit states, and then these limit state capacities are mapped to the corresponding damage states and functionalities of the system. Limit states must be defined by a metric consistent with the engineering demand parameters that can be evaluated in a computational model (e.g., ductility demands or displacement), and are characterized and represented by median values, S_c, and dispersion values, βc. To stay consistent with the demand models, which are assumed to take on lognormal distributions, the component capacity models are also assumed to have a lognormal distribution. There are three general methods used to create the capacity models: the prescriptive (physics-based) approach, the descriptive (judgmental) approach, or a combination of both using a Bayesian approach (Nielson and DesRoches 2007a).

The prescriptive method, also known as the physics-based method, is an approach that considers the mechanics of the structure to assess the level of damage and post-event functionality. A component's internal force or deformation is determined from a structural analysis and is used to evaluate the occurrence of damage that corresponds to a certain functionality level. For example, one can assume that at a column curvature ductility of 1.0 the longitudinal steel begins to yield; therefore, the traffic capacity must be reduced until the bridge is inspected.

The descriptive, or judgmental, approach attempts to subjectively correlate levels of component deformation or observed damage to post-event functionality and repair requirements based on expert opinion of bridge inspectors/officials. This data is typically gathered through surveys. Initial efforts were made through the FEMA-funded Applied Technology Council (ATC)-13 project to gather expert-opinions data for lifeline facilities in California to be used in developing the fragility curves found in HAZUS (Padgett 2007); however, the scope of the questionnaire was extremely broad (e.g., covering building, bridges, and utility system damage states) and the number of respondents with particular expertise in bridge engineering was low. Padgett (2007) designed and

conducted a survey to gather more extensive data focusing on bridges in the Central and Eastern United States (CEUS). In this survey, respondents were shown images of damaged bridge components (e.g., abutment settlement, expansion joint offsets, and column damage) from previous earthquakes, and they were asked to identify the level of functionality, repair procedures, and repair time associated with various levels of component deformation (e.g., abutment settlement or expansion joint offset displacements) or observed damage (e.g., column cracking, spalling, bar buckling, etc.). Survey data was collected from twenty-eight bridge engineers from nine different CEUS DOTs. This approach can be very subjective; however, expert-based opinion is thought to more accurately represent post-earthquake action decisions made by bridge officials.

The Bayesian approach recognizes that both the prescriptive (physics-based) and descriptive (survey-based) approaches offer valuable information, and thus combine data from both using Bayesian theory, which allows you to update probability distributions when additional information is acquired (Nielson 2005). This process is carried out by following Bayes' Theorem as:

$$P[B_i \mid A] = \frac{P[A \mid B_i]P[B]}{\sum_{j=1}^{n} P[A \mid B_i]} \tag{8-6}$$

where A is the new information that has been acquired, and B_i is the updated information. Figure 4.2 shows an example of the results for the updated moderate damage state for columns based on a combination of physics-based and survey-based capacity models. A full description of this method can be found in Nielson (2005).

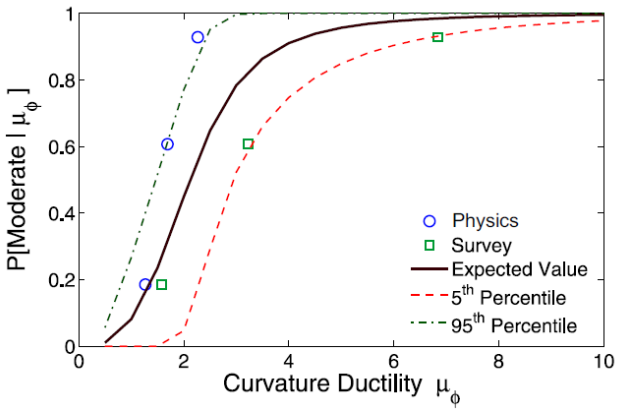

Figure 8.3: Bayesian updating of distribution of moderate damage state for columns (Nielson 2005)

A combination of all three of these techniques were used in determining the component capacities used in this study. The individual component limit state values are discussed in the following sections and are summarized in Table 8.11 at the end of this section. In early seismic fragility studies, it was common practice to use column capacity to represent the capacity of the bridge system (Karim and Yamazaki 2003; Mackie and Stojadinovic 2004; Shinozuka et al. 2000a);

however, more recent research has shown that all major vulnerable bridge components should be considered when determining system-level damage (Nielson and DesRoches 2007a; Tavares et al. 2013). Major bridge components considered in this study include: columns, bearings (steel and elastomeric), and abutments. Details regarding the damage state models that have been used for each of these components in this study are given in the sections below.

8.4.1. Columns

In previous bridge fragility studies (Nielson 2005; Ramanathan 2012; Tavares et al. 2013), the qualitative description of reinforced concrete column damage states remain consistent. These damage states and their descriptions are given as:

- Slight – yielding of outermost reinforcement steel and minor cracking
- Moderate – minor cracking and spalling
- Extensive – major cracking and spalling with exposed core concrete
- Complete – loss of confinement, buckling of reinforcing steel, and core crushing

The engineering demand parameters and values of the parameters used to evaluate the occurrence of these limit states, however, have varied from study to study. Drift, displacement ductility (μ_{Δ}), and curvature ductility (μ_{ϕ}) are all metrics that have been used to define the performance of reinforced concrete columns. In the more recent fragility studies, researchers tend to use curvature ductility as the performance metric of choice for columns as this value can be obtained from computational models employing fiber cross-section-based beam-column elements. Curvature ductility is defined as the maximum curvature demand from the response-history analysis divided by the curvature at yielding of the outer most reinforcing steel. Table 8.9 shows the comparison of performance metrics and limit state median values used in these previous studies.

Table 8.9: Column limit state comparison

Study	Damage State	Description	Performance Metric	Limit State Value
Hwang (2000)	Slight	Yielding	Displacement Ductility (μΔ)	1.00
	Moderate	Cracking		1.20
	Extensive	Spalling		1.76
	Complete	Reinforcement Buckling		4.76
Nielson (2005)	Slight	Yielding	Curvature Ductility (μϕ)	1.00
	Moderate	Cracking		1.58
	Extensive	Spalling		3.22
	Complete	Reinforcement Buckling		6.84
Ramanathan (2012) Pre 1971	Aesthetic damage	Cracking	Curvature Ductility (μϕ)	0.80
	Repairable minor damage	Minor Spalling		0.90
	Repairable major damage	Shear cracks, major spalling, exposed core		1.00
	Component replacement	Loss of confinement, reinforcement buckling		1.20
Ramanathan (2012) 1971 - 1990	Aesthetic damage	Cracking	Curvature Ductility (μϕ)	1.00
	Repairable minor damage	Minor Spalling		2.00
	Repairable major damage	Shear cracks, major spalling, exposed core		3.50
	Component replacement	Loss of confinement, reinforcement buckling		5.00
Ramanathan (2012) post 1990	Aesthetic damage	Cracking	Curvature Ductility (μϕ)	1.00
	Repairable minor damage	Minor Spalling		4.00
	Repairable major damage	Shear cracks, major spalling, exposed core		8.00
	Component replacement	Loss of confinement, reinforcement buckling		12.00

A major reason for the differences in column limit state values in the various studies is due to the regional column design and detailing practices or the design era of the columns in question. Ramanathan (2012) focused on columns in California bridges, but recognized the evolution in column design as brittle columns (pre-1971), strength-degrading columns (1971–1990), and ductile columns (post 1990). Figure 8.4 shows the expected behavior of columns from these three design eras, indicating the component damage thresholds (CDTs) along with photographic examples of these damage states. Note that as ductile detailing requirements improved in California over the decades, the curvature ductility values corresponding to the damage states increased. The Nielson (2005) study focused on bridge columns in the CEUS that were non-seismically detailed and had little to no confinement in the plastic hinge regions. In this particular study, limit state values were based on displacement ductility values from the Hwang (2000) seismic fragility study of Memphis, Tennessee bridges, but values were converted into curvature ductility values based on guidance from the *Seismic Retrofitting Manual for Highway Bridges*

(FHWA 1995). The displacement ductility selected in the Hwang (2000) study corresponded to key points in the cross-section flexural behavior (i.e., full yielding of the tension steel for the slight damage state, concrete reaching an assumed crushing strain of 0.002 for the moderate damage state, etc.). Note that the curvature ductility for these damage states had magnitudes similar to those from the 1971–1990 “strength-degrading” California columns from the Ramanathan (2012) study.

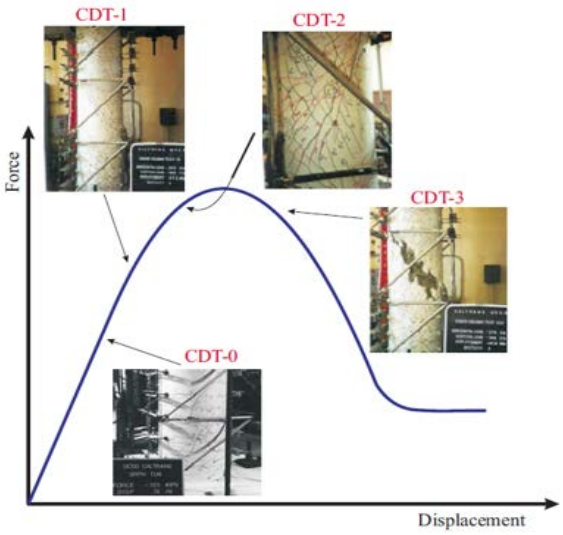

Designed before 1971

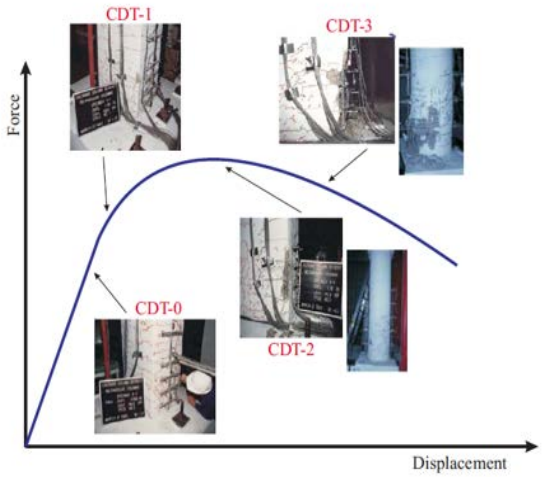

Designed between 1971 and 1990

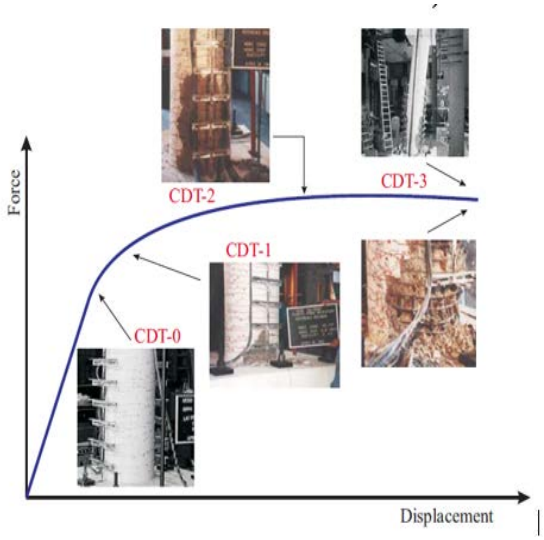

c) Designed after 1990

Figure 8.4: Depiction of column performance by design era (Ramanathan, 2012)

The engineering demand parameters and values of the parameters used to evaluate the occurrence of these limit states, however, have varied from study to study. Drift, displacement ductility (μ_{Δ}), and curvature ductility (μ_{ϕ}) are all metrics that have been used to define the performance of reinforced concrete columns. In the more recent fragility studies, researchers tend to use curvature ductility as the performance metric of choice for columns as this value can be obtained from computational models employing fiber cross-section-based beam-column elements. Curvature ductility is defined as the maximum curvature demand from the response-history analysis divided by the curvature at yielding of the outer most reinforcing steel. Table 8.9 shows the comparison of performance metrics and limit state median values used in these previous studies.

In the present study, to be consistent with the modeling approach suggested for columns, plastic rotation (Rot) is used to evaluate the performance of reinforced concrete columns. This metric has also been used in the work done by the ACI 369 committee (2016) for the ASCE 41-17 standard. In that work, plastic rotations are proposed for three different pre-defined limit states as immediate occupancy (IO), life safety (LS), and collapse prevention (CP), which are shown in Table 8.10. As seen in the table, these values depend on a_{nl} and b_{nl} which describe column inelastic rotation capacities to the points that limit the hardening region and strength degradation respectively (See Figure 7.35 for more details).

Table 8.10: Column limit state values suggested by ASCE 41-17

Limit State	Plastic rotation
IO	$0.15\ a_{nl} \leq 0.005$
LS	$0.5\ b_{nl}$
CP	$0.7\ b_{nl}$

Note: a_{nl} and b_{nl} are computed using the equations in Table 7.1.

The definition of these limit states is very similar to the slight, moderate, and extensive levels of damage suggested by HASUZ, respectively. Thus, the proposed values can be used for Slight, Moderate, and Extensive levels of damage. For Complete level of damage defined in Table 8.8, the present study considers b_{nl}, inelastic rotation capacity before strength degradation, as the limit state value. As seen in the table, the limit state values depend on the column properties. By investigating columns with different properties considered in this study, it is observed that the limit state values vary between 0.002 and 0.004 for Slight level of damage, between 0.011 and 0.033 for Moderate level of damage, between 0.018 and 0.046 for Extensive level of damage, and between 0.021 and 0.058 for Complete level of damage. Thus, the median values of 0.003, 0.01, 0.02, and 0.03 are considered for Slight, Moderate, Extensive, and Complete levels of damage, respectively.

It should be noted that the limit state values discussed above were developed only considering flexural behavior of columns; however, reinforced concrete columns that have not been seismically designed and do not provide adequate transverse reinforcing are also susceptible to a more brittle shear failure. In order to determine which failure mode (i.e., flexural or shear) governs a columns behavior, one must compare the shear and flexural strengths of the column. If the column reaches its nominal flexural capacity prior to reaching its nominal shear capacity, the column is considered flexure-controlled. All of the bridge columns in this study were found to be flexure-controlled; thus, column shear limit state values are not given in this report.

8.4.2. Bearings

Mander et al (1996) conducted extensive experimental research on the response of steel bearings subjected to cyclic loading, which has been the foundation for estimating limit state median values throughout several past bridge fragility studies. This experimental research showed that failure of the anchor bolts connecting the base of the bearing to the concrete support typically controls the behavior and critical limit state values for steel bearings. For past tests of high-type fixed steel bearings, noticeable damage was first observed at a deformation of 0.25 inch (6mm), when cracks tend to form around the concrete bearing areas (Mander et al, 1996). For this reason, a 0.25 inch bearing deformation is used for the "slight" limit state median value in this study. The limit state median value for the "moderate" damage state is assumed to be at a deformation of 0.75 inches (20mm), where prying action in the bearing is first observed. This behavior results in more significant cracking and spalling of the concrete bearing areas, and significant deformation of the anchor bolts can be observed. Based on observations of anchor bolt fracture in the past tests, a bearing deformation of 1.5 inches (40mm) is assumed for the "extensive" limit state median value, resulting in subsequent sliding or toppling of the bearing. Finally, the "complete" limit state is assumed to take place at a deformation that exceeds the typical width of the bridge seat, resulting in unseating of the girder and ultimately complete or partial collapse of the span.

While visually being able to determine if a bridge span has collapsed during post-earthquake inspection can be straightforward, determining a bearing deformation value that would indicate collapse in a numerical bridge model is not. Nielson (2005), using the prescriptive approach, suggests that unseating will occur at a displacement of 10 inches (255mm) based on the width of the bridge seat for the bridge population in question. Results from a survey of bridge officials in the CEUS, conducted in the Padgett study (2007), indicated an expected bearing deformation of greater than or equal to 6 inches to cause girder unseating. Nielson (2005), using Bayseian updating and the survey results to update the prescriptive expected value, suggests that an expected bearing deformation of 7.25 inches would causing girder unseating. More details on the Bayesian updating process can be found in Nielson (2005).

This variation in median values shows that there is some discrepancy in determining displacement consistent bearing deformations associated with girder unseating. Recognizing these challenges and uncertainties in determining the "complete" limit state median value for bearings, and due to the lack of experimental data of girder-bearing-seat subassemblies, it was determined to use the updated value, which takes into account engineering judgement, suggested in the Nielson study (2005). Through the investigation of TxDOT as-built drawings, it was determined that this value of 7.25 inches is also consistent with the typical distance between the centerline of bearing and the edge of the bridge seat.

Typical details for fixed steel bearing design provide the same number of anchor bolts providing restraint in either direction, indicating that fixed type steel bearings have similar behaviors in both the longitudinal and transverse directions (Nielson 2005). Also, while expansion type steel bearings are expected to accommodate more deformation in the longitudinal direction, the transverse behavior of a steel expansion bearing is expected to be similar to that of the fixed type

bearing. Thus, the limit states for the longitudinal and transverse fixed steel bearings, as well as the steel expansion bearings in the transverse direction are assumed to follow the same limit state values as discussed above and are summarized in Table 8.11.

For expansion bearings (e.g., rockers and sliding bearings) in the longitudinal direction, the damage of concern is instability of the bearing, which would result in significant movement in the superstructure, and in the worst cases unseating of the span (Pan 2007). The dimensions of the bearings and ultimately the width of the bridge seat generally govern this damage and instability. The experimental bearing tests conducted by Mander et al (1996) showed that instability of expansion bearings was first observed at a deformation of half the width of the masonry plate (100mm). Using these test results Choi (2002) proposed a displacement of 4 inches (100mm) as the "moderate" limit state for expansion bearings. Investigation of as-built drawings indicated that the size of the masonry plates used in older steel girder bridges in Texas varies with span length, ranging from a width of 6 inches up to 14 inches. For example, longer span lengths result in larger bearing forces, which requires a larger masonry plate. However, typical span lengths for steel girder bridges used in this study (e.g., spans less than 120ft) correspond to bearings with masonry plates ranging in width from 6 to 9 inches. Therefore, a "moderate" limit state median value of 3.75 inches is used in this study. Considering unseating of a span as the "complete" damage state, a displacement of 7.25 inches, as previously discussed, is used as the median value for the "complete" limit state. Following the work of Choi (2002) the "slight" and "extensive" limit state median values were picked between the "moderate" and "complete" values, and do not correspond to any designated observed damage. These values are 1.5 inches of displacement for "slight" damage, and 5 inches for "extensive" damage.

As previously mentioned, elastomeric bearings are common bearing types used with concrete superstructures (i.e., PC girder bridge class). The behavior of these type of bearings is typically characterized by sliding; however, unimpeded sliding can only occur after complete fracture of the retention dowels, if present (Nielson 2005). As discussed in Tech Memo 8, the only difference between expansion and fixed elastomeric bearings are the slotted holes in the elastomeric pad and girder allowing the longitudinal movement of the superstructure at the expansion bearing locations. Because dowels, which are embedded in the bridge seat and extend through the elastomeric pad into the bottom of the concrete girder, cannot be observed after construction, it is difficult for an inspector to visually differentiate between expansion and fixed elastomeric bearings. For this reason, it is common to use the same limit state values for the fixed and expansion elastomeric bearings, in both the longitudinal and transverse directions (Nielson 2005). This detailing, which causes the dowels to be hidden from outside inspection, also makes it difficult to visually inspect and identify damage in the retention dowels (e.g., yielding or fracture of the dowel). Thus, limit state expected values related to dowel fracture must be related to observable displacements that can be associated with capacity implications and possibly repair efforts, rather than observed dowel damage. For example, Nielson (2005) stated that a peak transient displacement of 1 inch is expected to result in permanent deformations in the bearing that can be easily observed by an inspector and may have caused minor dowel yielding but is expected to have little effect on bearing capacity. A peak bearing displacement of 3 inches would imply possible dowel fracture and may

require minor deck realignment. At 5 inches of peak bearing displacement, the dowels are expected to be fully fractured, resulting in not only deck realignment, but also requiring installation of a new retention mechanism for the concrete girders. At a bearing deformation of 7.25 inches, unseating of the span is expected to occur. Therefore, the values for the slight, moderate, extensive, and complete limit states used in this study are displacements of 1 inch, 3 inches, 5 inches, and 7.25 inches, respectively.

Other reinforced concrete superstructures (e.g., RC slab and girders) do not utilize elastomeric pads as the bearing between the superstructure and the substructure. These older details, which typically consist of ¾ inch dowels and roofing felt, do rely on the same type of restraint system (i.e., steel dowels connecting the superstructure and substructure) and are expected to have similar "sliding" type of behavior. For this reason, the limit state values for the elastomeric bearings, discussed above, will be used for the alternative concrete bearings typically used in the RC slab and girder bridge classes.

8.4.3. Abutments

Abutments primarily resist vertical loads and act as a retaining wall to the backfill supporting the approach slab; however, they do provide resistance against deformation and earthquake induced inertial forces from the bridge superstructure (Saini and Saiidi, 2013). Deformation of the abutment in the longitudinal direction can be resisted passively or actively. Passive resistance is developed as the abutment pushes into the soil backfill (compression), and active resistance is when the abutment is pulled away from the backfill (tension). The passive soil pressure and the foundation (e.g., piles or drilled shafts) provide resistance in passive action, while active action is resisted solely by the foundation (i.e., the soil is assumed to have no tensile resistance). Abutments also provide transverse stiffness, which can be attributed to the foundation or the wing walls, if present.

Typically, abutment limit states are defined in terms of the first yield point and ultimate displacement of the abutment foundation and backwall (Choi 2002; Tavares et al. 2013). Martin and Yan (1995) provide guidelines for estimating ultimate displacement in the passive direction, as they suggest a multi-linear behavior of abutments in the passive action, and their tests show that the ultimate passive earth pressure becomes mobilized at a displacement of 6% to 10% of abutment height, depending on the type of soil (e.g., cohesive vs cohesionless). Their tests also suggest abutments in the passive action see first yielding and second yielding at displacements of 0.6% and 1.5% of abutment height, respectively. Nielson (2005) proposed that an inspector would not be able to identify noticeable (i.e., "slight") damage until cracking of the abutment and backwall occurred at or around second yielding, and "moderate" damage would occur at a longitudinal displacement of about 6 inches. Nielson (2005) also proposed, based on survey results of practicing CEUS bridge engineers, that abutment deformation was highly unlikely to reach an "extensive" or "complete" limit state. This particular study adopts the limit state values proposed by Nielson (2005).

Limit states for abutments in the active or transverse directions are again typically defined in terms of first yield and ultimate deformations. When considering pile bent abutments, which are typical

in the CEUS and Texas, Caltrans (1999) proposes that ultimate displacement occurs around a displacement of 1 inch, and first yield will occur at 30% of the ultimate displacement. Using these Caltrans recommendations, coupled with relevant engineering judgment (i.e., survey results from practicing bridge engineers) through Bayesian updating, Nielson (2005) proposed that an abutment deformation of 0.375 inches should be considered as "slight" damage, 1.5 inches as "moderate" damage, and 3 inches as "extensive" damage in the active action and transverse direction. Similar to the behavior in the passive action, Nielson (2005) suggested that, based on engineering judgement and the lack of "complete" damage observed in abutments in past earthquakes, abutment displacement in the active or transverse direction during a seismic event would not cause "complete" damage to a bridge structure.

Due to the similar design and details of CEUS and Texas bridge abutments (e.g., seat type pile/shaft abutments), the limit states proposed by Nielson (2005) for abutments were used in this study. Assuming an average abutment height of 7 ft, based on review of as-built drawings and TxDOT Standards, the second yielding point of an abutment in the passive direction is expected to occur at a deformation of about 1.25 inches, which was considered as the "slight" limit state median value. An abutment deformation of 6 inches in the passive direction was used as the "moderate" limit state value in this study. For both the active and transverse abutment deformations, median values of 0.375 inches, 1.5 inches, and 3 inches are used as the "slight," "moderate," and "extensive" limit states, respectively.

8.4.4. Foundations and Expansion Joints

Foundations and expansion joints are two other bridge components that are potentially susceptible to damage during an earthquake event. These components are often considered as secondary components (Ramanathan 2012), as their damage does not necessarily compromise the overall stability of the system (i.e., in the case of expansion joints), or their fragility is far lower than other major components (e.g., damage in columns or bearings is much likelier to occur before damage in the foundation). In this particular study, the capacity of the foundation and columns are assumed to be related due to the typical integral drilled shaft/column foundation detail assumed. Depending on the design and detailing of this type of substructure component, the foundation and column can act as one component (e.g., with the same diameter column and shaft), or the column can be designed with a smaller diameter than the shaft, causing damage to occur in the smaller column section. In this study, foundation capacity is not considered explicitly and is instead implicitly included in the column capacity and median limit state values.

Expansion joints are an important component of a bridge structure and are expected to experience damage during an earthquake event (e.g., due to pounding and crushing of the concrete deck). Although this type of damage may affect the functionality or the required repair of the structure (e.g., resulting in reduced traffic speed due to rough joints, or required patching of joints that may increase repair costs), it is not expected to affect the overall stability of the structure. The capacity or damage of expansion joints is not typically considered explicitly in a fragility analysis; instead, it is common to map expansion joint damage to the limit states of other components. For example,

if an expansion bearing experiences a displacement of 3 inches (which is considered "moderate" damage), it is expected that there will be moderate cracking and spalling at the expansion bearings, which will increase the time and costs of structural repairs. For this reason, expansion joint behavior was considered when developing the qualitative structural level limit states but are not considered explicitly at the component level.

According to past studies (Cornell et al. 2002; Nielson 2005), it is assumed that the capacity for each limit state follows a lognormal distribution with a median of S_C and dispersion of β_C. The values of S_C are assumed based on engineering judgement and test results as previously discussed and as summarized in Table 8.11. To account for the uncertainty in capacity of each component, the coefficient of variation (COV) of 25% for slight and moderate, and 50% for extensive and complete limit states are taken into account, which results in β_C of 0.25 for slight and moderate, and β_C of 0.47 for extensive and complete limit states using the following equation:

$$\beta_C = \sqrt{1 + \mathrm{COV}^2} \tag{8-7}$$

Table 8.11: Limit state median and dispersion values for bridge components

Component		Slight		Moderate		Extensive		Complete	
		S_C	β_C	S_C	β_C	S_C	β_C	S_C	β_C
Column-Rotation (radian)	Rot	0.003	0.25	0.01	0.25	0.02	0.47	0.03	0.47
Steel Fixed bearing-Long. (in)	fx_L	0.25	0.25	0.75	0.25	1.5	0.47	7.25	0.47
Steel Fixed bearing-Trans. (in)	fx_T	0.25	0.25	0.75	0.25	1.5	0.47	7.25	0.47
Steel Expan. bearing-Long. (in)	ex_L	1.5	0.25	4.1	0.25	5.3	0.47	7.25	0.47
Steel Expan. bearing-Trans. (in)	ex_T	0.25	0.25	0.75	0.25	1.5	0.47	7.25	0.47
Elasto. Fixed bearing-Long. (in)	fx_L	1	0.25	3	0.25	5	0.47	7.25	0.47
Elasto. Fixed bearing-Trans. (in)	fx_T	1	0.25	3	0.25	5	0.47	7.25	0.47
Elasto. Expan. bearing-Long. (in)	ex_L	1	0.25	3	0.25	5	0.47	7.25	0.47
Elasto. Expan. bearing-Trans. (in)	ex_T	1	0.25	3	0.25	5	0.47	7.25	0.47
Abutment-Passive (in)	abut_P	1.45	0.25	5.8	0.25	8.0	0.47	10.0	0.47
Abutment-Active (in)	abut_A	0.375	0.25	1.5	0.25	3	0.47	8	0.47
Abutment-Trans (in)	abut_T	0.375	0.25	1.5	0.25	3	0.47	8	0.47

8.5. Component-Level Fragility Curves

Given demand and capacity models for each component, the probability of damage can be computed using Eq. (8-2). Figure 8.5 through Figure 8.11 show the fragility curves for different components of different bridge classes considered in this study. Each plot of the figures represents the fragility functions of the components for one specific limit state (e.g., slight, moderate, extensive, and complete). As seen in these figures, the probability of damage for columns and abutments are similar amongst the different bridge types; however, the probability of damage for bearings changes a lot from one bridge class to the others.

For steel girder bridges, as seen in Figure 8.5 and Figure 8.6, the bearings are the most vulnerable component and are most likely to experience damage during an earthquake. This is mainly due to the fact that this bridge class, based on the age of the bridge samples, have steel bearings which are known to be vulnerable to seismic hazards (NCHRP, 1977). Although this type of bearings has recently been replaced by elastomeric pads in modern steel girder bridges, as discussed in Section 6.4, the majority of the steel bridges constructed in Texas have steel bearings. Moreover, as seen in Figure 8.5, for continuous steel girder bridges, the expansion bearings are more vulnerable compared to fixed bearings, which is largely because of the instability of steel rocker bearings under large deformations. Moreover, fixed bearings in MSSTEEL bridges tend to be more vulnerable than fixed bearings in MCSTEEL bridges.

Figure 8.7 and Figure 8.8 respectively show the results for multi-span and single-span prestressed concrete girder bridge. As seen in the figure, for prestressed concrete girder bridge, like steel girder bridges, the bearings are the most vulnerable components of the bridges. As discussed in Chapter 6, prestressed girder bridges employ elastomeric bearings with elastomeric pad and dowels. The results indicate that although the elastomeric bearings have a slightly lower probability of damage compared to steel bearing, elastomeric bearings are the most vulnerable component of prestressed concrete girder bridges.

For reinforced concrete girder and slab, bridges i.e., MSRC, MCRC-Slab, and MSRC-Slab, as seen in Figure 8.9 through Figure 8.11, the column is the most vulnerable component. This observation is attributed to the fact that for these bridge classes, the bearings consist of numerous dowels and concrete-on-concrete friction, which provides significant strength and stiffness, resulting in lower deformations compared to steel and elastomeric bearings.

Finally, regardless of the bridge class, it is found that abutments are the least vulnerable component of the bridges. Due to their relative flexibility and lower strength, the bearings are expected to experience large deformations and subsequent damage, limiting the loads that can be transferred to the abutments. These fragility curves can be used as a guidance for post-event bridge inspection, to identify the critical components most likely to exhibit damage.

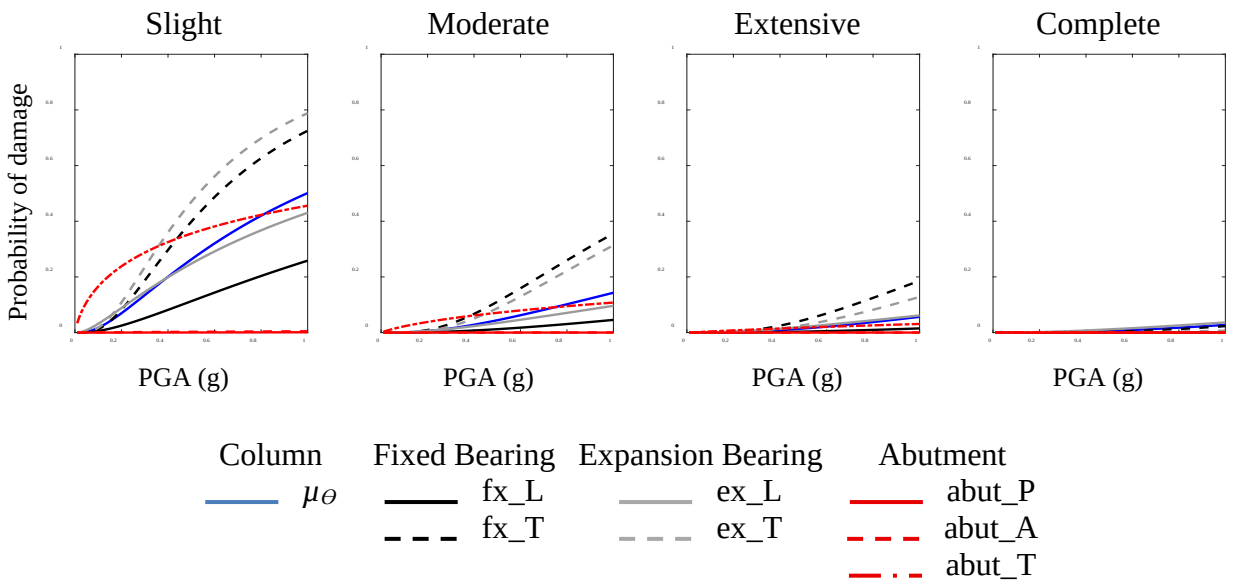

Figure 8.5: Component fragility curves of MCSTEEL bridges

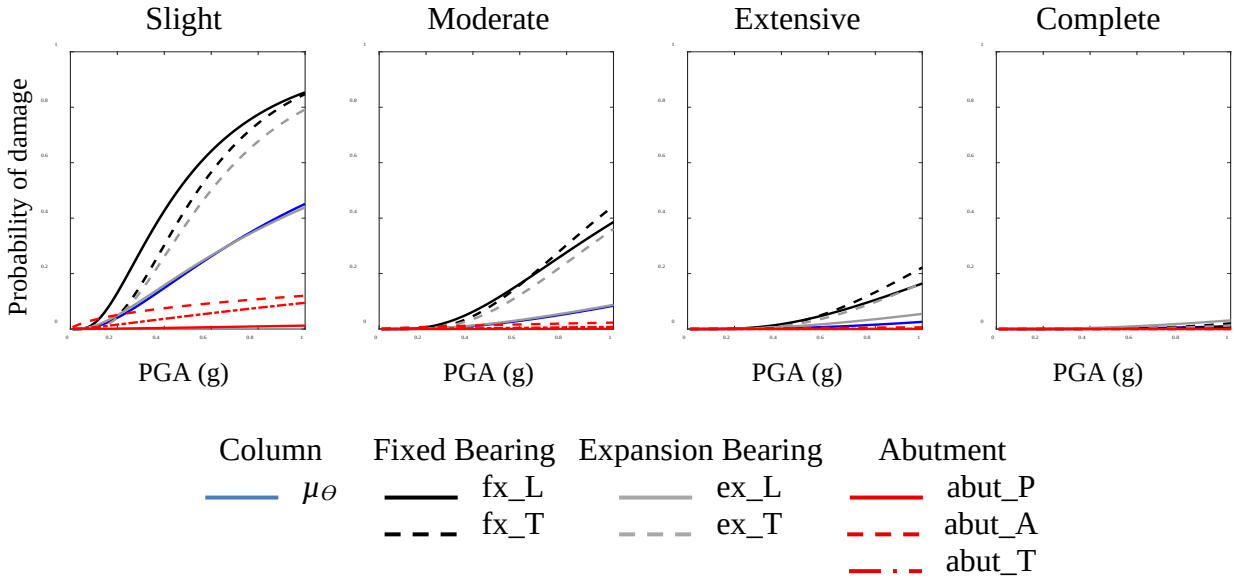

Figure 8.6: Component fragility curves of MSSTEEL bridges

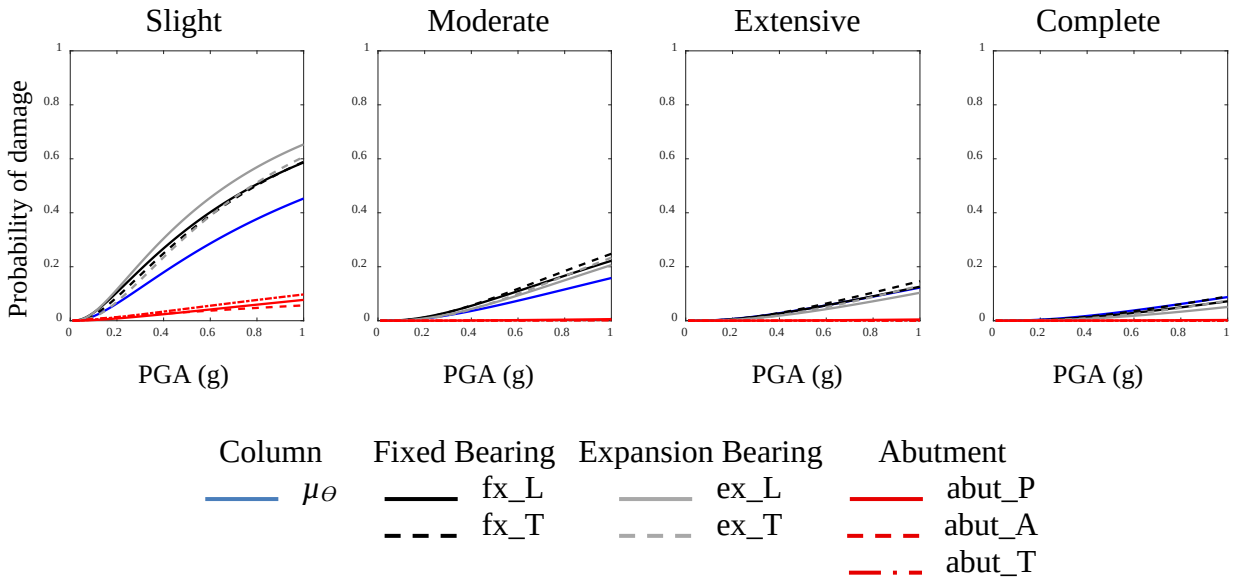

Figure 8.7: Component fragility curves of MSPC bridges

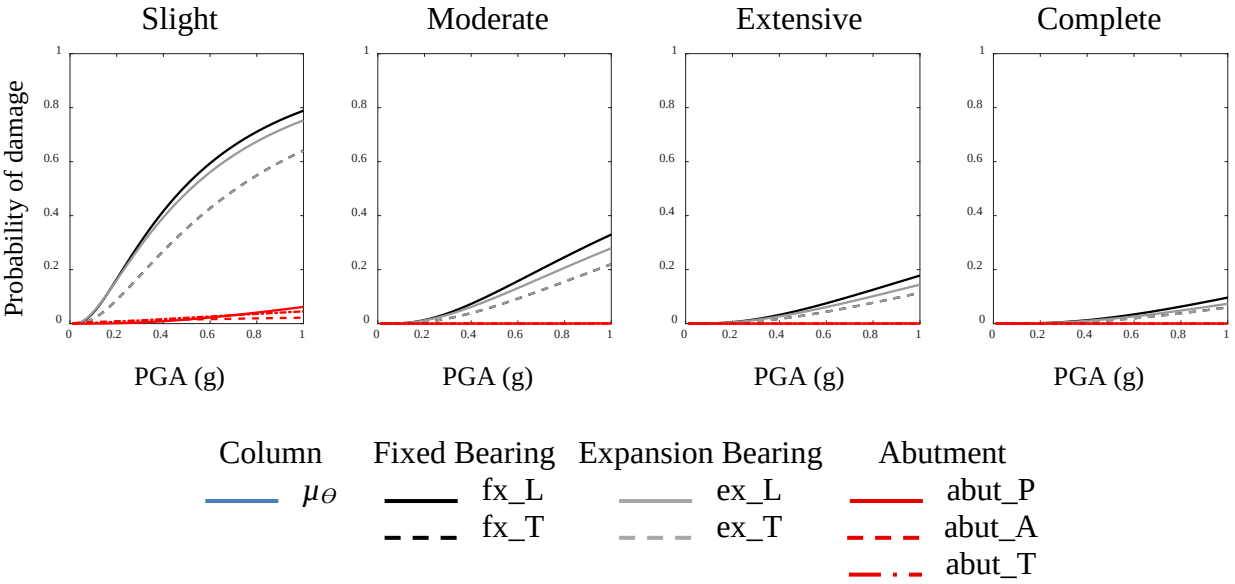

Figure 8.8: Component fragility curves of SSPC bridges

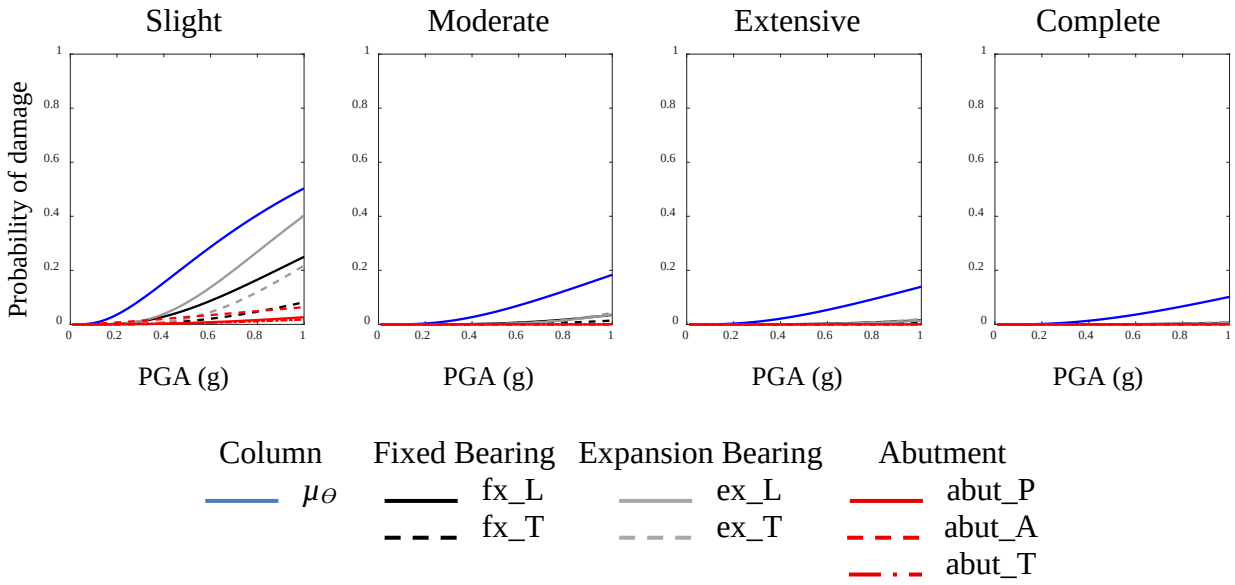

Figure 8.9: Component fragility curves of MSRC bridges

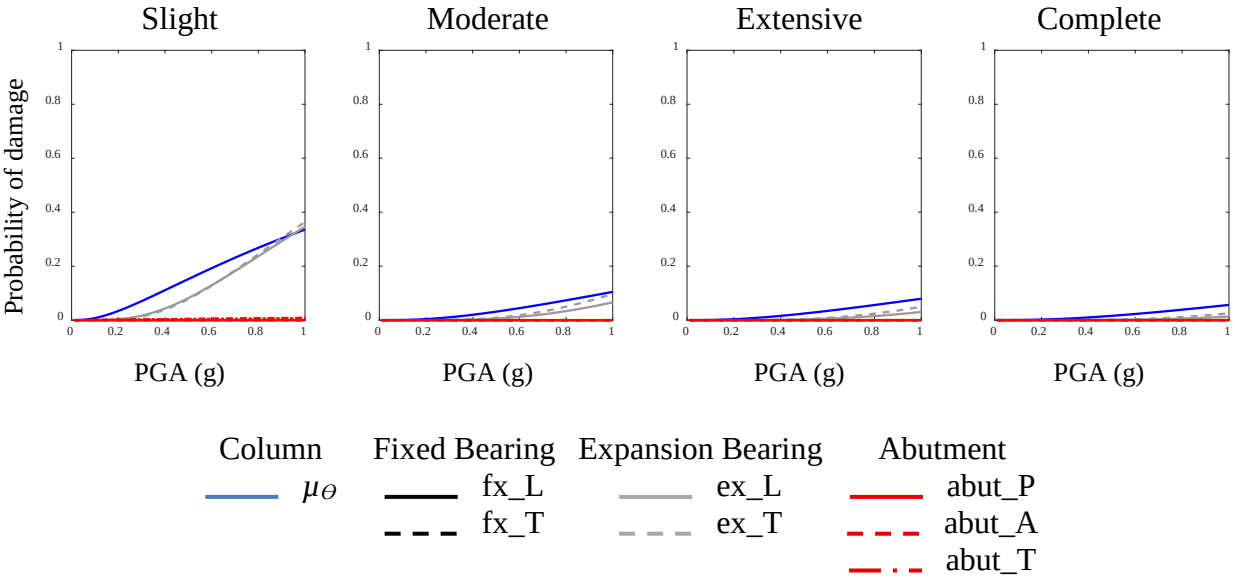

Figure 8.10: Component fragility curves of MCRC-slab bridges

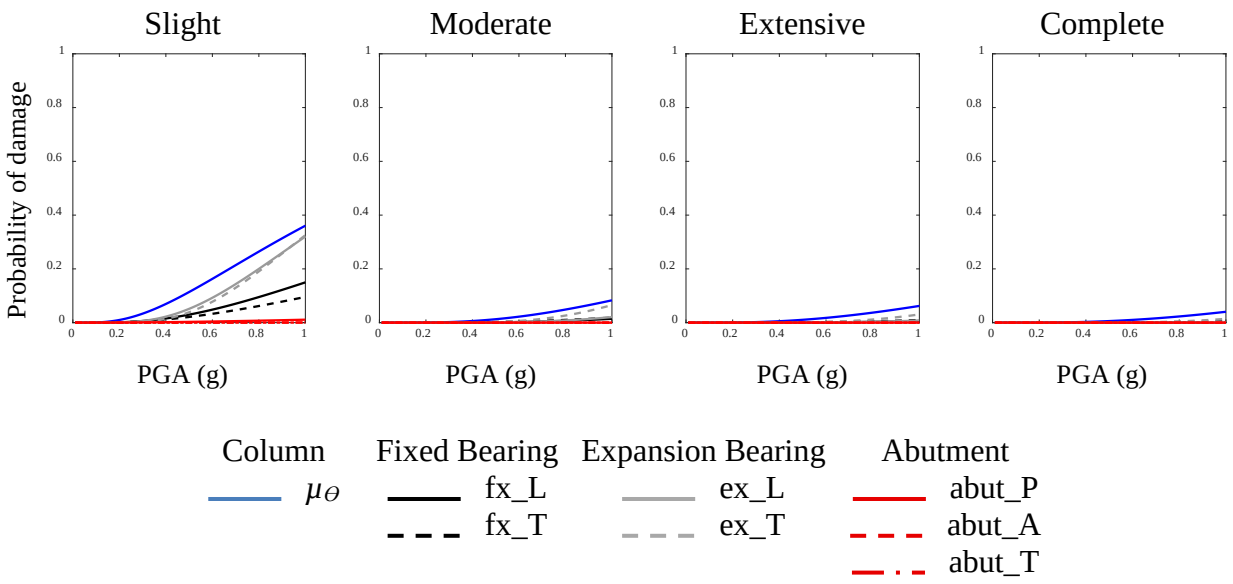

Figure 8.11: Component fragility curves of MSRC-slab bridges

8.6. System-Level Fragility Curves

System-level fragility curves provide an estimation of the vulnerability of the entire bridge system and are useful tools in developing post-event action plans or loss estimations. In early bridge studies, such as Karim and Yamazaki (2003), Mackie and Stojadinovic (2004), and Shinozuka et al. (2000b), it was assumed that the columns were most vulnerable part of the bridge, and thus the column fragility were assumed to represent the fragility of the entire bridge system. However, as shown in the previous section, it is observed that in most bridge classes, bearing is the most vulnerable component of the bridge system in the state of Texas. In this regard, more recent fragility studies, powered by advancements in computing capabilities, considered the vulnerability of multiple components to more accurately represent the fragility of the bridge system. The concept of combining multiple component fragilities into a single system-level fragility significantly increases the complexity of fragility analysis, which makes the use of closed form integration of multiple component fragilities extremely difficult, if not impossible. For this reason, researchers have explored several methods for developing system-level fragility curves. One common approach is the use of first-order reliability bounds (Nielson and DesRoches 2007a; Pan 2007). First-order reliability can be expressed as:

$$\max_{i=1}^{n}[P(F_{comp\_i})] \le P(\mathrm{F}_{\mathrm{system}}) \le 1-\prod_{i=1}^{m}[1-P(\mathrm{F}_{comp\_i})] \tag{8-8}$$

where $P(F_{comp\text{-}i})$ is the probability of failure of the i^{th} component. The lower bound assumes complete component correlation, where the entire bridge fragility is controlled by the most vulnerable component, which may underestimate the bridge fragility as it ignores potential damage in components with lower, yet still significant, vulnerabilities. The upper bound assumes no correlation between damage in different components, in which failure of a single component (i.e., a component exceeding a certain limit state) constitutes failure of the entire bridge. This upper

bound is mathematically represented by the product of the component survival probabilities and can overestimate the bridge fragility since it ignores likely correlation of damage among various components. Nielson and DesRoches (2007b) found that the upper bound provides a good estimation of the system fragility; however, they concluded that direct estimation of system-level fragility considering component correlation using numerical integration is a more accurate approach, showing a reduction in fragilities of up to 10 percent. This direct estimation approach has also been used in more recent studies such as Ramanathan (2012) and Tavares et al. (2013).

The direct estimation approach recognizes that there is some sort of correlation of damage among the components, as the component PSDMs are compiled into a joint seismic probability density model (JPSDM) for the system. As previously stated, it is assumed that, for a given PGA, the demands follow lognormal distributions, resulting in normal distributions in natural logarithm space (as demonstrated in Figure 8.2). The JPSDM is developed in natural logarithm space using the transformed marginal distributions of the components as well as taking into account the correlation between the component-level demands in the transformed space. Therefore, The JPSDM takes on a multivariate normal distribution in natural logarithm space and can be fully described by a vector of mean demands and a covariance matrix in natural logarithm space. Table 8.12 shows the correlation among the seismic demands of multi-span continuous steel girder bridges, i.e., MCSTEEL, in natural logarithm space. From Table 8.12, values in the matrix closer to 1.0 indicate higher correlation in component demands. For example, the largest value (other than self-correlation values of 1.0) of 0.9 in the location corresponding to ln(ex_T) and ln(fx_T) indicates that demands in the transverse direction of expansion and fixed bearings are highly correlated. The correlation among seismic demands of other bridge classes are available in Appendix F.

Table 8.12: Correlation of seismic demands for MCSTEEL bridges

	ln(Rot)	ln(fx_L)	ln(fx_T)	ln(ex_L)	ln(ex_T)	ln(abut_P)	ln(abut_A)	ln(abut_T)
ln(Rot)	1.00	0.58	0.62	0.93	0.54	0.63	0.53	0.50
ln(fx_L)	0.58	1.00	0.54	0.71	0.39	0.28	0.24	0.18
ln(fx_T)	0.62	0.54	1.00	0.60	0.72	0.43	0.49	0.62
ln(ex_L)	0.93	0.71	0.60	1.00	0.48	0.62	0.55	0.47
ln(ex_T)	0.54	0.39	0.72	0.48	1.00	0.19	0.01	0.15
ln(abut_P)	0.63	0.28	0.43	0.62	0.19	1.00	0.70	0.62
ln(abut_A)	0.53	0.24	0.49	0.55	0.01	0.70	1.00	0.90
ln(abut_T)	0.50	0.18	0.62	0.47	0.15	0.62	0.90	1.00

In order to develop fragility curves, the JPSDM must be integrated over all possible failure domains (i.e., for each limit state of each component). This integration provides the probability of failure for a particular system at a given value of PGA. To compute this integration in this study, it is assumed that if any component exceeds any level of damage, then the whole bridge exceeds that level of damage. It is a conservative assumption that provides equal weight to damage in any component regardless of the relative "importance" of each component, though it is consistent with other past research (Nielson and DesRoches 2007b). Thus, for each level of damage, it is assumed

that the probability of damage for a bridge is the union of the probabilities that bridge components exceed that limit state, given mathematically as:

$$P(\text{Fail}_{\text{system}} \mid \text{LS}) = \bigcup_{i=1}^{n} P(\text{Fail}_{\text{componenet-}i} \mid \text{LS}) \tag{8-9}$$

Therefore, with this approach, whole system is considered to be more fragile than any one of the bridge components. Figure 8.12a illustrates the bi-variate probability density function over the failure domain. This figure demonstrates the correlation between demands from two components (d_1 and d_2), as indicated by the contour lines showing the multivariate distribution of the JPSDM. The failure domain for the system is indicated by the shaded parts of the plot, where either component exceeding its capacity for a specific limit state constitutes the entire system exceeding that limit state.

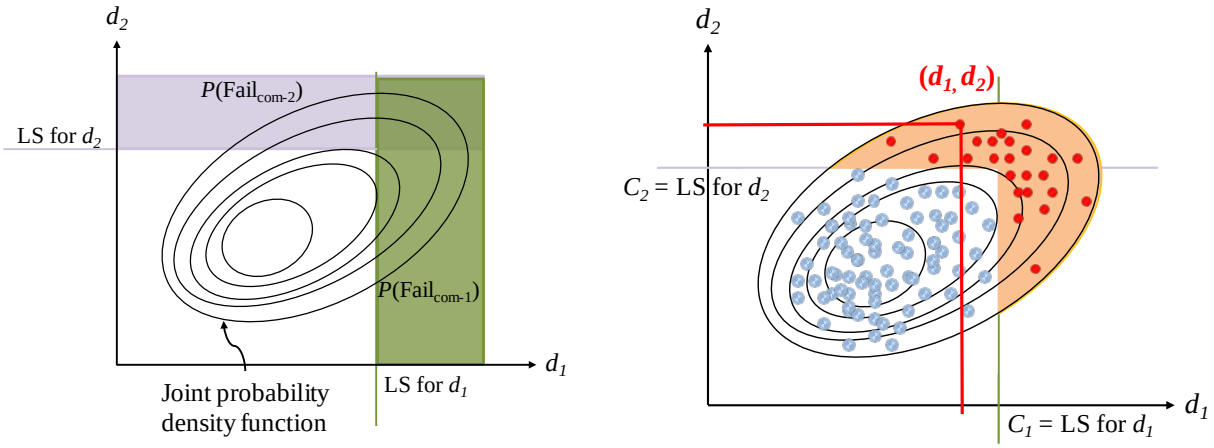

(a) JPSDM over failure domain at a given PGA (b) Monto Carlo Simulation at a given PGA

Figure 8.12: Bi-variate joint probability density function

Computing the system fragility from the JPSDM of multiple components is commonly computed using a numerical integration technique, such as Monte Carlo simulation (Figure 8.12b). In each sample of Monte Carlo simulation (indicated by the dots in Figure 8.12b), random realizations are generated for both the demand (d_1, d_2) and capacity (C_1, C_2) of each component. Then, the failure of each component and, in turn, the bridge system is evaluated by comparing the paired realizations. In the simulation process, the probability of failure given a PGA is computed using an indicator function, I_f. In each sample, if the demand of any of component exceeds the corresponding randomly generated capacity (as indicated by the red dots in Figure 8.12b), the indicator function is equal to one, indicating that the bridge fails; otherwise, I_f is equal to zero. By way of illustration, the indicator function for computing the integration for a bi-variate distribution, shown in Figure 8.12b, is as follows:

$$I_f = \begin{cases} 1 & \text{if } d_1 > c_1 \text{ or } d_2 > c_2 \\ 0 & \text{if } d_1 < c_1 \text{ and } d_2 < c_2 \end{cases} \tag{8-10}$$

where d_1 and d_2 are the randomly generated demands, and c_1 and c_2 are the corresponding randomly generated capacities given a specific value of PGA. To properly account for the uncertainty of demand and capacity, 10^6 number of realizations are generated in this study. Hence, probability of failure at a given PGA value is estimated as the number of samples that exceeded that limit state (i.e., failed) divided by the total number of samples, which is expressed mathematically using the following equation:

$$P\left[LS \mid \text{PGA}\right] = \frac{\sum_{i=1}^{N} I_{f_i}}{N = 10^6} \tag{8-11}$$

where P[LS|PGA] is the probability of exceeding a specific limit state (LS) at the system level given a PGA. This sampling is then carried out over a wide range of PGA values to compute the probability of failure for different values of PGA, which forms the underlying data for the generation of fragility curves. Fragility curves are assumed to follow a lognormal distribution and are, therefore, produced via a simple linear regression of the underlying failure probabilities at various PGA levels to estimate the median PGA (i.e., PGA corresponding to 50% likelihood of exceeding the specified limit state) and dispersion of the fragility functions. Table 8.13 presents the median PGA and dispersion values for the fragility curves of the bridge classes considered in this study. For instance, the median probability of exceeding the slight level of damage for MSSTEEL girder bridges is 0.27 g, which means that for ground motions with PGA of 0.27 g, there is 50% chance that bridges in that class experience slight or severe levels of damage. As seen in the table, regardless of the limit state, median PGA values for steel girder bridges are lower than other bridges, indicating the fact that steel girder bridges are more vulnerable than other bridges. This observation, as discussed in previous section, is mainly because of the higher vulnerability of steel bearings used in steel girder bridges compared to other bearing types.

Table 8.13: Median PGA (in units of g) and dispersion of fragility curves of the bridge systems

	Slight		Moderate		Extensive		Complete	
Bridge Class	Median	Dispersion	Median	Dispersion	Median	Dispersion	Median	Dispersion
MCSTEEL	0.26	0.97	0.82	0.76	1.33	0.84	3.53	1.03
MSSTEEL	0.27	0.72	0.64	0.72	0.99	0.75	2.69	0.83
MSPC	0.46	0.98	1.32	0.98	1.77	1.02	2.46	1.04
SSPC	0.37	0.90	1.17	0.88	1.65	0.93	2.44	0.94
MCRC-Slab	0.93	0.81	2.17	0.83	3.00	0.94	4.23	1.01
MSRC-Slab	0.99	0.66	2.26	0.69	2.92	0.78	3.71	0.80
MSRC	0.82	0.78	2.03	0.84	2.56	0.91	3.23	0.94

Figure 8.13 presents the fragility curves for all bridge classes based on the median and dispersion values shown in Table 8.13. Each plot of the figure represents the fragility curves for one specific

limit state. As seen in the figure, there are noticeable differences in the system-level bridge fragility curves of different bridge classes, which is mainly attributed to the relative vulnerability of the bearings used in each bridge class as previously discussed.

Figure 8.13 shows that steel girder bridges, both simply-supported and continuous ones, are the most vulnerable bridge types in Texas, which is mainly because of their bearing types, as discussed in the previous section on component fragility curves. Prestressed concrete girder bridges are expected to have slightly better seismic performance compared to steel girder bridges. This observation is attributed to the fact that they have elastomeric bearings which are believed to exhibit better seismic performance compared to the steel bearings common in steel girder bridges. Reinforced concrete girder and slab bridges, however, are expected to be the least vulnerable, which is attributed to their bearing performance as discussed in the previous section.

Recall that the largest PGA values recorded in the ground motions used in this report came from the November 7, 2016 Cushing, Oklahoma M5.0 event. The largest PGA recorded during this event was approximately 0.59g, which was at a hypocentral distance of 5.2km. Other stations ranging from 6.4km to 9.6km from the hypocenter recorded peak PGA values ranging from 0.20g to 0.32g. These data suggest that larger magnitude induced earthquake (M5+) have a significant likelihood of producing slight to moderate damage in steel and prestressed concrete girder bridges nearby the hypocenter (e.g., hypocentral distances less than approximately 10km). These fragility curves are used to develop a rapidly-deployable post-earthquake response plan for state officials. Establishing a post-event response plan facilitates economic and timely bridge inspections following a seismic event and can help ensure public safety. Details of this post-event response plan are discussed in Chapter 9.

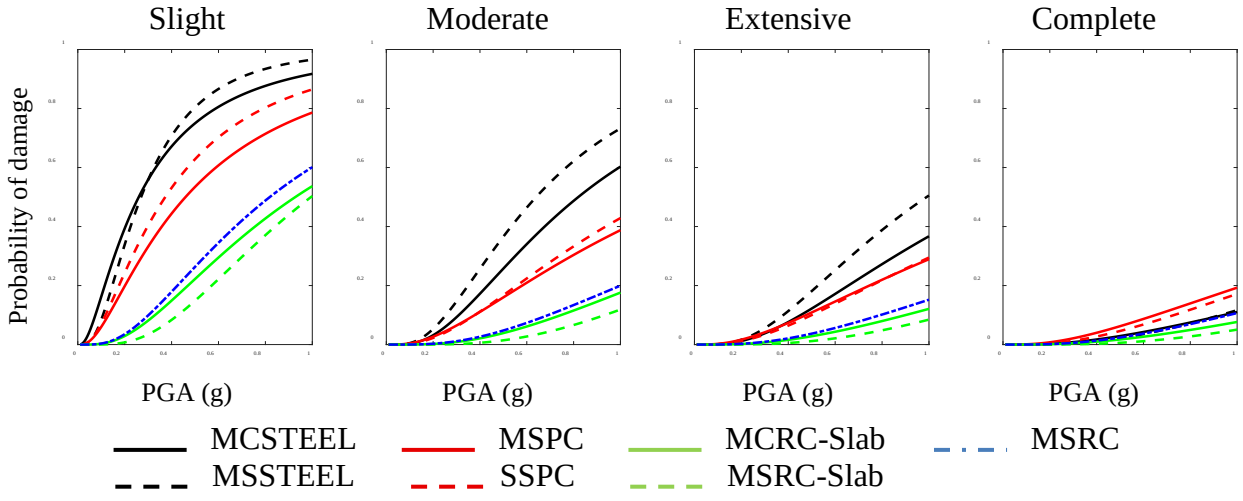

Figure 8.13: Bridge fragility curves

Finally, it should be noted that the findings here are limited to the modeling assumptions of this study and the available data for Texas bridges. Specific examples of assumptions made in this study that may affect the assessment of seismic vulnerability of Texas bridges include, but are not limited to:

- In this study, heavily skewed (skew angles greater than 15 degrees) and curved bridges are ignored in the modeling assumptions. Such bridges have been shown to be particularly vulnerable to seismic hazards (Noori et al. 2016; Zakeri et al. 2013a; b).
- The column height in the bridge samples in this study were determined using NBI underclearance data. Underclearance data is only provided for bridges that cross over navigable roadways; therefore, bridges that do not cross over navigable roadways or flyovers with multiple levels of roadway beneath are not represented in the bridge population statistics. Very tall bridges (e.g., tall flyovers) are expected to be much more flexible and may have very different seismic performance than the bridges considered in this study. Additionally, very short bridges, such as those over low-water crossings, may have short columns that are stiffer and more susceptible to shear failure modes, which may significantly affect seismic performance compared to the bridge samples considered in this study.
- In this study, it is assumed that the probabilistic seismic demand models follow a power function with respect to the intensity measure, i.e., PGA, or in other words, a linear model in log-log space. This assumed model for the PSDM regression may not accurately capture nonlinear variations of seismic demands in all ranges of ground shaking intensity. Further research should be done on the appropriateness of other regression models for relating seismic response to ground shaking intensity over a broader range of seismic intensities.
- The capacity models used in this study were largely based on those from previous bridge fragility studies. Due to the lack of data on the seismic performance of bearings used in reinforced concrete girder and slab bridges in Texas (i.e., those with dowels and simulated concrete-on-concrete friction), such bearings were assumed to have the same limit state capacity models as elastomeric bearings. The appropriateness of such an assumption should be evaluated as empirical seismic performance data from such bearings becomes available in future experimental research programs and earthquakes.
- In the nonlinear bridge models used in this study, flexural hinges are assumed to occur at the top and bottom of the columns, which is an appropriate assumption for pile foundations and drilled shafts with larger diameter than the column above. This assumed column hinge model does not capture the potential location of hinge formation in integral column-shaft foundations where the drilled shafts have the same diameter as the columns above. In such integral column-shaft foundations, flexural hinges may form below the ground surface, the location of which is dependent on drilled shaft and soil properties and can only be captured with more sophisticated modeling of soil-structure interaction. Development of hinges below the ground surface may affect the column deformations, and thus fragilities, compared to the column hinge models assumed in this study.

8.7. Summary

This chapter presents component-level and system-level fragile curves for the bridge classes considered in this study. The system-level fragility curves are developed considering the vulnerability of multiple components, i.e., bearings, columns, and abutments. To do so, the correlation of seismic demands in different components are taken into account. The system-level

fragility curves are generated by assuming that if any component exceeds any level of damage, the whole bridge exceeds that level of damage. The system-level fragility curves can used to inform post-earthquake inspection decisions (as will be discussed in the following chapter of this report), and the component-level fragility curves give a guidance to inspectors on which components are more vulnerable and may require additional attention during inspection. It is shown that steel girder bridges, both simply-supported and continuous bridges, are the most vulnerable bridge classes in Texas, which is mainly because of the steel bearings of these bridge classes. Furthermore, reinforced concrete bridges, both girder and slab types, are expected to have better seismic performance compared to the other bridge types in Texas. It is also shown that, regardless of the bridge class, abutments are the least vulnerable component of the bridges. Bearings are the most vulnerable components of the steel and prestressed concrete girder bridges, and columns are expected to be the most vulnerable component of reinforced concrete bridges. It should be also noted that the findings of this chapter are limited to the assumptions made in the bridge sampling and modeling process, which may warrant further investigation.

Chapter 9. Post-Earthquake Action Plans

9.1. Overview

The chapter proposes a procedure to use the previously described fragility functions in developing a post-earthquake action plan. First, the inspection or action criteria must be defined by decision makers (e.g., TxDOT officials). Then, the bridges the seismic fragility curves can be used in conjunction with ground shaking intensity maps to identify the bridges that require inspection or some other action. For this chapter, implementation of a post-event action plan is demonstrated using the deterministic seismic scenario maps described in Chapter 5 and two assumed inspection criteria. Finally, the number of bridges requiring inspection for the two assumed criteria are compared to the existing criterion in TxDOT's current post-event action plan.

9.2. Inspection Criteria

After an earthquake, TxDOT's initial approach is to inspect all the bridges within a specified radius of concern that depends on the earthquake magnitude, as given in Table 9.1. TxDOT would start its search within the radius of concern and would expand its inspection efforts outward if required. As seen in the table, the inspection plan only depends of the magnitude and location of the earthquake as does not account for bridge vulnerability or variability of ground motion shaking associated with soil conditions and event-to-event variability.

Table 9.1: Existing response plan of TxDOT to earthquake

Earthquake Magnitude	Radius of Concern (miles)
$M_w < 4.0$	N/A
$4.0 < M_w < 4.5$	6
$4.5 < M_w < 5.0$	9
$5.0 < M_w < 5.5$	14
$M_w > 5.5$	30

To make more informed inspection decisions, the fragility curves developed in Chapter 9 can be used to account for the relative vulnerability of different bridge types to prioritize inspection of those bridges most likely to be damaged. Additionally, using ground motion intensity maps specific to the earthquake event and the soil conditions (e.g., the ShakeMaps produced by USGS following all events of M>3.0) will provide accurate estimations of the geographic distribution of ground shaking intensities for identifying areas of most concern.

To develop a post-event action plan, first, a threshold for inspection must first be determined. Ultimately, TxDOT officials are responsible for determining this threshold based on the level of risk they are willing to assume. Here, as the purpose of demonstration, two examples of criteria are assumed as follows:

- Criterion 1: inspect all bridges that have at least a 10% probability of exceeding the Slight damage state.
- Criterion 2: inspect all bridges that have at least a 5% probability of exceeding the Moderate damage state.

Using the fragility curves developed in Chapter 9, one can find the threshold that correspond to the abovementioned criteria. For instance, Figure 9.1 shows the fragility curves that are developed for the MSSTEEL bridge class. As seen in the figure, the corresponding PGA values for the first and second criteria are 0.11 g and 0.19 g, respectively. In fact, for this bridge class, all the MSSTEEL bridges that are in areas with PGA $\geq$ 0.11 g and PGA $\geq$ 0.19 g would require inspection according to the first and second inspection criteria, respectively. The PGA thresholds for all other bridge classes can be computed by following in the same procedure. Table 9.2 presents the PGA thresholds for the two assumed inspection criteria for all bridge classes considered in this study. As seen in the table, MSSTEEL bridges have the lowest PGA values requiring inspection, representing the fact that MSSTEEL bridges are the most vulnerable bridges compared to all other bridge classes.

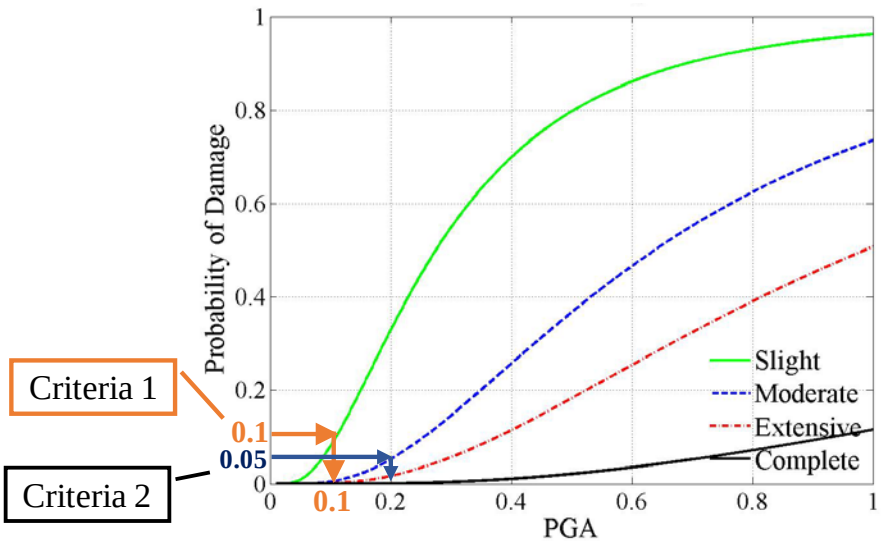

Figure 9.1: Fragility curves for MSSTEEL bridge class

Table 9.2: PGA threshold for different bridge classes

	PGA Threshold (g)	
Bridge Classes	First criteria	Second criteria
MCSTEEL	0.13	0.23
MSSTEEL	0.11	0.19
MSPC	0.13	0.26
MSRC	0.30	0.50
MCRC-SLAB	0.32	0.55
MSRC-SLAB	0.42	0.72

Right after the earthquake, USGS generates ShakeMaps providing geographic distribution of various ground shaking intensity measures, such as PGA, PGV, and spectral accelerations at certain natural periods. One can use the USGS ShakeMap PGA contours corresponding to the thresholds in Table 9.2 to identify the areas over which inspection is required for each bridge class. In the absence of ShakeMaps form recent Texas earthquakes, the deterministic hazard maps shown in Figure 5.5 through Figure 5.12 demonstrate that with increasing distance from the epicenter, the PGA values rapidly diminish.

9.3. Inspection Decisions for Fort Worth Earthquake Scenario

For purposes of demonstrating the post-event action plan, the M6 Fort Worth scenario presented in Chapter 5 of this report is considered. Figure 5.9 shows the deterministic hazard map developed for that earthquake scenario. As seen in the figure, the largest PGA in the vicinity of the earthquake epicenter is approximately 0.63g. Further from the epicenter, the values of PGA decrease. Figure 9.2 through Figure 9.7 show the locations of bridges from each bridge class overlaid on the scenario hazard map. The PGA contours correspond to the two example inspection criteria are shown for each bridge class, as well as the 30-mile radius of concern according to the existing TxDOT action plan. The location of each bridge is indicated by a dot in the figures. The existing inspection criteria requires that all bridges within the 30-mile radius of concern should be inspected, regardless of bridge class. However, the contours indicating the area for inspection using the two example criteria in the proposed action plan not only consider the relative vulnerability of each bridge class, but also take into account the effects of soil and ground motion characteristics specific to that particular earthquake event and location. These figures also show the locations of all the bridges that needs to be inspected for each bridge class.

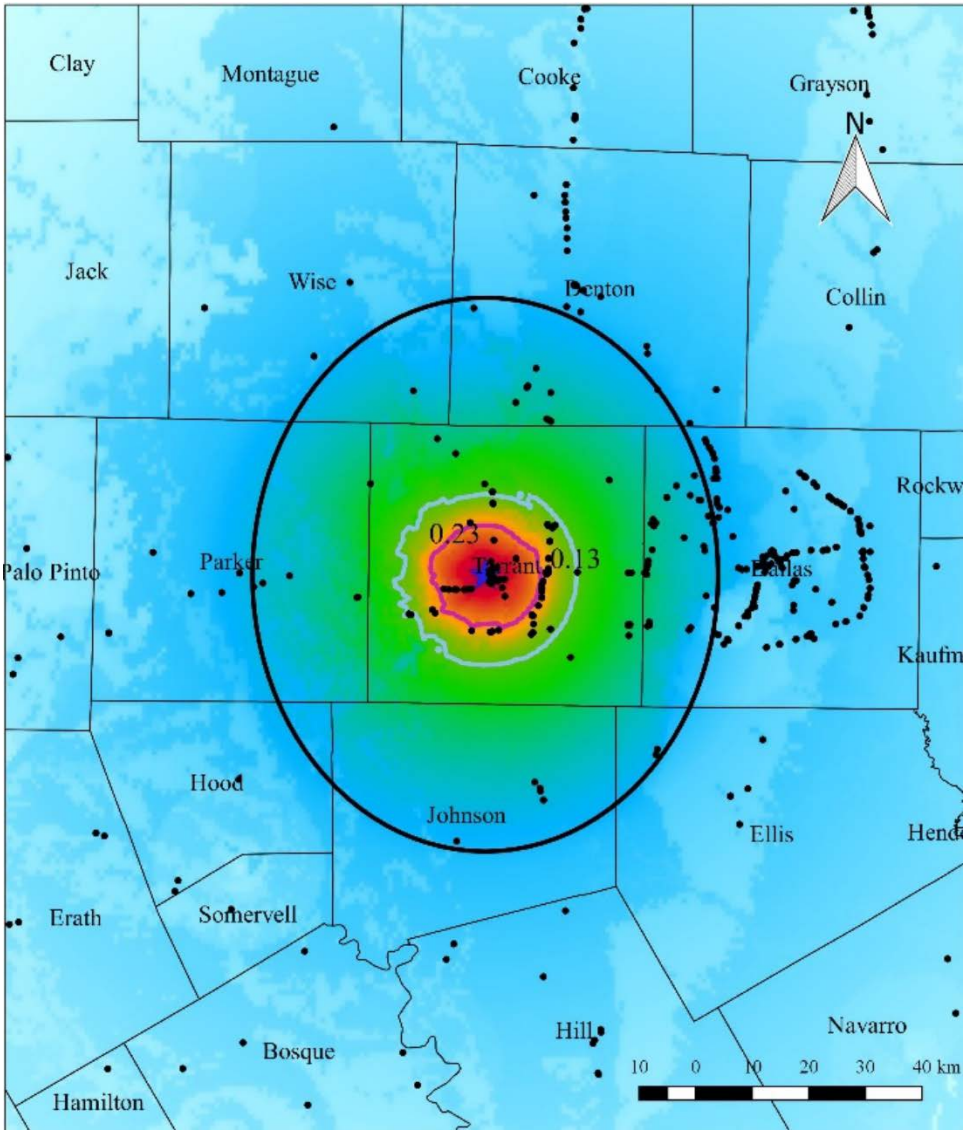

Figure 9.2: Hazard map with MCSTEEL bridges

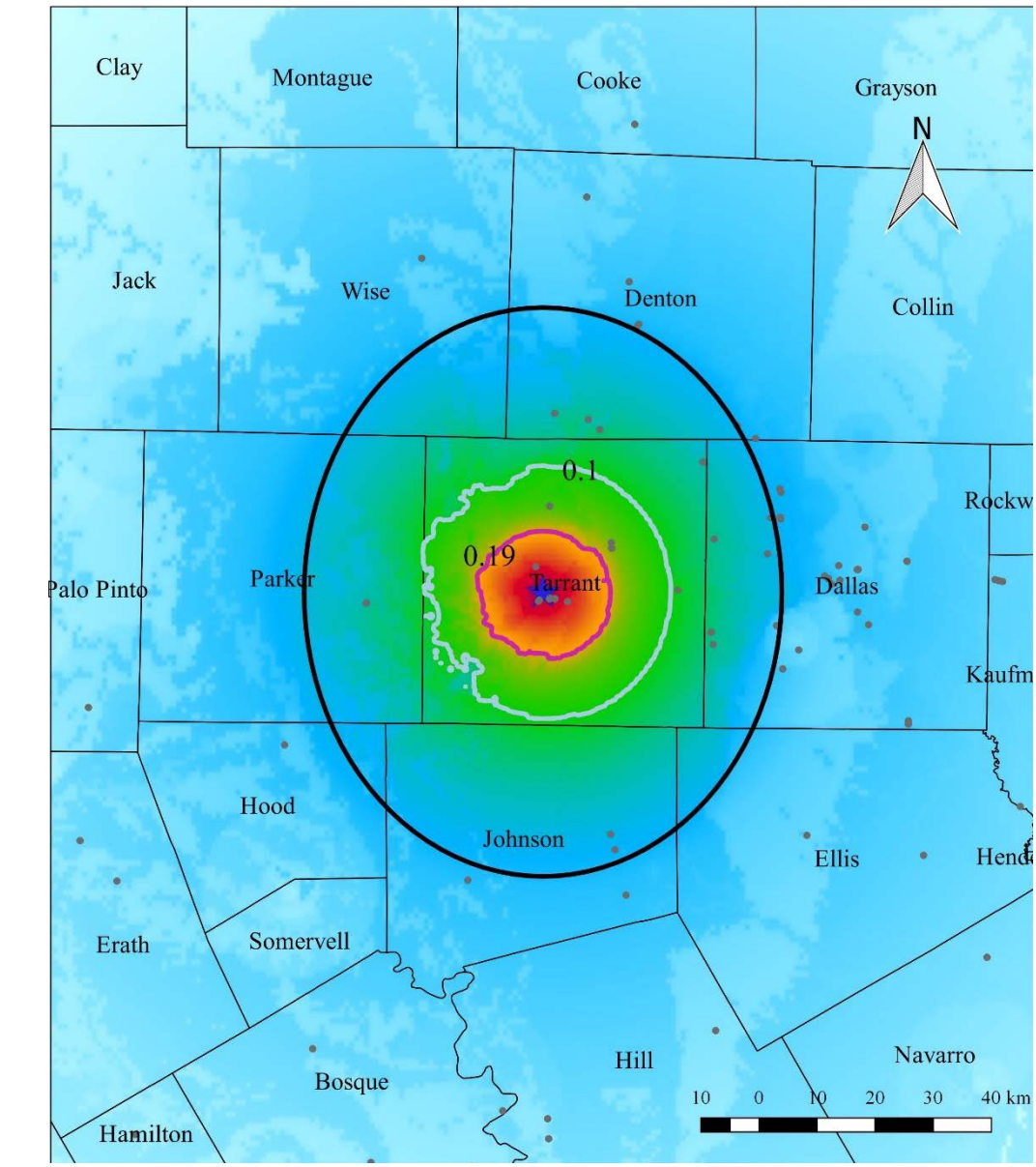

Figure 9.3: Hazard map with MSSTEEL bridges

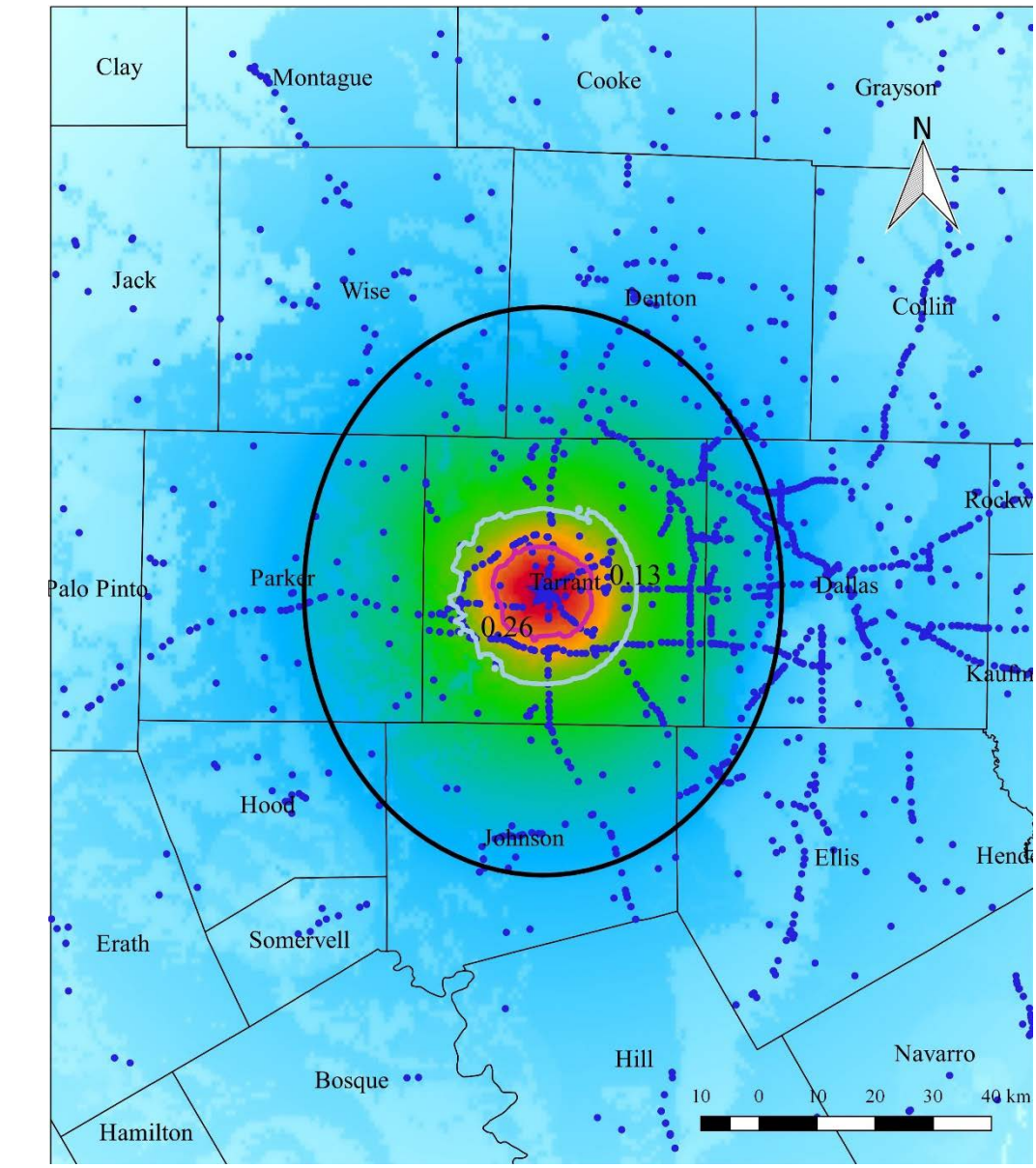

Figure 9.4: Hazard map with MSPC bridges

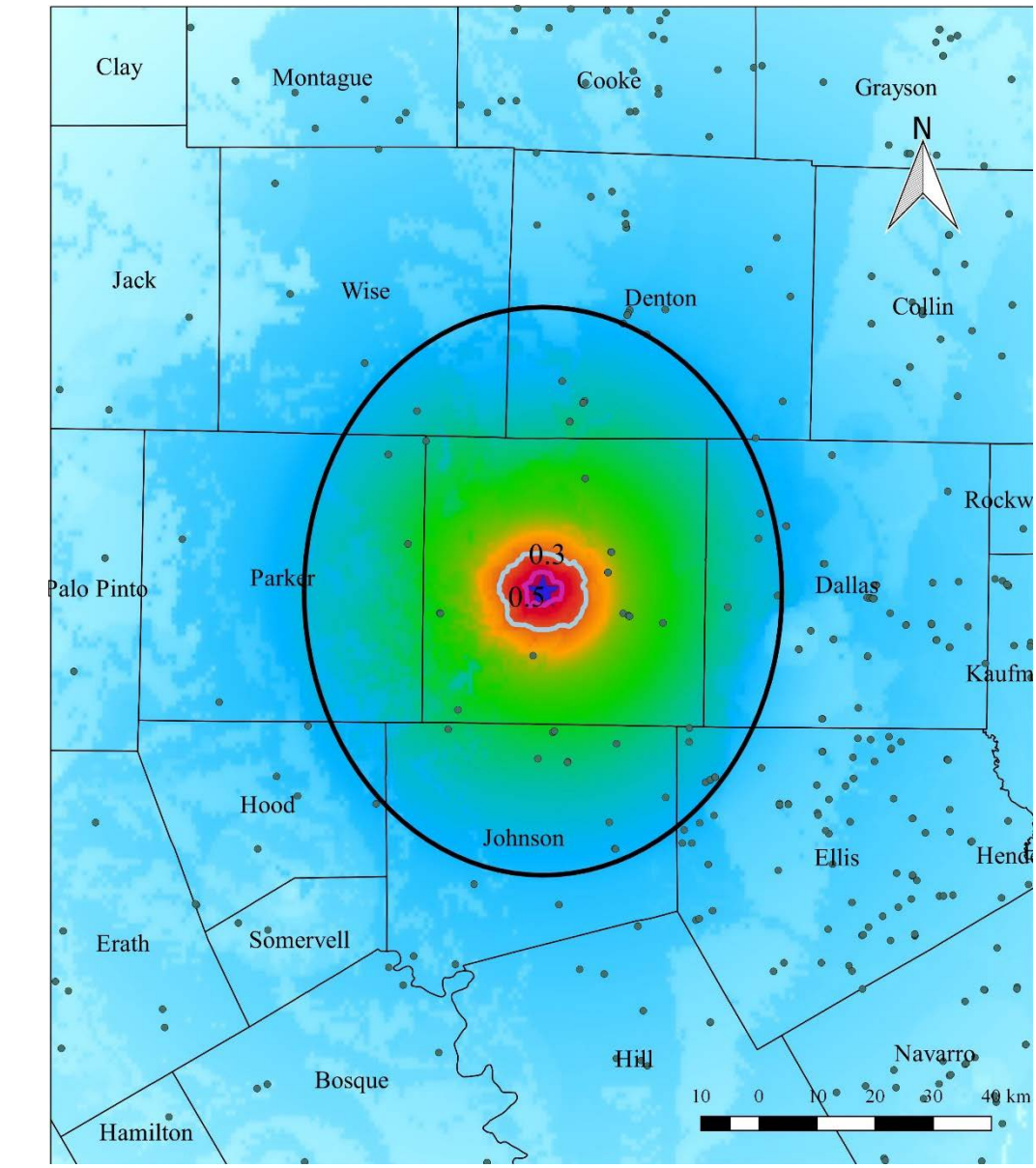

Figure 9.5: Hazard map with MSRC bridges

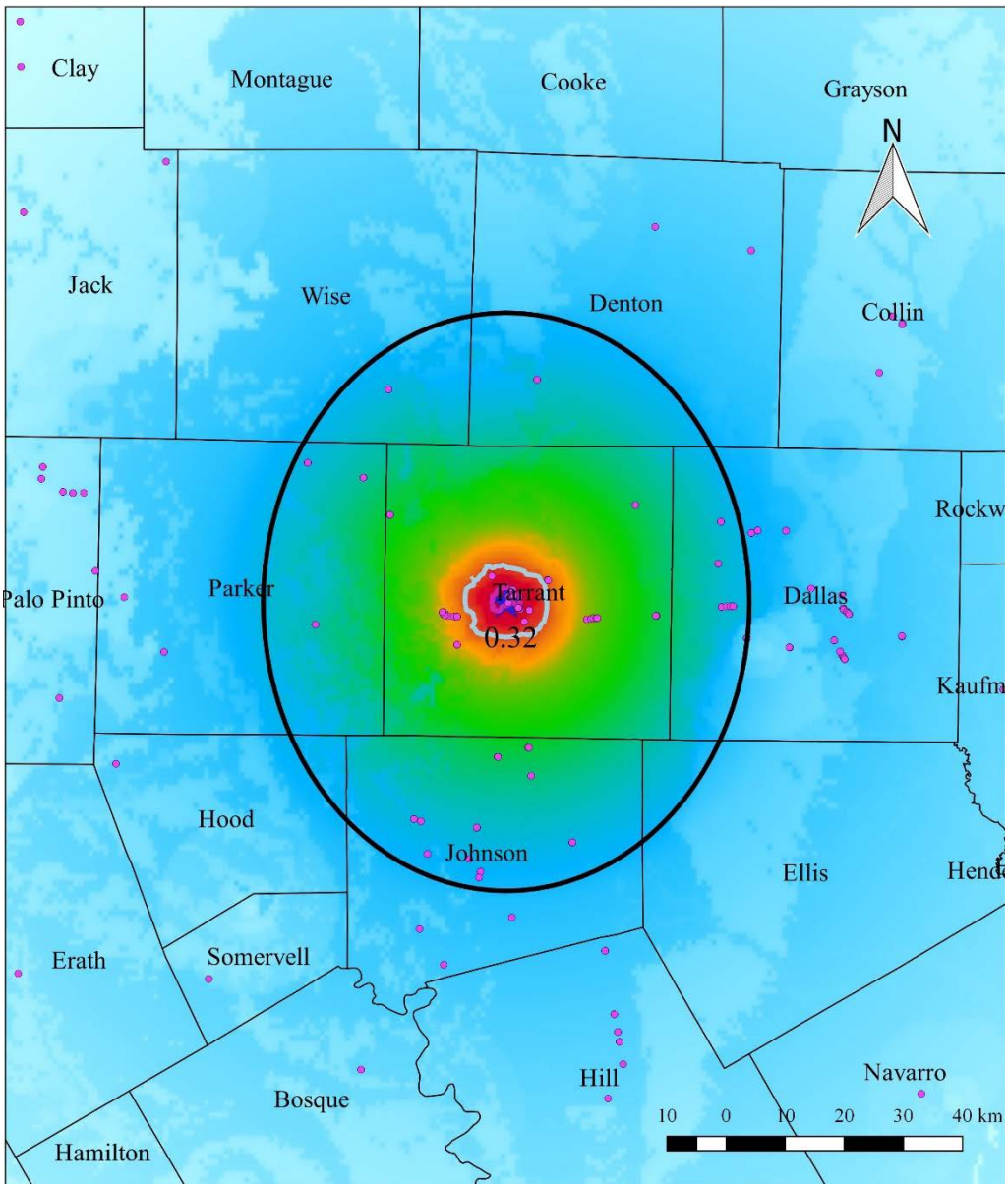

Figure 9.6: Hazard map with MCRC-slab bridges

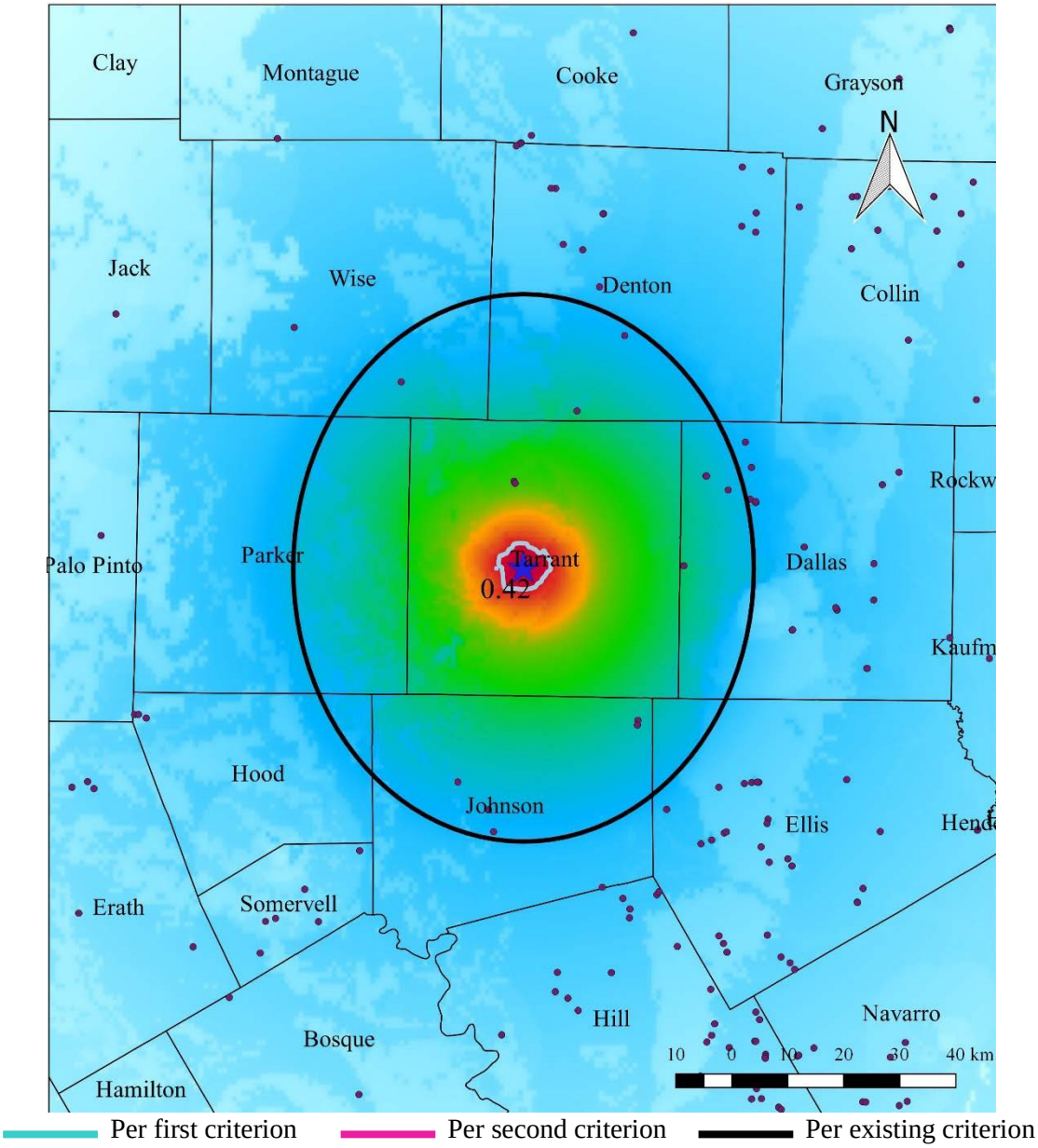

Figure 9.7: Hazard map with MSRC-slab bridges

Table 9.3 shows the number of the bridges that would require inspection for this assumed M6 Fort Worth earthquake scenario for the existing criterion and the two example criteria for the proposed action plan. As seen in the table, for each bridge, there is a noticeable difference between the number of the bridges that require inspection based on the proposed criteria and existing criterion. For instance, based on the existing criteria, 1014 MSPC bridges need to be inspected after this earthquake; however, the two example criteria used in the proposed action plan lead to significantly lower numbers. Moreover, although the MSSTEEL bridge class is the most vulnerable bridge class, the table shows that MSPC bridge class has the largest number of bridges that need to be inspected, which is because of the frequency of the latter bridge class in the area that the earthquake happened.

Table 9.3: Number of bridges requiring inspection after the hypothetical M6 Fort Worth earthquake scenario

	First criteria	Second criteria	Excising Criteria
Bridge Classes	10% probability of Slight damage	5% probability of Moderate damage	Bridge within 30 miles
MCSTEEL	102	57	188
MSSTEEL	12	8	28
MSPC	292	85	1014
MSRC	0	0	51
MCRC-SLAB	15	6	69
MSRC-SLAB	0	0	14
Total	421	156	1364

9.4. Summary

This chapter presents a post-earthquake action plan based on the fragility curves that were developed in this study for different bridge classes. For implementation of this action plan, the user (i.e., TxDOT officials) should define a threshold for the action; then, using the Texas-specific fragility curves, the corresponding intensity measure (i.e., PGA) threshold requiring action can be identified. Maps of ground motion shaking intensity produced immediately following an earthquake event, along with the previously determined PGA thresholds, can be used to determine the area requiring action for each bridge class. This methodology not only takes into account the effects of the earthquake shaking on different bridge classes, but also considers the ground motions characteristics and soil effects specific to each earthquake event. A demonstration of the proposed post-event action plan using two example criteria for inspection was discussed using a hypothetical M6 Fort Worth earthquake scenario previously developed in Chapter 5.

References

AASHTO. (2016). *AASHTO LRFD Bridge Design Specifications*. American Association of State Highway and Transportation Officials, Washington, DC.

Al Aawar, W. (2015). “Non-linear modeling parameters for reinforced concrete columns with inadequate lap splices.”

Abrams, M., and Hook, S. J. (1995). “Simulated ASTER data for geologic studies.” *IEEE Transactions on Geoscience and remote sensing*, IEEE, 33(3), 692–699.

ACI. (2016). *Code Requirements for Seismic Evaluation and Retrofit of Existing Concrete Buildings*. American Concrete Institute, Committee 369.

ACI Committee 318. (2014). *Building Code Requirements for Structural Concrete (ACI 318-14)*. American Concrete Institute, Farmington Hills, Michigan,.

Amirihormozaki, E., Pekcan, G., and Itani, A. (2015). “Analytical Modeling of Horizontally Curved Steel Girder Highway Bridges for Seismic Analysis.” *Journal of Earthquake Engineering*, 19(19).

Anagnostopoulos, S. A. (1988). “Pounding of buildings in series during earthquakes.” *Earthquake engineering & structural dynamics*, Wiley Online Library, 16(3), 443–456.

ASCE. (2014). *Seismic evaluation and retrofit of existing buildings*. ASCE/SEI 41-13, Reston, VA.

ATC. (1985). *Earthquake Damage Evaluation Data for California*. Report No. ATC-13, Applied Technology Council.

Atkinson, G. M., Greig, D. W., and Yenier, E. (2014). “Estimation of moment magnitude (M) for small events (M< 4) on local networks.” *Seismological Research Letters*, GeoScienceWorld, 85(5), 1116–1124.

Atkinson, G. M., and Mahani, A. B. (2013). “Estimation of moment magnitude from ground motions at regional distances.” *Bulletin of the Seismological Society of America*, Seismological Society of America, 103(1), 107–116.

Aviram, a., Aviram, a., Mackie, K., Mackie, K., Stojadinovic, B., and Stojadinovic, B. (2008). “Guidelines of Nonlinear Analysis of Bridge Structures in California.” *PEER report*, (August).

Basoz, N., and Kiremidjian, A. S. (1996). “Risk assessment for highway systems.” *Rep. No. 118, John A. Blume Earthquake Engineering Center*.

Boore, D. M. (2010). “Orientation-independent, nongeometric-mean measures of seismic intensity from two horizontal components of motion.” *Bulletin of the Seismological Society of America*, Seismological Society of America, 100(4), 1830–1835.

Boulanger, R. W., Curras, C. J., Kutter, B. L., Wilson, D. W., and Abghari, A. (1999). “Seismic soil-pile-structure interaction experiments and analyses.” *Journal of Geotechnical and Geoenvironmental Engineering*, American Society of Civil Engineers, 125(9), 750–759.

Bournonville, M., Dahnke, J., and Darwin, D. (2004). *Statistical analysis of the mechanical properties and weight of reinforcing bars*.

Bozorgzadeh, A., Megally, S. H., Ashford, S., and Restrepo, J. I. (2007). “Seismic response of sacrificial exterior shear keys in bridge abutments.” *SSRP*, 4, 14.

Brown, L. T., Diehl, J. G., and Nigbor, R. L. (2000). “A simplified procedure to measure average shear-wave velocity to a depth of 30 meters (VS30).” *Proceedings of 12th world conference on earthquake engineering*.

Caltrans. (1999). “Caltrans Seismic Design Criteria Version 1 . 1.” (July).

Caltrans. (2013). “Seismic Design Criteria Version 1.7.” *California Department of Transportation: Sacramento, CA, U.S.*, (April).

Chen, W., and Duan, L. (2003). *Bridge engineering: seismic design*. CRC press.

Choi, E. (2002). “Seismic Analysis and Retrofit of Mid-America Bridges.” Georgia Institute of Technology.

Choi, E., DesRoches, R., and Nielson, B. (2004). “Seismic fragility of typical bridges in moderate seismic zones.” *Engineering Structures*, 26(2), 187–199.

Chopra, A. (2012). *Dynamics of Structures: Theory and Applications to Earthquake Engineering*. Prentice Hall, New Jersey.

Cornell, C. A., Jalayer, F., Hamburger, R. O., and Foutch, D. A. (2002). “Probabilistic Basis for 2000 SAC Federal Emergency Management Agency Steel Moment Frame Guidelines.” 128(4), 526–533.

Cox, B. R., Bachhuber, J., Rathje, E., Wood, C. M., Dulberg, R., Kottke, A., Green, R. A., and Olson, S. M. (2011). “Shear wave velocity-and geology-based seismic microzonation of Port-au-Prince, Haiti.” *Earthquake Spectra*, 27(S1), S67–S92.

Crone, A. J., and Luza, K. V. (1990). “Style and timing of Holocene surface faulting on the Meers fault, southwestern Oklahoma.” *Geological Society of America Bulletin*, Geological Society of America, 102(1), 1–17.

CSI. (2016). “SAP200 v19. Retrieved from https://www.csiamerica.com/products/sap2000.”

Davis, S. D., and Frohlich, C. (1993). “Did (or will) fluid injection cause earthquakes?-criteria for a rational assessment.” *Seismological Research Letters*, GeoScienceWorld, 64(3-4), 207–224.

Davis, S. D., Nyffenegger, P. A., and Frohlich, C. (1995). “The 9 April 1993 earthquake in south-central Texas: Was it induced by fluid withdrawal?” *Bulletin of the Seismological Society of America*, Seismological Society of America, 85(6), 1888–1895.

DesRoches, R., and Fenves, G. L. (1997). *NEW DESIGN AND ANALYIS PROCEDURES FOR INTERMEDIATE HINGES IN MULTIPLE-FRAME BRIDGES*.

Doser, D. I., Baker, M. R., Luo, M., Marroquin, P., Ballesteros, L., Kingwell, J., Diaz, H. L., and Kaip, G. (1992). “The not so simple relationship between seismicity and oil production in the Permian Basin, West Texas.” *pure and applied geophysics*, Springer, 139(3-4), 481–506.

Douglas, J. (2016). *Ground motion prediction equations 1964–2016*. Department of Civil and Environmental Engineering, University of Strathclyde, Glasgow, United Kingdom,.

Eaton, D. W., and Mahani, A. B. (2015). “Focal mechanisms of some inferred induced earthquakes in Alberta, Canada.” *Seismological Research Letters*, GeoScienceWorld, 86(4), 1078–1085.

Elnashai, A. S., Borzi, B., and Vlachos, S. (2004). “Deformation-based vulnerability functions for

RC bridges." *Structural Engineering and Mechanics*, Taejon, Korea: Techno-Press, c1993-, 17(2), 215–244.

Fan, Z., Eichhubl, P., Gale, J., Olson, J. E., Frohlich, C., and Gono, V. (2014). "Was the Timpson, Texas, M4. 8 event induced by fluid injection?" *AGU Fall Meeting Abstracts*.

Fang, J. Q., Li, Q. S., Jeary, A. P., and Liu, D. K. (1999). "Damping of tall buildings: Its evaluation and probabilistic characteristics." *The Structural Design of Tall Buildings*, John Wiley & Sons, Ltd., 8(2), 145–153.

Farahbod, A. M., Kao, H., Cassidy, J. F., and Walker, D. (2015). "How did hydraulic-fracturing operations in the Horn River Basin change seismicity patterns in northeastern British Columbia, Canada?" *The Leading Edge*, Society of Exploration Geophysicists, 34(6), 658–663.

de Felice, G., and Giannini, R. (2010). "An efficient approach for seismic fragility assessment with application to old reinforced concrete bridges." *Journal of Earthquake Engineering*, Taylor & Francis, 14(2), 231–251.

FEMA. (2003). *HAZUS-MH MR4: Technical Manual*. Vol. Earthquake Model. Federal Emergency Management Agency, Washington DC.

FHWA. (1995). *Recording and Coding Guide for the Structure Inventory and Appraisal of the Nation's Bridges*. Vol. FHWA-PD-96-001. Office of Engineering Bridge Division, Federal Highway Administration, McLean, VA.

Filipov, E. (2012). "Nonlinear seismic analysis of quasi-isolation systems for earthquake protection of bridges."

Frohlich, C. (2012). "Two-year survey comparing earthquake activity and injection-well locations in the Barnett Shale, Texas." *Proceedings of the National Academy of Sciences*, National Acad Sciences, 109(35), 13934–13938.

Frohlich, C., and Brunt, M. (2013). "Two-year survey of earthquakes and injection/production wells in the Eagle Ford Shale, Texas, prior to the MW4. 8 20 October 2011 earthquake." *Earth and Planetary Science Letters*, Elsevier, 379, 56–63.

Frohlich, C., and Davis, S. D. (2002). *Texas earthquakes*. University of Texas Press.

Frohlich, C., Deshon, H., Stump, B., Hayward, C., Hornbach, M., and Walter, J. I. (2016a). "A Historical Review of Induced Earthquakes in Texas." *Seismological Research Letters*, 87(4), 1–17.

Frohlich, C., DeShon, H., Stump, B., Hayward, C., Hornbach, M., and Walter, J. I. (2016b). "A historical review of induced earthquakes in Texas." *Seismological Research Letters*, GeoScienceWorld, 87(4), 1022–1038.

Frohlich, C., Ellsworth, W., Brown, W. A., Brunt, M., Luetgert, J., MacDonald, T., and Walter, S. (2014). "The 17 May 2012 M4. 8 earthquake near Timpson, East Texas: An event possibly triggered by fluid injection." *Journal of Geophysical Research: Solid Earth*, Wiley Online Library, 119(1), 581–593.

Fumal, Te., and Tinsley, J. C. (1985). "Mapping shear-wave velocities of near-surface geologic materials." *Evaluating earthquake hazards in the Los Angeles region: an earth-science perspective, US Geol. Surv. Profess. Pap*, 1360, 101–126.

Ghannoum, W., and Sivaramakrishnan, B. (2012a). *ACI 369 rectangular column database*. Data

set. <http://www.nees.org/resources/3659>.

Ghannoum, W., and Sivaramakrishnan, B. (2012b). *ACI 369 circular column database*. Dataset. <http://www.nees.org/resources/3658>.

Goldsmith, W. (1978). *Impact: the theory and physical behaviour of colliding solids*. University Microfilms.

Goulet, C. A., Cramer, C. H., Darragh, R. B., Silva, W. J., Hashash, Y. M. A., Harmon, J., Stewart, J. P., Wooddell, K. E., and Youngs, R. R. (2014). "PEER NGA-East database." *PEER Report 2014*, 17.

Gupta, H. K. (2002). "A review of recent studies of triggered earthquakes by artificial water reservoirs with special emphasis on earthquakes in Koyna, India." *Earth-Science Reviews*, Elsevier, 58(3), 279–310.

Hamidreza, B., Ahmad, M. I., and Ian, G. B. (2010). "Guidelines for the Seismic Design of Ductile End Cross Frames in Steel Girder Bridge Superstructures." *Unr*, Report No.(July).

Harding, S. T. (1981). "Induced seismic Cogdell Canyon Reef oil field." *US Geol. Surv. Open-File Rept*, 67–81.

Hassani, B., and Atkinson, G. M. (2015). "Referenced Empirical Ground-Motion Model for Eastern North America." *Seismological Research Letters*, 86, 477–491.

Healy, J. H., Rubey, W. W., Griggs, D. T., and Raleigh, C. B. (1968). "The denver earthquakes." *Science*, 161(3848), 1301–1310.

Herrmann, R. B., Benz, H., and Ammon, C. J. (2011). "Monitoring the earthquake source process in North America." *Bulletin of the Seismological Society of America*, Seismological Society of America, 101(6), 2609–2625.

Hinton, D. D., and Olien, R. M. (2002). *Oil in Texas: the gusher age, 1895-1945*. University of Texas Press.

Holland, A. (2011). *Examination of possibly induced seismicity from hydraulic fracturing in the Eola Field, Garvin County, Oklahoma*. Oklahoma Geological Survey.

Hornbach, M. J., DeShon, H. R., Ellsworth, W. L., Stump, B. W., Hayward, C., Frohlich, C., Oldham, H. R., Olson, J. E., Magnani, M. B., Brokaw, C., and others. (2015). "Causal factors for seismicity near Azle, Texas." *Nature communications*, Nature Publishing Group, 6.

Horton, S. (2012). "Disposal of hydrofracking waste fluid by injection into subsurface aquifers triggers earthquake swarm in central Arkansas with potential for damaging earthquake." *Seismological Research Letters*, GeoScienceWorld, 83(2), 250–260.

Hough, S. E. (2014). "Shaking from injection-induced earthquakes in the central and eastern United States." *Bulletin of the Seismological Society of America*, Seismological Society of America.

Hough, S. E., Armbruster, J. G., Seeber, L., and Hough, J. F. (2000). "On the modified Mercalli intensities and magnitudes of the 1811--1812 New Madrid earthquakes." *Journal of Geophysical Research: Solid Earth*, Wiley Online Library, 105(B10), 23839–23864.

Huntington, D. E., and Lyrintzis, C. S. (1998). "Improvements to and limitations of Latin hypercube sampling." *Probabilistic Engineering Mechanics*, Elsevier, 13(4), 245–253.

Iman, R. L., and Conover, W.-J. (1982). "A distribution-free approach to inducing rank correlation among input variables." *Communications in Statistics-Simulation and Computation*, Taylor

& Francis, 11(3), 311–334.

Iwahashi, J., and Pike, R. J. (2007). "Automated classifications of topography from DEMs by an unsupervised nested-means algorithm and a three-part geometric signature." *Geomorphology*, Elsevier, 86(3), 409–440.

Janská, E., and Eisner, L. (2012). "Ongoing seismicity in the Dallas-Fort Worth area." *The Leading Edge*, Society of Exploration Geophysicists, 31(12), 1462–1468.

Justinic, A. H., Stump, B., Hayward, C., and Frohlich, C. (2013). "Analysis of the Cleburne, Texas, earthquake sequence from June 2009 to June 2010." *Bulletin of the Seismological Society of America*, Seismological Society of America, 103(6), 3083–3093.

Kahle, A. B., and Rowan, L. C. (1980). "Evaluation of multispectral middle infrared aircraft images for lithologic mapping in the East Tintic Mountains, Utah." *Geology*, Geological Society of America, 8(5), 234–239.

Karim, K. R., and Yamazaki, F. (2003). "A simplified method of constructing fragility curves for highway bridges." *Earthquake engineering & structural dynamics*, Wiley Online Library, 32(10), 1603–1626.

Keller, G. R., Rogers, A. M., and Orr, C. D. (1987). "Seismic Activity in the Permian Basin Area of West Texas and Southeastern New Mexico, 1975--79." *Seismological Research Letters*, GeoScienceWorld, 58(2), 63–70.

Kent, D. C., and Park, R. (1971). "Flexural members with confined concrete." *Journal of the Structural Division*.

Keranen, K. M., Weingarten, M., Abers, G. A., Bekins, B. A., and Ge, S. (2014). "Sharp increase in central Oklahoma seismicity since 2008 induced by massive wastewater injection." *Science*, American Association for the Advancement of Science, 345(6195), 448–451.

Kim, B., Hashash, Y. M. A., Rathje, E. M., Stewart, J. P., Ni, S., Somerville, P. G., Kottke, A. R., Silva, W. J., and Campbell, K. W. (2016). "Subsurface Shear Wave Velocity Characterization Using P-Wave Seismograms in Central and Eastern North America." *Earthquake Spectra*, Earthquake Engineering Research Institute, 32(1), 143–169.

Der Kiureghian, A. (2002). "Bayesian methods for seismic fragility assessment of lifeline components." *Acceptable Risk Processes--Lifelines and Natural Hazards*, 61–77.

Kottke, A. R., Hashash, Y., Stewart, J. P., Moss, C. J., Nikolaou, S., Rathje, E. M., Silva, W. J., and Campbell, K. W. (2012). "Development of geologic site classes for seismic site amplification for central and eastern North America."

Kramer, S. L. (1996). *Geotechnical earthquake engineering*. Prentice Hall, New Jersey.

Lou, K., and Cheng, F. Y. (1996). "Post-earthquake assessment of bridge colapso and design parameters." *11th World Conference on Earthquake Engineering, CD ROOM, paper*.

Mackie, K., and Stojadinovic, B. (2004). "Fragility curves for reinforced concrete highway overpass bridges." *13th World Conference on Earthquake Engineering*, 1–6.

Mackie, K., and Stojadinović, B. (2001). "Probabilistic seismic demand model for California highway bridges." *Journal of Bridge Engineering*, American Society of Civil Engineers, 6(6), 468–481.

Maison, B. F., and Kasai, K. (1990). "SLAM-2: A Computer Program for the Analysis of Structural Pounding (Extended Version)." *June, Available from the National Information*

Service for Earthquake Engineering, University of California, Berkeley, CA.

Mander, J. B., Priestley, M. J. N., and Park, R. (1988). "Theoretical stress-strain model for confined concrete." *Journal of structural engineering*, American Society of Civil Engineers, 114(8), 1804–1826.

Mander, J., Kim, D., Chen, S., and Premus, G. (1996). "Response of steel bridge bearings to the reversed cyclic loading." *Technical Report NCEER 96-0014, Buffalo, NY*.

McGann, C. R., Arduino, P., and Mackenzie-Helnwein, P. (2011). "Simplified procedure to account for a weaker soil layer in lateral load analysis of single piles." *Journal of Geotechnical and Geoenvironmental Engineering*, American Society of Civil Engineers, 138(9), 1129–1137.

McKenna, F., Fenves, G. L., Scott, M. H., and others. (2000). "Open system for earthquake engineering simulation." *University of California, Berkeley, CA.*

Mtenga, P. V. (2007). *Elastomeric Bearing Pads Under Combined Loading*. Report to the Florida Department of Transportation, Contract No: BC352-16, Tallahassee, FL.

Muthukumar, S. (2003). "A contact element approach with hysteresis damping for the analysis and design of pounding in bridges." Georgia Institute of Technology.

Ni, S., Li, Z., and Somerville, P. (2014). "Estimating subsurface shear velocity with radial to vertical ratio of local P waves." *Seismological Research Letters*, GeoScienceWorld, 85(1), 82–90.

Nicholson, C., and Wesson, R. L. (1990). *Earthquake hazard associated with deep well injection*. Alexandria, VA (United States); US Geological Survey.

Nicot, J.-P., and Scanlon, B. R. (2012). "Water use for shale-gas production in Texas, US." *Environmental science & technology*, ACS Publications, 46(6), 3580–3586.

Nielson, B. G. (2005). "Analytical fragility curves for highway bridges in moderate seismic zones." *Environmental Engineering*, (December), 400.

Nielson, B. G., and DesRoches, R. (2007a). "Analytical seismic fragility curves for typical bridges in the central and southeastern United States." *Earthquake Spectra*, 23(3), 615–633.

Nielson, B. G., and DesRoches, R. (2007b). "Seismic fragility methodology for highway bridges using a component level approach." *Earthquake Engineering & Structural Dynamics*, 36, 823–839.

Noori, H. Z., Amiri, G. G., Nekooei, M., and Zakeri, B. (2016). "Seismic fragility assessment of skewed MSSS-I girder concrete bridges with unequal height columns." *Journal of Earthquake and Tsunami*, World Scientific, 10(01), 1550013.

Olien, R. M. (2010). "Oil and gas industry." *Handbook of Texas Online, Texas State Historical Association, http://www. tshaonline. org/handbook/online/articles/doogz (last accessed August 2015*.

Olson, D. R., and Frohlich, C. (1992). "Research Note: Felt Reports from the 20 July 1991 Falls City Earthquake, Karnes County, Texas." *Seismological Research Letters*, GeoScienceWorld, 63(4), 603–604.

Olsson, A. M. J., and Sandberg, G. E. (2002). "Latin hypercube sampling for stochastic finite element analysis." *Journal of Engineering Mechanics*, American Society of Civil Engineers, 128(1), 121–125.

Padgett, J. E. (2007). “Seismic Vulnerability Assessment of Retrofitted Bridges Using Probabilistic Methods Seismic Vulnerability Assessment of Retrofitted Bridges Using Probabilistic.” *Environmental Engineering*, 1–10.

Padgett, J. E., and DesRoches, R. (2007). “Bridge functionality relationships for improved seismic risk assessment of transportation networks.” *Earthquake Spectra*, 23(1), 115–130.

Padgett, J. E., Nielson, B. G., and Desroches, R. (2008). “Selection of optimal intensity measures in probabilistic seismic demand models of highway bridge portfolios.” (December 2007), 711–725.

Pan, Y. (2007). “Seismic fragility and risk management of highway bridges in New York State.” 12(December), 10031.

Pan, Y., Agrawal, A. K., Ghosn, M., and Alampalli, S. (2010). “Seismic Fragility of Multispan Simply Supported Steel Highway Bridges in New York State. II: Fragility Analysis, Fragility Curves, and Fragility Surfaces.” *Journal of Bridge Engineering*, 15(5), 462–472.

Parker, G. A., Harmon, J. A., Stewart, J. P., Hashash, Y. M. A., Kottke, A. R., Rathje, E. M., Silva, W. J., and Campbell, K. W. (2017). “Proxy-Based VS30 Estimation in Central and Eastern North America.” *Bulletin of the Seismological Society of America*, Seismological Society of America.

Patel, R., Dubey, S. K., and Pathak, K. K. (2014). “Effect of depth span ratio on the behaviour of beams.” *International Journal of Advanced Structural Engineering (IJASE)*, Springer, 6(2), 3.

Pennington, W. D., Davis, S. D., Carlson, S. M., DuPree, J., and Ewing, T. E. (1986). “The evolution of seismic barriers and asperities caused by the depressuring of fault planes in oil and gas fields of south Texas.” *Bulletin of the Seismological Society of America*, Seismological Society of America, 76(4), 939–948.

Petersen, B. M. D., Mueller, C. S., Moschetti, M. P., Hoover, S. M., Rubinstein, J. L., Andrea, L., Michael, A. J., Ellsworth, W. L., Mcgarr, A. F., Holland, A. A., Anderson, J. G., Jewell, S., and Survey, U. S. G. (2015). “Incorporating Induced Seismicity in the 2014 United States National Seismic Hazard Model — Results of 2014 Workshop and Sensitivity Studies.” *USGS Open File Report*, 2015-1070, 75.

Petersen, M. D., Mueller, C. S., Moschetti, M. P., Hoover, S. M., Shumway, A. M., McNamara, D. E., Williams, R. A., Llenos, A. L., Ellsworth, W. L., Michael, A. J., and others. (2017). “2017 one-year seismic-hazard forecast for the Central and Eastern United States from induced and natural earthquakes.” *Seismological Research Letters*, GeoScienceWorld, 88(3), 772–783.

Petersen, M., Mueller, C. S., Moschetti, M. P., Hoover, S. M., Llenos, A. L., Ellsworth, W. L., Michael, A. J., Rubinstein, J. L., McGarr, A. F., and Rukstales, K. S. (2016a). “2016 One-Year Seismic Hazard Forecast for the Central and Eastern United States from Induced and Natural Earthquakes.” *Open-File Report*, (June), 1–50.

Petersen, M., Mueller, C. S., Moschetti, M. P., Hoover, S. M., Llenos, A. L., Ellsworth, W. L., Michael, A. J., Rubinstein, J. L., Mcgarr, A. F., Rukstales, K. S., Jewell, S., Kimball, S. M., and Survey, U. S. G. (2016b). “2016 One-Year Seismic Hazard Forecast for the Central and Eastern United States from Induced and Natural Earthquakes.”

Pottatheere, P., and Renault, P. (2008). “Seismic vulnerability assessment of skew bridges.”

Proceedings of Fourteenth World Conference on Earthquake Engineering. Beijing, China.

Pratt, W. E., and Johnson, D. W. (1926). "Local subsidence of the Goose Creek oil field." *The Journal of Geology*, University of Chicago Press, 34(7, Part 1), 577–590.

Priestley, M. J. N., Seible, F., and Calvi, G. M. (1996). *Seismic design and retrofit of bridges*. John Wiley & Sons.

Ramanathan, K. N. (2012). *Next generation seismic fragility curves for California bridges incorporating the evolution in seismic design philosophy*. Georgia Institute of Technology.

Ramelli, A. R., and Slemmons, D. B. (1990). "Implications of the Meers fault on seismic potential in the central United States." *Reviews in Engineering Geology*, Geological Society of America, 8, 59–76.

Rashidi, S., and Ala Saadeghvaziri, M. (1997). "Seismic Modeling of Multi-Span Simply-Supported Bridges UsingAdina." *Computers & Structures*, 64(5/6), 1025–1039.

RISA-Technologies. (2016). "RISA-3D. Retrieved from http://risa.com/p_risa3d.html."

Rogers, A. M., and Malkiel, A. (1979). "A study of earthquakes in the Permian Basin of Texas-New Mexico." *Bulletin of the Seismological Society of America*, Seismological Society of America, 69(3), 843–865.

Sanford, A., Balch, R., Jaksha, L., and Delap, S. (1993). "Location and Fault Mechanism of the 2 January 1992 Rattlesnake Canyon Earthquake in Southeastern New Mexico." *Open-File Rept*, 70.

Sellards, E. H. (1933). "The Wortham-Mexia, Texas, earthquake." *Contributions to Geology, Univ. Texas Bull*, 3201, 105–112.

Shinozuka, M., Feng, M. Q., Kim, H., Uzawa, T., and Ueda, T. (2003). *Statistical analysis of fragility curves. Report No. MCEER-03-0002, MCEER.*

Shinozuka, M., Feng, M. Q., Kim, H.-K., and Kim, S.-H. (2000a). "Nonlinear static procedure for fragility curve development." *Journal of engineering mechanics*, American Society of Civil Engineers, 126(12), 1287–1295.

Shinozuka, M., Feng, M. Q., Lee, J., and Naganuma, T. (2000b). "Statistical analysis of fragility curves." *Journal of engineering mechanics*, American Society of Civil Engineers, 126(12), 1224–1231.

Skoumal, R. J., Brudzinski, M. R., and Currie, B. S. (2015). "Earthquakes induced by hydraulic fracturing in Poland Township, Ohio." *Bulletin of the Seismological Society of America*, Seismological Society of America, 105(1), 189–197.

Stewart, J. P., Klimis, N., Savvaidis, A., Theodoulidis, N., Zargli, E., Athanasopoulos, G., Pelekis, P., Mylonakis, G., and Margaris, B. (2014). "Compilation of a local VS profile database and its application for inference of VS30 from geologic-and terrain-based proxies." *Bulletin of the Seismological Society of America*, Seismological Society of America, 104(6), 2827–2841.

Suckale, J. (2009). "Induced seismicity in hydrocarbon fields." *Advances in geophysics*, Elsevier, 51, 55–106.

Sullivan, I., and Nielson, B. G. (2010). "Sensitivity analysis of seismic fragility curves for skewed multi-span simply supported steel girder bridges." *Structures Congress 2010: 19th Analysis and Computation Specialty Conference*, 226–237.

Tavares, D. H., Suescun, J. R., Paultre, P., and Padgett, J. E. (2013). "Seismic Fragility of a

Highway Bridge in Quebec." *Journal of Bridge Engineering*, 18(11), 1131–1139.

Texas House Bill 2. (2015). *http://www.capitol.state.tx.us/tlodocs/84R/billtext/pdf/HB00002F.pdf, accessed 15 September 2015.*

Torbol, M., and Shinozuka, M. (2012). "Effect of the angle of seismic incidence on the fragility curves of bridges." *Earthquake Engineering & Structural Dynamics*, Wiley Online Library, 41(14), 2111–2124.

TxDOT. (1962). *As-built Drawing – NBI Bridge No. 161780032603016*. Texas Department of Transportation, Austin, TX.

TxDOT. (2004). *Bridge Standards – Steel Beam Spans 24' Roadway (SSB-24)*. Texas Department of Transportation, Austin, Tx. Retrieved from: http://www.txdot.gov/insdtdot/orgchart/cmd/cserve/standard/bridge-e.htm#STEELBEAMS.

TxDOT. (2005). *Bridge Standards – 30'-4" Concrete Slab and Girder Span – 24ft Roadway (CG-30-24)*. Texas Department of Transportation, Austin, TX. Retrieved from: http://www.txdot.gov/insdtdot/orgchart/cmd/cserve/standard/bridge-e.htm#CONCRETESLAB&GIRDER(PANFORM).

TxDOT. (2006). *Bridge Standards – Steel Beam Standard Design (SBSD)*. Texas Department of Transportation, Austin, Tx, Retrieved from: http://www.txdot.gov/insdtdot/orgchart/cmd/cserve/standard/bridge-e.htm#STEELBEAMS.

TxDOT. (2015). *Bridge Standards – Common Foundation Details (FD)*. Texas Department of Transportation, Austin, TX. Retrieved from: www.dot.state.tx.us/insdtdot/orgchart/cmd/cserve/standard/bridge-e.htm.

TxDOT. (2017). *Bridge Standards – Prestressed Concrete I-Girders*. Texas Department of Transportation, Austin, TX. Retrieved from: http://www.txdot.gov/insdtdot/orgchart/cmd/cserve/standard/bridge-e.htm#PRESTRESSEDCONCRETEI-GIRDERS.

U.S. Department of Transportation Federal Highway Administration. (2014). "LRFD Seismic Analysis and Design of Bridges - Reference Manual." (FHWA-NHI-15-004), 608.

Udden, J. A. (1926). *The Southwest Earthquake of July 30, 1925*. University of Texas at Austin.

Unanwa, C., and Mahan, M. (2012). "Statistical analysis of concrete compressive strengths for California highway bridges." *Journal of Performance of Constructed Facilities*, American Society of Civil Engineers, 28(1), 157–167.

Voss, J. A., and Herrmann, R. B. (1980). "A surface wave study of the June 16, 1978 Texas earthquake." *Seismological Research Letters*, GeoScienceWorld, 51(1), 1–14.

Wald, D. J., and Allen, T. I. (2007). "Topographic slope as a proxy for seismic site conditions and amplification." *Bulletin of the Seismological Society of America*, Seismological Society of America, 97(5), 1379–1395.

Walsh, F. R., and Zoback, M. D. (2015). "Oklahoma's recent earthquakes and saltwater disposal." *Science advances*, American Association for the Advancement of Science, 1(5), e1500195.

Walter, J. I., Dotray, P. J., Frohlich, C., and Gale, J. F. W. (2016). "Earthquakes in northwest Louisiana and the Texas--Louisiana border possibly induced by energy resource activities within the Haynesville Shale Play." *Seismological Research Letters*, GeoScienceWorld.

Weingarten, M., Ge, S., Godt, J. W., Bekins, B. A., and Rubinstein, J. L. (2015). "High-rate

injection is associated with the increase in US mid-continent seismicity." *Science*, American Association for the Advancement of Science, 348(6241), 1336–1340.

Wills, C. J., and Clahan, K. B. (2006). "Developing a map of geologically defined site-condition categories for California." *Bulletin of the Seismological Society of America*, Seismological Society of America, 96(4A), 1483–1501.

Wills, C. J., Petersen, M., Bryant, W. A., Reichle, M., Saucedo, G. J., Tan, S., Taylor, G., and Treiman, J. (2000). "A site-conditions map for California based on geology and shear-wave velocity." *Bulletin of the Seismological Society of America*, Seismological Society of America, 90(6B), S187–S208.

Wills, C. J., and Silva, W. (1998). "Shear-wave velocity characteristics of geologic units in California." *Earthquake Spectra*, 14(3), 533–556.

Wolf, J. P., and Skrikerud, P. E. (1980). "Mutual pounding of adjacent structures during earthquakes." *Nuclear Engineering and Design*, Elsevier, 57(2), 253–275.

Yamazaki, F., Hamada, T., Motoyama, H., and Yamauchi, H. (1999). "Earthquake damage assessment of expressway bridges in Japan." *Optimizing Post-Earthquake Lifeline System Reliability*, 361–370.

Yerkes, R. F., and Castle, R. O. (1976). "Seismicity and faulting attributable to fluid extraction." *Engineering Geology*, Elsevier, 10(2-4), 151–167.

Yong, A. (2007). "Geophysical site characterization using geomorphology, geology and integrated digital imaging methods on satellite data." California State University, Northridge.

Yong, A., Hough, S. E., Iwahashi, J., and Braverman, A. (2012). "A terrain-based site-conditions map of California with implications for the contiguous United States." *Bulletin of the Seismological Society of America*, Seismological Society of America, 102(1), 114–128.

Zakeri, B., Padgett, J. E., and Amiri, G. G. (2013a). "Fragility analysis of skewed single-frame concrete box-girder bridges." *Journal of Performance of Constructed Facilities*, American Society of Civil Engineers, 28(3), 571–582.

Zakeri, B., Padgett, J. E., and Ghodrati Amiri, G. (2013b). "Fragility assessment for seismically retrofitted skewed reinforced concrete box girder bridges." *Journal of Performance of Constructed Facilities*, American Society of Civil Engineers, 29(2), 4014043.

Zalachoris, G., Rathje, E. M. (2018). "Ground Motion Prediction Equation for Small-to-Moderate Earthquake Events in Texas, Oklahoma, and Kansas." *Earthquake Spectra*, (In prepar.

Zalachoris, G., and Rathje, E. M. (2017). "Ground Motion Models for Earthquake Events in Texas , Oklahoma , and Kansas." 3rd International Conference on Performance Based Design in Earthquake Geotechnical Engineering, Vancouver, BC, Canada.

Zalachoris, G., Rathje, E. M., and Paine, J. G. (2017). "V S30 Characterization of Texas , Oklahoma , and Kansas Using the P-Wave Seismogram Method." *Earthquake Spectra*, 33(3), 943–961.

Appendix A. Records of Earthquakes in Texas

This section addresses the ground motions recorded in Texas. In this regard, Table A.1 contains the catalog of Texas earthquakes having magnitude 3 or greater. This catalog is a compilation of earthquakes having magnitudes of 3 or greater as reported by Frohlich and Davis (2002), the International Seismological Centre (ISC), or the National Earthquake Information Centre. Focal mechanisms are available for entries in bold type. Tabled origin times and epicenters are as reported by the indicated agency, rounded to nearest second and 0.01° of latitude and longitude. Agencies are as cited in reference list: CMT – centroid moment tensor (Harvard University); GCMT – global centroid moment tensor (Columbia University); IDC – International Data Centre, Comprehensive Nuclear Test Ban Treaty (Austria); ISC – International Seismological Centre (United Kingdom); NEIC – National Earthquake Information Center (U.S.A.); SLM – St. Louis University moment tensor. Tabled magnitudes (Mag) are (1) those reported Frohlich and Davis (2002), if available; (2) moment magnitude M_W, if available; or otherwise (3) as reported by the U.S. Geological Survey. Magnitude types are: m_N – estimated from felt area; M_{corr} – corrected magnitude of Rogers and Malkiel (1979); M_C – coda-length magnitude; M_W – moment magnitude; M_L – local magnitude; M_S - surface wave magnitude; m_b – body-wave magnitude; m_{bLg} – magnitude derived from 1-second L_g waves. Values for maximum reported Mercalli intensity (I_{max}) are (1) as reported by Frohlich and Davis (2002); (2) as determined in a field investigation; or otherwise (3) as reported by the U.S. Geological Survey. Felt areas are as reported by Frohlich and Davis (2002) or as reported in a subsequent publication. Type is assessed from scores assigned for answers to questions as described in Table 1 and Table 2: score 0.0-1.0 – T: tectonic; score 1.5-2.0 – PsI: possibly induced; score 2.5-3.5 – PrI: probably induced; score 4.0-5.0 – ACI: almost certainly induced; ?? – possibly spurious report (i.e., may be grossly mislocated, or may not be an earthquake).

Then, Table A.2 presents catalog of Texas earthquakes, scored to assess whether event may be induced. Columns QT to QP show score for answers to questions 1 to 5 in Table 1 (0.0 for “No”, 0.5 for “possibly”, 1.0 for “yes”); sum column is sum of scores. Type is: T (tectonic) = 0.0 to 1.0; PsI (possibly induced) = 1.5 to 2.0; PrI (probably induced) = 2.5-3.5; ACI (almost certainly induced) = 4.0-5.0; ?? – possibly spurious report. Ref column indicates reference providing published evidence indicating the event is ACI or PrI.

Table A.1: Catalog of Texas earthquakes having magnitude 3 or greater

Date and origin time			Lat °N	Lon °W	Agency	Mag		I_{max}	Felt area (km^2)	Type/Location		County
14 Feb.	1847	02	29.6	98.0	Davis et al. (1989)	3.6	m_N	V	1200	T	Seguin	Guadalupe
1 May	1873	04:30	30.25	97.6	Docekal (1970)	3.1	m_N	III-IV	—	T	Manor	Travis
5 Jan.	1887	17:57	30.15	97.06	Davis et al. (1989)	4.1	m_N	V-VI	4600	T	Paige	Bastrop
31 Jan.	1887	22:14	30.53	96.3	Davis et al. (1989)	3.3	m_N	IV	—	T	Wellborn	Brazos
31 May	1889	20	32.	106.5	Davis et al. (1989)	3.6	m_N	V	—	T	El Paso	El Paso
8 Jan.	1891	06	31.7	95.2	Docekal (1970)	4.0	m_N	VI	—	T	Rusk	Cherokee
9 Oct.	1902	19	31.10	97.60	Davis et al. (1989)	3.9	m_N	IV-V	5600	T	Creedmoor	Travis
Apr.	1907		35.20	101.80	Northrup & Sanford (1972)	3.6	m_N	V		??	Amarillo	Potter
8 May	1910	17:30	30.10	96.00	Docekal (1970)	3.8	m_N	IV	2900	T	Hempstead	Waller
30 Dec.	1914	01:00	30.50	95.90	von Hake & Cloud (1971)	3.3	m_N	IV		T	Anderson	Grimes
28 Mar.	1917	29:56	35.40	101.30	Woolard (1968)	3.9	m_N	VI	7600	T	Panhandle	Carson
7 Mar.	1923	05:03	31.8	106.5	Docekal (1970)	4.7	m_N	VI	200,000	T	El Paso	El Paso
	1925		29.70	94.98	Pratt & Johnson (1926)					PrI	Goose Creek	Harris
29 July	1925	11:30	34.5	101.2	Docekal (1970)	3.3	m_N	IV	—	??	Silverton	Briscoe
30 July	1925	12:17	35.4	101.3	Docekal (1970)	5.4	m_N	VI	520,000	PsI	Panhandle	Carson
31 July	1925	18	35.5	101.1	Davis et al. (1989)	3.0	m_N	III	—	PsI	White Deer	Carson
16 Aug.	1931	08	30.7	104.6	Davis et al. (1989)	3.6	m_N	V	—	T	Valentine	Jeff Davis
16 Aug.	1931	11:15	30.7	104.6	Davis et al. (1989)	3.0	m_N	III	—	T	Valentine	Jeff Davis
16 Aug.	1931	11:40:22	30.7	104.6	Dumas et al. (1980)	6.3	M_W	VIII	1,000,000	T	Valentine	Jeff Davis
16 Aug.	1931	12:17	30.7	104.6	Davis et al. (1989)	3.0	m_N	III	—	T	Valentine	Jeff Davis
16 Aug.	1931	12:45	30.7	104.6	Davis et al. (1989)	3.3	m_N	IV	—	T	Valentine	Jeff Davis
16 Aug.	1931	13:35	30.7	104.6	Davis et al. (1989)	3.3	m_N	IV	—	T	Valentine	Jeff Davis
16 Aug.	1931	19:33	30.7	104.6	Davis et al. (1989)	3.6	m_N	V	—	T	Valentine	Jeff Davis
18 Aug.	1931	08:42	30.7	104.6	Davis et al. (1989)	3.0	m_N	III	—	T	Valentine	Jeff Davis
18 Aug.	1931	19:36	30.7	104.6	Davis et al. (1989)	4.2	m_N	V	20,000	T	Valentine	Jeff Davis
18 Aug.	1931	22	30.7	104.6	Davis et al. (1989)	3.0	m_N	III	—	T	Valentine	Jeff Davis
26 Aug.	1931	—	30.7	104.6	Davis et al. (1989)	3.6	m_N	III	6,800	T	Valentine	Jeff Davis
2 Oct.	1931	—	31.8	106.5	Docekal (1970)	3.2	m_N	II-III	—	T	El Paso	El Paso
3 Nov.	1931	15:50	30.7	104.6	Davis et al. (1989)	3.0	m_N	III	—	T	Valentine	Jeff Davis
9 Apr.	1932	10:17	31.7	96.4	Reagor et al. (1982)	4.0	m_N	VI	6,400	ACI	Wortham-Mexia	Limestone
12 Apr.	1934	01:40	33.9	95.5	Docekal (1970)	4.2	m_N	V	13,000	T	Trout Switch	Lamar

Date and origin time			Lat °N	Lon °W	Agency	Mag		I_{max}	Felt area (km^2)	Type/Location		County
19 June	1936	21	35.2	100.7	Davis et al. (1989)	3.0	m_N	III	—	PsI	Clarendon	Gray
20 June	1936	03:13:37	35.7	101.4	Docekal (1970)	3.9	m_N	III	—	PsI	Borger	Hutchison
20 June	1936	03:18:27	35.7	101.4	Docekal (1970)	3.9	m_N	III-IV	21,000	PsI	Borger	Hutchison
20 June	1936	03:24:06	35.7	101.4	Docekal (1970)	5.0	m_N	VI	110,000	PsI	Borger	Hutchison
8 Aug.	1936	01:40	31.8	106.5	Docekal (1970)	3.0	m_N	III	—	T	El Paso	El Paso
15 Oct.	1936	18	31.8	106.5	Docekal (1970)	3.0	m_N	III	—	T	El Paso	El Paso
31 Mar.	1937	23:45	31.8	106.5	Docekal (1970)	3.0	m_N	III	—	T	El Paso	El Paso
12 Mar.	1948	04:29	36.0	102.5	Reagor et al. (1982)	5.2	m_N	VI	240,000	T	Dalhart	Hartley
20 Mar.	1950	13:23	33.3	97.8	Docekal (1970)	3.3	m_N	IV	—	??	Chico	Wise
20 June	1951	18:37:10	35.0	102.0	Docekal (1970)	4.2	m_N	V	74,000	PsI	Amarillo	Randall
17 Oct.	1952	15:48	30.1	93.8	Reagor et al. (1982)	3.3	m_N	IV	—	PsI	Orange	Orange
27 Jan.	1955	00:37	30.6	104.5	Docekal (1970)	3.3	m_N	IV	—	T	Valentine	Jeff Davis
19 Mar.	1957	16:37:39	32.6	94.7	Docekal (1970)	4.7	m_N	V	45,000	PrI	Gladewater	Gregg
19 Mar.	1957	17:41:17	32.6	94.7	Docekal (1970)	3.0	m_N	III	3,000	PrI	Gladewater	Gregg
19 Mar.	1957	22:36	32.6	94.7	Docekal (1970)	3.0	m_N	III	3,000	PrI	Gladewater	Gregg
19 Mar.	1957	22:45	32.6	94.7	Docekal (1970)	3.0	m_N	III	3,000	PrI	Gladewater	Gregg
6 Mar.	1962	09:59:10	31.2	104.8	Frohlich & Davis (2002)	3.5	M_L	—	—	T	Van Horn area	Culberson
24 Apr.	1964	01:20:55	31.5	93.9	Davis et al. (1989)	3.7	m_b	V	—	T	Hemphill	Sabine
24 Apr.	1964	07:33:53	31.6	93.9	Davis et al. (1989)	3.7	m_b	IV	—	T	Hemphill	Sabine
24 Apr.	1964	12:07:07	31.3	93.8	Davis et al. (1989)	3.2	m_b	IV	—	T	Hemphill	Sabine
27 Apr.	1964	21:50:27	31.3	93.8	Davis et al. (1989)	3.2	m_b	IV	—	T	Hemphill	Sabine
28 Apr.	1964	21:18:35	31.3	93.8	Davis et al. (1989)	4.4	m_b	VI	2,700	T	Hemphill	Sabine
30 Apr.	1964	20:30:00	31.5	93.8	Davis et al. (1989)	3.0	m_b	III	—	T	Hemphill	Sabine
7 May	1964	07:33:53	31.2	94.0	Davis et al. (1989)	3.2	m_b	V	—	T	Hemphill	Sabine
2 June	1964	23:00:00	31.3	94.0	Davis et al. (1989)	4.2	m_b	V	—	T	Hemphill	Sabine
3 June	1964	00:00:00	31.3	94.0	Davis et al. (1989)	4.2	m_b	V	—	T	Hemphill	Sabine
3 June	1964	02:27:24	31.5	93.9	Davis et al. (1989)	3.1	m_b	III	—	T	Hamphill	Sabine
3 June	1964	09:37:00	31.0	94.0	Davis et al. (1989)	3.6	m_b	IV	—	T	Hemphill	Jasper
8 Nov.	1964	09:25:59	31.9	103.1	Sanford et al. (1978)	3.0	M_{corr}	—	—	PrI	Kermit	Winkler
21 Nov.	1964	11:21:22	31.9	103.1	Sanford et al. (1978)	3.1	M_{corr}	—	—	PrI	Kermit	Winkler
3 Feb.	1965	19:59:32	31.9	103.1	Sanford et al. (1978)	3.3	M_{corr}	—	—	PrI	Kermit	Winkler
30 Aug.	1965	05:17:30	31.9	103.0	Sanford et al. (1978)	3.5	m_b	—	—	PrI	Kermit	Winkler
20 July	1966	09:04:58	35.7	101.2	von Hake & Cloud (1968)	4.1	m_N	V	36,000	PsI	Borger	Hutchison
14 Aug.	1966	15:25:47	31.9	103.0	Sanford et al. (1978)	3.4	m_b	VI	50,000	PrI	Kermit	Winkler

Date and origin time			Lat °N	Lon °W	Agency	Mag		I_{max}	Felt area (km^2)	Type/Location		County
12 May	1969	08:26:19	31.8	106.4	von Hake & Cloud (1971)	3.9	M_L	VI	—	T	El Paso	El Paso
12 May	1969	08:49:16	31.8	106.4	von Hake & Cloud (1971)	3.6	M_L	VI	—	T	El Paso	El Paso
30 July	1971	01:45:51	31.72	103.00	Reagor et al. (1982)	3.0	m_b	—	—	PrI	Kermit	Winkler
31 July	1971	14:53:49	31.70	103.06	Reagor et al. (1982)	3.4	m_b	—	—	PrI	Kermit	Winkler
24 Sept.	1971	01:01:54	31.6	103.2	Reagor et al. (1982)	3.2	M_{corr}	—	—	PrI	Kermit	Ward
9 Dec.	1972	05:58:44	31.75	106.40	Davis et al. (1989)	3.0	M_L	IV	1,500	T	El Paso	El Paso
10 Dec.	1972	14:37:50	31.75	106.40	Davis et al. (1989)	3.0	M_L	III	100	T	El Paso	El Paso
25 Dec.	1973	02:46:10	28.82	98.20	Davis et al. (1989)	3.2	M_C	IV	—	ACI	Fashing	Atascosa
15 Feb.	1974	13:33:50	36.39	100.52	ISC	4.5	m_b	V	110,000	PsI	Perryton	Ochiltree
20 Apr.	1974	23:46:10	29.	98.	Frohlich & Davis (2002)	3.0	M_C	—	—	PsI	South Texas	Wilson
24 June	1974	18:03:10	29.	98.	Frohlich & Davis (2002)	3.4	M_C	—	—	PsI	South Texas	Wilson
1 Aug.	1974	13:33:10	29.	98.	Frohlich & Davis (2002)	3.0	M_C	—	—	PsI	South Texas	Wilson
30 Dec.	1974	08:05:27	30.9	103.1	Frohlich & Davis (2002)	3.7	M_L	—	—	T	Fort Stockton	Pecos
1 Aug.	1975	07:27:57	31.4	104.0	Coffman & Stover (1977)	4.8	m_b	II	—	T	Delaware Basin	Reeves
19 Jan.	1976	04:03:30	31.90	103.09	Gordon (1983)	3.5	M_L	IV	—	PrI	Kermit	Winkler
25 Jan.	1976	04:48:28	31.90	103.09	Gordon (1983)	3.9	M_L	V	2,000	PrI	Kermit	Winkler
5 Aug.	1976	18:53:09	31.6	103.0	Frohlich & Davis (2002)	3.0	M_L	—	—	PrI	Kermit	Ward
17 Sept.	1976	03:56:29	31.4	102.5	Frohlich & Davis (2002)	3.1	M_{corr}	—	—	PrI	Kermit	Crane
26 Apr.	1977	09:03:07	31.9	103.1	Keller et al. (1981)	3.3	M_L	IV	—	PrI	Kermit	Winkler
7 June	1977	23:01:20	33.0	100.7	Frohlich & Davis (2002)	3.1	M_C	—	—	ACI	Snyder	Scurry
22 July	1977	04:01:10	31.8	102.7	Frohlich & Davis (2002)	3.0	M_{corr}	—	—	PrI	Kermit	Ector
28 Nov.	1977	01:40:52	33.35	100.72	ISC	3.5				ACI	Spur	Kent
2 Mar.	1978	10:04:53	31.55	102.56	Gordon (1983)	3.5	M_L	III	—	PrI	Kermit	Crane
16 June	1978	11:46:54	33.01	100.72	ISC	4.6	m_{bLg}	V	100,000	ACI	Snyder	Scurry
16 June	1978	11:53:33	33.0	100.8	ISC	3.4	m_{bLg}	—	—	PrI	Snyder	Scurry
9 June	1980	22:37:10	35.50	101.05	ISC	4.3	m_N	V	35,000	PsI	Pampa	Gray
9 June	1981	01:46:33	31.76	94.28	Davis et al. (1989)	3.2	m_{bLg}	III	—	PsI	Center	Shelby
6 Nov.	1981	12:36:41	31.95	95.92	Davis et al. (1989)	3.3	m_{bLg}	V	800	PrI	Jacksonville	Anderson
4 Jan.	1982	16:56:10	31.18	102.35	ISC	3.9	m_{bLg}	III	2,500	PrI	Fort Stockton	Pecos
28 Mar.	1982	23:24:33	29.	98.	Frohlich & Davis (2002)	3.0	M_C	—	—	PsI	South Texas	Wilson
19 Sept.	1982	06:15:42	32.03	100.68	ISC	3.0	m_{bLg}			PsI	Silver	Coke

Date and origin time			Lat °N	Lon °W	Agency	Mag		I_{max}	Felt area (km^2)	Type/Location		County
14 Oct.	1982	12:52:46	36.05	102.53	ISC	3.9	m_{bLg}	III	8,200	T	Dalhart	Hartley
7 Nov.	1982	00:04:19	35.2	100.2	ISC	3.1	m_{bLg}	—	—	PsI	Wheeler Co.	Wheeler
28 Nov.	1982	02:36:48	32.92	100.85	ISC	3.3	m_{bLg}	IV	32,000	ACI	Snyder	Scurry
3 Apr.	1983	04:55:22	35.40	102.41	ISC	3.4	m_{bLg}			PsI	Oldham	Oldham
23 July	1983	15:24:39	28.82	98.18	Davis et al. (1989)	3.4	m_{bLg}	V	200	ACI	Fashing	Atascosa
3 Mar.	1984	01:03:26	28.87	98.50	Davis et al. (1989)	3.9	m_{bLg}	V	1,300	ACI	Pleasanton	Atascosa
3 Mar.	1984	01:58:25	28.87	98.50	Davis et al. (1989)	3.2	M_C	IV	100	ACI	Pleasanton	Atascosa
8 Mar.	1984	01:31:28	28.87	98.50	Davis et al. (1989)	3.1	m_{bLg}	IV	100	ACI	Pleasanton	Atascosa
3 Apr.	1984	04:55:24	35.32	102.4	Frohlich & Davis (2002)	3.4	m_{bLg}	—	—	PsI	Oldham Co.	Oldham
21 May	1984	13:30:14	35.4	102.4	Frohlich & Davis (2002)	3.1	m_{bLg}	—	—	PsI	Oldham Co.	Oldham
8 Aug.	1984	01:31:27	28.87	98.50	Davis et al. (1989)	3.1	m_{bLg}	IV	—	ACI	Pleasanton	Atascosa
11 Sept.	1984	14:47:33	31.96	100.66	Frohlich & Davis (2002)	3.0	m_{bLg}	—	—	PsI	Coke County	Coke
19 Sept.	1984	06:15:42	32.03	100.68	Frohlich & Davis (2002)	3.2	m_{bLg}	—	—	PsI	Coke County	Coke
18 Sept.	1985	15:54:05	33.55	97.02	ISC	3.3	m_{bLg}	V	700	PsI	Valley View	Cooke
30 Jan.	1986	22:26:37	32.02	100.70	ISC	3.3	m_{bLg}	IV	—	PsI	Silver	Coke
3 Mar.	1986	11:45:17	35.31	102.52	Frohlich & Davis (2002)	3.1	m_{bLg}	—	—	T	Oldham Co.	Oldham
20 July	1991	23:38:17	29.0	98.0	Olson & Frohlich (1991)	3.6	m_{bLg}	IV	110	PrI	Falls City	Karnes
2 Jan.	1992	11:45:36	32.36	102.97	ISC	4.6	m_b	V	440,000	PsI	Rattlesnake Canyon	Andrews
26 Aug.	1992	03:24:53	32.18	102.71	ISC	3.0	m_{bLg}			PsI	Andrews	Andrews
9 Apr.	1993	12:29:19	28.87	98.50	Frohlich & Davis (2002)	4.3	m_{bLg}	VI	5,000	ACI	Fashing	Atascosa
16 May	1993	15:30:19	28.9	98.5	Frohlich & Davis (2002)	3.0	m_{bLg}	IV	300	ACI	Fashing	Atascosa
29 Sept	1993	02:01	35.9	103.03	ISC	3.3	m_{bLg}			T	Dalhart	Hartley
30 Nov	1993	03:07	35.86	103.03	NEIC	3.3	m_{bLg}			T	Dalhart	Hartley
14 Apr.	1995	00:32:56	30.29	103.32	ISC	5.7	M_W	VI	760,000	T	Alpine	Brewster
14 Apr.	1995	02:19:38	30.5	103.1	ISC	3.3	m_{bLg}	felt	—	T	Alpine	Pecos
15 Apr.	1995	10:33:43	30.22	103.24	ISC	3.6	m_{bLg}			T	Alpine	Brewseter
15 Apr.	1995	14:33:30	30.26	103.33	ISC	4.0	m_{bLg}	VI	52,000	T	Alpine	Brewster
1 June	1995	01:06:16	30.28	103.35	Frohlich & Davis (2002)	3.5	m_{bLg}	IV	36,000	T	Alpine	Brewster
12 Nov.	1995	17:45:59	30.2	103.2	Frohlich & Davis (2002)	3.6	m_{bLg}	felt	—	T	Alpine	Brewster
25 Mar.	1996	06:43:47	35.61	102.60	ISC	3.5	m_{bLg}	—	—	PsI	near Channing	Huntley
23 Nov.	1996	10:54:18	35.11	100.60	Frohlich & Davis (2002)	3.0	m_{bLg}	possibly felt	—	PsI	near McLean	Donley

Date and origin time			Lat °N	Lon °W	Agency	Mag		I_{max}	Felt area (km^2)	Type/Location		County
12 Feb.	1997	23:53:11	35.11	100.60	Frohlich & Davis (2002)	3.0	m_{bLg}	IV	110	PsI	near McLean	Donley
15 Feb.	1997	09:08:55	35.11	100.60	Frohlich & Davis (2002)	3.2	m_{bLg}	V	110	PsI	near McLean	Donley
24 Mar.	1997	22:31:34	27.72	97.95	Frohlich et al. (2012)	3.8	m_{bLg}	V-VI	950	ACI	Alice	Jim Wells
31 May	1997	03:26:41	33.22	96.00	ISC	3.4	m_{bLg}	IV	1,100	T	Commerce	Hunt
15 Apr.	1998	10:33:42	30.23	103.24	ISC	3.6	m_{bLg}	III	3,900	T	Alpine	Brewster
27 Apr.	1998	15:22:46	35.42	102.27	ISC	3.2	m_{bLg}			T	Oldham	Oldham
7 Aug.	2000	17:19:06	35.36	101.84	ISC	3.3	m_{bLg}	III		PsI	Amarillo	Potter
7 Aug.	2000	18:34:09	35.39	101.81	NEIC	3.0	m_{bLg}	III		PsI	Amarillo	Potter
7 Aug.	2000	21:36:21	35.29	101.90	ISC	3.0	m_{bLg}	III		PsI	Amarillo	Potter
10 Aug.	2000	13:59:50	35.39	101.81	NEIC	3.0	m_{bLg}	III		PsI	Amarillo	Potter
17 Aug.	2000	01:08:05	35.36	101.70	ISC	3.9	m_{bLg}	V	5,000	PsI	Amarillo	Potter
16 Dec.	2000	22:08:53	35.23	101.78	ISC	3.9	m_{bLg}	IV		PsI	Amarillo	Potter
22 Nov.	2001	00:07:08	31.79	102.63	NEIC	3.1	m_{bLg}			PsI	Odessa	Ector
24 Sept.	2003	15:02:09	35.30	101.74	NEIC	3.3	m_{bLg}	IV		PsI	Amarillo	Potter
3 Apr.	2005	14:39:17	28.39	100.31	NEIC	3.5	m_{bLg}	IV		T	Eagle Pass	Maverick
18 Feb.	2006	05:49:41	35.67	101.79	NEIC	3.5	ml	III		PsI	Lake Meredith	Moore
28 Mar.	2006	23:55:11	35.36	101.87	NEIC	3.0	ml			PsI	Amarillo	Potter
27 Sept.	2007	15:21:02	35.47	100.11	NEIC	3.0	m_{bLg}			PsI	Wheeler	Wheeler
7 Oct.	2007	13:54:22	34.51	100.15	NEIC	3.1	m_{bLg}			T	Childress	Childress
29 Jan.	2008	10:24:53	32.90	100.84	NEIC	3.3	m_{bLg}			PrI	Snyder	Scurry
7 Apr.	2008	09:51:13	28.93	98.00	ISC	3.9	M_W	III		PrI	Falls City	Karnes
12 Oct.	2008	12:08:16	35.62	100.32	NEIC	3.0	m_{bLg}			PsI	Briscoe	Wheeler
14 Oct.	2008	03:07:28	35.77	100.75	ISC	3.7	M_W	IV		PsI	Miami	Roberts
31 Oct.	2008	05:01:55	32.84	97.03	NEIC	3.0	m_{bLg}	IV		ACI	Dallas-Fort Worth	Tarrant
16 May	2009	16:24:05	32.82	97.09	ISC	3.3	m_{bLg}	IV		ACI	Dallas-Fort Worth	Tarrant
16 May	2009	16:58:38	32.85	97.10	NEIC	3.0	m_{bLg}			ACI	Dallas-Fort Worth	Tarrant
27 Jan.	2010	04:59:33	32.87	100.90	Gan & Frohlich (2013)	3.1	m_{bLg}			PrI	Snyder	Scurry
4 Feb.	2010	09:41:28	35.49	102.62	NEIC	3.3	M_W	V		PsI	Borger	Oldham
8 Mar.	2010	23:47:28	28.94	98.03	NEIC	3.0		III		PrI	Falls City?	Karnes
25 Apr.	2010	02:10:42	27.72	97.95	Frohlich et al. (2012)	3.9	m_{bLg}		950	ACI	Alice	Jim Wells

Date and origin time			Lat °N	Lon °W	Agency	Mag		I_{max}	Felt area (km^2)	Type/Location		County
8 Aug.	2010	01:12:38	32.90	100.85	NEIC	3.4	M_W	III		PrI	Snyder	Scurry
9 Oct.	2010	07:42:28	32.95	100.90	Gan & Frohlich (2013)	3.1	m_{bLg}			PrI	Snyder	Scurry
26 Oct.	2010	06:56:29	32.93	100.90	Gan & Frohlich (2013)	3.1	m_{bLg}			PrI	Snyder	Scurry
21 Dec.	2010	13:53:18	28.64	98.04	NEIC	3.2				ACI	Fashing	Bee
17 Feb.	2011	18:25:34	30.11	103.30	NEIC	3.3	m_{bLg}			T	Marathon	Brewster
1 Mar.	2011	03:30:13	32.88	100.84	NEIC	3.1	m_{bLg}	II		PrI	Snyder	Scurry
12 Mar.	2011	15:22:00	32.88	100.90	NEIC	3.0	m_{bLg}			PrI	Snyder	Scurry
13 Mar.	2011	20:16:21	32.97	100.84	ISC	3.8	M_W	III		PrI	Snyder	Kent
14 Mar.	2011	00:19:49	32.96	100.81	NEIC	3.0	m_{bLg}			PrI	Snyder	Kent
19 Mar.	2011	23:24:01	32.98	100.77	NEIC	3.0	m_{bLg}			PrI	Snyder	Kent
28 Mar.	2011	09:12:12	32.91	100.82	NEIC	3.0	m_{bLg}			PrI	Snyder	Scurry
2 Apr.	2011	22:05:14	33.06	100.76	NEIC	3.0	m_{bLg}			PrI	Snyder	Kent
2 May	2011	19:07:15	33.04	100.79	ISC	3.2	m_{bLg}			PrI	Snyder	Kent
17 Jul.	2011	06:58:01	32.49	97.17	Frohlich (2012)	3.0	m_{bLg}	IV		PrI	Venus	Johnson
11 Sept.	2011	12:27:44	32.88	100.83	ISC	4.3	M_W	IV		PrI	Snyder	Scurry
12 Sept.	2011	14:18:34	32.80	100.83	ISC	3.4	m_{bLg}	III		PrI	Snyder	Scurry
20 Oct.	2011	12:24:42	28.85	98.15	ISC	4.8	M_W	VI	11,000	ACI	Fashing	Atascosa
12 Nov.	2011	10:34:54	28.88	98.23	ISC	3.5				ACI	Fashing	Atascosa
24 Nov.	2011	23:15:49	32.94	100.85	NEIC	3.1	m_{bLg}			PrI	Snyder	Scurry
9 Dec.	2011	18:47:32	32.94	100.88	ISC	3.5	m_{bLg}	III		PrI	Snyder	Scurry
17 Dec.	2011	14:46:58	32.81	100.85	NEIC	3.2	m_{bLg}	III		PrI	Snyder	Scurry
18 Jan	2012	22:30:54	32.36	97.49	ISC	3.3	m_{bLg}	IV		ACI	Cleburne	Johnson
24 Jan.	2012	18:21:03	30.32	103.38	NEIC	3.6	m_{bLg}	IV		T	Alpine	Brewster
4 Feb.	2012	12:48:09	28.82	98.17	ISC	3.0				ACI	Fashing	Atascosa
10 May	2012	15:15:39	31.88	94.40	Frohlich et al. (2014)	3.9	M_W	V		ACI	Timpson	Shelby
17 May	2012	08:12:01	31.89	94.41	Frohlich et al. (2014)	3.9	M_W	VII	20,000	ACI	Timpson	Shelby
15 Jun.	2012	07:02:32	32.48	97.25	ISC	3.3	m_{bLg}	IV		ACI	Cleburne	Johnson
24 Jun.	2012	08:55:59	28.40	98.41	ISC	3.4				ACI	Pleasanton	McMullen
24 Jun.	2012	17:46:43	32.49	97.26	ISC	3.5	m_{bLg}	IV		ACI	Cleburne	Johnson
12 Aug.	2012	00:36:04	35.42	101.85	ISC	3.3	m_{bLg}			PsI	Amarillo	Potter
30 Sept.	2012	04:04:59	32.87	97.00	ISC	3.4	m_{bLg}	IV		PrI	Irving	Dallas
30 Sept.	2012	04:09:03	32.83	96.96	NEIC	3.1	m_{bLg}			PrI	Irving	Dallas
7 Nov.	2012	17:38:00	27.25	98.82	ISC	3.4	m_b			PsI	Hebronville	Jim Hogg

Date and origin time			Lat °N	Lon °W	Agency	Mag		I_{max}	Felt area (km^2)	Type/Location		County
23 Jan.	2013	04:16:19	32.89	97.00	NEIC	3.0	m_{bLg}	III		PrI	Irving	Dallas
25 Jan.	2013	07:01:20	31.87	94.44	Frohlich et al. (2014)	3.9	M_W	V		ACI	Timpson	Shelby
6 May	2013	23:11:59	32.97	100.84	NEIC	3.0	m_{bLg}			PrI	Snyder	Kent
14 May	2013	00:05:40	31.14	104.78	NEIC	3.1				T	Van Horn	Culberson
2 Sept.	2013	21:52:37	31.85	94.30	IDC	4.2	M_W			ACI	Timpson	Shelby
2 Sept.	2013	23:51:15	31.96	94.50	IDC	4.3	M_W			ACI	Timpson	Shelby
9 Nov.	2013	19:54:31	32.93	97.69	NEIC	3.0	m_{bLg}	III		ACI	Azle	Parker
12 Nov.	2013	17:36:03	31.11	105.38	NEIC	3.1	m_{bLg}			T	Hudspeth	Hudspeth
20 Nov.	2013	00:40:35	33.09	97.68	IDC	3.6	m_{bLg}	IV		ACI	Azle	Wise
25 Nov.	2013	07:43:03	32.90	97.63	NEIC	3.3	m_{bLg}	III		ACI	Reno	Parker
26 Nov.	2013	14:24:03	32.89	97.53	NEIC	3.0				ACI	Reno	Parker
28 Nov.	2013	07:58:34	32.94	97.97	NEIC	3.6	m_{bLg}	IV		ACI	Mineral Wells	Parker
29 Nov.	2013	06:14:10	32.90	97.63	NEIC	3.1	m_{bLg}	III		ACI	Azle	Denton
8 Dec.	2013	06:10:01	33.01	97.34	IDC	3.6	m_{bLg}	IV		ACI	Azle	Parker
9 Dec.	2013	09:23:14	32.98	98.03	IDC	3.7	m_{bLg}	IV		ACI	Mineral Wells	Parker
22 Dec.	2013	17:31:55	32.92	97.58	NEIC	3.3	m_{bLg}	III		ACI	Reno	Parker
23 Dec.	2013	13:11:34	32.93	97.59	NEIC	3.3	m_{bLg}	IV		ACI	Reno	Parker
6 Jan.	2014	08:41:20	35.21	102.91	IDC	3.5		IV		T	Boise	Oldham
13 Jan.	2014	17:40:21	32.94	97.57	NEIC	3.1	m_{bLg}	III		ACI	Reno	Parker
28 Jan	2014	17:43:44	32.95	97.53	NEIC	3.0				PrI	Snyder	Scurry
14 May	2014	15:52:17	32.78	100.88	NEIC	3.1	m_{bLg}			PrI	Snyder	Scurry
10 Sept.	2014	17:53:24	28.84	98.67	NEIC	3.2	m_{bLg}			ACI	Jourdanton	Atascosa
14 Sept.	2014	09:19:00	32.91	100.82	NEIC	3.2	m_{bLg}			PrI	Snyder	Scurry
3 Oct.	2014	04:52:33	31.72	94.03	NEIC	3.1	m_{bLg}			PsI	Center	Shelby
23 Nov.	2014	03:15:47	32.84	96.89	NEIC	3.3	m_{bLg}	V		PrI	Irving	Dallas
30 Nov.	2014	05:52:24	32.53	97.19	IDC	3.4	m_{bLg}	V		PrI	Mansfield	Johnson
3 Dec.	2014	13:33:39	36.50	100.11	IDC	4.0	m_{bLg}			PsI	Follett	Lipscomb
31 Dec.	2014	18:31:40	32.93	100.85	NEIC	3.2	m_{bLg}			PrI	Snyder	Scurry
6 Jan.	2015	21:10:31	32.84	96.90	NEIC	3.5	m_{bLg}	IV		PrI	Irving	Dallas
6 Jan.	2015	21:55:19	32.92	100.85	NEIC	3.5	m_{bLg}			PrI	Snyder	Scurry
7 Jan.	2015	00:52:09	32.88	96.91	IDC	3.6	m_{bLg}	IV		PrI	Irving	Dallas
7 Jan.	2015	06:59:03	32.84	96.91	NEIC	3.1	m_{bLg}	V		PrI	Irving	Dallas

Date and origin time			Lat °N	Lon °W	Agency	Mag		I_{max}	Felt area (km^2)	Type/Location		County
20 Jan.	2015	20:25:49	32.84	96.90	NEIC	3.0	m_{bLg}	V		PrI	Irving	Dallas
31 Jan.	2015	02:17:02	28.86	98.13	NEIC	3.1	m_{bLg}			ACI	Fashing	Atascosa
2 Feb.	2015	00:39:27	35.23	101.75	IDC	3.1	m_{bLg}	IV		T	Amarillo	Potter
19 Feb.	2015	20:31:20	29.45	96.91	NEIC	3.1	m_{bLg}			PsI	Hallettsville	Lavaca
27 Feb.	2015	12:18:21	32.83	96.89	NEIC	3.1	m_{bLg}	IV		PrI	Irving	Dallas
2 Apr.	2015	22:36:21	32.85	96.94	NEIC	3.3	m_{bLg}	V		PrI	Irving	Dallas
4 Apr.	2015	00:16:33	31.16	103.25	NEIC	3.3	m_{bLg}			PsI	Pecos	Pecos
17 Apr.	2015	22:15:14	31.03	103.19	NEIC	3.1				PsI	Pecos	Pecos
3 May	2015	15:11:16	32.85	96.95	NEIC	3.2	m_{bLg}	V		PrI	Irving	Dallas
7 May	2015	22:58:05	32.48	97.10	NEIC	4.0	M_W	IV		PrI	Venus	Johnson
17 May	2015	22:15:13	31.05	103.19	NEIC	3.1	m_{bLg}			PsI	Pecos	Pecos
18 May	2015	18:14:29	32.87	96.96	NEIC	3.3	m_{bLg}	V		PrI	Irving	Dallas
4 Aug.	2015	15:06:32	31.17	103.28	NEIC	3.3	m_{bLg}			PsI	Pecos	Pecos
12 Aug.	2015	20:49:22	31.05	103.16	NEIC	3.0	m_{bLg}			PsI	Fort Stockton	Pecos
7 Nov.	2015	05:18:20	31.32	103.09	NEIC	3.0	m_{bLg}			PsI	Monahans	Ward
10 Nov.	2015	21:43:04	31.32	103.05	NEIC	3.2	m_{bLg}			PsI	Monahans	Ward
14 Dec.	2015	12:35:03	29.23	97.51	NEIC	3.0	m_{bLg}	IV		PsI	Nixon	Wilson
17 Dec.	2015	22:29:56	32.96	97.35	NEIC	3.0	m_{bLg}	V		PsI	Haslet	Tarrant

Table A.2: Catalog of Texas earthquakes, scored to assess whether event may be induced

Date	Year	Time	QT	QS	QD	QF	QP	Sum	Type	Ref	Location	County
14 Feb.	1847	02	0.0	0.0	0.0	0.0	0.0	0.0	T		Seguin	Guadalupe
1 May	1873	04:30	0.0	0.0	0.0	0.0	0.0	0.0	T		Manor	Travis
5 Jan.	1887	17:57	0.0	0.0	0.0	0.0	0.0	0.0	T		Paige	Bastrop
31 Jan.	1887	22:14	0.0	0.0	0.0	0.0	0.0	0.0	T		Wellborn	Brazos
31 May	1889	20	0.0	0.0	0.0	0.0	0.0	0.0	T		El Paso	El Paso
8 Jan.	1891	06	0.0	0.0	0.0	0.0	0.0	0.0	T		Rusk	Cherokee
9 Oct.	1902	19	0.0	0.0	0.0	0.0	0.0	0.0	T		Creedmoor	Travis
Apr.	1907								??		Amarillo	Potter
8 May	1910	17:30	0.0	0.0	0.0	0.0	0.0	0.0	T		Hempstead	Waller
30 Dec.	1914	01:00	0.0	0.0	0.0	0.0	0.0	0.0	T		Anderson	Grimes
28 Mar.	1917	1956	0.0	0.0	0.0	0.0	0.0	0.0	T		Panhandle	Carson
7 Mar.	1923	05:03	0.0	0.0	0.0	0.0	0.0	0.0	T		El Paso	El Paso
	1925		1.0	1.0	0.0	0.5	1.0	3.5	PrI	Pratt & Johnson (1926)	Goose Creek	Harris
29 July	1925	11:30							??		Silverton	Briscoe
30 July	1925	12:17	1.0	0.5	0.0	0.0	0.0	1.5	PsI		Panhandle	Carson
31 July	1925	18	1.0	0.5	0.0	0.0	0.0	1.5	PsI		White Deer	Carson
16 Aug.	1931	08	0.0	0.0	0.0	0.0	0.0	0.0	T		Valentine	Jeff Davis
16 Aug.	1931	11:15	0.0	0.0	0.0	0.0	0.0	0.0	T		Valentine	Jeff Davis
16 Aug.	1931	11:40:22	0.0	0.0	0.0	0.0	0.0	0.0	T		Valentine	Jeff Davis
16 Aug.	1931	12:17	0.0	0.0	0.0	0.0	0.0	0.0	T		Valentine	Jeff Davis
16 Aug.	1931	12:45	0.0	0.0	0.0	0.0	0.0	0.0	T		Valentine	Jeff Davis
16 Aug.	1931	13:35	0.0	0.0	0.0	0.0	0.0	0.0	T		Valentine	Jeff Davis
16 Aug.	1931	19:33	0.0	0.0	0.0	0.0	0.0	0.0	T		Valentine	Jeff Davis
18 Aug.	1931	08:42	0.0	0.0	0.0	0.0	0.0	0.0	T		Valentine	Jeff Davis
18 Aug.	1931	19:36	0.0	0.0	0.0	0.0	0.0	0.0	T		Valentine	Jeff Davis
18 Aug.	1931	22	0.0	0.0	0.0	0.0	0.0	0.0	T		Valentine	Jeff Davis
26 Aug.	1931	—	0.0	0.0	0.0	0.0	0.0	0.0	T		Valentine	Jeff Davis
2 Oct.	1931	—	0.0	0.0	0.0	0.0	0.0	0.0	T		El Paso	El Paso
3 Nov.	1931	15:50	0.0	0.0	0.0	0.0	0.0	0.0	T		Valentine	Jeff Davis

Date	Year	Time	QT	QS	QD	QF	QP	Sum	Type	Ref	Location	County
9 Apr.	1932	10:17	1.0	1.0	0.5	1.0	1.0	4.5	ACI	Sellards (1933)	Wortham-Mexia	Limestone
12 Apr.	1934	01:40	0.0	0.0	0.0	0.0	0.0	0.0	T		Trout Switch	Lamar
19 June	1936	21	1.0	1.0	0.0	0.0	0.0	2.0	PsI		Clarendon	Gray
20 June	1936	03:13:37	1.0	1.0	0.0	0.0	0.0	2.0	PsI		Borger	Hutchison
20 June	1936	03:18:27	1.0	1.0	0.0	0.0	0.0	2.0	PsI		Borger	Hutchison
20 June	1936	03:24:06	1.0	1.0	0.0	0.0	0.0	2.0	PsI		Borger	Hutchison
8 Aug.	1936	01:40	0.0	0.0	0.0	0.0	0.0	0.0	T		El Paso	El Paso
15 Oct.	1936	18	0.0	0.0	0.0	0.0	0.0	0.0	T		El Paso	El Paso
31 Mar.	1937	23:45	0.0	0.0	0.0	0.0	0.0	0.0	T		El Paso	El Paso
12 Mar.	1948	04:29	0.0	0.0	0.0	0.0	0.0	0.0	T		Dalhart	Hartley
20 Mar.	1950	13:23							??		Chico	Wise
20 June	1951	18:37:10	1.0	0.5	0.0	0.0	0.0	1.5	PsI		Amarillo	Randall
17 Oct.	1952	15:48	1.0	0.5	0.0	0.0	0.0	1.5	PsI		Orange	Orange
27 Jan.	1955	00:37	0.0	0.0	0.0	0.0	0.0	0.0	T		Valentine	Jeff Davis
19 Mar.	1957	16:37:39	1.0	1.0	0.0	0.0	0.5	2.5	PrI	Frohlich & Davis (2002)	Gladewater	Gregg
19 Mar.	1957	17:41:17	1.0	1.0	0.0	0.0	0.5	2.5	PrI	Frohlich & Davis (2002)	Gladewater	Gregg
19 Mar.	1957	22:36	1.0	1.0	0.0	0.0	0.5	2.5	PrI	Frohlich & Davis (2002)	Gladewater	Gregg
19 Mar.	1957	22:45	1.0	1.0	0.0	0.0	0.5	2.5	PrI	Frohlich & Davis (2002)	Gladewater	Gregg
6 Mar.	1962	09:59:10	0.0	0.0	0.0	0.0	0.0	0.0	T		Van Horn area	Culberson
24 Apr.	1964	01:20:55	0.0	0.0	0.0	0.0	0.0	0.0	T		Hemphill	Sabine
24 Apr.	1964	07:33:53	0.0	0.0	0.0	0.0	0.0	0.0	T		Hemphill	Sabine
24 Apr.	1964	12:07:07	0.0	0.0	0.0	0.0	0.0	0.0	T		Hemphill	Sabine
27 Apr.	1964	21:50:27	0.0	0.0	0.0	0.0	0.0	0.0	T		Hemphill	Sabine
28 Apr.	1964	21:18:35	0.0	0.0	0.0	0.0	0.0	0.0	T		Hemphill	Sabine
30 Apr.	1964	20:30:00	0.0	0.0	0.0	0.0	0.0	0.0	T		Hemphill	Sabine
7 May	1964	07:33:53	0.0	0.0	0.0	0.0	0.0	0.0	T		Hemphill	Sabine
2 June	1964	23:00:00	0.0	0.0	0.0	0.0	0.0	0.0	T		Hemphill	Sabine
3 June	1964	00:00:00	0.0	0.0	0.0	0.0	0.0	0.0	T		Hemphill	Sabine
3 June	1964	02:27:24	0.0	0.0	0.0	0.0	0.0	0.0	T		Hamphill	Sabine

Date	Year	Time	QT	QS	QD	QF	QP	Sum	Type	Ref	Location	County
3 June	1964	09:37:00	0.0	0.0	0.0	0.0	0.0	0.0	T		Hemphill	Jasper
8 Nov.	1964	09:25:59	1.0	1.0	0.0	0.0	1.0	3.0	PrI	Doser et al. (1992)	Kermit	Winkler
21 Nov.	1964	11:21:22	1.0	1.0	0.0	0.0	1.0	3.0	PrI	Doser et al. (1992)	Kermit	Winkler
3 Feb.	1965	19:59:32	1.0	1.0	0.0	0.0	1.0	3.0	PrI	Doser et al. (1992)	Kermit	Winkler
30 Aug.	1965	05:17:30	1.0	1.0	0.0	0.0	1.0	3.0	PrI	Doser et al. (1992)	Kermit	Winkler
20 July	1966	09:04:58	1.0	1.0	0.0	0.0	0.0	2.0	PsI		Borger	Hutchison
14 Aug.	1966	15:25:47	1.0	1.0	0.0	0.0	1.0	3.0	PrI	Doser et al. (1992)	Kermit	Winkler
12 May	1969	08:26:19	0.0	0.0	0.0	0.0	0.0	0.0	T		El Paso	El Paso
12 May	1969	08:49:16	0.0	0.0	0.0	0.0	0.0	0.0	T		El Paso	El Paso
30 July	1971	01:45:51	1.0	1.0	0.0	0.0	1.0	3.0	PrI	Doser et al. (1992)	Kermit	Winkler
31 July	1971	14:53:49	1.0	1.0	0.0	0.0	1.0	3.0	PrI	Doser et al. (1992)	Kermit	Winkler
24 Sept.	1971	01:01:54	1.0	1.0	0.0	0.0	1.0	3.0	PrI	Doser et al. (1992)	Kermit	Ward
9 Dec.	1972	05:58:44	0.0	0.0	0.0	0.0	0.0	0.0	T		El Paso	El Paso
10 Dec.	1972	14:37:50	0.0	0.0	0.0	0.0	0.0	0.0	T		El Paso	El Paso
25 Dec.	1973	02:46:10	1.0	1.0	0.5	0.5	1.0	4.0	ACI	Pennington et al. (1986)	Fashing	Atascosa
15 Feb.	1974	13:33:50	1.0	0.5	0.0	0.0	0.0	1.5	PsI		Perryton	Ochiltree
20 Apr.	1974	23:46:10	1.0	0.5	0.0	0.0	0.0	1.5	PsI		South Texas	Wilson
24 June	1974	18:03:10	1.0	0.5	0.0	0.0	0.0	1.5	PsI		South Texas	Wilson
1 Aug.	1974	13:33:10	1.0	0.5	0.0	0.0	0.0	1.5	PsI		South Texas	Wilson
30 Dec.	1974	08:05:27	1.0	0.5	0.0	0.0	0.0	1.5	PsI		Fort Stockton	Pecos
1 Aug.	1975	07:27:57	0.0	0.0	0.0	0.0	0.0	0.0	T		Delaware Basin	Reeves
19 Jan.	1976	04:03:30	1.0	1.0	0.0	0.0	1.0	3.0	PrI	Doser et al. (1992)	Kermit	Winkler
25 Jan.	1976	04:48:28	1.0	1.0	0.0	0.0	1.0	3.0	PrI	Doser et al. (1992)	Kermit	Winkler

Date	Year	Time	QT	QS	QD	QF	QP	Sum	Type	Ref	Location	County
5 Aug.	1976	18:53:09	1.0	1.0	0.0	0.0	1.0	3.0	PrI	Doser et al. (1992)	Kermit	Ward
17 Sept.	1976	03:56:29	1.0	1.0	0.0	0.0	1.0	3.0	PrI	Doser et al. (1992)	Kermit	Crane
26 Apr.	1977	09:03:07	1.0	1.0	0.0	0.0	1.0	3.0	PrI	Doser et al. (1992)	Kermit	Winkler
7 June	1977	23:01:20	1.0	1.0	0.5	0.5	1.0	4.0	ACI	Davis & Pennington (1989)	Snyder	Scurry
22 July	1977	04:01:10	1.0	1.0	0.0	0.0	1.0	3.0	PrI	Doser et al. (1992)	Kermit	Ector
28 Nov.	1977	01:40:52	1.0	1.0	0.0	0.0	0.0	2.0	PrI	Davis & Pennington (1989)	Spur	Kent
2 Mar.	1978	10:04:53	1.0	1.0	0.0	0.0	1.0	3.0	PrI	Doser et al. (1992)	Kermit	Crane
16 June	1978	11:46:54	1.0	1.0	0.5	0.5	1.0	4.0	ACI	Davis & Pennington (1989)	Snyder	Scurry
16 June	1978	11:53:33	1.0	1.0	0.5	0.5	1.0	4.0	ACI	Davis & Pennington (1989)	Snyder	Scurry
9 June	1980	22:37:10	1.0	1.0	0.0	0.0	0.0	2.0	PsI		Pampa	Gray
9 June	1981	01:46:33	0.5	0.5	0.0	0.0	0.5	1.5	PsI	Pennington & Carlson (1984)	Center	Shelby
6 Nov.	1981	12:36:41	1.0	1.0	0.0	0.0	0.5	2.5	PrI	Frohlich & Davis (2002)	Jacksonville	Anderson
4 Jan.	1982	16:56:10	1.0	1.0	0.0	0.0	0.5	2.5	PrI	Doser et al. (1992)	Fort Stockton	Pecos
28 Mar.	1982	23:24:33	1.0	0.5	0.0	0.0	0.0	1.5	PsI		South Texas	Wilson
19 Sept.	1982	06:15:42	1.0	1.0	0.0	0.0	0.0	2.0	PsI		Silver	Coke
14 Oct.	1982	12:52:46	0.0	0.0	0.0	0.0	0.0	0.0	T		Dalhart	Hartley
7 Nov.	1982	00:04:19	1.0	1.0	0.0	0.0	0.0	2.0	PsI		Wheeler Co.	Wheeler

Date	Year	Time	QT	QS	QD	QF	QP	Sum	Type	Ref	Location	County
28 Nov.	1982	02:36:48	1.0	1.0	0.5	0.5	1.0	4.0	ACI	Davis & Pennington (1989)	Snyder	Scurry
3 Apr.	1983	04:55:22	1.0	1.0	0.0	0.0	0.0	2.0	PsI		Oldham	Oldham
23 July	1983	15:24:39	1.0	1.0	0.5	0.5	1.0	4.0	ACI	Pennington et al. (1986)	Fashing	Atascosa
3 Mar.	1984	01:03:26	1.0	1.0	0.5	0.5	1.0	4.0	ACI	Pennington et al. (1986)	Pleasanton	Atascosa
3 Mar.	1984	01:58:25	1.0	1.0	0.5	0.5	1.0	4.0	ACI	Pennington et al. (1986)	Pleasanton	Atascosa
8 Mar.	1984	01:31:28	1.0	1.0	0.5	0.5	1.0	4.0	ACI	Pennington et al. (1986)	Pleasanton	Atascosa
3 Apr.	1984	04:55:24	1.0	0.5	0.0	0.0	0.0	1.5	PsI		Oldham Co.	Oldham
21 May	1984	13:30:14	1.0	0.5	0.0	0.0	0.0	1.5	PsI		Oldham Co.	Oldham
8 Aug.	1984	01:31:27	1.0	1.0	0.5	0.5	1.0	4.0	ACI	Pennington et al. (1986)	Pleasanton	Atascosa
11 Sept.	1984	14:47:33	1.0	1.0	0.0	0.0	0.0	2.0	PsI		Coke County	Coke
19 Sept.	1984	06:15:42	1.0	1.0	0.0	0.0	0.0	2.0	PsI		Coke County	Coke
18 Sept.	1985	15:54:05	1.0	1.0	0.0	0.0	0.0	2.0	PsI		Valley View	Cooke
30 Jan.	1986	22:26:37	1.0	1.0	0.0	0.0	0.0	2.0	PsI		Silver	Coke
3 Mar.	1986	11:45:17	0.0	0.0	0.0	0.0	0.0	0.0	T		Oldham Co.	Oldham
20 July	1991	23:38:17	1.0	1.0	0.0	0.5	1.0	3.5	PrI	Frohlich & Brunt (2013)	Falls City	Karnes
2 Jan.	1992	11:45:36	1.0	1.0	0.0	0.0	0.0	2.0	PsI		Rattlesnake Canyon	Andrews
26 Aug.	1992	03:24:53	1.0	1.0	0.0	0.0	0.0	2.0	PsI		Andrews	Andrews
9 Apr.	1993	12:29:19	1.0	1.0	0.5	0.5	1.0	4.0	ACI	Pennington et al. (1986)	Fashing	Atascosa
16 May	1993	15:30:19	1.0	1.0	0.5	0.5	1.0	4.0	ACI	Pennington et al. (1986)	Fashing	Atascosa
29 Sept	1993	02:01	0.0	0.0	0.0	0.0	0.0	0.0	T		Dalhart	Hartley
30 Nov	1993	03:07	0.0	0.0	0.0	0.0	0.0	0.0	T		Dalhart	Hartley
14 Apr.	1995	00:32:56	0.0	0.0	0.0	0.0	0.0	0.0	T		Alpine	Brewster
14 Apr.	1995	02:19:38	0.0	0.0	0.0	0.0	0.0	0.0	T		Alpine	Pecos

Date	Year	Time	QT	QS	QD	QF	QP	Sum	Type	Ref	Location	County
15 Apr.	1995	10:33:43	0.0	0.0	0.0	0.0	0.0	0.0	T		Alpine	Brewseter
15 Apr.	1995	14:33:30	0.0	0.0	0.0	0.0	0.0	0.0	T		Alpine	Brewster
1 June	1995	01:06:16	0.0	0.0	0.0	0.0	0.0	0.0	T		Alpine	Brewster
12 Nov.	1995	17:45:59	0.0	0.0	0.0	0.0	0.0	0.0	T		Alpine	Brewster
25 Mar.	1996	06:43:47	1.0	0.5	0.0	0.0	0.0	1.5	PsI		near Channing	Huntley
23 Nov.	1996	10:54:18	1.0	0.5	0.0	0.0	0.0	1.5	PsI		near McLean	Donley
12 Feb.	1997	23:53:11	1.0	0.5	0.0	0.0	0.0	1.5	PsI		near McLean	Donley
15 Feb.	1997	09:08:55	1.0	0.5	0.0	0.0	0.0	1.5	PsI		near McLean	Donley
24 Mar.	1997	22:31:34	1.0	1.0	1.0	1.0	1.0	5.0	ACI	Frohlich et al. (2012)	Alice	Jim Wells
31 May	1997	03:26:41	0.0	0.0	0.0	0.0	0.0	0.0	T		Commerce	Hunt
15 Apr.	1998	10:33:42	0.0	0.0	0.0	0.0	0.0	0.0	T		Alpine	Brewster
27 Apr.	1998	15:22:46	1.0	1.0	0.0	0.0	0.0	2.0	PsI		Oldham	Oldham
7 Aug.	2000	17:19:06	1.0	0.5	0.0	0.0	0.0	1.5	PsI		Amarillo	Potter
7 Aug.	2000	18:34:09	1.0	0.5	0.0	0.0	0.0	1.5	PsI		Amarillo	Potter
7 Aug.	2000	21:36:21	1.0	0.5	0.0	0.0	0.0	1.5	PsI		Amarillo	Potter
10 Aug.	2000	13:59:50	1.0	0.5	0.0	0.0	0.0	1.5	PsI		Amarillo	Potter
17 Aug.	2000	01:08:05	1.0	0.5	0.0	0.0	0.0	1.5	PsI		Amarillo	Potter
16 Dec.	2000	22:08:53	1.0	0.5	0.0	0.0	0.0	1.5	PsI		Amarillo	Potter
22 Nov.	2001	00:07:08	1.0	1.0	0.0	0.0	0.0	2.0	PsI		Odessa	Ector
24 Sept.	2003	15:02:09	1.0	0.0	0.0	0.0	0.0	1.0	PsI		Amarillo	Potter
3 Apr.	2005	14:39:17	0.0	0.0	0.0	0.0	0.0	0.0	T		Eagle Pass	Maverick
18 Feb.	2006	05:49:41	1.0	1.0	0.0	0.0	0.0	2.0	PsI		Lake Meredith	Moore
28 Mar.	2006	23:55:11	1.0	1.0	0.0	0.0	0.0	2.0	PsI		Amarillo	Potter
27 Sept.	2007	15:21:02	1.0	1.0	0.0	0.0	0.0	2.0	PsI		Wheeler	Wheeler
7 Oct.	2007	13:54:22	0.0	0.0	0.0	0.0	0.0	0.0	T		Childress	Childress
29 Jan.	2008	10:24:53	1.0	1.0	0.0	0.5	1.0	3.5	PrI	Gan & Frohlich (2013)	Snyder	Scurry
7 Apr.	2008	09:51:13	1.0	1.0	0.0	0.5	1.0	3.5	PrI	Frohlich & Brunt (2013)	Falls City	Karnes
12 Oct.	2008	12:08:16	1.0	1.0	0.0	0.0	0.0	2.0	PsI		Briscoe	Wheeler
14 Oct.	2008	03:07:28	1.0	1.0	0.0	0.0	0.0	2.0	PsI		Miami	Roberts

Date	Year	Time	QT	QS	QD	QF	QP	Sum	Type	Ref	Location	County
31 Oct.	2008	05:01:55	1.0	1.0	1.0	1.0	1.0	5.0	ACI	Frohlich et al. (2011)	Dallas-Fort Worth	Tarrant
16 May	2009	16:24:05	1.0	1.0	1.0	1.0	1.0	5.0	ACI	Frohlich et al. (2011)	Dallas-Fort Worth	Tarrant
16 May	2009	16:58:38	1.0	1.0	1.0	1.0	1.0	5.0	ACI	Frohlich et al. (2011)	Dallas-Fort Worth	Tarrant
27 Jan.	2010	04:59:33	1.0	1.0	0.0	0.5	1.0	3.5	PrI	Gan & Frohlich (2013)	Snyder	Scurry
4 Feb.	2010	09:41:28	1.0	1.0	0.0	0.0	0.0	2.0	PsI		Borger	Oldham
8 Mar.	2010	23:47:28	1.0	1.0	0.0	0.5	1.0	3.5	PrI	Frohlich & Brunt (2013)	Falls City?	Karnes
25 Apr.	2010	02:10:42	1.0	1.0	1.0	1.0	1.0	5.0	ACI	Frohlich et al. (2012)	Alice	Jim Wells
8 Aug.	2010	01:12:38	1.0	1.0	0.0	0.5	1.0	3.5	PrI	Gan & Frohlich (2013)	Snyder	Scurry
9 Oct.	2010	07:42:28	1.0	1.0	0.0	0.5	1.0	3.5	PrI	Gan & Frohlich (2013)	Snyder	Scurry
26 Oct.	2010	06:56:29	1.0	1.0	0.0	0.5	1.0	3.5	PrI	Gan & Frohlich (2013)	Snyder	Scurry
21 Dec.	2010	13:53:18	1.0	1.0	0.5	0.5	1.0	4.0	ACI	Frohlich & Brunt (2013)	Fashing	Bee
17 Feb.	2011	18:25:34	0.0	0.0	0.0	0.0	0.0	0.0	T		Marathon	Brewster
1 Mar.	2011	03:30:13	1.0	1.0	0.0	0.5	1.0	3.5	PrI	Gan & Frohlich (2013)	Snyder	Scurry
12 Mar.	2011	15:22:00	1.0	1.0	0.0	0.5	1.0	3.5	PrI	Gan & Frohlich (2013)	Snyder	Scurry
13 Mar.	2011	20:16:21	1.0	1.0	0.0	0.5	1.0	3.5	PrI	Gan & Frohlich (2013)	Snyder	Kent

Date	Year	Time	QT	QS	QD	QF	QP	Sum	Type	Ref	Location	County
14 Mar.	2011	00:19:49	1.0	1.0	0.0	0.5	1.0	3.5	PrI	Gan & Frohlich (2013)	Snyder	Kent
19 Mar.	2011	23:24:01	1.0	1.0	0.0	0.5	1.0	3.5	PrI	Gan & Frohlich (2013)	Snyder	Kent
28 Mar.	2011	09:12:12	1.0	1.0	0.0	0.5	1.0	3.5	PrI	Gan & Frohlich (2013)	Snyder	Scurry
2 Apr.	2011	22:05:14	1.0	1.0	0.0	0.5	1.0	3.5	PrI	Gan & Frohlich (2013)	Snyder	Kent
2 May	2011	19:07:15	1.0	1.0	0.0	0.5	1.0	3.5	PrI	Gan & Frohlich (2013)	Snyder	Kent
17 Jul.	2011	06:58:01	1.0	1.0	0.0	0.5	1.0	3.5	PrI	Frohlich (2012)	Venus	Johnson
11 Sept.	2011	12:27:44	1.0	1.0	0.0	0.5	1.0	3.5	PrI	Gan & Frohlich (2013)	Snyder	Scurry
12 Sept.	2011	14:18:34	1.0	1.0	0.0	0.5	1.0	3.5	PrI	Gan & Frohlich (2013)	Snyder	Scurry
20 Oct.	2011	12:24:42	1.0	1.0	0.5	0.5	1.0	4.0	ACI	Frohlich & Brunt (2013)	Fashing	Atascosa
12 Nov.	2011	10:34:54	1.0	1.0	0.5	0.5	1.0	4.0	ACI	Frohlich & Brunt (2013)	Fashing	Atascosa
24 Nov.	2011	23:15:49	1.0	1.0	0.0	0.5	1.0	3.5	PrI	Gan & Frohlich (2013)	Snyder	Scurry
9 Dec.	2011	18:47:32	1.0	1.0	0.0	0.5	1.0	3.5	PrI	Gan & Frohlich (2013)	Snyder	Scurry

Date	Year	Time	QT	QS	QD	QF	QP	Sum	Type	Ref	Location	County
17 Dec.	2011	14:46:58	1.0	1.0	0.0	0.5	1.0	3.5	PrI	Gan & Frohlich (2013)	Snyder	Scurry
18 Jan	2012	22:30:54	1.0	1.0	1.0	0.0	1.0	4.0	ACI	Justinic et al. (2013)	Cleburne	Johnson
24 Jan.	2012	18:21:03	0.0	0.0	0.0	0.0	0.0	0.0	T		Alpine	Brewster
4 Feb.	2012	12:48:09	1.0	1.0	0.5	0.5	1.0	4.0	ACI	Frohlich & Brunt (2013)	Fashing	Atascosa
10 May	2012	15:15:39	1.0	1.0	1.0	1.0	1.0	5.0	ACI	Frohlich et al. (2014)	Timpson	Shelby
17 May	2012	08:12:01	1.0	1.0	1.0	1.0	1.0	5.0	ACI	Frohlich et al. (2014)	Timpson	Shelby
15 Jun.	2012	07:02:32	1.0	1.0	1.0	0.0	1.0	4.0	ACI	Justinic et al. (2013)	Cleburne	Johnson
24 Jun.	2012	08:55:59	1.0	1.0	0.5	0.5	1.0	4.0	ACI	Pennington et al. (1986)	Pleasanton	McMullen
24 Jun.	2012	17:46:43	1.0	1.0	1.0	0.0	1.0	4.0	ACI	Justinic et al. (2013)	Cleburne	Johnson
12 Aug.	2012	00:36:04	1.0	1.0	0.0	0.0	0.0	2.0	PsI		Amarillo	Potter
30 Sept.	2012	04:04:59	0.5	0.5	1.0	1.0	0.0	3.0	PrI		Irving	Dallas
30 Sept.	2012	04:09:03	0.5	0.5	1.0	1.0	0.0	3.0	PrI		Irving	Dallas
7 Nov.	2012	17:38:00	1.0	1.0	0.0	0.0	0.0	2.0	PsI		Hebronville	Jim Hogg
23 Jan.	2013	04:16:19	0.5	0.5	1.0	1.0	0.0	3.0	PrI		Irving	Dallas
25 Jan.	2013	07:01:20	1.0	1.0	1.0	1.0	1.0	5.0	ACI	Frohlich et al. (2014)	Timpson	Shelby
6 May	2013	23:11:59	1.0	1.0	0.0	0.5	1.0	3.5	PrI	Gan & Frohlich (2013)	Snyder	Kent
14 May	2013	00:05:40	0.0	0.0	0.0	0.0	0.0	0.0	T		Van Horn	Culberson
2 Sept.	2013	21:52:37	1.0	1.0	1.0	1.0	1.0	5.0	ACI	Frohlich et al. (2014)	Timpson	Shelby
2 Sept.	2013	23:51:15	1.0	1.0	1.0	1.0	1.0	5.0	ACI	Frohlich et al. (2014)	Timpson	Shelby

Date	Year	Time	QT	QS	QD	QF	QP	Sum	Type	Ref	Location	County
9 Nov.	2013	19:54:31	1.0	1.0	1.0	1.0	1.0	5.0	ACI	Hornbach et al. (2015)	Azle	Parker
12 Nov.	2013	17:36:03	0.0	0.0	0.0	0.0	0.0	0.0	T		Hudspeth	Hudspeth
20 Nov.	2013	00:40:35	1.0	1.0	1.0	1.0	1.0	5.0	ACI	Hornbach et al. (2015)	Azle	Wise
25 Nov.	2013	07:43:03	1.0	1.0	1.0	1.0	1.0	5.0	ACI	Hornbach et al. (2015)	Reno	Parker
26 Nov.	2013	14:24:03	1.0	1.0	1.0	1.0	1.0	5.0	ACI	Hornbach et al. (2015)	Reno	Parker
28 Nov.	2013	07:58:34	1.0	1.0	1.0	1.0	1.0	5.0	ACI	Hornbach et al. (2015)	Mineral Wells	Parker
29 Nov.	2013	06:14:10	1.0	1.0	1.0	1.0	1.0	5.0	ACI	Hornbach et al. (2015)	Azle	Denton
8 Dec.	2013	06:10:01	1.0	1.0	1.0	1.0	1.0	5.0	ACI	Hornbach et al. (2015)	Azle	Parker
9 Dec.	2013	09:23:14	1.0	1.0	1.0	1.0	1.0	5.0	ACI	Hornbach et al. (2015)	Mineral Wells	Parker
22 Dec.	2013	17:31:55	1.0	1.0	1.0	1.0	1.0	5.0	ACI	Hornbach et al. (2015)	Reno	Parker
23 Dec.	2013	13:11:34	1.0	1.0	1.0	1.0	1.0	5.0	ACI	Hornbach et al. (2015)	Reno	Parker
6 Jan.	2014	08:41:20	0.0	0.0	0.0	0.0	0.0	0.0	T		Boise	Oldham
13 Jan.	2014	17:40:21	1.0	1.0	1.0	1.0	1.0	5.0	ACI	Hornbach et al. (2015)	Reno	Parker
28 Jan.	2014	17:43:44	1.0	1.0	0.0	0.5	1.0	3.5	PrI	Gan & Frohlich (2013)	Snyder	Scurry
14 May	2014	15:52:17	1.0	1.0	0.0	0.5	1.0	3.5	PrI	Gan & Frohlich (2013)	Snyder	Scurry
10 Sept.	2014	17:53:24	1.0	1.0	0.5	0.5	1.0	4.0	ACI	Pennington et al. (1986)	Jourdanton	Atascosa

Date	Year	Time	QT	QS	QD	QF	QP	Sum	Type	Ref	Location	County
14 Sept.	2014	09:19:00	1.0	1.0	0.0	0.5	1.0	3.5	PrI	Gan & Frohlich (2013)	Snyder	Scurry
3 Oct.	2014	04:52:33	0.5	0.5	0.0	0.0	0.5	1.5	PsI	Walter et al. (2016)	Center	Shelby
23 Nov.	2014	03:15:47	0.5	0.5	1.0	1.0	0.0	3.0	PrI		Irving	Dallas
30 Nov.	2014	05:52:24	1.0	1.0	0.0	0.0	1.0	3.0	PrI	Frohlich (2012)	Mansfield	Johnson
3 Dec.	2014	13:33:39	1.0	1.0	0.0	0.0	0.0	2.0	PsI		Follett	Lipscomb
31 Dec.	2014	18:31:40	1.0	1.0	0.0	0.5	1.0	3.5	PrI	Gan & Frohlich (2013)	Snyder	Scurry
6 Jan.	2015	21:10:31	0.5	0.5	1.0	1.0	0.0	3.0	PrI		Irving	Dallas
6 Jan.	2015	21:55:19	1.0	1.0	0.0	0.5	1.0	3.5	PrI	Gan & Frohlich (2013)	Snyder	Scurry
7 Jan.	2015	00:52:09	0.5	0.5	1.0	1.0	0.0	3.0	PrI		Irving	Dallas
7 Jan.	2015	06:59:03	0.5	0.5	1.0	1.0	0.0	3.0	PrI		Irving	Dallas
20 Jan.	2015	20:25:49	0.5	0.5	1.0	1.0	0.0	3.0	PrI		Irving	Dallas
31 Jan.	2015	02:17:02	1.0	1.0	0.5	0.5	1.0	4.0	ACI	Frohlich & Brunt (2013)	Fashing	Atascosa
2 Feb.	2015	00:39:27	0.0	0.0	0.0	0.0	0.0	0.0	T		Amarillo	Potter
19 Feb.	2015	20:31:20	1.0	1.0	0.0	0.0	0.0	2.0	PsI		Hallettsville	Lavaca
27 Feb.	2015	12:18:21	0.5	0.5	1.0	1.0	0.0	3.0	PrI		Irving	Dallas
2 Apr.	2015	22:36:21	0.5	0.5	1.0	1.0	0.0	3.0	PrI		Irving	Dallas
4 Apr.	2015	00:16:33	1.0	1.0	0.0	0.0	0.5	2.5	PrI	Doser et al. (1992)		Reeves
17 Apr.	2015	22:15:14	1.0	0.5	0.0	0.0	0.5	2.5	PsI	Doser et al. (1992)	Pecos	Pecos
3 May	2015	15:11:15	0.5	0.5	1.0	1.0	0.0	3.0	PrI		Irving	Dallas
7 May	2015	22:58:07	1.0	1.0	0.0	0.5	1.0	3.5	PrI	Frohlich (2012)	Venus	Johnson
17 May	2015	22:15:13	1.0	0.5	0.0	0.0	0.5	2.0	PsI	Doser et al. (1992)	Pecos	Pecos

Date	Year	Time	QT	QS	QD	QF	QP	Sum	Type	Ref	Location	County
18 May	2015	18:14:29	0.5	0.5	1.0	1.0	0.0	3.0	PrI		Irving	Dallas
4 Aug.	2015	15:06:32	1.0	0.5	0.0	0.0	0.5	2.0	PsI	Doser et al. (1992)		Reeves
12 Aug.	2015	20:49:22	1.0	0.5	0.0	0.0	0.5	2.0	PsI	Doser et al. (1992)	Fort Stockton	Pecos
7 Nov.	2015	05:18:20	1.0	0.5	0.0	0.0	0.5	2.0	PsI	Doser et al. (1992)	Monahans	Reeves
10 Nov.	2015	21:43:04	1.0	0.5	0.0	0.0	0.5	2.0	PsI	Doser et al. (1992)	Monahans	Ward
14 Dec.	2015	12:35:03	1.0	0.5	0.0	0.0	0.0	1.5	PsI		Nixon	Wilson
17 Dec	2015	22:29:56	1.0	1.0	0.0	0.0	0.0	2.0	PsI		Haslet	Tarrant

Appendix B. Information on the Selected Ground Motions

Table B.1: Information on selected ground motion recordings

Date	Time	Event Latitude	Event Longitude	Magnitude	Depth	Network	Station	Station Latitude	Station Longitude	V_{S30} (m/s)	Hypocentral Distance (km)	PGA (g)
11/6/2011	3:53:10	35.5501	-96.7579	5.7	7.5	TA	S37A	37.7597	-94.8279	1620	300.1	0.0025
11/6/2011	3:53:10	35.5501	-96.7579	5.7	7.5	TA	Z36A	33.2702	-96.4344	520	255.4	0.0025
11/6/2011	3:53:10	35.5501	-96.7579	5.7	7.5	TA	R36A	38.3237	-95.5040	636	328.0	0.0027
11/6/2011	3:53:10	35.5501	-96.7579	5.7	7.5	TA	Y35A	33.9059	-97.0374	812	184.8	0.0029
11/6/2011	3:53:10	35.5501	-96.7579	5.7	7.5	TA	X38A	34.6692	-94.8288	1202	201.1	0.0029
11/6/2011	3:53:10	35.5501	-96.7579	5.7	7.5	TA	ABTX	32.6238	-99.6431	975	420.1	0.0029
9/3/2016	12:02:44	36.4298	-96.9317	5.8	5.4	US	CBKS	38.8140	-99.7374	439	362.4	0.0030
11/6/2011	3:53:10	35.5501	-96.7579	5.7	7.5	TA	X37A	34.5892	-95.3713	1073	165.5	0.0042
11/6/2011	3:53:10	35.5501	-96.7579	5.7	7.5	TA	W38A	35.0704	-94.5184	1120	210.2	0.0042
11/6/2011	3:53:10	35.5501	-96.7579	5.7	7.5	US	WMOK	34.7379	-98.7807	1663	205.0	0.0047
9/3/2016	12:02:44	36.4298	-96.9317	5.8	5.4	N4	R32B	38.4225	-98.7111	666	271.7	0.0051
9/3/2016	12:02:44	36.4298	-96.9317	5.8	5.4	OK	LOOK	33.9924	-97.1800	764	272.0	0.0052
11/8/2011	2:46:57	35.5275	-96.7918	5.0	2.7	TA	W37B	35.1390	-95.4316	1321	130.8	0.0053
9/3/2016	12:02:44	36.4298	-96.9317	5.8	5.4	US	KSU1	39.1009	-96.6094	697	298.4	0.0053
2/13/2016	17:07:06	36.4905	-98.7056	5.1	8	GS	OK029	35.7966	-97.4549	630	136.5	0.0054
11/6/2011	3:53:10	35.5501	-96.7579	5.7	7.5	TA	Y36A	33.8996	-96.2848	781	188.7	0.0054
11/6/2011	3:53:10	35.5501	-96.7579	5.7	7.5	TA	Y38A	33.9278	-94.7311	826	258.6	0.0054
2/13/2016	17:07:06	36.4905	-98.7056	5.1	8	GS	OK031	35.9531	-96.8391	509	178.0	0.0055
9/21/2013	12:16:12	27.8013	-105.6794	5.4	10	IM	TX32	29.3338	-103.6670	1002	260.3	0.0058
10/2/2014	18:01:24	37.2447	-97.9553	4.5	5	GS	KAN13	37.0129	-97.4778	353	49.8	0.0062
1/7/2016	4:27:27	36.4955	-98.7254	4.7	4.1	GS	KAN08	37.2267	-97.9709	1055	105.5	0.0063
1/7/2016	4:27:27	36.4955	-98.7254	4.7	4.1	GS	KAN10	37.1235	-98.0951	946	89.7	0.0064
11/6/2011	3:53:10	35.5501	-96.7579	5.7	7.5	TA	Y37A	33.9789	-95.6210	532	203.4	0.0064
11/7/2016	1:44:24	35.9837	-96.7982	5.0	5	GS	OK032	36.8038	-98.2104	500	155.9	0.0065
11/8/2011	2:46:57	35.5275	-96.7918	5.0	2.7	TA	U35A	36.3709	-96.7318	969	94.0	0.0066
11/19/2015	7:42:12	36.6602	-98.4594	4.7	5.9	OK	QUOK	36.1714	-96.7080	503	166.0	0.0066
11/7/2016	1:44:24	35.9837	-96.7982	5.0	5	GS	OK029	35.7966	-97.4549	630	62.9	0.0066
11/7/2016	1:44:24	35.9837	-96.7982	5.0	5	GS	KS21	37.2865	-97.6630	374	164.2	0.0067
11/30/2015	9:49:12	36.7509	-98.0561	4.5	5.6	GS	KAN12	37.2974	-97.9980	524	61.2	0.0068
11/5/2011	7:12:45	35.5525	-96.7387	5.0	6.2	OK	OKCFA	35.4153	-97.4518	660	66.6	0.0069
11/5/2011	7:12:45	35.5525	-96.7387	5.0	6.2	TA	W37B	35.1390	-95.4316	1321	127.3	0.0070
11/6/2011	3:53:10	35.5501	-96.7579	5.7	7.5	TA	T35A	36.9161	-96.5121	849	153.7	0.0071
11/30/2015	9:49:12	36.7509	-98.0561	4.5	5.6	OK	DEOK	35.8427	-96.4983	906	172.4	0.0071

Date	Time	Event Latitude	Event Longitude	Magnitude	Depth	Network	Station	Station Latitude	Station Longitude	V_{S30} (m/s)	Hypocentral Distance (km)	PGA (g)
11/30/2015	9:49:12	36.7509	-98.0561	4.5	5.6	GS	KAN11	37.2060	-97.9133	995	52.5	0.0072
11/7/2016	1:44:24	35.9837	-96.7982	5.0	5	GS	KAN05	37.1080	-97.8715	765	157.6	0.0072
2/13/2016	17:07:06	36.4905	-98.7056	5.1	8	GS	OK025	35.5811	-97.3379	502	159.4	0.0073
11/7/2016	1:44:24	35.9837	-96.7982	5.0	5	NQ	KAN02	37.1977	-97.8787	1118	166.0	0.0073
11/7/2016	1:44:24	35.9837	-96.7982	5.0	5	GS	KAN06	37.2480	-97.8586	1008	169.5	0.0074
2/13/2016	17:07:06	36.4905	-98.7056	5.1	8	OK	QUOK	36.1714	-96.7080	503	182.6	0.0074
2/13/2016	17:07:06	36.4905	-98.7056	5.1	8	GS	KS21	37.2865	-97.6630	374	128.4	0.0077
11/19/2015	7:42:12	36.6602	-98.4594	4.7	5.9	OK	CCOK	35.3568	-97.6561	664	162.0	0.0078
11/7/2016	1:44:24	35.9837	-96.7982	5.0	5	GS	KAN17	37.0441	-97.7648	183	146.2	0.0078
7/20/2015	20:19:03	36.842	-98.2593	4.4	4.1	GS	KAN10	37.1235	-98.0951	946	34.8	0.0080
10/13/2010	14:06:30	35.2196	-97.3262	4.3	4.8	TA	Z34A	33.3712	-97.9158	740	212.6	0.0080
2/13/2016	17:07:06	36.4905	-98.7056	5.1	8	OK	CCOK	35.3568	-97.6561	664	157.7	0.0080
11/20/2015	22:40:40	36.9483	-97.8276	4.1	5	GS	KAN06	37.2480	-97.8586	1008	33.8	0.0083
1/7/2016	4:27:27	36.4955	-98.7254	4.7	4.1	OK	CROK	36.5047	-97.9834	493	66.5	0.0083
6/16/2014	10:47:35	35.5935	-97.3969	4.3	5	GS	OK028	35.5611	-97.0614	461	31.0	0.0084
2/13/2016	17:07:06	36.4905	-98.7056	5.1	8	GS	OK030	35.9278	-96.7838	448	183.6	0.0085
2/13/2016	17:07:06	36.4905	-98.7056	5.1	8	GS	KAN12	37.2974	-97.9980	524	109.9	0.0086
11/30/2015	9:49:12	36.7509	-98.0561	4.5	5.6	GS	KAN01	37.1535	-97.7592	825	52.3	0.0087
11/7/2016	1:44:24	35.9837	-96.7982	5.0	5	OK	CHOK	35.5611	-97.0613	525	52.9	0.0087
11/30/2015	9:49:12	36.7509	-98.0561	4.5	5.6	GS	OK031	35.9531	-96.8391	509	140.6	0.0088
10/10/2014	13:51:21	35.9466	-96.7594	4.3	5	OK	QUOK	36.1714	-96.7080	503	25.9	0.0089
11/7/2016	1:44:24	35.9837	-96.7982	5.0	5	GS	KAN14	36.9568	-97.9630	701	150.3	0.0090
11/30/2015	9:49:12	36.7509	-98.0561	4.5	5.6	GS	KAN13	37.0129	-97.4778	353	59.4	0.0090
11/30/2015	9:49:12	36.7509	-98.0561	4.5	5.6	GS	KAN08	37.2267	-97.9709	1055	53.7	0.0090
11/30/2015	9:49:12	36.7509	-98.0561	4.5	5.6	GS	KAN06	37.2480	-97.8586	1008	58.3	0.0091
10/13/2010	14:06:30	35.2196	-97.3262	4.3	4.8	TA	W35A	35.1527	-96.8745	521	42.0	0.0091
11/7/2016	1:44:24	35.9837	-96.7982	5.0	5	OK	RLOK	36.1676	-95.0268	1534	160.6	0.0091
2/13/2016	17:07:06	36.4905	-98.7056	5.1	8	GS	KAN17	37.0441	-97.7648	183	104.3	0.0092
7/20/2015	20:19:03	36.842	-98.2593	4.4	4.1	GS	KAN08	37.2267	-97.9709	1055	50.0	0.0094
11/7/2016	1:44:24	35.9837	-96.7982	5.0	5	GS	KS20	37.2297	-97.5543	299	154.2	0.0095
10/10/2015	9:20:43	36.7187	-97.9311	4.4	5.6	GS	KAN10	37.1235	-98.0951	946	47.6	0.0095
6/18/2014	10:53:02	35.5956	-97.3924	4.1	5	OK	BCOK	35.6567	-97.6093	796	21.3	0.0095
10/20/2011	12:24:41	28.8481	-98.1485	4.8	14.2	TA	735A	28.8553	-97.8081	430	36.1	0.0096

Date	Time	Event Latitude	Event Longitude	Magnitude	Depth	Network	Station	Station Latitude	Station Longitude	V_{S30} (m/s)	Hypocentral Distance (km)	PGA (g)
4/27/2015	22:22:17	35.918	-97.3256	4.1	5.3	GS	OK029	35.7966	-97.4549	630	18.6	0.0097
11/7/2016	1:44:24	35.9837	-96.7982	5.0	5	GS	KAN13	37.0129	-97.4778	353	129.7	0.0100
11/30/2015	9:49:12	36.7509	-98.0561	4.5	5.6	GS	KAN10	37.1235	-98.0951	946	42.0	0.0101
7/27/2015	18:12:15	35.9889	-97.5717	4.3	5	GS	OK029	35.7966	-97.4549	630	24.4	0.0101
2/13/2016	17:07:06	36.4905	-98.7056	5.1	8	GS	KAN10	37.1235	-98.0951	946	89.3	0.0101
11/19/2015	7:42:12	36.6602	-98.4594	4.7	5.9	GS	KAN16	37.2256	-98.0647	971	72.2	0.0103
11/7/2015	11:11:53	36.9528	-97.8552	4.1	5	GS	KAN06	37.2480	-97.8586	1008	33.2	0.0104
11/8/2011	2:46:57	35.5275	-96.7918	5.0	2.7	TA	W35A	35.1527	-96.8745	521	42.4	0.0104
2/13/2016	17:07:06	36.4905	-98.7056	5.1	8	GS	KAN06	37.2480	-97.8586	1008	113.3	0.0104
12/29/2015	11:39:19	35.6654	-97.4054	4.3	6.5	OK	BCOK	35.6567	-97.6093	796	19.6	0.0104
7/27/2015	18:12:15	35.9889	-97.5717	4.3	5	GS	OK031	35.9531	-96.8391	509	66.2	0.0109
10/10/2015	9:20:43	36.7187	-97.9311	4.4	5.6	GS	KAN09	37.1361	-97.6183	396	54.4	0.0110
2/13/2016	17:07:06	36.4905	-98.7056	5.1	8	GS	KAN14	36.9568	-97.9630	701	84.5	0.0110
11/7/2016	1:44:24	35.9837	-96.7982	5.0	5	GS	KAN01	37.1535	-97.7592	825	155.9	0.0112
11/7/2016	1:44:24	35.9837	-96.7982	5.0	5	NQ	KAN15	37.2998	-97.5727	1051	161.9	0.0112
11/30/2015	9:49:12	36.7509	-98.0561	4.5	5.6	GS	KAN05	37.1080	-97.8715	765	43.3	0.0113
11/19/2015	7:42:12	36.6602	-98.4594	4.7	5.9	GS	KAN01	37.1535	-97.7592	825	83.2	0.0114
10/10/2015	9:20:43	36.7187	-97.9311	4.4	5.6	GS	KAN06	37.2480	-97.8586	1008	59.5	0.0114
11/7/2015	11:11:53	36.9528	-97.8552	4.1	5	GS	KAN13	37.0129	-97.4778	353	34.5	0.0116
7/20/2015	20:19:03	36.842	-98.2593	4.4	4.1	OK	CROK	36.5047	-97.9834	493	45.0	0.0116
4/16/2013	6:56:29	35.685	-97.066	4.4	5	OK	FNO	35.2574	-97.4012	578	56.6	0.0117
11/19/2015	7:42:12	36.6602	-98.4594	4.7	5.9	GS	KAN12	37.2974	-97.9980	524	82.1	0.0117
11/19/2015	7:42:12	36.6602	-98.4594	4.7	5.9	GS	KAN11	37.2060	-97.9133	995	77.9	0.0117
11/7/2016	1:44:24	35.9837	-96.7982	5.0	5	GS	OK025	35.5811	-97.3379	502	66.3	0.0119
1/7/2016	4:27:27	36.4955	-98.7254	4.7	4.1	OK	U32A	36.3795	-99.0014	700	28.2	0.0119
11/5/2011	7:12:45	35.5525	-96.7387	5.0	6.2	TA	V35A	35.7626	-96.8378	598	25.8	0.0120
6/16/2014	10:47:35	35.5935	-97.3969	4.3	5	OK	BCOK	35.6567	-97.6093	796	21.0	0.0122
4/16/2013	6:56:29	35.685	-97.066	4.4	5	OK	BCOK	35.6567	-97.6093	796	49.4	0.0124
11/6/2011	3:53:10	35.5501	-96.7579	5.7	7.5	OK	X34A	34.6010	-97.8326	818	144.1	0.0124
11/20/2015	22:40:40	36.9483	-97.8276	4.1	5	GS	KAN05	37.1080	-97.8715	765	18.9	0.0125
11/30/2015	9:49:12	36.7509	-98.0561	4.5	5.6	GS	KAN17	37.0441	-97.7648	183	42.0	0.0125
10/10/2015	9:20:43	36.7187	-97.9311	4.4	5.6	OK	QUOK	36.1714	-96.7080	503	125.3	0.0127
11/7/2016	1:44:24	35.9837	-96.7982	5.0	5	OK	BCOK	35.6567	-97.6093	796	81.8	0.0128
11/7/2015	11:11:53	36.9528	-97.8552	4.1	5	GS	KAN01	37.1535	-97.7592	825	24.4	0.0129

Date	Time	Event Latitude	Event Longitude	Magnitude	Depth	Network	Station	Station Latitude	Station Longitude	V_{S30} (m/s)	Hypocentral Distance (km)	PGA (g)
2/13/2016	17:07:06	36.4905	-98.7056	5.1	8	OK	CROK	36.5047	-97.9834	493	65.1	0.0129
11/19/2015	7:42:12	36.6602	-98.4594	4.7	5.9	OK	CROK	36.5047	-97.9834	493	46.3	0.0129
11/12/2014	21:40:00	37.2713	-97.6206	4.9	4	GS	KAN14	36.9568	-97.9630	701	46.5	0.0130
11/7/2016	1:44:24	35.9837	-96.7982	5.0	5	OK	DEOK	35.8427	-96.4983	906	31.6	0.0131
11/6/2011	3:53:10	35.5501	-96.7579	5.7	7.5	TA	W35A	35.1527	-96.8745	521	46.1	0.0132
9/3/2016	12:02:44	36.4298	-96.9317	5.8	5.4	OK	X34A	34.6010	-97.8326	818	219.2	0.0132
11/30/2015	9:49:12	36.7509	-98.0561	4.5	5.6	GS	KAN09	37.1361	-97.6183	396	58.1	0.0136
11/7/2015	11:11:53	36.9528	-97.8552	4.1	5	GS	KAN09	37.1361	-97.6183	396	29.7	0.0139
11/19/2015	7:42:12	36.6602	-98.4594	4.7	5.9	GS	KS21	37.2865	-97.6630	374	99.4	0.0139
11/7/2016	1:44:24	35.9837	-96.7982	5.0	5	GS	KAN09	37.1361	-97.6183	396	147.7	0.0141
6/5/2015	23:12:41	37.2648	-97.9213	4.2	2.4	GS	KAN10	37.1235	-98.0951	946	22.1	0.0143
9/3/2016	12:02:44	36.4298	-96.9317	5.8	5.4	OK	U32A	36.3795	-99.0014	700	185.4	0.0145
11/7/2016	1:44:24	35.9837	-96.7982	5.0	5	GS	KAN12	37.2974	-97.9980	524	181.2	0.0147
11/7/2015	11:11:53	36.9528	-97.8552	4.1	5	GS	KAN05	37.1080	-97.8715	765	18.0	0.0148
10/2/2014	18:01:24	37.2447	-97.9553	4.5	5	GS	KAN14	36.9568	-97.9630	701	32.4	0.0150
10/10/2015	9:20:43	36.7187	-97.9311	4.4	5.6	GS	KAN14	36.9568	-97.9630	701	27.2	0.0155
4/16/2013	10:16:53	35.687	-97.109	4.2	5	OK	BCOK	35.6567	-97.6093	796	45.6	0.0158
2/13/2016	17:07:06	36.4905	-98.7056	5.1	8	GS	OK032	36.8038	-98.2104	500	56.8	0.0159
11/19/2015	7:42:12	36.6602	-98.4594	4.7	5.9	GS	KAN06	37.2480	-97.8586	1008	84.6	0.0160
11/20/2015	22:40:40	36.9483	-97.8276	4.1	5	GS	KAN09	37.1361	-97.6183	396	28.4	0.0161
11/19/2015	7:42:12	36.6602	-98.4594	4.7	5.9	GS	KAN09	37.1361	-97.6183	396	91.8	0.0163
11/19/2015	7:42:12	36.6602	-98.4594	4.7	5.9	GS	KAN05	37.1080	-97.8715	765	72.4	0.0166
11/30/2015	9:49:12	36.7509	-98.0561	4.5	5.6	OK	QUOK	36.1714	-96.7080	503	136.8	0.0169
1/1/2016	11:39:39	35.6688	-97.4065	4.2	5.8	OK	CHOK	35.5611	-97.0613	525	33.9	0.0172
4/7/2014	16:03:03	35.8913	-97.2752	4.2	5.1	GS	OK029	35.7966	-97.4549	630	20.0	0.0178
10/2/2014	18:01:24	37.2447	-97.9553	4.5	5	GS	KAN09	37.1361	-97.6183	396	32.6	0.0178
11/30/2015	9:49:12	36.7509	-98.0561	4.5	5.6	OK	CROK	36.5047	-97.9834	493	28.7	0.0182
11/19/2015	7:42:12	36.6602	-98.4594	4.7	5.9	GS	KAN17	37.0441	-97.7648	183	75.3	0.0185
11/19/2015	7:42:12	36.6602	-98.4594	4.7	5.9	GS	KAN10	37.1235	-98.0951	946	61.1	0.0196
8/19/2014	12:41:35	35.7727	-97.4677	4.1	4.5	OK	BCOK	35.6567	-97.6093	796	18.7	0.0201
11/19/2015	7:42:12	36.6602	-98.4594	4.7	5.9	GS	KAN14	36.9568	-97.9630	701	55.5	0.0202
11/8/2011	2:46:57	35.5275	-96.7918	5.0	2.7	OK	OKCFA	35.4153	-97.4518	660	61.1	0.0204
2/13/2016	17:07:06	36.4905	-98.7056	5.1	8	OK	U32A	36.3795	-99.0014	700	30.3	0.0219

Date	Time	Event Latitude	Event Longitude	Magnitude	Depth	Network	Station	Station Latitude	Station Longitude	V_{S30} (m/s)	Hypocentral Distance (km)	PGA (g)
1/7/2016	4:27:27	36.4955	-98.7254	4.7	4.1	GS	OK035	36.7082	-98.7097	123	24.0	0.0224
1/7/2016	4:27:57	36.4955	-98.7254	4.7	4.1	GS	OK035	36.7082	-98.7097	123	24.0	0.0224
11/30/2015	9:49:12	36.7509	-98.0561	4.5	5.6	GS	KAN14	36.9568	-97.9630	701	25.0	0.0246
11/12/2014	21:40:00	37.2713	-97.6206	4.9	4	GS	KAN08	37.2267	-97.9709	1055	31.7	0.0268
2/13/2016	17:07:06	36.4905	-98.7056	5.1	8	GS	OK035	36.7082	-98.7097	123	25.5	0.0299
9/3/2016	12:02:44	36.4298	-96.9317	5.8	5.4	GS	OK040	36.4829	-98.6741	330	156.0	0.0309
11/7/2016	1:44:24	35.9837	-96.7982	5.0	5	OK	QUOK	36.1714	-96.7080	503	22.9	0.0310
11/20/2015	22:40:40	36.9483	-97.8276	4.1	5	GS	KAN14	36.9568	-97.9630	701	13.1	0.0316
9/3/2016	12:02:44	36.4298	-96.9317	5.8	5.4	GS	KAN17	37.0441	-97.7648	183	101.0	0.0316
9/3/2016	12:02:44	36.4298	-96.9317	5.8	5.4	GS	OK029	35.7966	-97.4549	630	84.8	0.0322
5/17/2012	8:12:00	31.926	-94.369	4.4	5	US	NATX	31.7600	-94.6600	401	33.5	0.0325
9/3/2016	12:02:44	36.4298	-96.9317	5.8	5.4	OK	CROK	36.5047	-97.9834	493	94.6	0.0325
9/3/2016	12:02:44	36.4298	-96.9317	5.8	5.4	GS	KAN16	37.2256	-98.0647	971	134.3	0.0326
9/3/2016	12:02:44	36.4298	-96.9317	5.8	5.4	GS	KAN01	37.1535	-97.7592	825	109.2	0.0330
11/12/2014	21:40:00	37.2713	-97.6206	4.9	4	GS	KAN06	37.2480	-97.8586	1008	21.6	0.0339
9/25/2015	1:16:37	35.987	-96.7872	4.0	2.9	GS	OK030	35.9278	-96.7838	448	7.2	0.0344
9/3/2016	12:02:44	36.4298	-96.9317	5.8	5.4	OK	NOKA	36.6347	-98.9319	612	180.2	0.0352
9/3/2016	12:02:44	36.4298	-96.9317	5.8	5.4	GS	OK031	35.9531	-96.8391	509	53.9	0.0355
9/3/2016	12:02:44	36.4298	-96.9317	5.8	5.4	GS	KAN06	37.2480	-97.8586	1008	122.9	0.0360
9/3/2016	12:02:44	36.4298	-96.9317	5.8	5.4	NQ	OK915	35.9536	-96.7726	860	55.1	0.0366
11/8/2011	2:46:57	35.5275	-96.7918	5.0	2.7	TA	V35A	35.7626	-96.8378	598	26.6	0.0368
9/3/2016	12:02:44	36.4298	-96.9317	5.8	5.4	GS	KAN13	37.0129	-97.4778	353	81.3	0.0375
6/5/2015	23:12:41	37.2648	-97.9213	4.2	2.4	GS	KAN06	37.2480	-97.8586	1008	6.3	0.0381
11/12/2014	21:40:00	37.2713	-97.6206	4.9	4	GS	KAN05	37.1080	-97.8715	765	29.0	0.0386
9/3/2016	12:02:44	36.4298	-96.9317	5.8	5.4	GS	KS20	37.2297	-97.5543	299	104.9	0.0405
11/7/2016	1:44:24	35.9837	-96.7982	5.0	5	GS	OK033	36.0444	-96.9382	362	15.1	0.0405
9/3/2016	12:02:44	36.4298	-96.9317	5.8	5.4	GS	OK038	36.4782	-98.7422	254	162.1	0.0408
11/20/2015	22:40:40	36.9483	-97.8276	4.1	5	GS	KAN17	37.0441	-97.7648	183	13.0	0.0411
9/3/2016	12:02:44	36.4298	-96.9317	5.8	5.4	GS	KAN10	37.1235	-98.0951	946	129.3	0.0415
9/3/2016	12:02:44	36.4298	-96.9317	5.8	5.4	OK	CHOK	35.5611	-97.0613	525	97.4	0.0418
9/3/2016	12:02:44	36.4298	-96.9317	5.8	5.4	OK	RLOK	36.1676	-95.0268	1534	173.3	0.0419
10/2/2014	18:01:24	37.2447	-97.9553	4.5	5	GS	KAN10	37.1235	-98.0951	946	19.0	0.0433
9/3/2016	12:02:44	36.4298	-96.9317	5.8	5.4	GS	KAN05	37.1080	-97.8715	765	112.8	0.0440

Date	Time	Event Latitude	Event Longitude	Magnitude	Depth	Network	Station	Station Latitude	Station Longitude	V_{S30} (m/s)	Hypocentral Distance (km)	PGA (g)
9/3/2016	12:02:44	36.4298	-96.9317	5.8	5.4	GS	OK025	35.5811	-97.3379	502	101.3	0.0444
6/5/2015	23:12:41	37.2648	-97.9213	4.2	2.4	GS	KAN12	37.2974	-97.9980	524	8.1	0.0445
9/3/2016	12:02:44	36.4298	-96.9317	5.8	5.4	GS	KAN08	37.2267	-97.9709	1055	128.2	0.0446
11/7/2015	11:11:53	36.9528	-97.8552	4.1	5	GS	KAN17	37.0441	-97.7648	183	13.9	0.0448
11/6/2011	3:53:10	35.5501	-96.7579	5.7	7.5	TA	V35A	35.7626	-96.8378	598	25.8	0.0450
9/3/2016	12:02:44	36.4298	-96.9317	5.8	5.4	OK	CCOK	35.3568	-97.6561	664	136.1	0.0452
9/3/2016	12:02:44	36.4298	-96.9317	5.8	5.4	OK	QUOK	36.1714	-96.7080	503	35.4	0.0453
12/29/2015	11:39:19	35.6654	-97.4054	4.3	6.5	GS	OK025	35.5811	-97.3379	502	12.9	0.0457
9/3/2016	12:02:44	36.4298	-96.9317	5.8	5.4	GS	KAN09	37.1361	-97.6183	396	99.7	0.0463
6/5/2015	23:12:41	37.2648	-97.9213	4.2	2.4	GS	KAN16	37.2256	-98.0647	971	13.6	0.0465
9/3/2016	12:02:44	36.4298	-96.9317	5.8	5.4	GS	KAN14	36.9568	-97.9630	701	109.2	0.0472
10/2/2014	18:01:24	37.2447	-97.9553	4.5	5	GS	KAN05	37.1080	-97.8715	765	17.6	0.0501
9/3/2016	12:02:44	36.4298	-96.9317	5.8	5.4	GS	OK005	35.6549	-97.1911	591	89.4	0.0555
9/3/2016	12:02:44	36.4298	-96.9317	5.8	5.4	GS	OK030	35.9278	-96.7838	448	57.6	0.0568
6/20/2015	5:10:54	35.7392	-97.3865	4.0	3	GS	OK029	35.7966	-97.4549	630	9.4	0.0590
9/3/2016	12:02:44	36.4298	-96.9317	5.8	5.4	NQ	OK914	35.9708	-96.8048	672	52.6	0.0595
9/3/2016	12:02:44	36.4298	-96.9317	5.8	5.4	NQ	OK916	36.8073	-97.7477	524	84.2	0.0596
9/3/2016	12:02:44	36.4298	-96.9317	5.8	5.4	GS	OK032	36.8038	-98.2104	500	121.6	0.0598
1/1/2016	11:39:39	35.6688	-97.4065	4.2	5.8	GS	OK025	35.5811	-97.3379	502	12.9	0.0604
11/7/2015	11:11:53	36.9528	-97.8552	4.1	5	GS	KAN14	36.9568	-97.9630	701	10.8	0.0676
9/25/2015	1:16:37	35.987	-96.7872	4.0	2.9	GS	OK031	35.9531	-96.8391	509	6.7	0.0695
10/2/2014	18:01:24	37.2447	-97.9553	4.5	5	GS	KAN12	37.2974	-97.9980	524	8.6	0.0730
10/2/2014	18:01:24	37.2447	-97.9553	4.5	5	GS	KAN06	37.2480	-97.8586	1008	9.9	0.0743
11/19/2015	7:42:12	36.6602	-98.4594	4.7	5.9	GS	OK032	36.8038	-98.2104	500	28.0	0.0927
11/12/2014	21:40:00	37.2713	-97.6206	4.9	4	GS	KAN09	37.1361	-97.6183	396	15.6	0.0940
11/12/2014	21:40:00	37.2713	-97.6206	4.9	4	GS	KAN01	37.1535	-97.7592	825	18.4	0.0974
11/23/2015	21:17:46	36.8382	-98.2762	4.4	5	GS	OK032	36.8038	-98.2104	500	8.6	0.1157
10/10/2015	22:03:05	35.986	-96.8032	4.3	3.3	GS	OK030	35.9278	-96.7838	448	7.5	0.1329
8/19/2014	12:41:35	35.7727	-97.4677	4.1	4.5	GS	OK029	35.7966	-97.4549	630	5.4	0.1413
6/5/2015	23:12:41	37.2648	-97.9213	4.2	2.4	GS	KAN11	37.2060	-97.9133	995	7.0	0.1700
11/7/2016	1:44:24	35.9837	-96.7982	5.0	5	GS	OK031	35.9531	-96.8391	509	7.1	0.2085
11/7/2016	1:44:24	35.9837	-96.7982	5.0	5	GS	OK034	36.0102	-96.7132	718	9.6	0.2731
11/7/2016	1:44:24	35.9837	-96.7982	5.0	5	NQ	OK915	35.9536	-96.7726	860	6.4	0.3278
11/7/2016	1:44:24	35.9837	-96.7982	5.0	5	NQ	OK914	35.9708	-96.8048	672	5.2	0.5947

Appendix C. As-Built Drawings

Table C.1: As-built drawing inventory

	NBI Structure #	Year Built	# of Spans	Max Span Length (ft)	Deck width (ft)
MSPC	1092004518125	1970	3	80	42
	21200013405027	1993	3	80	45
	61869914991318	1983	4	83	40
	161780032603016	1964	2	80	50
	180710017204204	2003	3	80	40
MSSTEEL	41070003005030	1939	3	40	45
	90500018401019	1950	3	40	45
	102120024506026	1939	4	48	60
	141500015004027	1942	4	40	50
MCSTEEL	30390135001006	1964	3	75	25
	41800009003052	1969	4	75	28
	121020050201008	1952	3	75	82
	1813300049501150	1964	4	86	25
	230470103902014	1959	3	90	25
	161290112201002	1949	3	90	25
	120200017902050	1958	3	240	46
	120200017902098	2007	3	240	40
	151310007205174	1971	34	150	42
	180570035304135	1975	17	150	44
	180570009214192	1971	4	115	26
	180570044202067	1965	3	115	48
MSRC	32430221502001	1956	4	30	25
	52190078904002	1970	4	30	28
	102340049502017	1963	3	30	25
	30390082403007	1966	3	40	42
	141440033403048	1986	4	40	36
MSRC-Slab	10920051001007	1955	3	25	25
	130760033408021	1947	2	25	25
	112030263701002	1963	4	25	25
	15083001706216	1968	3	25	42
	111740181001004	1956	4	25	43
MCRC-Slab	240720212105065	1961	3	30	42
	240550000303112	1970	3	30	42
	230420007805034	1955	3	30	46
	210660032703047	1985	4	25	40
	142460203802006	1956	3	40	25

Appendix D. Girder and Column Spacing and Number

The number of girders and columns as well as their spacings are important parameters in developing representative bridge models. Table D.1 through D.6 present the number of girders and columns as well as the corresponding girder and column spacings for the relevant bridge classes. It should be noted that the reinforced concrete slab type bridges (i.e., MSRC-Slab, and MCRC-Slab), due to the slab type superstructure, do not have girders and are not listed in this section. Moreover, single span prestressed concrete girder (SSPC) bridges does not have columns, so the information related to columns are not listed for that specific bridge class.

Table D.1: Number and spacing of girder and column for MCSTEEL bridges

	Column		Girder	
Bridge Sample	Number	Spacing	Number	Spacing
1	5	16	11	7.00
2	3	9	5	5.67
3	3	10.5	5	6.67
4	4	14.5	9	6.00
5	3	15.5	6	7.33
6	4	11	7	6.33
7	3	15	5	9.00
8	3	12.5	6	6.00

Table D.2: Number and spacing of girder and column for MSSTEEL bridges

	Column		Girder	
Bridge Sample	Number	Spacing	Number	Spacing
1	5	11	8	6.67
2	3	9.5	4	7.33
3	4	11.5	7	6.33
4	4	11.5	6	7.33
5	4	12	6	7.67
6	4	12	6	7.67
7	4	10	5	8.33
8	3	12.5	5	7.00

Table D.3: Number and spacing of girder and column for MSPC bridges

	Column		Girder	
Bridge Sample	Number	Spacing	Number	Spacing
1	4	12	6	8.00
2	3	15.5	6	7.33
3	3	15	7	6.00
4	3	13	5	8.00
5	5	15.5	11	6.67
6	4	15.5	8	7.33
7	5	13	10	6.33
8	4	11.5	7	6.67

Table D.4: Number and spacing of girder and column for MSRC bridges

	Column		Girder	
Bridge Sample	Number	Spacing	Number	Spacing
1	4	12	15	3.00
2	3	8	9	3.00
3	3	11	11	3.00
4	3	14.5	13	3.00
5	3	9	10	3.00
6	3	16	14	3.00
7	3	7.5	8	3.00
8	4	11.5	15	3.00

Table D.5: Number and spacing of girder for SSPC bridges

	Girder	
Bridge Sample	Number	Spacing
1	7	6.33
2	11	5.67
3	10	8.67
4	6	6.33
5	8	6.00
6	7	6.00
7	7	6.67
8	8	6.00

Table D.6: Number and spacing of column for reinforced concrete slab bridges

	MCRC-Slab		MSRC-Slab	
Bridge Sample	Number	Spacing	Number	Spacing
1	5	12.5	3	9.5
2	4	12.5	4	12.5
3	4	14	4	12.5
4	4	12	3	11.5
5	3	14	3	10.5
6	4	12	3	10.5
7	4	14	3	10.5
8	4	12.5	4	14

Appendix E. Parameter Samples

The parameter samples for each geometric representative bridge sample used in this study are presented in this appendix. The parameter abbreviations and the units for the values in each of these tables can be found in Section 6.4.7. The parameter samples for the MSPC bridge class are presented in Section 6.7.3 of this report.

Table E.1: MCSTEEL modeling parameters for geometric sample 1

	Modeling Sample							
Parameter	1	2	3	4	5	6	7	8
Conc Str	4528	5820	4225	4333	3847	3172	4849	5213
Reinf Str	60568	45085	57684	53239	49924	56127	53439	66973
Steel Fix-Long	537.3	523.0	437.1	442.4	477.4	402.5	414.3	391.5
Steel Fix-Trans	25.5	27.3	27.0	22.5	30.3	26.8	20.9	22.7
Steel Fix COF-Long	0.221	0.186	0.233	0.241	0.200	0.202	0.227	0.214
Steel Fix COF-Trans	0.313	0.341	0.358	0.408	0.349	0.423	0.304	0.394
Steel Rocker COF-Long	0.046	0.038	0.037	0.036	0.045	0.038	0.042	0.036
Steel Rocker COF-Trans	0.084	0.096	0.085	0.119	0.110	0.110	0.104	0.085
Abt-Pas Stf	36.0	48.9	42.2	31.9	26.0	20.8	45.6	30.8
Pile Stf	53.0	32.2	56.8	53.8	24.0	54.6	54.6	52.7
Fnd-Rot Stf	508	759	1343	1077	984	841	653	1282
Fnd-Tran-Stf	200	317	378	361	293	445	232	147
Mass	137	114	120	132	112	126	134	123
Damp Ratio	0.041	0.047	0.045	0.034	0.054	0.066	0.053	0.025
Large Gap	5.26	4.11	2.26	1.16	3.43	5.09	3.63	1.63
Load Dir	273	323	148	237	95	87	210	45

Table E.2: MCSTEEL modeling parameters for geometric sample 2

	Modeling Sample							
Parameter	1	2	3	4	5	6	7	8
Conc Str	3547	5490	5063	4086	2701	5362	4544	4281
Reinf Str	52335	58206	45535	64328	53743	57475	54803	51441
Steel Fix-Long	550.0	417.0	526.1	477.2	458.9	483.6	541.4	550.5
Steel Fix-Trans	24.9	24.3	26.6	21.9	31.1	28.1	22.9	25.2
Steel Fix COF-Long	0.235	0.240	0.204	0.192	0.171	0.230	0.215	0.214
Steel Fix COF-Trans	0.346	0.411	0.405	0.321	0.324	0.380	0.346	0.373
Steel Rocker COF-Long	0.041	0.036	0.038	0.043	0.032	0.043	0.041	0.043
Steel Rocker COF-Trans	0.086	0.110	0.083	0.111	0.093	0.091	0.084	0.120
Abt-Pas Stf	48.1	31.2	20.0	20.2	24.2	42.1	37.4	34.1
Pile Stf	41.1	33.1	38.4	42.4	27.5	56.2	45.2	33.1
Fnd-Rot Stf	836	1193	1124	538	671	1410	974	811
Fnd-Tran-Stf	191	368	328	142	392	442	221	262
Mass	112	130	134	127	121	138	125	115
Damp Ratio	0.043	0.056	0.026	0.052	0.059	0.040	0.032	0.049
Large Gap	3.37	1.50	2.87	1.78	4.82	5.44	4.38	1.23
Load Dir	207	140	103	34	326	77	303	270

Table E.3: MCSTEEL modeling parameters for geometric sample 3

	Modeling Sample							
Parameter	1	2	3	4	5	6	7	8
Conc Str	6085	4950	4385	3605	2787	4646	5302	3951
Reinf Str	58724	42885	50579	55665	54468	63982	57947	52657
Steel Fix-Long	473.4	544.4	480.5	385.8	373.9	420.6	400.0	372.6
Steel Fix-Trans	25.0	29.2	22.3	22.5	25.0	22.5	29.1	30.9
Steel Fix COF-Long	0.186	0.240	0.192	0.223	0.240	0.181	0.217	0.226
Steel Fix COF-Trans	0.301	0.375	0.428	0.396	0.402	0.408	0.389	0.345
Steel Rocker COF-Long	0.047	0.036	0.048	0.044	0.035	0.041	0.045	0.042
Steel Rocker COF-Trans	0.107	0.092	0.083	0.117	0.100	0.105	0.088	0.101
Abt-Pas Stf	39.0	21.9	44.2	49.2	34.6	31.0	24.4	35.9
Pile Stf	46.3	23.8	48.6	44.1	33.3	48.4	34.2	51.3
Fnd-Rot Stf	1281	1170	891	1338	728	497	978	652
Fnd-Tran-Stf	234	430	371	214	404	269	321	148
Mass	122	113	119	127	117	134	131	116
Damp Ratio	0.047	0.041	0.075	0.056	0.035	0.026	0.038	0.052
Large Gap	4.11	4.94	2.84	5.36	1.60	3.54	1.04	2.17
Load Dir	65	101	142	217	274	40	326	237

Table E.4: MCSTEEL modeling parameters for geometric sample 4

	Modeling Sample							
Parameter	1	2	3	4	5	6	7	8
Conc Str	4173	5719	2789	4550	4827	5175	4268	3628
Reinf Str	55544	51683	57408	59076	62232	50159	54172	45434
Steel Fix-Long	397.5	436.7	473.9	381.7	434.4	493.3	525.2	515.7
Steel Fix-Trans	23.4	26.0	23.4	24.9	21.2	21.3	20.3	26.2
Steel Fix COF-Long	0.243	0.194	0.196	0.187	0.219	0.236	0.197	0.246
Steel Fix COF-Trans	0.376	0.410	0.300	0.388	0.322	0.373	0.428	0.434
Steel Rocker COF-Long	0.038	0.036	0.047	0.033	0.040	0.033	0.047	0.041
Steel Rocker COF-Trans	0.106	0.106	0.105	0.110	0.111	0.099	0.087	0.096
Abt-Pas Stf	29.3	39.1	46.3	21.6	27.1	35.3	44.0	31.7
Pile Stf	51.1	20.6	47.3	35.5	32.4	21.1	54.6	21.4
Fnd-Rot Stf	1341	630	1101	738	963	529	927	1254
Fnd-Tran-Stf	320	282	399	215	242	156	337	445
Mass	134	113	127	130	122	115	120	138
Damp Ratio	0.029	0.056	0.034	0.044	0.051	0.039	0.048	0.063
Large Gap	4.92	1.80	5.46	0.99	3.59	3.69	4.29	2.35
Load Dir	109	318	276	82	172	214	236	36

Table E.5: MCSTEEL modeling parameters for geometric sample 5

	Modeling Sample							
Parameter	1	2	3	4	5	6	7	8
Conc Str	4494	4551	3865	5397	5014	2998	6142	4144
Reinf Str	49105	51031	54780	56438	55141	58696	53035	63777
Steel Fix-Long	399.4	408.2	542.2	470.3	401.8	499.8	471.8	523.6
Steel Fix-Trans	25.7	23.9	25.3	23.5	22.9	23.3	30.5	25.9
Steel Fix COF-Long	0.231	0.195	0.199	0.220	0.239	0.244	0.227	0.247
Steel Fix COF-Trans	0.405	0.391	0.316	0.297	0.442	0.383	0.396	0.332
Steel Rocker COF-Long	0.047	0.032	0.043	0.036	0.038	0.037	0.033	0.047
Steel Rocker COF-Trans	0.095	0.115	0.096	0.090	0.103	0.085	0.081	0.090
Abt-Pas Stf	21.2	46.1	34.3	42.3	24.2	46.9	30.8	37.2
Pile Stf	43.5	31.4	50.7	56.2	46.3	59.6	55.0	26.0
Fnd-Rot Stf	889	666	1361	1220	713	1052	1087	520
Fnd-Tran-Stf	167	436	308	238	400	184	338	273
Mass	116	129	137	123	119	134	114	126
Damp Ratio	0.053	0.022	0.033	0.063	0.039	0.056	0.043	0.049
Large Gap	2.74	1.09	5.65	4.77	3.36	3.14	2.18	4.15
Load Dir	244	118	35	279	218	158	89	352

Table E.6: MCSTEEL modeling parameters for geometric sample 6

	Modeling Sample							
Parameter	1	2	3	4	5	6	7	8
Conc Str	4527	4916	4293	3490	6065	4039	3881	5201
Reinf Str	54110	63060	43998	52908	54963	58129	50949	58663
Steel Fix-Long	419.6	418.4	424.8	516.5	519.3	510.7	556.8	533.1
Steel Fix-Trans	25.8	30.7	22.6	30.5	24.6	23.6	28.3	22.6
Steel Fix COF-Long	0.213	0.239	0.235	0.174	0.210	0.233	0.182	0.244
Steel Fix COF-Trans	0.323	0.428	0.359	0.406	0.299	0.324	0.397	0.372
Steel Rocker COF-Long	0.047	0.046	0.044	0.035	0.037	0.047	0.046	0.041
Steel Rocker COF-Trans	0.087	0.088	0.106	0.109	0.118	0.102	0.091	0.095
Abt-Pas Stf	21.2	38.5	31.1	26.4	34.7	42.9	46.8	41.0
Pile Stf	20.2	51.9	37.8	38.5	44.1	41.4	37.6	35.1
Fnd-Rot Stf	950	824	695	589	1391	943	1223	1120
Fnd-Tran-Stf	229	421	209	356	319	402	265	142
Mass	117	125	111	121	130	138	135	126
Damp Ratio	0.049	0.062	0.014	0.059	0.047	0.041	0.034	0.042
Large Gap	3.23	5.10	3.78	1.22	1.37	1.92	5.53	2.30
Load Dir	65	307	241	92	201	338	144	41

Table E.7: MCSTEEL modeling parameters for geometric sample 7

	Modeling Sample							
Parameter	1	2	3	4	5	6	7	8
Conc Str	4698	5747	3306	4222	5254	4277	3837	5058
Reinf Str	63370	52091	56488	49499	42456	53414	58448	55088
Steel Fix-Long	527.9	486.2	512.4	545.3	429.5	455.4	386.2	387.4
Steel Fix-Trans	29.3	29.9	29.6	24.9	26.7	24.8	25.5	25.5
Steel Fix COF-Long	0.249	0.209	0.171	0.249	0.169	0.232	0.168	0.219
Steel Fix COF-Trans	0.359	0.305	0.409	0.443	0.302	0.371	0.399	0.406
Steel Rocker COF-Long	0.041	0.039	0.037	0.042	0.033	0.047	0.041	0.034
Steel Rocker COF-Trans	0.096	0.099	0.114	0.108	0.087	0.119	0.089	0.096
Abt-Pas Stf	30.4	36.3	21.6	41.4	47.7	24.8	45.2	33.5
Pile Stf	44.4	32.5	26.5	57.3	46.5	34.2	58.2	23.1
Fnd-Rot Stf	781	604	1033	1073	1311	1252	871	523
Fnd-Tran-Stf	148	419	300	282	384	213	351	231
Mass	113	123	136	117	118	134	127	132
Damp Ratio	0.037	0.047	0.024	0.042	0.057	0.034	0.064	0.051
Large Gap	2.15	4.16	3.32	5.41	2.44	2.60	4.56	0.83
Load Dir	329	131	6	228	311	142	49	224

Table E.8: MCSTEEL modeling parameters for geometric sample 8

	Modeling Sample							
Parameter	1	2	3	4	5	6	7	8
Conc Str	3239	5196	4455	3733	5699	4225	4924	4530
Reinf Str	49767	47536	58693	61042	51875	54584	57794	56106
Steel Fix-Long	419.0	459.7	511.8	395.8	469.9	387.3	454.0	446.0
Steel Fix-Trans	29.0	26.2	22.2	22.1	22.9	25.7	26.5	27.1
Steel Fix COF-Long	0.215	0.172	0.229	0.219	0.245	0.202	0.215	0.246
Steel Fix COF-Trans	0.311	0.322	0.374	0.315	0.415	0.304	0.414	0.334
Steel Rocker COF-Long	0.034	0.041	0.040	0.044	0.044	0.038	0.035	0.035
Steel Rocker COF-Trans	0.112	0.085	0.111	0.111	0.116	0.098	0.094	0.117
Abt-Pas Stf	31.0	33.7	43.2	41.1	35.1	25.2	22.5	46.5
Pile Stf	39.8	58.5	20.7	59.6	31.4	31.5	24.8	20.8
Fnd-Rot Stf	751	1111	1024	591	1402	858	1280	539
Fnd-Tran-Stf	447	372	172	253	285	182	394	327
Mass	117	131	119	133	124	128	138	113
Damp Ratio	0.057	0.047	0.070	0.045	0.053	0.020	0.040	0.035
Large Gap	5.46	4.25	3.55	2.62	3.00	1.85	4.63	2.80
Load Dir	314	5	234	120	150	77	318	212

Table E.9: MSSTEEL modeling parameters for geometric sample 1

	Modeling Sample							
Parameter	1	2	3	4	5	6	7	8
Conc Str	4528	5820	4225	4333	3847	3172	4849	5213
Reinf Str	60568	45085	57684	53239	49924	56127	53439	66973
Steel Fix-Long	462	491	487	414	540	484	388	416
Steel Fix-Trans	29	31	25	28	23	25	28	31
Steel Fix COF-Long	0.251	0.225	0.244	0.208	0.188	0.208	0.237	0.206
Steel Fix COF-Trans	0.415	0.360	0.346	0.436	0.395	0.395	0.352	0.382
Steel Rocker COF-Long	0.038	0.032	0.040	0.042	0.042	0.040	0.043	0.046
Steel Rocker COF-Trans	0.080	0.081	0.110	0.103	0.118	0.106	0.105	0.106
Abt-Pas Stf	40.4	23.0	34.8	20.9	44.2	49.4	35.6	49.2
Pile Stf	20.9	67.6	27.0	48.0	57.4	44.5	38.3	70.0
Fnd-Rot Stf	508	759	1343	1077	984	841	653	1282
Fnd-Tran-Stf	200	317	378	361	293	445	232	147
Mass	135	135	123	112	126	115	129	118
Damp Ratio	0.050	0.020	0.057	0.050	0.050	0.052	0.048	0.056
Small Gap	1.05	0.72	1.01	1.24	1.14	0.73	0.79	0.79
Large Gap	1.56	1.26	1.59	1.60	1.92	1.31	1.28	1.13
Load Dir	94	313	145	325	281	207	234	247

Table E.10: MSSTEEL modeling parameters for geometric sample 2

	Modeling Sample							
Parameter	1	2	3	4	5	6	7	8
Conc Str	3547	5490	5063	4086	2701	5362	4544	4281
Reinf Str	52335	58206	45535	64328	53743	57475	54803	51441
Steel Fix-Long	453	442	481	403	554	504	420	457
Steel Fix-Trans	30	31	30	29	20	24	29	24
Steel Fix COF-Long	0.171	0.179	0.243	0.244	0.242	0.173	0.229	0.204
Steel Fix COF-Trans	0.305	0.298	0.437	0.358	0.322	0.324	0.324	0.333
Steel Rocker COF-Long	0.041	0.039	0.043	0.039	0.044	0.039	0.037	0.038
Steel Rocker COF-Trans	0.098	0.087	0.090	0.107	0.088	0.111	0.103	0.099
Abt-Pas Stf	31.9	27.9	43.4	42.3	37.3	41.4	22.9	39.5
Pile Stf	63.3	33.8	25.8	33.0	55.0	44.2	48.5	69.4
Fnd-Rot Stf	836	1193	1124	538	671	1410	974	811
Fnd-Tran-Stf	191	368	328	142	392	442	221	262
Mass	139	118	113	120	120	118	139	117
Damp Ratio	0.036	0.033	0.037	0.057	0.033	0.058	0.053	0.044
Small Gap	1.06	0.88	1.18	1.01	0.90	1.11	0.90	1.22
Large Gap	1.43	1.53	1.20	1.11	1.51	1.69	1.16	1.83
Load Dir	288	209	27	340	140	22	263	66

Table E.11: MSSTEEL modeling parameters for geometric sample 3

	Modeling Sample							
Parameter	1	2	3	4	5	6	7	8
Conc Str	6085	4950	4385	3605	2787	4646	5302	3951
Reinf Str	58724	42885	50579	55665	54468	63982	57947	52657
Steel Fix-Long	455	523	410	414	453	413	521	551
Steel Fix-Trans	21	22	29	28	21	29	23	27
Steel Fix COF-Long	0.242	0.229	0.196	0.219	0.170	0.225	0.181	0.237
Steel Fix COF-Trans	0.355	0.442	0.432	0.441	0.315	0.351	0.359	0.339
Steel Rocker COF-Long	0.034	0.037	0.043	0.045	0.039	0.046	0.043	0.044
Steel Rocker COF-Trans	0.097	0.109	0.117	0.102	0.108	0.094	0.102	0.106
Abt-Pas Stf	31.0	30.1	41.5	35.0	25.5	35.0	44.5	44.0
Pile Stf	43.5	26.3	63.6	60.9	50.5	35.7	71.6	29.5
Fnd-Rot Stf	1281	1170	891	1338	728	497	978	652
Fnd-Tran-Stf	234	430	371	214	404	269	321	148
Mass	132	128	128	126	113	123	117	130
Damp Ratio	0.064	0.053	0.068	0.049	0.054	0.043	0.046	0.056
Small Gap	0.83	1.18	1.19	1.03	1.20	1.14	0.89	0.75
Large Gap	1.27	1.95	1.64	1.52	1.97	1.09	1.00	1.80
Load Dir	155	198	86	177	87	85	233	133

Table E.12: MSSTEEL modeling parameters for geometric sample 4

	Modeling Sample							
Parameter	1	2	3	4	5	6	7	8
Conc Str	4173	5719	2789	4550	4827	5175	4268	3628
Reinf Str	55544	51683	57408	59076	62232	50159	54172	45434
Steel Fix-Long	429	471	428	453	392	394	377	473
Steel Fix-Trans	30	31	31	24	29	29	28	23
Steel Fix COF-Long	0.245	0.177	0.227	0.220	0.209	0.172	0.223	0.175
Steel Fix COF-Trans	0.374	0.321	0.304	0.341	0.444	0.364	0.367	0.387
Steel Rocker COF-Long	0.047	0.035	0.042	0.043	0.033	0.040	0.043	0.043
Steel Rocker COF-Trans	0.098	0.099	0.091	0.097	0.089	0.106	0.115	0.102
Abt-Pas Stf	49.6	40.4	47.1	34.4	27.2	34.1	44.5	33.6
Pile Stf	67.5	59.8	45.8	25.3	35.8	49.2	71.2	29.9
Fnd-Rot Stf	1341	630	1101	738	963	529	927	1254
Fnd-Tran-Stf	320	282	399	215	242	156	337	445
Mass	120	111	124	130	128	126	130	135
Damp Ratio	0.045	0.044	0.032	0.040	0.037	0.049	0.067	0.047
Small Gap	1.01	0.91	0.81	1.06	0.92	0.96	1.24	0.98
Large Gap	1.75	1.27	1.80	1.84	1.20	1.40	1.28	1.92
Load Dir	328	52	44	176	145	127	162	225

Table E.13: MSSTEEL modeling parameters for geometric sample 5

	Modeling Sample							
Parameter	1	2	3	4	5	6	7	8
Conc Str	4494	4551	3865	5397	5014	2998	6142	4144
Reinf Str	49105	51031	54780	56438	55141	58696	53035	63777
Steel Fix-Long	466	437	459	430	420	427	544	469
Steel Fix-Trans	27	31	27	27	28	22	27	29
Steel Fix COF-Long	0.235	0.223	0.185	0.240	0.182	0.174	0.212	0.179
Steel Fix COF-Trans	0.358	0.312	0.405	0.400	0.321	0.441	0.314	0.335
Steel Rocker COF-Long	0.046	0.035	0.033	0.047	0.036	0.047	0.033	0.032
Steel Rocker COF-Trans	0.111	0.086	0.111	0.106	0.085	0.097	0.091	0.106
Abt-Pas Stf	21.1	24.1	46.7	47.1	46.6	21.8	41.7	33.0
Pile Stf	68.3	63.8	33.3	58.7	53.2	45.9	26.5	34.4
Fnd-Rot Stf	889	666	1361	1220	713	1052	1087	520
Fnd-Tran-Stf	167	436	308	238	400	184	338	273
Mass	128	123	131	122	133	124	119	120
Damp Ratio	0.065	0.031	0.047	0.055	0.037	0.042	0.037	0.049
Small Gap	1.29	0.75	0.77	1.16	1.20	0.93	0.85	0.72
Large Gap	1.90	1.25	1.50	1.92	1.11	1.30	1.55	1.14
Load Dir	65	307	66	122	35	296	197	281

Table E.14: MSSTEEL modeling parameters for geometric sample 6

	Modeling Sample							
Parameter	1	2	3	4	5	6	7	8
Conc Str	4527	4916	4293	3490	6065	4039	3881	5201
Reinf Str	54110	63060	43998	52908	54963	58129	50949	58663
Steel Fix-Long	467	546	415	543	448	431	507	415
Steel Fix-Trans	21	25	20	22	24	26	22	23
Steel Fix COF-Long	0.176	0.210	0.171	0.236	0.250	0.212	0.250	0.183
Steel Fix COF-Trans	0.393	0.351	0.336	0.395	0.301	0.319	0.383	0.418
Steel Rocker COF-Long	0.045	0.039	0.033	0.041	0.034	0.042	0.036	0.042
Steel Rocker COF-Trans	0.093	0.094	0.088	0.106	0.104	0.114	0.093	0.102
Abt-Pas Stf	46.6	41.6	30.0	38.3	20.9	40.5	24.5	44.8
Pile Stf	31.4	24.9	68.9	52.9	46.6	57.7	61.9	37.9
Fnd-Rot Stf	950	824	695	589	1391	943	1223	1120
Fnd-Tran-Stf	229	421	209	356	319	402	265	142
Mass	113	119	131	135	123	136	130	133
Damp Ratio	0.040	0.037	0.026	0.055	0.047	0.048	0.036	0.046
Small Gap	0.99	1.01	1.19	1.21	0.81	1.29	0.89	1.15
Large Gap	1.73	1.93	1.65	1.50	1.30	1.31	1.87	1.50
Load Dir	95	224	86	324	48	6	107	29

Table E.15: MSSTEEL modeling parameters for geometric sample 7

	Modeling Sample							
Parameter	1	2	3	4	5	6	7	8
Conc Str	4698	5747	3306	4222	5254	4277	3837	5058
Reinf Str	63370	52091	56488	49499	42456	53414	58448	55088
Steel Fix-Long	524	534	529	452	482	451	463	463
Steel Fix-Trans	23	29	30	28	31	25	21	26
Steel Fix COF-Long	0.190	0.233	0.231	0.216	0.228	0.176	0.223	0.201
Steel Fix COF-Trans	0.389	0.325	0.359	0.376	0.379	0.423	0.329	0.441
Steel Rocker COF-Long	0.036	0.034	0.037	0.037	0.036	0.047	0.036	0.038
Steel Rocker COF-Trans	0.111	0.104	0.091	0.107	0.098	0.113	0.085	0.109
Abt-Pas Stf	47.4	23.2	41.0	38.5	34.7	21.3	39.8	22.5
Pile Stf	67.1	22.1	53.5	68.5	55.2	30.2	42.8	33.9
Fnd-Rot Stf	781	604	1033	1073	1311	1252	871	523
Fnd-Tran-Stf	148	419	300	282	384	213	351	231
Mass	137	115	129	132	113	126	131	130
Damp Ratio	0.052	0.048	0.036	0.047	0.041	0.050	0.023	0.050
Small Gap	1.12	0.92	1.08	0.93	0.78	0.94	0.95	1.12
Large Gap	1.41	1.07	1.80	1.28	1.40	1.11	1.04	1.40
Load Dir	52	126	150	133	339	15	268	335

Table E.16: MSSTEEL modeling parameters for geometric sample 8

	Modeling Sample							
Parameter	1	2	3	4	5	6	7	8
Conc Str	3239	5196	4455	3733	5699	4225	4924	4530
Reinf Str	49767	47536	58693	61042	51875	54584	57794	56106
Steel Fix-Long	519	474	408	406	420	466	479	488
Steel Fix-Trans	26	22	31	20	20	27	26	28
Steel Fix COF-Long	0.196	0.228	0.210	0.183	0.210	0.237	0.235	0.238
Steel Fix COF-Trans	0.339	0.368	0.377	0.399	0.427	0.391	0.353	0.404
Steel Rocker COF-Long	0.042	0.042	0.040	0.034	0.039	0.036	0.043	0.047
Steel Rocker COF-Trans	0.099	0.088	0.084	0.105	0.098	0.090	0.118	0.101
Abt-Pas Stf	43.9	39.6	25.9	45.8	25.0	22.1	35.6	24.0
Pile Stf	51.1	68.2	30.4	37.2	21.6	44.8	58.1	67.2
Fnd-Rot Stf	751	1111	1024	591	1402	858	1280	539
Fnd-Tran-Stf	447	372	172	253	285	182	394	327
Mass	136	115	111	139	118	138	112	110
Damp Ratio	0.044	0.033	0.038	0.052	0.043	0.037	0.056	0.046
Small Gap	0.95	1.14	0.71	0.75	1.23	0.96	1.12	0.83
Large Gap	1.94	1.30	1.23	1.65	1.42	1.59	1.90	1.17
Load Dir	49	185	18	40	344	61	68	279

Table E.17: MSRC modeling parameters for geometric sample 1

	Modeling Sample							
Parameter	1	2	3	4	5	6	7	8
Conc Str	5580	3958	5032	5103	4598	3470	3830	4354
Reinf Str	63265	56497	53575	54845	47029	60568	51862	49629
COF MF	0.96	1.07	0.88	1.13	0.98	1.00	1.07	0.92
Dowel Str	6.30	6.89	6.42	6.74	7.48	7.77	7.32	7.04
Abt-Pas Stf	21.2	44.8	37.4	23.8	31.1	46.7	31.6	39.5
Pile Stf	23.5	42.1	35.7	55.0	62.0	31.5	70.2	53.0
Mass	130	135	117	138	121	125	110	125
Damp Ratio	0.033	0.063	0.029	0.040	0.047	0.058	0.042	0.052
Small Gap	1.62	1.98	1.05	0.80	0.32	0.71	1.34	0.12
Load Dir	203	70	160	346	22	112	278	234

Table E.18: MSRC modeling parameters for geometric sample 2

	Modeling Sample							
Parameter	1	2	3	4	5	6	7	8
Conc Str	4723	5908	5131	3991	4484	3785	3172	4941
Reinf Str	48304	60077	55571	50954	51681	60952	54703	56799
COF MF	1.15	0.89	0.88	1.01	0.96	1.08	1.04	1.00
Dowel Str	7.81	6.38	6.71	7.17	7.56	7.06	5.81	6.94
Abt-Pas Stf	47.1	23.1	39.3	23.8	44.3	27.9	36.5	34.4
Pile Stf	33.0	53.4	42.8	57.8	25.6	64.7	39.6	74.6
Mass	130	137	115	118	113	122	135	128
Damp Ratio	0.053	0.071	0.046	0.030	0.043	0.056	0.032	0.039
Small Gap	0.73	0.84	1.83	1.32	0.28	1.50	1.06	0.10
Load Dir	111	13	66	180	170	265	310	357

Table E.19: MSRC modeling parameters for geometric sample 3

	Modeling Sample							
Parameter	1	2	3	4	5	6	7	8
Conc Str	4620	3070	4220	4335	3799	5453	5813	5010
Reinf Str	61825	57218	50552	48025	56154	52469	53481	58431
COF MF	0.93	0.92	1.10	1.07	0.87	1.00	1.17	1.01
Dowel Str	7.62	6.97	7.13	6.49	6.64	7.30	8.17	6.34
Abt-Pas Stf	21.7	45.1	49.4	36.4	27.5	41.9	26.5	33.5
Pile Stf	39.5	28.5	55.3	52.0	42.8	66.1	23.2	69.3
Mass	137	125	115	128	121	111	135	130
Damp Ratio	0.043	0.038	0.036	0.049	0.058	0.068	0.046	0.026
Small Gap	1.83	0.88	0.45	1.48	1.54	0.71	0.21	1.08
Load Dir	10	130	257	169	291	356	72	220

Table E.20: MSRC modeling parameters for geometric sample 4

	Modeling Sample							
Parameter	1	2	3	4	5	6	7	8
Conc Str	3989	5160	3457	3736	4681	5765	4393	4941
Reinf Str	58601	55434	54113	52846	46407	51170	67862	56748
COF MF	1.12	0.83	1.10	1.01	0.99	1.06	0.91	0.95
Dowel Str	7.65	7.32	6.89	6.47	6.33	6.78	7.10	8.38
Abt-Pas Stf	42.2	31.3	25.1	22.9	29.7	49.5	37.7	45.3
Pile Stf	33.4	72.6	35.6	21.4	64.4	42.8	48.2	60.9
Mass	125	132	121	127	136	110	117	140
Damp Ratio	0.032	0.051	0.047	0.038	0.060	0.044	0.054	0.022
Small Gap	0.88	0.16	1.55	1.05	1.83	1.47	0.49	0.61
Load Dir	75	228	354	192	106	278	27	146

Table E.21: MSRC modeling parameters for geometric sample 5

	Modeling Sample							
Parameter	1	2	3	4	5	6	7	8
Conc Str	2413	4620	4848	4061	4493	5275	5690	3738
Reinf Str	58882	52927	62009	49260	50820	56921	53356	55072
COF MF	1.01	1.08	1.04	0.79	0.99	0.92	0.94	1.16
Dowel Str	6.21	7.57	6.85	6.65	6.53	7.10	7.90	7.30
Abt-Pas Stf	23.9	43.4	31.2	39.9	47.4	21.3	36.7	34.2
Pile Stf	34.4	48.1	57.2	45.2	62.3	23.8	68.8	33.5
Mass	119	112	117	123	136	130	127	140
Damp Ratio	0.058	0.047	0.050	0.043	0.041	0.034	0.067	0.027
Small Gap	1.34	0.61	1.64	1.93	1.12	0.81	0.31	0.11
Load Dir	326	131	195	247	82	273	153	25

Table E.22: MSRC modeling parameters for geometric sample 6

	Modeling Sample							
Parameter	1	2	3	4	5	6	7	8
Conc Str	4032	5282	3666	6073	4497	4625	3361	4786
Reinf Str	47417	56887	58767	52203	61690	54214	55427	51382
COF MF	0.96	0.99	1.11	1.04	0.91	1.22	1.03	0.86
Dowel Str	6.23	7.14	7.31	7.65	6.39	7.41	6.78	6.88
Abt-Pas Stf	41.7	36.7	28.4	26.2	48.3	43.9	20.3	34.4
Pile Stf	24.6	55.7	47.5	27.0	67.3	45.9	40.5	70.8
Mass	126	130	117	123	138	110	133	118
Damp Ratio	0.039	0.054	0.033	0.044	0.049	0.061	0.026	0.046
Small Gap	0.96	1.05	1.34	0.32	0.05	0.73	1.76	1.63
Load Dir	279	84	23	123	253	195	172	347

Table E.23: MSRC modeling parameters for geometric sample 7

	Modeling Sample							
Parameter	1	2	3	4	5	6	7	8
Conc Str	3961	3713	4611	4812	5460	5539	4391	3503
Reinf Str	55734	57021	65656	60106	51421	48480	52000	54427
COF MF	1.04	0.85	0.90	0.99	1.21	1.10	0.95	1.01
Dowel Str	6.32	7.52	7.33	7.72	7.02	6.59	6.83	6.76
Abt-Pas Stf	48.1	41.8	29.6	26.9	32.2	37.4	20.2	46.2
Pile Stf	24.9	53.1	34.3	60.8	43.5	63.7	29.3	69.1
Mass	119	124	131	126	113	139	134	116
Damp Ratio	0.034	0.041	0.041	0.052	0.069	0.030	0.057	0.048
Small Gap	0.71	1.29	1.55	1.93	0.19	0.42	0.79	1.04
Load Dir	274	135	106	265	88	332	19	182

Table E.24: MSRC modeling parameters for geometric sample 8

	Modeling Sample							
Parameter	1	2	3	4	5	6	7	8
Conc Str	4694	3018	3958	3568	4299	5354	4859	6313
Reinf Str	54033	56942	51790	59186	51066	60762	56297	48469
COF MF	0.76	1.03	1.25	1.10	0.96	0.99	0.92	1.04
Dowel Str	6.93	7.02	5.84	6.76	7.22	7.41	6.38	7.70
Abt-Pas Stf	24.6	29.4	22.2	47.7	35.5	32.5	40.5	45.1
Pile Stf	61.2	33.7	40.0	52.6	68.0	72.1	45.2	23.2
Mass	129	139	128	111	115	136	118	123
Damp Ratio	0.050	0.034	0.045	0.039	0.027	0.064	0.044	0.054
Small Gap	1.13	1.38	1.88	0.44	0.23	0.73	0.78	1.69
Load Dir	121	5	259	76	342	283	219	141

Table E.25: SSPC modeling parameters for geometric sample 1

	Modeling Sample							
Parameter	1	2	3	4	5	6	7	8
Conc Str	3894	3937	4334	5401	3278	4531	4904	5767
Reinf Str	59779	55321	51054	57668	48356	51937	62575	53885
Elasto Shear Mod	187	258	237	145	105	148	288	208
Elasto MF	1.12	0.85	1.16	1.02	0.92	1.00	1.06	0.94
Dowel Str	19.64	22.76	19.98	18.19	19.19	21.46	20.75	18.38
Dowel Gap	0.180	1.936	1.150	2.427	1.505	0.934	2.336	0.537
Abt-Pas Stf	42.5	49.2	20.7	26.1	33.3	30.8	39.6	37.0
Pile Stf	58.1	21.5	28.1	43.2	38.1	48.3	66.4	74.5
Mass	115	112	124	129	128	133	120	137
Damp Ratio	0.060	0.044	0.045	0.017	0.036	0.038	0.053	0.059
Large Gap	4.11	3.12	0.83	5.30	4.91	1.68	0.05	2.39
Load Dir	278	30	69	105	333	219	269	174

Table E.26: SSPC modeling parameters for geometric sample 2

	Modeling Sample							
Parameter	1	2	3	4	5	6	7	8
Conc Str	4560	4055	4351	3347	4901	3526	5819	5184
Reinf Str	52046	54624	55522	49848	61229	48284	57636	60290
Elasto Shear Mod	142	117	183	157	257	292	239	215
Elasto MF	1.00	1.12	0.87	0.92	1.04	1.03	1.13	0.96
Dowel Str	22.88	19.79	21.21	21.03	20.42	18.45	17.48	19.16
Dowel Gap	1.248	1.901	0.171	1.406	2.679	2.290	0.490	0.864
Abt-Pas Stf	26.9	38.0	21.1	42.7	32.6	46.7	30.4	39.9
Pile Stf	52.7	70.5	24.4	64.8	58.5	45.2	38.8	28.5
Mass	137	116	129	125	112	124	136	118
Damp Ratio	0.045	0.033	0.041	0.027	0.037	0.050	0.066	0.054
Large Gap	5.68	3.88	0.29	2.10	3.14	0.76	2.89	4.61
Load Dir	315	183	290	139	61	235	19	126

Table E.27: SSPC modeling parameters for geometric sample 3

	Modeling Sample							
Parameter	1	2	3	4	5	6	7	8
Conc Str	3752	4483	5015	4678	5542	4217	3309	5200
Reinf Str	52450	46517	57945	61079	55508	54775	60179	51105
Elasto Shear Mod	111	141	160	232	202	174	297	257
Elasto MF	0.90	0.97	0.86	1.02	1.15	1.05	1.11	0.96
Dowel Str	21.23	18.19	17.83	18.91	20.82	19.49	20.21	22.71
Dowel Gap	0.511	2.464	1.064	2.158	1.587	0.929	1.825	0.041
Abt-Pas Stf	29.4	47.3	35.9	45.2	41.8	27.3	33.4	21.1
Pile Stf	65.5	28.5	41.2	49.6	54.6	39.8	70.6	24.2
Mass	138	123	134	119	115	128	111	130
Damp Ratio	0.055	0.039	0.066	0.041	0.027	0.031	0.049	0.051
Large Gap	1.64	3.49	0.38	1.41	4.07	4.86	2.73	5.35
Load Dir	13	300	254	198	319	168	92	57

Table E.28: SSPC modeling parameters for geometric sample 4

	Modeling Sample							
Parameter	1	2	3	4	5	6	7	8
Conc Str	5413	4295	3084	3786	5565	4760	5042	3944
Reinf Str	63053	52270	55486	50589	54348	56559	58299	45967
Elasto Shear Mod	232	250	293	133	200	194	101	170
Elasto MF	1.09	1.25	0.95	0.84	1.03	0.93	0.99	1.03
Dowel Str	20.13	21.25	18.41	20.82	17.61	19.66	23.51	19.14
Dowel Gap	1.714	0.902	2.349	1.189	0.309	2.049	0.367	2.416
Abt-Pas Stf	22.0	48.7	45.0	38.4	41.0	26.6	33.2	28.6
Pile Stf	26.6	68.6	47.2	37.4	31.1	50.7	54.4	61.9
Mass	128	113	137	130	123	114	134	120
Damp Ratio	0.053	0.056	0.028	0.046	0.032	0.043	0.070	0.040
Large Gap	4.60	1.27	1.94	5.39	4.22	0.43	2.93	3.25
Load Dir	111	233	156	78	344	307	29	216

Table E.29: SSPC modeling parameters for geometric sample 5

	Modeling Sample							
Parameter	1	2	3	4	5	6	7	8
Conc Str	4146	3825	5338	5065	4252	5662	4706	3198
Reinf Str	47748	52731	75355	55429	54521	51234	57870	59266
Elasto Shear Mod	251	138	105	277	160	207	237	195
Elasto MF	1.13	0.98	0.82	1.10	1.06	1.01	0.94	0.92
Dowel Str	21.51	19.67	19.06	18.30	17.86	20.11	21.88	20.99
Dowel Gap	2.119	2.749	1.842	0.755	0.603	1.697	0.253	1.340
Abt-Pas Stf	22.9	33.8	44.9	37.9	40.0	28.5	27.5	48.7
Pile Stf	42.1	64.4	60.6	68.9	52.6	23.7	31.5	35.4
Mass	121	127	134	137	130	117	114	125
Damp Ratio	0.044	0.048	0.020	0.041	0.035	0.051	0.055	0.065
Large Gap	1.24	0.59	5.80	3.68	5.14	2.76	4.05	2.13
Load Dir	321	15	212	240	61	140	95	300

Table E.30: SSPC modeling parameters for geometric sample 6

	Modeling Sample							
Parameter	1	2	3	4	5	6	7	8
Conc Str	3475	5266	3825	4659	4937	3969	5648	4496
Reinf Str	56827	61464	54872	60530	51947	47938	54358	51513
Elasto Shear Mod	279	232	188	154	264	120	132	216
Elasto MF	0.93	0.97	1.09	0.87	1.21	1.04	0.98	1.02
Dowel Str	17.95	21.42	22.74	18.50	19.01	19.88	20.03	20.54
Dowel Gap	1.891	0.707	2.650	0.558	2.367	0.012	1.226	1.690
Abt-Pas Stf	21.5	49.7	30.5	24.6	41.2	35.6	45.7	32.4
Pile Stf	67.7	56.6	36.9	23.3	73.2	48.5	41.8	33.6
Mass	123	136	139	132	112	126	119	114
Damp Ratio	0.024	0.042	0.034	0.052	0.054	0.046	0.037	0.083
Large Gap	2.34	3.82	5.04	0.65	6.00	2.01	1.10	3.13
Load Dir	89	247	103	284	140	193	3	360

Table E.31: SSPC modeling parameters for geometric sample 7

	Modeling Sample							
Parameter	1	2	3	4	5	6	7	8
Conc Str	5752	4419	4841	3023	4516	5260	3739	3995
Reinf Str	46900	70603	54438	58345	56746	52398	51470	56032
Elasto Shear Mod	151	276	186	132	198	111	269	227
Elasto MF	1.08	1.00	0.92	0.96	1.06	1.16	0.82	1.02
Dowel Str	19.43	20.86	20.16	19.50	21.81	21.96	18.07	18.33
Dowel Gap	2.000	0.665	2.196	1.478	0.993	2.717	0.138	1.096
Abt-Pas Stf	21.3	45.4	31.3	49.7	41.0	35.1	29.4	25.2
Pile Stf	51.0	57.7	34.9	44.7	72.2	20.3	65.8	32.8
Mass	115	132	111	121	138	133	126	124
Damp Ratio	0.034	0.040	0.057	0.030	0.048	0.042	0.064	0.050
Large Gap	0.16	5.37	3.23	5.19	1.65	2.90	4.07	1.07
Load Dir	338	170	233	292	40	119	53	219

Table E.32: SSPC modeling parameters for geometric sample 8

	Modeling Sample							
Parameter	1	2	3	4	5	6	7	8
Conc Str	4635	3916	4122	4405	5348	4988	2925	6313
Reinf Str	67937	56886	52075	55018	53940	45614	60526	50057
Elasto Shear Mod	222	132	235	284	259	161	194	102
Elasto MF	1.08	0.90	1.26	0.87	0.94	1.00	0.97	1.05
Dowel Str	18.93	21.22	19.65	19.95	16.97	20.47	22.29	18.65
Dowel Gap	1.622	0.942	0.156	1.189	2.479	1.764	2.136	0.354
Abt-Pas Stf	23.1	46.7	33.0	35.1	26.4	42.7	40.2	28.3
Pile Stf	64.3	28.6	44.0	60.4	52.5	34.3	22.8	71.3
Mass	123	120	129	126	115	136	110	138
Damp Ratio	0.010	0.067	0.037	0.053	0.037	0.045	0.054	0.044
Large Gap	1.18	5.94	2.17	0.02	3.32	4.89	2.52	4.34
Load Dir	216	347	167	296	68	93	7	257

Table E.33: MCRC-slab modeling parameters for geometric sample 1

	Modeling Sample							
Parameter	1	2	3	4	5	6	7	8
Conc Str	5533	4871	3382	3846	4353	4663	5158	4116
Reinf Str	52786	50560	54011	55556	44698	56812	61025	58578
COF MF	1.01	0.97	1.04	1.00	1.29	1.11	0.92	0.89
Dowel Str	6.80	7.30	7.06	6.83	7.63	7.69	6.32	6.41
Abt-Pas Stf	23.5	44.8	31.2	47.8	32.9	42.5	36.5	26.1
Pile Stf	44.5	35.4	68.1	52.6	20.8	33.4	65.8	56.2
Mass	112	137	133	119	129	125	123	116
Damp Ratio	0.045	0.032	0.057	0.053	0.047	0.024	0.038	0.062
Small Gap	0.48	1.45	1.10	0.93	1.81	1.67	0.06	0.69
Load Dir	308	192	122	165	90	245	340	38

Table E.34: MCRC-slab modeling parameters for geometric sample 2

	Modeling Sample							
Parameter	1	2	3	4	5	6	7	8
Conc Str	5444	2633	3568	5600	4093	4829	4533	4320
Reinf Str	56470	50435	62754	52909	54856	59628	47971	53515
COF MF	1.03	1.00	0.94	0.91	1.07	0.88	1.21	1.10
Dowel Str	6.63	7.43	6.88	6.98	5.94	7.17	7.80	6.53
Abt-Pas Stf	44.6	39.3	32.5	36.9	29.9	24.9	49.6	23.6
Pile Stf	39.6	71.4	33.7	24.0	66.6	56.7	50.9	43.4
Mass	132	135	122	111	120	140	127	117
Damp Ratio	0.049	0.045	0.034	0.067	0.019	0.037	0.046	0.055
Small Gap	0.53	1.79	1.53	1.48	0.82	0.46	0.04	1.07
Load Dir	103	285	219	36	49	140	253	349

Table E.35: MCRC-slab modeling parameters for geometric sample 3

	Modeling Sample							
Parameter	1	2	3	4	5	6	7	8
Conc Str	5493	5223	4780	3913	4450	3179	4596	4132
Reinf Str	61067	50070	55086	54111	60443	53010	57683	49239
COF MF	1.10	0.93	0.84	0.94	1.02	1.13	1.03	0.99
Dowel Str	6.96	7.61	7.16	6.17	6.80	6.60	8.26	7.00
Abt-Pas Stf	47.3	40.7	35.6	45.9	23.7	26.2	29.4	34.2
Pile Stf	71.9	20.2	37.4	44.1	33.6	53.1	62.0	58.6
Mass	121	111	120	140	134	116	127	129
Damp Ratio	0.051	0.036	0.070	0.040	0.028	0.057	0.049	0.043
Small Gap	1.51	0.01	1.49	0.68	0.98	1.04	1.90	0.35
Load Dir	282	62	11	347	171	106	183	234

Table E.36: MCRC-slab modeling parameters for geometric sample 4

	Modeling Sample							
Parameter	1	2	3	4	5	6	7	8
Conc Str	4581	2751	3674	5178	4800	4343	4136	5480
Reinf Str	59270	47888	52311	56391	54252	51107	62313	55173
COF MF	1.07	1.18	0.96	0.86	0.99	1.09	1.01	0.91
Dowel Str	7.62	7.03	8.11	6.91	7.30	6.65	5.38	6.46
Abt-Pas Stf	49.9	34.6	46.1	30.6	39.4	21.7	38.1	24.0
Pile Stf	53.3	55.9	23.3	44.6	39.9	29.4	74.1	64.1
Mass	120	129	121	114	133	112	137	129
Damp Ratio	0.055	0.060	0.041	0.019	0.042	0.051	0.047	0.033
Small Gap	0.85	0.64	1.49	1.15	1.61	0.23	0.45	1.81
Load Dir	14	299	345	105	199	169	73	261

Table E.37: MCRC-slab modeling parameters for geometric sample 5

	Modeling Sample							
Parameter	1	2	3	4	5	6	7	8
Conc Str	4567	2484	3736	4356	4034	5548	5390	4857
Reinf Str	52463	59204	51536	46420	53627	55424	57453	62835
COF MF	0.90	1.04	0.94	1.21	0.88	1.09	1.00	1.02
Dowel Str	7.98	6.50	7.02	7.63	6.03	7.22	6.72	6.88
Abt-Pas Stf	43.1	26.6	28.4	22.7	33.7	41.3	38.5	49.7
Pile Stf	63.3	43.5	68.9	34.0	21.0	52.2	56.7	27.5
Mass	136	118	131	110	138	117	124	128
Damp Ratio	0.037	0.022	0.038	0.048	0.062	0.053	0.042	0.057
Small Gap	0.16	1.13	1.39	0.44	0.96	1.93	1.66	0.69
Load Dir	276	85	140	342	32	191	258	111

Table E.38: MCRC-slab modeling parameters for geometric sample 6

	Modeling Sample							
Parameter	1	2	3	4	5	6	7	8
Conc Str	3608	2451	4718	4359	4149	4943	6099	5312
Reinf Str	57201	50981	47986	52783	58849	60937	54339	55592
COF MF	1.12	0.89	0.99	0.91	1.00	0.95	1.09	1.04
Dowel Str	6.66	7.21	6.90	6.35	6.59	7.01	7.45	8.62
Abt-Pas Stf	22.2	47.5	31.1	36.0	38.8	33.6	44.3	24.6
Pile Stf	57.5	32.6	68.8	64.2	21.1	47.7	35.1	43.7
Mass	129	114	112	120	129	134	138	124
Damp Ratio	0.052	0.059	0.042	0.032	0.049	0.068	0.037	0.030
Small Gap	1.99	0.15	1.03	0.65	0.81	0.31	1.69	1.27
Load Dir	244	23	324	70	313	136	191	109

Table E.39: MCRC-slab modeling parameters for geometric sample 7

	Modeling Sample							
Parameter	1	2	3	4	5	6	7	8
Conc Str	4317	5024	3781	3151	4620	5606	4011	5105
Reinf Str	50702	45183	61666	53886	53095	56321	58000	59390
COF MF	0.89	1.03	1.07	0.99	1.18	0.92	1.11	0.95
Dowel Str	7.24	6.79	7.62	7.13	7.67	6.84	6.45	5.63
Abt-Pas Stf	34.2	38.1	39.0	42.9	22.3	27.0	30.7	50.0
Pile Stf	22.7	48.0	54.9	61.3	45.7	34.1	74.2	27.8
Mass	139	123	131	114	121	127	136	113
Damp Ratio	0.030	0.056	0.044	0.049	0.051	0.040	0.033	0.077
Small Gap	1.28	1.22	1.79	1.54	0.39	0.72	0.23	0.96
Load Dir	70	157	259	25	219	111	297	358

Table E.40: MCRC-slab modeling parameters for geometric sample 8

	Modeling Sample							
Parameter	1	2	3	4	5	6	7	8
Conc Str	4437	3831	4190	6211	3297	4775	5121	4571
Reinf Str	46036	62741	57933	49775	54470	59815	55885	51816
COF MF	0.84	0.97	0.93	1.03	0.94	1.14	1.07	1.11
Dowel Str	7.64	6.22	6.76	7.07	7.18	8.06	6.87	6.61
Abt-Pas Stf	25.1	33.0	40.6	36.1	29.8	21.4	48.8	45.9
Pile Stf	22.0	38.1	30.0	51.9	41.0	65.1	60.5	69.1
Mass	133	121	132	124	117	112	125	138
Damp Ratio	0.054	0.039	0.030	0.032	0.052	0.046	0.065	0.043
Small Gap	0.70	0.91	0.20	1.75	1.95	1.39	0.33	1.13
Load Dir	274	195	115	7	72	249	340	165

Table E.41: MSRC-slab modeling parameters for geometric sample 1

	Modeling Sample							
Parameter	1	2	3	4	5	6	7	8
Conc Str	4528	5820	4225	4333	3847	3172	4849	5213
Reinf Str	60568	45085	57684	53239	49924	56127	53439	66973
COF MF	0.98	1.02	1.18	0.93	1.05	0.97	0.86	1.10
Dowel Str	7.20	7.86	7.09	6.86	6.33	6.80	7.46	6.46
Abt-Pas Stf	36.0	48.9	42.2	31.9	26.0	20.8	45.6	30.8
Pile Stf	20.9	67.6	27.0	48.0	57.4	44.5	38.3	70.0
Mass	137	114	120	132	112	126	134	123
Damp Ratio	0.041	0.047	0.045	0.034	0.054	0.066	0.053	0.025
Small Gap	0.49	1.58	1.85	1.20	0.15	0.59	0.86	1.47
Load Dir	273	323	148	237	95	87	210	45

Table E.42: MSRC-slab modeling parameters for geometric sample 2

	Modeling Sample							
Parameter	1	2	3	4	5	6	7	8
Conc Str	3547	5490	5063	4086	2701	5362	4544	4281
Reinf Str	52335	58206	45535	64328	53743	57475	54803	51441
COF MF	1.03	0.93	0.87	1.01	1.27	0.98	1.10	0.94
Dowel Str	6.62	7.74	7.39	6.34	6.86	7.10	7.23	6.40
Abt-Pas Stf	48.1	31.2	43.7	20.2	24.2	42.1	37.4	34.1
Pile Stf	63.3	33.8	25.8	33.0	55.0	44.2	48.5	69.4
Mass	112	130	134	127	121	138	125	115
Damp Ratio	0.043	0.056	0.026	0.052	0.059	0.040	0.032	0.049
Small Gap	1.28	0.82	0.58	1.21	1.61	0.26	1.85	0.05
Load Dir	207	140	103	34	326	77	303	270

Table E.43: MSRC-slab modeling parameters for geometric sample 3

	Modeling Sample							
Parameter	1	2	3	4	5	6	7	8
Conc Str	6085	4950	4385	3605	2787	4646	5302	3951
Reinf Str	58724	42885	50579	55665	54468	63982	57947	52657
COF MF	0.94	1.05	1.01	0.99	1.07	0.87	0.93	1.14
Dowel Str	6.15	6.42	7.03	7.63	6.95	7.31	8.10	6.77
Abt-Pas Stf	39.0	21.9	44.2	49.2	34.6	31.0	24.4	35.9
Pile Stf	43.5	26.3	63.6	60.9	50.5	35.7	71.6	29.5
Mass	122	113	119	127	137	134	131	116
Damp Ratio	0.047	0.041	0.075	0.056	0.035	0.026	0.038	0.052
Small Gap	1.29	1.60	1.10	0.52	1.86	0.50	0.05	0.85
Load Dir	65	101	142	217	274	40	326	237

Table E.44: MSRC-slab modeling parameters for geometric sample 4

	Modeling Sample							
Parameter	1	2	3	4	5	6	7	8
Conc Str	4173	5719	2789	4550	4827	5175	4268	3628
Reinf Str	55544	51683	57408	59076	62232	50159	54172	45434
COF MF	1.03	1.04	0.94	0.92	1.23	0.82	0.99	1.11
Dowel Str	7.61	8.01	6.35	6.70	7.02	6.95	6.52	7.34
Abt-Pas Stf	29.3	39.1	46.3	21.6	27.1	35.3	44.0	31.7
Pile Stf	67.5	59.8	45.8	25.3	35.8	49.2	71.2	29.9
Mass	134	113	127	130	122	115	120	138
Damp Ratio	0.029	0.056	0.034	0.044	0.051	0.039	0.048	0.063
Small Gap	1.62	1.16	1.88	0.66	0.06	1.40	0.82	0.38
Load Dir	109	318	276	82	172	214	236	36

Table E.45: MSRC-slab modeling parameters for geometric sample 5

	Modeling Sample							
Parameter	1	2	3	4	5	6	7	8
Conc Str	4494	4551	3865	5397	5014	2998	6142	4144
Reinf Str	49105	51031	54780	56438	55141	58696	53035	63777
COF MF	0.92	1.13	0.96	1.08	0.79	1.01	1.06	0.99
Dowel Str	6.47	6.20	7.41	8.25	6.62	7.01	6.92	7.23
Abt-Pas Stf	21.2	46.1	34.3	42.3	24.2	46.9	30.8	37.2
Pile Stf	68.3	63.8	33.3	58.7	53.2	45.9	26.5	34.4
Mass	116	129	137	123	119	134	114	126
Damp Ratio	0.053	0.022	0.033	0.063	0.039	0.056	0.043	0.049
Small Gap	1.96	1.24	1.56	1.30	0.43	0.22	0.91	0.54
Load Dir	244	118	35	279	218	158	89	352

Table E.46: MSRC-slab modeling parameters for geometric sample 6

	Modeling Sample							
Parameter	1	2	3	4	5	6	7	8
Conc Str	4527	4916	4293	3490	6065	4039	3881	5201
Reinf Str	54110	63060	43998	52908	54963	58129	50949	58663
COF MF	1.03	1.13	1.12	1.02	0.94	0.92	0.99	0.78
Dowel Str	6.70	6.85	7.63	7.89	7.11	6.25	7.24	6.44
Abt-Pas Stf	21.2	38.5	31.1	26.4	34.7	42.9	46.8	41.0
Pile Stf	31.4	24.9	68.9	52.9	46.6	57.7	61.9	37.9
Mass	117	125	111	121	130	138	135	126
Damp Ratio	0.049	0.062	0.014	0.059	0.047	0.041	0.034	0.042
Small Gap	1.28	0.38	1.05	0.67	1.61	0.90	0.03	1.83
Load Dir	65	307	241	92	201	338	144	41

Table E.47: MSRC-slab modeling parameters for geometric sample 7

	Modeling Sample							
Parameter	1	2	3	4	5	6	7	8
Conc Str	4698	5747	3306	4222	5254	4277	3837	5058
Reinf Str	63370	52091	56488	49499	42456	53414	58448	55088
COF MF	0.93	0.94	0.79	1.12	1.01	1.04	0.99	1.13
Dowel Str	7.63	7.31	6.40	6.19	6.98	7.07	6.65	7.70
Abt-Pas Stf	30.4	36.3	21.6	41.4	47.7	24.8	45.2	33.5
Pile Stf	67.1	22.1	53.5	68.5	55.2	30.2	42.8	33.9
Mass	113	123	136	117	118	134	127	132
Damp Ratio	0.037	0.047	0.024	0.042	0.057	0.034	0.064	0.051
Small Gap	1.21	1.74	0.01	0.83	1.78	1.27	0.33	0.52
Load Dir	329	131	6	228	311	142	49	224

Table E.48: MSRC-slab modeling parameters for geometric sample 8

	Modeling Sample							
Parameter	1	2	3	4	5	6	7	8
Conc Str	3239	5196	4455	3733	5699	4225	4924	4530
Reinf Str	49767	47536	58693	61042	51875	54584	57794	56106
COF MF	1.26	0.87	1.00	0.96	0.93	1.04	1.03	1.09
Dowel Str	7.13	7.16	6.20	6.70	7.56	6.82	8.34	6.42
Abt-Pas Stf	31.0	33.7	43.2	41.1	35.1	25.2	22.5	46.5
Pile Stf	51.1	68.2	30.4	37.2	21.6	44.8	58.1	67.2
Mass	117	131	119	133	124	128	138	113
Damp Ratio	0.057	0.047	0.070	0.045	0.053	0.020	0.040	0.035
Small Gap	1.72	1.33	0.12	1.86	1.05	0.30	0.87	0.68
Load Dir	314	5	234	120	150	77	318	212

Appendix F. Correlation of Seismic Demands for Bridge Classes

Here, the correlation of the seismic demands in the natural logarithm space is shown for the bridge classes considered in this study (Table F.1 through F.7).

Table F.1: Correlation of the seismic demands for MCSTEEL bridges

	ln(Rot)	ln(fx_L)	ln(fx_T)	ln(ex_L)	ln(ex_T)	ln(abut_P)	ln(abut_A)	ln(abut_T)
ln(Rot)	1.00	0.58	0.62	0.93	0.54	0.63	0.53	0.50
ln(fx_L)	0.58	1.00	0.54	0.71	0.39	0.28	0.24	0.18
ln(fx_T)	0.62	0.54	1.00	0.60	0.72	0.43	0.49	0.62
ln(ex_L)	0.93	0.71	0.60	1.00	0.48	0.62	0.55	0.47
ln(ex_T)	0.54	0.39	0.72	0.48	1.00	0.19	0.01	0.15
ln(abut_P)	0.63	0.28	0.43	0.62	0.19	1.00	0.70	0.62
ln(abut_A)	0.53	0.24	0.49	0.55	0.01	0.70	1.00	0.90
ln(abut_T)	0.50	0.18	0.62	0.47	0.15	0.62	0.90	1.00

Table F.2: Correlation of the seismic demands for MSSTEEL bridges

	ln(Rot)	ln(fx_L)	ln(fx_T)	ln(ex_L)	ln(ex_T)	ln(abut_P)	ln(abut_A)	ln(abut_T)
ln(Rot)	1.00	0.78	0.65	0.91	0.62	0.62	0.36	0.56
ln(fx_L)	0.78	1.00	0.72	0.83	0.58	0.73	0.62	0.50
ln(fx_T)	0.65	0.72	1.00	0.69	0.90	0.40	0.31	0.65
ln(ex_L)	0.91	0.83	0.69	1.00	0.64	0.56	0.37	0.53
ln(ex_T)	0.62	0.58	0.90	0.64	1.00	0.19	0.06	0.67
ln(abut_P)	0.62	0.73	0.40	0.56	0.19	1.00	0.85	0.35
ln(abut_A)	0.36	0.62	0.31	0.37	0.06	0.85	1.00	0.34
ln(abut_T)	0.56	0.50	0.65	0.53	0.67	0.35	0.34	1.00

Table F.3: Correlation of the seismic demands for MSPC bridges

	ln(Rot)	ln(fx_L)	ln(fx_T)	ln(ex_L)	ln(ex_T)	ln(abut_P)	ln(abut_A)	ln(abut_T)
ln(Rot)	1.00	0.78	0.79	0.82	0.82	0.67	0.52	0.57
ln(fx_L)	0.78	1.00	0.83	0.92	0.79	0.81	0.65	0.50
ln(fx_T)	0.79	0.83	1.00	0.81	0.94	0.71	0.48	0.49
ln(ex_L)	0.82	0.92	0.81	1.00	0.83	0.72	0.59	0.60
ln(ex_T)	0.82	0.79	0.94	0.83	1.00	0.64	0.43	0.59
ln(abut_P)	0.67	0.81	0.71	0.72	0.64	1.00	0.76	0.44
ln(abut_A)	0.52	0.65	0.48	0.59	0.43	0.76	1.00	0.61
ln(abut_T)	0.57	0.50	0.49	0.60	0.59	0.44	0.61	1.00

Table F.4: Correlation of the seismic demands for MSRC bridges

	ln(Rot)	ln(fx_L)	ln(fx_T)	ln(ex_L)	ln(ex_T)	ln(abut_P)	ln(abut_A)	ln(abut_T)
ln(Rot)	1.00	0.78	0.78	0.78	0.78	0.68	0.36	0.54
ln(fx_L)	0.78	1.00	0.82	0.86	0.73	0.74	0.48	0.60
ln(fx_T)	0.78	0.82	1.00	0.73	0.79	0.81	0.44	0.58
ln(ex_L)	0.78	0.86	0.73	1.00	0.75	0.70	0.50	0.59
ln(ex_T)	0.78	0.73	0.79	0.75	1.00	0.57	0.27	0.54
ln(abut_P)	0.68	0.74	0.81	0.70	0.57	1.00	0.62	0.63
ln(abut_A)	0.36	0.48	0.44	0.50	0.27	0.62	1.00	0.85
ln(abut_T)	0.54	0.60	0.58	0.59	0.54	0.63	0.85	1.00

Table F.5: Correlation of the seismic demands for SSPC bridges

	ln(fx_L)	ln(fx_T)	ln(ex_L)	ln(ex_T)	ln(abut_P)	ln(abut_A)	ln(abut_T)
ln(fx_L)	1.00	0.78	0.99	0.78	0.81	0.29	0.37
ln(fx_T)	0.78	1.00	0.75	1.00	0.73	0.21	0.46
ln(ex_L)	0.99	0.75	1.00	0.75	0.75	0.31	0.38
ln(ex_T)	0.78	1.00	0.75	1.00	0.73	0.21	0.46
ln(abut_P)	0.81	0.73	0.75	0.73	1.00	0.36	0.38
ln(abut_A)	0.29	0.21	0.31	0.21	0.36	1.00	0.76
ln(abut_T)	0.37	0.46	0.38	0.46	0.38	0.76	1.00

Table F.6: Correlation of the seismic demands for MCRC-slab bridges

	ln(Rot)	ln(fx_L)	ln(fx_T)	ln(ex_L)	ln(ex_T)	ln(abut_P)	ln(abut_A)	ln(abut_T)
ln(Rot)	1.00	0.52	0.64	0.54	0.65	0.43	0.25	0.25
ln(fx_L)	0.52	1.00	0.69	0.74	0.63	0.39	0.15	0.10
ln(fx_T)	0.64	0.69	1.00	0.77	0.85	0.37	0.21	0.25
ln(ex_L)	0.54	0.74	0.77	1.00	0.85	0.38	0.30	0.25
ln(ex_T)	0.65	0.63	0.85	0.85	1.00	0.35	0.21	0.24
ln(abut_P)	0.43	0.39	0.37	0.38	0.35	1.00	0.45	0.40
ln(abut_A)	0.25	0.15	0.21	0.30	0.21	0.45	1.00	0.95
ln(abut_T)	0.25	0.10	0.25	0.25	0.24	0.40	0.95	1.00

Table F.7: Correlation of the seismic demands for MSRC-slab bridges

	ln(Rot)	ln(fx_L)	ln(fx_T)	ln(ex_L)	ln(ex_T)	ln(abut_P)	ln(abut_A)	ln(abut_T)
ln(Rot)	1.00	0.70	0.82	0.83	0.84	0.58	0.34	0.42
ln(fx_L)	0.70	1.00	0.82	0.80	0.69	0.73	0.57	0.60
ln(fx_T)	0.82	0.82	1.00	0.71	0.75	0.77	0.50	0.56
ln(ex_L)	0.83	0.80	0.71	1.00	0.80	0.53	0.37	0.41
ln(ex_T)	0.84	0.69	0.75	0.80	1.00	0.47	0.25	0.42
ln(abut_P)	0.58	0.73	0.77	0.53	0.47	1.00	0.63	0.56
ln(abut_A)	0.34	0.57	0.50	0.37	0.25	0.63	1.00	0.91
ln(abut_T)	0.42	0.60	0.56	0.41	0.42	0.56	0.91	1.00